Coherence and superfluidity of Bose gases in reduced dimensions: from harmonic traps to uniform fluids

Lauriane Chomaz

To cite this version:

Lauriane Chomaz. Coherence and superfluidity of Bose gases in reduced dimensions: from harmonic traps to uniform fluids. Physics [physics]. Ecole Normale Supérieure, 2014. English. NNT : . tel-01099789

HAL Id: tel-01099789
https://hal.science/tel-01099789

Submitted on 5 Jan 2015

École Normale Supérieure
Ecole Doctorale "Physique en Ile de France"

Laboratoire Kastler Brossel
Collège de France

THÈSE de DOCTORAT de l'ÉCOLE NORMALE SUPÉRIEURE
Spécialité : Physique Quantique

présentée par
Lauriane Chomaz
pour obtenir le grade de DOCTEUR de l'ÉCOLE NORMALE SUPÉRIEURE

Coherence and superfluidity of Bose gases in reduced dimensions: from harmonic traps to uniform fluids

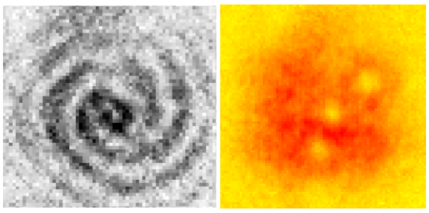

Soutenue le 10 Novembre 2014
devant le jury composé de :

M.	**Gabriele Ferrari**	Rapporteur
M.	**Bruno Laburthe–Tolra**	Rapporteur
Mme.	**Patrizia Vignolo**	Examinateur
M.	**Christoph Westrook**	Examinateur
M.	**Jean Dalibard**	Directeur de thèse
M.	**Jerôme Beugnon**	Membre Invité

There is no point in rushing an old lady...

Contents

Remerciements

Je voudrais ici remercier toutes les personnes avec qui j'ai travaillé et plus généralement toutes celles avec qui j'ai partagé ces quatre années de thèse, ce sont elles qui ont fait cette thèse et qui font de moi la personne que je suis maintenant.

Avant tout autre, je tiens à remercier chaleureusement et pleinement Jean Dalibard, qui a accepté d'encadrer cette thèse et qui m'a donné une place dans son groupe. Je me joins aux éloges unanimes concernant ces qualités tant scientifiques qu'humaines et sa personnalité hors paire. C'est l'estime que j'ai toujours eu de ses grandes qualités qui m'a guidé des sièges de l'amphithéâtre Arago aux chaises du Master 2 de "Physique Quantique" aux tabourets de la salle S6. L'association de cette ingéniosité, de cette rigueur scientifique et de cette bonté de caractère sont les fondements d'un environnement de travail rêvé, que j'ai trouvé à ces côtés et que je souhaiterais pouvoir préserver par la suite. Je n'oublierai pas de ci tôt le moment au milieu de ma rédaction où, lui faisant part de mon anxiété, il a pris sur lui de proposer du jour au lendemain un plan d'article cohérent avec l'ensemble un peu brouillon des données expérimentales dont nous disposions (et qui a été la base de l'analyse présentée dans les chapitres 7 et 8 de ce manuscrit). Je n'oublierai pas non plus son soutien dans mes choix et je suis fière des marques de confiance qu'il a pu me donner, particulièrement au cours de cette dernière année.

Je souhaite aussi remercier Jérôme Beugnon qui a commencé à encadrer notre équipe au cours de ma thèse. Son humour, son calme et sa solidité ont été des soutiens essentiels au cours des deux dernières années. J'ai été très touchée de tous les efforts que Jérôme a entrepris pour que l'organisation de l'équipe se déroule au mieux pour nous tous (et très sûrement sauf pour lui) ainsi que du temps qu'il a libéré dans son emploi du temps déjà extrêmement chargé pour relire intégralement mon manuscrit (y compris les appendices!). Il a eu un rôle majeur dans la confiance que j'ai pu gagner en mon travail (même si elle est faible, elle n'est plus nulle) et je le remercie de tout coeur pour cela. Enfin je tiens à remercier Sylvain Nascimbène qui a rejoint l'équipe encore plus récemment et avec qui ce fut également un réel plaisir de travailler tant par sa bonne humeur que par son talent. Je le remercie du temps qu'il a passé à essayer de comprendre nos problèmes et à souvent les résoudre avec brio et Mathematica. Ce trio a su guider avec tact et optimisme notre petite équipe Rubidium soumise aux caprices de notre expérience vieillissante, confrontée aux éléments déchaînés de notre sous-sol de l'ENS, assujettie aux pannes des amplis infrarouge, mais célébrant aussi de nombreuses réussites, petites ou grandes, toujours de manière adaptée (un certain nombre de cadavres de bouteilles de champagne le prouve).

Je remercie également tous les membres de cette équipe que j'ai côtoyé aux cours de mes quatre années de thèse. Je tiens en particulier à remercier Rémi qui m'a introduit à cette vieille dame qu'était Feu expérience Rb II, qui m'a le plus appris tout en m'entrainant à suivre un débit dépassant les 400 mots par minute. Sa grande capacité de compréhension et d'adaptation, son intuition ont marqué très positivement mes premières années de thèse tant sur le plan professionnel que personnel et je le remercie chaleureusement pour cela; j'espère que notre amitié perdurera, que l'on puisse ou non retourner au Brewberry de temps en temps. Je remercie également Christof qui a grandement contribué à l'expérience le temps de son post-doc parisien et pas seulement par l'introduction de la musique classique dans notre programmation musicale. Sa rigueur scientifique, sa grande capacité d'organisation, son ardeur au travail ont été un modèle important et très instructif. Sa joie de vivre, son humour bien qu'allemand et son manque de résistance à la bière belge ont par ailleurs marqué de joie ses années que nous avons partagées. Je remercie Tarik pour toutes ces histoires (véridiques ou "enjolivées") qui ont diverti ma première année de thèse; il savait mettre de la joie dans chaque instant même au cours de cette année qui maintenant je sais être la plus éprouvante du doctorat, celle de la rédaction. Je remercie Laura pour ses fortes capacités et son volontarisme. Je remercie Tom pour sa bonne humeur et ses toujours bonnes appréciations. Je remercie David pour avoir essayé de mettre de la bonne humeur dans les moments difficiles de cette dernière année. Je remercie toutes les autres personnes que j'ai côtoyé moins longtemps sur cette expérience ou sa successeure – Ken, Benno, Julian, Katharina, Andrea, Jean-Loup. Je leur souhaite à tous bonne chance et bon courage avec la nouvelle génération, susnommée Rb III.

Cette thèse a été effectué au sein du Laboratoire Kastler Brossel sur deux sites successifs, le département de physique de l'Ecole Normale Supérieure et l'institut de physique du Collège de France. Je tiens à remercier les directeurs successifs de ces différentes institutions – Paul Indelicato qui m'a reçu avec le souvenir de ma mère, Antoine Heidmann, Werner Krauth et Serge Haroche – pour m'avoir accueilli dans cette environnement scientifique et humain exceptionnel et pour toujours s'être soucier du sort des membres les plus jeunes (dont je faisais encore partie) sous leur responsabilité. Je remercie également tous les membres de ces différentes institutions, tant les chercheurs, les services techniques qu'administratifs pour leur grande aide et leur grande sympathie. Je remercie en particulier Monique, Christophe, Thierry, Jean-Michel, Didier, Carmen (et leurs équipes) pour leur soutien particulier. Je remercie également l'Ecole Polytechnique de m'avoir permis de revenir enseigner en ses murs pour différents cours de Physique et de Mécanique que j'avais moi-même éprouvés auparavant. Je remercie mes élèves avec qui se fut toujours intéressant d'interagir et je remercie Linda pour l'organisation. Je remercie la DGA de m'avoir financé pendant 3 ans, le Collège de France pendant 1 an (et aussi pour l'année de prolongement de financement qui me permettra de finir confortablement mon travail de doctorat) et la fondation L'Oréal non seulement pour son soutien financier et l'appréciation de mon mérite mais aussi de m'avoir permis plusieurs journées d'évasion par des séances "shooting" inhabituelles où j'ai pu côtoyer un monde fondamentalement différent du mien. Je remercie Jean-François Dars et Anne Papillault pour les autres espaces de liberté qu'ils m'ont offerts, pour leur écoute et leur présence si particulière.

Je remercie grandement Bruno Laburthe-Tolra, Gabriele Ferrari, Patrizia Vignolo et Chris Westbrook d'avoir accepté de juger ce travail de thèse, de s'être attelé avec beaucoup d'attention et d'intérêt à mon manuscrit de thèse (malgré sa longueur) et d'avoir fait le déplacement pour participer à l'évaluation de ma soutenance de thèse.

Je souhaite remercier tous les membres du groupe "Atomes froids" pour les nombreux moments que nous avons partager et pour l'atmosphère chaleureuse qui marque nos journées de travail ou nos soirées au cours desquelles le point focal s'éloignait joyeusement de la science. En premier lieu, je tiens à remercier l'équipe Sodium - David, Luigi, Tilman, Vincent, Camille - qui nous a laissé traverser sa salle d'expérience comme un moulin pendant toutes ces années à l'ENS et qui nous ont, malgré ce dérangement permanent, toujours prévenu quand l'alarme incendie se déclenchait. Je remercie tous les occupants de S18 pour la bonne agitation qui y régnait - Juliette, Fred, Nir, Andrew, Ulrich, Benno, Igor, Marion, Sebastien, Sebastian, Alexandre, Matthias, Daniel, Quentin, Wilfried, Davide, Tian, Chayma, Leonid... Je remercie les Fermix - Armin, Tom, Franz, Diogo, Norman, Daniel - pour leurs emprunts réguliers de matériels. Je remercie aussi Christophe pour les nombreuses discussions que nous avons eues, pour son excellente humeur et pour partager son amour de la montagne. Je remercie les théoriciens, en particulier Yvan et Christian, pour des discussions parfois énigmatiques. Je tiens à remercier très particulièrement Vincent pour avoir partagé cette dernière année de doctorat, ces longues heures d'écriture ou de "Matlabing" et surtout les nombreux verres de vin, de bière, et plateaux de fromage qui achevaient fréquemment nos journées arasantes et nous les rendaient appréciables. Je le remercie pour sa sensibilité, sa compréhension et son soutien.

Je remercie aussi tous mes amis au delà du groupe d'atomes froids qui m'ont fait apprécier ces années. Je remercie mes amis grimpeurs – Hélène, David, Arthur, Guillaume, Sylvain, Mélanie, Toptop, Margaux, Yves...– en particulier pour les nombreux week-ends où ma tête s'est complètement vidée pour se concentrer sur le calcaire. Je remercie le master LKB (et assimilés) – Benjamin, Michele, Raul, Théo, Romain, Pu – pour de nombreuses bières-frites et discussions politiques, les plus à gauche que j'ai expérimenté. Je remercie les atomes froids de l'Institut et en particulier Guillaume pour les nombreuses fois où il m'a ramenée sur Paris après mes enseignements platalisants, en passant bien entendu par la case Murmur. Je remercie Raphael pour les nombreux déjeuners que nous avons partagés aux Arènes ou à la cafét à discuter de tout et de rien ainsi qu'un certain nombre de moments dansant qui m'ont redonné de la bonne humeur. Je le remercie aussi, et le félicite, pour son écriture pinçante, comme son humour. Je remercie Arthur pour avoir partagé mes trois premières années de doctorat, pour le réconfort qu'il m'a apporté face à mes doutes et mon manque de confiance en moi, pour m'avoir tant ouvert de voies (verticales ou non) et associé à sa vie. Je remercie bien sûr mes parents, Philippe et Patricia, et ma famille, en particulier Pierrot, Lucile et Jean-Marc pour m'avoir toujours soutenu et pour avoir fait autant pour moi spécialement au cours de ma rédaction et pour mon pot de thèse, pour avoir supporté mes moments d'angoisse de cette dernière année même si cela se traduisait par un coup de fil au milieu de la nuit. Toutes ces personnes m'ont progressivement appris à vivre et à chercher, je les remercie sincèrement et leur dédie ce travail.

Introduction

Bose–Einstein Condensate (BEC) is a special state of dilute matter in which quantum physics manifests at a macroscopic scale. It was predicted in 1925 by Einstein [1] generalizing Bose's work [2] on photons (the massless elementary particles of light quanta). One of the cornerstones of quantum mechanics is that a (massive) particle, which is described classically by a trajectory, is in fact more rigorously depicted as a wave. Its wavelength is set by the de Broglie relation [3] $\lambda = h/p$ where p is the particle momentum and h the Planck constant. In a gas at thermal equilibrium (temperature T), the coherence length in the dilute regime is characterized by the thermal wavelength $\lambda_{\mathrm{T}} \propto 1/\sqrt{T}$ (which is roughly the average of λ for the particles in the gas). At very low temperature, this typical coherence length becomes larger than the mean inter-particle distance such that the particle waves overlap and interfere (without need for them to interact). These interferences when constructive lead to the establishment of a gigantic wave over the cloud represented by the complex field (the wavefunction) $\psi(\boldsymbol{r})$, which embodies the Bose–Einstein condensate. A second cornerstone of quantum mechanics lies in two points: (i) the time-evolution of a particle-wave is fully dictated by a special operator named the Hamiltonian; (ii) the state of an assembly of independent identical particles is entirely described by the number of particles which populate each of the eigenstates of this single-particle Hamiltonian. The emergence of a macroscopic quantum state along the Bose–Einstein condensation is intimately linked to the specific statistics of the population of these single-particle states in a gas of identical particles at thermal equilibrium. One distinguishes (in our 3D world) two kinds of particles with respect to this statistics, the Fermions and the Bosons. For non-interacting Bosons, the statistics causes an accumulation of the atoms in the particle state of minimal energy (ground-state) for a sufficiently low temperature, corresponding to the occurrence of the constructive interferences described above and to the BEC transition. Even if several earlier phenomena are considered to realize a state equivalent to the BEC such as the superfluidity in liquid ^{4}He [4, 5] [1], the superconductivity of an electron gas in a metal [7, 8] [2] or even the lasing of an optical cavity [11] [3], the cooling of atomic Bose gas

---

[1] ^{4}He is a liquid rather than a gas such that interactions are very strong, complicating both the measurements and the theory. In particular, this system only have a minority of atom in their minimal energy single-particle state [6].

[2] Electrons are Fermions and thus are not expected to undergo a BEC transition. However at low enough temperature the free electrons can loosely bound in pairs and superconductivity can be interpreted as a condensation of these pairs of electrons, namely the Cooper pairs, that sort of behave as Bosons. However these pairs of electron are massively delocalized over the system such that all electrons of the gas participate to the pairing and this arises at the same time as the condensation itself. This results in a significantly distinct phenomenon compared to a BEC of molecules and leads to important modifications of the theoretical prediction in this case. A similar state as also been observed in ^{3}He [9, 10], in atom nuclei (between the protons and neutrons that formed it) and other aspect of nuclear physics.

[3] Laser beams can be seen as BECs of photons in one mode of the cavity. However this system is intrinsically out of thermal equilibrium and thus do not hold within Einstein's considerations.

enables the first[4] experimental realization in 1995 [17–19] of Einstein's prediction in its original formulation (see footnotes 1-3).

This experimental achievement was permitted by the invention half a century ago of the laser source [11, 20] which set the ground for the development of techniques for cooling and trapping of atomic assemblies. While the laser is often associated with the idea of heat - it can melt, weld, cut ... - the purity of the light emitted by this source also serves to cool collections of atoms at temperatures down to a few billionths of a degree above absolute zero (nK scale) and thus enables experimental observation of BEC in atomic Bose gases. Note that this ultra-cooling is not limited to Bosonic atoms but was also performed on Fermionic ensembles [21–23].

Ultracold atomic physics blossoms by rising massive interest beyond the pristine demonstration of BEC [17–19] and the consecutive study of the condensed phase properties [24–28] due to two main characteristics : (i) the accuracy of simple theoretical modeling for these systems in which impurities are essentially absent; (ii) the versatility and tunability of the energy landscapes designed for being experienced by the atoms. It indeed results in highly controllable systems in which a wide range of physical problems can be tackled so that it opens groundbreaking perspectives in many other domains of research in physics. I will briefly illustrate this tremendous input of ultracold atomic gases.

First, the physics of cold atomic gases is not limited to the weakly interacting regime and many-body problems can also be addressed. A flexible method to control the strength of interactions between the atoms (and reach the strongly interacting regime) is based on Feshbach resonances [29, 30], for the species presenting this special feature[5]. These resonances occurring in the collision scheme are controlled via the application of a uniform magnetic field whose variations effectively lead to the tuning of the strength and the sign of the interactions. This feature for example permitted the experimental observation in Fermi gases of the crossover from a BEC [31–33] of the molecules that form in the strongly repulsive case [34] to a superfluid of loosely bound pairs of atoms [35–38] that arise at low temperature in the weakly attractive regime along Bardeen–Cooper–Schieffer (BCS) theory (see footnote 2).

Second, the controllability of the energy landscapes – by modifying the equation of motion dictating the evolution of the system (its Hamiltonian) – brings a wide variety of problems as potential subjects of study. In particular, due to the universality of quantum physics, we can reproduce, on our cold atom gases, problems (Hamiltonians) from other domains of physics and study their properties on our copy system. This illustrates the notion of *quantum simulation* put forward by Feynman in 1982 [39]. The customization of the Hamiltonian is eased in our setups by the use of laser beams. For example, the trapping potential can be shaped by finely designing these beams intensity and phase profiles or by patterning the intensity variations from interferences between several of them. Cutting-edge developments have been achieved in the past

---

[4] Latter realizations include exciton polariton BEC [12–14], magnon BEC [15] and photon BEC [16]. Note that the two former systems are not exactly at equilibrium and thus do not strictly realized the Einstein's prediction. They are said to realize quasi-equilibrium BEC.

[5] The results I will present in this manuscript have been measured on a ^{87}Rb vapor which does not show these interesting resonances in a simply accessible range of magnetic field.

several years:

- — The use of strongly anisotropic (and tight along some directions) confinement enables one to change the dimensionality of the gas under study by freezing the motion of the atoms in one or two directions of space. Then the specificities of both 1D (*e.g.* [40, 41]) and 2D (*e.g.* [42]) physics as the crossover between these regimes become experimentally explorable.
- — The possibility of generating periodic potential of tunable strength from interference patterns enables to investigate the physics arising in lattices (*e.g* [43]). In this case, the atoms arrange themselves in the periodically spaced energy wells, similarly to the electrons in a solid crystal and reproduce the so-called Bose-Hubbard Hamiltonian. In this system, a transition from a superfluid phase (at weak lattice height) to a Mott-insulating phase with a suppression of the fluctuations of the number of atom per lattice site and the absence of phase coherence over the system (at strong lattice depth) was observed [44]. This setup also enables to achieve a strongly interacting regime and opens the way to a large spectrum of investigations [45–48].
- — Further control of the spatial dependencies of the trap confining a bulk (in opposition to the lattice) systems is also of huge interest to test various physical properties. Due to common laser beam profiles, the trapping potentials happen to be usually non homogeneous (harmonic). It was recently achieved to change it into a quasi-uniform box [49], closer to the textbook models. In this system, complementary measurements and more rigorous comparison to theory can be achieved and a novel insight in physical phenomena can be gained, opening a new field of investigation.
- — In a somehow opposite direction, one can also reproduce a disordered potential with a tunable range and strength by using for example a laser beam transmitted through a diffusive plate generating a speckle pattern. A particular point of interest is the effect of disorder on the diffusion of the atoms in the gas and particularly of the occurrence of the transition toward a localized state predicted by Anderson [50]. Cold gases enabled a first direct observation of the localization [51–53] which triggered novel investigations for example toward the issue of the interplay between the disorder and the interactions between particles.

Many other research efforts may also be quoted. For example, efforts are pointing toward the implementation of two essential points for quantum simulation purpose that are the realization of (strong) synthetic gauge fields (that reproduce in the Hamiltonian the effect of a magnetic field on a charged particle like the electron) [54–59], and the implementation of long-range interactions between atoms [60–62]. A complementary very active theme of research aims toward ultra-cold chemistry [63].

With these ingredients, the thermodynamics properties of a great number of systems become accessible with cold atom ensembles. For example, beyond the simple observation of the thermodynamics transitions whose few examples have been quoted above, efforts have been undertaken to precisely describe the complete equilibrium behavior of the gases. This steady behavior is embodied by an equation-of-state (EoS) which relates the appropriate number of dimensionless quantities to fully determine the state of the gas. Thus, from the measurement of the EoS, we can deduce all the thermodynamics quantities and determine at which values a thermodynamic transition occurs by observing the discontinuities of some of these variables. Such relations have been measured in both Bose and Fermi gases [64–71].

Another flourishing trend in atomic physics consists in the study of the dynamical properties of the system. This study is enabled in cold atom systems due to the unique possibility of controlling dynamically both the interaction between the atoms and the energy landscape they feel. Then many dynamical problems can be addressed. Such investigations bring important complementary information on the gas state. The manifestation of a macroscopic quantum behavior is generally linked to the establishment of a so-called "superfluid" state that is primitively characterized by its response to a flow. Hence, beyond the historical observation of the collective excitations [72, 73], flow [74–82] and transport [83–87] experiments have raised great interest.

Linked to the dynamical study, another long-lasting question bears on how a BEC forms in experiments and how coherence emerges in an initially incoherent gas. This question can be seen as a specific case of a more general problem, which encompasses the general question of the coherence establishment when a system is driven through a thermodynamic transition in a short time ("critical quench"). Close to any transition point, the microscopic details of the system are predicted to become irrelevant (critical universality), then a general mechanism may hold for all "critically-quenched" systems. In this way, studying cold atoms enables to access general properties for any system, from the cosmology to the particle physics. Such an ubiquitous mechanism was put forward by Kibble [88] and extended by Zurek [89] and is based on the universal divergences that occurs when approaching a point where a transition toward a coherent state occurs. In particular the typical equilibration time diverges at this point. Then, in the case of a finite time evolution through this transition, a specific time emerges at which the actual evolution can no longer follows these divergent behaviors. At this time, the evolution reaches a non-equilibrium regime. Kibble and Zurek predicted that a memory of this non-equilibrium evolution may be kept inside the final coherent state by the presence of specific long-lived excitations. Quench-induced excitations have been observed in cold atom experiments [90, 91]. Moreover, the counting of these excitations may bring crucial information on the phase transition that is crossed. Such a quantitative analysis has also been carried out with cold atom assembly confirming thus the Kibble-Zurek model [92–95].

The work presented in this manuscript focuses on the properties of two-dimensional (2D) physical systems via the experimental investigation of Bose gases with their motion frozen out in one direction of space (relying to this aim on the highlighted versatility of the potential shaping). These low dimensional systems are of interest as they show properties that are dramatically altered compared to the three-dimensional (3D) case but also vastly distinct from the one-dimensional (1D) fluid. It has been theoretically shown [96, 97] that in an infinite, homogeneous system of one or two dimensions with short range interaction, there cannot exist a phase transition associated with the spontaneous breaking of a continuous symmetry. For example, as noticed as early as 1934 by Peierls [98], in a 1D or 2D world crystals (salt, diamond, snow ...) would not exist. In such a world thermal and quantum fluctuations have a much more predominant role than in our common 3D universe and they prohibit the emergence of a long-range order.

However, some specificities of the 2D case rely on the fact that the thermodynamic limit within which these conclusions hold is only reached for exponentially large systems (compare to the introduced thermal length λ_{T}) leading to the famous statement that "the sample would need to be bigger than the state of Texas for the Mermin–Wagner theorem to be relevant”[6]. Then for a gas produced in a typical cold atom experiment, which is of a few tens of micrometers large, the size of the system plays a predominant role in its thermodynamic. In particular, the considerable range of coherence (the size over which the particles interfere and thus cohere) in dense and cold 2D gases makes it possible to recover a transition similar to Bose–Einstein condensation even in the absence of interactions. We also emphasize that the quantum statistics of the ideal Bose gas also plays an important role at the dimensional crossover from a 3D to a 2D system. As in Bose condensation phenomenon, it helps establishing a macroscopic population of a single-particle state but primarily in the more tightly confined direction of the trap. Indeed along this direction the quantized energy levels are more spaced and so condensation regime easier to achieve. Then if the trap is anisoptropic enough, the 3D BEC phenomenon splits in two steps of condensation, leading first to the establishment of reduced dimensionality physics (transverse condensation) and then, if it is allowed by the thermodynamic of the lower dimensional system, to an overall condensation. Due to the specific 2D marginality, such a Bose-driven crossover may lead to an important change in the coherence properties of the remaining 2D system.

On the other hand, even at the thermodynamic limit, a 2D gas of interacting particles undergoes a phase transition to an ordered state with an even slower decay of the coherence than the ideal 2D gas. This state shows a superfluid behavior. The necessarily fundamentally different mechanism behind this transition was described by Berezinskii [100] and Kosterlitz and Thouless [101]. In this mechanism, quasi long-range coherence and superfluidity are microscopically enabled by the pairing of special defects in the gas wavefunction ψ, the vortices, in vortex-antivortex bound pairs of small spatial extent (on a scale set by the interaction strength). The vortices are points around which the phase of the complex field ψ winds, then at the vortex center the density of the gas $|\psi|^2$ goes to zero but this perturbation is only local. Their pairing leads to a suppression of the windings of the phase drastically increasing the coherence range. Since this mechanism does not rely on the breaking of a symmetry, all the thermodynamical variables are continuous at the transition and it is said of infinite order.

Previous experimental investigations of 2D ultra cold gases mainly focus on properties around the BKT transition point, the critical region. The occurrence of a BKT-type transition was demonstrated by interference measurement showing the emergence of a coherent state in which free vortex proliferation is proscribed [42].The pre-superfluid state that is the seat for free vortices proliferation ahead of the BKT transition was studied in [102, 103]. Thermally activated vortex pairs linked to the BKT mechanism were observed [104]. The continuity of the EoS around the critical point and its approxi-

---

[6] This statement was published in [99] in the context of 2D magnetism but is nevertheless representative of the 2D specificity.

mate scale-invariance in the weakly interacting regime were experimentally verified [69]. Density and phase fluctuation scalings within the critical region were also investigated [105, 106]. All these experiments were performed in inhomogeneous gases and their results were linked back to the homogeneous system by considering the gas as locally equivalent to a uniform one (local density approximation). In these systems, the spatial variations of the gas properties lead to an intricate dependency between the location on the sample and the gas degrees of degeneracy.

In the present work, we vary the shape of our gas "container" from a common inhomogeneous (harmonic) one to a novel flat bottom box-like trap. We thus enrich both the properties that can be measured and the physical effects under study. This manuscript is then mainly divided in three parts:

1. In Chapters 1-3, we present the general principle of the investigations undertaken. We introduce both the main theoretical results for the relevant regime of parameters of our ultracold Bose gases and the experimental apparatus that we have built along with the sequence that we have optimized for producing and analyzing our cold atomic samples.
2. In Chapters 4-5, we show results obtained in a 2D harmonically confined gas. In these cases we use the space-dependent degree of degeneracy to investigate a wide range of homogenous-equivalent parameters within a unique cloud configuration.
3. In Chapters 6-8, we present our experimental realization of an in-plane uniform trapping and investigate some specific key features of the 2D gas. Here we use the space independent degree of degeneracy to explore long-range coherence and the space-independent populations of the transverse excitations to study the Bose-driven dimensional crossover.

The detailed outline is the following:

Detailed Outline

In chapter 1, we present a few theoretical results that we will aim to investigate in the remaining part of this manuscript. The first part focuses on the gas in the full 2D regime (the transverse motion is nearly perfectly frozen). We present results for both of a non-interacting and an interacting gas in either a homogeneous or an inhomogeneous trap. We demonstrate how to link back the inhomogeneous case to the homogeneous one but also allude to specificities of each configuration. In the second part we consider a gas in a highly anisotropic trap, but whose transverse motion is not frozen. Then we introduce a more general description of our gases. We briefly discuss the possible corrections to retrieve results for a perfectly 2D gas from the case of a weakly excited transverse motion (which is experimentally relevant). We finally focus on the specificity of the dimensional crossover in an anisotropic trap, considering highly excited transverse motion. For the specific case of an in-plane uniform trapping, a non-conventional transition of BEC type arises which we will characterize in detail. This partial condensation will be the main focus of our investigation in our flat trap experiment.

Chapter 2 presents the experimental apparatus used to produce ultra-cold 2D ^{87}Rb gases. In a first part we present the overall sequence along which we generate and investigate our uniform 2D samples. We mainly detail the changes made during my PhD on the experimental apparatus whose main frame was designed and constructed by former PhD students [107–111]. These modifications are two-fold: (i) We switch from a magnetic to a hybrid magnetic and optical trap to produce a 3D BEC (that we will latter load in the 2D trap) in order to increase repetition rate.(ii) We switch for an all optical 2D trap which enables in plane uniform confinement. In a second part we detail the method used to create a tight transverse confinement and reach (quasi-)2D regime. We specifically detail calculations of all possible side effects of this 2D confinement that can be of importance in the scope of producing in-plane uniform traps. Finally we present preliminary tests of an improved scheme for generating this 2D confinement that will allow higher trapping frequencies and improved loading of the initial 3D gas.

In chapter 3 we detail the imaging procedure used to measure the gas properties at the end of the experimental sequence. We first present the specific regime in which we use the mainstream absorption imaging technique in order to overcome the 2D special diffusion effects. We then present the two experimental setups implemented to acquire images of the clouds. Finally we present an exhaustive and renewed calibration of the analysis of the in-plane density profiles. Due to change in the 2D trapping configuration, the imaging environment has been changed, demanding thus a calibration campaign to be performed (the previous one was carried out in 2010 [110]).

In chapter 4, we present a measurement of the equation of state (EoS) of the homogeneous 2D Bose gas computed from the in-situ density distribution $n(r)$ of harmonically trapped 2D ^{87}Rb gases. We develop a robust and flawless technique to infer the EoS from the density profile without any fit of these experimental data. First we develop a general formalism (inspired from the procedure introduced by Ku et al.[71] for the unitary 3D Fermi gas) for deriving the EoS in any scale invariant system investigated within a cold atom experiment. We then apply this formalism to our measurements of the 2D gas. We extract a highly accurate measurement of the EoS that can be extensively compared to theoretical predictions and serves as a benchmark for them. This work was published [112], and is reproduced with minor modifications.

In chapter 5, we present a direct measurement of the superfluid behavior of the 2D homogeneous Bose gas, by moving a local defect in an inhomogeneous 2D sample on trajectories of equi-density (thus probing a unique homogeneous equivalent configuration). We show evidence for both a normal and a superfluid response to this motion, depending on the local degree of degeneracy of the gas at the defect position. We compare the results to theoretical predictions of the homogeneous gas. This work was also published [113], and is reproduced without modifications.

Chapter 6 presents the experimental setup for the production of our box-like potential. We first set some requirements on the trap «box-like character» from simple theoretical calculations on the atomic configurations of interest. The conditions bear on the maximal fluctuations of the potential inside the trapping region and on the stiffness of its variation at the edges of this region. We compare two possible realizations using the same laser beam (far-blue detuned compared to the atomic resonance). One method is based on the shaping of a beam with an optical phase plate whereas the other relies on the simple imaging of a dark mask. In both cases we precisely characterize the trap uniformity from the beam intensity profile. We also consider the achieved potential height. The comparison of these characteristics leads to the choice of the second method which we implement on our atomic samples in the aim of further physical investigations.

In chapter 7, we present an experimental investigation of the emergence of quantum coherence in a 2D uniform gas. In our system a coherent behavior is said to be established when the characteristic length of the inter-particle correlations (embodied by the one-body correlation function $g_1(r)$) is notably larger than the value predicted by Boltzmann statistics, which is set by the thermal wavelength. To measure the degree of coherence in our gas we use two complementary methods. A first one is based on the appearance of a bimodal distribution after a free expansion of the gas. The coherence manifests by a sharp peak in the final density spatial distribution. A second method is based on matter wave interferences between two initially spatially separated clouds. In both cases we identify a crossover between an incoherent regime and an extended coherence. Using appropriate thermodynamic variables we find a universal behavior for the variation of this crossover. We tested both the quasi-2D regime where the transverse motion is nearly frozen, and the 3D-to-2D crossover (starting with an initially high population of the transverse excitations). In the first case, we note the emergence of a quantum coherence at a point matching quasi-condensation regime, ahead from BKT or BEC transition. In the second case we measure the effect of a partial condensation (along transverse motion) on the in-plane coherence.

Finally, in chapter 8, we present a dynamical investigation of the establishment of coherence via a finite-time ramp from a thermal to a deep superfluid state. This experimental investigation relates to the Kibble Zurek mechanism which encompasses a large range of physical systems. We start by presenting a theoretical description of this mechanism highlighting its applicability in our experimental realization. We investigate quenches through the Bose-driven dimensional crossover. We then present two experimental measurements of the quench dynamics by detecting and counting topological defects nucleated via the KZ mechanism. In a first experiment, we directly observe bulk vortices by revealing their core density hole with a short time of flight. In the second one we use an annulus geometry and reveal establishment of phase winding via matter wave interference with a reference central disk of atoms. In both cases, we first demonstrate that the observed defects are linked to the quench dynamics. Then we fit an exponent for the defect number dependency as a function of the quench time that we compare to some theoretical predictions.

1. Elements of theory on quasi-two-dimensional Bose gases, from harmonic to uniform trapping

In this first chapter, our aim is to introduce the theoretical concepts that establish the relevance of our experimental setup to study an interesting and challenging physics. We will point out the specific features of Bose gases in two dimensions (2D). We will show in particular that conventional phase transitions do not take place and full long-range order is not achievable in an ideal infinite 2D gas at non-zero temperature ($T > 0$) . As a corollary property, thermal and quantum fluctuations have an enhanced role in this system, leading to unusual thermodynamic regimes. Moreover, due to the marginality of the 2D (that is intermediate between three-dimensional (3D) physics in which long-range order (LRO) survives thermal fluctuations and the most incoherent one dimensional (1D) physics), we will show that finite-size effects are here of great importance to recover coherence over the gas. Interactions between particles constitute an additional ingredient to restore such a quasi-long-range order and a superfluid behavior. For all these characteristics behaviors we will highlight the specificities of both harmonic and uniform trapping as we will experimentally investigate both of these configurations in the rest of this work. In this theoretical description, we do not aim to exhaustivity as a more complete picture can be found in recent reviews, such as [114, 115] or former PhD works in our group [109–111].

We will also point out the particularities of establishing 2D physics within our 3D world for a gas of Bosonic atoms. We will show that 2D physics is achieved by the freezing out of one motional degree of freedom in our gas. Such a freezing out can be established by a simple but constraining condition on the temperature of the gas. In the specific case of a gas uniformly confined in-plane, we will show that Bose stimulation enables establishment of a 2D regime prior the thermal condition is achieved, resulting in a sharp dimensional crossover. This crossover is linked but not equivalent to usual 3D Bose–Einstein condensation (BEC) phenomenon. We will describe in detail the occurrence of such a transition.

1.1. Specificity of two-dimensional physics

1.1.1. Absence of true long-range order in 2D systems

Usual phase transitions in the 3D space, like Bose–Einstein condensation, arise from spontaneous breaking of a continuous symmetry and are associated with the emergence of true long-range order. For the BEC case, spontaneous breaking of gauge invariance occurs by the specific choice of the phase of the macroscopic wavefunction ψ that constitutes the order parameter of this phase transition.

Bogoliubov [116], Hohenberg [97] and Mermin and Wagner [96] studied the appearance of such spontaneous symmetry breaking transitions in lower dimensional spaces (dimension $d < 3$). They conclude that true LRO is unachievable in the thermodynamics limit and at non-zero temperature for systems with short range interactions and showing Hamiltonian symmetry. In this case, the order is destroyed by long wavelength thermal fluctuations, more specifically in our atomic gases, by phonons. In a general way, the coherence is characterized by describing the one-body correlations and we consider their matrix $\mathcal{G}_1(\boldsymbol{r}_1, \boldsymbol{r}_2) \equiv \langle \hat{\psi}^\dagger(\boldsymbol{r}_1)\hat{\psi}(\boldsymbol{r}_2)\rangle$ (where $\hat{\psi}(\boldsymbol{r})$ is the annihilation operator of a particle at position $\boldsymbol{r}$ and $\langle . \rangle$ stands for the average over the equilibrium state at temperature T). In a uniform system $\mathcal{G}_1$ is simply a function of the distance $\boldsymbol{r} = \boldsymbol{r}_1 - \boldsymbol{r}_2$ and we define the one-body correlation function

$$g_1(\boldsymbol{r}) \equiv \langle \hat{\psi}^\dagger(\boldsymbol{r})\hat{\psi}(0)\rangle. \tag{1.1}$$

and the range of coherence as being the characteristic length ℓ_c of g_1 decay with the distance $|\boldsymbol{r}|$. Penrose and Onsager [117] generalization of Einstein's argument consists in stating that condensation occurs when an eigenvalue of $\mathcal{G}_1$ is macroscopically populated. Then in an infinite uniform system, it is the case if g_1 tends to a non-zero value when $|\boldsymbol{r}|$ grows to infinity and the condensate density n_0 identifies with this limit:

$$n_0 \equiv \lim_{|\boldsymbol{r}|\to\infty} g_1(\boldsymbol{r})\ , \tag{1.2}$$

we see that the absence of true long-range order is equivalent to the absence of Bose–Einstein condensation as $g_1(\boldsymbol{r}) \xrightarrow{|\boldsymbol{r}|\to\infty} 0$.

We should note that:

- In this analysis all the phase transitions are not precluded but only the ones relying on a mechanism linked to symmetry breaking. We will see that in fact in our 2D gases and in the presence of interactions between the atoms, a transition of a different kind is expected to occur, reestablishing a «quasi long-range order».
- The proscription of Bose–Einstein condensation is only relevant in the thermodynamics limit. Considering again Penrose and Onsager argument, we see that finite-size effect can lead to an effective condensation when the correlation length ℓ_c is larger than the characteristic size L of the system itself.

In this section, we will first describe the ideal 2D Bose gas and compute the BEC transition point while varying the 2D confining potential. Then, we will present the case of an interacting gas.

1.1.2. Realizing a 2D Bose gas in a 3D world: the deep thermal 2D regime

Before entering in the details of the physics of a 2D gas, we present here how to realize such a gas in our 3D world. This description gives an insight on the emergence and the treatment of the 2D wavefunction and its Hamiltonian. This will also facilitate the introduction of interactions between particles.

Experimentally producing a gas of reduced dimension necessitates to freeze out the motion in one of the direction of space. For our atomic gases, this translates into imposing a very tightly confining potential along this direction. If we impose a harmonic confinement along z such that

$$V(\boldsymbol{r}) = U(\boldsymbol{\rho}) + \frac{1}{2} m\omega_z^2 \, z^2 \tag{1.3}$$

($\boldsymbol{r} = \boldsymbol{\rho} + z\boldsymbol{u}_z$ stands for the 3D position vector, $\boldsymbol{\rho}$ for the 2D one), freezing out of the motion along z is achieved if the inter-level spacing $\hbar\omega_z$ is large enough. Deep 2D regime (with almost full freezing of the motion along z) corresponds to $\hbar\omega_z \gg k_{\mathrm{B}}T$ where T is the temperature of the gas, such that z-motion excited states can not be reached via thermal excitations. Note that the interaction energy may also be considered, we will discuss in details how to account for the interaction potential in the following and postpone its discussion there (see 1.1.4.1).

Assuming a freezing of the z motion, the 3D wavefunction $\psi(\boldsymbol{r})$ of any particle can be factorized along

$$\psi(\boldsymbol{r}) = \phi(\boldsymbol{\rho}) \; \varphi_0(z) \;\text{ with } \varphi_0(z) = \frac{\chi_0(z/\ell_z)}{\sqrt{\ell_z}} \tag{1.4}$$

(where χ_0 stands for the zeroth order Hermite function and $\ell_z = \sqrt{\frac{\hbar}{m\omega_z}}$), and the interesting part of the state is restricted to the 2D wavefunction $\phi(\boldsymbol{\rho})$ (which is unspecified here). The quantum field operator $\hat{\psi}(\boldsymbol{r})$ (defined in Eq. 1.1) can be consequently replaced by

$$\hat{\psi}(\boldsymbol{r}) \to \hat{\phi}(\boldsymbol{\rho}) \; \varphi_0(z) \tag{1.5}$$

where $\varphi_0(z)$ is the classical field given in Eq. 1.4 and $\hat{\phi}(\boldsymbol{\rho})$ is a 2D quantum field operator (which annihilates a particle at position $\boldsymbol{\rho}$ in plane). Then, by simply integrating the 3D Hamiltonian $\hat{H}$ of the atomic assembly along z, we can deduce a 2D Hamiltonian $\hat{\mathcal{H}}$ for the 2D gas. In the following, we first present the simple case of a non-interacting gas, for which such a description of the 3D environment behind the 2D gas is not crucial and then turn to the description of an interacting gas for which it is essential to see the gas as part of the 3D world (and even only being in a quasi-2D regime for the interactions).

1.1.3. The ideal two-dimensional Bose gas

In the case of non-interacting particles, the splitting between in-plane and z motions is simplified as the ideal 3D Hamiltonian $\hat{H}_{id}$ for a gas of N particles is the sum of N identical single-particle hamiltonian $\hat{h}$, which in turn directly decompose in:

$$\begin{aligned} \hat{h} &= \hat{h}_\rho + \hat{h}_z && (1.6)\\ \text{with } \hat{h}_z &= -\frac{\hbar^2 \partial_z^2}{2m} + \frac{1}{2} m\omega_z^2 \, z^2 && (1.7)\\ \text{and } \hat{h}_\rho &= -\frac{\hbar^2 \partial_\rho^2}{2m} + U(\boldsymbol{\rho}) && (1.8) \end{aligned}$$

Then the ideal 2D Hamiltonian $\hat{\mathcal{H}}_{id}$ is also the straightforward sum of N identical single-particle hamiltonian $\hat{h}_\rho$ and the integration along z simply turns into a constant energy contribution to $\hat{\mathcal{H}}_{id}$ equal to $N\hbar\omega_z/2$.

Now let us focus on the physics of the 2D component $\phi(\boldsymbol{\rho})$ (dictated by $\hat{\mathcal{H}}_{id}$). We assume that the eigenstates $|\phi_i\rangle_{i\in\mathbb{N}}$ and eigenvalues ϵ_i of the single-particle 2D Hamiltonian $\hat{h}_\rho$ are known. Then, within the grand canonical ensemble, the occupancy of the state i is equal to the Bose–Einstein factor $f(\epsilon_i)$ with:

$$f(\epsilon) = \frac{1}{e^{\beta\,(\epsilon-\mu)} - 1} \tag{1.9}$$

where $\beta = 1/k_\mathrm{B}T$, and μ is the chemical potential. For this non-interacting case, μ is necessarily smaller than the ground state energy ϵ_0. We take this reference energy to be zero, $\epsilon_0 = 0$. For now on, we call $Z = e^{\mu/k_\mathrm{B}T}$ the fugacity of the gas, and in the non-interacting case, Z varies from 0 to 1. The function f of Eq. 1.9 depends on β and Z for the gas we consider. By definition, the number of atoms N in the gas is then given by:

$$N = \sum_{i=0}^{\infty} f(\epsilon_i) \tag{1.10}$$

If we assume that the (in-plane) level spacing is small compared to the thermal energy $k_\mathrm{B}T$, the summation of Eq 1.10 is well approximated by the semi-classical limit:

$$N \;=\; \int_0^\infty D(\epsilon) f(\epsilon)\mathrm{d}\epsilon \tag{1.11}$$

where $D(\epsilon)$ is the density of states at energy ϵ (*i.e.* the number of states whose energy is comprised between ϵ and $\epsilon + \mathrm{d}\epsilon$, divided by $\mathrm{d}\epsilon$).

For a gas of characteristic size L in plane, we can then deduce the mean 2D phase-space-density (PSD) $\mathcal{D}^{(2D)} \equiv n\lambda_\mathrm{T}^2$ as the mean surface density equals $n = N/L^2$ and can be computed from Eqs. 1.10–1.11, and the thermal wavelength λ_T is given by $\lambda_\mathrm{T} = \sqrt{2\pi\hbar^2\beta/m}$.

More generally, we can compute the mean value of any one-particle observable $\hat{A}$ in our 2D Bose gases by:

$$\langle\hat{A}\rangle \;=\; \frac{1}{N}\sum_{i=0}^{\infty}\langle\phi_i|\hat{A}|\phi_i\rangle f(\epsilon_i) \tag{1.12}$$

We have to specify the trapping potential $U(\boldsymbol{\rho})$ to compute these sums or integrals.

1.1.3.1. The uniform 2D gas

In this section, we assume that the atoms are uniformly trapped in the horizontal plane with $U(\boldsymbol{\rho}) = 0$ within the confining region[1]. Then the eigenenergies are given by the kinetic energy term $\epsilon_{\boldsymbol{k}} = \hbar^2\boldsymbol{k}^2/2m$ where $\boldsymbol{k}$ is the particle wave vector.

In the infinite case, $\boldsymbol{k}$ is not quantized and the eigen-wavefunctions are simply $\psi_{\boldsymbol{k}}(\boldsymbol{\rho}) = e^{i\boldsymbol{k}.\boldsymbol{\rho}}/2\pi$.

---

[1] outside this region, $U(\boldsymbol{\rho}) = U_\mathrm{barrier}$ with a very high energy barrier compared to the other energy scales of the problem, for example, $U_\mathrm{barrier} \gg k_\mathrm{B}T$.

If we assume that the gas is constrained in a square region of the plane of length L and that we apply periodic boundary conditions on this box, we find $\boldsymbol{k}$ components are quantized by multiple integers of $2\pi/L$:

$$\boldsymbol{k} = \frac{2\pi}{L}\left(j_x \boldsymbol{u}_x + j_y \boldsymbol{u}_y\right) \text{ with } j_x, j_y \in \mathbb{Z} \tag{1.13}$$

where $\boldsymbol{u}_x$ and $\boldsymbol{u}_y$ are the unit vectors along the axes of the trapping square. Then the eigenfunction and the eigenenergy corresponding to the eigenstate (j_x, j_y) write

$$\psi_{j_x,j_y}(\boldsymbol{\rho}) = \frac{1}{L}\exp\left(i\frac{j_x \pi x}{L}\right)\exp\left(i\frac{j_y \pi y}{L}\right) \tag{1.14}$$

$$\epsilon_{j_x,j_y} = \frac{2\hbar^2\pi^2}{mL^2}\left(j_x^2 + j_y^2\right). \tag{1.15}$$

The exact sum from Eq. 1.10 can be computed numerically for this square box but also for more complex trapping geometries after determining the eigenenergies in these precise cases. From this simple square box description, we can deduce in general the semi-classical limit for any uniform trap (in this limit the trap size L tends toward infinity, then all details on the trap geometry become irrelevant.).

Semi-classical limit and equation of state For this square, the density of state is uniform and equal to $D(\epsilon) = mL^2/(2\pi\hbar^2)$. If $L^2 \gg \pi\lambda_T^2$, Eq. 1.10 is well approximated by Eq. 1.11 and the phase-space-density simply verifies[2]:

$$\mathcal{D}^{(2D)} = -\ln(1 - Z) \tag{1.16}$$

Eq. 1.16 linkes $\mathcal{D}^{(2D)}$ to μ and $k_B T$ and is the equation of state (EoS) of the homogeneous ideal 2D Bose gas. We note that the PSD does not admit an upper bound contrarily to the 3D case. This is a signature of the announced absence of Bose–Einstein condensation in the ideal 2D gas at thermodynamic limit ($L \to \infty$).

State occupancies in the semi-classic limit Using Eq. 1.16, we can easily study the two limiting cases of the weakly (for which $\mathcal{D}^{(2D)} \ll 1$) and strongly (for which $\mathcal{D}^{(2D)} \gg 1$) degenerate gases in terms of the occupancies of the various single-particle states ϕ_k:

- In the **weakly degenerate cases**, we deduce that

  $$\mathcal{D}^{(2D)} \approx Z\ (\ll 1), \tag{1.17}$$

  and then $|\mu| \gg k_B T$. The Bose distribution is then close to the Boltzmann one $f(\epsilon_k) \sim e^{-\beta\epsilon_k}$.
- In the **highly degenerate cases**, the fugacity Z is close to 1 so that $|\mu| \ll k_B T$. We

---

[2] This condition is in general valid in experiments as for a typical $T = 100\,\text{nK}$, $\lambda_T = 0.6\,\mu\text{m}$ leading to a thermal surface $\pi\lambda_T^2 \sim 1\,\mu\text{m}^2$ while trap surfaces realized experimentally vary typically from $100\,\mu\text{m}^2$ to $1000\,\mu\text{m}^2$.

find that

$$\mathcal{D}^{(2D)} \approx \ln\left(k_{\mathrm{B}}T/|\mu|\right) \ (\gg 1). \tag{1.18}$$

The population of an excited state depends on the relative importance of its energy $\epsilon_{\boldsymbol{k}}$ compared to the thermal energy $k_{\mathrm{B}}T$:

- For the highly excited states with $\epsilon_{\boldsymbol{k}} \gg k_{\mathrm{B}}T$ (that is $|\boldsymbol{k}| \gg \sqrt{4\pi}/\lambda_{\mathrm{T}}$), the population is still close to the Boltzmann prediction $f(\epsilon_{\boldsymbol{k}}) \sim e^{-\beta\epsilon_{\boldsymbol{k}}}$.
- Whereas for the low energy states, with $\epsilon_{\boldsymbol{k}} \ll k_{\mathrm{B}}T$ (that is $|\boldsymbol{k}| \ll \sqrt{4\pi}/\lambda_{\mathrm{T}}$), the occupation tends to a Lorentzian dependency in $|\boldsymbol{k}|$ as $f(\epsilon_{\boldsymbol{k}}) \sim k_{\mathrm{B}}T/(\epsilon_{\boldsymbol{k}} + |\mu|^2)$ (with $\epsilon_{\boldsymbol{k}} = \hbar^2\boldsymbol{k}^2/2m$). Moreover as $\epsilon_{\boldsymbol{k}}$ and $|\mu|$ are both negligible compared to $k_{\mathrm{B}}T$, the population of these state verifies $f(\epsilon_{\boldsymbol{k}}) \gg 1$ such that they have a major contribution to the total phase-space-density.

One-body correlation function and coherence properties Characterizing g_1 enables to investigate how the range of coherence evolves with the gas parameters. We define the coherence length ℓ_{c} as the distance $|\boldsymbol{\rho}|$ at which g_1 is equal to $g_1(0)/e$. In the infinite homogeneous case, g_1 is simply given by

$$g_1(\boldsymbol{r}) = \frac{1}{(2\pi)^2}\int_0^{\infty} \frac{e^{i\,\boldsymbol{k}.\boldsymbol{r}}}{e^{\beta(\hbar^2k^2/2m)}/Z - 1}\mathrm{d}^2\boldsymbol{k}, \tag{1.19}$$

which is the Fourier transform of the Bose population $f(\epsilon_{\boldsymbol{k}})$ of the state of momentum $\boldsymbol{k}$.

From the two limiting behaviors of the occupancy $f(\epsilon_{\boldsymbol{k}})$, we deduce that:

- In **weakly degenerate cases**, $g_1(\boldsymbol{r}) \propto e^{-\pi r^2/\lambda_{\mathrm{T}}^2}$ which decays rapidly to zero and the characteristic width is
$$\ell_{\mathrm{c}}^{(th)} = \frac{\lambda_{\mathrm{T}}}{\sqrt{\pi}}. \tag{1.20}$$
- In **strongly degenerate cases**, $g_1(\boldsymbol{r})$ develops a bimodal structure as $f(\epsilon_{\boldsymbol{k}})$ varies from a Lorentzian to Gaussian shape according to the norm of the wave vector $|\boldsymbol{k}|$ compared to $1/\ell_{\mathrm{c}}^{(th)}$. Then, the Lorentzian contribution dominates for $|\boldsymbol{r}| \gg \ell_{\mathrm{c}}^{(th)}$ in Eq. 1.19 and it translates into a long distance exponential decay of $g_1(\boldsymbol{r})$ whose characteristic length is $\ell = \hbar/\sqrt{2m|\mu|}$:
$$g_1(\boldsymbol{r}) \underset{|\boldsymbol{r}|\gg\lambda_{\mathrm{T}}}{\sim} e^{-|\boldsymbol{r}|/\ell} \tag{1.21}$$
and, using Eq. 1.18 we find that the characteristic width follows
$$\ell = \frac{\lambda_{\mathrm{T}}}{\sqrt{4\pi}} e^{\mathcal{D}^{(2D)}/2}. \tag{1.22}$$

For highly enough degenerate cases, the gaussian contribution to g_1 is negligible such that $\ell_c = \ell$.

Naive approach to the recovery of BEC in a finite box In the previous paragraph, we found that $g_1(\boldsymbol{r})$ decays to zero at long distances even in the strongly degenerate regime and so an ideal uniform 2D gas does not show Bose–Einstein condensation in the thermodynamic limit. However, due to the exponential growth of ℓ_c with $\mathcal{D}^{(2D)}$ at $\mathcal{D}^{(2D)} \gg 1$, a condensation can be easily induced by the finite-size of the system along Penrose and Onsager argument. Recovery of a condensation is then roughly expected when $L \sim \ell_c$ which occurs at $\mathcal{D}^{(2D)} \sim \ln(4\pi L^2/\lambda_T^2)$.

Exact calculation of the BEC critical point in a finite box In the previous paragraph, we estimated the threshold for the emergence of a BEC using calculations for an infinite system and in a final step reintroducing the size L as a cut to the coherence length ℓ_c. The exact condensation point depends in fact on the specific shape of the uniform potential and the induced specific quantization of the energy levels.

It must be computed using a full quantum treatment of the eigenstates summations. For each configuration, we can numerically compute the sum over the energy states of Eq. 1.10 and deduce at which $\mathcal{D}^{(2D)}$ the saturation of the excited states occurs. We call this value the critical PSD and denote it $\mathcal{D}^{(2D)}_{\text{BEC}}$.

Calculations are performed for a square-shaped and disk-shaped trap in [111] and reveal corrections of these full quantum results compared to the semi-classical rough approach. We describe $\mathcal{D}^{(2D)}_{\text{BEC}}$, by similarity to the semi-classical description, by the empirical model

$$\mathcal{D}^{(2D)}_{\text{BEC}} \approx \xi \ln\left(\eta \frac{L^2}{\lambda_T^2}\right). \tag{1.23}$$

Conclusions from the calculations are that:

- The full quantum description mainly reduces the value of the coefficient η , up to a few percents of its semi-classical value (equal to 4π), whereas ξ stays close to 1.
- The dependance on the shape (square, disk) is very weak: results are highly similar in terms of this critical point as long as we consider traps of the same total area $\mathcal{A}$ and it gives $\eta \approx 0.4$.

We note that the prediction of Eq. 1.23 is in good agreement with the intuitive view of the occurrence of BEC when the semi-classical integral of Eq. 1.11 do not properly account for the population of the ground state $(j_x = 1, j_y = 1)$. This is typically the case when $|\mu|$ is chosen smaller than the gap between the ground state of the box and the first excited state: $\mu_{\text{BEC}} \approx -(2\pi\hbar)^2/(2mL^2)$. As when BEC occurs the degeneracy must be high[3], $\mathcal{D}^{(2D)}$ follows Eq. 1.18 and at the critical chemical potential

$$\mathcal{D}^{(2D)}_{\text{BEC}} \approx \ln\left[L^2/(\pi\lambda_T^2)\right]. \tag{1.24}$$

Here $\xi = 1$ and $\eta = 1/\pi \approx 0.31$ which is close to their respective numerical values of 0.99 and 0.39.

---

[3] as at this point, the Bose statistics has to be relevant. From the estimate of μ deduced here ($|\mu| \approx (2\pi\hbar)^2/(2mL^2)$), we infer $Z \sim \exp\left(-\pi\lambda_T^2/L^2\right)$ which is typically close to 1 (see footnote 2) and justifies $\mathcal{D}^{(2D)} \gg 1$.

1.1.3.2. The harmonic 2D gas

In experiments, the most widespread trap is well described by a harmonic potential. This is for example the case for the dipolar potential created by a far red-detuned gaussian beam shined on the atoms. Such a configuration has been widely described elsewhere [109, 110, 115, 118]. I remind here some of the specific properties of a 2D ideal gas trapped in an harmonic trap of frequency $\omega/2\pi$, that is $U(\boldsymbol{\rho}) = \frac{1}{2}m\omega^2\boldsymbol{\rho}^2$:

- By integrating Eq. 1.11 with $D(\epsilon) = \epsilon/(\hbar\omega)^2$, we deduce that in such a trap, condensation occurs even in the thermodynamic limit and the critical atom number is $N_c = \frac{\pi^2}{6}\left(\frac{k_\mathrm{B}T}{\hbar\omega}\right)^2$.
- If the trapping potential varies smoothly enough, we can apply the local density approximation (LDA) and consider that around each point $\boldsymbol{\rho}$, the gas is locally at thermal equilibrium. At this local scale, the potential can be considered as uniform but then the effective chemical potential in the region surrounding $\boldsymbol{\rho}$ is reduced compared to its value at the trap center μ_0 by $\mu(\boldsymbol{\rho}) = \mu_0 - U(\boldsymbol{\rho})$. Then, if $\hbar\omega \ll k_\mathrm{B}T$ the semi-classical approximation applies and the local PSD follows:

$$\mathcal{D}^{(2D)}(\boldsymbol{\rho}) \equiv n(\boldsymbol{\rho})\lambda_\mathrm{T}^2 = -\ln\left(1 - \exp\left(\beta\mu_0 - \beta U(\boldsymbol{\rho})\right)\right) \qquad (1.25)$$

  We note that such a trapping configuration is remarkably advantageous compared to the uniform case with respect to the possibility of probing several $\mathcal{D}^{(2D)}$ using a unique experimental realization as the effective chemical potential varies from μ_0 at center to $-\infty$ in the far wings. In this manuscript, we will show how to take advantage from this specific property to measure the thermodynamics properties of the equivalent homogeneous gas. In particular, we measured the EoS of the 2D uniform gas using density profiles of a harmonically trapped sample and applying LDA.

1.1.4. The interacting quasi-two-dimensional gas

Until now, we only considered the ideal case of non-interacting atoms and described single-particle physics. In our experiments, the gases differ from this description as atoms are colliding with one another leading to more complex physics possibly involving many-particles phenomena. In 2D, the consideration of this contribution to the Hamiltonian leads to a new type of phase transition. In this section, I will expose how to describe interactions occurring in our cold 2D gases. I will then remind the important physical properties of the gases within this description. I will not dwell on their demonstrations as they have been extensively reviewed in previous works [109, 110, 115, 118].

1.1.4.1. The «collisionnally» quasi-2D regime and scale invariance

To describe how interactions occurs in our 2D samples, we have to go back considering it as part of a 3D environment as presented in 1.1.2. Since we consider very dilute Bose gases at low temperature, we can only account for binary-collisions occurring in the *s*-wave channel. In the 3D world, the resulting interaction is well approximated by a contact potential:

$$V(\boldsymbol{r}_i - \boldsymbol{r}_j) = \frac{4\pi\hbar^2}{m} a_s \delta^{(3D)}(\boldsymbol{r}_i - \boldsymbol{r}_j) \tag{1.26}$$

where $\boldsymbol{r}_i$ (resp. $\boldsymbol{r}_j$) stands for the position of the i-th (resp. j-th) atom of the gas ($i, j \in [[1, N]]$) and the range of these interactions are characterized by the s-wave scattering length a_s. For our ^{87}Rb atoms, $a_s = 5.1$ nm. We denote $g^{(3D)} = \frac{4\pi\hbar^2}{m} a_s$ the 3D interaction strength.

In a pure 2D world, the description of such s-wave interactions would be much more intricate. This 2D picture would be relevant when the scattering range is much smaller than the vertical extent of our gas. To be in the **«collisionnally two-dimensional»** regime, we must impose $\ell_z \ll a_s$. We note that this constraint is much more stringent than the «thermally 2D» condition deduced in 1.1.2 of $\ell_z \ll \lambda_\mathrm{T}/\sqrt{2\pi}$. For our typical gases, the temperature is of the order of $T \approx 100$ nK so that $\lambda_\mathrm{T}/\sqrt{2\pi} \approx 240$ nm $\gg a_s$.

Confinement frequencies enabling the experimental study of two-dimensional physics turn out to verify $\ell_z \gg a_s$, and the interactions are described by the simple 3D picture of Eq. 1.26. This regime is called **«collisonally quasi–two-dimensionality»**. As previously described, the 2D hamiltonian $\hat{\mathcal{H}}$ is simply deduced by integrating the 3D one $\hat{H}$ along z while replacing the quantum field $\hat{\psi}(\boldsymbol{r})$ along Eq. 1.5. Then the 2D interaction potential operator is given by

$$\hat{V}_{int} = \frac{g^{(3D)}}{2\sqrt{2\pi}\ell_z} \int \hat{\phi}^\dagger(\boldsymbol{\rho})\hat{\phi}^\dagger(\boldsymbol{\rho})\hat{\phi}(\boldsymbol{\rho})\hat{\phi}(\boldsymbol{\rho}) d^2\rho. \tag{1.27}$$

We note $g^{(2D)} = g^{(3D)}/(\sqrt{2\pi}\ell_z)$ the coupling strength of this 2D potential [4]. We point out that the reduced coupling strength

$$\tilde{g} \equiv \frac{m}{\hbar^2}\, g^{(2D)} = \sqrt{8\pi}\, \frac{a_s}{\ell_z} \tag{1.28}$$

is a dimensionless quantity in this 2D case. Hence, there is no breaking of the scale invariance due to the interactions [5] and it results in a specific property of the 2D EoS: the phase-space-density $\mathcal{D}^{(2D)}$ (or any dimensionless thermodynamics quantity) must only be a function of the dimensionless quantity $\mu/k_\mathrm{B}T$ formed from the temperature and the chemical potential and of the interaction parameter $\tilde{g}$. We will present an experimental analysis of this property in Ch. 4.

---

[4] A more general and rigorous deduction of the two-dimensional coupling constant $g^{(2D)}$ was set by Petrov *et al.* [119, 120]: For our experimental parameters, this general expression is well approximated by the naive derivation done in the main text.

[5] in fact it is only an approximate scale invariance that is preserved due to corrections mentioned in footnote 4 from [119, 120]. This approximate scale invariance is maintained for weakly interacting gases, up to some corrective factors.

1.1.4.2. Reduction of the density fluctuations and quasi-condensation

The interaction energy is given by

$$E_{int} \equiv \langle \hat{V}_{int} \rangle = \frac{g^{(2D)}}{2} \int \langle n(\boldsymbol{\rho})^2 \rangle d^2\rho, \tag{1.29}$$

such that the interaction energy per particle is locally $\epsilon_{int}(\boldsymbol{\rho}) = g^{(2D)} \langle n(\boldsymbol{\rho})^2 \rangle / \langle n(\boldsymbol{\rho}) \rangle$. As for stability reasons, the interactions in our gases are repulsive ($a_s > 0$), minimizing this energy contribution turns out to be equivalent to minimizing the density fluctuations $\Delta n^2 = \langle n^2 \rangle - \langle n \rangle^2$ at constant average density $n \equiv \langle n \rangle$. In an ideal thermal gas, $\langle n^2 \rangle = 2n^2$ (and $\epsilon_{int} = 2gn$) whereas when the fluctuations are completely suppressed $\langle n^2 \rangle = n^2$ (and $\epsilon_{int} = gn$). Comparing the lower bound of $\epsilon_{int} \geq gn$ to $k_B T$, we find that density fluctuations induced by thermal excitations are strongly suppressed in a 2D gas when $\mathcal{D}^{(2D)} \gtrsim 2\pi/\tilde{g}$.

More accurately, a thorough analysis of Bogoliubov excitations [115] shows that density fluctuations at low temperature are given by:

$$\frac{\Delta n^2}{n^2} \approx \frac{2}{n\lambda_T^2} \ln\left(\frac{k_B T}{gn}\right) \tag{1.30}$$

and are strongly suppressed as long as $\mathcal{D}^{(2D)} \gg 1$ for any length scale larger than the healing length ς. We will study experimentally the reduction of those fluctuations in F.3.

The same Bogoliubov analysis shows that phase fluctuations are the only contribution to long-wavelength phonons and are not suppressed at low temperature in 2D. Physical description at low T, high $\mathcal{D}^{(2D)}$ and at distances larger than ς can be made by only considering these phase fluctuations.

This state where density fluctuations are suppressed at length scale larger than ς but not phase fluctuations is called a «**quasi-condensate**» or «**presuperfluid**» [102, 103].

1.1.4.3. Equation of state of an interacting 2D gas in two limiting cases

Due to the complexity introduced by the interactions between particles, there is no general prediction for the EoS of an interacting gas. However in some limiting cases we can perform approximations that give access to the EoS for restricted range of parameters.

Hartree-Fock approximation. The simplest way to take interactions into account is to use a Mean Field description in which the effect of neigbourghing atoms is approximated by an average effect. The development of Hartree-Fock formalism leads to modification of the single-particle Hamiltonian of Eq. 1.8 by $U(\boldsymbol{\rho}) \rightarrow U(\boldsymbol{\rho}) + 2g^{(2D)} n(\boldsymbol{\rho})$ in the weakly degenerate regime. Then applying the LDA, the EoS is obtained as in Eq. 1.25 by replacing $\mu \rightarrow \mu - 2gn$, resulting in the implicit relation

$$\mathcal{D}^{(2D)}(r) = -\ln\left(1 - e^{\mu/k_B T - \tilde{g}\mathcal{D}^{(2D)}/\pi}\right) \tag{1.31}$$

in the case of a uniform confinement $U = 0$. With the relation of Eq. 1.31, we note that μ is no more constrained to $\mu \leq 0$ in this interacting case. This development is valid for gases with low enough densities, typically up to $\mathcal{D}^{(2D)} \lesssim 4$ as it assumes large density fluctuations.

Thomas-Fermi approximation In the opposite case of strongly degenerate gases $\mathcal{D}^{(2D)} \gg 1$, the Hamiltonian of Eq. 1.8 is modified along $U(\boldsymbol{\rho}) \to U(\boldsymbol{\rho}) + g^{(2D)} n(\boldsymbol{\rho})$ leading to the so-called Gross-Pitaevskii equation [6]

$$\mu\phi(\boldsymbol{\rho}) = \left(-\frac{\hbar^2}{2m}\Delta + U(\boldsymbol{\rho}) + g^{(2D)} n(\boldsymbol{\rho}) \right) \phi(\boldsymbol{\rho}). \tag{1.32}$$

for the macroscopic 2D wavefunction $\phi(\boldsymbol{\rho})$. Then in the highly degenerate regime, we can apply the Thomas–Fermi approximation, neglecting the kinetic term of Eq. 1.32 and considering a uniform confinement $U = 0$, we find $\mu = gn$ and:

$$\mathcal{D}^{(2D)} = \frac{2\pi}{\tilde{g}} \frac{\mu}{k_\mathrm{B} T} \tag{1.33}$$

We note that in this case $\mu > 0$.

1.1.4.4. The superfluid state at low T and Berezinskii–Kosterlitz–Thouless mechanism:

From the Bogoliubov analysis, we also find that at low T, the dispersion relation shows a non-zero minimal velocity $\mathrm{d}\omega_k/\mathrm{d}k$. Then the system is expected to be superfluid according to the Landau criterion. We will present in Chapter 5 an experimental study of the superfluid behavior of the 2D gas.

By neglecting the density fluctuations at distances larger than ς, we can estimate the dependency of $g_1(\boldsymbol{\rho})$ in this superfluid regime. We find that $g_1(\boldsymbol{\rho})$ shows algebraic decay in this case [118]:

$$g_1(\boldsymbol{\rho}) = n_s \left(\frac{\varsigma}{|\boldsymbol{\rho}|} \right)^{1/(n_s \lambda_\mathrm{T}^2)} \quad \text{for } |\boldsymbol{\rho}| \gg \varsigma \tag{1.34}$$

where n_s is the density of the superfluid part of the gas. This decay is consistent with the absence of true long-range order as it goes to zero at infinite distances. It is nevertheless very slow compared to the ideal gas behavior and corresponds to a so-called **«quasi–long-range order»**.

The transition toward this low-T superfluid phase with quasi long-range order occurs via a novel mechanism that is not linked to any continuous symmetry breaking as

---

[6] This also results from a Mean Field treatment of the interactions but now considering a fully condensed gas. We assume that the atoms all populate the same macroscopic wavefunction $\phi(\boldsymbol{\rho})$ so that the quantum field $\hat{\phi(\boldsymbol{\rho})}$ of Eq. 1.27 is approximated by a classical field. The factor 2 difference compared to Hartree-Fock description can be understood from the suppression of density fluctuations in the degenerate case (see 1.1.4.2). The quantity $\langle n^2 \rangle$ thus evolves from $2n^2$ in the thermal regime to n^2 in the degenerate one.

stated in 1.1.1. The mechanism was first described by Berezinskii [100] and Kosterlitz and Thouless [101]. It relies on the appearance and binding of special phase defects in the gas, namely the vortices that will preclude or enable superfluid behavior of the fluid.

At low enough temperature, density fluctuations are strongly suppressed and some coherence appears in the gas (Eq. 1.34) so that we are able to define a phase over the cloud. Vortices are points at which the density cancels and around which the phase winds by a multiple of 2π. The density is here affected only on a small length scale of the order of ς. Above the critical point, the vortices proliferate freely so that they significantly modify the phase of the gas, preventing the appearance of a superfluid state. Below the critical point, formation of vortex pairs of opposite «charges» (that is to say of opposite winding directions) is energetically favorable. The total circulation of the phase around such a pair cancels and thus they only perturb the gas locally, on the scale of the pair size that is also typically of the order of ς. A superfluid behavior is thus enabled. Pairs of vortices in the critical regions were observed in [121].

Such a transition is not described by an order parameter and is said of «infinite order». Most of the thermodynamics parameters vary smoothly across the transition. Only the superfluid density n_s jumps from 0 to a universal value of $4/\lambda_{\mathrm{T}}^2$ at the transition [122]. This jump was measured in liquid He films [123] but a direct measurement of the jump is difficult to implement in our cold atom gas.

BKT theory does not describe quantitatively the transition point in terms of temperature and chemical potential. In a general manner, this proves to be a difficult problem. A computation via classical field Monte-Carlo simulations gives an estimate of the transition point in the weakly interacting limit that is a good approximation for our experimental realization. Such calculations have been performed by Prokof'ev, Ruebenacker and Svistunov [124] and they found:

$$\mathcal{D}_{\mathrm{BKT}}^{(2D)} \equiv \frac{2\pi\hbar^2 n_{\mathrm{BKT}}}{m\, k_{\mathrm{B}}\, T_{\mathrm{BKT}}} = \ln\left(\frac{380}{\tilde{g}}\right) \tag{1.35}$$

$$\mu_{\mathrm{BKT}} = k_{\mathrm{B}} T_{\mathrm{BKT}} \frac{\tilde{g}}{\pi} \ln\left(\frac{13.2}{\tilde{g}}\right) \tag{1.36}$$

For a typical $\tilde{g} = 0.1$ we expect $\mathcal{D}_{\mathrm{BKT}}^{(2D)} \approx 8.2$ and $\mu_{\mathrm{BKT}} = 0.16 k_{\mathrm{B}} T$. We note that due to the very slow decay of the g_1 function for $\mathcal{D}^{(2D)} \geq \mathcal{D}_{\mathrm{BKT}}^{(2D)}$ (Eq. 1.34), the BKT transition always induce condensation via finite-size effects in any practical situation. To determine if the condensation that occurs in a specific configuration is driven by interactions (BKT physics) or by Bose statistics, we must compare $\mathcal{D}_{\mathrm{BKT}}^{(2D)}$ to the previously deduced critical PSD for Bose–Einstein condensation in finite traps $\mathcal{D}_{\mathrm{BEC}}^{(2D)}$ (Eq. 1.23 for example).

Prokof'ev and Svistunov [125] also performed Monte Carlo simulations around the critical point and numerically computed the EoS $\mathcal{D}^{(2D)} = f(\mu/k_{\mathrm{B}}T, \tilde{g})$ for an homogeneous infinite system, which enables to interpolate between the two known limits presented in 1.1.4.3. In Ch. 4, we will compare our experimental measurement of the EoS to these numerical predictions which thus provides an experimental validation of the classical field approaches.

Finally, we point out that the correlation length for the (exponential) decay of the g_1 function above the transition diverges exponentially with the temperature when approaching the transition point:

$$\ell_c \approx \lambda_T \exp\left(\frac{\sqrt{aT_{\mathrm{BKT}}}}{\sqrt{T - T_{\mathrm{BKT}}}}\right) \tag{1.37}$$

where a is a dimensionless constant. This exponential law is specific to the 2D marginal behavior.

1.2. 3D-2D crossover in a uniform trap: transverse condensation phenomenon

From now on we denote $\zeta = k_B T/\hbar\omega_z$. Previously, we described properties of a Bose gas in the «deep thermal 2D regime», that is when $\zeta \ll 1$ (1.1.2), both for non-interacting particles and for weakly interacting ones. In this part, we want to go further in describing Bose gases in a strongly anisotropic confinement linked to a 2D geometry[7] (oblate traps) but not in the «deep thermal 2D regime». As long as $\zeta \not\ll 1$, we must consider that the full 3D wavefunction correctly pictures the state of our gas. In particular, we must not only consider the z-motion ground state but also its excitations. We denote $|\varphi_{j_z}\rangle_{j_z\in\mathbb{N}^*}$ the eigenstates of the z-harmonic confinement, of energies[8] $j_z\hbar\omega_z$.

We are interested in two cases:

- We want to describe cases close to the 2D regime but for which the «deep thermal 2D regime» condition is not achieved, that is $\zeta \gtrsim 1$. In this case we cannot consider that the motion is frozen along the z direction and we must take excitations into account to precisely picture the gas. As pointed out in [126], such considerations are important in particular with respect to the temperature determination.
- We want to describe the evolution of the gas in a strongly anisotropic oblate confinement from a 3D regime (that corresponds to a weakly populated z-motion ground-state $j_z = 0$) to a 2D one (that is when the z excited states $j_z > 0$ are populated in minority). In this case we start in a regime with $\zeta \gg 1$ and we are interested in describing the evolution of the population of the z excited states j_z when varying the total phase-space-density $\mathcal{D}^{(2D)}_{\mathrm{tot}}$.

1.2.1. Relevance of the uniform case

In this section, we will thoroughly describe the case of a gas that is uniformly confined in-plane and harmonically confined along z, with an adjustable strength of confinement $\hbar\omega_z$ compared to the thermal energy $k_B T$. We study the case of a strongly anisotropic confinement with $L \ggg \ell_z$.

- In the case $\zeta \gtrsim 1$ we will deduce corrections to the equation of state Eq. 1.16.

---

[7] Using previous notation, in the case of a uniform confinement in-plane, anisotropic traps must verify $\ell_z \ll L$, and in the case of an harmonic one $\omega \ll \omega_z$.

[8] as previously, we choose the energy origin so that the ground state has a zero energy.

We note that using LDA we can generalize the corrected EoS to any type of confinement by replacing $\mu \rightarrow \mu_0 - V(\boldsymbol{r})$ similarly as in Eq. 1.25.
We can also generalize this description to an interacting gas using a standard simplifying assumption [127, 128] for weakly interacting cases [9]. It consists in asserting that the different atomic assemblies corresponding to the various states j_z of z-motion are not coupled. Then starting from the results for the ideal case, we can reintroduce interactions in each of these 2D atomic assemblies following lines developed in 1.1.4.3. These developments consist in replacing $\mu \rightarrow \mu - g^{(2D)}\langle n^2\rangle / \langle n\rangle$ (in the two extreme cases of very weakly and very strongly degenerate gases) where $g^{(2D)}$ is the 2D interaction parameter. Note that here $g^{(2D)}$ takes a specific value for each level j_z as it is obtained by performing integration over z as in Eq. 1.27. The integration must then be performed in each specific subspace and it gives in $g^{(2D)}_{j_z} = g^{(3D)} \int |\varphi_{j_z}(z)|^2 \mathrm{d}z$

— In the case $\zeta \gg 1$ and in this specific trapping configuration, Bose stimulation plays a crucial role in the occurrence of the 3D to 2D crossover by the introduction of the notion of transverse condensation (BEC$_\perp$) that we will present in details in the following. We note that the occurrence of a distinct transverse condensation phenomenon does not hold in the case of an in-plane harmonic confinement. Indeed, while LDA implies that Bose stimulation locally enhances effectively the population of the ground state of the z-motion, such an enhancement will depend on the position $\boldsymbol{\rho}$ and be negligible in the distant wings of the cloud (due to a lower density). A distinct condensation phenomenon for the z direction is then precluded by the occurrence of a full condensation phenomenon (at a similar PSD). As stated in [129], two step condensation is valid only if the reduced dimensional system does not show condensation at the thermodynamic limit (the second step of condensation then results from finite-size effects). In the opposite case, the two condensation phenomena can not be distinguished. In the non-uniform case, 2D physics can only be established over the whole cloud via the thermal condition $\zeta \lesssim 1$.

1.2.2. General description of an non-interacting gas in an oblate confinement uniform in-plane

As in 1.1.3.1, we consider a non-interacting gas confined in a square region of the xy plane of length L inside which the potential is simply $U(\boldsymbol{\rho}) = 0$ and for which we apply the periodic boundary conditions. Then the eigenenergies and eigen-wavefunctions

---

[9] For a more complete description of interactions in quasi-2D gases see [109]. We note that inter-level interactions can be taken into account in first approximation by modifying intra-level value of the 2D interaction parameter.

are:

$$\begin{aligned} E_{\boldsymbol{j}} &= \frac{2\pi^2\hbar^2}{mL^2}(j_x^2+j_y^2)+j_z\hbar\omega_z, & (1.38)\\ \psi_{\boldsymbol{j}}(\boldsymbol{r}) &= \frac{1}{L\sqrt{\ell_z}}\exp(i\frac{\pi j_x x}{L})\ \exp(i\frac{\pi j_y y}{L})\ \chi_{j_z}(\frac{z}{\ell_z}), & (1.39)\\ \text{with} &\quad j_x,\ j_y \in \mathbb{Z} \text{ and } j_z \in \mathbb{N}, & (1.40)\end{aligned}$$

where χ_j stands for the j-th Hermite function. The occupancy of state $\boldsymbol{j}$ is given by the Bose–Einstein factor $f(E_{\boldsymbol{j}})$ with f defined in Eq. 1.9 and we can compute direct summation over these energies states in a similar way as in Eqs. 1.10-1.12 to deduced the gas properties (see Annex A). We note that each 2D assembly of atoms corresponding to a given j_z is simply described by results of 1.1.3.1 while shifting the chemical potential μ by the energy of state j_z: $\mu^{(j_z)} = \mu - j_z\hbar\omega_z$. This enables to access any dimensionless gas parameter A whose 2D equation of state is known $A = f_A(\mu/k_BT)$ (using results of 1.1) via:

$$A = \sum_{j_z=0}^{\infty} f_A(\beta\mu - j_z\zeta) \tag{1.41}$$

If $L^2 \gg \pi\lambda_T^2$, the semi-classical limit applies in the xy plane and we transform the sum over $j_\rho \equiv (j_x, j_y)$ in an integral. For example the EoS for the total 2D PSD $\mathcal{D}_{\text{tot}}^{(2D)}$ is given by:

$$\begin{aligned} \mathcal{D}_{\text{tot}}^{(2D)} &= \sum_{j_z=0}^{+\infty} \mathcal{D}^{(2D)}(j_z) & (1.42)\\ \mathcal{D}^{(2D)}(j_z) &= -\ln\left(1 - Ze^{-j_z/\zeta}\right) & (1.43)\end{aligned}$$

For a gas in the deep thermally two-dimensional regime where $\zeta \ll 1$, only $j_z = 0$ contributes and we find back the previous results $\mathcal{D}^{(2D)} \approx -\ln(1-Z)$. In the opposite case where $\zeta \gg 1$, we can apply the semi-classical limit in the vertical direction also, and find:

$$\begin{aligned} \mathcal{D}_{\text{tot}}^{(2D)} &= -\int_0^{+\infty} \ln\left(1 - Ze^{-u/\zeta}\right)\ \mathrm{d}u & (1.44)\\ &= \sum_{n=1}^{+\infty}\int_0^{+\infty}\frac{Z^n}{n}e^{-nu/\zeta}\ \mathrm{d}u = \zeta\sum_{n=1}^{+\infty}\frac{Z^n}{n^2} = \zeta\, g_2(Z). & (1.45)\end{aligned}$$

where $g_\alpha(Z) = \sum_{n=1}^{+\infty} Z^n/n^\alpha$ is the polylogarithm of α order. In the intermediate regime $\zeta \gtrsim 1$, we must use the discrete summation of Eq. 1.42 to predict the EoS of the phase-space-density with μ/k_BT.

1.2.3. Transverse condensation phenomenon of a in-plane uniform gas in an oblate confinement

In this section, in order to investigate the transverse condensation phenomenon (BEC$_\perp$), we focus on the case $\zeta \gg 1$ where the semi-classical approximation is valid for all quantum number j_x, j_y and j_z. Then each corresponding discrete sum in Eq. 1.12 can be approximated by the integrals of Eqs. 1.11 and 1.44.

1.2.3.1. Saturation of z excitation populations and transverse condensation phenomenon.

In this case of $\zeta \gg 1$, the 2D PSD is given by Eq. 1.45 which results in

$$\mathcal{D}^{(2D)} \quad = \quad \zeta\, g_2(Z). \tag{1.46}$$

Since $Z<1$ and $g_2(Z)$ remains finite when $Z \to 1$ [$g_2(1) = \pi^2/6$], this semi-classical approximation leads to the paradoxical result that for a given ζ, the total 2D phase-space-density is bounded from above by $\zeta\pi^2/6$. The paradox is lifted by noticing that when the fugacity Z approaches 1, the population of the lowest vibrational state $|j_z = 0\rangle$ is not properly accounted for when one replaces the discrete sum in Eq. 1.42 by the integral Eq. 1.44. More precisely within this semi-classical approximation, when the total phase-space-density approaches the value $\zeta\pi^2/6$, the result above must be replaced by

$$\mathcal{D}^{(2D)}_{\text{tot}} = \mathcal{D}^{(2D)}_{0} + \mathcal{D}^{(2D)}_{\text{exc}} \tag{1.47}$$

$$\text{with, for } Z \approx 1: \qquad \mathcal{D}^{(2D)}_{0} = -\ln(1-Z), \qquad \mathcal{D}^{(2D)}_{\text{exc}} = \zeta\,\pi^2/6. \tag{1.48}$$

Therefore, when the total phase-space-density $\mathcal{D}^{(2D)}_{\text{tot}}$ is significantly larger than $\zeta\,\pi^2/6$, the phase-space-density $\mathcal{D}^{(2D)}_{\text{exc}}$ saturates and additional atoms accumulate essentially in the $j_z = 0$ state. This is the **transverse condensation phenomenon** (BEC$_\perp$) [129].

In the case of an infinite box ($L \to \infty$), only accumulation in the ground state of the z motion $j_z = 0$ is expected and no true 3D BEC occurs. Indeed, once BEC$_\perp$ takes place, conclusion of 1.1.3.1 for a infinite 2D gas holds and no condensate fraction can arise for the xy motion. In the case of a finite system however, the same reasoning leads to a two-step condensation. The gas first reaches reduced dimensionality regime via BEC$_\perp$ and then condenses in this reduced dimensionality system (BEC$_{\text{full}}$) to the overall 3D ground state as result of finite-size effects (as described in 1.1.3.1). Hence BEC$_{\text{full}}$ occurs when 2D phase density of $j_z = 0$ state reaches the critical value $\mathcal{D}^{(2D)}_{0,\text{BEC}_{\text{full}}}$ given by Eq. 1.23. Then the two condensation phenomena, BEC$_\perp$ and BEC$_{\text{full}}$, can be distinguished when the values of $\mathcal{D}^{(2D)}_{0}$ at which they occur are (clearly) separated: $\mathcal{D}^{(2D)}_{0,\text{BEC}_\perp} \ll \mathcal{D}^{(2D)}_{0,\text{BEC}_{\text{full}}}$. We intuitively understand that this will be the case for an anisotropic enough trap with $\ell_z \ll L$. We will give in following section 1.2.3.2, a quantitative analysis of this separation of the 2 steps of condensation.

In Fig. 1.1, we show the evolution of $\mathcal{D}^{(2D)}_{\text{exc}}$ and $\mathcal{D}^{(2D)}_{0}$ with $\mathcal{D}^{(2D)}_{\text{tot}}$ in the case of a finite square box (see Annex A for calculation principle) of size L chosen [10] at $L = 200\,\lambda_{\text{T}}$ while ℓ_z is given by $\ell_z = \sqrt{\zeta/2\pi}\ \lambda_{\text{T}}$. Our calculations are made for $\zeta \leq 20$ which corresponds to a minimal anisotropy factor $L/\ell_z \geq 112$.

---

[10] In this case, $\mathcal{D}^{(2D)}_{0,\text{BEC}_{\text{full}}} \approx 9.5$ and we have restricted our analysis to the domain of parameters such that $\mathcal{D}^{(2D)}_{0} \lesssim 9$, in order to avoid the regime dominated by finite-size effects.

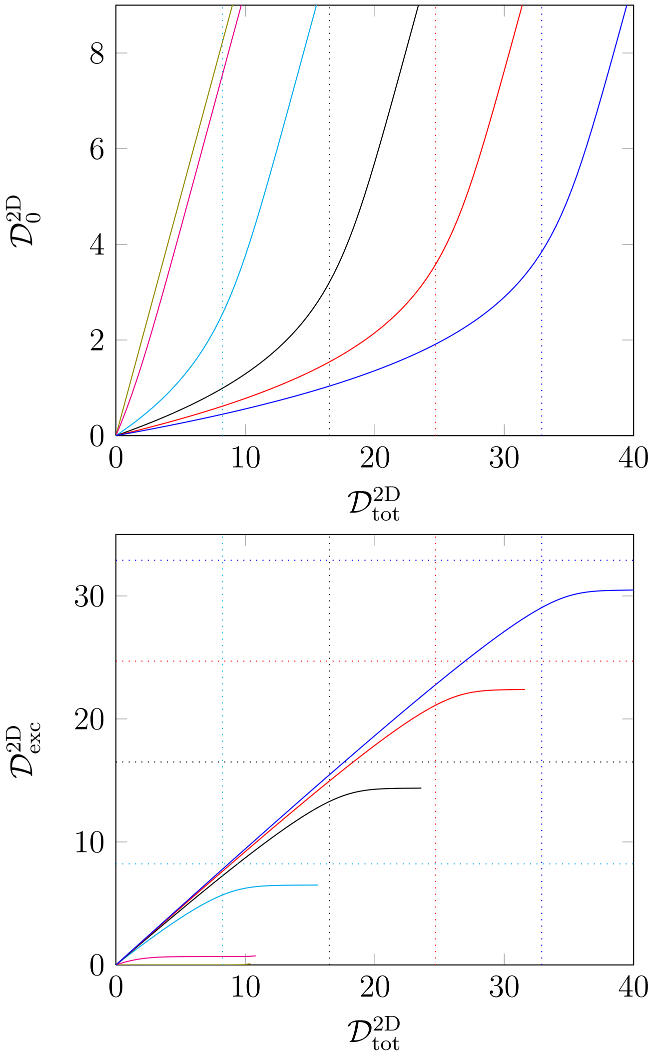

Figure 1.1.: *Top: Variations of the 2D phase-space-density in the* $|j_z = 0\rangle$ *ground state of the* z *motion with the total 2D phase space-density* $\mathcal{D}_{\mathrm{tot}}^{\mathrm{2D}}$. *Bottom: Variations of the phase-space-density of the excited states of the* z *motion with* $\mathcal{D}_{\mathrm{tot}}^{(2D)}$. *The calculation is made for an ideal gas confined in a square box with periodic boundary conditions in the* xy *plane, with a size* $L = 200\,\lambda_{\mathrm{T}}$. *The values of* ζ *are: 0.1 (olive), 1 (magenta), 5 (cyan), 10 (black), 15 (red), 20 (blue). The dotted lines indicate the critical phase-space-density* $\zeta\,\pi^2/6$ *(same color code). For large* $\mathcal{D}_{\mathrm{tot}}^{(2D)}$, *all* $\mathcal{D}_0^{(2D)}$ *tend to parallel linear behavior corresponding to a slope* $\mathcal{D}_{\mathrm{tot}}^{(2D)}/\mathcal{D}_0^{(2D)} = 1$. *For* $\zeta \leq 1$ *we do not notice any significant modification from this linear behavior. For* $\zeta > 1$, *we point out that the change in curvature in* $\mathcal{D}_0^{(2D)}$ *coincides with the saturation of* $\mathcal{D}_{\mathrm{exc}}^{(2D)}$ *when* $\mathcal{D}_{\mathrm{tot}}^{(2D)}$ *is close to the predicted critical value of* $\zeta\,\pi^2/6$.

1.2.3.2. Population of z ground-state at transverse condensation point

Let us estimate the 2D phase-space-density associated to the ground state of the z-motion when the threshold for transverse condensation

$$\mathcal{D}^{(2D)}_{\text{tot,BEC}_\perp} = \zeta\, \pi^2/6 \tag{1.49}$$

is reached. Transverse condensation occurs when the population of the $j_z = 0$ state is significantly different from that of $j_z = 1$, so that it cannot be accounted for properly by the integral Eq. 1.44. At this moment the chemical potential is on the order of $-\hbar\omega_z$ and then $Z \sim e^{-1/\zeta}$. Then, from Eq. 1.48, we predict $\mathcal{D}^{(2D)}_{0,\text{BEC}_\perp} = -\ln(1-Z) \sim \ln(\zeta)$. More precisely, a numerical calculation using full quantum 3D computation of Annex A gives at the transverse condensation point

$$\mathcal{D}^{(2D)}_{0,\text{BEC}_\perp} \approx \ln(\zeta) + 0.9. \tag{1.50}$$

for ζ between 5 and 20 (see Table 1).

ζ	$\mathcal{D}^{(2D)}_{\text{tot,c}}$	Z	$\mathcal{D}^{\text{2D}}_0$	$r_{1/20}/\lambda_T$	ℓ'_c/λ_T	ℓ'_c/ℓ_z
5	8.2	0.921	2.5	2.2	0.80	0.90
10	16.5	0.959	3.2	2.6	1.07	0.85
15	24.7	0.972	3.6	2.9	1.27	0.82
20	32.9	0.979	3.8	3.1	1.43	0.80

Table 1.1.: Values of relevant parameters at the point where BEC$_\perp$ occurs. The parameters are calculated numerically using a finite box of $L = 200\lambda_\text{T}$ and following lines of Annex A. The correlation length is calculated along lines of 1.2.3.4.

The condition for distinguishing BEC$_\perp$ from the full condensation phenomenon BEC$_\text{full}$ is that $\mathcal{D}^{(2D)}_{0,\text{BEC}_\perp} \ll \mathcal{D}^{(2D)}_{0,\text{BEC}_\text{full}}$. $\mathcal{D}^{(2D)}_{0,\text{BEC}_\perp}$ is given in Eq. 1.50 while $\mathcal{D}^{(2D)}_{0,\text{BEC}_\text{full}}$ is given by Eq. 1.23 as BEC$_\text{full}$ occurs when 2D phase density of $j_z = 0$ state reaches the critical value obtained for the deep 2D regime in 1.1.3.1. Then owing $\ell_z^2/\lambda_T^2 = \zeta/2\pi$:

$$\mathcal{D}^{(2D)}_{0,\text{BEC}_\text{full}} \approx \ln(0.4\frac{L^2}{\lambda_\text{T}^2}) = \mathcal{D}^{(2D)}_{0,\text{BEC}_\perp} + 2\ln(0.16\frac{L}{\ell_z}). \tag{1.51}$$

The 2 step condensation picture is then valid for:

$$2\ln(0.16L/\ell_z) \gg 1 \;\Rightarrow\; L \gg 10 \times \ell_z \tag{1.52}$$

1.2.3.3. Link to 3D Bose–Einstein condensation phenomenon

A similar calculation as Eqs 1.42-1.46 gives the value of the 3D phase-space-density $\mathcal{D}^{(3D)}_\text{tot} \equiv n^\text{3D}_\text{tot}(0)\lambda_\text{T}^3$ in the center $\boldsymbol{r} = 0$. Indeed using the general expression of Eq. 1.12

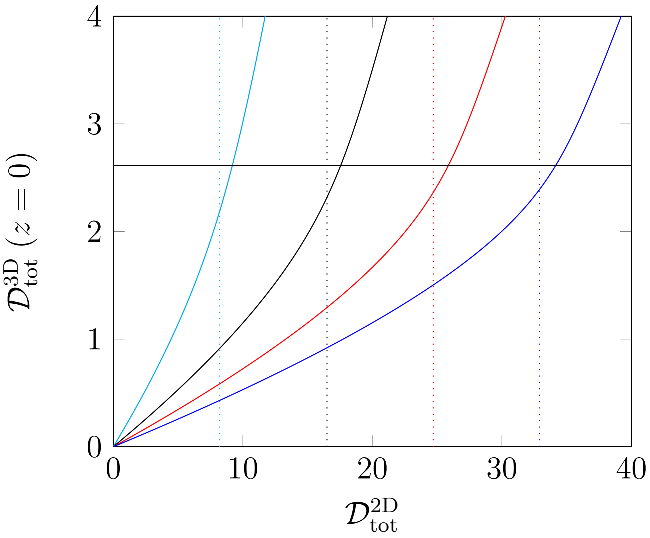

Figure 1.2.: Total 3D phase-space-density in the plane $z = 0$, as a function of the total 2D phase-space-density (same color code as in Fig. 1.1). These quantities are here deduced for a full quantum treatment of ideal Bose law taking $L = 200\lambda_T$. The horizontal line corresponds to $\mathcal{D}^{(3D)}_{\rm tot}(z = 0) = 2.612$, which is the predicted threshold for BEC$_\perp$. We notice a change in curvature at $\mathcal{D}^{(3D)}_{\rm tot} \approx 2.612$. We note a slight discrepancy between the crossing of $\mathcal{D}^{(2D)}_{\rm tot}(z = 0) = \zeta\pi^2/6$ (dotted lines) and $\mathcal{D}^{(3D)}_{\rm tot}(z = 0) = 2.612$ for each of the curves – the latter occurring at higher $\mathcal{D}^{(2D)}_{\rm tot}$.

for $\hat{A} = N\psi^\dagger(\boldsymbol{r})\psi(\boldsymbol{r})$, we find:

$$n^{\rm 3D}_{\rm tot}(\boldsymbol{r}) = \sum_{j_z=0}^{\infty}\sum_{j_x,j_y=1}^{\infty} f(E_j)|\psi_j(\boldsymbol{r})|^2 \tag{1.53}$$

where E_j and $\psi_j(\boldsymbol{r})$ are given in Eqs. 1.38-1.39. We deduce in the semi-classical limit:

$$\mathcal{D}^{(3D)}_{\rm tot} = -\sqrt{\frac{2\pi}{\zeta}}\sum_{j_z=0}^{+\infty}|\chi_{j_z}(0)|^2 \ln\left(1 - Ze^{-j_z/\zeta}\right) \approx g_{3/2}(Z). \tag{1.54}$$

For the last step of the calculation we used the asymptotic result for the value of the Hermite functions in $z = 0$: $|\chi_j(0)|^2 \approx (\pi\sqrt{j})^{-1}$, and we replaced the sum over j_z by an integral (semi-classical approximation). We reach here again a paradoxical result: since $g_{3/2}(1)$ is finite, the 3D total density seems to be bounded. As above, the solution to the paradox is that the semi-classical treatment does not properly account for the population of the $j_z = 0$ state when Z approaches 1. More precisely, above the transverse condensation threshold, one has

$$\mathcal{D}^{(3D)}_{\rm tot} = \mathcal{D}^{(3D)}_0 + \mathcal{D}^{(3D)}_{\rm exc.} \tag{1.55}$$

$$\text{with, for } Z \approx 1: \qquad \mathcal{D}_0^{(3D)} = -\sqrt{2/\zeta}\ \ln(1-Z), \qquad \mathcal{D}_{\mathrm{exc}}^{(3D)} \approx g_{3/2}(1) = 2.612, \tag{1.56}$$

whereas $\mathcal{D}_0^{(3D)} \ll \mathcal{D}_{\mathrm{tot}}^{(3D)}$ and $\mathcal{D}_{\mathrm{exc}}^{(3D)} \approx \mathcal{D}_{\mathrm{tot}}^{3\mathrm{D}} \approx g_{3/2}(Z)$ below the threshold for BEC$_\perp$ if $\zeta \gg 1$. Evolution of $\mathcal{D}_{\mathrm{tot}}^{(3D)}$ is plotted in Fig. 1.2 versus $\mathcal{D}_{\mathrm{tot}}^{(2D)}$.

In other words, transverse condensation occurs when the central 3D phase-space density approaches the value 2.612, which corresponds to the point where full BEC occurs in a weakly anisotropic[11] gas $\ell_z \sim L$. Here due to the strong anisotropy, full condensation does not occur at this point but only a partial one that results in projecting the gas in a lower dimensional state. Then the gas is governed by the specific physics arising in this reduced dimension space, possibly leading to prediction of other phase transition(s) at $\mathcal{D}_0^{(2D)} > \mathcal{D}_{0,\mathrm{BEC}_\perp}^{(2D)}$, following specific theory of the reduced dimensionality (presented in 1.1 in our case).

1.2.3.4. Influence of transverse condensation on in-plane coherence

As the BEC$_\perp$ phenomenon leads to the establishment of 2D physics for which a majority of atoms populates the ground state of z-motion, the coherence length ℓ_c in the xy plane is also affected following results of 1.1.3.1. A rough estimate for ℓ_c is obtained by plugging the approximate value $\mathcal{D}_0^{(2D)} \sim \ln\zeta$ into the expression for the coherence length of a 2D gas in the degenerate regime of Eq. 1.22, which gives

$$\ell_\mathrm{c} \approx \lambda_\mathrm{T}\sqrt{\zeta/4\pi} = \ell_z/\sqrt{2}, \tag{1.57}$$

A more precise estimate is given in Table 1.1 for the relevant range of values for ζ and using a full quantum 3D treatment as explained in Annex A for $L = 200\lambda_\mathrm{T}$. To obtain these results, we computed numerically the variations of the one-body correlation function $g_1(\boldsymbol{r})$ for $\boldsymbol{r}$ in the xy plane, and we looked for the wings of this function. More precisely we considered the point $r_{1/20}$ where the function g_1 is divided by 20 with respect to its value in $r = 0$. At this point we define ℓ'_c as

$$\frac{1}{\ell'_\mathrm{c}} = -\left.\frac{\mathrm{d}\ln[g_1(r)]}{\mathrm{d}r}\right|_{r=r_{1/20}}. \tag{1.58}$$

If g_1 had an exponential variation for all r, this quantity would take the same value independently of the location r where it is calculated and $\ell_\mathrm{c} = \ell'_\mathrm{c}$. For a non-strictly exponential g_1, the present definition is a good compromise between considering the far wings of g_1 in order to monitor the appearance of an extended coherence, and restricting to sufficiently small values of r so that the values of g_1 are still significant. The variation of $\ell'_\mathrm{c}/\lambda_\mathrm{T}$ with $\mathcal{D}_{\mathrm{tot}}^{(3D)}$ for various values of ζ is shown in Fig. 1.3.

For Boltzmann statistics, $g_1(\boldsymbol{\rho}) \propto e^{-\pi\rho^2/\lambda_\mathrm{T}^2}$ and $\ell_\mathrm{c}'^{th} = 0.16\,\lambda_\mathrm{T}$. We see in table 1.1 that at BEC$_\perp$, the value of ℓ'_c is increased by a factor $6-9$ for $\zeta = 10-20$ with respect to ℓ_c^{th}. More precisely the result of Eq. 1.57 states that at the threshold for BEC$_\perp$, the coherence

---

[11] It is also the threshold for an infinite uniform 3D gas.

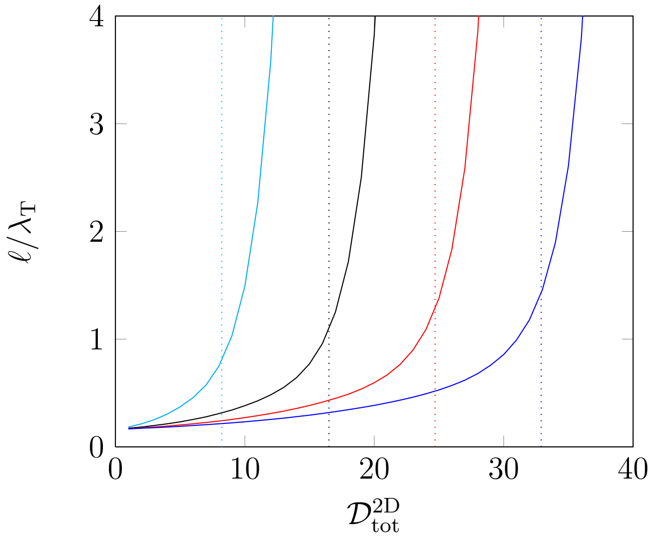

Figure 1.3.: *Variations of the coherence length ℓ_c' defined in Eq. 1.58 with the total 2D phase-space-density (same color code as in Fig. 1.1).*

length in the xy plane is comparable to the size of the ground state along the z direction. The physical meaning of Eq. 1.57 is related to the fact that the 3D phase-space-density in the plane $z = 0$ reaches the value 2.612 when BEC$_\perp$ occurs. For a uniform, infinite 3D gas with this spatial density, the coherence length ℓ_c would diverge, signaling the occurrence of a true Bose–Einstein condensation. Here the z-confinement limits the extension of the coherent part of the gas along z to ℓ_z, which prevents the divergence of ℓ_c and limits its value also to ℓ_z in the xy plane. In the regime $\zeta \gg 1$, the appearance of a large coherence length in the xy plane and the occurrence of transverse condensation for the z degree of freedom are thus linked.

1.3. Conclusion

In this chapter, we presented the main theoretical ingredients of the physics of a two-dimensional Bose gas. In the case of perfectly 2D atomic samples, we detailed the occurrence of Bose–Einstein condensation BEC$_{\text{full}}$ to the 2D atomic ground state for an ideal (*i.e.* non-interacting) gas, both in an harmonic trap and in a finite uniform box, while in an infinite uniform 2D gas condensation is fundamentally absent at non zero temperature due to the general argument of Mermin Wagner. We also pointed some modifications of the thermodynamics properties of the gas due to the presence of interactions between the particles. We quoted in particular the appearance of a transition of a novel kind, described by the Berezinskii-Kostlerlitz-Thouless mechanism. A second point in this chapter is to highlight the relevance of this 2D physics in our 3D world by presenting a regime of confining configurations (the «deep thermal 2D regime») where the 2D description applies. We then pointed out some corrections due to the non perfect realization of this regime. Finally, we presented a specific way to reach the 2D regime, linked to the BEC phenomenon in a strongly oblate uniform confinement. In this case the BEC phenomenon does not occur fully (in one step) but divides in two steps, separated in phase space densities, due to the strong anisotropy of the confinement. First the condensation occurs in the tighter direction so that a reduced dimensionality physics is established in the remaining gas. Then low dimensionality (2D in our case) applies and leads to a full condensation along the lines precised above. We note that this two step condensation is fundamentally linked to the assumption of a uniform trapping in the 2D plane as it necessitates that BEC does not hold in the thermodynamic limit for the considered 2D trap.

In the following parts of this manuscript we will present experimental investigations of the different properties highlighted here. A first part of this manuscript (Chapters 4 and 5) will be devoted to the study of harmonic 2D gases. In this geometry, we will study the interacting 2D gases physics. We will link back the obtained results to the uniform case using LDA. In a second part of the manuscript, we will present results directly obtained in a uniform trapping geometry (Chapters 7 and 8). In this case, we will investigate the specific transverse condensation phenomenon, in particular via its consequence on the in-plane coherence of the atomic sample. Before presenting our results, we will detail the experimental setup that we have built to investigate the specific regime of the (quasi-)two dimensional gases.

2. Experimental methods for producing two–dimensional Bose gases

Since the experimental apparatus used to produce the results presented in this thesis has been running for several years, the main part of the setup has been built by previous PhD students. A detailed description of the various setup elements and their evolution can be found in their successive manuscripts [107–111].

In this chapter, I will present the main line of the production of two–dimensional degenerate Bose gases, highlighting the improvements realized during the three years I spent on the experiment. I will first quickly described the line followed for producing a tri–dimensional Bose–Einstein Condensate (3D BEC). I will then insist on the specific operations we developed and used during the last year of my PhD to study uniform 2D Bose gases. The specificity of the production scheme for the necessary flat bottom potential will be addressed in a following chapter (Ch. 6).

In the second part of this chapter, I will more precisely focus on the experimental realization of the 2D–trapping. I will first characterize the in–place setup whose parameters were slightly modified since last overview [111]. I will point out the limitations of such a realization especially in the prospect of creating uniform Bose gases. These stems from the residual horizontal potential created by the beam which is mainly used to create the tight trapping along the vertical direction. I will then present preliminary test on a new and advantageous setup for producing strong confinement in one direction. Such a new optical setup will soon be implemented on the experiment.

2.1. Experimental setup

Here I will describe our specific implementation of a cold atom experiment to study the physics of the 2D Bose gas and produce the experimental results reported in this manuscript.

2.1.1. Overall description of the experimental setup

As in any cold atoms experiment our setup consists of a vacuum system in which we can trap and cool atomic sample at the nano-Kelvin scale. The specificity of our own setup is that it is constituted of two separated chambers with two different vacuum pressures:

- a steel «MOT chamber» with moderate vacuum in which we trap a sample of ^{87}Rb atoms from the background vapor and perform preliminary cooling on it.
- a glass «science cell», in which cooling is carried further to reach degeneracy and in which the 2D gas is produced and studied.

These two chambers are linked by a differential pumping stage along which atoms are magnetically transported. To reach the desired regime of degenerate 2D Bose gas within this global setup, a sequence of tens of events mainly consisting in modifying either the strength of the magnetic fields or the intensity of the optical beams is necessary. These are controlled and synchronized at the microsecond scale. The control is realized via a computer based program developed in MIT by Aviv Keshet [130] communicating with nine analog or digital National Instruments cards and two GPIB devices.

These tens of unit events can be decomposed in typically ten global phases. I will describe them, distinguishing the creation of a 3D BEC and the further study of a 2D degenerate Bose gas.

2.1.2. Experimental sequence toward tri–dimensional Bose–Einstein Condensation

First, I will recall the specific sequence leading to condensation of an atomic sample in our specific scheme. Until 2012, we were using a magnetic *Time Orbiting Potential* (TOP) trap that I will not describe here (for a description of this previous implementation, see [109, 110]). We are now using an *hybrid* magnetic and optical trap as implemented in [131] and [132]. The basic principle of the new procedure was presented in [111] so I will mainly report on the experimental parameters currently in use. Such a sequence can be divided in five phases:

1. **MOT and loading of the first magnetic trap** (8.5 s)
   This phase is constituted of all the events occurring in the first «MOT chamber». We load a magneto-optical trap from a background ^{87}Rb vapor in 8 s. The loading time constant of this trap is typically of 2s for our setup and we typically trap 1×10^{10} atoms in this first step. We then lower the magnetic gradients while shifting the MOT laser to higher detuning and reducing the power of the repumping beam to further cool this set of atoms. The resulting temperature at the end of this stage is typically of $T = 200\,\mu K$. We then use a step of optical molasses in which we switch off the magnetic gradient to reach $T = 100\,\mu K$. The atoms are then optically pumped into the internal state $|\,F = 2, m_F = 2\,\rangle$ before being transferred to a first quadrupole trap with magnetic gradient $b'_z = 140\,\mathrm{G/cm}$. In this trap, we manage to collect 5×10^9 atoms, at $T = 450\,\mu K$ that we want to transfer to the science cell before being limited by cloud lifetime. This short lifetime of 1.2s results from the collisions between the trapped atoms and the background vapor. In the current setup, the quality of the vacuum in this chamber is maintained via two cooling Peltier setups (commonly named «cold fingers»).
2. **Magnetic transport (6 s)**
   We transport the atoms over a 50 cm distance, from the «MOT chamber» to the «science cell», using a series of nine pairs of coils in which we accurately control the currents [107, 133]. The resulting smooth displacement of the trap center is set to be nearly adiabatic. The main source of heating is the limited lifetime in the «MOT chamber». We thus impose a fast initial acceleration to leave quickly the collision area and reach a region with better vacuum. The first steps of the

transport constitute the limiting factor to the overall transfer efficiency. They induce losses and heating as shown by round trip transport measurements [1]. At the end of this transport stage, we load a second quadrupole trap in the science cell with $b'_z = 90\,\mathrm{G/cm}$. In this trap we can characterize our cloud using horizontal absorption imaging in the high intensity regime (cf. 3.2.1) and with magnification $\mathcal{M} = 1$. We measure $N \sim 10^9$ atoms and $T \sim 150\,\mu K$ after compressing the cloud to a upper gradient of $b'_z = 140\,\mathrm{G/cm}$ in order to increase the collision rate.

3. **Radio-frequency evaporation in the quadrupole trap (16 s)**
   To further enhance the collision rate and the phase-space-density before loading the 3D hybrid trap, we then evaporatively cool the gas in this magnetic trap. We apply a radio–frequency (RF) pulse that induces transitions between different Zeeman sub–states at a given distance of the zero–field trap center. The frequency of this RF is then ramped linearly from 30 MHz to 3 MHz. In a quadrupole trap the evaporation is limited by Majorana spin-flips due to the cancelation of the magnetic field at the trap center and thus this technique is not sufficient to reach degeneracy. The value of the final frequency results from a compromise between a cloud cold enough so that it is efficiently loaded into the later used dipole trap and a not too cold one to prevent Majorana spin flips. At the end of this phase the atom number is reduced to $N \sim 2 \times 10^8$ atoms and the temperature to $T \sim 30\,\mu K$.

4. **Loading the hybrid trap (2.5 s)**
   In order to circumvent Majorana losses and push evaporation further down to reach degeneracy, we choose to add a red-detuned optical dipole trap to the quadrupole gradient, as implemented in [131] and [132]. In our case, such a dipole trap is created by a laser beam at 1064 nm wavelength with a waist $w_h = 50\,\mu\mathrm{m}$ and a maximal power $P_h^{\max} = 8.4\,\mathrm{W}$. We set its propagation along the horizontal x axis. We should note that its Rayleigh length along x is large – $x_R = 7.4\,\mathrm{mm}$ – so the confinement along the beam propagation direction results only from the remaining magnetic gradient b'_x (In our coil configuration, $b'_x = b'_z/2$). The dipole beam is switched on at the loading power $P_h^{\mathrm{load}} = 6.7\,\mathrm{W}$ at the beginning of the experimental sequence. We load this optical trap from the magnetic one, by lowering the magnetic gradient to a small but non–zero value, so that the atoms drop into the additional trap where they are still magnetically confined in the x direction. We choose to lower the magnetic gradient down to $b'_z = 12.5\,\mathrm{G/cm}$ which is below the gravity-equivalent gradient $b_z'^{mag} = mg/\mu = 15.4\,\mathrm{G/cm}$ for atoms in $|\, F = 2, m_F = 2\,\rangle$ state. The beam center in the yz plane is set to be vertically below the quadrupole trap center at a distance d_z^{load}. We optimized the position of the zero of the magnetic field in terms of the number of atoms transferred in the hybrid trap so that $d_z^{\mathrm{load}} \approx 100\,\mu\mathrm{m}$. The loading is performed in 2 s and the

---

[1] We cannot directly image the cloud during transport, then to image the gas we needed it to be in either the MOT chamber or the science cell. In the round trip measurements, we image the atomic sample coming back in the MOT Chamber after the desired number of transport steps (in total there are eleven steps). The back transport steps are simply defined by reversing the time dependency of the currents used in the corresponding forth step (of course time reversal is also applied for defining steps order). We should note that such a simple definition can create additional heating especially for the first steps due to abrupt change in center of mass velocity and acceleration at the reversing point.

remaining atomic ensemble contains 7×10^7 atoms at a temperature $T = 10.5\,\mu K$. We can quantitatively describe the trapping potential in this hybrid trap:

$$\begin{aligned} V_{\text{hybrid}}(x,y,z) &= V_{\text{mag}}(x,y,z) + V_{\text{dip}}(y,z) - mgz & (2.1)\\ \text{where } V_{\text{mag}}(x,y,z) &= \mu b'_z \sqrt{(z+d_z)^2 + \frac{x^2+y^2}{4}} & (2.2)\\ V_{\text{dip}}(y,z) &= \mathcal{U}_{\text{H}} \exp\left(-2\frac{y^2+z^2}{w^2}\right). & (2.3) \end{aligned}$$

$\mathcal{U}_{\text{H}}$ is the trap depth due to the dipolar force $\mathcal{U}_{\text{H}} = \alpha \times P_h/(\pi w^2)$ (P_h stands for the dipole beam power). α is deduced from the general expression of the dipolar force for our parameters, taking into account the beyond *Rotating Wave Approximation* term and neglecting thedetuning difference to the fine structure: $\alpha = -\frac{3\pi c^2}{2\omega_0^3}\left(\frac{\Gamma}{\omega_0-\omega} + \frac{\Gamma}{\omega_0-\omega}\right)$. ω is the laser pulsation $\omega = 2\pi \times 2.82 \times 10^{14}\,\text{Hz}$, ω_0 is the mean value of the atomic pulsation $\omega_0 = \omega_{D_1}/3 + 2\omega_{D_2}/3 = 2\pi \times 3.80 \times 10^{14}\,\text{Hz}$ (taking into account Clebsch–Gordan coefficients) and Γ the mean natural width $\Gamma = \Gamma_{D_1}/3 + 2\Gamma_{D_2}/3 = 2\pi \times 5.97 \times 10^6\,\text{Hz}$. We deduce $\alpha = -k_{\text{B}} \times 157\,\text{mK}\,\mu\text{m}^2/\text{W}$ and so $\mathcal{U}_{\text{H}}/P_h = -k_{\text{B}} \times 20\,\mu\text{K}/\text{ W}$. The loading trapping depth is so $\mathcal{U}_{\text{H}}^{\text{load}} = -k_{\text{B}} \times 134\,\mu K$

In Eq. 2.1, the coordinates origin is taken to be the center (in yz) and focus location (in x) of the dipole beam. We set the zero of the magnetic field to be centered in the horizontal directions x and y on the cloud[2]. Then a polynomial approximation of Eq. 2.1 gives the trapping frequencies:

$$\begin{aligned} \omega_y^{\text{hybrid}} = \omega_z^{\text{hybrid}} &\approx \sqrt{\frac{4\mathcal{U}_{\text{H}}}{mw^2}} & (2.4)\\ \omega_x^{\text{hybrid}} &= \sqrt{\frac{\mu b'_z}{4md_z}} & (2.5) \end{aligned}$$

ω_y^{hybrid} and ω_z^{hybrid} are dominated by dipolar potential effect. They vary from several hundreds at loading to several tens of Hz after optical evaporation (see next item). Along the beam propagation, ω_x^{hybrid} is dominated by the magnetic potential and is typically of a few tens of Hz for the considered d_z (also varying during optical evaporation). At loading, the frequencies are summarized in Table 2.1.

5. **Optical evaporation in the hybrid trap** (13 s)
Once the hybrid trap is loaded, the collision rate is enhanced by a tighter trapping, Majorana losses are bypassed and now evaporation can be pushed further down. Here, we use optical evaporation in the dipole trap, simply lowering the beam power to P_h^{evap}. P_h^{evap} may vary from the initial value of $P_h^{\text{load}} = 6.7\,\text{W}$ to our laser seed power[3] $P^{\text{seed}} \approx 40\,\text{mW}$. We performed the evaporation in $t_{\text{evap}}^h = 13\,\text{s}$ and

---

[2] this is automatically true for the x direction as it is magnetically trapped but it needs to be aligned in y direction

[3] Our laser is a fiber laser from *Azur Light System* with a fully integrated servo control of the power. It

Axis i	ω_i^{hybrid}
x	$2\pi \times 22.5\,\text{Hz}$
y	$2\pi \times 719\,\text{Hz}$
z	$2\pi \times 719\,\text{Hz}$

Table 2.1.: Summary of all trapping frequency at the loading of the hybrid trap ($P^{\text{load}} = 6.7\,\text{W}$).

reach degeneracy for $P_h^* \approx 76\,\text{mW}$.

The value of d_z^{load} reveals insufficient to fully prevent Majorana losses as the magnetic field at the cloud center is only $b_z' d_z^{\text{load}} = 0.125\text{G}$. It is thus compulsory to displace the zero of the magnetic field to a greater distance from the dipole trap center $d_z^{\text{evap}} > d_z^{\text{load}}$ before performing the evaporation ramp. It is also important not to increase d_z too much as it results in a decompression of ω_x^{hybrid}, which unwantedly decreases the collision rate. d_z is optimized on the final BEC to the highest condensate fraction and is set to $d_z^{\text{evap}} \approx 300\,\mu\text{m}$. Typical trapping frequencies at the end of the evaporation ramp (up to the condensation threshold $P_h^{\text{evap}} = P_h^*$) are given in Table 2.2. The ramping slope is set to be exponential with time constant $\tau = 0.125 \times t_{\text{evap}}^h$. We can select P_h^{evap} to tune the final T and N of the 3D cloud and thus vary the resulting 2D cloud configuration.

Axis i	ω_i^{hybrid}
x	$2\pi \times 13\,\text{Hz}$
y	$2\pi \times 76\,\text{Hz}$
z	$2\pi \times 76\,\text{Hz}$

Table 2.2.: Summary of all trapping frequencies in the hybrid trap obtained from Eq. 2.5 at the end of the optical evaporation ramp to laser power $P_{evap}^* \approx 76\,\text{mW}$ at which degeneracy is reached. There $d_z = d_z^{\text{evap}} \approx 300\,\mu\text{m}$

2.1.3. Experimental sequence from 3D BEC to the study of two–dimensional gases

At the end of these five first experimental stages, we reach 3D degeneracy in typically 46 s. In our experiment, we want to study 2D physics. In this aim, we need to change the trapping configuration of our cloud for it to enter a 2D (or quasi-2D) regime (see 1.1.2). We must care about implementing such changes in an efficient way so that the 2D cloud created covers interesting physical regimes. In this section, I will describe the experimental phases necessary to create and to study clouds confined in a uniform 2D geometry. I will present the specific shaping of the trapping beams in other parts of the manuscript (section 2.2 and Ch. 6).The evolution of the various beam powers of the 2D and 3D traps as well as of the magnetic gradient are schematized in Fig. 2.1.

---

is based on the amplification of a seed power. For varying the power at the output of the laser, only the amplification is mastered. When the amplification is completely switch off, the remaining output is then the seed power that so constitutes the minimal power reachable.

1. **Transfer into the Hermite–Gauss and box–traps (1 s)**
   We start by ramping the power of the beam that creates the 2D tight confinement (along z); it is blue detuned compared to the atomic resonance line and shaped with a Hermite-Gauss profile (see 2.2 for a description of the beam shaping and the confinement induced). The beam propagates along x and its profile in the yz plane at the atom position consists of two bright lobes aligned along y such that the 2D cloud is trapped in between in a resulting tight vertical (z) harmonic confinement of pulsation ω_z. Due to its shape, we commonly name this beam the *«light-sheet»* (LS). The first loading step consists in ramping up the LS power to an intermediate power P_{LS}^{load} in 0.5 s, onto the BEC (we previously aligned the beam at the position of the 3D gas). Typically at P_{LS}^{load}, $\omega_z/2\pi = 300\,\text{Hz}$. During this loading, the initial 3D cloud is split into one central – horizontally spread and vertically tightly confined – component (the 2D cloud) and two possibly remaining side clouds above and below. Only the central part is of interest. This loading must not be too fast in order to circumvent important heating of the cloud and en-

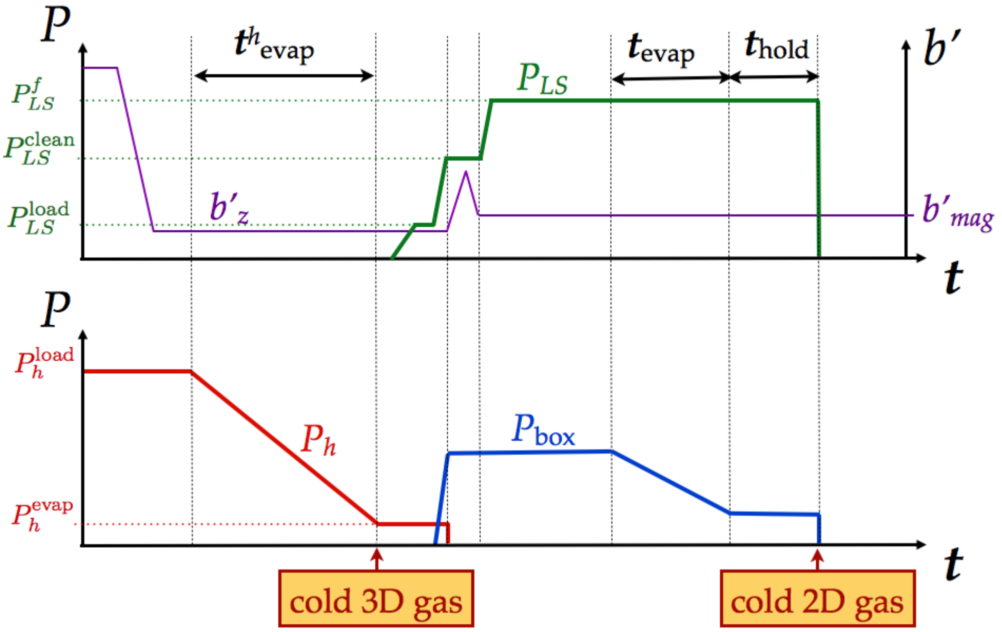

Figure 2.1.: Schematic representation of the evolution of (a, violet) the magnetic gradient b'_z (note that due to coil configuration $b'_x = b'_y = b'_z/2$), of the (b, red) power in the beam used in the hybrid trap P_h, of (a,green) the beam used to create the 2D (z) confinement P_{LS} and of (b,blue) the beam used to create the 2D in-plane (xy) uniform confinement P_{box}. Durations of the various steps and powers are not to scale. This scheme enable to visualize the order of the variations of these 4 variable along the experimental sequence. At the end of t^h_{evap}, we have achieved a 3D cold gas in the hybrid trap (2.1.2). We load this gas in the 2D trap by successive increases of P_{LS} and P_{box} (2.1.3). A 2D gas is achieved at the end of t_{evap}. The 2D experiment is achieved with a compensated gravity field $b'_z = b'_{\text{mag}}$.

abling a good loading efficiency in the 2D trap. This first step reveals indeed the most sensitive one in terms of losses and heating. This is also the reason why we choose to progressively increase the light sheet power all along the whole loading stage (see below).

After this initial step, we quickly (in 10 ms) ramp up an additional optical dipole trap propagating along z and that confines the atoms in a specific region of the 2D plane. It is created by a blue detuned laser beam presenting a dark region at its center (see Ch. 6 for a description of the beam shaping and the confinement induced). We commonly call this trapping potential the «*box–trap*».

In Fig. 2.2, we show the geometric arrangement of the various beams as well as the magnetic coils around the science cell.

After switching on the box–trap, we can switch off the hybrid trap previously used for 3D confinement. That is to say:

— we switch off the remaining power of the dipole trap. This is done thanks to a mechanical shutter as the seed of the laser cannot be switched off (see footnote 3).

— we change the magnetic gradients. We can then set b'_z and d_z to any convenient values b'^{2D}_z and d^{2D}_z as long as it does not result in a negligible confinement[4]. We choose b'_z so that it compensates the gravity field ($b'^{2D}_z = b'^{mag}_z$). We also set the magnetic zero further away from the atomic sample $d^{2D}_z = 1.5\,\mathrm{mm}$. As

---

[4] compared to the box confinement and the 2D cloud characteristic energies, namely the thermal energy $k_B T$ and the interaction energy per particle ϵ_{int}

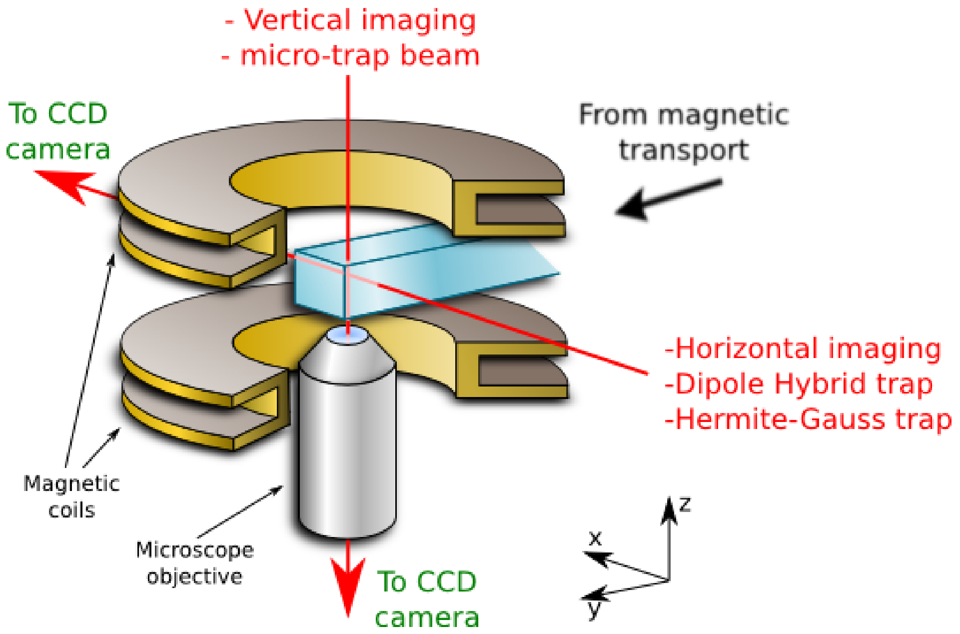

Figure 2.2.: Schematic representation of the science cell and its surroundings. red arrows represent the two used optical access to the atomic cloud in science cell and is stated in red the optical beams propagating on these axes. The coordinate trihedron give the latter used coordinates names.

described in Annex C, we choose the precise position of the magnetic zero in the xy plane so that the in–plane atomic distribution is uniform (the resulting magnetic gradient can compensate a residual curvature of the light sheet potential). The choice of a higher d_z enables a better control of the in-plane uniformity.

In the same time as we switch off the hybrid trap (in 150 ms), we ramp up the LS power to a higher intermediate power P_{LS}^{clean}. Typically at P_{LS}^{clean}, $\omega_z/2\pi = 1.1\,\text{kHz}$ and the trap depth along z is increased. At this stage, we get rid of the remaining atoms outside of the central 2D cloud, which are situated above it[5]. For this, we effectively reverse the gravity by applying a magnetic gradient $b_z'^{\text{clean}} > b_z'^{mag}$. Then the atoms feel the effective gravity potential

$$
\begin{aligned}
mg^{\text{eff}}z &= \mu b_z'^{\text{clean}}z - mgz & (2.6)\\
\Rightarrow g^{\text{eff}} &= g\frac{b_z'^{\text{clean}} - b_z'^{mag}}{b_z'^{mag}} \geq 0. & (2.7)
\end{aligned}
$$

We typically choose $b_z'^{\text{clean}} = 27.5\,\text{G/cm}$, so $g^{\text{eff}} = 7.7\,\text{m/s}^2$. We apply it during $\tau = 150\,\text{ms}$ before coming back to the levitating value of the magnetic field $b_z' = b_z'^{mag}$. Then the atoms initially located above the central cloud are accelerated upwards and they hit the upper face of the glass cell (situated at $\approx 7.5\,\text{mm} \ll g^{\text{eff}}\tau^2/2$ off the atoms). We note that increasing the energy barrier between the 2D cloud and the residual atoms by $P_{LS}^{\text{load}} \to P_{LS}^{\text{clean}}$ is essential to keep the atoms of the 2D cloud in place during the cleaning process.

2. **Final preparation of the 2D–cloud (2.15 s)**

   Once we have isolated our atomic plane and confined the atoms in the box–trap, we ramp the LS power to its final value P_{LS}^{f}. We can vary this value to set the vertical confinement frequency[6] at a value varying from $\omega_z/2\pi \sim 300\,\text{Hz}$ to $\omega_z/2\pi \sim 2\,\text{kHz}$.

   Finally, we can evaporatively cool the gas in the box–trap by lowering the power of the corresponding beam. We typically divide this power by 1.25 to 50 in $t_{\text{evap}} = 2\,\text{s}$ by applying a linear ramp. We ultimately let the cloud equilibrate for typically $t_{\text{hold}} = 500\,\text{ms}$. During this whole stage, we keep the magnetic gradient at a constant value, compensating the gravitation: $b_z' = b_z'^{mag} = mg/\mu_{\text{B}}$. We can estimate the resulting trapping potential from the magnetic gradients. Due to the coil geometry, $b_x' = b_y' = b_\perp' = b_z'/2$. The potential at distance $\boldsymbol{r} = \boldsymbol{\rho} + d_z\boldsymbol{u}_z$ for the magnetic zero is

$$V_{\text{mag}}(\boldsymbol{r}) = \mu\left[(b_z'd_z)^2 + b_\perp'^2\boldsymbol{\rho}^2\right]^{1/2} \tag{2.8}$$

   As the cloud center matches $\boldsymbol{\rho} = 0$ and $d_z = d_z^{2D} = 1.5\,\text{mm}$ we deduce that for all

---

[5] Usually the atom populating the symmetric lobe, below the central plane were expelled due to gravity effect. If it was not the case, we could perform a symmetric step by increasing the effective magnetic field compared to its value in presence of $b_z' = 12.5\,\text{G}$

[6] In fact for the experimental results shown in Ch. 7 and 8, we preferred to vary the distance of the atomic sample to the focus of the LS beam (see 2.2.2 for a detailed description of this effect and 7.1.3.1 for a detailed description of the experimental choices).

position within the cloud[7] $|\boldsymbol{\rho}| \ll d_z$. Then any atom within the cloud (located in $\boldsymbol{\rho}$) feels a potential that approximates as

$$V_{\text{mag}}(\boldsymbol{\rho}) \approx \mu b'_z d_z^{2D} + \frac{\mu b'^2_\perp}{2 b'_z d_z^{2D}} \boldsymbol{\rho}^2 = m g d_z^{2D} + \frac{mg}{8 d_z^{2D}} \boldsymbol{\rho}^2, \tag{2.9}$$

and the resulting trapping frequencies in xy plane are

$$\nu_x = \nu_y = \nu_{\text{mag}} = \frac{1}{2\pi}\sqrt{\frac{g}{4 d_z^{2D}}} \approx 6.4\,\text{Hz}. \tag{2.10}$$

3. **Possible Time–of–Flight (some ms)**
   Depending on the quantities we want to measure, we have the possibility to let the cloud expand freely along certain directions of space for some milliseconds before imaging it. This technique is usually named Time–of–Flight (ToF) measurement. More precisely, we may switch off:
   — The light-sheet confinement that tightly confines the atoms in the vertical direction. This switching off can be done by fast electronic control of Acousto Optic Modulator (AOM) on the order of the microsecond. When we only switch off this trap, the gas expands along the vertical direction but not in the xy plane. Such an expansion is called «one–dimensional Time–of–Flight » which we abbreviate in 1D ToF[8].
   — The box–trap confinement that keeps the atoms in a restricted region of space in the 2D plane. This switching off can be done in $\sim 10\,\mu s$. When we only switch this trap, the gas expands in the xy plane but not along z. Such an expansion is called «two–dimensional Time–of–Flight » (2D ToF). To perform such a Time–of–Flight we usually ramp down the light sheet power to reduce the effect of possible defects and rugosities of the light-sheet potential (see 2.2.1). We typically choose a remaining confinement of $\sim 350\,\text{Hz}$.
   — When switching off simultaneously both traps, the gas is expanding in the three-dimensional free-space and this is conventional «three-dimensional time of flight» (3D ToF).

   We implement these Time–of–Flights without modifying the magnetic fields. Such changes would induce strong Eddy currents (especially in the translation stage holding the microscope objective for vertical imaging setup) and thus strong perturbations to the later imaging process. We choose the value of this gradient to $b'^{2D}_z = b'^{mag}_z$ so that it exactly compensates the effect of gravity. This is highly convenient as it enables to keep the cloud center of mass in place for all ToF durations. Hence, we can produce long free–expansion without being limited by the gas hitting the glass cell and the cloud stays advantageously at the imaging focus position. The remaining gradients do not imply any important modification to ToF dynamics as the resulting frequencies are small enough (some Hz).

---

[7] Maximal extension of the cloud is set by the box size and varies typically from $5\,\mu$m to $15\,\mu$m

[8] For this type of ToF we are concerned by the box-potential defects that arise at a small distance ($d_{\text{defect}} \lesssim 6\,\mu$m) of the focus of this beam (see 6). For $\omega_z = 2\pi \times 2$kHz, this is reached after an expansion time of $d_{\text{defect}} \times \sqrt{m/h\omega_z} \approx 2\,\text{ms}$)

4. **Absorption Imaging of the cloud (some ms)**
   To effectively measure the physical properties of our gas, we image its density distribution at the end of the sequence. We implement an absorption imaging technique. We shine on the atoms a close to resonance laser beam, collect it at the output of the cloud thanks to lenses and finally image it on a CCD camera. We then compare the output intensity profile to the input one. For this we implement a succession of exposures of our camera to record the cloud image and some reference images in a short time lapse. This process is described in details in Ch. 3.

2.2. Current realization of tight transverse confinement for 2D trapping: the Hermite-Gaussian beam

To experimentally realize quasi–two–dimensional confinement of our gas of cold atoms, we need to generate a trap with very tight confinement in one direction. Such a tight confinement must freeze out atomic motion in the considered direction (see 1.1.2). The freezing is realized when the energy gap between the ground state and the first excited state is much smaller than both the thermal energy $k_{\mathrm{B}}T$ and the interaction energy per particle ϵ_{int}. If the z confinement is harmonic with pulsation ω_z, we enter the quasi-2D regime when $\hbar\omega_z \gtrsim k_{\mathrm{B}}T,\ \epsilon_{\mathrm{int}}$. In our typical 2D experiments, the temperature T is of the order of $T \sim 100\,\mathrm{nK}$ and the chemical potential $\mu \sim k_{\mathrm{B}} \times 50\,\mathrm{nK}$. Then the quasi-2D regime necessitates $\omega_z \gtrsim 2\pi \times 2\,\mathrm{kHz}$.To implement this tight trapping, we use an optical dipole trap generated via a specially shaped blue–detuned laser beam (typically $\lambda = 532\,\mathrm{nm}$) showing an anisotropic geometry.

2.2.1. Producing an Hermite–Gauss beam

The shaping of this beam is realized in the current setup via the use of a phase plate as previously implemented in [134]. This phase plate shows a step in phase along one direction and it imprints a phase of π on the upper half of the beam ($z > 0$) with respect to the other half ($z \leq 0$):

$$\phi\,(z) = \pi \text{ if } z > 0\,,\, \phi\,(z) = 0 \text{ if } z \leq 0 \tag{2.11}$$

The phase plate is placed on the path of elliptic collimated beam (see below for the choice of the yz aspect ratio). We refocus this beam after the phase plate at the atom position by a converging lens of focal $f = 100\,\mathrm{mm}$ so that the phase imprinted translates into a specific Hermite–Gaussian intensity profile. To quantitatively describe the effect of this far blue detuned ($\lambda = 532\,\mathrm{nm}$) beam on the atoms, we need to calculate the spatial dependance of the dipolar force. Hence, we are interested in the intensity profile I_{HG} at the position of the atoms. The resulting dipole potential is $U = \alpha I_{HG}$ where α can be computed as previously done in 2.1.1. As $\omega = 2\pi \times 5.63 \times 10^{14}\,\mathrm{Hz}$, we take into account the beyond *Rotating Wave Approximation* term and neglect the detuning difference to the fine structure. Thus $\alpha = -\frac{3\pi c^2}{2\omega_0^3}\left(\frac{\Gamma}{\omega_0 - \omega} + \frac{\Gamma}{\omega_0 - \omega}\right)$ and numerical application gives $\alpha = k_{\mathrm{B}} \times 59\mathrm{mK}\,\mu\mathrm{m}^2/\mathrm{W}$. We then need to calculate the I_{HG}.

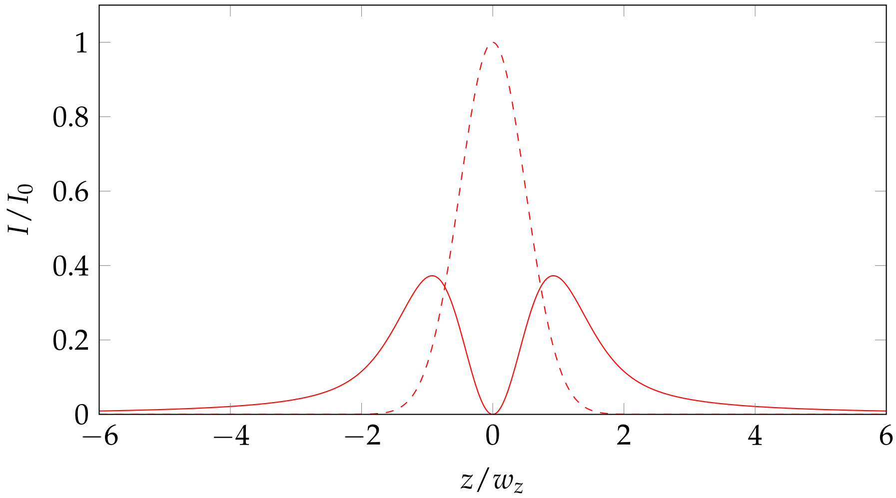

Figure 2.3.: Normalized intensity profile in the focal plane of the lens (red full line). For comparison, the intensity profile without a phase plate is presented in red dashed line

Detailed calculations on the beam propagation where done by previous PhD student P. Rath [109] in paraxial approximation. In this approximation, the electric field at the focus of the lens, is simply the Fourier transform of the electric field after the phase plate, that is the Gaussian beam profile multiplied by the special phase distribution imprinted.

At the center of the output beam $z = 0$, the dephasing of π of the incoming beam results in destructive interferences between the two halves of the beam so that the arising intensity is zero (Fig. 2.3). Close to this dark center, as represented in Fig. 2.3, the intensity distribution can be approximated by

$$I(y, z \ll w_z) \approx I_0 \frac{4}{\pi w_z^2} z^2 e^{-2\frac{y^2}{w_y^2}} \text{ with } I_0 = \frac{2P_0}{\pi w_y w_z} \tag{2.12}$$

which leads to an harmonic confinement along z of pulsation

$$\omega_z(y) = \frac{4}{\pi}\sqrt{\frac{\alpha P_0}{m w_z^3 w_y}} e^{-\frac{y^2}{w_y^2}} \tag{2.13}$$

where w_z and w_y are the beam waists on the atoms (after the focusing lens) in the z and y directions.

Therefore, the smaller these waists are, the tighter the confinement is. Nevertheless we can not choose w_y too small as we want a uniform confinement along y. From Eq. 2.12, we note that the potential varies with y as the gaussian intensity $\propto e^{-2y^2/w_y^2}$. The cloud size along y is set by the box–trap radius R_{box} (varying from $R_{\text{box}}^{min} \approx 5\,\mu$m to $R_{\text{box}}^{max} \approx 15\,\mu$m). We typically require $w_y \gtrsim 3R_{\text{box}}$ so that the potential varies of $\lesssim 20\%$ [9]. We also note that along x, the 2D trap extent is given by the Rayleigh range of the

---

[9] this means that the transverse trapping frequency ω_z (that varies as $\propto \sqrt{I}$ as shown in Eq. 2.13) varies of $\lesssim 10\%$ and the interaction parameter $\tilde{g}$ (that is proportional to a_s/a_z and so varies as $\propto \sqrt{\omega_z}$) of $\lesssim 5\%$

laser $x_R = \pi w_z^2/\lambda$[10]. From the specific dependency of the Hermite–Gauss intensity $I_{HG} \propto (1+(x/x_R)^2)^{3/2}$, this size must verify $x_R \gtrsim 2.5 R_{\mathrm{box}}$ so that the potential varies of $\lesssim 20\%$. These constraints sum up as follow:

- w_z must be as small as possible as long as $x_R \gtrsim 2.5 \times R_{\mathrm{box}}^{max}$. Thus $w_z \gtrsim \sqrt{2.5\,\lambda\, R_{\mathrm{box}}^{max}/\pi} \approx 2.5\,\mu$m for $\lambda = 532\,$nm.
- w_z is limited by the numerical aperture of the focusing lens. In our setup, this reads $w_z \gtrsim 5\,\mu$m.
- w_y must be as small as possible (to not reduce the confinement along z) but larger than $w_y \gtrsim 3 \times R_{\mathrm{box}}^{max} \approx 45\,\mu$m.

In our setup, we choose $w_y = 50\,\mu$m and we have $w_z \approx 5\,\mu$m at the focus. We use cylindric lenses to give the wanted aspect ratio to the beam.

When these conditions are fulfilled, the variations of $\omega_z = \frac{4}{\pi}\sqrt{\frac{\alpha P_0}{m w_z^3 w_y}}$ over the cloud are less than 10%. We can thus neglect the corresponding variation of the zero point energy. The expected value is $\omega_z = 2\pi \times 6.08\,$kHz for $P_0 = 1\,$W. This corresponds to a harmonic oscillator length $\ell_z = \sqrt{\hbar/m\omega_z} = 138$ nm, and a 2D interaction parameter $\tilde{g} = \sqrt{8\pi} a_s/\ell_z = 0.18$.

2.2.2. Focusing the beam on the atoms by frequency measurement:

Such a tight confinement is in fact realized only if we put the atoms in the focus of the Hermite–Gauss beam. If not, then the trapping frequency varies along the beam, mainly due to the broadening of vertical waist w_z: $w_z(x) = w_z^0\sqrt{1+(x-x_0)^2/(x_R)^2}$. We now denote w_z^0 the waist at focus ($w_z^0 \approx 5\,\mu$m). Then the frequency depends on the position of the focus x_0 compared to the atomic position x_{at} via

$$\omega_z(x_{at};\omega_z^0, x_0, x_R) = \frac{\omega_z^0}{\left(1+((x_{at}-x_0)/x_R)^2\right)^{3/4}}. \tag{2.14}$$

where ω_z^0 is the value of ω_z at the focus given in Eq. 2.13.

2.2.2.1. Finding the focus

We first note that by experimentally varying the focusing of the beam on the atoms, we can deduce from Eq. 2.14 both:

1. the position of the focus of the LS beam x_0 compared to the atom position x_{at}. We should note that x_0 is not readily available by direct methods. In particular, we can not directly image the beam focus with the horizontal imaging setup due to chromatic shift in the optical elements (we measure a displacement of the expected focus of 600μm). Varying the beam focusing on the atoms may also manifest in various measurable signals on the atomic sample that we could study to detect x_0. For example, when we get closer to the focus the number of atoms

---

[10] We also note from P. Rath calculations that for position out of the focus –$x \neq 0$ – the beam intensity still cancel at $z = 0$ so the Rayleigh is the unique source of variation in the confinement along that direction, collinear to the beam propagation.

loaded in the 2D trap decreases. However this also depends very sensitively on the accuracy in side alignment procedures. Trapping frequency measurements appear to be the most accurate method to find x_0.

2. the waist values w_z and w_y of the LS beam at the atom position can be checked using the fitted values of x_R and ω_z^0 and assuming that the beam power P_0 on the atoms is known. I will give later in this paragraph a numerical example of such a check. I want to emphasize here that this calibration of the beam waists serves as a validation of the light sheet alignment procedure.

We can easily perform this inspection of the dependency ω_z toward $(x_{at} - x_0)$ by repeating oscillation measurements while varying the position of the focusing lens $x_{0,F}$ (and so varying x_0 by the same quantity) as this lens is set on a translation stage directed along x. We thus measure the dependency $\omega_z(x_{0,F})$ at a fixed position x_{at} of the atomic cloud. To produce one frequency measurement, we observe the breathing mode after performing an excitation of the vertical confinement. We excite the cloud at the end of the evaporative ramp of the box–trap by abruptly lowering [11] the LS power from P_{LS}^f to $P_{LS}^{\mathrm{exc}} \sim P_{LS}^f/4$. After this abrupt reduction of the confinement we hold the system for a varying $t_{\mathrm{hold}}^{\mathrm{exc}}$ up to a few milliseconds in which the oscillation occurs. In order to reveal the oscillatory phenomenon, we perform a 3D ToF (typically of 5 ms) and image the cloud in horizontal imaging. We focus on the variation of the vertical size (that contains information on the z velocity distribution) with $t_{\mathrm{hold}}^{\mathrm{exc}}$ as we expect oscillations at frequency $\nu = 2 \times \omega_z^{exc}/2\pi$ where ω_z^{exc} is the value of ω_z at LS power P_{LS}^{exc}. From ν we can deduce ω_z at any beam power P_{LS} by $\omega_z(P_{LS}) = \omega_z^{exc}\sqrt{P_{LS}/P_{LS}^{exc}}$. We observe such oscillations and fit it by a damped sine of frequency ν (see Fig. 2.4**(a)**). The oscillations indeed show a damping, whose time scale varies with the distance to the focus. In Fig. 2.4**(b)** we show the resulting variation of ω_z at LS power P_{LS}^f with the position $x_{0,F}$, arising from the various measurements performed.

We fit $\omega_z(x_{0,F})$ to Eq. 2.14. We find:

— $x_R = 147.5 \pm 9.5\,\mu$m, which gives $w_z^0 = 5.00 \pm 0.16\,\mu$m, in agreement with the theoretical value $w_z^0 = 5\,\mu$m.

— $\omega_z^0(P = 190 \pm 20\,\mathrm{mW}) = 2.76 \pm 0.1\,\mathrm{kHz}$. If we assume $w_y = 50\,\mu$m, we deduce $w_z^0 = 4.93 \pm 0.33\,\mu$m, in agreement with previous value. From both x_R and ω_z^0, we can also compute $w_y = 48 \pm 9\,\mu$m, in agreement with theoretical value $w_y = 50\,\mu$m.

We conclude that the optical setup is well aligned, and we also gain the knowledge of the relative position of the focus and the atoms.

2.2.2.2. Choosing the right position for loading the trap

In practice, we cannot work with the atomic cloud in the focus of the Hermit Gaussian beam for severals reasons:

---

[11] due to servo power control problems, we are not able to switch abruptly the trap to a higher value in a controlled way. We are so obliged to perform the frequency measurement at a lower power of the light sheet and to rescaled it afterwards

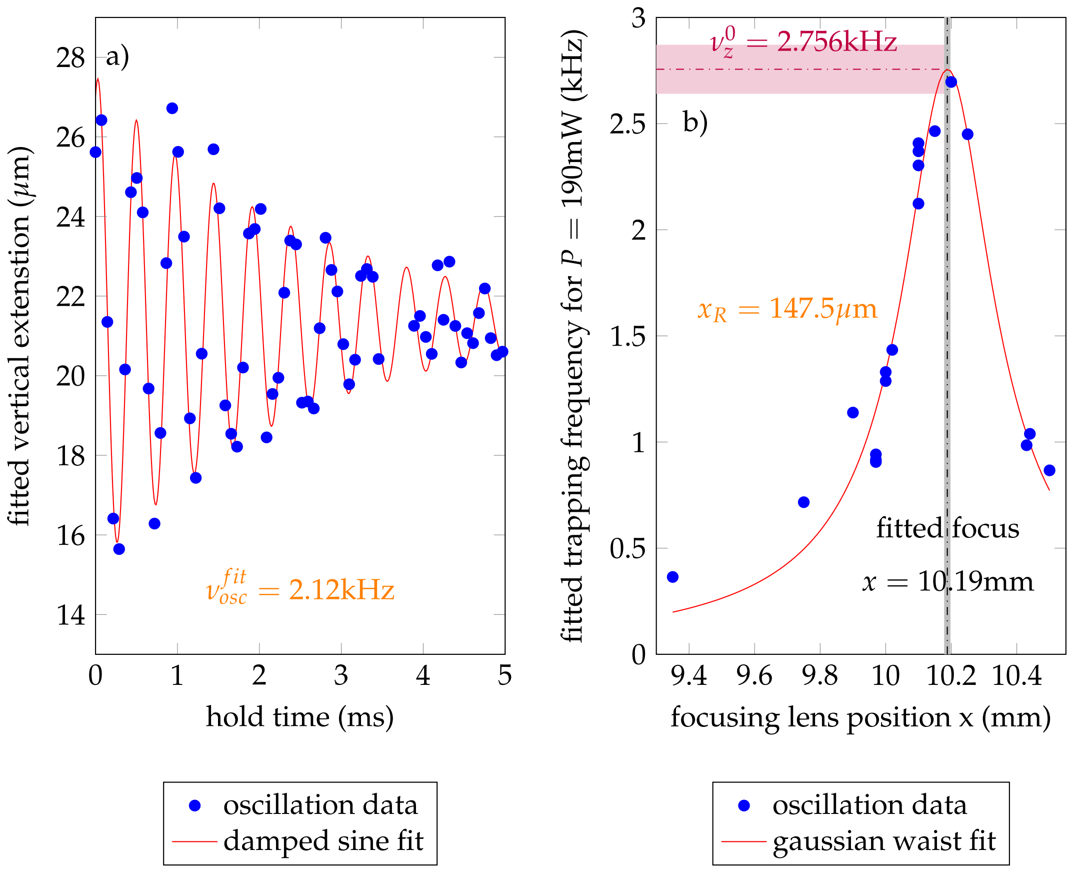

Figure 2.4.: (**a**) Example of an excited oscillation on the vertical size of the cloud distribution after 5 ms of 3D ToF. We fit the oscillations to a damped sine. Here the frequency fitted is $\nu = 2.12$ kHz and the damping time constant $\tau = 2.58$ ms. The frequency $\nu$for the breathing mode is twice the trapping frequency expected at the excitation power of the light sheet P_{LS}^{exc} that is here of 47.5 mW. In **b**, we represented the summary of the oscillation measurement (performed in a 3 day measurement campaign essentially). ω_z is calculated at the light sheet power $P = 190$ mW. We then fit the distribution of ω_z by Eq. 2.14. We find the position of the focus $x_{0,F}$ and the beam characteristics x_R and ω_z^0.

1. The vertical extension of the 2D–trap (set by $w_z(x)$) fixes the overlap ratio between the 3D atomic distribution (at the end of the evaporation in the hybrid trap) and the 2D–trap. Then, the closer we are to the focus, the less important the overlap and the lower the loading efficiency. At focus, the atomic density loaded remains very low and reveals insufficient to reach degeneracy along the box–trap ramp.
2. In its experimental realization, the Hermite–Gauss beam shows defects along y and these defects are more important (with a higher amplitude and showing also higher spatial frequency) when we get closer to the focus. The defects characteristics also change from one side to the other of the focus (that is to say if the atoms are loaded upstream or downstream compared to the focus position).
3. Finally when ramping up the light-sheet alone (no box–trap) on the 3D cloud and

imaging it in vertical imaging, we see that close to the focus the atomic sample is deformed compared to the shape of the 3D cloud and is displaced from its original position along x. The amplitude of the displacement varies with the distance to the focus from $\gtrsim 100\,\mu$m at focus to nearly none at $300\,\mu$m away from the focus. These defects can also explain the oscillation damping we observed in the vertical frequency measurement (Fig. 2.4). Roughly speaking, the more important the defects are, the shorter the damping time constant.

We can link these two last points to defects in the LS beam profile. These can be directly observed by imaging the intensity distribution. They can also be characterized by their effects on the atomic distribution. We will develop such an analysis in the next section. For now, we want to conclude on the choice of $(x_{at} - x_0)$ to realize a satisfying 2D confinement. From previous observations, we want to find a compromise value of $(x_{at} - x_0)$ due to the opposite characteristics:

- We want to get far enough from the focus so that the densities loaded are sufficiently large and the rugosities of the potential have a negligible influence on the radial trapping potential.
- We want to be close enough to the focus so that the confinement is tight enough $\omega_z \gtrsim 2\pi \times 2\,$kHz to realize a (quasi-)2D regime.

We find the optimum by trapping the atoms upstream to the focus of the Hermite–Gauss beam ($(x_{at} - x_0) < 0$ if the beam propagates toward $x > 0$) and at $|x_{at} - x_0| = 190\,\mu\text{m} = 1.28 x_R$. In Table 2.3, we compute the beam characteristics at this position.

Parameters	Expected value at focus	Exp. value at $\lvert x - x_0\rvert = 190\,\mu$m
w_z	5μm	8.15μm
w_y	50μm	50μm
$\omega_z(P_{LS} = 1\text{W})$	$2\pi \times 6.08$ kHz	$2\pi \times 2.92$ kHz

Table 2.3.: Summary of the beam characteristics at focus and at a distance $|x - x_0| = 190\,\mu$m. ω_z is obtained along Eqs. 2.13 and 2.14.

2.2.3. Characterizing the resulting potential in the radial plane

In the previous subsection, we saw how to characterize the trapping of the Hermite–Gauss along the z direction but we have not yet considered the possible effects of this beam in the xy plane. As we want to superimpose this trap with a flat bottom one in xy to create a uniform 2D gas (see Ch. 6), we need to precisely characterize all effects in the xy plane of the 2D confining beam. These can be divided in two parts:

1. An unavoidable effect of the LS beam that stems from the finite size of the beam and the resulting spatial dependencies of the the beam profile. This results in a variation of the zero–point energy $\hbar\omega_z/2$ along the beam propagation and so in de–confining potentials in xy directions. We can describe these easily using Eqs. 2.13 and 2.14. I will give typical numbers corresponding to our specific setup in the following paragraph.

2. Unwanted irregularities of the beam profile resulting in defects in the potential. These stem from non-perfect optics and phase plate realizations. We cannot suppress them completely and we thus need to characterize them.

2.2.3.1. Deconfining Potentials

As we saw previously the Hermite-Gaussian beam creates a trapping potential $U_{HG} = \alpha I(x, y, z)$ that can be considered in first approximation as harmonic along z: $U_{HG} = \frac{1}{2} m\omega_z^2 z^2$. As stated in 1.1.2, the 2D Hamiltonian $\hat{\mathcal{H}}$ is obtained from integrating the 3D one $\hat{H}$ along z after replacing the 3D quantum field operator $\hat{\psi}(\boldsymbol{r})$ by $\hat{\phi}(\boldsymbol{\rho})\varphi_0(z)$ with $\varphi_0(z)$ being a 1D classical field and $\hat{\phi}(\boldsymbol{\rho})$ a 2D quantum one (see Eq. 1.5). If the confinement is tight enough, $\varphi_0(z)$ is simply the ground state of the harmonic oscillator. The integration of $\hat{H}$ introduces a term depending on the z confinement in $\hat{\mathcal{H}}$, it is an additive term $+\frac{\hbar\omega_z}{2}\hat{\phi}^\dagger\hat{\phi}$. Then the dependency of ω_z with x and y leads to small radial trapping potentials that are not completely negligible. In particular, if we are interested in generating a uniform in-plane trapping, we need to estimate it carefully.

If we set $x_0 = 0$ and the beam center (y_0, z_0) at coordinates origin, we deduce from Eqs. 2.13-2.14:

$$\frac{\hbar\omega_z(x,y)}{2} = \frac{\hbar\omega_z(0,0)}{2}\left(\frac{w_z(0)}{w_z(x)}\right)^{3/2} e^{-\frac{y^2}{w_y^2}} \tag{2.15}$$

$$\text{with } w_z(x) = w_z(0)\sqrt{1+(x/x_R)^2}. \tag{2.16}$$

This dependency of the zero–point energy results in a «de–confining» potential as it can be approximated by an harmonic potential with imaginary trapping frequencies. Trapping frequencies ω_x and ω_y along x and y can be estimated by a polynomial approximation of Eq. 2.15. For a cloud trapped in the focus of the LS beam we perform the approximation around $(x, y) = (0, 0)$ which gives

$$\frac{\hbar\omega_z(x,y)}{2} = \frac{\hbar\omega_z(0,0)}{2} \times \left(1 - \frac{3x^2}{4x_R^2}\right) \times \left(1 - \frac{y^2}{w_y^2}\right) \tag{2.17}$$

$$= \frac{\hbar\omega_z(0,0)}{2} - \frac{3\hbar\omega_z(0,0)}{8x_R^2}x^2 - \frac{\hbar\omega_z(0,0)}{2w_y^2}y^2. \tag{2.18}$$

We deduce

$$\omega_x = i\frac{\sqrt{3}}{2}\frac{\sqrt{\hbar\omega_z(0,0)/m}}{x_R} \tag{2.19}$$

$$\omega_y = i\frac{\sqrt{\hbar\omega_z(0,0)/m}}{w_y} = \frac{2x_R}{\sqrt{3}w_y}\omega_x \tag{2.20}$$

For our experimental parameters, we found $\omega_x = 1.96\omega_y$. De–confining frequencies varies as a square-root of ω_z. Typical values of $|\omega_x|$ are of a few Hz. For $\omega_z = 2\pi \times 2$ kHz, we calculate $\omega_y = 2\pi \times i\,9.65\,\text{Hz}$ and $\omega_x = 2\pi \times i\,4.92\,\text{Hz}$

We should compare these to the residual magnetic confinement $\omega_{\text{mag}} = 2\pi \times 6.4\,\text{Hz}$

(Eq. 2.10). The resulting trapping term in xy is the sum of these two contributions:

$$U_{res}(x,y) = \frac{1}{2}m\left[\omega_{\text{mag}}^2((x-x_{\text{mag}})^2+(y-y_{\text{mag}})^2)+\omega_x^2x^2+\omega_y^2y^2)\right] \tag{2.21}$$

where x_{mag} and y_{mag} are the coordinates of the magnetic zero.

We may complete this analysis by computing ω_x and ω_y when the cloud center (x_c, y_c) is not coinciding with the LS beam focus $(x_0 = 0, \ y_0 = 0)$. As we saw in 2.2.2, it is experimentally the case along x: the atoms are trapped at a distance $x_c > x_R$ to the focus of the LS beam. This may also be the case along y due to a misalignment but with smaller importance (typically $|y_c| \lesssim 10\,\mu$m). The detailed analysis of the effects of this decentering is performed in Annex. C and here we remind the conclusions of these calculations.

- For both x and y directions, the potential gradient created (potential terms $\propto x$ or y) by a possible miscentering $x_c \neq 0$ or $y_c \neq 0$ can be easily corrected by a small miscentering $x_{\text{mag}} \neq 0$ or $y_{\text{mag}} \neq 0$ in the opposite directions of the magnetic zero of typically a few tens of μm.
- x_{mag} and y_{mag} stay negligible compared to the vertical miscentering of the magnetic zero d_z. Thus the residual magnetic trapping frequencies are not affected by such a compensating discentering.
- Realistic value of y_c gives $|y_c| \lesssim 0.2\ w_y$ so that the change in ω_y is negligible (up to 4%): $\omega_y^c \approx \omega_y$.
- The chosen defocusing x_c of the LS beam at the atom position (see 2.2.2) induces a significant change in the zero point energy dependency toward x. In particular, it can change from an anticonfining to a confining configuration as evidenced in Table 2.4.
- In the case $x_c \neq 0$ and $y_c \neq 0$, the rotation of the proper oscillation axis compared to x can be neglected.

The trapping frequencies for the chosen distance to the focus $x_c = 190\,\mu$m are summarized in Table 2.4.

$\omega_z/2\pi$	$\omega_y/2\pi$	$\omega_x/2\pi$	$\omega_{\text{mag}}/2\pi$
2 kHz	$i\,9.65$ Hz	1.89 Hz	6.4 Hz
1.6 kHz	$i\,8.63$ Hz	1.69 Hz	6.4 Hz
1.1 kHz	$i\,7.15$ Hz	1.4 Hz	6.4 Hz
0.8 kHz	$i\,6.10$ Hz	1.19 Hz	6.4 Hz
0.3 kHz	$i\,3.74$ Hz	0.73 Hz	6.4 Hz

Table 2.4.: All trapping frequencies for the experimental configuration (i.e.. defocusing of the LS beam of $x_c = 190\,\mu$m)

2.2.3.2. Defects on the beam profile

As pointed out in 2.2.1, we noticed loading shortcomings along both y and z axis. Such deficiencies are stronger as we get closer to the focus of the LS beam.

We can directly observe these defects by a side imaging of the light-sheet intensity profile [12]. In these profiles, we notice higher intensity regions, oriented perpendicularly to y axis. These bright lines result in barrier potentials $V_{\mathrm{add}}(y)$ for our ^{87}Rb atoms. This potential is expected to be anharmonic as the defects are not smoothly varying.

Similar rugosities in the potential along transverse directions to the light-sheet propagation were also pointed out in [110]. At that time, it was easier to characterize anharmonicity along y, as the trapping was harmonic in the three directions of space (now confinement along y is quasi-uniform. See 6). Defects along y were characterized by the damping of the oscillations along this axis while exciting this movement and comparing it to oscillations in absence of LS beam. As shown in 4.2.1.2, the potential along y can be reconstructed from density distribution measurements in this harmonic trap.

In our case, we can characterize these potential defects by density measurements:

- By operating a bad alignment of the light-sheet [13], we can directly see the defects by in–situ imaging of the density distribution. In this case, the potential is the sum of both contributions of the flat bottom box–trap and of the light-sheet and cold atomic configuration are greatly influenced by the potential rugosities created by the light-sheet along y directions.
- We can also characterize the light-sheet defects by comparing experimental and simulated two–dimensional Time–of–Flight expansion of a cold gas inside the light sheet [14]. We found that the expansion along x is well described by the simulation whereas the y expansion shows deviations that can be attributed to an additional anharmonic trapping potential.

2.3. A new setup for tight transverse confinement: the accordion setup

In this section, I will present the scheme of principle and preliminary tests of an alternative setup for shaping a blue detuned laser beam into a light-sheet-like potential showing highly anisotropic geometry and creating a tight confinement along one direction (z). We wanted to develop a new scheme for this tight confinement for several reasons:

- to reach a higher 2D interaction parameter $\tilde{g}$ using the same optical power.
- to improve the loading efficiency of the 2D plane from the 3D BEC and reach higher phase-space-densities.
- to be able to study multiple planes at once
- to have a more versatile apparatus whose parameters can be changed via a computer control and even varied dynamically.
- to get rid of the specific potential defects linked to the use of a phase plate.

---

[12] Due to the presence of a dichroic plate transmitting 780 nm and reflecting 532 nm in the imaging path, we can not directly nicely image the light sheet potential on the horizontal imaging camera (we see interferometric perturbation on this image). Instead, we implement a side imaging setup in the path of the dichroic plate reflection. In these side images, we do not have a sharp resolution of the central trapping region that is of only one or two pixels.

[13] We choose an alignment of the light-sheet beam by minimizing the density defects

[14] description of a simulation of 2D ToF along with a comparison to experimental results can be found in 3.3.3

2.3.1. The accordion scheme of principle

This new setup is not based on a specific shaping of a single beam but on the interference between two beams issued from the same laser source. The two beams are set to arrive along parallel paths distant by D on a lens of focal length f. The two beams converge after the lens and they overlap in the lens focal plane resulting in an interference pattern. The atoms should be positioned in this focal plane so that they feel the potential resulting from this special intensity pattern. A scheme of this geometric principle is given in Fig. 2.5. We set x the axis of the beam propagation upstream to the lens and z the orthogonal axis of the plane containing both beams. Here we assume that the lens is in the yz plane. Then after the lens the wave vectors of each beam are

$$\boldsymbol{k}_{+} = \frac{2\pi}{\lambda}\left(\cos(\theta/2)\,\boldsymbol{u}_x + \sin(\theta/2)\,\boldsymbol{u}_z\right) \tag{2.22}$$

$$\boldsymbol{k}_{-} = \frac{2\pi}{\lambda}\left(\cos(\theta/2)\,\boldsymbol{u}_x - \sin(\theta/2)\,\boldsymbol{u}_z\right) \tag{2.23}$$

where $\boldsymbol{u}_i$ is the unit vector along axis i (with $i \in \{x, y, z\}$) and $\lambda = 532\,\mathrm{nm}$ is the wavelength of the beam. θ is the angle between the two beams after the lens and is given by

$$\theta = 2\arctan\left(\frac{D}{2f}\right). \tag{2.24}$$

We assume that both beams have a similar intensity profile, equals to $I_0(x,y,z)/2$ with $I_0(x,y,z)$ being the intensity profile of the (gaussian) beam that would have the unsplit beam propagating through the lens center [15]. In the focal plane $x = f$, the intensity is modulated along

$$I(\boldsymbol{r}) = \frac{I_0(f,y,z)}{2}\left|e^{i\boldsymbol{k}_{+}\boldsymbol{r}} + e^{i(\boldsymbol{k}_{-}\boldsymbol{r}+\varphi)}\right|^2 = 2I_0(f,y,z)\cos^2\left(\frac{2\pi\sin(\theta/2)}{\lambda}z + \frac{\varphi}{2}\right). \tag{2.25}$$

where φ is the dephasing between the two beams. Mainly it is set by the path difference δ between the two beams and $\varphi = 2\pi\delta/\lambda$. Then a fringe pattern appears along z:

---

[15] The intensity profile of each beam in the focal plane are in fact distinct. In this footnote, we denote then $I_{+}(x,y,z)$ and $I_{-}(x,y,z)$ for the beams propagating along $\boldsymbol{k}_{+}$ and $\boldsymbol{k}_{-}$ respectively. They can be considered similar if

— the corresponding incident beam profiles $I_{+}^{(i)}(x,y,z)$ and $I_{-}^{(i)}(x,y,z)$ are identical. This would be the case if the path difference δ between the two beams is zero. In our case $\delta \neq 0$ but its effect is usually negligible due to the very large waist w' upstream to the lens (δ is very small compared to the Rayleigh length x_R). If we use numerical values of footnote 16 $w' = w'_z = w'_y \approx 340\,\mu\mathrm{m}$, we find $x_R = 680\,\mathrm{mm}$. And in the setup of Fig 2.6, $\delta \lesssim 100\,\mathrm{mm} \ll x_R$.

— we can neglect the effect of the difference between the wave vectors of the two beams (Eqs. 2.22-2.23) on the intensity profiles in the focal-plane $x = f$. This is the case if we consider a configuration where $4|z|f\sin(\theta/2)\cos(\theta/2) = 2Dz\frac{f^2}{D^2/4+f^2} \ll w_z^2$ where w_z is the beam waist along z at the atom position. z must cover all the abscissa range investigated by the atoms in the trap. Then D must be small (d large) and z close to the beams centers (such that $Dz \ll w_z^2$ typically).

$I(z) \propto \cos^2(\pi z/d + \varphi/2)$ with a fringe spacing d of

$$d = \frac{\lambda}{2\sin(\theta/2)} = \frac{\lambda\sqrt{D^2/4+f^2}}{D} \tag{2.26}$$

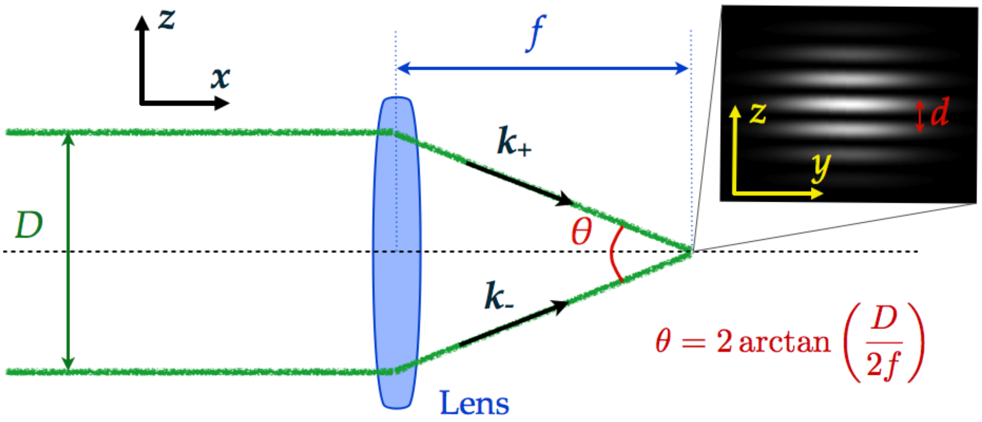

Figure 2.5.: Scheme of the interference setup. Two parallel (propagating along x) beams issued from the same laser source ($\lambda = 532\,\mathrm{nm}$) are set incident on a converging lens of focal f. The two beams interfere at the focal point (if the incidence is at $\pi/2$ as in the scheme. If not, they will overlap in an other point of the focal plane). Interference pattern happens along z-direction and its spacing is d.

2.3.2. Choices for experimental implementation

The lens used to combine the two beams is an achromatic triplet ($f = 100\,\mathrm{mm}$) in order to reduce astigmatism or other aberrations due to the fact that the beams go through the edges of the lens. The diameter of the lens fixes an upper bound to D, in our case $D \lesssim D_{\mathrm{max}} = 26\,\mathrm{mm}$ so that the minimal d that we can realize is $d_{\mathrm{min}} = 2\,\mu\mathrm{m}$. A maximal value of d will be introduced by the way the two beams are split (see 2.3.4) and is typically of $d_{\mathrm{max}} = 20\,\mu\mathrm{m}$.

The extent of the fringe pattern is fixed along z and y by the waists w_z, w_y of the beams at the position of the atoms and along x by the overlap region of the two beams which is of

$$x_{\mathrm{ext}} \sim \frac{w_z}{\tan(\theta/2)} = \frac{2fw_z}{D} \tag{2.27}$$

As in 2.2.1, to produce a tight 2D confinement along z we must impose that the extent of the potential along x and y are large enough compared to the in-plane cloud extent ($\gtrsim 3R_{\mathrm{box}}^{max}$). In order not to reduce the intensity I_0 (and so the confining strength, see

2.3.3), the waists must also be as small as possible. Then the waists are constrained along:

- — $w_y \gtrsim 3R_{\text{box}}^{max} \approx 45\,\mu\text{m}$.
- — w_z must be large enough so that $x_{\text{ext}} \gtrsim 3R_{\text{box}}^{max}$ for all D. The most constraining case is for $D = D_{\max}$ and $w_z \gtrsim 3R_{\text{box}}^{max} D_{\max}/(2f) = 6\,\mu\text{m}$.
- — w_z must be large enough so that the two beams intensity profiles can be considered as equal over the trapping region (see footnote 15). Typically we want to trap the atoms in the dark fringe closest to the beam center so that the trap center verifies $|z| \leq d/2$ (see 2.3.3). If we consider the extreme case of a trap center in $z = d/2$, the atoms typically investigates $0 \leq z \leq d$. Then condition $2Dz\frac{f^2}{D^2/4+f^2} \ll w_z^2$ obtained in footnote 15 is maximally constraining for $z = d$ and implies $w_z^2 \gg 2\lambda f^2/\sqrt{D^2/4+f^2} = 106\,\mu\text{m}^2$.
- — w_z must be large enough to contain at least two fringes maxima and $w_z \gtrsim 2d$. The most constraining case is for $d = d_{\max}$ and $w_z \gtrsim 2d_{\max} = 40\,\mu\text{m}$ in our case. Note that this value strongly depends on the requirement on $d_{\max}$ used at the loading of the 2D trap and is mainly set by the extent σ_z of the 3D gas we load (see 2.3.4). It happens to be the most constraining of the three last points in our case.

For the preliminary tests we have chosen an isotropic configuration $w_y = w_z \approx 50\,\mu\text{m}$.

2.3.3. Characterizing the transverse confinement (toward tighter trapping)

As in the current setup described in previous section, the patterned intensity profile $I(\boldsymbol{r})$ would lead, if we position the atoms at $x \sim f$, to a dipolar potential $U(x,y,z)$ tightly confining along z:

$$U(x,y,z) = 2\alpha I_0(x,y,z)\cos^2\left(\frac{\pi}{d}\left(z+\frac{\delta d}{\lambda}\right)\right). \tag{2.28}$$

where $\alpha = k_B \times 59\,\text{mK}\,\mu\text{m}^2/\text{W}$ (see 2.2.1). If we assume that the beams are focused in the lens focal plane then $I_0(x=f,y,z) \approx \frac{2P_0}{\pi w_z w_y}\exp\left(-2\left(\frac{z^2}{w_z^2}+\frac{y^2}{w_y^2}\right)\right)$. The atoms can be trapped around any intensity minimum which are positioned in $z_p = (1/2 - \delta/\lambda + p)\,d$ with $p \in \mathbb{Z}$. To maximize the confinement frequency, we will choose the minimum p such that z_p is the closest to the beam center $z = 0$. It is $z_c = d\left((1/2-\delta/\lambda)\,[1] - 1/2\right)$ where $[.]$ denotes the modulo operator and $-d/2 \leq z_c < d/2$. We note that we must be able to set $z_c = 0$by selecting δ/λ. Near the trap center the potential of Eq. 2.28 can be approximated to

$$U(x,y,z) \sim \frac{2\pi^2\alpha I_0(x,y,z_c)}{d^2}\,(z-z_c)^2\,. \tag{2.29}$$

corresponding to an harmonic frequency of

$$\omega(x,y) = \frac{2\pi}{d}\sqrt{\frac{\alpha I_0(x,y,z_c)}{m}} \tag{2.30}$$

In the focal plane and assuming $d \ll w_z, y \ll w_y$:

$$\omega(x,y) \approx \omega_z = \frac{2\pi}{d}\sqrt{\frac{2\alpha P_0}{\pi m w_z w_y}} \tag{2.31}$$

We report in Table 2.5 the expected confinement frequencies ω_z and the resulting 2D interaction parameters $\tilde{g}$ for our ^{87}Rb atoms for two total beam power $P_0 = 1\,\mathrm{W}$ and $P_0 = 250\,\mathrm{mW}$ and typical interference spacings that we will consider in our setup. We note that at same power, the confinement frequency $\omega_z/2\pi$ is a factor >3 larger compared to the phase plate shaping detailed in 2.2.1.

d	$\omega_z/2\pi$ (1 W)	$\tilde{g}$ (1 W)	$\omega_z/2\pi$ (250 mW)	$\tilde{g}$ (250 mW)
$d_{\mathrm{min}} = 2\,\mu\mathrm{m}$	19 kHz	0.33	9.4 kHz	0.23
$d_{\mathrm{max}} = 20\,\mu\mathrm{m}$	1.9 kHz	0.1	945 Hz	0.07
$4\,\mu\mathrm{m}$	9.4 kHz	0.23	4.7 kHz	0.16

Table 2.5.: Value of ω_z and $\tilde{g}$ in the case of a trapping from an interference pattern of spacing d varying from d_{min} to d_{max} and for two values of the maxima power $P_0 = 1\,\mathrm{W}$ and $P_0 = 250\,\mathrm{mW}$. In these calculations we use selected value of $w_z = w_y = 50\,\mu\mathrm{m}$ (see 2.3.2).

2.3.4. Dynamical variation of the confinement strength (toward optimal loading of the 2D-trap)

We tested on a bench setup an experimental design to vary dynamically the fringe spacing d within the experimental sequence. We image the fringe patterns in the focal plane of the achromat lens thanks to a microscope objective (magnification ×20) on a CCD camera (WinCamD camera from DataRay inc.).

Such a dynamical variation of d is highly interesting for experimental applications for several reasons. First due to current atoms imaging issues, we actually want to study a unique 2D trap and then load the atoms of our 3D gas in a unique fringe of the interference pattern (see 2.1.3 and Fig. 2.1 for a description of a typical loading scheme). Second the loading efficiency of the atoms of the 3D cold gas in the 2D trap is roughly proportional to the overlap of a single dark region in the fringe pattern and of the considered 3D cloud (and thus to the ratio of the cloud-size σ_z along z to d). From this two first remarks, we conclude that we want to use a large value of d at loading so that $\sigma_z \sim d$ and $\sigma_z \lesssim 2d$. On the other hand ω_z is inversely proportional to d (Eq. 2.31) so that in the final configuration we want to use a small value of d. Then, a variation of d from a large value d_{max} to the optimal trapping value d_{min} enables both an efficient loading of a unique plane (if we choose $d = d_{\mathrm{max}}$ at loading) and an optimally tight confinement at the end of the experimental sequence (if we vary d down to d_{min} at the end of the 2D cloud preparation).

In our case, we choose to implement a dynamical variation of d using an experimental setup schematize in Fig. 2.6 and inspired from [135]. In this setup the two beams are separated by the use of two polarizing beam splitters. The power in each beam is

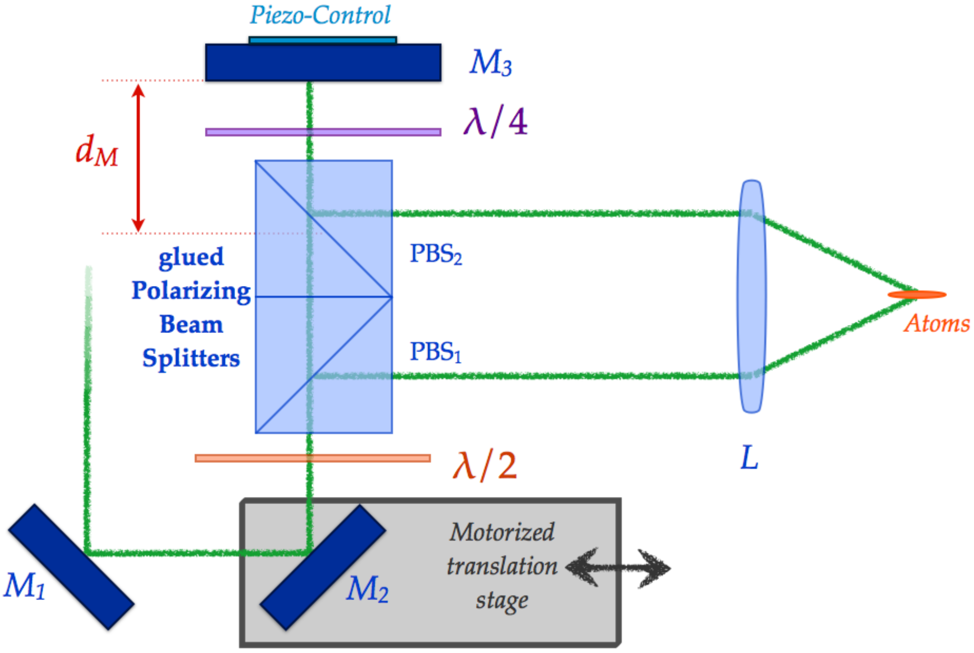

Figure 2.6.: Scheme of the specific setup used for a dynamical control of the fringe pattern. A unique translation stage is used, bearing mirror M_2 and fiwing the beam position at its output compared to a set of two cubes. The cubes are two Polarizing Beam Splitters (PBS). The $\lambda/2$ plate is set so that half of the power is transmitted by PBS_1. It is then transmitted by PBS_2 to a position-piezo-controlled mirror M_3. On its return way due to the double crossing of a $\lambda/4$ plate, the beam is transmuted via PBS_2. D is varied as twice to the distance of the the beam at output of M_2 to the cube edges. d_M sets the path difference between the 2 beams.

controlled by a $\lambda/2$-waveplate. The distance D between the two beams is set by the impact point of the beam on the coated interface of the beam-splitters. This impact point can be dynamically varied by moving the mirror M_2 positioned upstream to the $\lambda/2$-waveplate. This mirror is placed on the translation stage. This setup verified the following crucial constraints for being used with atomic ensembles:

- to have an especially robust setup: The difference of path between the two beams, in terms of absolute length δ but also of physical spatial separation, must be minimized. In our selected scheme the spatial separation of the beam is minimized but the absolute path difference is not zero. More precisely δ is set by the distance d_M of the mirror M_3 to the center of the cube PBS_2 and by the length of the cubes L_{cube}, $\delta = D + 2(d_M + L_{cube}/2 - D/2) = L_{cube} + 2d_M$. Thus we want to minimize both L_{cube} and d_M. Typically $d_M \sim 40\,\text{mm}$ so that $\delta \sim 100\,\text{mm}$.
- to have an especially reliable setup: The number of moving elements that enables to vary the beam separation D from D_{min} to D_{max} must also be minimized. In the implemented setup only one mirror is set on a translation stage (Fig. 2.6).
- the motorized translation stage on which we place the moving element(s) of the setup must be carefully selected (for a use on the atoms): The stage must be linear

and must travel over $D_{\mathrm{max}} - D_{\mathrm{min}} \sim 25\,\mathrm{mm}$ in a time $\lesssim 1\,\mathrm{s}$. The restricting point lies in the smoothness of this motion (a discontinuity in d may lead to heating of the atomic sample) whereas the reproducibility and the exactness are not limiting. We have chosen the linear stage LS110 1" from PI miCos GmbH with DC motor. Its travel range is of 26 mm and its maximal velocity of 90 mm/s, which match our requirements. The DC motor provides a very smooth operation.

— a fine and dynamic tuning of the position of the dark parts of the fringe pattern must be implemented. In our case it relies on a fine control of the path difference δ by means of a piezo-control on the position of mirror M_2 (not yet tested).

— the system must be isolated from the vibrations and other perturbations such that the fringe pattern is highly stable. For this we designed two specific elements: (i) We draw a special mount made of brass that holds all the optical elements on the path of the beam after its splitting (*i.e.* the two cubes, the mirror M_3 and the $\lambda/4$-waveplate). (ii) We designed a box that isolates the whole setup from the outside (air movement, heating, mechanical vibrations...) by surrounding it with plexiglass and stain. Then the unwanted changes of δ are minimized (note that the fine control on δ presented in previous item may in addition enable to dynamically correct for the residual ones, if they are not occurring on a too short time scale).

The dynamical variations of d have been tested on a camera. In this setup, the minimal D is imposed by the clipping of the beam at the edges of the cubes. This clipping leads to a loss in the beam power at the atoms position and ultimately to deformations of the fringe pattern. We measured a maximally acceptable value of $d_{\mathrm{max}} = 15 - 20\,\mu\mathrm{m}$. It must depend on the specific choice[16] of f, w_z and w_y. For this minimal separation of the beam, we see 2 to 3 fringes on the pattern. We measured $d_{\mathrm{min}} \approx 2.2\,\mu\mathrm{m}$. We tested by stopping the motion at intermediate values that the fringe position and contrast are not modified by moving the beam apart, that is that the beam images are not shifted by a displacement over the lens. We have not yet tested the smoothness of the evolution of the fringe pattern during the operation of the translation stage and its dependency to the velocity used.

We have tested the stability of a fixed fringes pattern on various time scales, from the ms to the day. We measured the stability by the evolution of the fringe contrast within a continuous exposure of the camera. We note that both the holding mount and the isolation box strongly enhanced the stability both over short and long times. We have not yet performed test neither of a final version of the isolation box we designed nor of a setup where a piezo control of the mirror M_3 is implemented. In the isolated and solidly mounted setup test we did not measure fringes fluctuations at short time scale, we noticed blurring of the fringe position due to drift in the alignment from time scales of $\sim 1\,\mathrm{h}$ (reduction of the contrast over the full exposure of $\approx 20\%$). Such a stability

---

[16] We note that upstream to the lens the beam waists are given by $w'_i = \lambda f/\pi w_i$ $(i = y, z)$. For our choice of waists at the atom position $w = w_z = w_y = 50\,\mu\mathrm{m}$ we found $w' = w'_z = w'_y \approx 340\,\mu\mathrm{m}$. $d = d_{\mathrm{max}} = 20\,\mu\mathrm{m}$ gives $D = D_{\mathrm{min}} = 2.66\,\mathrm{mm}$ so that the beams are distant from the edges of the cubes by $D_{\mathrm{min}}/2 \sim 4w'$. The quality of the coating of cube edges and their corner quality must also be taken into account. Note that we have chosen our cubes for the importance of the certified clear aperture ($\geq 85\%$ of the central dimension). The cubes are PBS-532-100 from Melles Griot.

seems encouraging for an experimental use of the setup even if some complementary tests are still needed.

2.4. Conclusion

In this chapter we detailed the experimental setup and the experimental sequence that we implemented to produce and study 2D Bose gases. We insisted on the implementation of the 2D tight confinement potential in our experiment and pointed out its possible drawbacks. In particular we have been recently (see Chs. 6-8) more concerned by the incidental spatially dependent in-plane potential compared to previous study as our aim evolves toward producing in-plane uniform gases. We also presented an alternative way to implement the 2D trapping that must palliate some of these defects. To deduce physical results from the produced gases, we must be able to quantitatively determine some of their parameters. This is commonly performed thanks to density distribution imaging. We will now discuss the validity of absorption imaging for 2D gases and present the specific implementation of this imaging in our current setup.

3. Imaging of our experimental gases

In this chapter I will present the experimental choices made for imaging our 2D cloud density distribution $n(x, y)$. Usually $n(x, y)$ is deduced from investigating emitted, absorbed or scattered photons by the considered atomic sample. In our setup, we implemented the common absorption imaging technique that consists in shining a quasi-resonant laser beam onto the atoms and observing the "shadow" of the cloud with a camera. In [136] (reproduced in Annex D) we highlighted restrictions to absorption imaging in its traditional implementation due to multiple scattering between atoms of a 2D cloud. To circumvent its limitations, we associate both low and high probing intensities. In the first part of this chapter, I explain why such a combination enables a quantitative analysis of the atomic density of our sample: I give an explicit model to deduce these profiles from light intensity measurements and shed to light its validity domains in terms of imaging parameters. Then I present our experimental setup in which we implement this imaging technique. Finally, I present a full calibration procedure of our imaging setup in this extended regime of imaging parameters.

3.1. Non-saturating and saturating absorption imaging

The traditional implementation of absorption imaging uses a low intensity probe beam and Beer–Lambert law

$$d(x, y) \equiv \sigma_0 \, n(x, y) = \ln[I_\mathrm{i}(x, y) / I_\mathrm{f}(x, y)] \tag{3.1}$$

to deduce the atomic density $n(x, y)$ from the incoming $I_\mathrm{i}(x, y)$ and outgoing $I_\mathrm{f}(x, y)$ intensity profile (σ_0 is the (constant) absorption cross section). Beer Lambert law relies on a mean-field treatment of the effect of the atoms on the electric field (via their average density). This mean-field approach is not valid for too high densities. In a 2D gas, we show in Annex D that collective scattering effects make the absorption cross-section dependent on n when n exceeds a few atoms per $\mu\mathrm{m}^2$ and the gas thickness is smaller than a few wavelengths. This induces a deficit of detectivity in the traditional absorption imaging analysis when used in the high density regions of our cloud constrained to 2D. In Annex D, we develop a theoretical description of this detectivity deficit in the simplified case of a $J = 0 \rightarrow J' = 1$ transition. This gives a qualitative understanding of the phenomenon but does not enable a quantitative description of the modified relation between $n(x, y)$, $I_\mathrm{f}(x, y)$ and $I_\mathrm{i}(x, y)$.

To circumvent this lack of quantitative understanding of the conventional absorption imaging, we developed a new imaging procedure that I will briefly described here (as it has been done in more details in [110]). This new imaging technique keeps using absorption of a close to resonance laser beam. The difference is that it relies on the saturation of the atomic transition at high probing beam intensity, as it was first developed in the 3D case by G. Reinaudi *& al* [137].

3.1.1. Principle of saturating absorption imaging

Using intensities of the order of several tens of atomic transition saturation intensity I_{sat} strongly excites the atomic ensemble: each atom is then permanently driven to its higher energy state by incoming photons from the probe beam. As, in this saturation regime, each atom spends half of its time in the excited state, it becomes less sensitive to photons from the desexcitation of the neighboring particles. Thus, collective effects due to multiple scattering of a single photon are reduced.

Quantitatively, in this regime, if Γ stands for the natural line width of the atomic transition, each atom scatters $\Gamma/2$ photons per second. If we probe a 2D cloud of atomic density $n(x,y)$ with a beam of incoming intensity $I_i(x,y)$ and of frequency $\omega_{\text{L}}/2\pi$ (close to the atomic resonance) then the intensity detected on the camera is

$$I_{\text{f}}(x,y) = I_{\text{i}}(x,y) - n(x,y) \times \frac{\Gamma}{2} \times \hbar\omega_{\text{L}}. \tag{3.2}$$

Thus we can deduce $n(x,y)$ from the intensity profiles I_{i} and I_{f}:

$$d(x,y) \equiv n(x,y)\sigma_0 = \frac{I_{\text{i}}(x,y) - I_{\text{f}}(x,y)}{I_{\text{sat}}} \tag{3.3}$$

where σ_0 is the low intensity absorption cross section $\sigma_0 \equiv \Gamma\hbar\omega_{\text{L}}/2I_{\text{sat}}$. This technique gives access to a quantity (the optical density (OD) d) proportional to the atomic density n for all range of n by detecting the intensity profiles I_{i} and I_{f}.

3.1.2. Absorption imaging at arbitrary intensity, some theoretical analysis

In the previous subsection, we described the high intensity absorption imaging technique as a reliable measurement of n. Nevertheless, as it uses higher probing intensity than the traditional non-saturating absorption imaging, it also results in higher noise on the measured atomic density due to photon shot noise in I_{i} and I_{f}. The lower n is, the higher the relative importance of this noise. In the regions of low n, both saturating and non-saturating techniques reliably estimate the atomic density and then we prefer using the non-saturating one. We thus implement an imaging procedure that is a combination of the novel saturating technique reliable in the regions of high n with the traditional non saturating mode which is more precise in the regions of low n (for example in the wings of an harmonically trapped cloud). In the following, we will give a general description of the relation between $n(x,y)$ and $I_{\text{i}}(x,y)$ and $I_{\text{f}}(x,y)$ both in the low and the high intensity regimes and deduce a unique relation between these quantities. The calibration of our imaging procedure will then relies on the assessment of the unknown empirical parameters of this description.

The interaction between a probe beam (frequency $\omega_{\text{L}}/2\pi$) and a single atom is characterized by the absorption cross section σ defined by the relation $\gamma = \sigma I/(\hbar\omega_{\text{L}})$, where γ is here the photon scattering rate and I the intensity of the beam on the atoms. In the case of a monochromatic resonant beam probing a two-level atom:

$$\gamma = \frac{\Gamma}{2}\frac{I}{I + I_{\text{sat}}}. \tag{3.4}$$

In the limit where $I \ll I_{\text{sat}}$ the absorption cross section is $\sigma_0 \equiv \Gamma\hbar\omega_{\text{L}}/2I_{\text{sat}}$.

In practice, this simple relation is modified as one must take into account stray magnetic fields, non-zero linewidth of the probe laser, optical pumping effects, etc. To model this complex situation, we heuristically replace I_{sat} by an effective saturation intensity αI_{sat} and Γ by an effective linewidth $\beta\Gamma$. Then the number of photons N_{p} scattered during an imaging pulse of duration τ writes

$$N_{\text{p}} \equiv \gamma\tau = \frac{\beta\Gamma}{2}\frac{I}{I + \alpha I_{\text{sat}}}\tau, \tag{3.5}$$

or equivalently

$$\sigma = \sigma_0 \frac{\beta}{\alpha + I/I_{\text{sat}}}. \tag{3.6}$$

At low intensity N_{p} is proportional to I as in the two-level case, but with a multiplicative coefficient β/α due (for example) to the broadening of the resonance line. At large intensity the number of scattered photons saturates at $\beta\Gamma\tau/2$ instead of $\Gamma\tau/2$, which models a reduction of the scattering rate that can be caused (for instance) by magnetic shift of the resonance. We note that, in our setup described in Ch. 2 [1], trapping is all–optical at the end of our sequence, thus stray magnetic field are negligible. Then, we expect $\beta = 1$. We check this identity experimentally (see 3.3.4).

The intensity of the beam at the output of the cloud is given by

$$-\ln\left(\frac{I_{\text{f}}(x,y)}{I_{\text{i}}(x,y)}\right) = \sigma\, n(x,y), \tag{3.7}$$

where σ depends on the effective intensity I on the atoms (Eq. 3.6). If the optical thickness of the cloud is large, *i.e.* if the intensity I_{f} just after the plane of atoms is significantly lower than the intensity I_{i} just before this plane, the effective intensity I must be determined in a self-consistent manner by imposing:

$$I_{\text{f}} = I_{\text{i}} - n\,\sigma(I)\,I. \tag{3.8}$$

The elimination of the effective intensity I from Eqs. 3.6-3.8 yields to the generalized OD [2]

$$d(x,y) \equiv n\sigma_0\,\beta = -\alpha\ln\left(\frac{I_{\text{f}}}{I_{\text{i}}}\right) + \frac{I_{\text{i}} - I_{\text{f}}}{I_{\text{sat}}}. \tag{3.9}$$

as in [137]. The first member of the right-hand side of Eq. 3.9 dominates in the low intensity limit ($I_i \ll I_{\text{sat}}$), and corresponds to the Beer–Lambert law. In the high intensity

---

[1] This setup is the one used for uniform 2D-trapping (see Chs. 6-8). We develop a calibration, for this specific setup in 3.3. For measurement in 2d harmonic trap calibrations are details in [110].

[2] In Eq. 3.9, the OD is in fact multiply by β compared to the physical one. Nevertheless, we saw that we expect $\beta = 1$ thus d must be equal to the physical OD.

limit ($I_i \gg I_{\mathrm{sat}}$), the second member of the right-hand side dominates and matches the saturating regime of Eq. 3.3. We note that α enables coherence between data taken at different imaging intensities and with varying exposure times. β links the measured atomic density distribution to the physical one.

3.1.3. Constraints on the imaging parameters

In the previous subsection, we have seen that shining a resonant beam on an atom assembly enables the determination of its density distribution $n(x,y)$, whatever the incident intensity I_{i} is. From absorption and scattering effects, the spatial distribution of the outgoing beam intensity $I_{\mathrm{f}}(x,y)$ is linked to $n(x,y)$ and $I_i(x,y)$ along Eq. 3.9. We will now identify some limitations to the accuracy of this measurement and point out that the couple formed by the pulse duration τ, and the intensity of the beam $I = sI_{\mathrm{sat}}$ at the atom position must be chosen with care.

While shining a laser beam close to resonance on an atomic ensemble, the photons are not only absorbed but also exert a force on the atoms - the radiative pressure - which perturbs the atomic distribution we want to detect. To be reliable, the absorption measurement must use a beam that does not affect too much $n(x,y)$ while still enabling its detection on a camera at the output of an imaging setup. More precisely, the action of the beam on the atoms is due to the fact that each photon absorbed by an atom transfers to it its momentum $\hbar\boldsymbol{k}$. Then, the resulting force is directed along the beam propagation and is in average equal to $\gamma \times \hbar k$ where γ is the photon scattering rate given in Eq. 7.23. For monochromatic resonant beam, the resulting average acceleration for an two-level atom is then

$$a = \frac{\hbar k}{m}\frac{\Gamma}{2}\frac{I}{I + I_{\mathrm{sat}}} \tag{3.10}$$

If τ stands for the duration of the atom exposure to the probe light, then this acceleration results in a non zero global velocity $v_\tau = a\tau$ and in a global displacement $d_\tau = a\tau^2/2$.

3.1.3.1. Doppler effect

The acquisition of a non-zero v_τ leads to a Doppler shift of the probing beam frequency seen by the atoms. It becomes of importance in the imaging process when it shifts the detuning of the beam δ on the order of a fraction of the atomic linewidth broadened[3] by the beam intensity $I = sI_{\mathrm{sat}}$ on the atoms $\Gamma\sqrt{1+s}$.

As the atoms are put in motion in the direction of the beam propagation, the resulting detuning is $\delta_{\mathrm{Doppler}} = \delta_{\mathrm{L}} - kv_\tau$, where $\delta_{\mathrm{L}} = \omega_{\mathrm{L}} - \omega_{\mathrm{at}}$ is the laser detuning compared to the atomic transition frequency $\omega_{\mathrm{at}}/2\pi$. The Doppler shift kv_τ depends thus linearly on τ. We can define for a given saturation parameter s, the value of τ denoted τ_Γ for

---

[3] If we shine a two–level atom with a beam of intensity $I = sI_{\mathrm{sat}}$ and arbitrary detuning δ then the photon scattering rate is given by:

$$\gamma = \frac{\Gamma}{2}\frac{s}{(1+s) + 4\delta^2/\Gamma^2}. \tag{3.11}$$

which corresponds to a Lorentzian function of δ with a broadened linewidth $\Gamma\sqrt{1+s} \geq \Gamma$.

which the Doppler shift equals the intensity–broadened linewidth:

$$\Gamma\sqrt{1+s} = kv_\tau \quad \Rightarrow \quad \tau_\Gamma = T_0\sqrt{s(1+1/s)^3} \tag{3.12}$$

$$\text{where } T_0 \quad = \quad 2m/\hbar k^2 = 42.8\,\mu s \tag{3.13}$$

τ_Γ shows a minimum in $s = 2$ with $\tau_\Gamma\,(s=2) = \sqrt{27}/2T_0$. Typically we put as an upper bound $\tau \lesssim \tau_\Gamma/4$. Then, for the intermediate saturation parameters $s \sim 2$, we must restrict to $\tau \lesssim 25\,\mu s$. For lower saturation parameters ($s \approx 1/4$), we can choose imaging pulses of some tens of microseconds (typically up to $60\,\mu s$).

3.1.3.2. Atomic displacement

In the previous paragraph, we have seen that, because of the Doppler effect, τ is constrained to a few tens of microseconds. The atomic displacement d_τ can also become problematic when it leads to driving the atoms out of focus. For our high resolution vertical imaging setup [4], the depth of field (DoF) is $\sim 10\,\mu$m (see 3.2.2 for details) and we require that the atoms move by less than this distance. We can deduced for each τ, the maximally acceptable value of s denoted $s^*(\tau)$ for which the induced displacement equals the DoF:

$$\text{DoF} \quad = \quad d_\tau = d_1\,(\tau)\,\frac{s^*(\tau)}{s^*(\tau)+1} \tag{3.14}$$

$$\text{with } d_1\,(\tau) \quad = \quad \frac{v_{\text{rec}}}{\Gamma} \times \left(\frac{\Gamma\tau}{2}\right)^2 \tag{3.15}$$

where $v_{\text{rec}} = \hbar k/m$ denotes the recoil velocity. We deduce:

$$s^* = \begin{cases} \left((\tau/T_1)^2 - 1\right)^{-1} & \text{if } \tau > T_1 \\ \infty & \text{if } \tau \leq T_1 \end{cases} \tag{3.16}$$

where T_1 corresponds to $d_1\,(\tau = T_1) = \text{DoF}$ and equals to:

$$T_1 = \frac{2}{\Gamma}\sqrt{\frac{\text{DoF}\times\Gamma}{v_{rec}}} = 13.4\,\mu s \tag{3.17}$$

Then for $s \gg 1$, τ must not exceed T_1 so that $d_\tau \leq \text{DoF}$. For longer τ, the displacement effect is also more constraining than the Doppler effect as the former depends quadratically in time and not linearly. This leads for $\tau \sim 50\,\mu s$ to a very low bound in s: $I \lesssim 0.08 I_{\text{sat}}$. This happens to be experimentally difficult to work with as it leads to very small numbers of counts for our vertical imaging setup large magnification (see 3.2.2). Typically, we do not want to work with intensity $I \leq I_{\text{sat}}/4$. Then $\tau \lesssim T_1\sqrt{1+1/s_{\text{min}}} \approx 30\,\mu s$ with $s_{\text{min}} \approx 0.25$.

---

[4] This constraint does not apply for our horizontal imaging setup (see 3.2.1 for details) where the DoF is much larger ($\sim 100\,\mu$m)

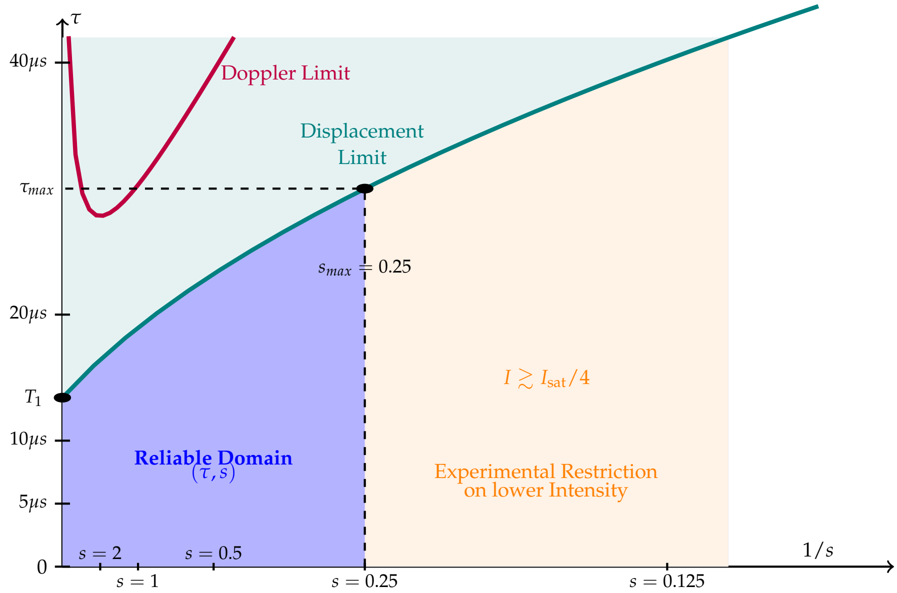

Figure 3.1.: Reliable and unreliable domains of imaging parameters due to Doppler effect and displacement over the pulse duration τ for varying saturation parameter s.

3.1.3.3. Summary

The constraints depicted above can be summarized by defining which couples (τ, s) lead to accurate detection under both conditions of small Doppler detuning and small displacements. We can plot reliable and unreliable domains in the convenient $(1/s, \tau)$ planar representation as done in Fig. 3.1. The constraints can be summarized in this plane by two threshold curves $(1/s^*, \tau^*)$ whose equations are deduced from above calculations [Eqs. 3.12-3.17] to be:

$$\begin{aligned} \text{Detuning: } \tau^* &= \frac{T_0}{4}\sqrt{s^*(1+1/s^*)^3}, \text{with } \frac{T_0}{4} = 10.7\,\mu s \qquad (3.18) \\ \text{Displacement: } \tau^* &= T_1\sqrt{1+1/s^*}, \text{with } T_1 = 13.4\,\mu s \qquad (3.19) \end{aligned}$$

The limit of acceptable domain of τ as a function of $1/s$ is defined by the lower value of these two curves as plotted in Fig. 3.1. Doppler effect happens to never be the most constraining of the two effects: We are always limited for our choice of imaging parameters by the small DoF. We deduce that there is no limitation on s for $\tau < T_1 \sim 13\,\mu s$. From pulse time $\tau > 13\,\mu s$, we must restrict to $I \leq s^*(\tau)\, I_{\text{sat}}$ where $s^*(\tau)$ is set along Eq. 3.19.

We conclude this analysis by choosing the relevant range of imaging parameters for both regimes of saturating and non saturating absorption imaging:

- **For our saturating imaging pulse, we choose $\tau = 4\,\mu s$, that lies in the "unconstrained" τ domain. We can then choose imaging intensities up to several hundreds of I_{sat}. In fact, we do not want to use too high I as it leads to higher photon shot noise on the detection of n. We typically use $I = 40 I_{\text{sat}}$.**

— As stated in the previous paragraph, we do not want to use $I < I_{\mathrm{sat}}/4$ for detection reasons. Then we must restrict to $\tau \lesssim 30\,\mu s$ (as represented in the Fig. 3.1). **For our non saturating imaging pulse, we choose $\tau = 20\,\mu s$, which enables s as high as** 0.8.

3.2. Imaging setup

In our experimental apparatus we are able to image our gases in two orthogonal directions of space:

— Along the x horizontal axis, with a moderately precise setup that mainly serves during the alignment procedure.

— Along the z vertical axis, with a highly precise setup that serves for the diagnostic of our gas configuration.

As absorption imaging is a destructive process we can not image the same cloud successively in the two directions and must repeat the production sequence to obtain images of similar clouds in varying imaging configurations.

With this two setups we can perform absorption imaging of the ^{87}Rb atoms close to the resonance of their D_2 line ($5^2S_{1/2} \rightarrow 5^2P_{3/2}$). We can adjust the detuning of our probing beam of approximately $\pm 3\,\Gamma$ around the atomic transition thanks to an acousto-optic modulator. We can also vary the intensity of the probing beam from 0.2 to 60 I_{sat} at the position of the atomic sample thanks to a second acousto-optic modulator and use both high and low intensity imaging. In both cases, we use linearly polarized light such that we do not have to worry about the magnetic field direction during imaging. Such a polarization does not correspond to an (approximately) cycling transition and we have to take into account corrections linked to averaging over hyperfine sublevels (such corrections modify the value of coefficient α of Eq. 3.9 by a factor 15/7 in the stationary regime). In this configuration, we must also ensure that the steady state of the Bloch Optics equations is reached and be sure that population has redistributed over the sublevels.

3.2.1. Horizontal Imaging

The horizontal imaging beam is collinear with both the hybrid trap and the light–sheet beams (propagating along x) and perpendicular to the box–trap beam (propagating along z, see Ch. 2 and Fig. 2.2 for an overall description of the experimental setup).

The beam intensity is collected via an achromatic triplet of focal length $f = 150$ mm from Melles–Griot. The in–situ distribution of the 2D atomic cloud is then appearing as a thin stroke limited by optical resolution along this imaging axis. Typically, we fit a gaussian of $3\,\mu$m waist, in agreement with the expected imaging triplet resolution. We deduce the DoF of this setup to be $\sim 100\,\mu$m.

The outgoing beam intensity distribution is detected by a CCD camera (*Ace*, Basler) of quantum efficiency of 24% at 780 nm [5]. The camera is placed after a telescope formed by the imaging triplet and an optical doublet so that it images the central plane of

---

[5] Its quantum efficiency is of 54% at 545nm. We need to multiple this value by the relative response at 780nm that is of 0.45.

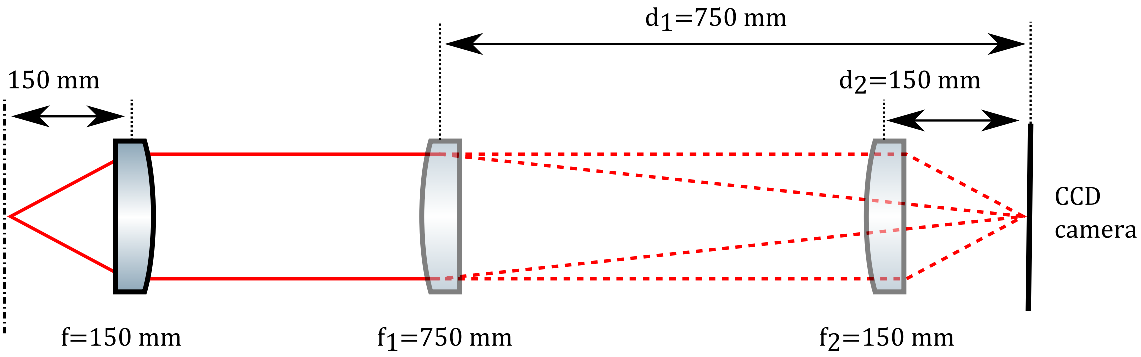

Figure 3.2.: Optical scheme for the horizontal imaging. The second lens can be chosen to adjust the magnification: either $\mathcal{M} = 5$ with $f_1 = d_1 = 750$ mm or $\mathcal{M} = 1$ with $f_2 = d_2 = 150$ mm.

the atomic cloud (see Fig. 3.2). The magnification of this imaging system can be either $\mathcal{M} = 1$ or $\mathcal{M} = 5$, by exchanging the second doublet of the telescope, as indicated in Fig. 3.2.

We can use both low intensity technique with[6] an exposure time $\tau_{\text{exp}} = 40\,\mu$s and an intensity $I \approx I_{\text{sat}}/5$, and the high intensity one with $\tau_{\text{exp}} = 4\,\mu$s and $I \approx 40\,I_{\text{sat}}$ by adding an optical density filter ($\mathcal{OD} = 1$) after the telescope to not saturate the camera. This imaging axis is primarily a diagnostic tool: it is mainly used to align the different optical dipole traps on each other and to perform some calibration measurements (for example frequency measurements of 2.2.2). We did not carefully calibrate the imaging parameters on this axis and the density is only determined up to a global multiplicative factor.

3.2.2. Vertical Imaging

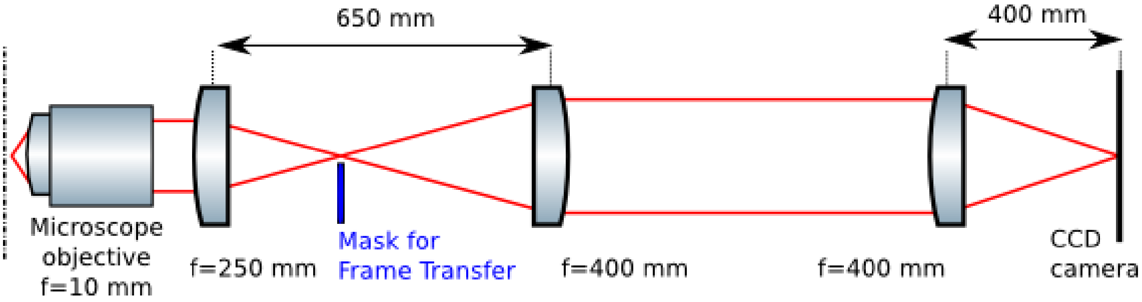

Figure 3.3.: Optical scheme for the vertical imaging. A specially designed high $\mathcal{NA}$ ($= 0.45$) is positioned just below the glass cell to image the cloud position. The total magnification is $\mathcal{M} = 25$. The mask for the frame transfer is placed at the intermediate focus.

---

[6] We remind that the constraints in 3.1.3 only hold for the vertical imaging setup. In this setup, the DoF is ten times smaller so that the constraints due to displacement effect are stronger. The magnification of the setup is also 5 to 25 times greater resulting in a stronger constraint on the minimal s (even though the quantum efficiency also has to be taken into account in this last statement.).

The vertical imaging beam is perpendicular to the 2D atomic plane and is propagating downward along this vertical axis (see Ch. 2 and Fig. 2.2 for an overall description of the experimental setup). This axis is used for precise measurements of the atomic density distribution.

As described in previous works [110], [111], this precision relies on a custom made microscope objective of high numerical aperture ($\mathcal{N}\mathcal{A} = \prime.\triangle\triangledown$) so that it enables high resolution on the atomic density. The tests carried out on a reference target by T. Yefsah [110] showed a resolution $\sim 1\,\mu$m. Together with a triplet, this objective forms an intermediate image of the atoms with magnification $\mathcal{M}_1 = 25$. This intermediate image makes a source for a telescope of magnification $\mathcal{M}_2 = 1$, finally projecting the image on a CCD camera (see Fig. 3.3). The total magnification of this system is $\mathcal{M} = 25$ so that the pixels correspond to an effective size of $0.52\,\mu\text{m} \times 0.52\,\mu\text{m}$ (real size of $13\,\mu$m). From an analysis of atomic images, we deduced that the total imaging system had a resolution better than $2\,\mu$m. We infer the DoF of this setup to be $\sim 10\,\mu$m.

The camera (*Pixis 1024*, Princeton Instruments) is also a fundamental element for our precision requirement as it has a very high quantum efficiency ($>95\%$ at $\lambda = 780\,$nm) and a low-noise readout which leads to shot-noise limited images.

To use the previously described imaging procedure for a quantitative analysis of our cloud, several calibrations are necessary:

— On the camera the intensities I_i and I_f are known only through the number of counts on the CCD frame and the high intensity term of Eq. 3.9, $(I_\mathrm{i} - I_\mathrm{f})/I_\mathrm{sat}$, is normalized to a theoretically known value I_sat. We will thus need to precisely calibrate the number of counts on the camera corresponding to the actual intensity $I = I_\mathrm{sat}$ on the atoms (see 3.3.2) .

— We will need to calibrate the imaging parameters α (see 3.3.3) and β (see 3.3.4) used in Eq. 3.9 to link the physical atomic density to measured intensities in this specific setup.

— We will also introduce a third parameter, γ, absent from Eq. 3.9, due to the specific mode in which we use our camera (see 3.3.1).

3.3. Calibrating absorption imaging coefficients.

3.3.1. Frame Transfer and additional intensity per frame exposure: introducing a new coefficient γ

As described in detail in [110], for measuring precisely the 2D density distribution, we use the high efficiency camera of 3.2.2 in the so-called *Frame Transfer* mode. This mode enables to take several pictures in a very short time lapse (less than 1 ms between two images).

Such a high repetition rate is of great importance in our absorption imaging procedure. As implied by Eq. 3.9, we need to know at the same time, the outgoing $I_\mathrm{f}(x, y)$ and the incoming $I_\mathrm{i}(x, y)$ intensity distributions in the atomic plane. To this aim, we experimentally take two successive images of our probing beam intensity, $\mathcal{I}_{\text{w. at.}}$ is taken with the laser shined in the presence of the atoms and $\mathcal{I}_{\text{no at.}}$ in their absence[7]. $\mathcal{I}_{\text{w. at.}}$

---

[7] Between the two images, the atoms are depumped to the $F = 1$ ground state

and $\mathcal{I}_{\text{no at.}}$ cannot be measured at the exact same time but we want to minimize the time lapse in between in order to filter out the effect of temporal fluctuations in intensity and pointing (that would result in unwanted discrepancy between the two images). We also take a third *dark* picture $\mathcal{I}_{\text{dark}}$ with no imaging beam pulse during the exposure time to distinguish ambient lighting from interesting photons coming through the atomic slab. It must also be taken close in time to the two first images to minimize variations but it is less sensitive than imaging beam fluctuations. In the imaging sequence we thus need three successive (useful) exposures of the CCD camera. The first one is necessarily the image of the atomic cloud $\mathcal{I}_{\text{w. at.}}$, then comes the most sensitive reference $\mathcal{I}_{\text{no at.}}$ and we finish taking $\mathcal{I}_{\text{dark}}$. The imaging sequence is represented in Fig. 3.4. We then compare the matrices of the counted number of incoming photons $\mathcal{I}_i = \mathcal{I}_{\text{no at.}} - \mathcal{I}_{\text{dark}}$ with the counted number of photons transmitted through the atomic cloud $\mathcal{I}_f = \mathcal{I}_{\text{w. at.}} - \mathcal{I}_{\text{dark}}$.

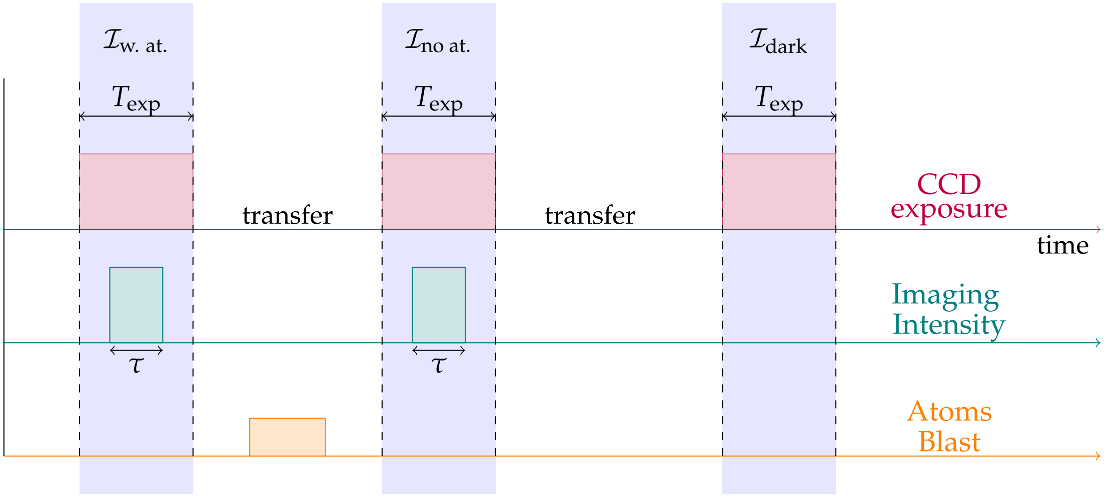

Figure 3.4.: Imaging sequence in the *Frame Transfer* mode. We successively expose during a time T_{exp} the **acquisition region** of the CCD frame to acquire $\mathcal{I}_{\text{w. at.}}$, $\mathcal{I}_{\text{no at.}}$ and $\mathcal{I}_{\text{dark}}$. During each exposure we displace the information contained by the pixels to the **storage region** (transfer). Between $\mathcal{I}_{\text{w. at.}}$ and $\mathcal{I}_{\text{no at.}}$, we depump the atomic sample to the $F = 1$ ground state.

A high repetition rate is traditionally difficult to achieve with a high efficiency camera as ours without adding unwanted noise or errors. It is achieved in the *Frame Transfer* mode by not reading out the different pictures between the successive exposures of the CCD frame. The successive pictures are simply moved very rapidly from one set of pixels to an other - not-exposed - one where they are so preserved until the final reading out process. We name this preserved region of the CCD the **storage region**. Then the initially exposed region of the CCD is blank and can be exposed again. We name this region of the CCD which collects photons during the exposure periods the **acquisition region**. The CCD frame is finally entirely (storage region and acquisition region) read out after the number of desired exposures.

The separation of the CCD frame in the **acquisition region** and the **storage region** must then be effective both in the computation process but also in a physical manner:

In order to preserve the information gathered, the **storage region** must be physically hidden to not receive photons during the camera exposure periods. To implement this acquisition mode we need to optically mask a part of the CCD chip. In our design, we physically hide a region optically-conjugated to the **storage region** in the intermediate image plane after the first triplet as shown in Fig. 3.3. The sharp cut separating both regions is realized thanks to a razor blade. A few unwanted photons can nevertheless reach the **storage region** and can be counted up to the stored data at each successive exposure period. Then, instead of being fixed from their initial exposure in the **acquisition region**, the pixels value of the data stored are increased for each exposure time following there initial transfer to the **storage region**. We denote $\mathcal{C}$ the average number of these extra counts per exposure. The exposure time T_{exp} being fixed for all our light pulse durations τ ($T_{exp} = 70\,\mu s$), $\mathcal{C}$ is a constant of our setup.

We experimentally observed an additional exposure of the stored frame in our experimental data. We calibrated $\mathcal{C}$ by comparing the over-exposure of the first and second frame compared to the third one when blocking the imaging beam. We took 20 absorption images while blocking the imaging beam and compared the three frames corresponding to the useful one for *Frame Transfer* (see Fig. 3.4). As the beam is blocked, in the ideal case where $\mathcal{C}$ is zero, these three frames must correspond to the same mean number of counts. If $\mathcal{C}$ is non zero then we must measure some discrepancy between the three frames: The first (resp. second) frame must have in average $\Delta_{13} = 2\mathcal{C}$ (resp. $\Delta_{23} = \mathcal{C}$) counts in more than the third. On the three frames, we compared the mean numbers of counts in a region of interest of 101×101 pixels centered on the atomic cloud position and away from the frame edges. We measured $\Delta_{13} = 17.6(7)$ and $\Delta_{23} = 8.2(4)$ (errorbars are standard deviations). From this, we deduce $\mathcal{C} = 8.5(4)$. We can easily repeat this calibration procedure regularly simply taking a few images with the beam blocked and check that $\mathcal{C}$ is not modified.

We check that $\mathcal{C}$ is not changed if we unblock the probing beam but take image in the absence of atoms. In that case we compare only the two first frames in which the pulse beam is produced (see Fig. 3.4). We found $\mathcal{C} = 11(4)$. In this case, we found a higher error due to higher photon shot noise.

In our imaging analysis, we take this correction into account and correct $\mathcal{I}_{\text{w. at.}}$ by subtracting $2\mathcal{C}$ and $\mathcal{I}_{\text{no at.}}$ by subtracting $\mathcal{C}$. Eq. 3.9 is then corrected along

$$d \equiv n\sigma_0\,\beta = -\alpha \ln\left(\frac{I_\mathrm{f} - 2\gamma}{I_\mathrm{i} - \gamma}\right) + \frac{I_\mathrm{i} - I_\mathrm{f} + \gamma}{I_\mathrm{sat}}. \tag{3.20}$$

with γ is the intensity corresponding to the photon number $\mathcal{C}$, $\gamma = \mathcal{C}\,\hbar\omega_L/(T_\mathrm{exp}\,\mathcal{A}_\mathrm{px})$ wihere $\mathcal{A}_\mathrm{px}$ the effective area of a pixel of the camera at the atom location, $\gamma = 11.5(5)\,\mu\mathrm{W/cm^2}$. Such a correction is important for non-saturating imaging procedure and it mainly affects the low–density regions of the cloud.

3.3.2. Calibrating the number of counts to the actual intensity seen by the atoms: efficiency η

To use high intensity absorption imaging, we need to accurately determine the number of CCD counts per imaging pulse $\mathcal{I}_\mathrm{sat}^\mathrm{cam}$ corresponding to $I = I_\mathrm{sat} = 1.67\,\mathrm{mW/cm^2}$ in the atomic plane. The expected value for a pulse of duration τ imaged along a perfect path and by an ideal camera is $\mathcal{I}_{\text{sat}}^{0} = \tau\, \mathcal{A}_{\text{px}}\, I_{\text{sat}}/\hbar\omega_L$. The correction η to this value is due both to the transmission efficiency of our imaging setup η_{path} and to the camera quantum efficiency η_{cam}.

We directly estimate η_{path} by power measurements along the path. We take into account corrections due to the two uncoated diopters of (the upper face of) the glass cell and to the irrelevant power loss due to the razor blade[8]. We find $\eta_{\text{path}} = 0.43$. This low value is explained by:

- the two uncoated diopters of (the bottom face of) the glass cell ton the beam path in between the atomic sample and the camera.
- the large number of optical diopters of the specially designed and large aperture microscope objective used in this setup.

We also directly measure the quantum efficiency of our Princeton camera by comparing the measured power just in front of the chip to the power deduced from the total number of counts $\mathcal{I}_{\text{count}}$ on the CCD frame[9]: $P_{\text{count}} = \mathcal{I}_{\text{count}}\, \tau\, \hbar\omega_L$. We find $\eta_{\text{cam}} = 0.89$ compatible with the theoretical value[10] of $\eta_{\text{cam}}^{(th)} = 0.855$. We choose to use this value of $\eta_{\text{cam}} = 0.855$. The global efficiency is then $\eta = \eta_{\text{path}}\, \eta_{\text{cam}} = 0.365$.

3.3.3. Calibration of the α coefficient

Once the conversion from the number of counts $\mathcal{I}_i$ and $\mathcal{I}_f$ to the intensity I_{i} and I_{f} is determined (via η and γ), we can address the calibration of the coefficients appearing in Eq. 3.9, namely α and β. In this equation, α is the coefficient enabling coherence between all sets of imaging parameters (various pulse durations τ and probe beam intensities $I = sI_{\text{sat}}$). Indeed, it corrects the relative amplitudes of the "high" and the "low" intensity terms contributing to the optical density (OD). The principle of the calibration of the coefficient α relies on this aim of consistency: When we vary the imaging parameters τ and s as we keep constant the atomic density n (the cloud configuration), it must exist an appropriate value of α, denoted α^*, for which the OD distribution $d_\alpha\,(x,y)$ computed along

$$d_\alpha\,(x,y) = -\alpha \ln\left(\frac{I_{\text{f}}\,(x,y)}{I_{\text{i}}\,(x,y)}\right) + \frac{I_{\text{i}}\,(x,y) - I_{\text{f}}\,(x,y)}{I_{\text{sat}}}, \tag{3.21}$$

similar to Eq. 3.9, is a constant. α^* is then the value of α for which the estimate of Eq. 3.21 is proportional to the physical atomic density (to the multiplicative factor $\beta\sigma_0$).

3.3.3.1. Need for a new calibration of the α coefficient

Calibrations of the coefficient α (and of the detectivity coefficient β) for our experiment were completed in 2010 as described in [110]. It needed to be redone since the

---

[8] The purpose of the razor blade is to block a part of the imaging beam that is far from the image of the atomic sample in this intermediate image plane. So the power loss induced by this mask is not a loss of information on the atomic density. Only useless photons are eliminated and they must not be taken into account in our efficiency calibration

[9] We also correct for out of frame intensity by performing a Gaussian fit

[10] taking into account the interferometric filter at the entrance of the camera

experimental setup has been deeply modified since then (see Ch. 2). In particular, the magnetic fields applied during the imaging pulse have substantially changed. We do not anymore trap the 2D atomic sample with a magnetic confinement as the *Trap Orbiting Potential* (TOP) in use until 2012. Now the atoms in the 2D plane are only held by optical potentials (the light–sheet and the box–trap). Nevertheless, we use a magnetic gradient to levitate our atomic ensemble and compensate the gravity ($b'_z = 15\,\mathrm{G/cm}$) in our fully-optical trap [11].

Furthermore, the calibration procedure needed to be modified for recent experiments. As described in [110], we previously calibrated α using *in-situ* images of a 3D cloud at varying imaging parameters. At that time, both the 2D and the 3D clouds were confined in a TOP trap and so the in–situ environment of both clouds were the same. Moreover, in the TOP trap, our gases were harmonically confined so that we were able to probe with a unique in–situ cloud a wide range of densities. Finally, to circumvent density effects, we could focus on the low-density wings of this cloud.

In our new setup, all these attributes are modified. First due to the switch to a fully optical 2D trap loaded from an hybrid magnetic and optical trap, the environment between the 3D and the 2D trap is changed (see 2.1.2) [12]. To calibrate the imaging, we prefer to directly use the final 2D configuration to be sure not to perturb our calibration by changes in the environment. Second, the uniform potential in the 2D (xy)-plane precludes using *in–situ* images for the calibration. Indeed, in such a potential, we cannot investigate a varying range of n by *in–situ* imaging. To overcome this, we use 2D Time–of–Flight (see 2.1.3) to let the density distribution expands into a non-uniform one, while remaining confined in the 2D plane. We can also use an additional 3D ToF to lower the density of the atomic cloud but short enough so that the measurement is not perturbed by out–of–focus effects. As the depth–of–field is $\mathrm{DoF} = 10\,\mu\mathrm{m}$, for typical temperature $T = 100\,\mathrm{nK}$, we are limited to ToF duration $\leq 3\,\mathrm{ms}$. Note that we keep the levitating magnetic gradient active (with constant b'_z and d_z) during these ToFs and the imaging process so that the *in–situ* magnetic environment is preserved until imaging (in particular no Eddy currents may perturb the calibration).

3.3.3.2. Principle of the calibration procedure for α coefficient

In a general manner, the experimental procedure to calibrate α consists in the following steps:

1. We select an appropriate experimental configuration for our 2D expanding cloud. In practice, we choose the values of the final powers of the hybrid–trap and the box–trap beams and the ToF durations [13].
2. We take a set of N absorption images of the cloud prepared in this reference configuration [14] with various couples (τ, s). We choose $\tau \in \{4, 8, 10, 12, 16, 20\}\,\mu\mathrm{s}$.

---

[11] The zero of the magnetic field is above the atoms at a distance $d_z \approx 1.5\,\mathrm{mm}$ (see 2.1.3). The resulting magnetic field is thus $B_0 = b'_z d_z = 2.25\,\mathrm{G}$.

[12] Due to the reduced values $d_z \approx 300\,\mu\mathrm{m}$ and $b'_z = 12.5\,\mathrm{G/cm}$ used for the hybrid trapping, the magnetic field at the atom position is $B_0 \approx 0.4\,\mathrm{G}$ in this case.

[13] In fact we will select two of these configurations, and do the following procedure for both.

[14] as the imaging process is destructive, we cannot image several times the same cloud so we repeat

As pointed out in 3.1.3, we must care that (τ, s) corresponds to a reliable configuration in terms of radiative pressure effects. For each image $k \in [1, N]$, we obtain the matrices $\mathcal{I}^{(k)}_{\text{w. at.}}$, $\mathcal{I}^{(k)}_{\text{no at.}}$ and $\mathcal{I}^{(k)}_{\text{dark}}$ of the number of counts on the camera for the various exposures of Fig. 3.4.

3. Then we compute for each image $k \in [1, N]$ and for each pixel (x, y) the intensity distributions of the input and output beams:

$$\begin{aligned} I_{\text{i}}\left(x,y;k\right) &= \left(\mathcal{I}^{(k)}_{\text{no at.}} - \mathcal{I}^{(k)}_{\text{dark}} - \mathcal{C}\right)\hbar\omega_L/\left(\tau\mathcal{A}_{\text{px}}\right) && (3.22)\\ I_{\text{f}}\left(x,y;k\right) &= \left(\mathcal{I}^{(k)}_{\text{w. at.}} - \mathcal{I}^{(k)}_{\text{dark}} - 2\mathcal{C}\right)\hbar\omega_L/\left(\tau\mathcal{A}_{\text{px}}\right). && (3.23)\end{aligned}$$

and deduce the log part $d_{\log}$ (corresponding to the "low" intensity term) and the difference part d_{diff} (the "high" intensity term) of Eq. 3.21:

$$\begin{aligned} d_{\log}\left(x,y;k\right) &\equiv -\ln\left(\frac{I_{\text{f}}\left(x,y;k\right)}{I_{\text{i}}\left(x,y;k\right)}\right) && (3.24)\\ d_{\text{diff}}\left(x,y;k\right) &\equiv \frac{I_{\text{i}}\left(x,y;k\right) - I_{\text{f}}\left(x,y;k\right)}{\eta I_{\text{sat}}}. && (3.25)\end{aligned}$$

4. We want to compare the behaviors of $d_{\log}$ and d_{diff} while varying (τ, s) and deduce α^* the value of α for which

$$d_\alpha\left(x,y;k\right) = \alpha d_{\log}\left(x,y;k\right) + d_{\text{diff}}\left(x,y;k\right) \qquad (3.26)$$

is a constant. We point out that in Eqs. 3.22-3.26 , we took into account the previously calibrated imaging coefficients [15] $\mathcal{C}$ and η.

The comparison of the N images must be carried out considering the variation of the density n (or equivalently of d) within the cloud configuration. The most severe way to account for these variations is to treat each pixel (x, y) independently (as they correspond to independent tiny regions of the cloud of fixed density $n(x, y)$). To improve the calibration quality, we perform some averaging of our data on pixels sets with the same (expected) n. We use disk-shaped box–trap potentials. After some 2D or 3D expansion times, the uniformity of the density distribution is lost but the azimuthal symmetry of the initial profile is preserved. Then, we perform azimuthal averaging and examine optical density in terms of distance to the cloud center r [16]: $d_{\log}\left(r;k\right)$, $d_{\text{diff}}\left(r;k\right)$ and $d_\alpha\left(r;k\right)$.

3.3.3.3. A new calibration procedure for α coefficient

To perform this calibration, we have in fact developed two methods:

---

the same preparation.

[15] In the previous calibrations (performed in 2010), γ was unknown and so set to zero and η was set to 1. We infer from this that the newly calibrated value of α and β must be strongly modified from the previously values $\alpha^{(2010)} = 2.6$ and $\beta^{(2010)} = 0.4$ even if the physical apparatus was not changed.

[16] We take the residual anisotropy of the cloud distribution into account in the definition of r. We first perform a gaussian fit of our data and account for the fitted ellipticity. These fits also give the position of the cloud center.

1. The historical analysis procedure developed by G. Reinaudi [137]. It is based on minimizing the standard deviation of the optical density $d_\alpha(x,y;k)$ over α for a set of (τ, s). This was used in the previous calibration campaign in 2010 [110]. The results of this method for our 2014 calibration campaign are detailed in Annex E. It leads to unexpected observations inspiring us the development of a new analysis procedure.
2. The new and more straightforward method we settled at the occasion of the 2014 campaign. It is based on a simple linear fit on the set of the N couples $(d_{\log}(x,y;k), d_{\mathrm{diff}}(x,y;k))$ from which we deduce the optical density d and the parameter α^*. It, in particular, enables a better analysis of our experimental data points, a discrimination of outlying points, a study of possible deviations to the expected law for some sets of imaging parameters and an estimate of the fit confidence on our calibrated coefficient.

We implemented these analysis for two cloud configurations:

— one **«cold » configuration** where the cloud shows high densities. The 2D traps are directly loaded from a 3D BEC and the box–trap height is then lower to very small final value to reach cold temperature and highly degenerate 2D regime. We then use a 2D ToF of 6ms followed by a 3D ToF of 2 ms to reduce the possible multiple-scattering effects.

— one **«hot » configuration** where the density is lower and the cloud is not degenerate. The 2D traps loaded from a 3D thermal gas and only moderately evaporated. We then use a 2D ToF of 3ms but not the 3D ToF as the densities are already sufficiently low to avoid 2D multiple scattering effects [17].

Both configurations were measured during two different series so we analyzed in total data from 4 different series.

3.3.3.4. Description of the new calibration procedure: direct fit of the optical density terms.

In this analysis we directly compare the two terms $d_{\log}(r;k)$ and $d_{\mathrm{diff}}(r;k)$ defined in Eqs. 3.24-3.25 contributing to the optical density (Eqs. 3.9 and 3.26).We remind here their definition:

$$d_{\log}(x,y;k) \equiv -\ln\left(\frac{I_{\mathrm{f}}(x,y;k)}{I_{\mathrm{i}}(x,y;k)}\right) \tag{3.27}$$

$$d_{\mathrm{diff}}(x,y;k) \equiv \frac{I_{\mathrm{i}}(x,y;k) - I_{\mathrm{f}}(x,y;k)}{\eta I_{\mathrm{sat}}}. \tag{3.28}$$

The log term has a dominant contribution for small probing intensity ($I \lesssim I_{\mathrm{sat}}$) and the difference term prevails at high probing intensity ($I \gg I_{\mathrm{sat}}$). Then the couple $(d_{\log}(r;k)$, $d_{\mathrm{diff}}(r;k))$ roughly varies from $(\alpha^* d(r), 0)$ to $(0, d(r))$ when $s(= I/I_{\mathrm{sat}})$ varies from $s \sim$

---

[17] the 2D ToF is performed at a lower power of the LS beam so that the confinement along z is reduced to $\omega_z/2\pi = 300Hz$. The thickness of the cloud is then enlarged to $\ell_z \approx 880\,\mathrm{nm}$ so that multiple scattering effect are already negligible at optical densities $d \lesssim 2$ as $k\ell_z = 7.1$(cf Annex D)

0 to $s \ggg 1$ (where $d\left(r\right)$ is the OD at radius r - $d\left(r\right) = \beta\sigma_0 n\left(r\right)$ - and α^* is the physical value of the α coefficient.).

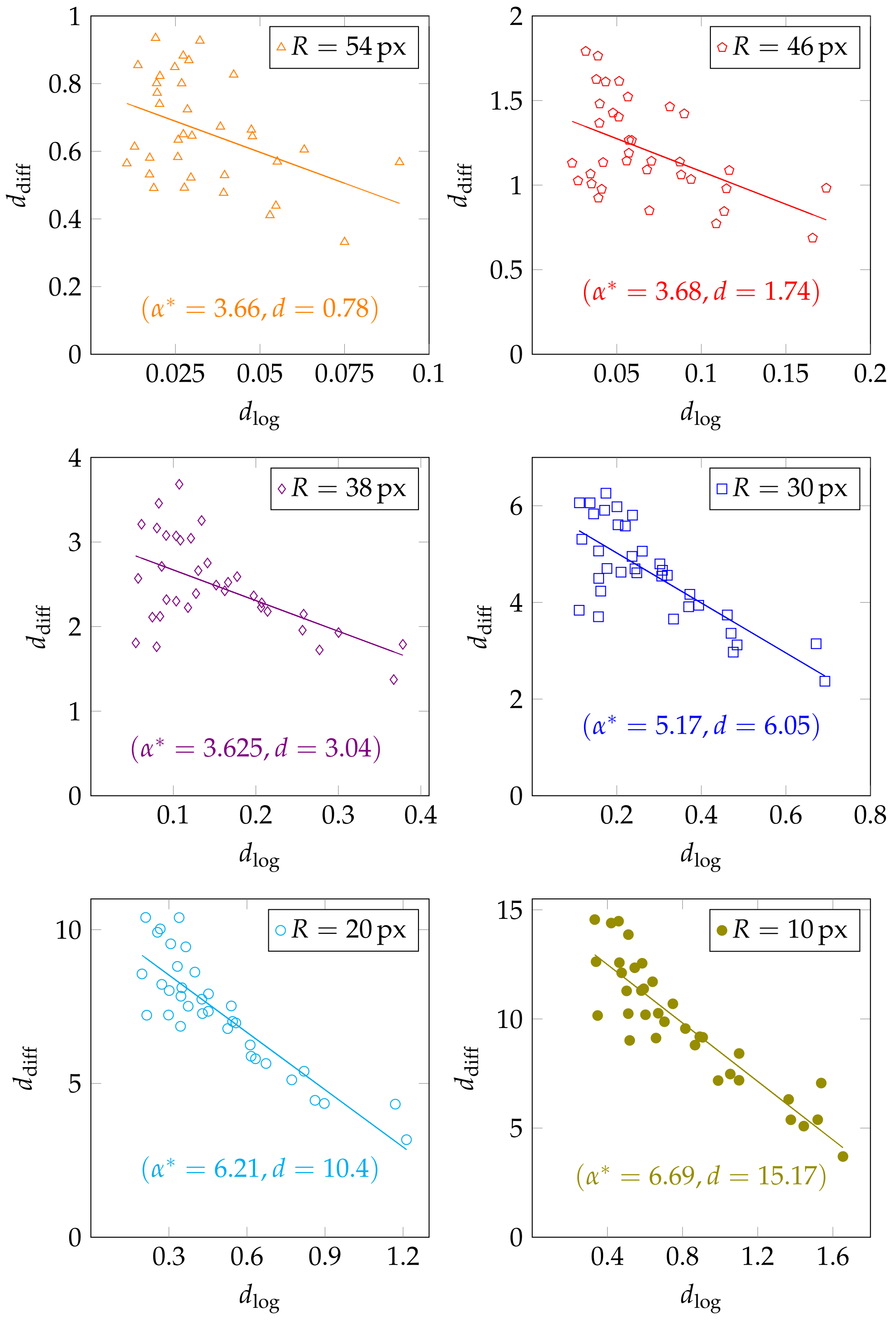

Figure 3.5.: Six examples of sets of couples $(d_{\log}(R;k), d_{\mathrm{diff}}(R;k))$ corresponding to four distinct atomic densities $n(R)$. The set correspond to data from one of the «cold» series. They are obtained from azimuthal averaging at radius $R = 10\,\mathrm{px}$, $R = 20\,\mathrm{px}$, $R = 30\,\mathrm{px}$, $R = 38\,\mathrm{px}$, $R = 46\,\mathrm{px}$, $R = 54\,\mathrm{px}$ (in camera pixels). Each point corresponds to one picture and thus to one specific imaging configuration. The solid lines is the linear fit and the two parameters resulting from this fit are indicated below.

In fact, according to Eq. 3.9, we expect that all couples (for all imaging parameters τ and s) collapse into a line of equation

$$d_{\mathrm{diff}}\left(r;k\right) = d\left(r\right) - \alpha^{*} d_{\log}\left(r;k\right) \tag{3.29}$$

We can then directly evaluate α^* and $d(r)$ by a linear regression of our experimental set of $\left(d_{\log}\left(r;k\right), d_{\mathrm{diff}}\left(r;k\right)\right)$ at a given radius r. This fit gives an estimate of α^* for each radius r denoted $\alpha^*_{\mathrm{lin}}(r)$. We expect $\alpha^*_{\mathrm{lin}}(r)$ to be approximately constant (equal to α^*).

In this analysis, we may visualize any possible defect of the experimental data as we directly plot the physical contributions $d_{\log}\left(r;k\right)$ and $d_{\mathrm{diff}}\left(r;k\right)$. For all series of data and all r, we do not detect any flaw in the sets of $\left(d_{\log}\left(r;k\right), d_{\mathrm{diff}}\left(r;k\right)\right)$ as shown in Fig. 3.5, for an example of six sets corresponding to distinct atomic densities $n(R)$ obtained at different R within the same data series. One point in these graphs corresponds to one couple (τ, s). We observe no systematic deviation of the point sets to the linear law (distribution of the residuals of the fit is centered around zero) for all investigated $n(R)$. Moreover, the dispersion of the $d_{\mathrm{diff}}\left(r;k\right)$ data points stays of the same relative order for all $d_{\log}\left(r;k\right)$ in each data set and does not reveal any pathologic behavior. We conclude that we can rely on the linear fits (as long as the data points are themselves of good enough quality that is for example for a high enough $n(R)$).

It is also clear from Fig. 3.5 that the slope of the linear fits $\alpha^*_{\mathrm{lin}}(R)$ depends on $n(R)$. In the six sets shown, it seems that $\alpha^*_{\mathrm{lin}}(R)$ increases with $n(R)$ (as shown in $d(R)$ fitted values or from the simple fact that $n(R)$ decreases with R).

Thus this dependency has to be interpreted as a physical phenomenon and not as a flaw of the experimental data. We will attempt to give a physical explanation in the next section but before we will use the results of the linear fit to conclude on α^* value. These direct linear fit has the advantage to give an estimation of the experimental confidence in α^* and thus of the uncertainty of the calibration contrarily to the historical procedure (see Annex E). From this knowledge, we can effectively and quantitatively point out the discrepancies of the fitted α^* according to the atomic density n on the overall set of data and enhance it as a physical effect. We can directly represent α^* as a function the estimated density $n \propto d$ by plotting the couples of fitted parameters $\left(d_{\mathrm{lin}}\left(r\right), \alpha^*_{\mathrm{lin}}(r)\right)$ as done in Fig. 3.6. We notice a change in $\alpha^*(d)$ dependency and identify:

- A plateau $\alpha^*(d) = \alpha^*_{\mathrm{low}}$ at low density $d \leq 5$. The fits seems reliable for $d \geq 0.7$ (relying on error bars amplitude). In this restricted range of d, the weighted average of $\alpha^*(d)$ gives $\alpha^*_{\mathrm{low}} = 3.73(13)$.
- A deviation toward larger α^* at high density $d > 5$. We fit a linear dependency to $\alpha^*(d)$ and find $\alpha^*_{\mathrm{high}}(d) = 3.75(37) + [0.21(3)] \times d$.

3.3.3.5. Qualitatively (possible) physical explanation to the α^* dependency on the atomic density n:

We conclude in the previous section that $\alpha^*(d)$ dependency must be understood as a physical effect. As the highlighted dependency occurs at high d (Fig. 3.6), one is tempted to incriminate multiple scattering effects once again. In this section, I will explained why such an effect may potentially explain the observed variation of α^* with

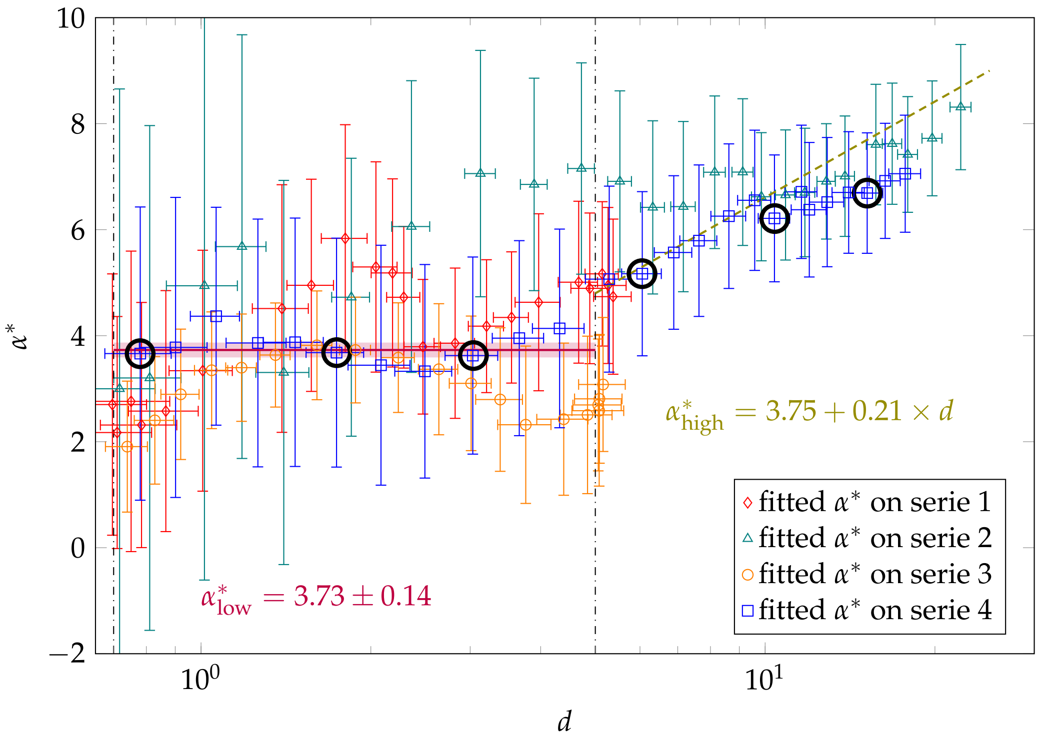

Figure 3.6.: Fitted values of $d\,(r)$ and $\alpha^*\,(r)$ for all series (1 and 3 correspond to the hot configuration. 2 and 4 to the cold one). The error bars represents the 95% confidence interval of the linear fit. In this graph, we circle the data represented in Fig. 3.5 (from series 4). We identify a plateau for $d \in [0.7; 5]$. The thick solid line represent the weighted average on this plateau $\alpha^*_{\text{low}} = 3.73(13)$. For $d \geq 5$, we characterized the variation of α^* by a linear dependency $\alpha^*_{\text{high}}(d) = 3.75(37) + [0.21(3)] \times d$. We do not plotted data with $d \leq 0.7$ as they lead to unreliable values of the fitted coefficients $d\,(r)$ and $\alpha^*\,(r)$. The dash-dotted black line identifies the separation between the different regimes.

d. However, I will not give any quantitive model to this.

Multiple scattering effects occur in the very dense regions of the cloud. In the model developed in Annex D, we saw that the effect becomes negligible for thick enough cloud with $k\ell_z \gg 1$ (ℓ_z stands for the thickness of the cloud). We calculated for example that, for $d \lesssim 4$, the effect disappears for $k\ell_z \gtrsim 20$. But in our samples we deduce from the linear fits that the OD [18] can be as large as $d \sim 25$ (in the center of our «cold» clouds). In such a regime, the thickness threshold on $k\ell_z$ for neglecting multiple scattering effects must be strongly increased. In our experiment, we restrict to cloud transverse extension smaller than the imaging depth of field DoF $= 10\,\mu$m, leading to $k\ell_z \leq k\,\text{DoF} \sim 80$. Then, in the very dense regions of the cloud, multiple scattering effects can still be of importance.

Intuitively, multiple scattering effects tend to decrease the number of photons scat-

---

[18] In these fits, we, in fact, deduced the OD up to the multiplicative factor β. Nevertheless, we expect (see 3.1.2) and will experimentally confirm (see 3.3.4) that $\beta = 1$.

tered by the cloud. In consequence, the outgoing beam intensity $I_\mathrm{f}^\mathrm{mes}$ measured after crossing the cloud is greater than the value $I_\mathrm{f}^\mathrm{exp}$ expected from application of the law of Eq. 3.9 with a constant α extracted from the reliables low density region ($\alpha = \alpha^*_\mathrm{low}$): $I_\mathrm{f}^\mathrm{mes} \geq I_\mathrm{f}^\mathrm{exp}$. Then, both the log part and the difference part of the measured OD are lower than the predictions:

$$d_\mathrm{log}^\mathrm{exp} = -\ln\left(\frac{I_\mathrm{f}^\mathrm{exp} - 2\gamma}{I_\mathrm{i} - \gamma}\right) \geq d_\mathrm{log}^\mathrm{mes} = -\ln\left(\frac{I_\mathrm{f}^\mathrm{mes} - 2\gamma}{I_\mathrm{i} - \gamma}\right) \tag{3.30}$$

$$d_\mathrm{diff}^\mathrm{exp} = \frac{I_\mathrm{i} - I_\mathrm{f}^\mathrm{exp} + \gamma}{\eta I_\mathrm{sat}} \geq d_\mathrm{diff}^\mathrm{mes} = \frac{I_\mathrm{i} - I_\mathrm{f}^\mathrm{mes} + \gamma}{\eta I_\mathrm{sat}} \tag{3.31}$$

These multiple scattering effects should become of less and less importance as we increase the probing beam intensity I_i. At the limit $I_\mathrm{i} \to \infty$, they must disappear. Then the shifts $d_\mathrm{log}^\mathrm{exp} - d_\mathrm{log}^\mathrm{mes}$ and $d_\mathrm{diff}^\mathrm{exp} - d_\mathrm{diff}^\mathrm{mes}$ are decreasing functions of I_i. As demonstrated in previous section, $I_\mathrm{i} \ll I_\mathrm{sat}$ corresponds in the plane $(d_\mathrm{log}, d_\mathrm{diff})$ to high $d_\mathrm{log} \sim \alpha d$ and low $d_\mathrm{diff} \ll d$. In the contrary, $I_\mathrm{i} \gg I_\mathrm{sat}$ corresponds to low $d_\mathrm{log} \ll d$ and high $d_\mathrm{diff} \sim d$.

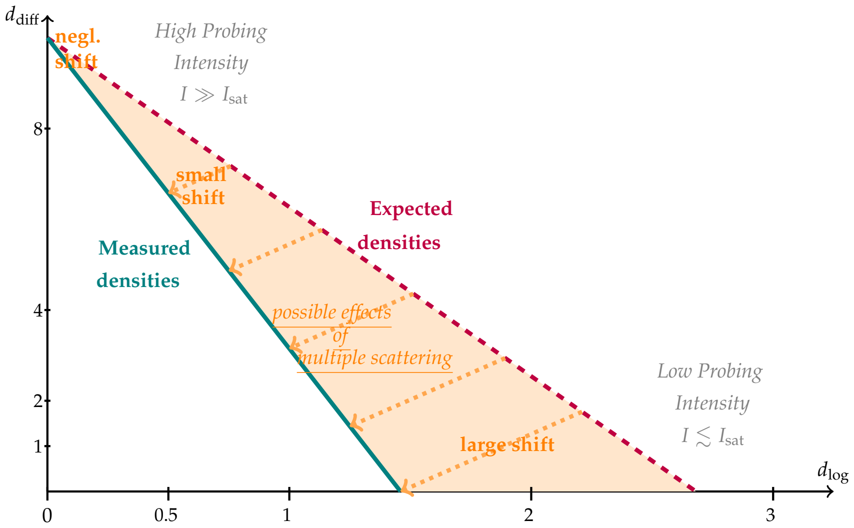

Figure 3.7.: Graphical representation of the possible effects of multiple scattering on $(d_\mathrm{log}, d_\mathrm{diff})$ distribution at a high d and varying imaging parameters. We consider a fixed $d (= 10)$, the expected distribution set along $d_\mathrm{diff}^\mathrm{exp} = d - \alpha^* d_\mathrm{log}^\mathrm{exp}$ and is represented by the dotted purple line. For a given $(d_\mathrm{log}^\mathrm{exp}, d_\mathrm{diff}^\mathrm{exp})$, we expect from multiple scattering effect a shift of both measured quantities $(d_\mathrm{log}^\mathrm{mes}, d_\mathrm{diff}^\mathrm{mes})$ with $d_\mathrm{log}^\mathrm{mes} \leq d_\mathrm{log}^\mathrm{exp}$ and $d_\mathrm{diff}^\mathrm{mes} \leq d_\mathrm{diff}^\mathrm{exp}$. It is represented by the orange arrows. The shift is larger when s is lower that is to say in the lower right corner of the plane (see text). The solid teal line shows the schematic resulting behavior of $(d_\mathrm{log}^\mathrm{mes}, d_\mathrm{diff}^\mathrm{mes})$.

Then, as represented in Fig. 3.7, multiple scattering effects induce a shift in the relation $d_\mathrm{diff} = f(d_\mathrm{log})$ that can be interpreted as an increase of the absolute value of the slope as the shift $d_\mathrm{diff}^\mathrm{exp} - d_\mathrm{diff}^\mathrm{mes}$ decreases with decreasing value of d_log. The relation $d_\mathrm{diff} = f(d_\mathrm{log})$ may or may not stay linear while the multiple scattering effects decrease with increasing I. As shown in Fig. 3.5, experimental observations are in agreement with a new linear dependency. To fully explain this new linear law requires a more quantitative model of the disappearance of multiple scattering effects with increasing probing intensity. Nevertheless, the effect deduced from this analysis is in qualitative agreement with the observed increase of α^* with the optical density for $d \geq 5$.

3.3.3.6. Conclusion on α analysis:

In conclusion, we think that multiple scattering effects explain the observed variation of the imaging coefficient α^* with atomic density n. We then rely on α^* value only for low enough densities ($d \leq 5$ or equivalently $n \leq 17\,\mu\text{m}^{-2}$) and take $\alpha^* = 3.73(13)$.

To compute n in the denser regions of the cloud, we must develop a new procedure. As we experimentally shown that the d_{diff} still follows a linear dependency in d_{log}, we deduce that Eq. 3.9 remains an (empirically) valid relation to compute the physical density. Nevertheless, we then need to compute a specific value of α for each n with $\alpha(n) \geq \alpha^*$. We implement an empirical model for $\alpha(n)$ deduced from a new fit of the set of the experimental couples (d, α^*) of Fig. 3.6. We fit the total set (d, α^*) to a «slope–breaking» function given by

$$\alpha(d) = \alpha^*_{\text{break}} + c_{\text{break}} \times \left((d - d_{\text{cut}}) + |d - d_{\text{cut}}|\right)/2 \tag{3.32}$$

We chose to set d_{cut} to 2.5. We then fitted $\alpha^*_{\text{break}} = 3.75(14)$ which is in agreement with the value of α^*, and $c_{\text{break}} = 0.26(2)$. We will then use the empirical model:

$$\alpha(n) = \alpha^* + 0.13 \times \left((n - n_{\text{cut}}) + |n - n_{\text{cut}}|\right) \tag{3.33}$$

where $n_{\text{cut}} = d_{\text{cut}}/\sigma_0 = 8.6\,\mu\text{m}^{-2}$ and $\alpha^* = 3.73$.

Then the procedure to compute $\alpha(n)$ and n for each pixel (x, y) of an absorption image will be iterative and proceed as follow:

1. We compute $d_{\text{log}}(x, y)$ and $d_{\text{diff}}(x, y)$ according to Eqs. 3.24–3.25.
2. We compute a first estimate of the OD by $d_0(x, y) = \alpha^* \, d_{\text{log}}(x, y) + d_{\text{diff}}(x, y)$.
3. Then there are two possibilities. If $d_0(x, y) \leq 2.5$ then $n(x, y) = d_0(x, y)/\sigma_0$ and $\alpha(x, y) = \alpha^*$. Otherwise, we compute $n(x, y)$ and $\alpha(x, y)$ by an iterative process:
    a) We compute an approximate value of α by $\alpha_0(x, y) = \alpha(d_0(x, y)/\sigma_0)$ from Eq. 3.33 and using the first estimate of the OD, $d_0(x, y)$.
    b) We deduce a new guess of the OD by $d_1(x, y) = \alpha_0(x, y)\, d_{\text{log}}(x, y) + d_{\text{diff}}(x, y)$.
    c) We appraise the accuracy of this new estimate by comparing the two successive evaluations $d_0(x, y)$ and $d_1(x, y)$. We consider that the process has converged when these two quantities are different by less than a few percent (typically 5%) from their mean value. If it is the case, then we set $n(x, y) = d_1(x, y)/\sigma_0$, $\alpha(x, y) = \alpha_0(x, y)$ and we exit the looping process[19].

---

[19] We note that to treat burnt pixels we also impose $\alpha \leq \alpha_{max}$. We choose $\alpha_{max} = 30$ so that it corresponds to a maximal OD $d_{max} \approx 100$

d) If the process has not converged yet, we calculate a new guess of the coefficient α, $\alpha_1(x,y) = \alpha(d_1(x,y)/\sigma_0)$ from Eq. 3.33 taking into account the modification of the OD.

e) We deduce a third assessment of the OD $d_2(x,y) = \alpha_1(x,y)\, d_{\log}(x,y) + d_{\text{diff}}(x,y)$ and compare it to $d_1(x,y)$. As previously, if the discrepancy is small enough to consider that the process has converged we set $n(x,y) = d_2(x,y)/\sigma_0$, $\alpha(x,y) = \alpha_1(x,y)$ and we exit the looping process.

f) As long as the process has not converged, we recompute an k^{th} estimate $\alpha_{k-1}(x,y) = \alpha(d_{k-1}(x,y)/\sigma_0)$ and $d_k(x,y) = \alpha_{k-1}(x,y)\, d_{\log}(x,y) + d_{\text{diff}}(x,y)$. The discrepancy between $d_{k-1}(x,y)$ and $d_k(x,y)$ decreases with k and reach the «process–convergence» condition at a given k. We then set $n(x,y) = d_k(x,y)/\sigma_0$, $\alpha(x,y) = \alpha_{k-1}(x,y)$ and we exit the looping process.

Such an iterative computation must converge fast if the imaging parameters have been correctly chosen. Usually, less than five iterations are needed. We note that if there are some very dense regions in the cloud, then the higher the probing intensity is, the more efficient this procedure. It also turns more accurate as it lower the influence of bad calibration of the empirical model $\alpha(n)$.

3.3.4. Calibrating the global detectivity factor β

In Eq. 3.9, β is the coefficient that links the model to the physical reality: it ensures the correspondence between the measured density distribution to the physical one. To find its experimental value, we must rely on other physical properties that depend on the gas density distribution. For our setup we choose to use **two–dimensional expansion of a highly degenerated uniform 2D cloud.**

In a 2D ToF, the interactions play an substantial role (if they are already important *in-situ*) in the expansion dynamics as the $2D$ confinement remains active and the gas does not expand along z. If we assume the gas is highly degenerate, we can model its expansion using (2D) Gross–Pitaevskii (GP) equation (see Annex B) in which the interacting terms has an «amplitude» $\propto \tilde{g}N$ (where N is the total atoms number and $\tilde{g}$ is the 2D interaction parameter for the expanding cloud). The evolution of the in–plane density distribution depends on this interaction term and so on N. Hence, we can estimate N by comparing the experimental evolution $n(x,y,t_{\text{ToF}})$ ($\propto d_{\alpha^*}(x,y,t_{\text{ToF}})$) to distribution resulting from GP simulations for various N and varying the time–of–flight duration t_{ToF}. By comparing this dynamical estimate of N denoted $N_{\text{2D ToF}}$ to a simple sum over the optical density matrix $d_{\alpha^*}(x,y)$ (Eq. 3.26), we deduce the physical value of β, denoted β^*.

This technique is experimentally robust as it is based:

— on one hand, on the overall description of a dynamical evolution (with t_{ToF}), which filters out defects appearing for a specific t_{ToF}.

— on the other hand, on the integration of the density distribution over the cloud, which is a robust operation, reducing sensitivity to noise.

To characterize the 2D ToF evolution of both the experimental and the simulated density distributions (and then compare them), we simply use two fitted parameters that are the widths $\sigma_x(t_{\text{ToF}})$ and $\sigma_y(t_{\text{ToF}})$ of a gaussian fit of these distributions. We keep differentiating both x and y axis sizes as they are not similar in terms of residual trapping potentials[20]. The evolution is recorded over a set of t_{ToF} typically varying from 0 to 26 ms with 14 different values.

We took experimental data for these 2D-ToF, in a unique and highly degenerated experimental configuration. To experimentally characterize the evolution of $n_{\text{mes}}(x,y)$, we combine both high (HI) and low (LI) intensity imaging techniques (see 3.2.2). For short t_{ToF}, we expect the LI imaging to be unreliable due to high densities. We indeed measure an effective broadening of the LI values of $\sigma_x(t_{\text{ToF}})$ and $\sigma_y(t_{\text{ToF}})$ for $t_{\text{ToF}} < 12$ ms compared to the HI ones. For these times, we must rely on the HI measurements. Nevertheless, the longer t_{ToF}, the more the density drops so that for $t_{\text{ToF}} > 14$ ms we find that the HI technique leads to greater noise in $\sigma_x(t_{\text{ToF}})$ and $\sigma_y(t_{\text{ToF}})$ than the LI measurements. We then set the experimental values of the sizes $\sigma_x^{exp}(t_{\text{ToF}})$ and $\sigma_y^{exp}(t_{\text{ToF}})$ to the LI values for $t_{\text{ToF}} \geq 14$ ms and otherwise to the HI values. We average over three repetitions. Finally, we note that the evolution of both sizes becomes different for $t_{\text{ToF}} \gtrsim 16$ ms. This time must be the characteristic time for the potential defects along y (see 2.2.3.2 for details) to manifest. Thus we will not consider the evolution of σ_y^{exp} for $t_{\text{ToF}} > 16$ ms.

To simulate the evolution of the gas, we use the 3D version of Gross-Pitaevskii simulations as detailed in Annex B. The specific parameters for this simulation are

— The z confinement is reduced for the 2D ToF and equals $\omega_z/2\pi = 360$ Hz .

— The box–trap is a disk of radius $R_{\mu T}$. It is on for $t \leq 0$ and abruptly switch off at $t = 0$. We adjust $R_{\mu T}$ so that the gaussian widths fitted at $t_{\text{ToF}} = 0$ ms matches the experimental ones. It gives $R_{\mu T} = 12.25\,\mu$m for a theoretical expectation of $R_{\mu T} = 12\,\mu$m.

— The residual confinement described in 2.2.3.1 leads to frequencies $\nu_x = 0.3$ Hz and $\nu_y = i \times 4.1$ Hz.

— The magnetic confinement leads to $\nu_x^{(mag)} = \nu_y^{(mag)} = 6.5$ Hz (see 2.1.3).

In this simulation, we do not account for the potential defects described in 2.2.3.2 but we eliminated data that can be perturbed by their effects.

We repeat this simulation for N varying from 40000 to 150000. We fit the resulting column density distribution $n_{col}(x,y,t_{\text{ToF}}|N) = \int \mathrm{d}z |\psi(x,y,z,t_{\text{ToF}}|N)|^2$ (where ψ is the computed 3D wavefunction) by a gaussian that gives the characteristics sizes $\sigma_x^{\text{sim}}(N,t_{\text{ToF}})$ and $\sigma_y^{\text{sim}}(N,t_{\text{ToF}})$.

To compute the experimental value of $N_{\text{2D ToF}}$, we want to find the best matching N comparing $(\sigma_x^{exp}(t_{\text{ToF}}), \sigma_y^{exp}(t_{\text{ToF}}))$ to $(\sigma_x^{\text{sim}}(N,t_{\text{ToF}}), \sigma_y^{\text{sim}}(N,t_{\text{ToF}}))$ for all time–of–flight $t_{\text{ToF}} \in [0,26]$ ms. We in fact notice that we could not find a perfectly matching N for all t_{ToF} as shown in Fig. 3.8. In particular, we notice that for $t_{\text{ToF}} < 6$ ms , the experimentally fitted values $(\sigma_x^{exp}(t_{\text{ToF}}), \sigma_y^{exp}(t_{\text{ToF}}))$ seem to expand more quickly than expected from their longer time evolution. Such a fast evolution at short times must be an imaging artifact due again to multiple scattering effects in this highly degenerate configuration. We will thus not consider $t_{\text{ToF}} < 6$ ms. We also notice discrepancies in the fitted and

---

[20] As characterized in 2.2.3, the light–sheet beam induced in–plane de–confining potentials and uncontrolled rugosities that are different for x and y axis.

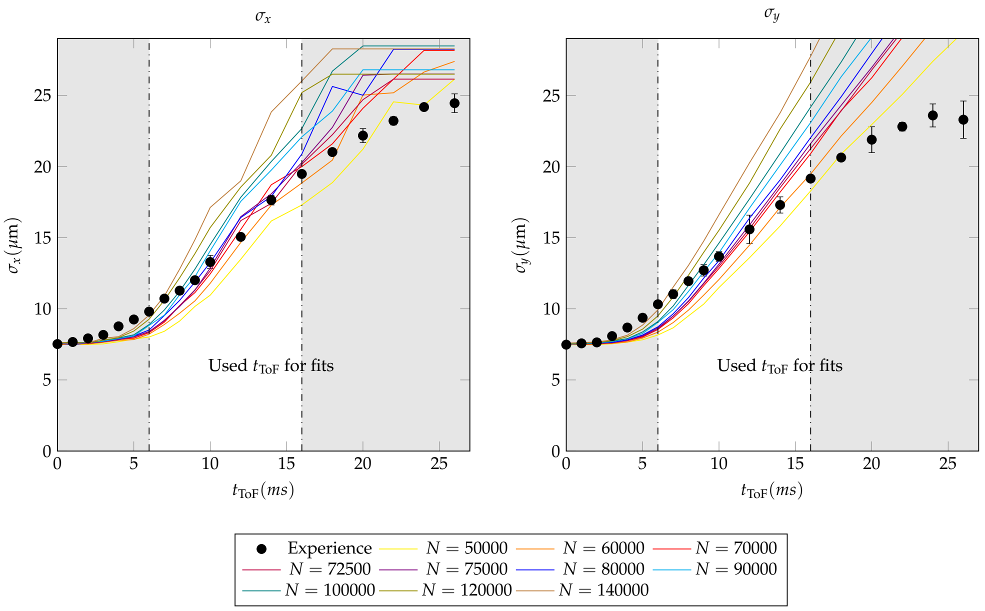

Figure 3.8.: Gaussian sizes along the 2D ToF expansion (t_{ToF}) for the experimental data (dots) and the simulations (solid lines): (left) σ_x and (right) σ_y. We lighten the considered t_{ToF} for the analysis and darken the unused ones.

simulated sizes at $t_{\text{ToF}} \geq 20\,\text{ms}$. This can both be due to loss in experimental signal quality (as indicated by the increase in error bars) or some flaw in the modeling of residual trapping effects. For our calibration, we will then rely on $t_{\text{ToF}} \in [6; 18]$ ms for σ_x and for $t_{\text{ToF}} \in [6; 14]$ ms for σ_y.

From these data, we compute χ^2 between simulated and experimental size over all considered t_{ToF}, for each axis and for each N. We deduce N by fitting the set of $\chi^2(N)$ according to:

$$\chi^2(N) = a^2 + c^2 \times (N - N_0)^2 \tag{3.34}$$

N_0 is the best matching atom number. We found for σ_x, $N_0 = 76.5 \times 10^3 \pm 1.5 \times 10^3$ and for σ_y, $N_0 = 74.7 \times 10^3 \pm 2.6 \times 10^3$. As both directions x and y do not exactly give the same results, we consider the mean value of these fits. We deduce: $N_{\text{2D ToF}} = 75.6 \times 10^3 \pm 2.1 \times 10^3$.

We will then compare this estimation to a simple integration of $d_{\alpha^*}(x, y) / \sigma_0$ from Eq. 3.26 and taking into account the the imaging coefficient $\mathcal{C} = 8.5$, $\eta = 0.365$ and $\alpha^* = 3.73$. We also take into account the correction of α at high density by Eq. 3.33 and compute the optical density $d(x, y)$ as described in conclusion of of the subsection 3.3.3. Then:

$$N_{\text{count}} = \int_{\text{Cloud}} \frac{d(x, y)}{\sigma_0} \tag{3.35}$$

$$= \int_{\text{Cloud}} n(x, y) \times \beta = \beta N \tag{3.36}$$

We directly perform this integration on the 2D ToF images previously fitted. As we pointed out, for the shortest time–of–flight $t_{\mathrm{ToF}} < 6$ ms, multiple scattering effects are not negligible and so we will not take these data into account. We found $N_{\mathrm{count}} = 71.8 \times 10^3 \pm 5.3 \times 10^3$. Then the physical value of β is given by $\beta^* = N_{\mathrm{count}} / N_{\mathrm{2D\,ToF}}$ and $\beta^* = 0.95(10)$. Such a value of β^* is compatible with the expected value $\beta^* = 1$ (from the fact that magnetic fields are negligible during the imaging process). We will then use $\beta^* = 1$.

3.4. Conclusion

In this chapter, we presented an imaging technique which is reliable for a two–dimensional gas whatever its density is. This technique is based on absorption imaging used in the saturating together with the non–saturating regimes. We inferred that the relation between the incoming intensity distribution I_{i}, the outgoing one I_{f} and the atomic density n is given by:

$$n(x,y)\sigma_0\,\beta = -\alpha \ln\left(\frac{I_{\mathrm{f}}(x,y) - 2\gamma}{I_{\mathrm{i}}(x,y) - \gamma}\right) + \frac{I_{\mathrm{i}}(x,y) - I_{\mathrm{f}}(x,y) + \gamma}{\eta I_{\mathrm{sat}}}. \tag{3.37}$$

taken into account the specificity of our acquisition process.

This relation is valid for all sets of imaging intensities and pulse durations as long as we are not perturbed by:

- Multiple scattering effects occurring in the dense regions of the cloud when using low probing intensity and when the cloud is thin, as presented in Annex D. In this chapter, we pointed out that multiple scattering effects are still visible in the high intensity images of our densest uniform 2D clouds. We can empirically take into account these effects by introducing a dependency of α with n as carried out in 3.3.3.6. The introduced dependency $\alpha(n)$ is simply fitted on a set of calibration data and does not rely on a theoretical model, it could then bring up flaws in the density measurement. The lower the probing intensity is, the higher the importance of multiple scattering effects and the larger the resulting defects. We then only allow to use this dependency $\alpha(n)$ for the high intensity images and discard the low intensity images in these dense regions.
- Modifications of the imaged atomic distribution due to radiative pressure effects that Doppler shifted the probing beam compared to the atomic transition and displace the atoms out of focus, as pointed out in 3.1.3.

When these conditions are fulfilled, the optical density is given by Eq. 3.37. In this chapter, we presented a calibration of all free coefficients necessary for a quantitative analysis of absorption images along this line:

1. We precisely calibrated the acquisition error by estimating the photons over–counts $\mathcal{C}$ (and corresponding intensity γ) due to dark–exposures before the reading–out process in the *Frame Transfer* mode.
2. We quantitatively estimated the global efficiency of our imaging setup η so that we precisely know the number of counts $\mathcal{I}_{sat}^{\mathrm{cam}} = \eta \mathcal{I}_{sat}^{0}$ corresponding to the saturation intensity of our ^{87}Rb atoms, $I_{\mathrm{sat}}^{0} = \mathcal{I}_{sat}^{0} \hbar\omega_L / \tau$. Then the highly saturating regime of absorption imaging is calibrated (up to the factor β that we expect

equals to 1).

3. To fully estimate the detectivity for all range of imaging parameters, we calibrate the coefficient α linking the high to the low intensity regime. We found the expected constant value α^*, valid for low densities ($n \lesssim 17.2\,\mu\mathrm{m}^{-2}$). We noticed a dependency of α on n for higher n. We calibrate the dependency law $\alpha(n)$.
4. After performing these three calibrations, we coherently checked that $\beta = 1$.

We summarize these calibrations in Table 3.1:

Coefficient	Calibrated Value
η	0.365
$\mathcal{C}$	$8.5(4)$
α^*	$3.7(1)$
$\alpha(n)$	$3.73 + 0.13 \times ((n - n_{\mathrm{cut}}) + \lvert n - n_{\mathrm{cut}} \rvert)$
β^*	1

Table 3.1.: Summary of all the calibration of imaging coefficients.

We estimate that the density profile obtained from this method may show 10% to 20% systematic errors.

4. Fit-free determination of the equation of state of the 2D Bose gas and scale invariance

In this chapter we are interested in an experimental investigation of the equation of state EoS of a (homogeneous) 2D Bose gas which is the relation between its 2D phase space density (PSD) $\mathcal{D} \equiv n\lambda_{\mathrm{T}}^2$, its temperature T and its chemical potential μ as introduced in Ch. 1. To experimentally investigate this relation over a wide range of μ and T we use an inhomogeneous (harmonically trapped) gas. We finally use the local density approximation (LDA) to relate this measurements to the homogeneous system as introduced in 1.1.3.2.

We performed a first measurement of this EoS in 2011 [70] whose results are reproduced in Annex F. It relies on the determination of T and μ_0 the chemical potential at the center of the cloud by a fit of the wings of the *in-situ* density distribution (based on the dependency of the in-plane confinement $U(\boldsymbol{\rho})$) for each cloud realization to the known theoretical results in the dilute regime (see 1.1.4.3). The local density approximation (LDA) then enables to deduce the chemical potential $\mu(\boldsymbol{\rho}) = \mu_0 - U(\boldsymbol{\rho})$ in each point of the trap [65] and relates it to the local value of the PSD $\mathcal{D}(\boldsymbol{\rho}) = n(\boldsymbol{\rho})\lambda_{\mathrm{T}}^2$ (where the density is determined along lines of Ch. 3). From this measurement we checked the (approximate) scale invariance of the EoS of a 2D Bose gas (see 1.1.4.1). It states that for all cloud configurations $\mathcal{D}$ only depends the ratio $\mu/k_{\mathrm{B}}T$ (and of the 2D interaction parameter $\tilde{g}$ but it is not varied in our measurements). In general, the scale invariance occurs in any fluid where no explicit energy/length scale is associated to the (binary) interaction potential.

The (approximate) scale invariance of the EoS makes possible to measure it using a more robust procedure which do not use any fitting parameter. This method is inspired from the procedure introduced by Ku et al.[71] for the unitary 3D Fermi gas (which also shows scale invariance). In this chapter, we formally generalize this "fit free" method of determination to any scale invariant EoS measured in any quantum gas in a known trapping potential. Then we apply this formalism to the set of data used in our former measurement of the EoS [70]. The main lines of this work has been developed by a former PhD student in our group, Rémi Desbuquois. This procedure leads to a much more accurate determination of the relation with no systematic errors. Then it enables a comparison to theoretical predictions for an interacting gas (see 1.1.4) that are of particular interest in the critical region (beyond the approximation of 1.1.4.3). In particular it provides an important experimental test for classical field approaches (such as the ones developed by Prokof'ev and Svistunov [125], see 1.1.4.4) which are believed to accurately describe quantum systems in the weakly interacting but non-perturbative regime.

The following chapter has been initially published in [112], and is reproduced here. Important modifications are announced by brackets.

4.1. General "fit free" formalism for determination of a scale-invariant EoS

Homogeneous matter at thermal equilibrium is described by an equation of state, *i.e.*, a functional relation between thermodynamic variables of the system. While the EoS is analytically known for ideal gases, one must resort to approximations or numerical calculations to determine the EoS of interacting fluids, which must then be compared to experiments. Thanks to a precise control of temperature, confining potential and interaction strength, cold atomic gases constitute a system of choice for the experimental determination of quantum matter EoS [65]. While performed on atomic systems, such measurements often provide crucial insight on generic physical problems, well beyond the atomic physics perspective. Prominent examples are the recent measurements of the EoS of atomic Fermi gases [66, 68, 71, 138], which provided a precious quantitative support for our understanding of strongly interacting fermions at low temperature. [Here we are interested in another important paradigm accessible to atomic gases that is the 2D systems and their specific Berezinskii-Kosterlitz-Thouless (BKT) transition briefly introduced in 1.1.4.4.

In this section, we want to generalize the method put forward in [71] which overcome systematic errors of the usual methods for determining the EoS of a cold atomic (see Annex F and [69, 70] in which an imperfect calibration of imaging system will lead to misestimate of $n(\boldsymbol{\rho})$ thus of $\mathcal{D}$ and through the fitting process in μ and T. The method of [71] is based on the use of two specific thermodynamic variables, the pressure and the compressibility; in addition, absolute energy scales T and μ are replaced by a single relative scale $\mathrm{d}\mu$, which was itself determined by the LDA through $\mathrm{d}\mu = -\mathrm{d}U$. Our method does not rely on specific thermodynamic variables but rather provides a generic formalism that can readily be applied to other quantum systems.]

4.1.1. A set of new dimensionless variables X_ν

We start our analysis by considering an atomic gas in thermodynamic equilibrium confined in a known potential $U(\boldsymbol{\rho})$. The only hypothesis for the method is the LDA, which entails that $n(\boldsymbol{\rho})$ depends on position only through the local value of the trapping potential: $n(\boldsymbol{\rho}) = n[U(\boldsymbol{\rho})]$. Although this method is applicable to any dimension, we focus here on the particular case of the two-dimensional gas for the sake of clarity. Let us introduce the energy $E[U(\boldsymbol{\rho})]$ with $\boldsymbol{\rho} = (x, y)$, defined by [1]

$$E = \frac{\hbar^2}{m} n, \tag{4.1}$$

which we want to combine with other relevant energies in order to form useful dimensionless variables. Though no absolute energy scales are readily available, a relative energy scale is provided by the variation of the trapping potential $\mathrm{d}U$. Furthermore, quantities formed in this manner are directly connected by the LDA to the properties of the uniform gas using the relation $\mathrm{d}\mu = -\mathrm{d}U$. Thus, we define the dimensionless

---

[1] In dimension d, this equation takes the general form $E = \hbar^2 n^{2/d}/m$

quantities

$$X_\nu \equiv E^{\nu-1}\frac{\partial^\nu E}{\partial\mu^\nu} = (-1)^\nu\, E^{\nu-1}\frac{\mathrm{d}^\nu E}{\mathrm{d}U^\nu}\,, \tag{4.2}$$

where ν is an integer. By convention, $X_0 = 1$ and a negative ν will instead correspond to $|\nu|$ successive integrations of E with respect to U, with for example

$$X_{-1} = \frac{1}{E^2}\int_U^\infty E(U')\,\mathrm{d}U'\,. \tag{4.3}$$

From a given image of the gas $n(\boldsymbol{\rho})$, one can thus construct all functions $X_\nu(V)$ (assuming that $U(\boldsymbol{\rho})$ is well known.

4.1.2. Determination of the EoS by mean of the X_ν

In the case of a scale invariant system, the knowledge of a single thermodynamic variable X_ν is sufficient to determine the state of the fluid, hence the values of all other variables $X_{\nu'}$. In other words, all individual measurements must collapse on a single line in each plane $\{X_\nu,\ X_{\nu'}\}$, irrespective of their temperature and chemical potential. Such a line is a valid EoS of the fluid under consideration.

Once the X_ν are known, all other thermodynamic quantities can be determined, up to an integration constant. In particular, one can derive the phase-space density $\mathcal{D}$ and the ratio $\alpha = \mu/k_\mathrm{B}T$. Let us suppose that a point $(X_\nu^{(0)},\ X_{\nu'}^{(0)})$ can be identified in a known portion the EoS, and that it corresponds to the values α_0 and $\mathcal{D}_0$. The link between the set $\{X_\nu\}$ and $(\alpha, \mathcal{D})$ is provided by

$$\mathcal{D}(X_\nu^{(1)}) = \mathcal{D}_0 \exp\left(\int_{X_\nu^{(0)}}^{X_\nu^{(1)}} \frac{X_1}{(\nu-1)X_1X_\nu + X_{\nu+1}}\mathrm{d}X_\nu\right), \tag{4.4}$$

$$\alpha(X_\nu^{(1)}) = \alpha_0 + \frac{1}{2\pi}\int_{X_\nu^{(0)}}^{X_\nu^{(1)}} \frac{\mathcal{D}(X_\nu)}{(\nu-1)X_1X_\nu + X_{\nu+1}}\mathrm{d}X_\nu\,. \tag{4.5}$$

The determination of $(\alpha, \mathcal{D})$ thus requires the knowledge of a triplet $\{X_1, X_\nu, X_{\nu+1}\}$. This requirement can be weakened by choosing $\nu = 1$ or $\nu = -1$, in which case only the pairs $\{X_1, X_{-1}\}$ or $\{X_1, X_2\}$ are needed.

4.1.3. Some examples

[We illustrate here in larger details this general formalism with the examples of the EoS established in Ch. 1.

4.1.3.1. The non interacting 2D gas

In 1.1.3, we established the EoS of the ideal 2D gas confined in a potential U in terms of the PSD along Eq. 1.25. As $E = \mathcal{D}k_\mathrm{B}T/2\pi$, we deduce the general relation

$$E[U] = -\frac{k_\mathrm{B}T}{2\pi}\ln\left(1 - Z[U]\right) \text{ with } Z[U] = e^{(\mu_0 - U)/k_\mathrm{B}T} \tag{4.6}$$

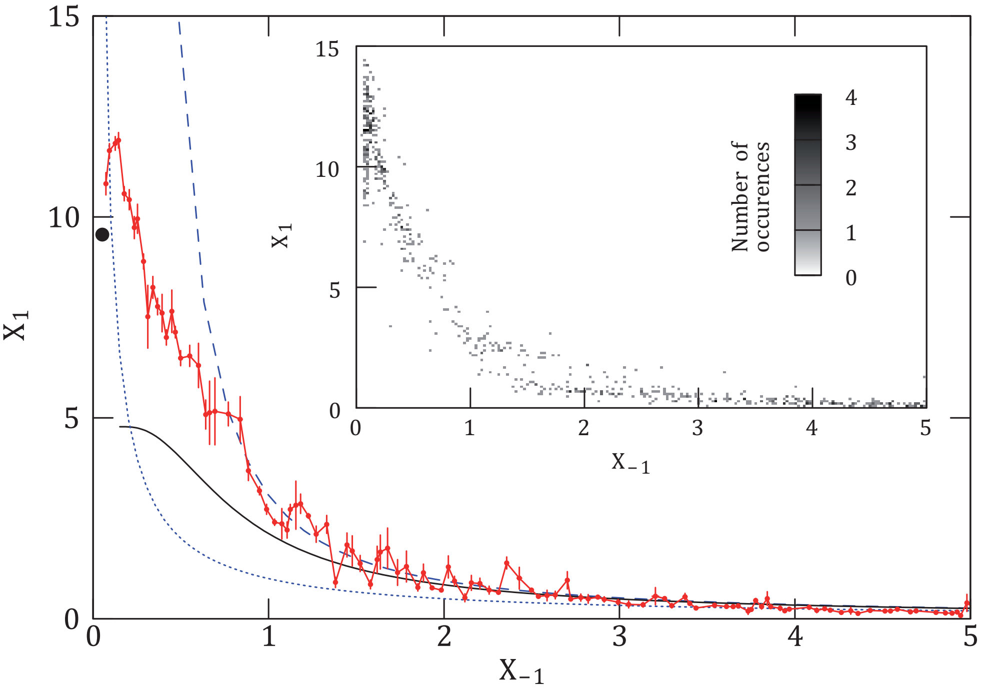

Figure 4.1.: Determination of the EoS with variables X_{-1} and X_1, along with known limits. The simple cases of the ideal Bose gas (Boltzmann gas) is shown in blue dashed (dotted) line. The known limits of the EoS of the weakly interacting 2D Bose gas are indicated by a black point for the Thomas–Fermi limit and by a black full line for the Hartree–Fock mean field theory. The red line results from the averaging over all the separate intensity profiles, with the error bars corresponding to the standard error introduced by the averaging procedure. The data shown here contains ~ 100 different values of X_{-1}. Inset: distribution of measured values of X_{-1} and X_1. The gray level indicates the number of individual data points falling in each pixel.

(where $\mu_0 \leq 0$ is the chemical potential at the trap center). From this relation we can deduce the dependencies of the X_ν's in the local fugacity $Z \equiv Z[U]$, which lead to implicit relations between any couple of X_ν's. For example in the three simplifying cases that we shed to light in previous section :

$$X_1[Z] = \frac{1}{2\pi}\frac{1}{1/Z-1} \tag{4.7}$$

$$X_{-1}[Z] = 2\pi\frac{g_2(Z)}{[\ln(1-Z)]^2} \tag{4.8}$$

$$X_2[Z] = \frac{1}{(2\pi)^2}\frac{-Z\ln(1-Z)}{(1-Z)^2}. \tag{4.9}$$

where g_2 is the second polylogarithm function. The corresponding EoS can be simply plotted by varying the fugacity Z from 0 to 1.

Maxwell-Boltzmann approximation If we consider now a gas in the very weakly degenerate regime (with $|\mu_0| \gg k_{\mathrm{B}}T$) then the EoS linking $\mathcal{D}$ to Z can be simplify along Eq. 1.17 and we recover the classical Boltzmann prediction $\mathcal{D} = Z$. We deduce from $Z[U]$ dependency (Eq. 4.6) the simple dependencies of the X_ν's (in the three cases of interest):

$$\begin{aligned} X_1[Z] &= Z/2\pi && (4.10)\\ X_{-1}[Z] &= 2\pi/Z && (4.11)\\ X_2[Z] &= (Z/2\pi)^2 && (4.12) \end{aligned}$$

and the EoS are simply $X_{-1} = 1/X_1$ (as shown in Fig. 4.1) and $X_2 = X_1^2$. In a general manner, the EoS in terms of the X_ν's can be obtained analytically in this classical description.

4.1.3.2. The interacting 2D gases

For an interacting 2D gas, the EoS is not known analytically; however for the Bosonic case, it can be approximated in two limiting cases (see 1.1.4.3).

Hartree Fock Approximation In the weakly degenerate regime, Hartree–Fock approximation applies and leads to the EoS of Eq. 1.31. It rewrites as an implicit equation of $E[U]$

$$E[U] = -\frac{k_{\mathrm{B}}T}{2\pi} \ln\left(1 - e^{(\mu_0 - U - 2\tilde{g}E[U])/k_{\mathrm{B}}T}\right), \tag{4.13}$$

from which we extracted numerically the values of X_{-1} and X_1 and plotted the corresponding EoS in Fig. 4.1.

Thomas Fermi Approximation In the opposite case of a strongly degenerate gas ($\mu > k_{\mathrm{B}}T$), the gas is described by the Thomas–Fermi equation (Eq. 1.33) and

$$E[U] = -\frac{\mu_0 - U}{2\pi\tilde{g}}. \tag{4.14}$$

Then, all X_ν are constant, with

$$\begin{aligned} X_{-1} &= \tilde{g}/2 && (4.15)\\ X_1 &= 1/\tilde{g} && (4.16)\\ X_2 &= 0 && (4.17) \end{aligned}$$

The Thomas Fermi approximation then leads to a single point EoS in any $(X_\nu, X_{\nu'})$ representation as shown in Fig. 4.1]

4.2. Application to the 2D Bose gas across BKT transition

[We now turn to the practical implementation of this method for processing data obtained with a quasi-2D rubidium weakly interacting gas. First we will present the experimental procedure to acquire the density profiles $n[U]$ in terms of the in-plane trapping potential. We note that in our 2D geometry (contrarily to [71]), the spatial density $n(\boldsymbol{\rho})$ is directly accessible from an image of the cloud. Then we will follow the procedure described in the first part of this chapter to our experimental profile and deduce a measurement of EoS $(\mu/k_\mathrm{B}T, \mathcal{D})$ around the critical BKT point with unprecedented accuracy.]

4.2.1. Acquiring Experimental profile $n(U)$

4.2.1.1. Experimental sequence

Our experimental preparation follows the lines detailed in [70, 110, 139]. We start with a 3D gas of ^{87}Rb atoms, confined in their $F = m_F = 2$ state in a magnetic trap. To create a 2D system, we shine an off-resonant blue-detuned laser beam on the atoms, with an intensity node in the plane $z = 0$. The resulting potential provides a strong confinement perpendicular to this plane, with oscillation frequency $\omega_z/2\pi = 1.9\,(2)\,\mathrm{kHz}$, which decreases at most by 5% over typical distribution radii. This corresponds to the interaction strength $\tilde{g} = \sqrt{8\pi}\, a_s/\ell_z \approx 0.1$, where a_s is the 3D scattering length and $\ell_z = \sqrt{\hbar/m\omega_z}$ (see 1.1.4.1). The energy $\hbar\omega_z$ is comparable to the thermal energy $k_\mathrm{B}T$, which ensures that most of the atoms occupy the ground state of the potential along z (see 4.2.2.3 and Annex F). For the analysis presented below, we used a data set of 80 samples, with temperatures ranging from 30 nK to 150 nK and atom numbers from 25 000 to 120 000.

4.2.1.2. Characterization of the in-plane trapping potential

[Though the method presented above relies neither on a thermometry of individual images nor on a precise determination of the detectivity of the imaging system, a precise knowledge of the trapping potential along xy is required. In this data set, the in-plane trapping is mainly provided by the TOP trap which results in an harmonic confinement. The mean oscillation frequency is measured via excitation of the center of mass oscillation and $\omega_r/2\pi = 20.6\,(1)\,\mathrm{Hz}$. However as outlined in 2.2.3 the intensity profile of the beam that freezes the z degree of freedom may also affects this $U(\boldsymbol{\rho})$ and leads to some anharmonicity.]

The following section was initially published as part of the supplemental material of [70], and is reproduced without modifications

These imperfections are revealed by looking at the center of mass oscillations $x_\mathrm{cm}(t)$ and $y_\mathrm{cm}(t)$, shown in Fig. 4.2a,b. Whereas the oscillation along the direction of propagation of the “freezing laser" (x) shows no deviation with respect to harmonic motion, the oscillation along y is damped. This is likely caused by irregularities of the transverse intensity profile of the freezing laser. In order to cope with these defects we have abandoned the standard technique consisting in making angular average of the images to produce radial density profiles. Instead we take advantage of the separability of the potential in the xy plane: $U(x,y) = m\omega_x^2 x^2/2 + \delta U(y)$, where $\delta U(y)$ accounts for the magnetic trapping potential and the irregularities of the freezing laser. We consider cuts of the measured density profile along the x direction, measured for various y_i's with $i = 1, \ldots, q$. In practice, we consider the $q = 31$ central lines of our images. We expect that two cuts corresponding to y_1 and y_2 coincide, provided we shift the second one by making the substitution $m\omega_x^2 x^2 \to m\omega_x^2 x^2 + \delta U(y_2) - \delta U(y_1)$. In practice we perform a least-square fit to optimize the superposition of the various cuts, taking the numbers $\delta U(y_i)$ as parameters. We use a single set of $\delta U(y_j)$ to fit a whole series of images taken at a given temperature. The robustness of the procedure is excellent, as shown in Fig. 4.2c, where we give the reconstructed potential $\delta U(y)$, with bars corresponding to the statistical errors of the $\delta U(y_j)$'s for various series of images acquired at different temperatures.

4.2.1.3. Imaging procedure

After letting the cloud equilibrate for 3 s in this combined magnetic and dipole trap, we measure the density distribution $n(\boldsymbol{r})$ by performing *in-situ* absorption imaging with a probe beam perpendicular to the plane of the atoms. [Following lines presented in Ch. 3, we use a combination of saturating (typically, the intensity shined on the atoms is $I \approx 40 I_{\text{sat}}$) and non-saturating (typically $I/I_{\text{sat}} \approx 0.7$) absorption imaging technique. The first one is reliable for all n but suffers from bad signal-to-noise ratio at low n. The second is less noisy but suffers systematic errors at high n (see Annex D). Since both

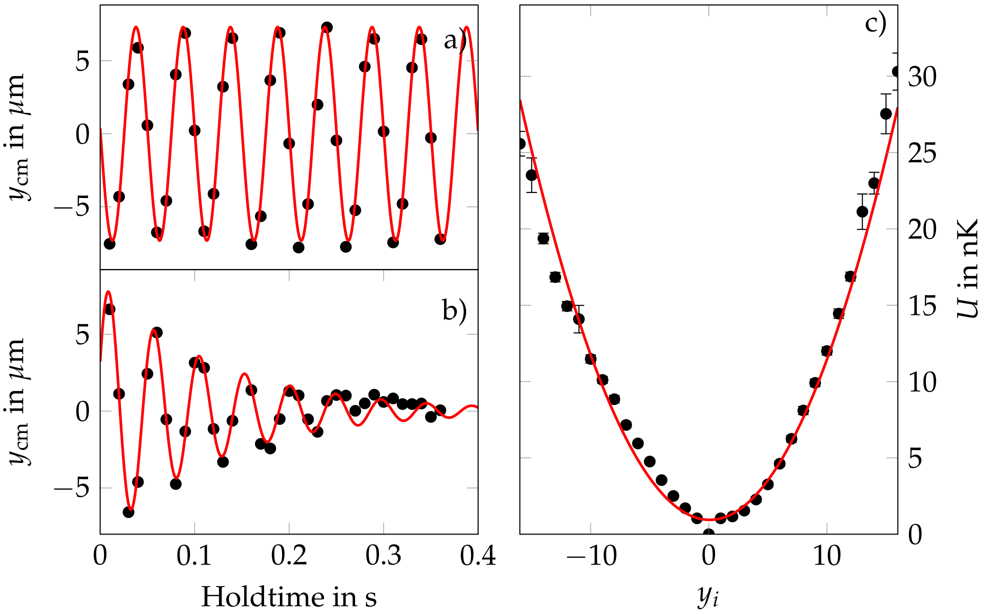

Figure 4.2.: (a) and (b) Center of mass oscillations (hollow circles ∘) along x (a) and y (b). The red lines correspond to a fit with a sine (a) and a damped sine (b). (c) Reconstructed potential along the y axis (filled circles •) and a harmonic fit (red line).

imaging processes destroy the atomic distribution, each sample is prepared twice and imaged successively in the low and high intensity regime.]

In Fig. 4.3 we show typical density distributions of 2D atomic clouds, together with the corresponding function $n[U(\rho)]$. The cloud (a) exhibits a significant thermal fraction, contrarily to cloud (b), which is essentially in the Thomas-Fermi regime. The latter illustrates the power of this fit-free method, since it can be incorporated as such in our determination of the EoS. On the opposite, it would be discarded in a conventional approach, owing to the impossibility to assign it a temperature.

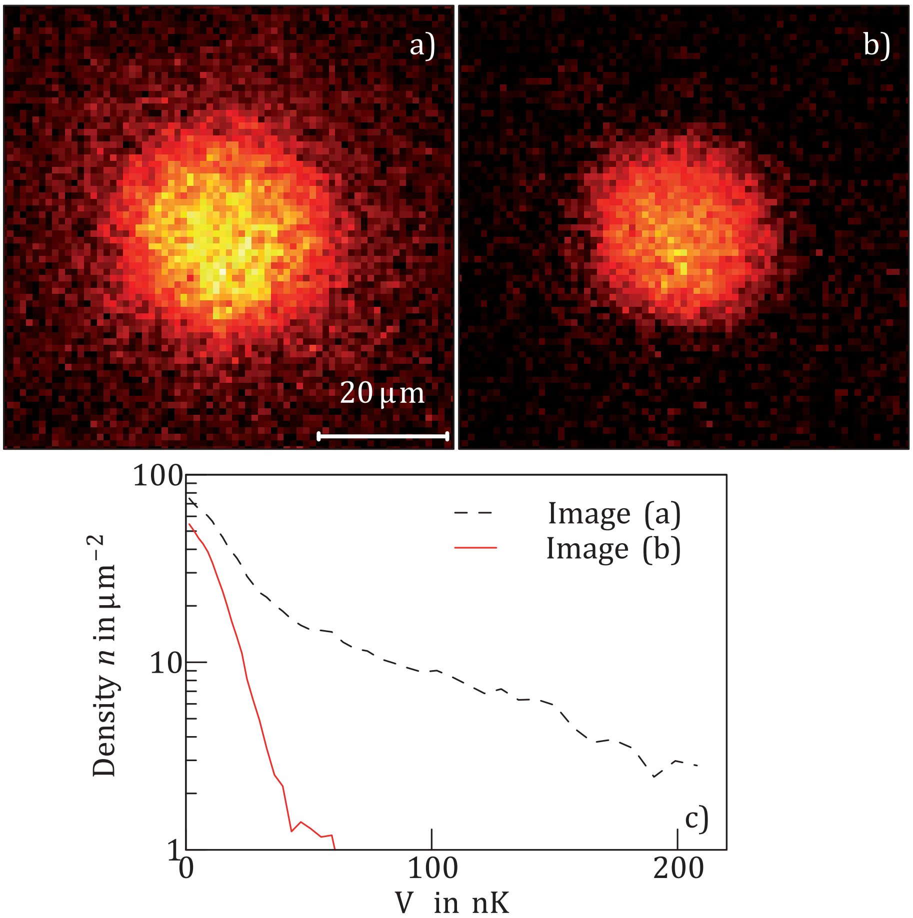

Figure 4.3.: (a) and (b) Density distributions of 2D atomic samples of ^{87}Rb corresponding to a partially degenerate (a) and a strongly degenerate cloud (b). (c) Corresponding function $n[U(\rho)]$resulting from azimuthal averaging. The distributions are obtained with high intensity imaging.

4.2.2. Implementation of the "fit-free" method

4.2.2.1. EoS in terms of the new variables X_ν

Though both choices of variables (X_{-1}, X_1) and (X_1, X_2) are in principle possible, the latter requires the experimental evaluation of a second-order derivative, which often suffers from a poor signal-to-noise ratio. By contrast the choice (X_{-1}, X_1), also adopted in [71] when writing the EoS in terms of pressure and compressibility, appears particularly robust[2]. For each image, we perform an azimuthal average and compute a set of ≈ 70 data points $(X_{-1},\ X_1)$, where the low (high) values of X_{-1} correspond to the high (low) density regions of the image.

In a first step, we combine all sets obtained from images acquired at various temperatures and various atom numbers to test the scale invariance. As explained above, each individual measurement should sit on the same universal curve in the (X_{-1}, X_1) plane, provided the interaction strength $\tilde{g}$ is constant. We show in the inset of Fig. 4.1 the repartition of data points in the (X_{-1}, X_1) plane, which fall as expected around a single curve. In the main panel we plot the corresponding average curve, which provides the EoS of our gas[3].

4.2.2.2. EoS for the conventional variables $\mu/k_\mathrm{B}T$ and $\mathcal{D}$

In order to re-express this EoS in terms of the more traditional variables α and $\mathcal{D}$, we now need to apply the transformations of Eqs. 4.4 and 4.5. However, this transformation must be adapted to account for possible imperfections in the calibration of the detectivity of our imaging setup. Indeed, as in most cold atoms experiments, we only measure the density up to a global multiplicative factor β[4], which is defined as the ratio between the unknown actual absorption cross-section and the ideal one expected for monochromatic probe light in the absence of stray magnetic fields. Taking this calibration factor into account amounts to replacing Eqs. 4.4 and 4.5 by

$$\mathcal{D}(X_\nu^{(1)}) = \mathcal{D}_0 \exp\left(\int_{X_\nu^{(0)}/\beta^\nu}^{X_\nu^{(1)}/\beta^\nu} \frac{X_1}{(\nu-1)X_1X_\nu + X_{\nu+1}}\mathrm{d}X_\nu\right) \tag{4.18}$$

$$\alpha(X_\nu^{(1)}) = \alpha_0 + \frac{\beta}{2\pi}\int_{X_\nu^{(0)}/\beta^\nu}^{X_\nu^{(1)}/\beta^\nu} \frac{\mathcal{D}(X_\nu)}{(\nu-1)X_1X_\nu + X_{\nu+1}}\mathrm{d}X_\nu \tag{4.19}$$

where the bounds of the integrals now depend on β and where $X_\nu^{(0)}/\beta^\nu$ corresponds to the reference values α_0 and $\mathcal{D}_0$. The value of β is *a priori* unknown; however, it can be determined by fitting the measured EoS to the Hartree–Fock mean-field (HFMF) theory, which is a good approximation in the region $\alpha < 0$. This procedure applies to any other quantum gas, provided one has a good knowledge of the EoS in a given segment of the parameters space.

---

[2] In our case, the compressibility is given by $\kappa = X_1/(n^2\,h^2/m)$ and the pressure by $P = X_{-1}\,n^2\,h^2/m$

[3] We extract data points with $X_{-1} < 2.5$ ($X_{-1} > 2.5$) from high (low) intensity imaging.

[4] This factor is taken into account in Eq. 4.1 by $E = \beta(\hbar^2/m)n$. The definition of X_ν is unchanged.

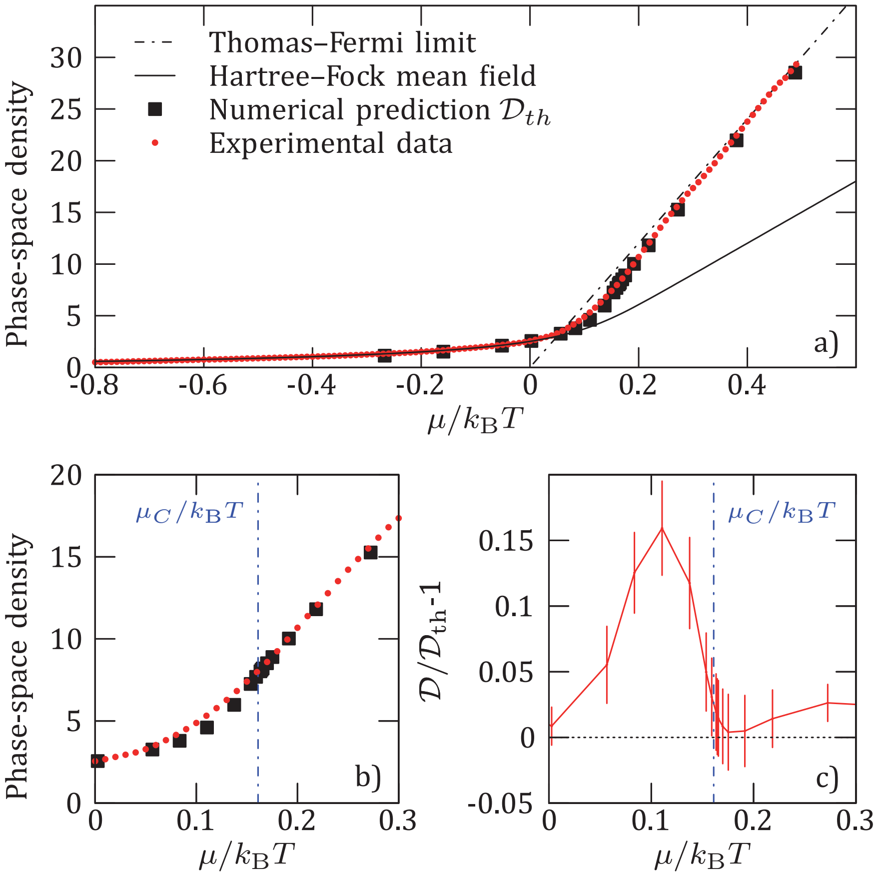

Figure 4.4.: (a) Equation of state of the 2D Bose gas, determined with Eqs. 4.4 and 4.5 (red points), with a detailed view of the critical region around the BKT transition (blue dash-dotted line) in (b). Statistical error bars are too small to be shown on these plots. We show for comparison the classical field Monte Carlo prediction $\mathcal{D}_{\mathrm{th}}$ [125] in black squares, the Thomas–Fermi limit in black dash-dotted line and the HFMF theory in black full line. We provide a quantitative estimate of the difference between measurement and prediction in (c). There, we plot $\mathcal{D}/\mathcal{D}_{\mathrm{th}} - 1$, where zero indicates perfect agreement. The error bars result from a boostrap analysis of the experimental data.

We choose the bound of Eqs. 4.18 and 4.19 at $X^0_{-1} = 3$, which corresponds to a phase-space density $\mathcal{D}_0 = 1.45$ and $\alpha_0 = -0.22$, well within the HFMF regime, and find a detectivity factor $\beta = 0.456\,(1)$ [5] after taking into account the contribution of the transverse excitations as we will describe in next paragraph.

4.2.2.3. Removing the contribution for thermally populated transverse states

The method presented in the main text assumes the EoS to be strictly scale invariant. However, when the temperature T of an individual realization is on the order of

---

[5] The error bar on this value is calculated through a bootstrap analysis. The result is consistent with our (less precise) previous estimate for the same setup, $\beta = 0.40(2)$, which was based on a different method [70].

the harmonic oscillator level spacing $\hbar\omega_z/k_B \sim 100$ nK, a fraction of the atoms occupy transverse excited states of the confinement potential. Their contribution can be evaluated and self-consistently removed in the following manner.

1. We calculate the EoS in variables (X_{-1}, X_1) with the method described above. This process yields a preliminary determination of the EoS, as well as a value for the detectivity $\beta_{(0)} = 0.481(4)$. Both these measurements contain a systematic error introduced by the thermally populated transverse levels.
2. We measure the temperature and the chemical potential of the atomic distribution of each individual image by fixing the detectivity β to the value determined above, and by fitting with the EoS measured previously. Since the EoS contains excited levels in its determination, we expect that the measured temperature will also be affected. Note that the population of the excited states is only 10% of the total population at most: we therefore expect a similarly small shift of the temperature and chemical potential.
3. We self-consistently evaluate the contribution of the excited levels to the total density, assuming the atoms in the excited states of the z motion to be in the HFMF regime [70, 103, 109] (see also Annex F) and subtract them to obtain an estimate of the population of the ground state. We find that the phase-space density associated with the excited states is at most 0.5, which justifies to describe these states with the HFMF approximation.
4. With the new estimate of the population of the ground state for each image, we generate a new EoS with the method outlined above. We also determine a more accurate value of the detectivity, and find $\beta = 0.456(1)$.
5. In principle, this process can be iterated to obtain an even more accurate determination of the temperature for each image. However, this does not lead to an improved measurement.

As shown in Fig. 4.5, the subtraction of the excited states does not significantly affect the EoS, though the detectivity is significantly modified.

4.2.2.4. Comparison to theory predictions

The EoS in terms of the variables $(\alpha, \mathcal{D})$ – obtained after a small correction due to excited states of the z motion – is shown in Fig. 4.4a, along with the numerical prediction $\mathcal{D}_{\text{th}}$ [125]. The reconstructed EoS is remarkably smooth and doesn't display any particular feature at the transition point. This observation is also made on the EoS for pressure, entropy and heat capacity(see 4.2.2.5). This illustrates the "infinite order" nature of the BKT transition, which is not associated to any singularity of thermodynamic quantities[6], as opposed to phase transitions driven by the breaking of a continuous symmetry, such as the second order lambda transition observed at MIT [71]. To compare quantitatively the reconstructed EoS with the numerical prediction, we plot the quantity $\mathcal{D}/\mathcal{D}_{\text{th}} - 1$ in Fig. 4.4c, and find it to lie consistently below 15 %, and even

---

[6] A singularity however appears in the superfluid density, which has to be distinguished from the total density, as the former enters only in the response of the system to an external drag or rotation.

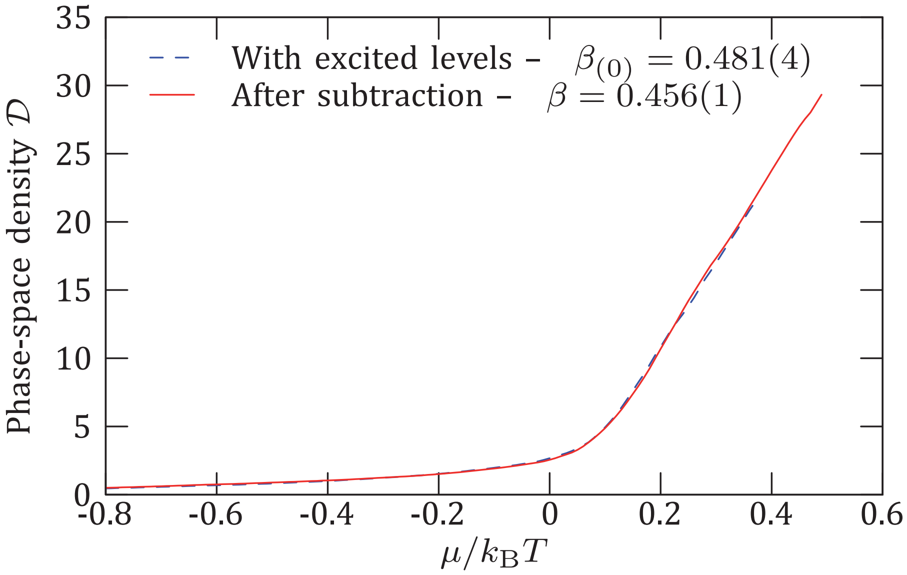

Figure 4.5.: EoS of the 2D Bose gas, determined with Eqs. 4.4 and 4.5. The measurement without (with) subtraction of the population of the excited levels is shown in blue (red) line.

below 5 % around the phase transition, which occurs at $\mu_C/k_\mathrm{B}T \approx 0.17$ [125]. The deviation observed in the fluctuation region below the critical chemical potential might signal deviations to the classical field picture which is expected to be accurate for $\tilde{g} \ll 1$ [124, 125]. Theoretically this deviation could be addressed using Quantum Monte Carlo methods [127, 140].

4.2.2.5. EoS in other variables

Owing to the scale invariance of the two dimensional Bose gas, the EoS with any pair of variables can in principle be deduced from the one for $\mathcal{D}$ and α. We show in Fig. 4.6 three measurements of such EoS. For example, the pressure is deduced from the density by $n = (\partial P/\partial \mu)_T$ and is expressed in dimensionless units:

$$\mathcal{P} = \frac{P\,\lambda_\mathrm{T}^2}{k_\mathrm{B}} = \frac{1}{2\pi}\mathcal{D}^2\,X_{-1}. \tag{4.20}$$

Once the pressure is known, extensive variables such as the entropy and the heat capacity can be deduced. The former is derived from the entropy per unit area $s = (\partial P/\partial T)_\mu$, and the latter from the internal energy $C = (\partial U/\partial T)_\mu$. Expressed in terms of previously determined thermodynamic quantities, we have

$$\frac{S}{N\,k_\mathrm{B}} = 2\frac{\mathcal{P}}{\mathcal{D}} - \alpha \quad \text{and} \quad \frac{C}{N\,k_\mathrm{B}} = \frac{\mathcal{P}}{\mathcal{D}} - \alpha + \alpha\,X_{-1}\,X_1 \tag{4.21}$$

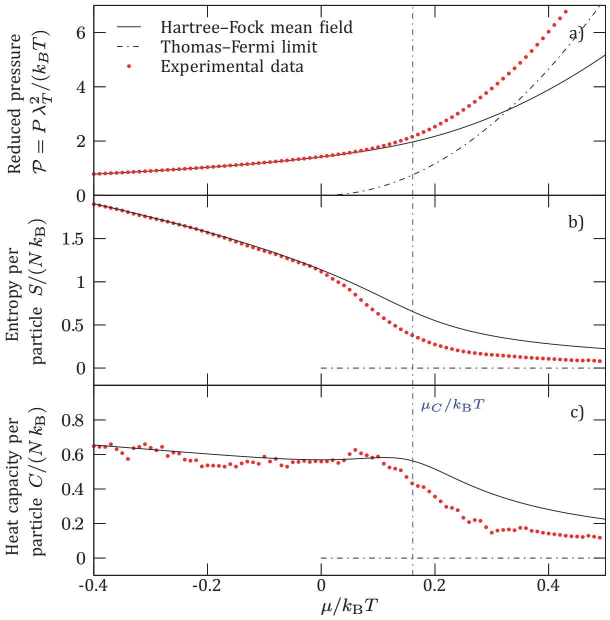

Figure 4.6.: Equations of state of the 2D Bose gas, derived from the HFMF theory (black line) and reconstructed following our method (red points), expressed with (a) the pressure P, (b) the entropy per particle S/N and (c) the heat capacity per particle C/N.

4.3. Conclusion

In conclusion, we have presented a method to determine the EoS of a scale-invariant fluid. This method does not rely on thermometry of individual images, nor on the precise calibration of the detectivity, and leads to a strong reduction of the noise level in the measurement. We have applied it to the case of a weakly interacting Bose gas and obtained its EoS with a precision of few percents, in excellent agreement with a theoretical prediction obtained from a classical Monte Carlo simulation. Using the response of the gas to a gauge field, originating for example from a rotation, this method could be extended to access the superfluid fraction of the gas along the lines proposed in [65]. In principle, this method is not limited to scale invariant systems, and could be extended to any situation described by two independent dimensionless parameters, such as the zero temperature limit of the Fermi gas, either for a spin-balanced gas with varying interactions [138], or for a unitary spin-imbalanced Fermi gas [64].

5. Superfluidity in two dimensions

In this chapter we are interested in a direct experimental proof of the superfluid behavior of the 2D Bose gas. Following theoretical description of the beginning of 1.1.4.4, this is characterizing the absence of heating (up to a critical velocity v_c) of the 2D fluid when excited by a moving obstacle (at velocity v). In this work, we perform "heating" measurements of our cloud after rotating a potential defect for a time τ. We use harmonically trap 2D gases and move the defect along an equi-potential such that, by applying local density approximation (LDA), we investigate a fixed phase space density $\mathcal{D} \equiv n\lambda_T^2$. We vary the velocity v of the defect and the value of $\mathcal{D}$ investigated in order to map the emergence of the superfluid behavior in the corresponding homogeneous system.

The following chapter was initially published in [113], and is reproduced without modifications

'Flow without friction' is a hallmark of superfluidity [141]. It corresponds to a metastable state in which the fluid has a non-zero relative velocity v with respect to an external body such as the wall of the container or an impurity. This metastable state is separated from the equilibrium state of the system ($v = 0$) by a large energy barrier, so that the flow can persist for a macroscopic time. The height of the barrier decreases as v increases, and eventually passes below a threshold (proportional to the thermal energy) for a critical velocity v_c. The microscopic mechanism limiting the barrier height depends on the nature of the defect and is associated to the creation of phonons and/or vortices [141]. While the quantitative comparison between experiments and theory is complicated for liquid ^{4}He, cold atomic gases in the weakly interacting regime are well suited for precise tests of many-body physics. In particular, superfluidity was observed in 3D atomic gases by stirring a laser beam or an optical lattice through bosonic [74–77, 142] or fermionic [78] fluids and by observing the resulting heating or excitations. Here we transpose this search for dissipation-less motion to a disc-shaped, non homogeneous 2D Bose gas. We use a small obstacle to locally perturb the system. The obstacle moves at constant velocity on a circle centered on the cloud, allowing us to probe the gas at a fixed density. We repeat the experiment for various atom numbers, temperatures and stirring radii and identify a critical point for superfluid behavior.

5.1. Data acquisition

5.1.1. Experimental scheme

Our experiments are performed with 2D Bose gases of $N = 35000$ to 95000 ^{87}Rb atoms confined in a cylindrically symmetric harmonic potential $V(r) + W(z)$ (see [70]). The trap frequencies are $\omega_r/2\pi = 25.0(5)$ Hz in the horizontal plane and $\omega_z/2\pi =$

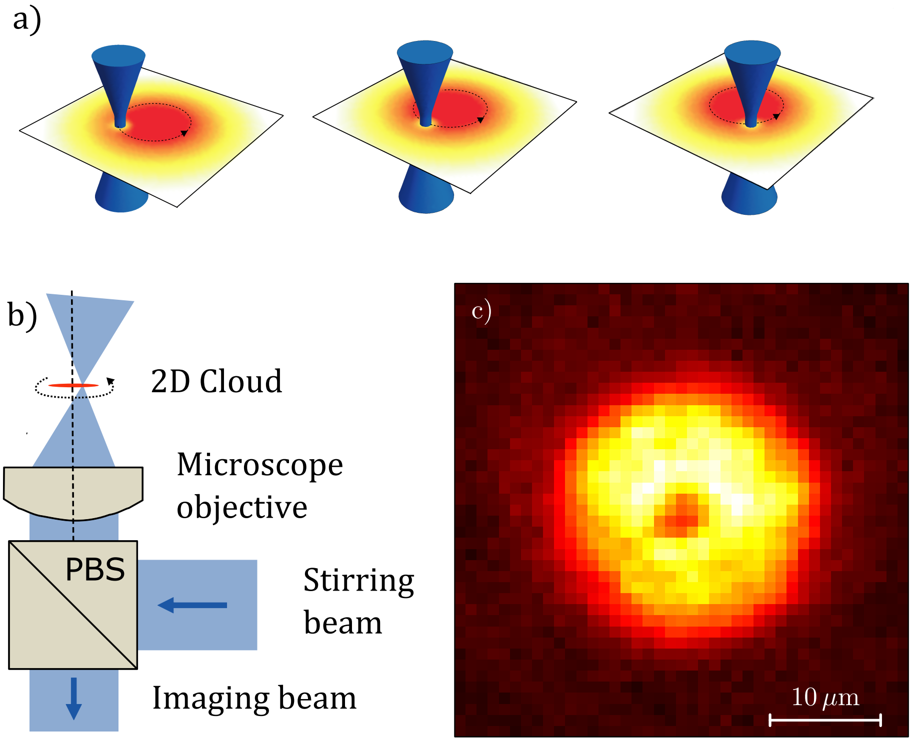

Figure 5.1.: Stirring a 2D Bose gas. **a**, A trapped 2D gas of ^{87}Rb atoms is perturbed by a focussed laser beam, which moves at constant velocity on a circle centred on the cloud. The stirring beam has a frequency larger than the ^{87}Rb resonance frequency ('blue detuning' of $\approx$ 2 nm) and thus creates a repulsive potential which causes a dip in the density profile. **b**, The stirring beam is focussed onto the 2D cloud via a microscope objective of numerical aperture 0.45, which is also used for imaging. We overlap the two beam paths with a polarizing beam splitter cube (PBS). The position of the stirring beam is controlled by a two-axis piezo-driven mirror. **c**, *in situ* false-color image of the 2D cloud in the presence of the laser beam (average over six images). From the dip in the density we deduce the waist of the laser beam as $w_0 = 2.0(5)\,\mu$m. In this image, the intensity of the beam is chosen three times higher than in the stirring experiment to make the hole well visible even in the center of the cloud. We use similar images, but with the stirring beam switched off, to determine the temperature T and the chemical potential μ from a fit of the Hartree-Fock prediction to the wings of the cloud [70].

1.4 (1) kHz in the vertical direction. We use gases with temperature T and central chemical potential μ in the range 65-120 nK and $k_B \times$ (35-60) nK, respectively. The interaction energy per particle is given by $U_{\text{int}} = (\hbar^2 \tilde{g}/m)n$, where n is the 2D spatial density (typically 100 atoms/μm^2 in the center), m the atomic mass and $\tilde{g}$ the dimensionless interaction strength. Here $\tilde{g} = \sqrt{8\pi}a/l_z = 0.093$, where $a = 5.3$ nm is the 3D scattering length and $l_z = \sqrt{\hbar/m\omega_z}$. The energy $\hbar\omega_z$ ($k_B \times 70$ nK) is comparable to $k_B T$ and U_{int} ($\sim k_B \times 40$ nK at the trap center). Thanks to Bose statistics, which limits to typically 10% the fractional atomic density in the axially excited states at the obstacle position, our gas is well described by the quasi-2D fluid model (see Supplemental Material of [70]).

We stir the cloud with a laser beam which creates a repulsive potential with height $V_{\mathrm{stir}} \approx k_{\mathrm{B}} \times 80\,\mathrm{nK}$. This is at least twice the local chemical potential $\mu_{\mathrm{loc}}(r) = \mu - V(r)$. The beam has a Gaussian profile with a waist of $w_0 = 2.0\,(5)\,\mu\mathrm{m}$, which is larger than the local healing length $\xi = 1/\sqrt{\tilde{g}n}$ ($\approx 0.3\,\mu\mathrm{m}$ at the trap center), but small compared to the size of the cloud (full width at half maximum $\approx 25\,\mu\mathrm{m}$) (see Fig. 5.1). We stir for typically $t_{\mathrm{stir}} = 0.2\,\mathrm{s}$ at constant velocity v in a circle of radius r centered on the cloud. The intensity of the stirring beam is ramped on and off in $\approx 5\,\mathrm{ms}$ without any significant additional heating. Once the stirring beam is switched off, we let the cloud relax for 0.1 s and measure the temperature T_{f}.

5.1.2. Heating response and fit

For each configuration (N, T, r), we repeat this experiment for various v from 0 to $2\,\mathrm{mm/s}$ and a fixed stirring time t_{stir}. We find two different regimes for the response and we show an example of each in Fig. 5.2. In Fig. 5.2**a**, there is a clear threshold behavior with no discernable dissipation below a critical velocity. In contrast, in Fig. 5.2**b**, the temperature increases without a threshold. We identify these behaviors as the superfluid and normal response, respectively. To model these data we choose for a given configuration the fit function

$$T_{\mathrm{f}}(v) = T_{\mathrm{f},0} + \kappa \cdot t_{\mathrm{stir}} \cdot \max[(v^2 - v_{\mathrm{c}}^2), 0], \tag{5.1}$$

which describes the heating of a 2D superfluid in the presence of a moving point-like defect [143]. In equation (5.1) the three fit parameters are the temperature at zero velocity $T_{\mathrm{f},0}$, the heating coefficient κ, and the critical velocity v_{c}. In the normal state, the fit finds $v_{\mathrm{c}} \sim 0$ and the according quadratic heating stems from the linear scaling of the drag force. In the absence of the stirring beam, there is no significant heating and we measure the temperature T_{i}. The presence of the stirring beam at zero velocity leads to a 'background heating' $T_{\mathrm{f},0} - T_{\mathrm{i}} \sim 10\,\mathrm{nK}$, which we attribute to photon scattering. In the following, we use the mean temperature $\bar{T} = (T_{\mathrm{i}} + T_{\mathrm{f},0})/2$ to characterize the cloud.

5.2. Observation of a critical velocity

In Fig. 5.3, we summarize our data obtained for different configurations (N, $\bar{T}$, r). We show in Fig. 5.3**a** the fitted critical velocities versus the single parameter $\mu_{\mathrm{loc}}(r)\,/k_{\mathrm{B}}\bar{T}$. The relevance of this parameter results from (i) the local character of the excitation, so that the response of the fluid to the moving perturbation is expected to be similar to that of a uniform gas with the same temperature and the chemical potential μ_{loc}, (ii) the scale invariance of the weakly-interacting 2D Bose gas, whose thermodynamical properties do not depend separately on μ and T, but only on the ratio $\mu/k_{\mathrm{B}}T$ (see [69, 70, 125]). In particular, this ratio is univocally related to the phase space density, and thus characterizes the degree of degeneracy of the cloud.

Quite remarkably, the ensemble of our data for v_{c} when plotted as a function of $\mu_{\mathrm{loc}}/k_{\mathrm{B}}\bar{T}$ shows a threshold between values compatible with zero and clearly non-zero values. This threshold is located at $\mu_{\mathrm{loc}}/k_{\mathrm{B}}\bar{T} \approx 0.24$, somewhat above the prediction

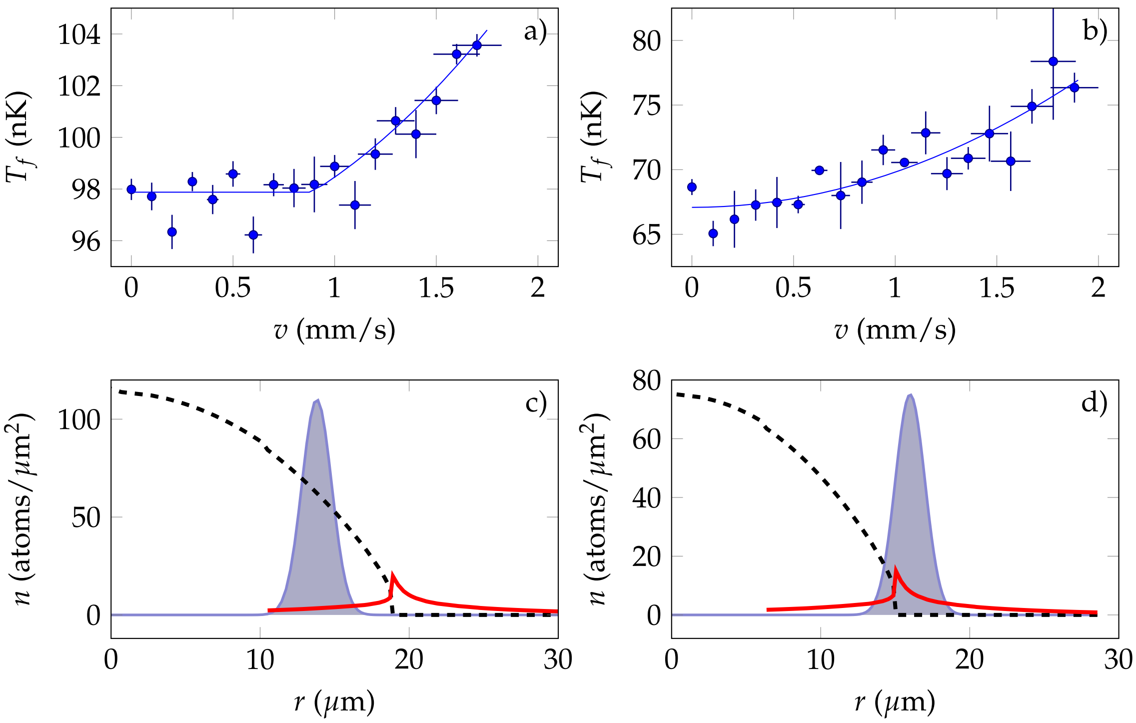

Figure 5.2.: Evidence for a critical velocity. Two typical curves of the temperature after stirring the laser beam at varying velocities. **a**, In the superfluid regime, we observe a critical velocity (here $v_c = 0.87(9)$ mm/s), below which there is no dissipation. **b**, In the normal regime, the heating is quadratic in the velocity. The fitted heating coefficients are $\kappa = 18(3)\,\mathrm{nK}\cdot\mathrm{s/mm}^2$ and $\kappa = 26(3)\,\mathrm{nK}\cdot\mathrm{s/mm}^2$ in **a** and **b**, respectively. The experimental parameters are (N, $\bar{T}$, μ, r)=(87000, 89 nK, $k_B \times 59$ nK, 14.4 ¯m) and (38000, 67 nK, $k_B \times 39$ nK, 16.6 ¯m) for **a** and **b**, respectively, yielding $\mu_{\mathrm{loc}}/k_B\bar{T} = 0.36$ and $\mu_{\mathrm{loc}}/k_B\bar{T} = 0.04$. The data points are the average of typically ten shots. The y error bars show the standard deviation. The x error bar denotes the spread of velocities along the size of the stirring beam ($1/\sqrt{e}$ radius). The solid line is a fit to the data according to equation (5.1). The stirring time is 0.2 s for all data points. Note that the three low-lying data points in **a** correspond to the completion of an odd number of half turns. For these data points, where we see a downshift of the temperature by approximately 1.5 nK, we also observe a displacement of the center of mass of the cloud by a few μm. **c** and **d**, Calculated radial density distribution for the clouds in **a** and **b**, respectively. The dashed blue curve shows the superfluid density, the solid red curve shows the normal density. The stirring beam potential is indicated by the grey shaded area (in arbitrary units). The densities are calculated via the local density approximation from the prediction for an infinite uniform system [125]. The jump of the superfluid density from zero to a universal value of $4/\lambda_{\mathrm{dB}}^2$ (where λ_{dB} is the thermal de Broglie wavelength) is a prominent feature of the BKT transition. The normal density makes a corresponding jump to keep the total density continuous.

$(\mu/k_B T)_c = 0.15$ for the superfluid phase transition in a uniform system [125] with $\tilde{g} = 0.093$. If we assume that the stirrer must stand entirely in the superfluid core in order to yield a non-zero critical velocity, then the deviation can be attributed to the non-zero width of the stirring beam. The range of $\mu_{\mathrm{loc}}/k_B\bar{T}$ corresponding to the extent of this beam is indicated by the horizontal error bars in Fig. 5.3**a**. Note that the finite size of our trapped atomic clouds might also shift the BKT transition, but the effect is expected to be small (a few percent) and in the opposite direction [125].

We limit the presented stirring radii to $r \geq 10\,\mu\text{m}$ such that the stirring frequencies $\omega = v/r$ for the relevant velocities $v \sim v_\text{c}$ are well below ω_r. Indeed, smaller radii correspond to a larger centripetal acceleration. This could lead to additional heating via the phonon analog of synchrotron radiation, as observed in the formally similar context of capillary waves generated by a rotating object [144].

5.3. Comparison with theory and previous measurements

For a homogeneous system, the value of the critical velocity is limited by two dissipation mechanisms, the excitation of phonons or vortices. For a point-like obstacle [143], phonon excitation dominates and v_c is equal to the speed of sound, given in the zero temperature limit by $c_\text{s} = \hbar\sqrt{\tilde{g}n}/m$ ($\approx 1.6\,\text{mm/s}$ for $n = 50\,\text{atoms}/\mu\text{m}^2$) (this situation is described by the celebrated Landau criterion [141]). When the obstacle size w_0 increases and becomes comparable to ξ, dissipation via the nucleation of vortex-antivortex pairs (vortex rings in 3D) becomes significant [145–147]. The corresponding v_c is then notably reduced with respect to c_s. In the limit of very large obstacles ($w_0 \gg \xi$), an analytical analysis of the superfluid flow stability yields $v_\text{c} \sim \hbar/mw_0 \ll c_\text{s}$ (see [148, 149]). With an obstacle size $w_0 \gtrsim \xi$, our experimental situation is intermediate between these two asymptotic regimes. For a non-homogeneous system like ours with the stirring obstacle close to the border of the expected superfluid regime, one can also excite surface modes [132, 150], which constitute an additional dissipation mechanism.

Our measured critical velocities are in the range 0.5–1.0 mm/s, *i.e.*, $v_\text{c}/c_\text{s} = 0.3 - 0.6$. By contrast, previous experiments in 3D clouds found lower fractions $v_\text{c}/c_\text{s} \sim 0.1$ (see [75]). The difference may be due to the larger size of the obstacles that were used, and to the average along the axis of the stirring beam of the density distribution in the 3D gas [151]. The dominant dissipation mechanism could be revealed by e.g. directly observing the created vortex pairs as in [142] or interferometrically detecting the Cerenkov-like wave pattern for $v > c_\text{s}$ as in experiments with a non-equilibrium 2D superfluid of exciton-polariton quasi-particles [152].

5.4. Heating coeficient

Fig. 5.3**b** shows the fitted heating coefficients κ for the normal (red circles) and superfluid data (blue circles). In the normal region, we expect the heating to scale linearly with the normal density n_no (see [76]). Using the prediction of [125] for $\bar{n}_\text{no}$ (averaged over the size of the stirring beam) we fit $\kappa = a_1 \cdot \bar{n}_\text{no}$ and obtain $a_1 \approx 3 \cdot 10^{-6}\,\text{nK} \cdot \text{s}$. This value is in reasonable agreement with the prediction of a model [76] of a single particle with a thermal velocity distribution of mean $\bar{v} = \sqrt{\pi k_\text{B} T/2m}$ colliding with a moving hard wall of width $L = w_0$ yielding $a_1 = 16mL\bar{v}/\pi N k_\text{B} \sim 6 \cdot 10^{-6}\,\text{nK} \cdot \text{s}$ (for $N = 65000$ and $T = 90\,\text{nK}$). In particular our data nicely reproduce the maximum of $\bar{n}_\text{no}$ around the expected superfluid transition point. In the superfluid case and $v > v_\text{c}$,

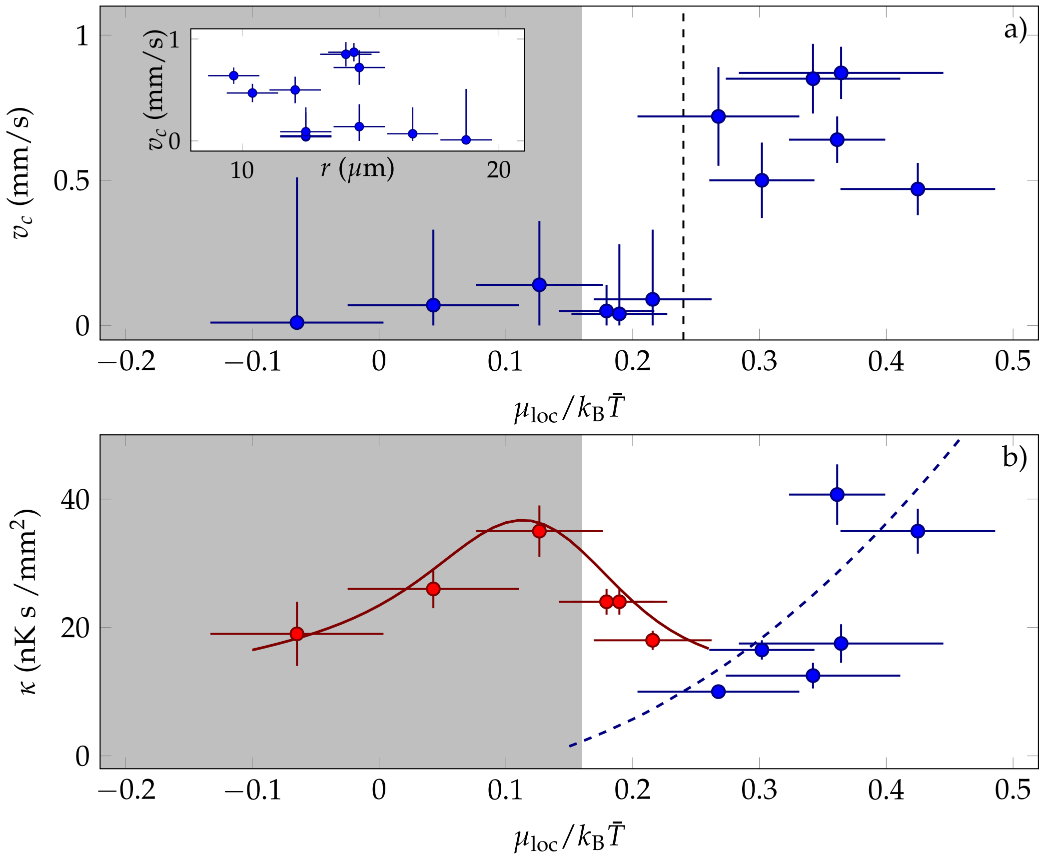

Figure 5.3.: Superfluid behaviour across the BKT transition. **a**, The critical velocities v_c obtained from the curves as in Fig.(5.2) plotted versus the single parameter $\mu_{\mathrm{loc}}/k_B\bar{T}$, which is the relevant quantity due to the scale invariance of the weakly-interacting 2D Bose gas. Our data show a threshold between critical velocities compatible with zero and clearly non-zero critical velocities. It is located at $\mu_{\mathrm{loc}}/k_B\bar{T} \approx 0.24$ (dashed line), somewhat above the prediction $(\mu_{\mathrm{loc}}/k_B T)_c = 0.15$ for the BKT transition in an infinite uniform system [125] (the grey shaded area indicates the normal state by this prediction). The x error bars indicate the region of $\mu_{\mathrm{loc}}/k_B\bar{T}$ that is traced by the stirring beam due to its size (using the $1/\sqrt{e}$ width of the beam) and due to the 'background heating'. The y error bar is the fitting error. The inset to **a** shows the critical velocity plotted versus the stirring radius r. Due to the different atom numbers and temperatures of the clouds, we can find superfluid or normal behaviour for the same radius. **b**, The heating coefficient κ as a function of $\mu_{\mathrm{loc}}/k_B\bar{T}$ for the normal data (red circles) and the superfluid data (blue circles). The red solid line shows a fit of κ linear in the normal density, as expected from a single-particle model. The blue dashed line shows an empirical fit quadratic in the superfluid density. The calculation for the densities assumes $\bar{T} = 90\,\mathrm{nK}$ and the densities are averaged over the size of the stirring beam.

we empirically fit a quadratic scaling of the heating with density $\kappa = a_2 \cdot n_{\mathrm{SF}}^2$ and find $a_2 = 8 \cdot 10^{-9}\,\mathrm{nK} \cdot \mathrm{s} \cdot$ ¯m^2. In principle, one could develop a more refined model to describe the superfluid region, by taking into account the coexistence of the normal and superfluid states via the sum of two heating terms. However, within the accuracy of our data, we did not find any evidence for the need of such a more refined description.

5.5. conclusion

We have presented a direct proof of the superfluid character of a trapped 2D Bose gas. An interesting extension of our work would be the study of superfluidity from the complementary point of view of persistent currents, by adapting to 2D the pioneering experiments performed in 3D toroidal traps [79–81].

6. The uniform two-dimensional Bose gas

In this chapter, I will present our experimental development toward the production of a two–dimensional uniform atomic gas. For creating such an unusual atomic sample, we need to shape the confining potential into a box-like one in the radial directions whereas along the vertical axis the confinement is still set by the light–sheet beam (see 2.2). The resulting radial potential must show:

- — a central uniform region where the potential is constant (equals to U_{bottom}) and where the atoms can be trapped. We characterized this central region by its typical radial extension R_{box}.
- — a high energy barrier of height U_{barrier} delimiting this central trapping region from the outer anti-confining one. This edge domain where the potential varies from U_{bottom} to U_{barrier} must ideally be of zero spatial extent (that is to say of infinite sharpness).

Of course, every possible experimental implementation of such a trapping configuration would present some defects compared to these ideal characteristics, which are non–uniformities of the central trapping region and a finite stiffness of the edges. The relative importance of these defects for the various implementation options dictates an experimental choice between them.

In a first part, I will introduce specifications on the potential properties emanating from the particular gas configurations we want to study. Then, I will detail two schemes for creating uniform trapping using a single laser beam, far blue-detuned compared to the atomic resonance. These two schemes consist in two ways of shaping the beam to display a dark center at the position of the atoms. In both cases, I will present a quantitative and detailed characterization of the potential created, both theoretically and experimentally to justify our choice.

6.1. Experimental specifications for our 2D Uniform trap

In this section, I deduce specific constraints on the uniform trapping potential stemming from a theoretical analysis of the range of cloud parameters we want to study. These constraints will give rise to specifications for our experimental realization of uniform trapping, that I will present later on. It will lead to a choice between the different possibilities. I start by presenting the physical regime we are interested in for our gas and deduce the atomic configurations we want to achieve in terms of atom number N, temperature T and interaction energy per particle ϵ_{int}. I then define the resulting constraints on the trap height, on the uniformity of its central region and on the steepness of its edges. Finally, I present various possibilities for experimentally realizing such a trapping configuration and select two of them for further experimental tests.

6.1.1. Physical properties of the gas under study

The physical configuration of the 2D gas we want to create, which is characterized by N, T and ϵ_{int}, is constrained by the combination of the range of physical properties of interest in our studies and of the characteristics of our 2D trapping configuration.

In our experiments, we want to vary these cloud parameters to test the thermodynamic transitions described in Chapter 1 – namely the partial condensation along transverse condensation (BEC$_\perp$), the condensation to the full ground state induced in 2D by finite-size effects and the Berezinskii–Kosterlitz–Thouless (BKT) transition. In our configuration, BEC$_\perp$ arises at total 2D phase–space density (PSD) $\mathcal{D}^{(2D)}_{\text{tot}} \equiv n^{(2D)}\lambda_{\text{T}}^2$ equals to $\mathcal{D}^{(2D)}_{\text{tot, BEC}_\perp} \sim \pi^2/6 \times k_{\text{B}}T/\hbar\omega_z$ (where $n^{(2D)}$ stands for the total 2D atomic density, λ_{T} for the thermal wavelength and ω_z stands for the oscillation frequency of the transverse motion). Due to the requirement on the trap anisotropy for the relevance of the two step condensation picture (see 1.2.3.2), we restrain ourselves to $k_{\text{B}}T \lesssim 15\hbar\omega_z$ so that typically[1] $\mathcal{D}^{(2D)}_{\text{tot, BEC}_\perp} \lesssim 25$. The two latter transitions (BEC and BKT) occur at a larger 2D phase–space density (PSD) verifying $\mathcal{D}^{(2D)}_0 \approx \mathcal{D}^{(2D)}_{0,\text{BEC}}, \mathcal{D}^{(2D)}_{0,\text{BKT}} \sim 8$. For studying gas properties around these transitions, we thus want to cover a typical range of phase–space density $\mathcal{D}^{(2D)}_{\text{tot}}$ varying from 1 to 100.

As the typical atom number achievable in our 2D gases varies from $N = 10^3$ to $N = 10^5$ and the box surface ranges[2] in $\mathcal{A}_{\text{box}} = 300\text{–}900\,\mu\text{m}^2$, the typical atomic density varies from $n^{(2D)} = 1$ to $150\,\mu\text{m}^{-2}$. For realizing the desired PSDs, we then roughly study T around 100 nK, typically varied from a few tens up to a few hundreds nK. In these cases, we can estimate the interaction energy of our gas, by:

- using predictions from classical Monte Carlo simulations [124, 125] or solving Gross Pitaevskii equation (see Annex B). These predictions are valid for our coldest cloud (compared to temperature associated with transverse trapping energy gap $\hbar\omega_z/k_{\text{B}}$ which varies from 20 nK to 100 nK) and for high enough value of $\mathcal{D}^{(2D)}$ (see Ch. 1). Note that in Thomas–Fermi approximation it simplifies in $\epsilon_{\text{int}} \sim \mu/2 \sim k_{\text{B}}T\,\tilde{g}\mathcal{D}^{(2D)}/4\pi$ (for the most degenerate cases).
- performing a first order approximation from ideal Bose law calculations (see Annex A for details). We perform such an estimate for the hottest clouds and lowest trapping frequency $\omega_z/2\pi = 350\,\text{Hz}$ for which previous prediction does not apply. In this approximation, we find $\epsilon_{\text{int}} \lesssim k_B T$ for the considered atomic numbers N and temperatures T.

6.1.2. Deduced constraints on the trapping potential

The techniques that I will present in this chapter to create a box–like potential are based on the use of a single far–blue–detuned ($\lambda = 532\,\text{nm}$) laser beam of intensity I. This beam gives rise to a dipolar potential $U = \alpha I$ on the atoms with $\alpha = k_{\text{B}} \times$

---

[1] Note that in this case the 2D PSD corresponding to the ground state of the z-motion $\mathcal{D}^{(2D)}_0 \equiv n^{(2D)}_0\lambda_{\text{T}}^2$ ($n^{(2D)}_0$ is the 2D density of atoms populating the ground-state of the z-motion) is logarithmically smaller than $\mathcal{D}^{(2D)}_{\text{tot, BEC}_\perp}$ (see Eq. 1.51) , which gives $\mathcal{D}^{(2D)}_{0,\text{BEC}_\perp} \lesssim 4$

[2] This is set by the radial extent of the LS beam that provides transverse confinement (see 2.2.1).

59 mK μm^2/W (as for the 2D light–sheet potential. see 2.2.1 for details). We thus want to shape its intensity profile at the position of our sample to create a «hollow beam», that presents:

- a central dark region of constant (and small) intensity I_{bottom}, that constitutes an «intensity hole».
- a sharp intensity variation at the edges of this «hole» to a high maximal value I_{barrier}.
- a smoothly varying outer region from this intensity maximum toward the outer and dark region of the beam.

I will present in next sections how to create such a profile, I now focus on the constraints on this intensity profile due to the specific cloud configurations under study, as introduced above.

The constraints bear on three main characteristics:

6.1.2.1. The maximal energy barrier U_{barrier} confining the atoms in the central region

To be able to load a 3D gas of temperature T in the box–trap potential without evaporatively cutting its thermal excitations distribution, the necessary energy barrier must verifies $U_{\text{barrier}} \gtrsim 10$ to $20 \times k_B T$. As we want to load gases of $T \gtrsim 250$ nK, the resulting condition reads

$$U^{\text{load}}_{\text{barrier}} = \alpha I^{\text{load}}_{\text{barrier}} \gtrsim k_B \times 5\,\mu K. \tag{6.1}$$

From this inequality, we infer the total power $P^{\text{load}}_{\text{box}}$ needed in the beam depending on the specific setup used for creating this trap geometry.

6.1.2.2. The uniformity of the trap center:

In order to avoid perturbing the atomic distribution, the variations of the confining potential in the central uniform region must be small compared to the largest energy scale between the gas temperature $k_B T$ and its interaction energy ϵ_{int}. We call δU the typical variation of the potential height in the central region[3].

We want to characterize the maximally acceptable variation $\delta U_{\max}$ compared to the energy barrier U_{barrier}[4]. We impose[5] $\delta U_{\max} = k_B T/2$. As, due to evaporation condition, the ratio of the potential barrier and the temperature is typically bounded to $U_{\text{barrier}}/k_B T \lesssim 10$, then, in the intensity profile at the position of the atoms, **the maximal variation of intensity in the central region must be less than** 5% **of the maximal**

---

[3] We will see at the end of the paragraph how to self-consistently define such a central region: It will be delimited by an upper potential bound $U_{\min} = U_{bottom} + \delta U_{\max}$ where $\delta U_{\max}$ is the maximally acceptable value for δU

[4] We compare the variation δU and the barrier U_{barrier} realized at the same laser power P_{box}. As they are both proportional to this power, the final condition on ratio $\delta U_{\max}/U_{\text{barrier}}$ will be independent on P_{box}

[5] Note that, for the most degenerate gases ($\mathcal{D}^{(2D)} \gtrsim 4\pi/\tilde{g}$), the condition given in Eq. 6.2 on the trap bottom flatness is relaxed due to the prevailing interaction energy $\epsilon_{\text{int}} \gtrsim k_B T$ that introduces a higher energy scale tending to uniformize cloud density.

intensity:

$$\delta U \lesssim \delta U_{\mathrm{max}} = \frac{U_{\mathrm{barrier}}}{20}. \tag{6.2}$$

We coherently define the central trapping region to be the domain in which the potential varies by less than $\delta U_{\mathrm{max}} = U_{\mathrm{barrier}}/20$. It is then defined by the value of the potential at its edges $U_{\mathrm{min}} = U_{\mathrm{bottom}} + U_{\mathrm{barrier}}/20$.

6.1.2.3. The steepness of the walls:

Due to the relation between the temperature and the total energy barrier of the potential, $U_{\mathrm{barrier}} \gtrsim 5\text{–}10 \times k_{\mathrm{B}}T$, U_{barrier} happens not to be the relevant reference for defining the edges felt by the atoms: The potential barriers seen by the atomic ensemble is more accurately described by a fraction of the total height, typically we take it to $U_{\mathrm{max}} = U_{\mathrm{min}} + U_{\mathrm{barrier}}/5$ where U_{min} is the previously introduced potential limit to the inner trapping region. To describe quantitatively the steepness of this part of the potential, we will measure two quantities:

1. First, we define the characteristic length on which the potential varies from U_{min} to U_{max}. This length scale will be called the «stiffness» of the uniform trap and it will be denoted by η in the rest of this chapter. If r stands for the abscissa along straight paths going from the center of the beam to its edges:

$$\eta = \langle R_{\mathrm{barrier}} - r_{\mathrm{min}} \rangle_{\mathrm{paths}} \;/\; \left\{ \begin{array}{l} U(R_{\mathrm{barrier}}) = U_{\mathrm{max}} \equiv U_{\mathrm{bottom}} + U_{\mathrm{barrier}}/4 \\ U(r_{\mathrm{min}}) = U_{\mathrm{min}} \equiv U_{\mathrm{bottom}} + U_{\mathrm{barrier}}/20 \end{array} \right. \tag{6.3}$$

   To be sharp, the edges must correspond to an η that is short compared to the other characteristic macroscopic lengths of the problem. This is commonly the trap extension[6] R_{box} and **we impose $\eta \lesssim R_{\mathrm{box}}/3$**. Typically, R_{box} ranges in 5–15 μm resulting in $\eta \lesssim 1.7\text{–}5\,\mu$m. η must also be smaller than or comparable to the microscopic length of the problem, that is commonly the healing length ξ defined by $\xi = 1/\sqrt{\tilde{g}n}$. For our configuration, we typically have $\xi = 0.5\text{–}1.5\,\mu$m. and **we impose $\eta \lessapprox \xi$**. In conclusion, η **characterizes the relevant edges of the potential and we require it to be of a few micrometers or less.**

2. To consider our trap as a box-like one, we also want to differentiate it from the commonly used harmonic-trap. To do so, we need to characterize the way the potential varies from its center to the edges. We thus perform a power–law fit of the potential from $r = 0$ to $r = R_{\mathrm{barrier}}$ that is the abscissa[7] for which the potential is equal to U_{max} defined in Eq. 6.3. The fitting function used is:

$$f_{\mathrm{fit}}(r) = I_{\mathrm{bottom}} + B\,(r/R_{\mathrm{barrier}})^{\beta} \tag{6.4}$$

---

[6] For anisotropic trap, we would in fact define several stiffness, one for each symmetry axis . To do so, we perform averages in Eq. 6.3 over paths along each symmetry axis. We would compare each of them to the corresponding axis characteristic size.

[7] Before performing such a fit, we in fact usually realize some averaging of the potential profile to convert dependency $U(x,y) \to V(r)$. For box-trap presenting rotation symmetry, we perform usual azimuthal averaging. For trap presenting no rotation symmetry, we will use averaged cut along each symmetry axis. This will usually result in several power law fits characterization, one for each axis.

We will impose [8] a power–law coefficient $\beta \gtrsim 5$.

Those two quantities are related as, for a given radius R_{box}, the lower β is, the larger η. But the precise relation between them depends on the radius R_{box} of the trapping region. Both quantities give, in their respective way, an interesting insight on the confinement of our cloud. We are thus interested in computing both quantities for each of our experimental implementation.

6.1.3. Choice on experimental technique to realize the uniform trap

Several techniques have been developed over years to realize a box–like or at least non–harmonic potential. In most of these previous experimental realizations, we note that the potential needed to be three–dimensional. In this section, I will briefly introduced selected examples. I will point out two realizations we have tested experimentally in our setup and that I will detail in the rest of the chapter.

A first technique have been developed to create dark non–harmonic potentials using **phase plates** [153]. This strategy is very similar to the solution we have implemented for creating the 2D light–sheet potential (see 2.2). A specific phase is imprinted on an initially Gaussian beam that is then focused with a lens. The phase profile is then converted into an intensity profile. Various choices have been made concerning the specific phase imprint used in these setups. The first proposals were only using one plate generating, after conjugation, either a Laguerre–Gaussian beam [153] or a Hermite–Gaussian one [154]. Due to typical 3D geometry used in experiments, it was profitable to combine several of them as in [155, 156]. In our advantageous 2D geometry, we can keep using a unique plate. We choose to test this technique experimentally on our atoms.

Axicon lenses have been used to create collimated beam exhibiting an hollow center as in [157] and [158]. The hollow center is robust along the beam propagation. It nevertheless needs to be cleaned to be of a sufficient quality to uniformly trap atoms. Such a cleaning is done using a dark spot in combination with this special lenses (see [157]).

In our specific configuration, due to the huge advantage of 2D geometry, we in fact develop a much simpler method, only using the cleaning **mask** to create the hollow beam at the specific image position. This technique only manipulates intensity profiles using diffraction on the mask. Then the cancelation of the beam profile is not extended along the beam propagation and has a short «depth of field», that is that the central hollow region is deformed and blurred when getting away from the precise focus position. Nevertheless, due to our planar geometry, we were comforted in trying this simple method prior to any complication using special optics devices.

One can use a **rapidly rotating laser beam** that creates the desired barrier by time-averaging (if the rotation frequency is high enough compared to the evolution time of the atomic cloud). Such a method has been implemented using a Acousto–Optic Modulator in [159]. It is a very versatile procedure but it has only been implemented for creating large traps (typical radius of 100 μm) confining hotter clouds (typically of sev-

---

[8] This choice is arbitrary and simply sets to be significantly different from an harmonic behavior. Previous PhD student Rémi Desbuquois [111] in fact imposes a more severe constraint ($\beta \gtrsim 10$) in order to inverse BKT and BEC transitions apparition order.

eral tens of μK). We did not consider this technique in our setup. We were in particular concerned by heating issues.

In Hadzibabic group [49], 3D uniform potential are created via the use of a **Spatial Light Modulator (SLM)**. This technique also use a phase imprint but here the phase imprinted can be controlled dynamically to correct for optical defects. This technique was first implemented in [160]. The specific refreshing frequency of such a device made them unusable for our specific experimental setup. For this reason, we discard this possible implementation.

In the rest of the chapter, I will present the experimental implementation of the two methods pointed out as relevant for our specific configuration. For each of them, I will characterize the uniform potential and compare the results to the specifications defined in this section. This will lead to an experimental choice between them:

1. We first developed a holographic method using a phase plate to generate a Laguerre Gaussian beam of high order. Even though seemingly robust (as the cancelation of the intensity profile is topologically ensured), such a technique reveals experimentally limited in terms of both barrier height and trap bottom quality. As not complying with the experimental requirements for our gases, we decided to discard it.
2. We then developed a simple geometrical imaging method using a blocking mask that we image at the position of the atoms. Even though the cancelation of the beam profile only occurs at the exact image position of the mask, we experimentally select this second method as the most relevant to simulate uniform trapping in our specific 2D geometry (Note that such a conclusion would not hold for the 3D case).

6.2. Uniform trap via holographic shaping

6.2.1. Principle

The first method we implemented to create a box-like potential is an holographic method using an optical phase plate. The experimental setup is described in Fig. 6.1**(b)** and follows the same principle as the 2D shaping (see 2.2). The phase plate imprints a specific phase on a collimated Gaussian beam. This beam is then focused on the atoms with a lens so that the phase imprint translates into a special amplitude profile at this position. The phase imprint chosen for creating the desired «hollow beam» at the lens focus is a linear function of the angle while a constant with the radius so that it results in a phase winding when completing a revolution around the plate[9] (see Fig. 6.1**(a)**. The overall phase winding must be a multiple n of 2π. Such a phase is thus similar to the one found in a n-fold vortex.

As for the 2D shaping (see 2.2.1), the resulting trapping potential U is deduced from the intensity profile I_{HG} at the focus of the lens by $U = \alpha I_{HG}$. Detailed calculations of the intensity profile I_{HG} in the paraxial approximation were performed by previous

---

[9] We should note that in practice the phase is not continuously varying with the angle but use discrete steps defining tiny phase sectors (typically our phase plates are made of 96 sectors)

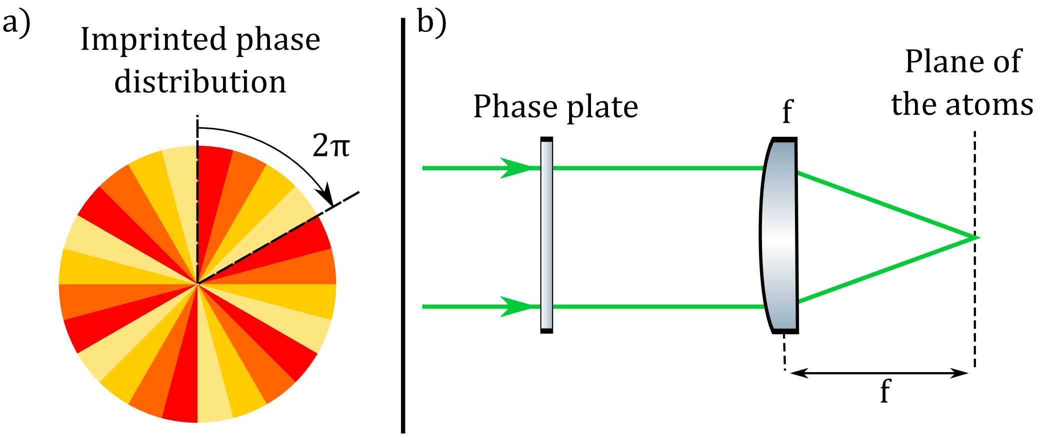

Figure 6.1.: **(a)** Six-fold phase vortex imprinted by the phase plate. Though only four phase sectors per 2π step are represented, our phase plates have 16 sectors per 2π step. **(b)** Experimental setup required to create a stadium with a phase plate.

PhD student P. Rath [109]. I will summarize them here. For a phase winding of $n \times 2\pi$, the electric field in the focal plane (parameterized by the polar coordinates (ρ, ϕ)) of the lens of focal length f is given by

$$E(\rho, \phi) = \int r \,\mathrm{d}r \,\mathrm{d}\theta E_0(r, \theta)\, e^{i\,n\theta} e^{i\,\frac{k}{f} r\,\rho\,\cos(\theta-\phi)} \tag{6.5}$$

where E_0 is the electric field distribution in the plane of the phase plate (parameterized by the polar coordinates (r, θ)) and $k = 2\pi/\lambda$. For a Gaussian profile E_0 of waist w_0 (at the phase plate location), this integral can be fully evaluated. Around the origin, the electric field can be approximated at the lowest order by

$$E(\rho \to 0, \phi) \propto \sqrt{\frac{2\,P_{\mathrm{box}}}{\pi w_0'^2}} e^{i\,n\phi} \left(\frac{\rho}{w_0'}\right)^n \tag{6.6}$$

where P_{box} is the total power of the beam, and w_0' is the waist at the focus of the lens and writes $w_0' = \lambda\, f / \pi\, w_0$. We note that the intensity distribution I_{HG} ($\propto |E|^2$) and so the trapping potential U is proportional to $(\rho/w_0')^{2n}$ for $\rho \to 0$. Then the higher n is, the flatter the central confining region. In practice, we choose to use a phase plate with $n = 6$.

6.2.2. Theoretical expectations

Using the general formula obtained by exact integration of Eq. 6.5 for all radius ρ and for a Gaussian beam (see [109] for details), we compute the whole intensity profile at the focus of the lens and show it in Fig. 6.2. From this theoretical profile, we deduce the expected properties for the trapping potential.

First, we note that, in the center, the intensity cancels perfectly $I(\rho = 0) = 0$. The intensity shows thus a maximum (denoted I_{barrier}) at an intermediate radius R_{barrier} and we find $R_{\mathrm{barrier}} \approx 3.2\, w_0'$. For $\rho \geqslant R_{\mathrm{barrier}}$, the intensity is decreasing slowly and the initial beam power is redistributed all along this important outer region. In particular, for $\rho \geqslant 5\,w_0'$, we fit a decay behavior $I \propto \rho^{-3}$. We now characterize the inner trapping region and its edges.

6.2.2.1. Radius of the box-trap

We define the extent of the central dark region by giving the radius inside which the intensity do not exceed 5% of the intensity peak $I_{\text{min}} = I_{\text{barrier}}/20$. This radius denoted R_{box} corresponds to the radius of the resulting uniform-trap on the atoms and we find

$$I(R_{\text{box}}) = I_{\text{barrier}}/20 \qquad \Rightarrow \qquad R_{\text{box}} \approx 1.5\,w_0'. \tag{6.7}$$

For the range of R_{box} of interest, w_0' must vary from $3\,\mu$m to $10\,\mu$m. To create such a small size, we need a specially designed optical setup to strongly focus our beam onto the atoms. The minimally achievable value of the trap radius will be limited by the resolution σ of our imaging setup ($R_{\text{box}} \gtrsim 1.5\,\sigma$).

6.2.2.2. Barrier height of the box-trap

Due to the slow decay in the wings of the profile, I_{barrier} is only a small fraction of the intensity maximum $I_0 = 2P/(\pi w_0^2)$ of the same Gaussian beam in the absence of the phase plate. We find

$$I_{\text{barrier}} \approx 0.014\ I_0 \Rightarrow U_{\text{barrier}} = 0.014\ \frac{2P_{\text{box}}\,\alpha}{\pi(R_{\text{box}}/1.5)^2} = 0.02\frac{\alpha\ P_{\text{box}}}{R_{\text{box}}^2}. \tag{6.8}$$

For a typical box-trap of radius $R_{\text{box}} = 10\,\mu$m, we expect $U_{\text{barrier}} = 11.8\,\mu K$ for $P_{\text{box}} = 1$ W. From the constraint of Eq. 6.1, we deduce that for the same $R_{\text{box}} = 10\,\mu$m, we need a total power of $P_{\text{box}} = 850$ mW. We note that the power needed depends strongly on the box-trap radius as $P_{\text{box}} \propto R_{\text{box}}^2$. Since only $P_{\text{box}} \sim 500$ mW are available in our experimental setup, we then have to restrict to $R_{\text{box}} \lesssim 8\,\mu$m.

6.2.2.3. Steepness of the edges of the box-trap

First, we note that the intensity varies from I_{min} to I_{barrier} in a characteristic length that is $R_{\text{barrier}} - R_{\text{box}} = 1.7w_0' \sim R_{\text{box}}$ (seeFig. 6.2). As we pointed out previously, only the sharp variation of the potential at small values is relevant to define the steepness of the resulting potential barrier seen by the atomic ensemble. We then characterize this steepness as introduced in 6.1.2 and compute:

— The stiffness $\eta = R_{\text{barrier}} - r_{\text{min}} = 0.41w_0' = 0.27R_{\text{box}}$.
— The power–law coefficient $\beta = 6.55 \pm 0.07$.

For such an implementation, the theoretical steepness is limited, but still marginally satisfies the requirements $\eta \leq R_{\text{box}}/3$ and $\beta \geq 5$ defined in 6.1.2. Then, if it is realized experimentally, it must be sufficient to realize a box potential with sharp edges.

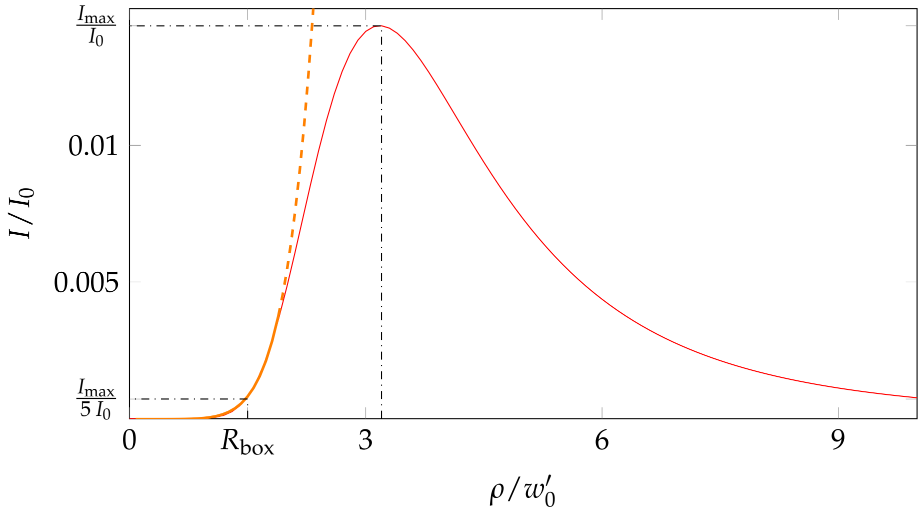

Figure 6.2.: In red solid line, intensity distribution for a phase plate with a 12π phase winding in paraxial approximation. This beam profile is extracted from exact integration of Eq. 6.5 for a Gaussian beam. I_0 is the intensity in the center of a Gaussian beam with the same total power P. In orange is presented the power low fit of the trap edges using Eq. 6.4. The fit gives $\beta = 6.55 \pm 0.07$.

6.2.3. Experimental results and reasons for abandon

Such a scheme of principle have been tested in a previous campaign on a simplified optical setup by former PhD students P. Rath [109] and D. Jacob. While still noticing some defects, the results were supporting for an experimental test on the atoms. I recall here briefly the deviations compared to the theoretical expectations they pointed out:

— They observed steeper walls than expected.

— The resulting hollow shape is slightly hexagonal, certainly due to the discrete sectors on the plate. We must take this into account for our detailed cloud analysis but it does not constitute a stringent limitation.

— An intensity bump occurs at the center of the profile when looking exactly at the focus of the lens. They manage to get rid of this non–uniformity by moving away from the focus [10].

Following these conclusions, we decided to implement such a trapping potential on our main experimental setup.

In this first experimental implementation on the atoms, the box-trap was propagating upward and so counter–propagating compared to the vertical imaging beam (see 3.2.2 and Fig. 3.3 for a description of the imaging setup). It was superimposed with the imaging beam just before the microscope objective and imaged on the atoms by this same microscope objective [11].

---

[10] Note that we perform the same trick for aligning the light-sheet beam which is also generated from a phase-plate (see 2.2.2)

[11] We should note that the microscope objective was design for use with 780 nm wavelength light. Then some chromatic effects may occur.

In this setup, we can image the intensity profile of the beam on a side imaging setup with a camera set at a conjugated position to the location of the atomic plane. This imaging setup enable to estimate the potential that is effectively felt by the atoms. An example of the measured intensity distribution is presented in Fig. 6.3**(a)**, and an azimuthal averaging is performed in Fig. 6.3**(b)**. For our implementation on the main experimental setup, we obtain similar results than in the preliminary tests described above but with stronger defects of the potential center. We perform a quantitative analysis of the trap characteristics as described in the following.

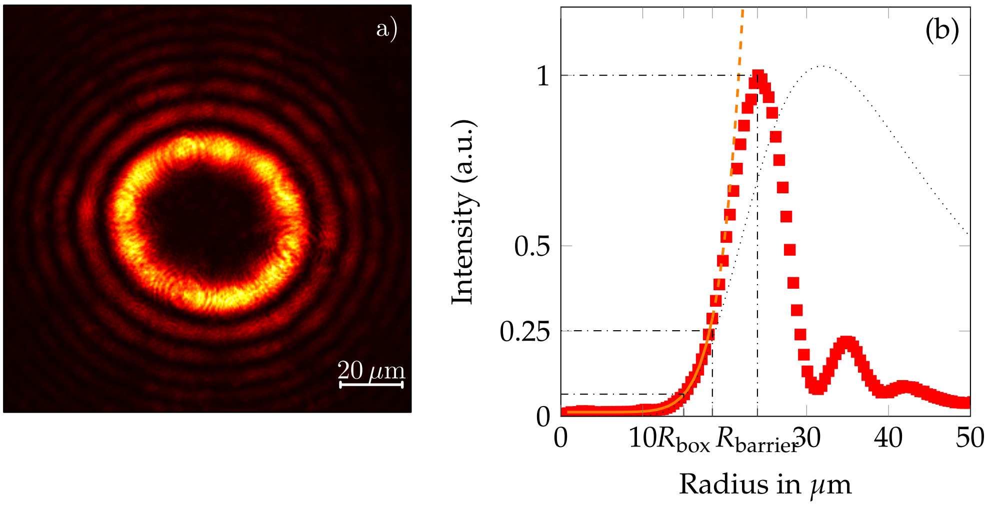

Figure 6.3.: **(a)** Intensity distribution created by a phase plate with a 12π winding. **(b)** Radial average of the intensity distribution (red line), along with a fit of the central region with the fitting function from Eq. 6.4 (orange line). The fit is performed for $r \leq R_{\text{box}}$ (see Eq. 6.7), and the fitted power is $\beta = 7.98$ instead of 6.55 as expected from previous theoretical analysis. The black dotted line correspond to the theoretical profile with a waist given by $R_{\text{box}}/1.5 = 10\,\mu$m. This plot enhance the increased steepness of the potential barrier in the experiment.

6.2.3.1. Radius of the box-trap and trap bottom

The mean intensity in the trapping center in this distribution is $I_{\text{bottom}} = 0.015 I_{\text{barrier}}$. We characterize as previously the radius of the uniform trap to be the distance at which the intensity is equals to $I_{\text{min}} = I_{\text{bottom}} + (I_{\text{max}} - I_{\text{bottom}})/20$. We find here $R_{\text{box}} = 15\,\mu$m and deduce $w_0' = 10\,\mu$m. We should note that, in this precise experimental realization, we displaced the atomic plane away from the focus of the box-trap beam in order to lower the effect of the central bump already observed in preliminary tests. The radius value results then from a compromise between the unwanted increase in the beam waist size due to this defocusing and the gain in uniformity of the central trapping domain. $R_{\text{box}} = 15\,\mu$m corresponds to the maximally acceptable extent of the box-trap in terms of light sheet radial waist (see 2.2). We highlight that:

1. This configuration gives rise to a limited energy barrier of $U_{\text{barrier}} \sim 2.6\,\mu K$ for the available power $P_{\text{box}} \approx 500\,$mW bounding then the temperature of the loaded

gas.

2. Due to the use of the maximally acceptable R_{box} and thus the maximal defocusing of the box-trap beam, this configuration corresponds to the most favorable one in terms of the trap bottom fluctuations and edges steepness. Configurations with smaller radii will necessary lead to more important defects.

6.2.3.2. Steepness of the edges of the box-trap

The intensity maximum I_{barrier} is found at $R_{\text{barrier}} = 24\,\mu\text{m}$ which is smaller than expected. Such an observation agrees with the preliminary-test conclusion that the walls are steeper than expected. Then the intensity varies from approximately I_{bottom} to I_{barrier} in a characteristic extent of $R_{\text{barrier}} - R_{\text{box}} = 0.9\ w'_0$. The walls steepness is quantitatively characterized by the variation at small values of the potential as introduced in 6.1.2 and we find:

— A stiffness $\eta = 0.34\ w'_0 = 0.23\ R_{\text{box}}$ that is 20% shorter than expected stiffness and satisfies the required $\eta \lesssim R_{\text{box}}/3$.

— A power–law coefficient $\beta = 7.98 \pm 0.01$ that is also steeper than expected and satisfies the requirements.

6.2.3.3. Uniformity of the trap bottom

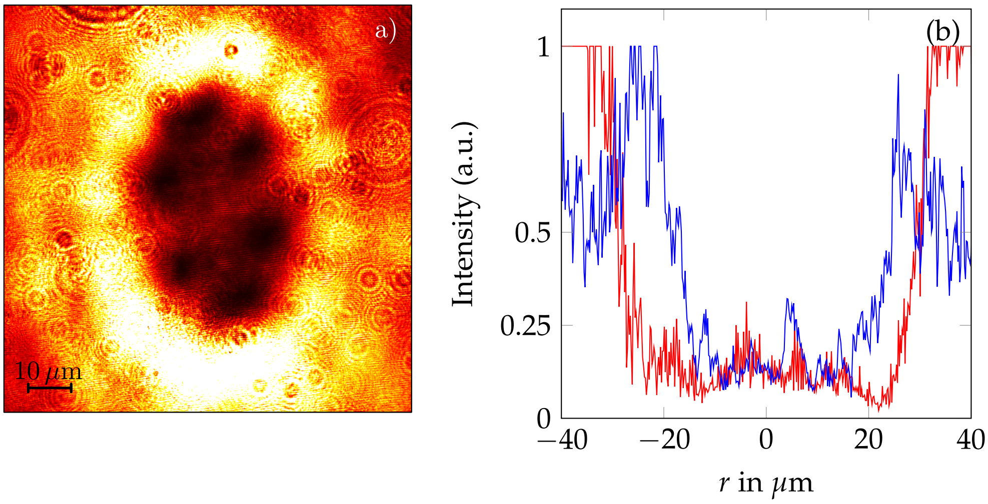

Figure 6.4.: **(a)** Intensity distribution created by a phase plate. The intensity has been rescaled to reveal the features in the center of the beam. **(b)** Two cuts of the intensity distribution shown in **(a)**.

The uniformity of the central part of the intensity distribution is our major concern. Contrarily to what was observed in the preliminary tests, we could not get rid of the bump at the center of the trap. This is due to the fact that we had to limit the displacement from the focus to keep $R_{\text{box}} \lesssim 15\,\mu\text{m}$. The intensity profile is presented in Fig. 6.4**(a)** with a rescaled intensity that reveals several defects:

- We clearly distinguish six intensity minima. This can be understood if we consider the phase plate as an imprint of six individual phase vortices, instead of a single six-fold vortex. For an ideal phase plate, the centers of the vortices coincide so that they are equivalent to the expected six-fold vortex. If the phase plate presents some defects, the vortex centers can be shifted so that the resulting total phase distribution is only equivalent to a six-fold vortex in the wings of the intensity distribution and not in its inner region.
- These six minima result in intensity bumps, at the center as well as along six radial lines, which remain important even when moving away from the focus.
- The edges are not perfectly symmetric and also show some defects. Thus the energy of barrier U_{barrier} is not a constant along all path that goes from the center to the wings of the intensity profile. We must then compare the variation of intensity in the center δU to the minimum barrier height over the straight paths, denoted by their angle θ , $U^{\text{tot}}_{\text{barrier}} \equiv \min(U_{\text{barrier}}(\theta))$.

Then for the intensity profile shown in Fig. 6.4**(b)**, the maximal intensity defect is as large as 40% of the barrier height (and its mean value is $\langle \delta U \rangle \sim 0.07\ U^{\text{tot}}_{\text{barrier}}$) which is too important for our applications (see Eq. 6.2).

In short, this implementation of an uniform trap does not fulfill the prerequisite defined at the beginning of the chapter. For this reason, we present in the following section an alternative method for producing a uniform confinement.

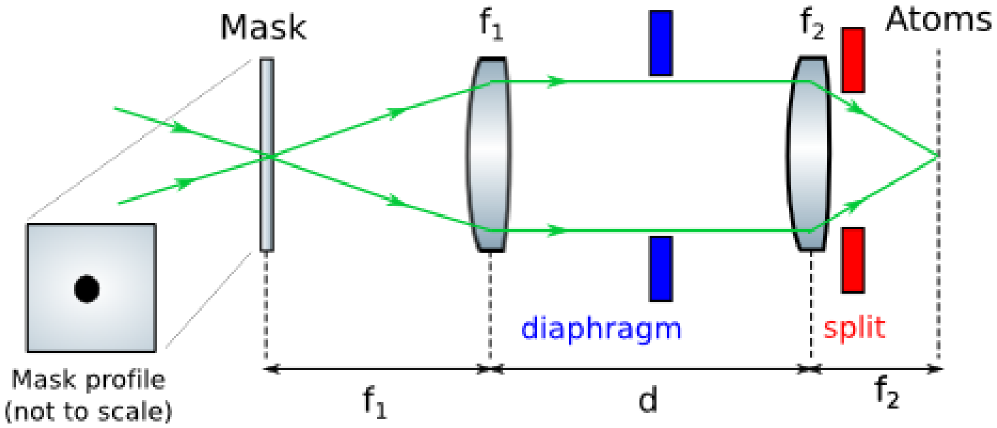

Figure 6.5.: Optical setup for the creation of a stadium potential in the experiment. In this setup we use to lenses of focal lengths $f_1 = 500$mm and $f_2 = 150$mm respectively. We place them such that either the glass plate holding the masks imprint or the atoms are located at their focus. In between the two lenses, the beam profile is cut by either the intrinsic setup aperture that is limited by a slit placed just after the second lens or a deliberate diaphragm placed inside the telescope to control at with order we do cut the diffraction pattern.

6.3. The dark spot method

6.3.1. Principle and theoretical expectations.

A straightforward way for creating a hollow-core beam consists in simply putting a mask at a given position on its path and forming the image of the mask plane at the wanted location. The mask can be of any shape. As the mask does not transmit light, just after the mask position, the intensity profile is simply the Gaussian profile truncated to zero by the mask shape. Mathematically, if we call $t(x,y)$ the transmission in the plane of the mask, $t(x,y)$ is defined by $t(x,y) = 0$ if (x,y) is inside the mask shape and $t(x,y) = 1$ elsewhere. Then the intensity profile just after the mask plate is defined by

$$I_i(x,y) = \frac{2P_{\text{box}}}{\pi\, w_0^2} e^{-2r^2/w^2}\ t(x,y) \tag{6.9}$$

where w_0 is the waist of the laser at the position of the mask and P_{box} is the available laser power.

This intensity will be reformed, up to a magnification factor $\mathcal{M}$, onto the atoms by the imaging setup as presented schematically in Fig. 6.5. In the limit of infinite and perfect optical elements and paraxial beam propagation, the intensity profile $I_{\text{f}}(x',y')$ is equal to $I_{\text{i}}(x,y)$ with $(x',y') = \mathcal{M}\ (x,y)$:

$$I_f(x',y') = I_i(x'/\mathcal{M}, y'/\mathcal{M}) = \frac{2P_{\text{box}}}{\pi\, w^2} e^{-2r'^2/w^2}\ t(x'/\mathcal{M}, y'/\mathcal{M}) \tag{6.10}$$

where we defined $w = \mathcal{M} w_0$, the waist if the beam at the position of the atoms.

For now on, to compare to the previous implementation using a phase plate imprint, we will consider a disk–shaped mask of radius R_{mask} and note r (resp. r') the radial coordinate in the mask (resp. atom) plane. Then

$$I_f(r') = \frac{2P_{\text{box}}}{\pi\, w^2} e^{-2r'^2/w^2}\,,\ \text{if}\ r' > R_{\text{box}} \qquad \text{and} \qquad I_f(r') = 0\,,\ \text{if}\ r' \leq R_{\text{box}} \tag{6.11}$$

where $R_{\text{box}} = \mathcal{M} R_{\text{mask}}$ is the hollow-core size at the position of the atoms.

6.3.1.1. Barrier height and optimal waist

For a fixed laser power P_{box} and a fixed mask radius R_{box}, the intensity barrier (*i.e.* the intensity at the edges of the mask) is maximal for $w = \sqrt{2}\, R_{\text{box}}$. Then, the energy barrier is given by

$$U_{\text{barrier}} = \frac{\alpha}{e\pi} \frac{P_{\text{box}}}{R_{\text{box}}^2}. \tag{6.12}$$

For a given power P_{box}, the energy barrier corresponding to this setup is then 5.8 times greater than the one expected in the holographic method (see Eq. 6.8) for the same trap radius R_{box}. We then only need $P_{\text{box}} = 325\text{mW}$ for $R_{\text{box}} = 15\,\mu\text{m}$ to satisfy Eq. 6.1, which is available in our setup.

6.3.1.2. Steepness of the edges and flatness of the bottom of the trap:

In the previously used limit of infinite and perfect optical elements and paraxial beam propagation, both the steepness of the barrier and the flatness of the bottom of the potential are expected to be infinite (or set by the mask quality). In practice, these will be limited by the numerical aperture of the imaging system.

6.3.1.3. Aperture Effects on the trap quality

I present a detailed simulation of the effect of a finite aperture on the beam propagation and resulting trap quality in Annex G. The aperture is a disk of radius R_{diaphr} centered on the beam and placed inside the telescope that image the mask onto the atomic sample (as it is experimentally relevant to simulate the actual effect of the clipping objects in our setup, see Fig. 6.5 and comments in Annex G). I summarize here the conclusions of this analysis.

For our setup characteristics, the aperture affects the trap quality at the level of the experimental requirements defined in 6.1.2 if $R_{\text{diaphr}} \lesssim 15\,\text{mm}$. This is thus in practice a relevant effect. Both the edge steepness and the trap bottom uniformity are affected by the finite aperture. The overall tendency is the larger the aperture, the shorter the stiffness length η, the higher the power law coefficient β, the flatter the trap bottom. For aperture sizes $R_{\text{diaphr.}} \gtrsim 3\text{mm}$ the limiting feature is the variation of the potential in the central region compared to the barrier height, while both the stiffness η and the power law coefficient β comply with their required values. However this tendency is only true in average. In fact, every parameter shows oscillatory behavior with the aperture size. We explain this oscillation by the position of the cut realized by the diaphragm compared to the intensity extrema of the beam pattern inside the telescope (which depend on the specific mask size and shape used). For aperture smaller than $R_{\text{diaphr}} \lesssim 15\text{mm}$, we can still reach a satisfying regime of uniform trapping by finely tuning the effective aperture of our optical system (and in particular by reducing it). For this reason we place a diaphragm of adjustable aperture inside the telescope as shown in Fig. 6.5.

6.3.2. Experimental setup

In our experimental setup, the box-trap is propagating downward onto the atoms. It is thus collinear to the vertical imaging beam with which it is superimposed using a dichroic plate. Both beams are focused onto the atoms via an achromatic doublet of focal length $f_2 = 150\,\text{mm}$ and radius $\mathcal{R} = 15\,\text{mm}$. Ahead of this imaging lens, the beam is focused on the atomic plane. We place a first spherical lens of focal $f_1 = 500\,\text{mm}$ so that the glass plate holding the mask imprint is at the focus of this lens. The two lenses are separated by $d = f_1 + f_2$ so that the resulting magnification of the global setup is $\mathcal{M} = 0.3$.

Just after the imaging doublet, the beam profile is cut by a geometrically unavoidable slit of radius [12] $\mathcal{R} = 9\,\text{mm}$. We also deliberately insert a diaphragm inside the telescope

---

[12] This limiting element for the aperture of the system is in fact an asymmetric slit made in the bread-

to advantageously control the cut performed in the diffraction pattern as explained in previous section (see Annex G for more details). We manually choose the aperture of this diaphragm for each of the used dark masks to optimize the bottom flatness of the resulting box-trap. This setup is schematized in Fig. 6.5.

As we aim to create a stadium of radius R_{box} varying from 5 to 15 μm, we use physical dark masks whose sizes R_{mask} vary from 15 μm to 50 μm. We choose [13] a beam waist at the position of the mask $w_0 = 160\,\mu$m.

The masks are realized by a clean–room deposit on a wedged AR coated glass plate of good surface quality [14]. We deposit a 80 nm gold film on the non-wedged face by electro–lithography. The resolution of deposit is then of the order of a few tens of nm. Rare parasite drops of the metal are also deposited outside the mask regions during the process but the probability of such an error is low. In our experimental realization of the dark spot–plate no error spot are found at less than 300 μm of any of our masks and so are not seen by the laser beam. Our deposit were realized by the engineer José Palomo. On a single glass plate we imprint several patterns. In the actual setup, we imprint at the center of the plate a grid of 6 × 6 patterns distant of 2.5mm. Along this grid:

1. the typical half–size (half–length or radius according to the shape) of the masks varies from $R_{\text{mask}} = 15\,\mu$m to $R_{\text{mask}} = 50\,\mu$m in real space.
2. the shape of the mask itself changes between a disk, a square, a rectangle, an annulus, a target or a set of two-parallel rectangles.

The glass plate is set on a three-axis translation stage so that we can change easily from one pattern to the other and adjust the conjugation of its plane to the atom position.

Even though the box-trap beam is superimposed with the vertical imaging one, due to the presence of a dichroic plate and of an interferometric filter, it is not easy to directly image the mask using the atomic imaging path. We thus implemented a side imaging setup using the reflection of the dichroic plate just after the microscope objective. In this setup, we image the box-trap beam at a conjugate position of the atoms. This side imaging gives a good insight of the potential seen by the atoms. We indeed noticed a good match between the defects seen in this side imaging and the one observed in a

---

board to transmit the beams toward the glass cell. Its minimal half width corresponds to the indicated value $\mathcal{R} = 9$.

[13] We are not varying this waist with the radius of the mask selected for a given experiment. Hence, we cannot be in an optimized configuration where $w_0 = \sqrt{2}R_{\text{mask}}$ for all our trap configurations. We decided to get away from this optimal configuration and choose a much larger beam than our masks. In this configuration, the barrier height at a given power is reduced but it results less sensitive to any change in the trap properties (size or shape) and then on the mask considered. For our experimental values, we found a maximal potential barrier at the center of the beam of $U^{(0)}_{\text{barrier}} = 8\,\mu K$ at the full available power $P_{\text{box}} = 500\,$mW. When we vary the trap extent R_{box}, the effective barrier is only a fraction of $U^{(0)}_{\text{barrier}}$. For the considered boxes in this manuscript, this fraction varies from 0.98 for a disk of radius $R_{\text{box}} = 5\,\mu$m to 0.83 for a disk of radius $R_{\text{box}} = 15\,\mu$m and 0.69 for a square of same half width $L_{\text{box}}/2 = 15\,\mu$m. Then, U_{barrier} is varying with the trapping configuration but less drastically than if we choose a smaller beam. We also note that the maximal barrier height is in good agreement with the experimental specification

[14] Thorlabs WW11050-C10 glass plate. The reflection is specified to be of 0.2% for $\lambda = 532\,$nm, the wedge define the small angle between both faces and it is of 30 arc minute, and the surface flatness is specified to be of $\lambda/20$ at $\lambda = 633\,$nm.

very cold atomic sample trapped in the box potential that we reset to its full power at the end of the experimental sequence (*i.e.* at the end the evaporation ramp).

6.3.3. Experimental results and reason for the choice

We show in Fig. 6.6**(a)** the intensity distribution measured on the side imaging setup for a disk–shaped mask of radius $R_{\text{mask}} = 40\,\mu\text{m}$ [15]. A thorough analysis of this type of images leads to the conclusions described in the following.

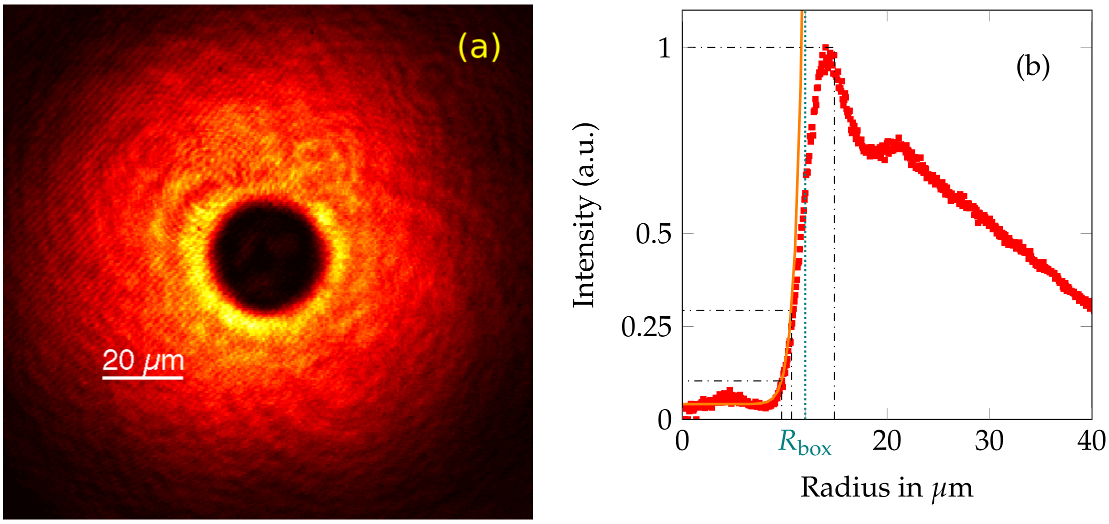

Figure 6.6.: **(a)** Intensity distribution created by a disk shaped dark spot of radius $R_{\text{mask}} = 40\,\mu\text{m}$ in the atomic plane. The magnification of the side imaging setup is calibrated along lines detailed in footnote 15 **(b)** Radial average of the intensity distribution (red points), along with a fit of the central region using the fitting function from Eq. 6.4 (orange line). The fit is performed for $r \leq R_{\text{barrier}}$ (see Eq. 6.7), and the fitted power is $\beta = 15$.

6.3.3.1. Potential Barrier and Radius of the box-trap

The maximum in the intensity profile of Fig. 6.6**(a)** is denoted I_{Max}. As the trap is not perfectly symmetric [16], there exist paths from the center to the edges along which the intensity always remains below I_{Max}. Then, the trap barrier I_{barrier} corresponds to the

---

[15] In this scheme, we do not know precisely the magnification of our side imaging setup. Nevertheless, we precisely know the expected size of the box–trap created from the size of the mask imaged and the magnification of main setup $R_{\text{box}} = \mathcal{M} R_{\text{mask}}$. We thus calibrate the side magnification $\mathcal{M}_{side}$ by an analysis of the imaged intensity profile similar to Fig. 6.6**(a)**. More precisely, we compute the transmitted fraction of the initial beam $T = P_{\text{trunc}}/P_{\text{inc}}$ that is the ratio of the power in the imaged truncated profile P_{trunc} to the incident power P_{inc}. We estimate T from a Gaussian fit on the wing of the beam (outside of the dark spot). By matching T to the expected value of the transmission $T_{\text{exp}} = exp(-\frac{2R_{\text{box}}^2}{w^2})$ (for a disk-shaped mask), we deduce an effective pixel size of $0.38\,\mu\text{m}$ on the side imaging camera and a magnification factor $\mathcal{M}_{side} = 16$.

[16] We note that such a dissymmetry of the barrier could come from a misalignment of the center of the mask compared to the center of the beam. We indeed fitted a displacement of the center of the Gaussian beam compared to the center of the trapping region of $\sim 2\,\mu\text{m}$ along both horizontal axis in Fig. 6.6

smallest intensity barrier encountered along these paths. For shown intensity profile, we find $I_{\text{barrier}} \sim 0.6\ I_{\text{Max}}$ and the barrier potential is located at $R_{\text{barrier}} = 14.9\,\mu\text{m}$ of the trap center. The mean intensity in the central dark region of this distribution is $I_{\text{bottom}} = 0.056\ I_{\text{barrier}}$. We then define the trapping region as the central domain whose edges are characterized by an intensity equals to $I_{\text{min}} = I_{\text{bottom}} + (I_{\text{barrier}} - I_{\text{bottom}})/20$, its radius is typically of $9.7\,\mu\text{m}$.

6.3.3.2. Uniformity of the trap bottom

We are here interested in the potential variations in the central trapping region defined in the intensity profile by the edge intensity I_{min}. In this experimental image obtained with a disk–shaped mask of radius $R_{\text{mask}} = 40\,\mu\text{m}$, we notice the appearance of three bumps in the intensity profile with a $\sim 120\,^\circ$ rotation symmetry that are also revealed in the radial average of the beam. We show in Fig. 6.7**(a)**, a zoom of the intensity profile on the center with a rescaling of the intensity to enhance the defects of the distribution. In this central region, we measure a maximal defect of 12% of I_{barrier} whereas the standard deviation of the potential in this central region is only 3% of I_{barrier}. This is a drastic improvement compared to the phase plate realization (see 6.2.3) since Eq. 6.2 is now fulfilled in terms of standard deviation and and the maximal defects are strongly reduced.

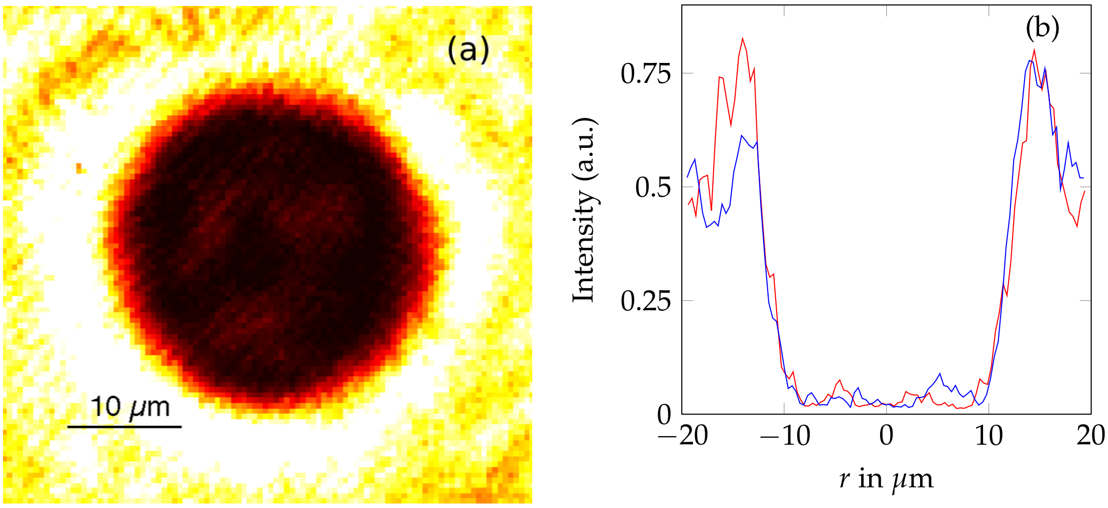

Figure 6.7.: **(a)** Intensity distribution created by the dark spot. The intensity has been rescaled to reveal the features in the center of the beam. **(b)** Two cuts of the intensity distribution shown in **(a)**.

6.3.3.3. Steepness of the edges of the box-trap:

We are now interested in the variations of the intensity up to the intermediate value I_{max}. We compute:

— The stiffness $\eta = 1.18 \pm 0.28\,\mu\text{m}$.

— The power–law fit exponent (Eq. 6.4) $\beta = 15 \pm 1.6$.

We note that this steepness is greatly improved compared to the phase plate realization (see 6.2.3) and complies with the given specifications.

6.3.3.4. Various shapes of the potential

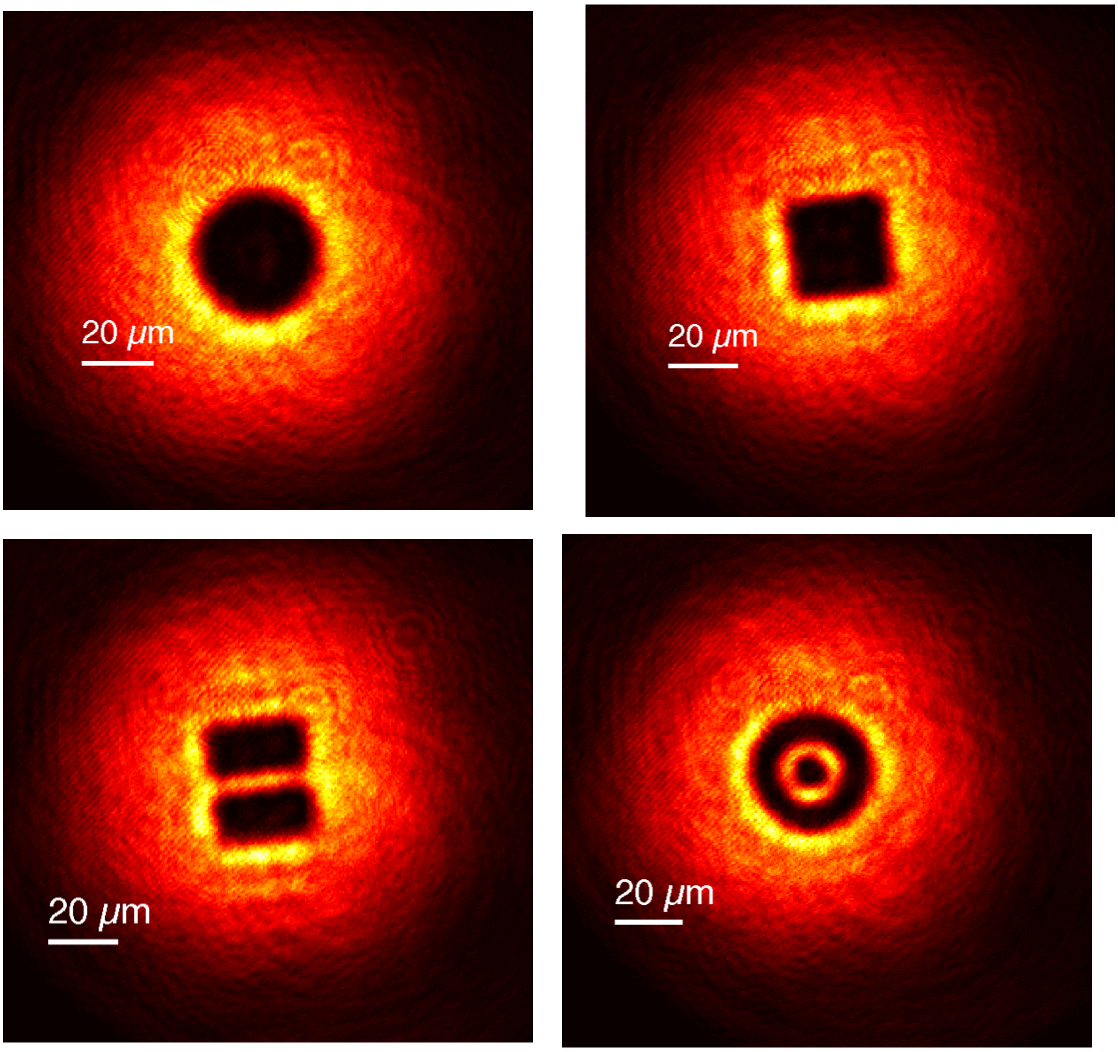

Figure 6.8.: Example of the possible changes in shape or in size of the box-trap. We show the intensity profile for: a disk (upper left) of larger radius than previously ($R_{\text{box}} = 15\,\mu\text{m}$ instead of $R_{\text{box}} = 12\,\mu\text{m}$), a square (upper right), two rectangles (we can also produce a unique rectangle of the same size – lower left), a target that is made of a central disk circled by an annulus (lower right).

We can versatilely change the shape of our box-trap potential by changing the mask placed on the path of the beam. Examples of the different intensity profiles realized are given in Fig. 6.8. As the characteristic lengths and symmetries of the diffraction pattern generated vary with this shape, the resulting trap attributes are also modified. Such modifications are particularly stringent for mask shapes like the set of two rectangles or the target where both the trapping region and the separation between the disconnected traps show shorter characteristic length scales. This results in:

- A smother variation of the trap edges with r. For both the target (central disk and annulus) and the two rectangles (small axis) presented in Fig. 6.8, we fit power law of $\beta \sim 4$. We note that this decrease of the power law coefficient only occurs along direction presenting small characteristic lengths. For the rectangles for example, we fit $\beta \sim 10$ along their long axis.
- A lower intensity barrier at the edge of these traps (*i.e.* the minimum of the intensity barrier over the straight paths going from the center to the outer regions of the traps) compared to a disk geometry of similar area. According to the pattern, this can be due either to the non–respect of the initial beam symmetry (for the square and the rectangles for example) or to the small characteristic length of traps separation (for the twin–rectangles and the target). In this latter case, the intensity separation between the trap is affected by the finite steepness of the intensity variations when imaging the traps separation.
- An increasing importance in the trap bottom bumps due to both the relative lowering of the energy barrier to which we have to compare the defects and the shortening of the characteristic lengths of the mask. This shortened length translates into an increase of the characteristic length in the diffraction pattern appearing within the imaging telescope. Thus, the effect of the finite aperture of the imaging system is strengthened as described in Annex G.

In these potentials, we manage to trap two–dimensional atomic samples and to investigate their parameters space by evaporatively cool them in the box-trap (see 2.1.3 for details on the experimental procedure). We will present in the remaining part of this manuscript the results we obtain with this setup. I show in Fig. 6.9 examples of in-situ atomic density distributions obtained at the end of the experimental sequence and for various shapes of the box-trap mask.

6.4. Conclusion

In this chapter, I presented the experimental techniques we use to produce radial trapping potentials that can be considered as uniform over the whole atomic sample. They are created by shaping a far–blue–detuned laser beam showing a hollow center at the position of the atoms. I quantitatively described the specifications on the intensity profile characteristics imposed by the atomic configurations we want to study. These specifications bear on:

- The absolute value of the intensity maximum found at the edges of the hollow center that should be used for the loading of the trap.
- The smallness ($\lesssim 5\%$) of the variations of the intensity inside the hollow center compared to the edge barrier intensity.
- The spatial extent ($\lesssim$ few μm) and the intensity spatial dependency (power law coefficient $\gtrsim 5$) at the edges of the hollow center.

We selected a shaping technique based on a simple dark mask imaging at the atoms position, which complies with these specifications. The most restrictive point is the rugosity of the trap center. We achieved a rms value of $\sim 3\%$ of U_{barrier}. One way to improve further the setup is to increase the aperture of the mask imaging setup. We

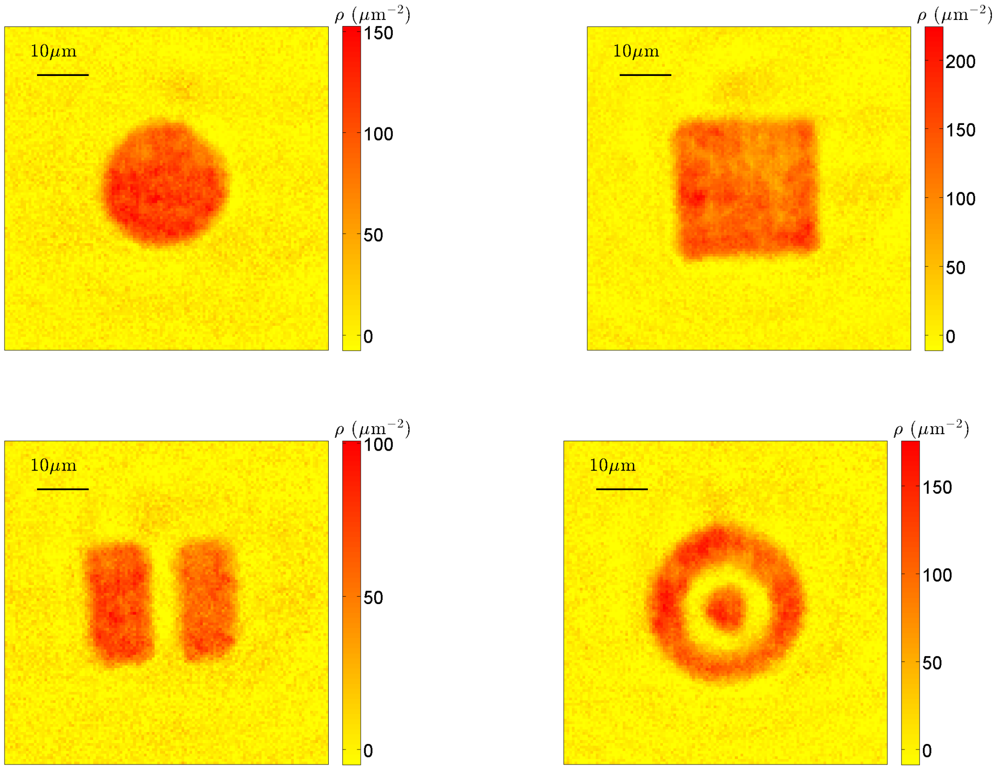

Figure 6.9.: Examples of atomic density distributions measured after evaporation toward the degenerate regime in the box-trap. In these four examples, we vary the shape of the mask. We used respectively a disk of radius $R_{\text{mask}} = 40\,\mu\text{m}$; a square of size $L_{\text{mask}} = 80\,\mu\text{m}$; two rectangle of widths $L_{\text{mask}} = 80\,\mu\text{m}$ and $l_{\text{mask}} = 40\,\mu\text{m}$ spaced by $d_{\text{mask}} = 15\,\mu\text{m}$ along their small axis; a target of inner, intermediate and outer radii $R_{\text{mask}} = 15,\ 30,\ 50\,\mu\text{m}$ respectively.

can think of using optical elements with a larger numerical aperture like for example replacing the imaging doublet by a microscope objective. An other source of improvement relies on the possibility of a dynamical control of the shape of the mask. Such an improvement can be made using a set of computer–controlled movable micro–mirrors instead of a static deposit on a glass plate. Preliminary tests of this type of devices have been performed by Master student David Perconte.

7. Coherence of the Uniform 2D Bose gas

In this chapter, we present our experimental investigation of the apparition of a coherent behavior in 2D uniform gases while varying the cloud atom number N and temperature T. In a first part, we describe how we measure these cloud parameters and in particular how we perform thermometry. In this challenging 2D uniform geometry, temperature is determined by an original method based on an empirical description of the loading of the 2D traps and of the final evaporative cooling realized via ramping the box-potential height. Then, we demonstrate emergence of coherence in this gas along with changes in the loading conditions or the evaporation ramp end point. First we measure the appearance of bimodality in the velocity distribution by a Time-of-Flight (ToF) technique. Second, we develop a matter-wave interference technique between two quasi-identical and coplanar clouds from which we characterize coherence via a description of the fringe patterns observed after an in-plane expansion.

7.1. Thermometry of 2D uniform Bose gases

Determining the temperature T and the chemical potential μ of a degenerate uniform 2D Bose gas reveals being highly challenging tasks. For example, compared to previous measurements performed in 2D harmonic traps (see Chapters 4 and 5), we cannot benefit here from any specific spatial dependency of in-situ density distribution as the density is uniform over the sample for any cloud parameters (see Fig. 6.9 for examples of in-situ distributions).

It is then necessary to use Time-of-Flight (ToF) measurements of the atomic density distribution (see 2.1.3 for technical details). In such a measurement, we let the cloud expands freely by releasing all the trapping potentials, then the initial momentum distribution is converted into the density distribution and can be characterized. However, performing a fit of this ToF density distribution enabling determination of T and μ or even the condensed fraction Π_0 happens to be excessively involved. Usual methods for such a characterization used, for example, for 3D harmonically-trapped gases rely on a two-independent-components description of the gas. The thermal part is then commonly described by ideal Bose law [161, 162], assuming fugactity $z = 1$ when gas reaches condensed behavior, so that it is possible to determine the temperature T by a (single-parameter) fit of the outer part ("wings") of the ToF density distribution. The condensed fraction Π_0 is then deduced from the ratio of atom numbers integrated from each fitted component of the bimodal density distribution and the chemical potential μ is deduced from description of condensed distribution for example using Thomas Fermi approximation.Specificity of 2D uniform gases leads to divergence of Bose law prediction at limit $z \to 1$ (see Chapter 1) making the assumption $z = 1$ irrelevant. Moreover, fitting simultaneously z and T from wings shape of the density distribution reveals very unstable. We notice such a fit instability even for simulated ideal distribution. Both dependencies occurs to be too entangled by the fitting law to be effectively determined without any further inputs.

Finally, in our experimental setup, transverse excitations play a major role in the establishment of the physics under interest (see following and Chapter 1), complicating further the description of our experimental gases. Then the definition of a fitting function valid for every cloud configurations under study is extremely complicated as, in this case, neither purely 2D nor semi-classical 3D description are accurately depicting the relevant energy states and their populations.

To address these difficulties, we developed an original approach of the temperature establishment in our gases leading to the deduction of a general empirical model. Using fits of a partial data set along with this empirical model, we deduce temperature for all cloud configurations.

7.1.1. Measuring Velocity Distribution Variance

As introduced, to determine the temperature T of our 2D uniform gases, it is necessary to perform Time-of-Flight (ToF) expansion and image the resulting density distribution after a given duration τ. The imaged distribution gives access to characteristics of the initial velocity distribution. For example, the variance of initial velocity distribution Δv^2 can be deduced from the variance of the expanded spatial distribution Δx^2 by the simple relation

$$\Delta x^2 = \Delta x_0^2 + \Delta v^2 \tau^2 \tag{7.1}$$

where Δx_0 is the in-situ width of spatial distribution[1].

We perform ToF of duration ranging from 8 to 16 ms. We choose the specific duration for each mask shape considered so that the fitted size Δx after expansion is several times larger than the extent of initial spatial distribution Δx_0 for all non-purely-condensed situations[2]. Then we can deduce Δv from the knowledge of Δx and Δx_0 with small error.

We image the in-plane density distribution of the cloud using low intensity absorption imaging technique along vertical axis (see Chapter 3). We image all considered atomic configurations after the same Time-of-Flight duration τ. The upper limit for τ comes from reduction of signal to noise ratio in density measurements while imaging the hottest and sparsest cloud configurations with increasing Time-of-Flight duration. Examples of ToF density distributions are given in Fig. 7.1.

---

[1] The relation of Eq. 7.1 neglect influence of interaction between particles during the expansion.This is valid in our geometry due to the very fast expansion along the tightly confined direction of space (z). Then atomic density drops within very short time scale and the interaction term immediately becomes negligible compared to the kinetic one. We quantitatively checked the negligible effect of the interactions on the time-of-flight expansion for our experimental parameters by performing 3D Gross-Pitaevskii simulations (see B) which enables to simulate the evolution of either an interacting or a non-interacting gas at $T = 0$ after releasing all traps.

[2] Rigorous choice of this duration is explained in details in next section. It is based on the expected thermal width from Boltzmann prediction of any of the considered distributions. The width expected from thermal expansion is given by $\Delta x_{\text{Boltz}} = \sqrt{k_B T/m}\,\tau$. We impose that, for all considered T, Δx_{Boltz} to be at least twice Δx_0: $\Delta x_{\text{Boltz}} \geq 2\Delta x_0$

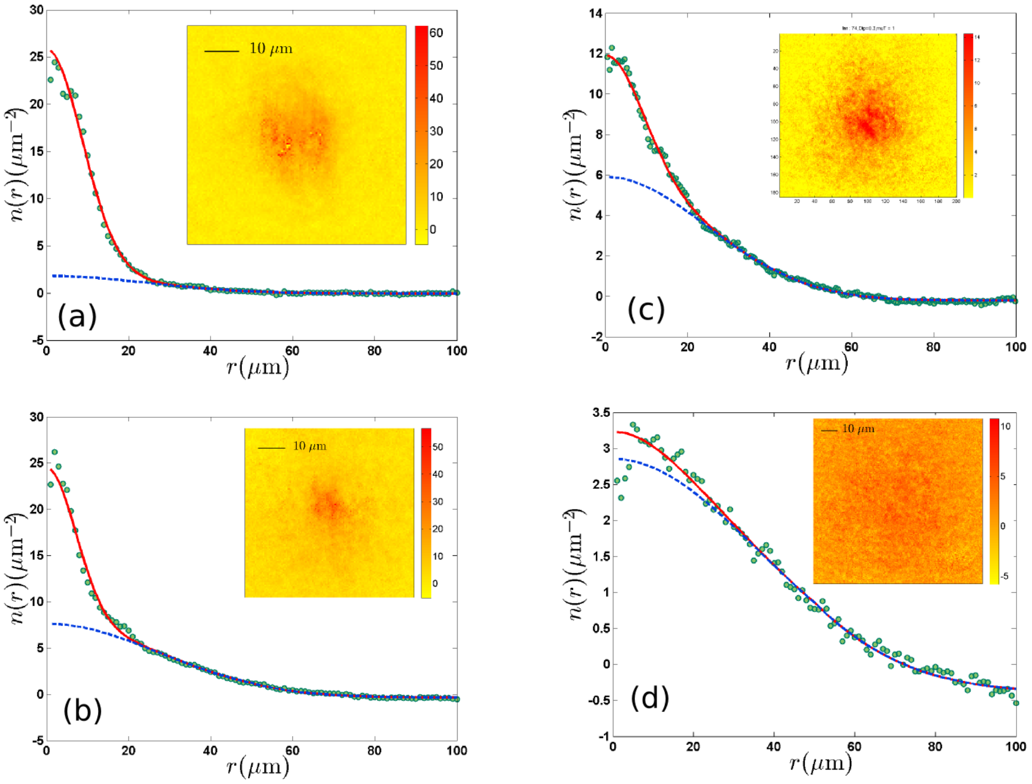

Figure 7.1.: Examples of density distribution after 12 ms of ToF from a cloud initially confined in a square of size $L = 24\mu$m after azimuthal average (blue dots) and corresponding average for the 2D double Gaussian fit performed (red solid line) and Gaussian of largest width of this fit (green dashed line). The four plots correspond to four different cloud configurations with varying end of 3D and 2D evaporation ramps. The respective couples of parameters (N, T) are **(a)**: $(19 \times 10^3, 27\text{ nK})$, **(b)**: $(38 \times 10^3, 145\text{ nK})$, **(c)**: $(27 \times 10^3, 91\text{ nK})$ and **(d)** : $(27 \times 10^3, 145\text{ nK})$. Insets: corresponding 2D density distribution.

We fit the ToF in-plane density distribution by a sum of two 2D Gaussian functions of same 2D center of coordinates (x_0, y_0), ellipticity[3] ϵ and orientation θ but different amplitudes A_1 and A_2 and sizes σ_1 and σ_2:

$$f(x,y) = A_1 \exp(-\frac{X^2+\epsilon^2 Y^2}{2\sigma_1^2}) + A_2 \exp(-\frac{X^2+\epsilon^2 Y^2}{2\sigma_2^2}) + B \quad (7.2)$$

$$X = (x - x_0)\cos\theta + (y - y_0)\sin\theta \quad (7.3)$$

$$Y = (y - y_0)\cos\theta - (x - x_0)\sin\theta \quad (7.4)$$

As illustrated in Fig. 7.1, this double-Gaussian-fit nicely takes into account the bimodality of the density distribution measured and so enables determination of both the atom number N and standard deviation of density distribution Δx with good accu-

---

[3] such an ellipticity enables to take into account effects of remaining anisotropy in the levitating fields and effects of initial trapping configuration and enables a better fit to experimental data. We checked that for a given configuration the orientation is not strongly varying and that ellipticity remains close to 1.

racy via

$$N = 2\pi\,(A_1\sigma_1^2 + A_2\sigma_2^2)/\epsilon \tag{7.5}$$

$$\Delta x^2 = (A_1\sigma_1^4 + A_2\sigma_2^4)/\epsilon(A_1\sigma_1^2 + A_2\sigma_2^2) \tag{7.6}$$

We then deduce Δv from the precise Time-of-Flight duration τ and the initial distribution width Δx_0. Δx_0 is estimated from a preliminary fit, performed once for each of the box-potential, as it is, in very good approximation, fixed by the shape of this box and independent of the atomic cloud configuration, in this uniform setup.

7.1.2. Estimate of temperature T for the less interacting clouds

From the measurement of Δv and N, we can infer values for the temperature T and the fugacity z of the gas by neglecting effects of interactions between atoms in the in-situ configuration and applying ideal Bose prediction (details on these calculations can be found in Annex A).

7.1.2.1. Self-consistent validation of the estimate

Such an estimate will be relevant only for gas configurations in which the interaction energy is negligible. We auto-coherently distinguish the "suited" configurations by computing a first order contribution of the interaction potential to the (single-particle) Hamiltonian by $gn(\mathbf{0})$, following lines developed in A.3 (g is the 3D interaction parameter and $n(\mathbf{0})$ the ideal estimate of the central 3D density of the cloud). We will consider as relevant the ideal law estimate for gases that self-consistently verify $gn(\mathbf{0}) \leq k_\mathrm{B} \times 4.5$nK as it corresponds in practice to $gn(\mathbf{0}) \lesssim \hbar\omega_z/4,\ k_\mathrm{B}T/10$ for all the considered situations (then within this condition the interaction energy contribution is negligible compared to the kinetic and potential energies). In this case, we assume that the eigenstates wavefunction spatial dependencies, energies and populations are negligibly modified compared to the ideal predictions and so the temperature T and the fugacity z are accurately assessed from an ideal interpolation from the known values of Δv and N.

7.1.2.2. Fit via Bose law computation

To perform ideal Bose law prediction for our gas configuration, we consider a full quantum 3D treatment of Bose statistics as described in Annex A. In this description, the eigenstates of the single-particle Hamiltonian are labelled by three integers $\boldsymbol{j} = (j_x, j_y, j_z)$ corresponding to the eigenenergy $E_{\boldsymbol{j}}$ (Eq. A.1). Their populations at thermal equilibrium in a gas of chemical potential μ (Grand canonical description) are given by Bose Einstein factor $f_{\boldsymbol{j}} \equiv f(E_{\boldsymbol{j}}, T, e^{\beta\mu}) = (\exp\left[(E_{\boldsymbol{j}} - \mu)/k_\mathrm{B}T\right] - 1)^{-1}$. Then, we obtain numerical estimates of N and Δv from the knowledge of the fugacity $z = e^{\beta\mu}$ and the temperature T via the formulae

$$N = \sum_j f(E_j, T, z) \tag{7.7}$$

$$\Delta v^2 = \left(\frac{\pi\hbar}{Lm}\right)^2 \sum_j \frac{j_x^2 + j_y^2}{2} f(E_j, T, z) \tag{7.8}$$

We numerically inverted this relation using grid values of N, Δv and T. Evaluation points are spaced by "logarithmic" [4] steps of 0.2 and typically vary from 10^3 to 10^5 for N, from 0.5mm/s to 8mm/s for Δv and from 10 nK to 1μK for T. We deduce an estimate of (z, T) for each experimental point $(N, \Delta v)$ using this pre-computed abacus.

7.1.3. Empirical model for temperature dependency

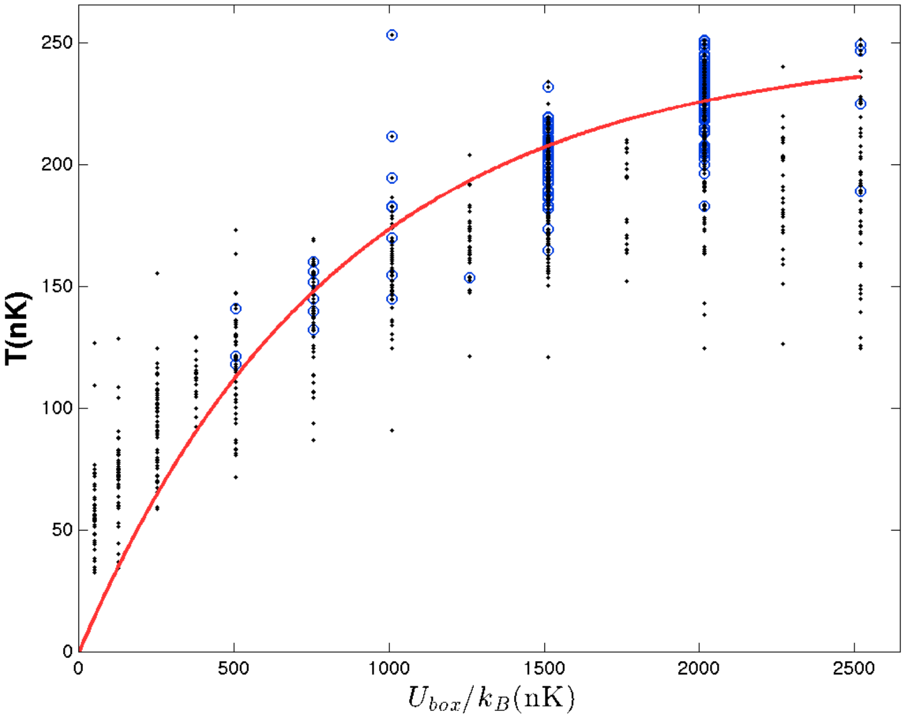

Figure 7.2.: Example of data sets (and fits) $T(U_{\text{box}})$ for a disk of radius $R = 12\,\mu$m at $\omega_z/2\pi = 365\,$Hz. For each density distribution imaged, we compute T from a ideal 3D full quantum Bose law treatment (black points). We only consider data point with $gn(\mathbf{0}) \lesssim k_B \times 4.5\,$nK (blue circled points). We fit the empirical model of Eq. 7.10 on these selected data points (red line).

We then look at the dependency of the estimated temperature T for a range of very

---

[4] For a quantity $\mathcal{Q}$ within N, Δv and T, the $(n+1)^{\text{th}}$ value is defined from n^{th} value used by $\mathcal{Q}(n+1) = (1+f)\mathcal{Q}(n)$ where f is called the "logarithmic step".

weakly interacting cloud configurations with the energy barrier height of the box-potential U_{box} as shown in Fig. 7.2. As T is set by the final ramp of U_{box} via evaporative cooling of the 2D uniform gas (see 2.1 for details), we expect an "evaporative" scaling between these two quantities. From the measured weakly-interacting configurations, we indeed notice an approximately constant T for a fixed value of U_{box} and for a given trapping configuration, that is a given transverse frequency $\omega_z/2\pi$ and given box size and shape. Standard deviations of T are typically of the order of 10% (see Fig. 7.2 and Fig. 7.4 **(a)**).

7.1.3.1. Justification of the temperature dependency at loading

We observe that this scaling relation extends for all the considered barrier height U_{box} even at the loading condition $U_{\mathrm{box}}^{\mathrm{load}}$. We do not see any effect of the 3D gas temperature that we load in the 2D traps on the resulting 2D gas temperature T_{load}. T_{load} is a constant for a given trapping configuration.

This independency on the 3D gas temperature is actually justified by the fact that the loaded gas is first evaporatively cooled in its volume by the 2D confining beam as we will evidence here. In this case, the loaded 2D configuration is only influenced by the initial 3D configuration in its atom number N_{load} and not in its temperature T_{load}. Such a primary cooling is explained by the limited 2D light-sheet potential height $V_{\mathrm{LS,0}}$ at the moment we load the 3D gas in it, that is when switching off the hybrid trap (see 2.1.3). In the following, we estimate $V_{\mathrm{LS,0}}$ at trap center using paraxial approximation calculations (see 2.2.1 and Fig. 2.3) and estimating the beam power P_{LS} at the corresponding moment of the experimental sequence.

In this chapter we present results for two different transverse confinement configurations of frequencies $\omega_z/2\pi = 365\,\mathrm{Hz}$ and $\omega_z/2\pi = 1460\,\mathrm{Hz}$. These two confinement configurations correspond to two different experimental sequences in terms of loading of the 2D traps. The value of $V_{\mathrm{LS,0}}$ is then estimated differently in both cases:

- **Configuration $\omega_z/2\pi = 1460\,\mathrm{Hz}$** matches to the optimal situation whose experimental sequence is detailed in Chapter 2. In this case, the hybrid trap is switched off while ramping the 2D power between P_{LS}^{load} (corresponding to transverse frequency $\omega_z^{\mathrm{load}}/2\pi = 330\,\mathrm{Hz}$ and $V_{\mathrm{LS,0}}^{\mathrm{load}} = k_{\mathrm{B}} \times 430\,\mathrm{nK}$) and P_{LS}^{clean} (corresponding to transverse frequency $\omega_z^{\mathrm{clean}}/2\pi = 1100\,\mathrm{Hz}$ and $V_{\mathrm{LS,0}}^{\mathrm{clean}} = k_{\mathrm{B}} \times 5.1\,\mu K$). It is then complex to precisely estimate the relevant height for 3D gas evaporation due to the time dependency introduced. As the ramp lasts 150 ms, the hybrid trap is switched off after 10ms and the relevant thermalization time is $\sim$ 10 ms, the relevant height must be $V_{\mathrm{LS,0}} \sim$ 1–2 μK.
- **Configuration $\omega_z/2\pi = 365\,\mathrm{Hz}$** is linked to a simpler situation and a thorough analysis can be performed. Indeed, to lower the trapping frequency, the maximal power P_{LS}^{f} is actually not changed but the atoms are simply put further away – at distance x_0 – from the focus of the Hermite-Gaussian beam. From this procedure, the loading of the gas is eased while the trapping frequency is decreased (as detailed in 2.2.2). The chosen distance is $x_0 = 840\,\mu\mathrm{m}$ instead of $190\,\mu\mathrm{m}$ in the optimal configuration. In this case, the loading of the 3D gas is directly performed at full power P_{LS}^{f} and the relevant barrier height is $V_{\mathrm{LS,0}} = k_{\mathrm{B}} \times 1.9\mu\mathrm{K}$.

As the maximal temperatures observed are $T_{\mathrm{load}} \sim 250$ nK, these values of $V_{\mathrm{LS},0}$ are compatible with a typical evaporation factor of order $\eta_{\mathrm{LS}} \equiv V_{\mathrm{LS},0}/T_{\mathrm{load}} \sim 8$.

We can push this investigation further by estimating the effective potential height $V_{\mathrm{LS},\mu T}$ taking into account the radial waist of the 2D beam $w_y = 50\,\mu$m and extent of the box-potential in-plane. We denote d_{max} the maximal in-plane distance from both the box and the light-sheet centers (that are assumed to be the same) explored by the atoms confined in this given box. For the different uniform trap shapes, we roughly observe that T_{load} scales inversely with d_{max}. We estimate the effective potential height seen by the atoms via

$$V_{\mathrm{LS},\mu T} = V_{\mathrm{LS},0} \exp(-2d_{\mathrm{max}}^2/w_y^2) \tag{7.9}$$

We find an approximately constant evaporation factor $\eta_{\mathrm{LS},\mu T} \equiv V_{\mathrm{LS},\mu T}/T_{\mathrm{load}} = 7.65$ for all trap configurations with fluctuation of 3.5% over the four investigated configurations at $\omega_z/2\pi = 365\,\mathrm{Hz}$ that are disk-shaped boxes of radius $R = 9\,\mu$m, $R = 12\,\mu$m and $R = 15\,\mu$m and a square-shaped box of size $L = 24\,\mu$m (see Fig. 7.3).

7.1.3.2. Choice of the empirical model

Starting from this "general" loading condition, we assume that the scaling of the temperature with the barrier height of the box-potential U_{box} observed for weakly interacting gases is in fact verified for all atomic configurations. Such an ubiquitous scaling is validated by the universality of evaporation mechanism involved while ramping the box-potential height $U_{\mathrm{box}} = U(t)$ at the end of the experimental sequence.

We want to characterize this dependency of T over U_{box} by a simple empirical model $T = f_{\mathrm{box},\omega_z}(U_{\mathrm{box}})$ representing the variation of the temperature along the evaporation ramp $U_{\mathrm{box}} = U(t)$ and simply depending on the shape and size of the uniform box and transverse trapping frequency $\omega_z/2\pi$ (via the loading condition), *i.e.* the overall 2D trapping configuration.

Due to the loading effect of the 2D-confining beam, evaporation factor $\eta = U_{\mathrm{box}}/k_{\mathrm{B}}T$ decreases along evaporation ramp. As the temperature evidently decreases to zero when $U_{\mathrm{box}} \to 0$, we find that the temperature can be empirically fitted by the simple dependency

$$T(U_{\mathrm{box}}) = T_0 \left(1 - e^{-U_{\mathrm{box}}/U_0}\right) \tag{7.10}$$

where T_0 and U_0 are the two fitting parameters, T_0 is the characteristic loading temperature, U_0 is a characteristic energy scale of the evaporation in the box. For $T \to 0$, the evaporation factor is simply given by $\eta_0 = U_0/k_{\mathrm{B}}T_0$. $\eta(U_{\mathrm{box}})$ typically varies from 11 to 4 for transverse frequency $\omega_z/2\pi = 365\,\mathrm{Hz}$ and from 14 to 4 for transverse frequency $\omega_z/2\pi = 1460\,\mathrm{Hz}$.

In Fig. 7.2, we give examples of an experimental data set (U_{box}, T) measured for a given trapping configuration and the related fit by Eq. 7.10. We summarize in Fig. 7.3, the various computed relations for a set of investigated uniform trap shapes and transverse confinements.

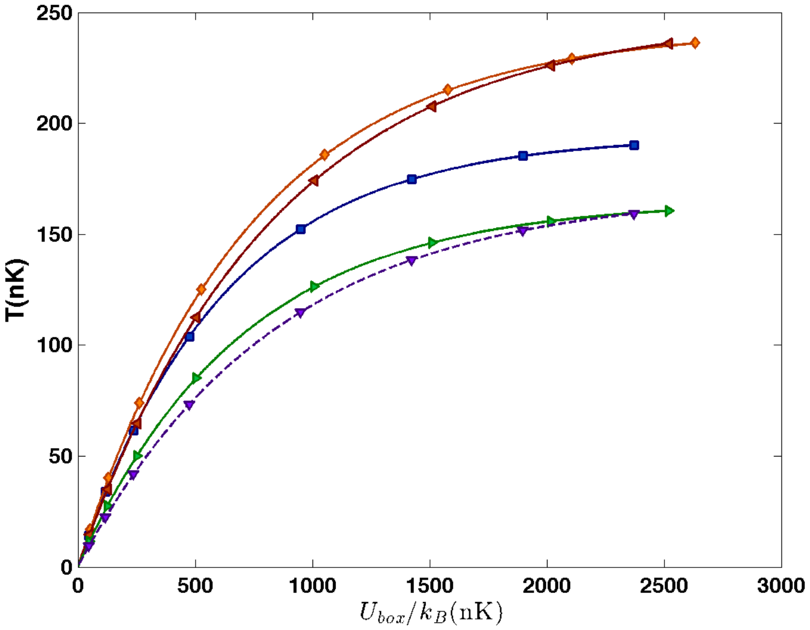

Figure 7.3.: Fitted relations (solid lines and points) $T(U_{\mathrm{box}})$ for various trap shapes and confinement: disks of radius $R = 9\,\mu$m (orange right triangles), $R = 12\,\mu$m (red squares) at frequency $\omega_z/2\pi = 365\,$Hz, square of size $L = 24\,\mu$m (blue left triangles) at same frequency and disk of radius $R = 12\,\mu$m at $\omega_z/2\pi = 1460\,$Hz (green circles). The dash line and corresponding points represent the approximated relation for square of size $L = 24\,\mu$m (purple circles) at $\omega_z/2\pi = 1460\,$Hz assuming a decoupling of the dependancies. The shown points correspond to the predicted T for the usual experimentally used values of the trap potential. The highest of them matches the loading configuration.

7.1.3.3. Generalization of the temperature relation

We may also deduce the relation $T = f_{\mathrm{box},\omega_z}(U_{\mathrm{box}})$ for any given trapping configuration bypassing the necessity of a direct measurement campaign of a data set (U_{box}, T) in this configuration.

To perform such a deduction, we assume that:

— T dependency in box shape can be fully embodied in a simple function of the previously introduced maximal extent d_{max} (see 7.1.3.1).

— T dependencies in d_{max} and ω_z are decoupled such that $T(U_{\mathrm{box}}; d_{\mathrm{max}}, \omega_z) = g(U_{\mathrm{box}}, \omega_z) \times h(U_{\mathrm{box}}, d_{\mathrm{max}})$.

Such assumptions are verified experimentally at the loading point as we studied that $T \propto \omega_z^2 \exp(-2d_{\mathrm{max}}^2/w_y^2)$. For further evaporatively cooled points, we note that evaporation dynamics only depends on this initial condition and on the box potential height U_{box}. In our setup where we use a box-potential beam of constant waist w_{box} (see 6.3.2), this height depends on the box shape and is clearly independent on ω_z, justifying the decoupling assumption for all U_{box}.

With these assumptions, we can compute the relation $T = f_{\mathrm{box},\omega_z}(U_{\mathrm{box}})$ for a couple

$(d_{\text{max}}, \omega_z)$ via a simple cross-multiplication of measured complementary relations[5]. We perform such a cross-multiplication to compute relation for a square box of size $L = 24\,\mu\text{m}$ at $\omega_z/2\pi = 1460\,\text{Hz}$ as represented in Fig. 7.3.

More precisely, we note that U_{box} is simply deduced from the central height of the box-potential beam $U_{\text{box},0}$ and from the maximal spatial extent of the box trapping region d_{max} via

$$U_{\text{box}} = U_{\text{box},0}\, e^{-2d_{\text{max}}^2/w_{\text{box}}^2} \tag{7.11}$$

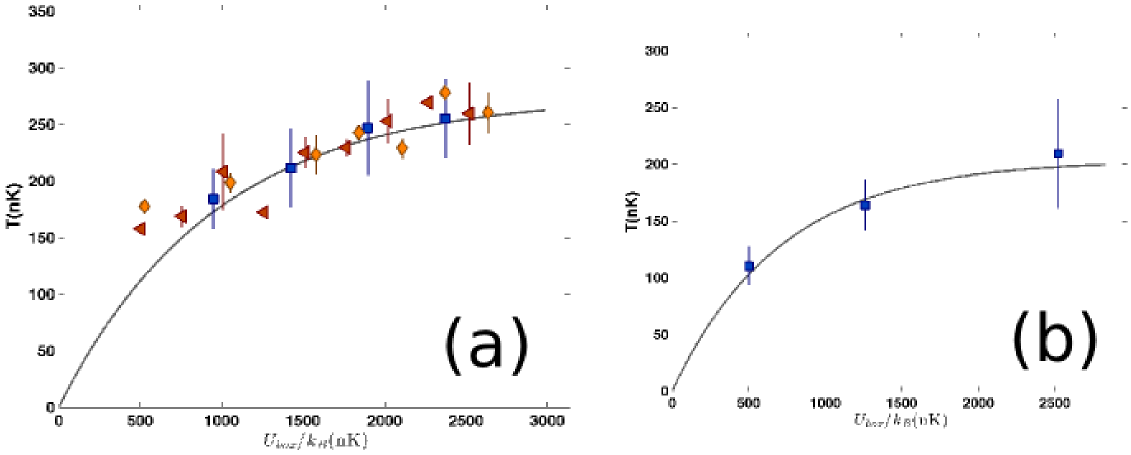

Figure 7.4.: Renormalized temperature $\mathcal{T}_0$ defined in Eq. 7.12. **(a)** Mean data points $T(U_{\text{box}})$ at $\omega_z/2\pi = 365\,\text{Hz}$ and for various trap shapes and confinement: disk of radius $R = 9\,\mu\text{m}$ (orange right triangles), $R = 12\,\mu\text{m}$ (red left triangles), square of size $L = 24\,\mu\text{m}$ (blue squares). Gray line shows global fit of these data points by Eq. 7.10. We find agreement with independency toward box shape. **(b)** Mean data points $T(U_{\text{box}})$ at $\omega_z/2\pi = 1460\,\text{Hz}$ for a disk of radius $R = 12\,\mu\text{m}$ (blue squares).Gray line shows global fit of these data points by Eq. 7.10. As we have less data at our disposal for this trapping configuration we impose $\eta_0 \equiv U_0/T_0$ at the value found for data at $\omega_z/2\pi = 365\,\text{Hz}$: $\eta_0 = 3.5$ as it dictates the temperature evolution at very low box potential and must so be independent from the loading condition.

In our specific experimental setup, we can in fact produce a more in-depth analysis by noticing that both the box-potential-beam and the 2D-beam have very similar radial waists $w_{\text{box}} = 48\,\mu\text{m}$ and $w_y = 50\,\mu\text{m}$. As the previously enhanced dependencies of T on d_{max} manifest via factors $e^{-2d_{\text{max}}^2/w_{\text{box}}^2}$ and $e^{-2d_{\text{max}}^2/w_y^2}$, we can approach T dependency at all points of the evaporation ramp by a unique multiplicative factor $e^{-2d_{\text{max}}^2/w^2}$ with $w \sim 50\,\mu\text{m}$. To check this dependency, we compute the estimated temperatures $\mathcal{T}$ at trap center by renormalizing the measured temperatures T by:

$$\mathcal{T}(U_{\text{box},0}, d_{\text{max}}, \omega_z) = T(U_{\text{box},0}, d_{\text{max}}, \omega_z)\, e^{2d_{\text{max}}^2/w^2}. \tag{7.12}$$

---

[5] for example from 3 complementary measurments performed at $(d'_{\text{max}}, \omega_z)$, $(d_{\text{max}}, \omega'_z)$ and $(d'_{\text{max}}, \omega'_z)$

We observe that the renormalized temperature $\mathcal{T}$ only depends on $U_{\mathrm{box},0}$ and ω_z (Fig. 7.4). Then the temperature dependency can be simply expressed as:

$$T(U_{\mathrm{box}}) = \mathcal{T}(U_{\mathrm{box},0}, \omega_z)\, e^{-2d_{\mathrm{max}}^2/w^2}\ ,\ w = 50\mu\mathrm{m} \tag{7.13}$$

$$\mathcal{T}(U_{\mathrm{box},0}, \omega_z) = \mathcal{T}_0(\omega_z)\left(1 - e^{-U_{\mathrm{box},0}/\mathcal{U}_0(\omega_z)}\right). \tag{7.14}$$

With these last relations, we can compute $T(U_{\mathrm{box}})$ for any box shape at these two frequencies. We fit the renormalized experimental data of $U_{\mathrm{box},0}$ (Eq. 7.11) and $\mathcal{T}$ (Eq. 7.12) by Eq. 7.14. As we have less data at our disposal at $\omega_z/2\pi = 1460\,\mathrm{Hz}$, we impose a fixed value for $\eta_0 \equiv \mathcal{U}_0/k_B\mathcal{T}_0$ that is the factor that governs the temperature evolution at very low U_{box}. Indeed, as only the loading condition is changed between the various confinement configurations, η_0 must be independent from ω_z. We then impose η_0 at the value resulting from the fit of the data at $\omega_z/2\pi = 365\,\mathrm{Hz}$, $\eta_0 = 3.50(25)$. Then the fit of the data at $\omega_z/2\pi = 1460\,\mathrm{Hz}$, only has one free parameter. We note that the result from this constrained fit lies within the error bar of a free fit for which we found $\eta_0 = 4.3 \pm 1.3$ and $\mathcal{T}_0 = 216(31)$ nK. The fitted coefficients are summarized in Table 7.1.

$\omega_z/2\pi$	$\mathcal{T}_0$	$\mathcal{U}_0/k_B$	η_0
365 Hz	275(8) nK	969(75) nK	3.49(25)
1460 Hz	203(18) nK	712[115] nK	3.50[25]

Table 7.1.: Summary of fitted parameters $\mathcal{T}_0, \mathcal{U}_0, \eta_0 = \mathcal{U}_0/k_B\mathcal{T}_0$ for fit of function $\mathcal{T}(U_{\mathrm{box},0}, \omega_z)$ defined in Eq. 7.13. Fitted function is given in Eq. 7.14. For $\omega_z/2\pi = 1460\,\mathrm{Hz}$, we impose value of η_0 to 3.5 that is the fitted value for $\omega_z/2\pi = 365\,\mathrm{Hz}$. The error bars in square brace on $\mathcal{U}_0$ and η_0 are obtained by taking the same error bar on η_0 than for $\omega_z/2\pi = 365\,\mathrm{Hz}$.

7.2. Emergence of Coherence seen in the momentum distribution

From the density distribution measured in ToF, whose examples are given in Fig. 7.1, we may further characterize the velocity distribution. Beyond the simple assessment of its variance Δv studied in the previous section, we will now describe in more details its shape. As we are interested in featuring the emergence of a phase coherence in 2D uniform gases, we are willing to describe a deviation of the population of low-energy states compared to Boltzmann prediction. These states are associated to the central part of the density distribution observed after a long Time-of-Flight expansion.

We quantitatively observed that, whereas for the hottest and least dense atomic configurations (Fig. 7.1 **(d)**) the distribution has a quasi-pure Gaussian-like shape, the distribution shows some bimodal features when performing further evaporative cooling (*i.e.* lowering the temperature: Fig. 7.1**(a)** and **(c)**) or loading a denser 3D cloud in our 2D traps (*i.e.* increasing the atom number: Fig. 7.1**(b)**). A sharp peak emerges at center of the ToF density distribution. This peak translates an "abnormal" (*i.e.* non-Boltzmanian) occupation of the low-momentum states. Such a feature in the ToF density distribution also features the occurrence of a conjugated bimodality in the g_1 correlation function as it is simply the Fourier transform of the momentum distribution of our uniform gas (see Eq. 1.19). This bimodality matches an increase of the g_1 characteristic decay length ℓ_c as the sharp peak observed in ToF is associated by conjugation to a broad component in the g_1 spatial distribution. It is then effectively a signature of an increasing phase coherence within the gas. In this section our aim is to characterize quantitatively the apparition of this coherent peak with a varying cloud configuration (N, T).

7.2.1. Estimating the population of the low excited states

To characterize the population of the low-energy states and quantitatively report for the observed bimodal momentum distribution, we use the same measurements of the density distribution of a single uniform cloud after a 3D ToF but now consider all accessible cloud configurations, whatever their interaction energy is. We use ToF of duration $\tau = 8$–16 ms according to the initial size of the cloud and use the same duration τ for all evaporation parameters considered. More quantitatively now, the value of τ is chosen for each trap shape considered so that it is long enough for the size expected from a thermal expansion $\Delta x_{\mathrm{Boltz}} = \tau\sqrt{k_B T/m}$ (Note that temperature used are $T \gtrsim 10$ nK) to be at least twice the initial standard deviation of the spatial distribution Δx_0: $\Delta x_{\mathrm{Boltz}} \geq 2\Delta x_0$.

We use the same double Gaussian fit as given in Eq. 7.3 but we now impose σ_2 to at least 1.75 time larger[6] than σ_1 to clearly associate the first Gaussian with a central peak of small extension compared to thermal wings fitted in the second Gaussian. We also impose that σ_1 varies in a limited range so that it is neither too small compared to the initial size of the cloud nor too large compared to the expected width $\Delta x_{\mathrm{Boltz}}$ from Boltzmann predictions. Typically we admit variations of ±50% around a mean value obtained from a first run of the fit over the whole set of data taken in a given trapping configuration.

We denote N_1 (resp. N_2) the number of atoms fitted in the sharpest (resp. broadest) Gaussian:

$$N_{1,2} \quad = \quad 2\pi A_{1,2}\, \sigma_{1,2}^2/\epsilon \tag{7.15}$$

and N, the total atom number given in Eq. 7.6, is simply $N = N_1 + N_2$. We characterize the importance of the central peak compared to the thermal wings by the ratio $\Delta = N_1/N$. This ratio gives an empirical characterization of the peakiness of the velocity distribution and so the deviation from the Boltzmann predictions of the population of the low-energy states. We note that this characterization does not enable to deduce the population of the overall ground-state $N_{(0,0,0)}$ which would be deduced from N by subtracting the population of all excited states N'. Due to Bose statistics, density distribution of all the excited states cannot be described by a Gaussian behavior and $N_2 \neq N'$. No further physical interpretation of the measured atoms numbers N_1 and N_2 is then permitted and Δ is not an estimation of the condensed fraction Π_0.

---

[6] we checked that the results are not strongly modified if we impose $\sigma_2 \geq 2.25\sigma_1$

7.2.2. Phase Diagram for Δ

7.2.2.1. Measurements

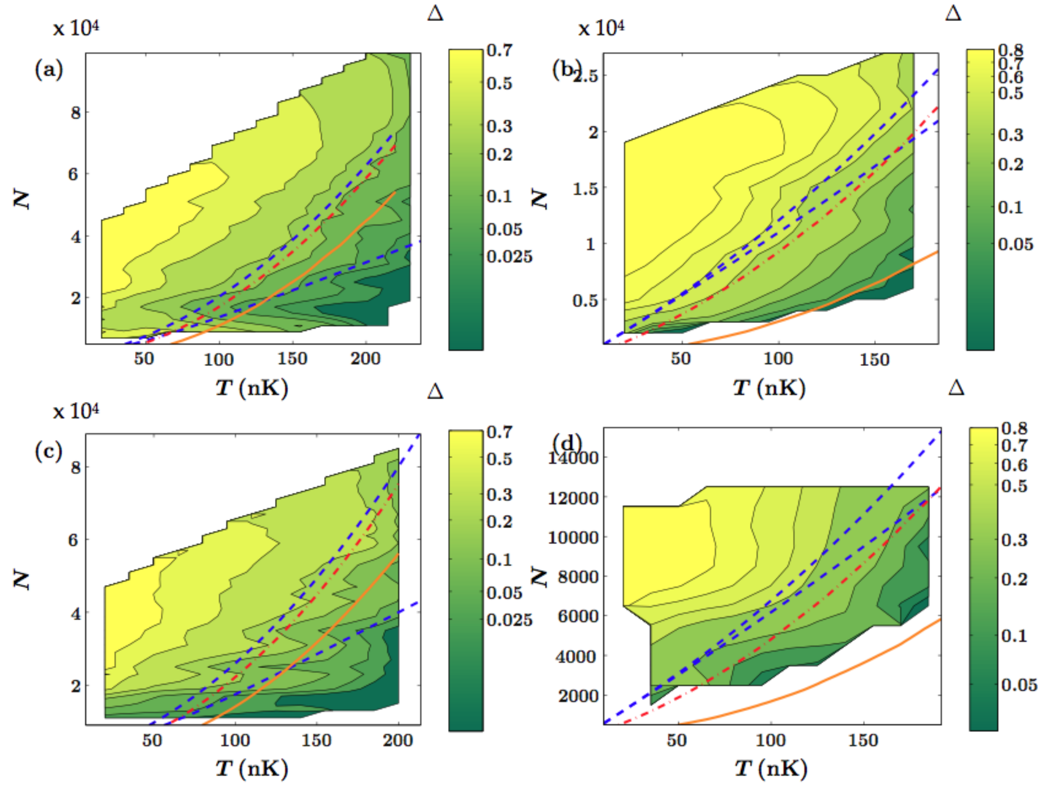

Figure 7.5.: Contour plot representation of the evolution of Δ with the cloud parameters (N, T) for an initial gas confined in **(a)** a disk of radius $R = 12\mu$m transversely confined in an harmonic trap of frequency $\omega_z/2\pi = 365$ Hz (colors are interpolated from a set of 517 images); **(b)** a disk of radius $R = 12\mu$m with $\omega_z/2\pi = 1460$ Hz (colors are interpolated from a set of 195 images); **(c)** a square of size $L = 24\mu$m with $\omega_z/2\pi = 365$ Hz (colors are interpolated from a set of 154 images); and **(d)** a disk of radius $R = 9\mu$m with $\omega_z/2\pi = 365$ Hz (colors are interpolated from a set of 123 images). The expected evolution of coherence is highlighted by predicted critical lines of $\mathrm{BEC}_\perp$ (solid orange line), $\mathrm{BEC}_{\mathrm{full}}$ (dash-dotted red line) phenomena and higher and lower bounds for BKT transition (dashed blue line).

We record Δ while varying the cloud parameters (N,T) by displacing the end points of the two evaporation ramps used in our experiment, that are (see 2.1 for details):

— the 3D (hybrid-trap) evaporation that changes the loaded 3D gas configuration,

— the 2D (box-trap) evaporation ramp that sets the final temperature.

For a given trapping configuration, we measure a large number of experimental density distributions corresponding to an also large number of cloud configurations. For each of them we compute the triplet of parameters (N, T, Δ). Typically T varies from 10 to

250 nK and N varies[7] from 10^3 to 10^5.

We repeat these measurements for different shapes and areas of the box potential and for different transverse confinement frequencies. Varying the shape and size of the box potential enables to test universality and robustness of the coherent behavior in a finite-size uniform 2D trap. Changing the transverse confinement frequency enables to test the emergence of 2D physics via transverse condensation (BEC$_\perp$) phenomenon (see 1.2.3 and following) and the resulting effect on the appearance of n extended coherence in-plane. Indeed, the two ranges spanned by ω_z and T allow us to explore both the frozen ($\zeta \ll 1$) and unfrozen ($\zeta \gg 1$) regimes for the z-motion, where $\zeta \equiv k_\mathrm{B}T/\hbar\omega_z$. We show the resulting phase diagram of variation of Δ in false colors in Fig. 7.5 for a set of four trapping configurations with:

- two distinct trapping frequencies $\omega_z/2\pi = 365\,\mathrm{Hz}$ and $\omega_z/2\pi = 1460\,\mathrm{Hz}$, differing by a factor 4.
- two different mask shapes: disk and square.
- a varied area of box-potential between $254\mu\mathrm{m}^2$ and $576\mu\mathrm{m}^2$ changing thus by a factor 2.3.

7.2.2.2. Comparing to theoretical predictions

We compare the evolution of Δ with N and T to theoretical expectations. Intuitively, we expect coherence to emerge close to the crossing of the thermodynamics transitions predicted to occur in the gas. In our case they are the Bose–Einstein Condensation (BEC) or Beresinskii–Kosterlitz–Thouless (BKT) transitions (see 1.1.3.1 and 1.1.4.4). We also note that due to the use of a small trapping frequency $\omega_z/2\pi = 365\,\mathrm{Hz}$, transverse excitations are not frozen for all considered cloud parameters. Then freezing of z-motion is reached through transverse condensation (BEC$_\perp$) and transverse excitations play a major role in establishment of a coherent behavior (see 1.2.3 and in particular 1.2.3.4). Thanks to BEC$_\perp$ mechanism, freezing of the z-motion is reached even if $k_B T > \hbar\omega_z$ ($\zeta > 1$). In a finite system, it leads to a two-step condensation by first reaching reduced dimensionality regime via transverse condensation and then condensing in this reduced dimensionality system (BEC$_\mathrm{full}$) to the overall 3D ground-state. In this section we describe the specific computations we performed to picture the expected transition lines for our specific experimental configuration.

Theoretical prediction for BEC transitions We compute the critical atom number for BEC phenomena using the full quantum 3D treatment of the ideal Bose law presented in Annex A (as in 7.1.2). In short, we consider a vertical harmonic confinement of frequency $\omega_z/2\pi$ and a perfectly uniform in-plane trap of square shape with size $L = \sqrt{\mathcal{A}}$ where $\mathcal{A}$ is the area of the experimental uniform trap. The eigenstates of the single-particle Hamiltonian are labelled by $\boldsymbol{j} = (j_x, j_y, j_z)$.

For each trapping configurations of interest, we consider a set of temperatures T and atom numbers N and compute the populations of the transverse $|j_z = 0\rangle$ and overall

---

[7] More precisely, N ranges from 10^4 to 10^5 for the weak z-confinement configuration $\omega_z/2\pi = 365\,\mathrm{Hz}$ and from 10^3 to 3×10^4 for the strong z-confinement configuration $\omega_z/2\pi = 1460\,\mathrm{Hz}$

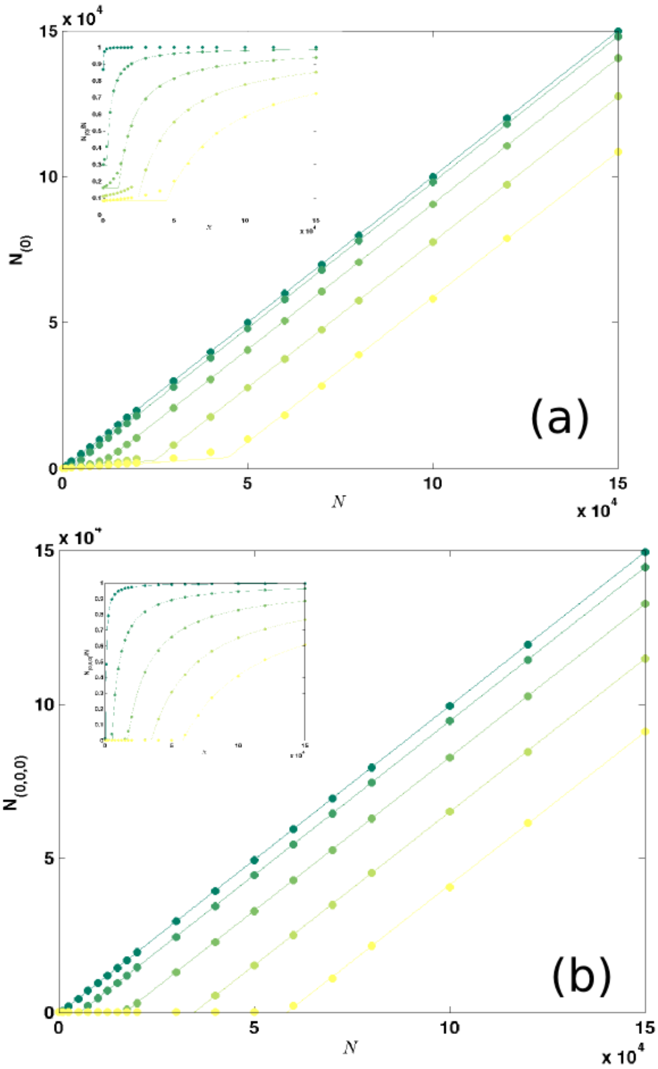

Figure 7.6.: **(a)** (resp. **(b)**). Fit performed on simulated populations of the **(a)** transverse (resp. **(b)** overall) ground-state for T =10 nK (dark green), 50nK, 100nK, 150 nK, 200nK. transverse trapping confinement is set to $\omega_z/2\pi = 365\,\text{Hz}$ and in-plane uniform trap is of square shape with the same area than a disk of $R = 12\,\mu\text{m}$. We compute $N_{(0)}$ (resp. $N_{(0,0,0)}$) for N ranging from 100 to 1.5×10^5 (circles). We fit (solid lines) the atom number in the respective ground-state to N by a linear increase from a threshold value that we identify with the critical atom numbers N_c for $\text{BEC}_\perp$ (resp. BEC_{full}). Insets: Same data and fits but representing the condensed fraction that is the ratio of the atom number in the ground-state to the overall atom number $N_{(0)}/N$ (resp. $N_{(0,0,0)}/N$). We note deviation of the transverse condensed fraction to the hyperbolic function with a smoother dependency observed.

ground-state $|0,0,0\rangle$ [8] of the system that we respectively denote $N_{(0)}$ and $N_{(0,0,0)}$ (see

---

[8] In Annex A (and in our calculations) we in fact consider Dirichlet boundary conditions such that $j_x, j_y \geq 1, j_z \geq 0$, then the overall ground-state $|0,0,0\rangle$ corresponds to $|j_x = 1, j_y = 1, j_z = 0\rangle$. We however decided to keep the more "comprehensive" notation $|0,0,0\rangle$ for the ground-state.

A.2.1). For a given temperature, we fit the differences between Bose and Boltzmann predictions for these populations by a linear threshold function toward the total atom number N as shown in Fig. 7.6. We identify the critical atom number for the transverse condensation $N_{(0)}^{\mathrm{BEC}}$ (respectively the overall condensation $N_{(0,0,0)}^{\mathrm{BEC}}$) to the value of the fit threshold parameter obtained when fitting the difference in $N_{(0)}$ (resp. $N_{(0,0,0)}$). Note that for $\zeta \lesssim 1$, the notion of transverse condition becomes insignificant as Boltzmann law directly predicts that a majority of atoms populates $|j_z = 0\rangle$.

Theoretical predictions for BKT transition To infer a prediction on the critical point of the BKT transition, we rely on the classical Monte Carlo calculation performed by Prokof'ev, Ruebenacker and Svistunov [125] in the weakly interacting limit and in the absence of transverse excitations (tight transverse confinement regime of $\zeta \ll 1$). In this regime, the authors infer a numerical prediction for critical 2D phase-space-density (PSD, denoted for the rest of this chapter $\mathcal{D}$):

$$\mathcal{D}_{\mathrm{c}} = \ln\left(\frac{380(3)}{\tilde{g}}\right) \tag{7.16}$$

where $\tilde{g}$ is the 2D reduced interaction parameter and the 2D PSD is defined by $\mathcal{D} \equiv n^{(2D)}\lambda_T^2$ with $n^{(2D)}$ being the atomic surface density $n^{(2D)} = \int \mathrm{d}z \; n^{(3D)}(z)$. In the weakly interacting and tight transverse confinement limit, the interaction parameter is simply given by $\tilde{g}^{(0)} = \sqrt{8\pi}a_s/\ell_z$ (where a_s is the 3D scattering length, $a_s = 5.1$ nm for ^{87}Rb , and ℓ_z is the vertical oscillator length $\ell_z = \sqrt{\hbar/m\omega_z}$) and the atomic surface density by $n^{(2D)} = N/\mathcal{A} = N_{(0)}/\mathcal{A}$ for our uniform setup.

As these calculations are only strictly valid for a pure 2D gas whereas in our experimental configuration transverse excitations play an important role, we cannot directly rely on their result. However, we can use it to deduce upper and lower bounds for the transition point implementing two different views on the values of the 2D PSD and of the reduced interaction parameter $\tilde{g}$ contributing to BKT physics in these transversely excited gases.

To obtain an upper bound to the critical atom number for BKT transition, we consider that only atoms in the transverse ground-state $|j_z = 0\rangle$ contribute to the 2D transition and so 2D PSD is obtained by taking $n^{(2D)} = N_{(0)}/\mathcal{A}$. In this case, we use a more refined estimate $\tilde{g}^{\mathrm{eff}}$ of the reduced interaction parameter, taking into account the non-zero contribution of the interaction between the z ground-state and the z excited states populations to mean interaction energy for the particles in $|j_z = 0\rangle$

$$\tilde{g}^{\mathrm{eff}} = \frac{m}{\hbar^2}\frac{\mathcal{A}\int d^3r \; \langle j_z = 0|\hat{V}_{\mathrm{int}}(\boldsymbol{r})|j_z = 0\rangle}{N_{(0)}^2} \geq \tilde{g}^{(0)} \tag{7.17}$$

where $\hat{V}_{\mathrm{int}}$ is the interaction potential operator given in Eq. A.10. We compute $\tilde{g}^{\mathrm{eff}}$ from the estimate of the density distribution in each transverse excited state obtained by solving the full quantum 3D treatment of the ideal Bose law (Annex A). This procedure gives a first order correction to $\tilde{g}$, depending on N and T, denoted $\tilde{g}^{\mathrm{eff}}(N, T)$. We then deduce the upper critical number for the BKT transition $N_{\mathrm{up}}^{\mathrm{BKT}}$ by recursively solving the implicit relation

$$N_{(0)}(N,T)\frac{\lambda_T^2}{\mathcal{A}} = \ln\left(\frac{380}{\tilde{g}^{\mathrm{eff}}(N,T)}\right) \tag{7.18}$$

To estimate a lower bound for the critical atom number for BKT transition, we consider the opposite approximation where all atoms contribute equally to the 2D transition so that the 2D PSD is given by taking $n^{(2D)} = N/\mathcal{A}$. In this case, the reduced interaction parameter is given by integrating the overall interaction term along z (Eq. A.12) and we denote it $\tilde{g}'$. It is then reduced compared to $\tilde{g}^{(0)}$ due to broadening of this density distribution compared to the ground-state width ℓ_z:

$$\tilde{g}' = 4\pi a_s \int dz\, n_{(1D)}^2(z) \;\leq\; \tilde{g}^{(0)} \tag{7.19}$$

where $n_{(1D)}(z)$ is the axial density distribution ($n_{(1D)}(z) = \int \mathrm{d}\boldsymbol{\rho}\, n^{(3D)}(\boldsymbol{\rho}, z) \sim \mathcal{A}n^{(3D)}(z)$). We compute $\tilde{g}'$ from the estimation of this axial density distribution by solving the same full quantum 3D treatment of the ideal Bose law. This procedure also gives a first order correction to $\tilde{g}$, depending on N and T, denoted $\tilde{g}'(N,T)$. We then deduce the lower critical number for BKT transition $N_{\mathrm{low}}^{\mathrm{BKT}}$ by recursively solving the second implicit relation

$$\frac{N}{\mathcal{A}}\lambda_T^2 = \ln\left(\frac{380}{\tilde{g}'(N,T)}\right) \tag{7.20}$$

In Fig. 7.5, we show the four resulting theoretical lines $N(T)$ that represent the expected evolution of coherence with cloud parameters. We note that variation of Δ quantitiavely follows the curvature of these lines.

7.2.3. Critical Atom Numbers for Δ

From the contour plot of Fig. 7.5, that summarizes the ensemble of our data, we note a typical variation of a sharp cross-over (or a phase transition), with essentially no bimodality ($\Delta \ll 1$) below a critical atom number $N_c(T)$ and a fast increase of Δ for $N > N_c(T)$. We fit the critical atom number N_c for the appearance of bimodality in velocity distributions by considering sets of data at fixed T (*i.e.* at fixed U_{box}).

We fit each resulting collection of $\Delta(N)$ by a threshold function of type:

$$f(N) = (1 - N_c/N)\Theta(N \geq N_c) \tag{7.21}$$

where Θ stands for the Heaviside function. This is the expected relation for the true condensed fraction $\Pi_0 = N_{(0,0,0)}/N$. As we do not rigorously measure Π_0, the fit by Eq. 7.21 reveals a practical yet empirical way to determine the point where Δ rises above zero. As we do not developed a rigorous insight on the behavior of Δ, we decided not to rely on the $N_c(T)$ fitted on data collections where no $\Delta \approx 0$ "plateau" were observed (*i.e.* all measured data shown some bimodal features). The limit was set to 4 experimental raw points with $\Delta < 0.1$. Examples of reliable fits are shown in Fig. 7.7 after binning of the raw data. We summarize the variations of N_c with T in Fig. 7.8. Reliable N_c are represented with plain dark green circles whereas the fitted N_c in absence of an observed zero plateau are represented by light green stars. In this case, we must considered that

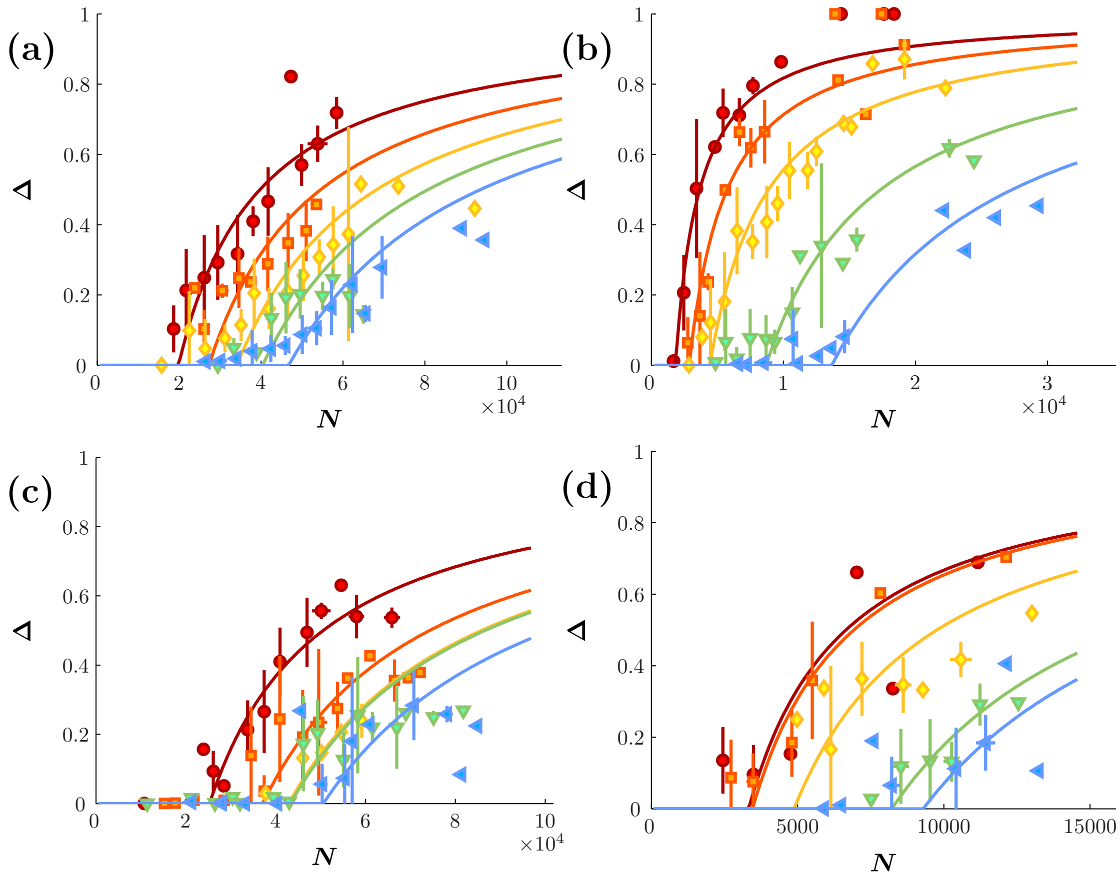

Figure 7.7.: Example of data sets (N, Δ) at fixed T and associated fits along Eq. 7.21 for **(a)** a disk of radius $R = 12\mu$m transversely confined in an harmonic trap of frequency $\omega_z/2\pi = 365$ Hz for 4 different $T = 170$ nK, 190 nK,222 nK and 228 nK; **(b)** a disk of radius $R = 12\mu$m with $\omega_z/2\pi = 1460$ Hz for 5 different $T = 33$ nK, 60 nK, 100 nK, 157 nK and 178 nK. **(c)** a square of size $L = 24\mu$m with $\omega_z/2\pi = 365$ Hz for 3 temperatures $T = 172$ nK, 185 nK and 209 nK **(d)** a disk of radius $R = 9\mu$m with $\omega_z/2\pi = 365$ Hz for 5 temperatures $T = 85$ nK, 104 nK, 164 nK, 183 nK and 173 nK. The represented data are binned in N and error bars represents standard deviation on the binned ranges (ranges width is 1000 atoms for data at $\omega_z/2\pi = 1460$ Hz and 4000 for $\omega_z/2\pi = 365$ Hz. Colors match the different temperatures; with increasing T, the color order is red, orange, yellow, green, cyan, light blue, dark blue, purple, magenta, salmon.

the critical atom number is comprised between 0 and the lowest measured number as indicated by the corresponding errors bars.

Clearly the bimodal behavior that we observe in our gases appears for atom numbers N_c lower than the critical values for both BEC_{full} and BKT transitions at fixed T. This reveals that Bose law significantly affects the population of the low-excited states and the resulting extent of the phase coherence prior to these transitions. In other world, this

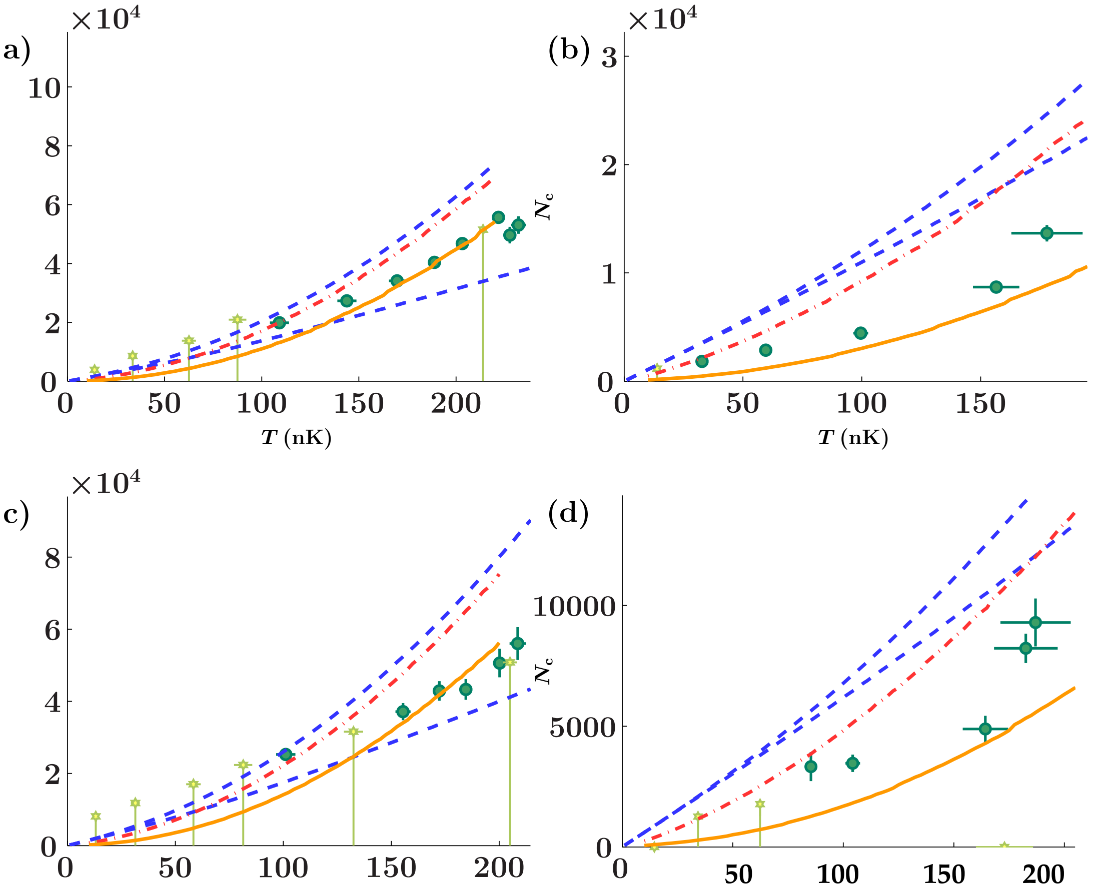

Figure 7.8.: Evolution of fitted critical number N_c for Δ with the temperature T for an initial gas confined in **(a)** a disk of radius $R = 12\mu$m transversely confined in an harmonic trap of frequency $\omega_z/2\pi = 365\,$Hz. **(b)** a disk of radius $R = 12\mu$m with $\omega_z/2\pi = 1460\,$Hz. **(c)** a square of size $L = 24\mu$m with $\omega_z/2\pi = 365\,$Hz. **(d)** a disk of radius $R = 9\mu$m with $\omega_z/2\pi = 365\,$Hz. The expected evolution of coherence is highlighted by the predicted critical lines of BEC$_\perp$ (solid light green line), BEC$_{\text{full}}$ (dash-dotted dark green line) phenomena and higher and lower bounds for BKT transition (dashed blue line). Dark green circles show reliable fits of $N_c(T)$ as exemplified in Fig. 7.7. Light green stars represent unreliable fitted values of N_c from data set presenting no zero plateau of Δ. In this latter case, error-bars represent the observation uncertainty from zero to the first atom number observed corresponding to non zero Δ.

modification implies an increase of the characteristic length ℓ_c for the decay of the g_1 such that it results significantly different from its thermal value $\lambda_T/\sqrt{\pi}$ (see Eq. 1.20). Moreover, we highlight that the coherence revealed from these ToF measurements always appears at similar (or higher) critical numbers than the ones needed for BEC$_\perp$ to occur. Thus, the measured coherence must be understood as a signature of 2D–ness of the gas. We will describe in more details the deviation and the matches of this experimental lines to theories in 7.4.

7.3. Matter-wave interferences

Matter-wave interference between independent atomic or molecular clouds is a powerful tool to monitor the emergence of extended coherence [24, 42, 49, 163, 164]. In our experimental setup, thanks to the versatility of the box-trapping configuration, we were able to implement and detect the fringes patterns resulting from interferences of two coplanar similar clouds. In this section I will present our procedure to make interfere two independent gases and characterize the coherence from the resulting fringes patterns. Such measurements nicely complement the one described in previous section and we will see in a last part that they both eventually fall in a common curve describing the evolution of coherence in our gas in terms of dimensionless parameters.

7.3.1. Detecting matter-wave interference

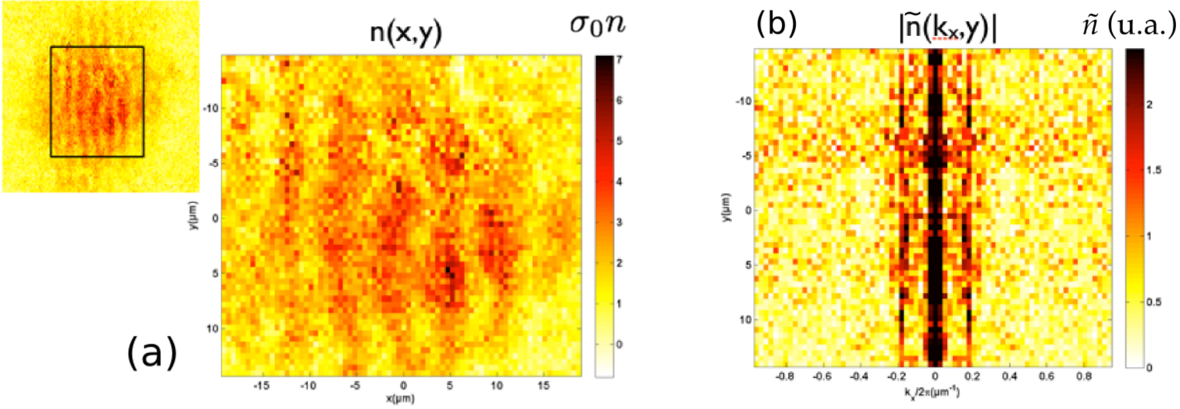

Figure 7.9.: **a**, Example of density distribution after a 16 ms in-plane expansion of two coplanar clouds. Insets: frame of the selected region for Fourier transform. **b**, 1D Fourier transform of each line y of the density distribution.

Using a mask shape showing a double site structure, we create two coplanar (*i.e.* positioned in the same vertical plane) rectangular 2D gases of same size (see Fig. 6.9 for example of in-situ density distribution) and initially spatially separated. In our setup the two rectangles are set parallel along their long axis y of extent $L = 24\,\mu$m. Along their short axis x, they extend over $l = L/2$ and are spaced by $d = 4.5\,\mu$m. Our setup is designed so that the long rectangle axis y is aligned with the vertical axis of our CCD camera frame.

To study matter-wave interference between the two clouds, we perform a 2D ToF (see 2.1.3 for details). It consists in abruptly switching off the box-potential while keeping the confinement along the z-direction. In this way, both gases expand in-plane. This point ensures that the atoms stay in focus with our imaging system, which allows us to observe interference fringes with a good resolution in the region where the two clouds overlap[9]. We observe that the two gases start to overlap for expansion times $\tau \gtrsim 4$ ms

---

[9] We note that in such a type of expansion the interactions between atoms may play a role. Indeed,

and then, in some configurations, we note the appearance of fringe patterns as shown in Fig. 7.9**(a)**.

We record the fringes patterns for longer expansion times $\tau \geq 10$ ms so that they are observed over the whole cloud and that the atomic density drops sufficiently to be able to use low intensity absorption imaging technique to observe these fringes in the density distribution [136]. This imaging technique is only partially quantitative in our 2D geometry. Nevertheless, we choose to use this incomplete imaging technique as it offers a larger signal to noise ratio compared to a fully-quantitative high intensity technique [137] and so ultimately a better diagnosis of the fringe patterns. Note that multiple scattering saturation effects may result in underestimating the fringe contrast for the densest clouds [10] and shortest expansion times used as the optical densities measured are as high as 2.

7.3.2. Characterizing fringes pattern

The observed fringe patterns are approximately rectilinear and parallel to the long rectangle axis (and so to the camera CCD frame vertical axis y) but commonly present some distortions. We analyze the fringes pattern line by line on a selected central region of the camera image (see Fig 7.9**(a)**). This line by line analysis enables a characterization of the fringe contrast that is not influenced by the importance of the distortions. The size of the region for performing the analysis is fixed for all cloud configurations at a given Time-of-Flight duration τ and is typically of 48 to 76 lines per 62 to 100 columns for τ varying from 10 to 20 ms.

We perform a fit of the density $n(x, y_l)$ on each line l of pixels by

$$n(x) = n_0 \left(e^{-x^2/(2\sigma_0^2)} + c e^{-x^2/(2\sigma^2)} \cos(k_0 x + \phi) \right) \tag{7.22}$$

where σ_0 is the Gaussian width of the overall cloud, σ is the Gaussian width of the interference domain, k_0 is the momentum component associated with the fringe spacing $\lambda = 2\pi/k_0$, ϕ is the fringe phase and c is the fringe contrast. We impose the interference region to be large enough $\sigma \geq 7\lambda$ but not necessarily equals to the total cloud size σ_0. We let k_0 fluctuate around its expected value by $\pm 25\%$ to 30% depending on τ to take into account distortion effects and other fluctuations in fringe patterns.

By Fourier transforming the density dependency $n(x)$ resulting from the fit to Eq. 7.22, we compute for each line l an estimate of the one dimensional Fourier transform $\tilde{n}[k_x, y_l]$ of $n(x, y_l)$. An example of $|\tilde{n}[k_x, y_l]|$ obtained by a direct Fourier transform from experimental distribution is given in Fig. 7.9**(b)**. Each line shows typically 3 characteristic

---

compared to the previous 3D expansion where the fast dynamics along z axis leads to a sudden drop of the atomic 3D density, here the density remains of the order its initial value and the same conclusion holds for the interaction energy. However, we note that for all points where we observe emergence of an extended phase coherence, interaction are in practice negligible in the in-situ configuration and hence play no role in the 2D expansion (see 7.4. A Bose law treatment described in Annex A self-consistentlypredicts $gn^{(3D)}(0) \lesssim k_B \times 10\,\text{nK} \lesssim \hbar\omega_z, k_B T$). Interactions may play a role at higher densities, thus when full coherence is already established. This may lead to a reduction in the fringe contrast in this case.

[10] We however expect that for the configurations where we measure emergence of an extended phase coherence, these multiple scattering effects to be negligible (similarly to the negligible effects of the interactions between particles).

peaks, one at zero momentum corresponding to the total cloud and two at opposite k_x of approximately constant value over the whole distribution. These auxiliary peaks correspond to the fringes pattern and arise at momentum $k_x = \pm k_0$. The phase of the complex value $\tilde{n}(k_0, y_l)$ is then equal to the phase of the fringes ϕ. The use of the result of the fit to Eq. 7.22 enables a more accurate estimate of the peak position k_0, phase ϕ and amplitude.

We consider the complex value of this hybrid density $\tilde{n}[k_x, y_l]$ at the momentum $k_x = k_0(y_l)$ and compute an equivalent of the one body correlation function:

$$\gamma(d) = \left| \langle \tilde{n}[k_0(y), y] \tilde{n}^*[k_0(y+d), y+d] \rangle_y \right| \tag{7.23}$$

where * denotes the complex conjugation. For two infinite rectangles of zero thickness and of identical initial one body correlation function $g_1(y) \equiv \langle \hat{\psi}(y) \hat{\psi}^\dagger(0) \rangle$ (where $\hat{\psi}(y)$ is the annihilation operator for a particle at position y), a simple integration gives $\gamma(d) = |g_1(d)|^2$ [165]. Here the non-zero extension of the rectangles along x and their finite initial size along y make it more difficult to provide an analytic relation between γ and the initial $g_1(\boldsymbol{r})$ of the gases. However $\gamma(d)$ remains a useful and quantitative tool to characterize the fringe pattern.

In an incoherent gas, $g_1(\boldsymbol{r})$ is expected to be a Gaussian of width $\lambda_T/\sqrt{2\pi}$. To study the coherence of the initial gas on a spatial scale larger than this thermal width, we study $\gamma(d)$ for $d \gtrsim \lambda_{\min}$ where $\lambda_{\min}$ is the thermal length λ_T for the lowest temperature observed (and is thus approximately four times larger than the largest width of $|g_1(\boldsymbol{r})|^2$). We also restrict ourselves to relatively small values of d due to distortions of the fringes over long distances (d must be short compared to L but still long compared to $\lambda_{\min}$). Typically $\lambda_{\min} \approx 2\,\mu$m (as minimal temperature investigated are as low as $\sim$ 10nK) and we consider the averaged value of $\gamma(d)$ for d varying between $\sim 2\,\mu$m and $\sim 6\,\mu$m. As a camera pixel corresponds to $0.52\,\mu$m on the atomic sample, we effectively consider the discrete average of $\gamma(d)$ for d varying from 4 to 10 pixels [11]:

$$\Gamma \equiv \langle \gamma(d) \rangle_{d \in [1,3]\lambda_{\min}} = \sum_{d=4\text{px}}^{10\text{px}} \gamma(d) \tag{7.24}$$

For the parameter Γ to take a value significantly different from 0, one needs a relatively large contrast on each line, and relatively straight fringes over the relevant distances d, so that the phases of the different complex contrasts $\tilde{n}[k_0(y), y]$ do not average out.

We note that the challenging point in this characterization lies in the quality performances of the fit to Eq. 7.22 for each line l. In this fit function six free parameters have to be determined whereas the single density lines may show important shot noise (from photonics noise inherent to absorption imaging technique) making each fit very sensitive to initial condition. We describe our effort for performing a good initialization of this fit in Annex H.

---

[11] We note that the results depend very weakly on the precise choice of this averaging range. In practice, we note that $\gamma(d)$ shows very similar behavior with (N, T) for $d \in [1, 40]$. Restricting the averaging range to $[4, 10]$ enables to increase signal to noise ratio.

7.3.3. Phase Diagram and critical atom number for Γ

7.3.3.1. Phase Diagram

As for the velocity distribution phase diagrams, we measure a large number of experimental fringe patterns corresponding to an also large number of cloud configurations (N, T). We deduce (N, T) for these fringes pattern configurations from Time-of-Flight measurements performed on a single square box of same total area that is with $L = 24\mu$m (as in Fig. 7.5) as similar densities [12] are observed in both cases after identical preparation sequence (*i.e.* same evaporation ramps) [13].

We compute the value of Γ from the measured interference patterns so that for each image we get a triplet (N, T, Γ). In Fig. 7.10, we plot Γ while varying the cloud parameters (N, T). We show results obtained for two trapping frequencies, $\omega_z/2\pi = 365\,$Hz and $\omega_z/2\pi = 1460\,$Hz. As for the equivalent plot for the bimodality parameter Δ shown in Fig. 7.5, no indication of coherence appears in the lower right corner ($\Gamma \sim 0$ for large T and small N), and Γ increases for larger N/lower T. For a given T, the variation of Γ with N shows the same threshold-type behavior as Δ.

7.3.3.2. Critical atom number for Γ

We then also estimate the critical atom numbers N_c for observing fringe patterns with a significant contrast by fitting the variation of Γ with N at fixed T by fitting:

$$f(N) = A_0(1 - N_c/N)\Theta(N \geq N_c) \tag{7.25}$$

where Θ stands for the Heaviside function. Note that here we do not assume a rise to unity of the fitting function contrarily to Eq. 7.21 as Γ may take arbitrary values. This implies the use of a second fitting parameter A_0 that might increase the error on the determination of the critical atom number in this case. The fitting parameter N_c reliably estimates the atom number N for which Γ rises above zero for all data collections where a significant $\Gamma \approx 0$ "plateau" is observed (*i.e.* clouds without fringes were observed). We summarize the variations of N_c with T in Fig. 7.11. Reliable N_c are represented with plain dark green circles whereas the fitted N_c in absence of an observed zero plateau are represented by light green stars. In this case, as for Δ, we must considered that the critical atom number is comprised between 0 and the lowest measured number as indicated by the errors bars. We note an overall very similar evolution of the fringes signal compared to the one extracted from the bimodality of the velocity distribution. We conclude that both Time-of-Flight characterization of velocity distributions and matter-wave interferences give a similar insight on the emergence of phase coherence in 2D uniform Bose gases.

---

[12] Each rectangle in this setup presents half the area of the square cloud studied but also half number of atoms so that the spatial density is equivalent to this square case.

[13] We then assume that the separation d has negligible influence on the setting of the cloud configuration (N, T) via evaporation ramps and that in particular the same law $T(U_{\text{box}})$ as the one deduced in 7.1 for the square of size $L = 24\,\mu$m applies. For each preparation sequence we deduce N from averaging ~ 5 ToF measurements

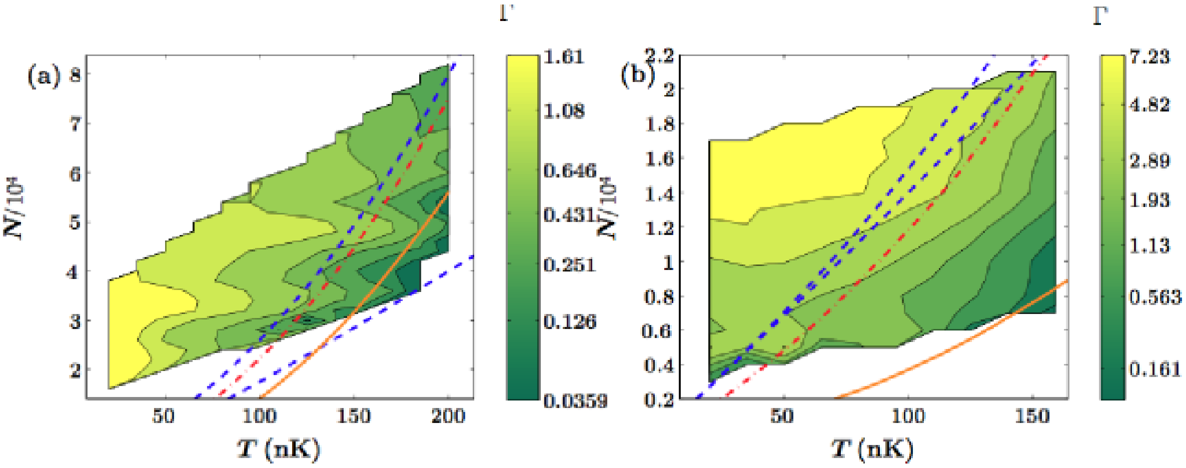

Figure 7.10.: Contour plot representation of the evolution of Γ with the clouds parameters (N, T), for two initially rectangular gases of sizes $L = 24\,\mu$m and $l = 12\,\mu$m, spaced by $d = 4.5\mu$m and transversely confined in an harmonic trap of frequency **(a)** $\omega_z/2\pi = 365\,$Hz **(b)** $\omega_z/2\pi = 1460\,$Hz. N is the total atom number of the two clouds and we checked by complementary in situ measurement that each cloud contains approximately $N/2$ atoms. T is obtained from empirical law $T(U_{\mathrm{box}})$ deduced in 7.1 for the square of size $L = 24\,\mu$m. To observed the fringes patterns, we performed 2D ToF of 16 ms (resp. 10 ms) for **(a)** (resp. **(b)**) Colors are interpolated from a set of 100 (resp. 140) images over which we consider in average 61 (resp. 48) lines. As in 7.5, we represent theoretical critical lines of $\mathrm{BEC}_\perp$ phenomenon (solid orange line), $\mathrm{BEC}_{\mathrm{full}}$ phenomenon (dash-dotted red line) and higher and lower bounds for BKT transition (dashed blue line). The theoretical lines are computed for a square of $L = 24\,\mu$m

7.4. Scaling Laws for emergence of Coherence

From the two experimental characterizations described above, we are now interested in highlighting universal features in the appearance of coherence in 2D uniform gases and, more precisely, while looking at various $\zeta \equiv k_{\mathrm{B}}T/\hbar\omega_z$. We have summarized in Fig. 7.12 the ensemble of our results for $N_{\mathrm{c}}(T)$ obtained in the two regimes $\zeta \gg 1$ (achieved for $\omega_z/2\pi = 365\,$Hz) and $\zeta \lesssim 1$ ($\omega_z/2\pi = 1460\,$Hz). It gives the variations of the critical phase-space-density $\mathcal{D}_{\mathrm{c}} = N_{\mathrm{c}}\lambda_{\mathrm{T}}^2/\mathcal{A}$ for the emergence of both bimodality as described in 7.2 (full symbols) and fringe patterns as described in 7.3 (open symbols) as a function of ζ. The results lie on a universal curve, independent of the shape and size of the gas: $\mathcal{D}_{\mathrm{c}}$ is approximately constant for $\zeta \lesssim 1$, whereas it increases linearly with ζ when $\zeta \gg 1$. This is in line with our understanding of the transverse condensation $\mathrm{BEC}_\perp$ phenomenon.

In the regime of a strong confinement in the z-direction, $\zeta \lesssim 1$, Bose and Boltzmann statistics do not lead to dramatically different descriptions of the z degree of freedom. Both indicate that a majority of atoms occupy the ground-state $|j_z = 0\rangle$, independently of the surface density. Then, from the theoretical description of ideal 2D gases (see 1.1.3), one expects that the coherence length in the xy-plane increase sufficiently to

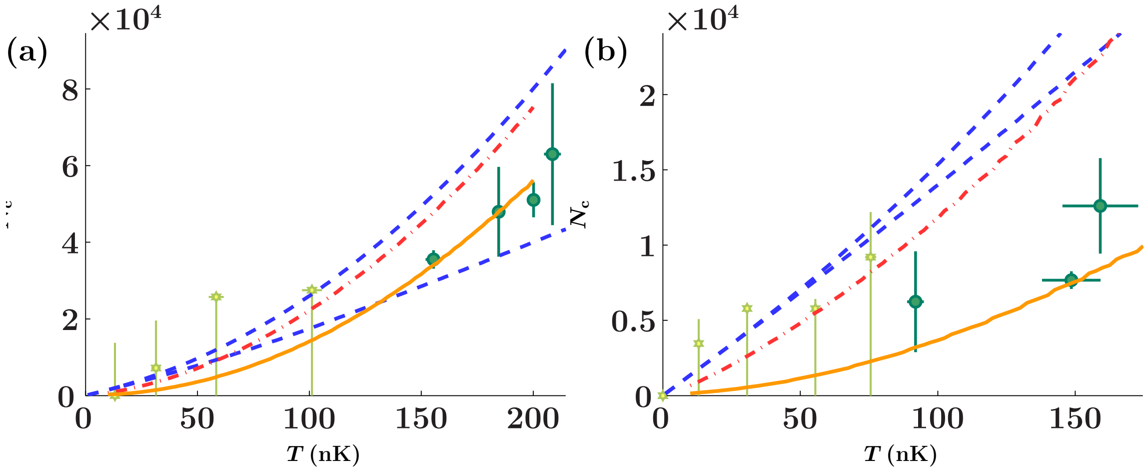

Figure 7.11.: Fitted critical atoms numbers N_c from Eq. 7.25, for the fringes contrast parameter Γ shown in 7.10. Transverse confinement is varied: **(a)** $\omega_z/2\pi = 365\,\text{Hz}$ **(b)** $\omega_z/2\pi = 1460\,\text{Hz}$. N is the total atom number of the two clouds. T is obtained from empirical law $T(U_{\text{box}})$ deduced in 7.1 for the square of size $L = 24\,\mu\text{m}$ We represent theoretical critical lines of BEC$_\perp$ phenomenon (solid orange line), BEC$_{\text{full}}$ phenomenon (dash-dotted red line) and higher and lower bounds for BKT transition (dashed blue line).The theoretical lines are computed for a square of $L = 24\,\mu\text{m}$

lead to a bimodal velocity distribution and to interference patterns when the 2D phase-space-density $\mathcal{D} \equiv n\lambda_T^2$ (where n stands here for the surface density $n^{(2D)}$) significantly exceeds 1. More precisely, as detailed in 1.1.3.1 (Eqs. 1.17–1.22) in the case $\mathcal{D} \gtrsim 1$, $g_1(r)$ acquires a bimodal structure: in addition to its incoherent Gaussian structure of $1/e$–width $\lambda_T/\sqrt{\pi}$, a broader feature $\propto \exp(-r/\ell)$ develops, with the characteristic length given in Eq. 1.22 and reminded here:

$$\ell = \frac{\lambda_T}{\sqrt{4\pi}} \exp(\mathcal{D}/2). \tag{7.26}$$

The fast (exponential) increase of ℓ with $\mathcal{D}$, which is specific to 2D physics, entails that the phase coherence is strongly enhanced, with a factor larger than 4 between the widths at $1/e$ of the Gaussian and the Lorentzian components, as soon as $\mathcal{D} \geq 4$. Then we expect coherence to arise at a constant value of $\mathcal{D}$:

$$\mathcal{D} = \mathcal{D}_{\text{c,2D}} \gtrsim 1 \tag{7.27}$$

In the weaker confinement regime in the z-direction, $\zeta \gtrsim 1$, BEC$_\perp$ phenomenon becomes relevant and leads to discrepancies between Bose and Boltzmann descriptions. As thoroughly described in 1.2, Bose statistics implies that the 2D phase-space-density that can be accumulated in the excited states of the z-motion $\mathcal{D}' = \mathcal{D} - \mathcal{D}_0$ is bounded $\mathcal{D}' \leq \mathcal{D}'_{\text{max}}$ (see 1.2.3.1). When $\mathcal{D}'$ reaches this bound, every additional atom must accu-

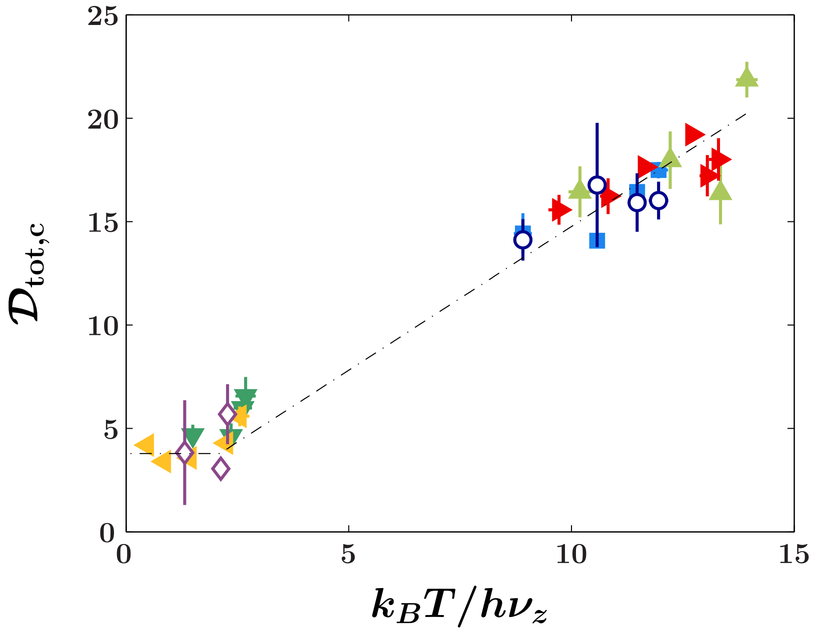

Figure 7.12.: Scaling law for the emergence of coherence in a quasi2D Bose gas. Variation of the critical phase-space-density $\mathcal{D}_{\mathrm{tot,c}}$ for observing a bimodal distribution (full symbols) and distinct matter-wave interferences (open symbols), as a function of the dimensionless parameter $\zeta = k_\mathrm{B}T/(h\nu_z)$. This plot summarizes data obtained for various confinement shapes and sizes, as well as two different trapping frequencies, $\nu_z = 365\,\mathrm{Hz}$: disk $R = 12\,\mu\mathrm{m}$ (red left triangles), disk $R = 9\,\mu\mathrm{m}$ (light green up triangle), square $L = 24\,\mu\mathrm{m}$ (blue square), $\nu_z = 1460\,\mathrm{Hz}$: disk $R = 12\,\mu\mathrm{m}$ (yellow right triangles), disk $R = 9\,\mu\mathrm{m}$ (green down triangles). Interferences are also observed at the same two frequencies : $\nu_z = 365\,\mathrm{Hz}$ (dark blue open circles) and $\nu_z = 1460\,\mathrm{Hz}$ (violet open diamonds). Black dash-dotted line shows a fit to the overall data set of a linear increase of $\mathcal{D}_{\mathrm{tot,c}}$ with a threshold at low ζ. We obtain a plateau at $\mathcal{D}_{\mathrm{tot,c}} = 3.8(7)$ for $\zeta \leq 2.1(8)$, which gives from Eq. 7.26 a correlation length $\ell = 1.9(7)\lambda_T$. The linear increase show a ramp of 1.39(9) close to the semi-classical expectation of $\pi^2/6$. We note for ideal Bose law computations (see methods), that ℓ/λ_T is approximately constant over the transition line and equals to 1.6(2).

mulate in the ground-state $|j_z = 0\rangle$ of the z-motion, which is associated to the PSD $\mathcal{D}_0$ and then the total PSD is $\mathcal{D} = \mathcal{D}'_{\mathrm{max}} + \mathcal{D}_0$. In the case $\zeta \gg 1$, a semi-classical treatment leads to:

$$\mathcal{D}'_{\mathrm{max}} = \frac{\pi^2}{6}\zeta. \tag{7.28}$$

In this case, BEC$_\perp$ occurs when $\mathcal{D}_0$ is not properly accounted by the semi-classical approximation which leads to $\mathcal{D}_{\mathrm{c}} \sim \mathcal{D}'_{\mathrm{max}}$ and $\mathcal{D}_0\,[\sim \ln(\zeta)] \gtrsim 1$ (see 1.2.3.2, Eq. 1.50). Then, it appears from Eq. 7.26 that a bimodal structure arises in g_1 and the coherence length in the xy-plane becomes large compared to its thermal value $\ell_{\mathrm{c}}^{(th)} = \lambda_{\mathrm{T}}/\sqrt{\pi}$ (see 1.2.3.4 for more details). In the regime $\zeta \gg 1$, the appearance of a large coherence length in the xy-plane and the occurrence of transverse condensation for the z degree of freedom are thus linked. Then, the expected threshold line for emergence of coherence on $\mathcal{D}$ must show some increase with ζ. From Eq. 7.28, in the regime where $\zeta \gg 1$, we expect an approximately linear [14] increase of the critical PSD with a slope of $\frac{\pi^2}{6}$:

$$\mathcal{D} \approx \frac{\pi^2}{6}\zeta + \mathcal{D}_{\mathrm{c},3D} \tag{7.29}$$

We fit the overall data set of $\mathcal{D}_{\mathrm{c}}$ by a linear increase with a threshold at low ζ:

$$\mathcal{D}_{\mathrm{c}} = \mathcal{D}_{\mathrm{c},0} + \alpha(\zeta - \zeta_0)\,\Theta(\zeta \geq \zeta_0) \tag{7.30}$$

We obtain a plateau at $\mathcal{D}_{\mathrm{c},0} = 3.8\,(7)$ for $\zeta \leq \zeta_0 = 2.1\,(8)$. We note that the $\mathcal{D}_{\mathrm{c}}$ for emergence of coherence is much lower (approximately half of it) than the expected value for the BEC/BKT transitions. This is due to the fast growth of the correlation length with $\mathcal{D}$ of Eq. 7.26 and it thus matches the above theoretical description of the tight confining regime. The linear increase for $\zeta \geq \zeta_0$ presents a slope of $1.4\,(1)$ compatible with the semi-classical expectation of $\pi^2/6$. Note that the error bars given here do not take into account uncertainties on N and T determinations.

Using ideal Bose law computations described in Annex A, we can compute the spatial dependency of the one-body correlation function $g_1(\boldsymbol{r})$ for all couples (N_{c}, T) appearing in Fig. 7.12. We estimate the width ℓ_{c} at $1/e$ of g_1 in the xy-plane and we found it that it is approximately constant over the transition line $\ell_{\mathrm{c}} = 1.6(7)\ell_{\mathrm{c}}^{(th)}$.

From this ideal description, we have also calculated for all couples (N_{c}, T) the maximal interaction energy per particle $E_{\mathrm{int}}^{\mathrm{max}} = (4\pi\hbar^2 a_s/m)n^{(3\mathrm{D})}(\mathbf{0})$. For all points we find that $E_{\mathrm{int}}^{\mathrm{max}} \lesssim k_{\mathrm{B}} \times 10\,\mathrm{nK}$ is smaller than both $\hbar\omega_z$ and $k_{\mathrm{B}}T$, justifying *a posteriori* the ideal gas approximation. The emergence of bimodality is therefore driven by single-particle physics and not by interactions, contrarily to the superfluid transition expected for larger phase-space densities (BKT physics). The regime corresponding to the transition threshold in Fig. 7.12 is similar to the quasi-condensate/pre-superfluid state observed in [102, 103] for ^{87}Rb atoms in a 2D harmonic potential. In that case, the analysis is complicated by the fact that the BEC$_\perp$ phenomenon is position-dependent,

---

[14] More precisely, from our theoretical development in 1.2.3, we expect BEC$_\perp$ to occur at $\mathcal{D}_{\mathrm{c}} = \mathcal{D}'_{\mathrm{max}} + \mathcal{D}_{0,\mathrm{c}}$ with $\mathcal{D}'_{\mathrm{max}} = \frac{\pi^2}{6}\zeta$ and $\mathcal{D}_{0,\mathrm{c}} \approx \ln(\zeta) + 0.9$ (Eqs. 1.47–1.50), leading to a logarithmic correction to the linear dependency.

as evidenced by Quantum Monte Carlo calculations [166]. The advantage of our homogeneous setup is that extended coherence emerges simultaneously over the whole sample, and is thus easier to discriminate from interaction effects expected for larger spatial densities.

7.5. Conclusion

In this chapter, we presented our results on the steady state behavior of 2D uniform Bose gases.

Firstly, we presented an original thermometry of our 2D uniform gases based on an empirical description of the trap loading and evaporative cooling phenomena. From an experimental investigation of temperature from Bose law calculations performed on a partial data set (considering only cloud with negligible interaction energy contribution) we deduced a general relation between the temperature T and the box-potential height U_{box}. This relation depends on the transverse trapping configuration – more precisely on the potential height V_{LS} when we load the 3D gas into the 2D traps – and on the box-potential shape – more precisely on the maximally explored distance from the trap center d_{max}. The final relation reads

$$\begin{aligned} T(U_{\mathrm{box}}; V_{\mathrm{LS}}, d_{\mathrm{max}}) &= \mathcal{T}(U_{\mathrm{box}}\, e^{\frac{2d_{\mathrm{max}}^2}{w^2}}; V_{\mathrm{LS}})\, e^{-\frac{2d_{\mathrm{max}}^2}{w^2}} && (7.31) \\ \mathcal{T}(U; V_{\mathrm{LS}}) &= \mathcal{T}_0(V_{\mathrm{LS}}) \left(1 - e^{-\frac{U}{\eta k_{\mathrm{B}} \mathcal{T}_0(V_{\mathrm{LS}})}}\right), \; w = 50\mu\mathrm{m}. && (7.32) \end{aligned}$$

We computed the characteristic loading temperature $\mathcal{T}_0$ for our two reference trapping configurations and the global factor η as summarized in Table 7.1.

Secondly, we presented two sets of measurements characterizing the emergence of a coherent behavior in our 2D uniform gases while varying the cloud atom number N and temperature T. We characterize this phase coherence in two complementary ways:

1. We highlighted an abnormal population of the in-plane low-momentum states by characterizing the bimodality of the density distribution measured after a Time-of-Flight expansion.
2. We outlined the wave-like behavior of 2D uniform gases by characterizing the interference generated when making two identical but initially separated gases overlap.

Finally, we highlighted a universal variation of the critical phase-space-density for the emergence of an extended coherence as a function of $\zeta \equiv k_{\mathrm{B}}T/\hbar\omega_z$, which characterize the strength of the transverse confinement compared to the temperature. For the tight confining regime, $\zeta \lesssim 1$, we show that coherence appears in a 2D uniform gas at a constant phase-space-density $\mathcal{D}_{\mathrm{c},0} \sim 4$ that is smaller that the expected critical PSD for BEC and BKT transitions $\mathcal{D}_{\mathrm{c,BKT}} \sim \mathcal{D}_{\mathrm{c,BEC}} \sim 8$. Such a deviation reveals the rapid increase of the correlation length ℓ_{c} as soon as $\mathcal{D} \gtrsim 1$ in the 2D geometry and corresponds to the quasi-condensation or pre-superfluid regime [102, 103, 125]. For weaker transverse confinements $\zeta \gg 1$, we highlight a linear variation of $\mathcal{D}_{\mathrm{c}}$ with ζ which matches the description of the transverse condensation phenomenon $\mathrm{BEC}_{\perp}$ [129].

In these measurements, the coherence is considered as an equilibrium property of the gas. In our experiment, it is in fact established via a forced evaporative cooling over a finite ramp time. The finite duration of the evaporation ramp also implies interesting dynamical features of the coherence establishment that we will study in next chapter.

8. Kibble–Zurek mechanism at the dimensional crossover

Dynamics at the crossing of a thermodynamic transition is a widespread topic of investigation in physics, from the study of the early universe to nanoscopic laboratory experiments.

Generally speaking, when approaching a transition point, both the thermalization time τ and the correlation length ξ diverge. First the divergence of ξ leads to the emergence of a universal behavior close to the transition point: as ξ grows to infinity, microscopic details of the system under interest become irrelevant. Behavior of the system is then dictated by the universality class[1] of the transition that is crossed. The universality of this behavior is embodied in thermodynamic critical exponents characterizing the steady–state power-law dependencies of interesting physical quantities close to the transition point with respect to the distance to this point (in terms of a given control parameter). If the transition is crossed via a finite ramp of a control parameter, however, ξ would never reach its predicted infinite value. Indeed, as the thermalization time τ also diverges, there will be a time $\hat{t}$ before the transition occurs for which thermalization is no longer possible and ξ will be *frozen out* at $\hat{t}$ before the transition. Such a *freezing out* leads to the formation of independent domains of characteristic size $\hat{\xi}$ in each of which a choice of the order parameter value is made. These domains will merge after the transition is crossed[2] leading to the formation of robust topological defects at their boundaries that subsist within the globally coherent system. The size of the independent domains and the density of defects are intimately linked to the equilibrium description of the considered transition and may serve to identify the class of universality at which it belongs.

This ubiquitous mechanism was first put forward by Kibble [88] concerning cosmological systems and extended by Zurek [89] to condensed matter field. Kibble and Zurek description enable a quantitative prediction of the scaling of both the size of the independent domains and the consequent density of defects. Signatures of Kibble–Zurek physics and quantitative scaling properties have been studied in a variety of experimental systems such as liquid crystals [167], helium [168, 169], ion chains [170, 171], superconducting loops [172] and cold atom gases [91, 93–95].

In this chapter, I present a quantitative analysis of KZ mechanism for our specific uniform quasi-2D setup. Thanks to the uniformity of our gas, we get closer to the original prediction from Kibble and Zurek than previous experiments realized on cold

---

[1] Universality classes constitutes a categorization of phase transitions coming from the application of the Renormalization Group (RG). Phase transitions belonging to the same universality class are equivalent under the renormalization transformations around the critical point. They have the same relevant observables (*i.e.* the ones that grow under the renormalization transformations) and only differ by irrelevant observables (the ones that decay under the renormalization transformations). Then they have the same values of their critical exponents.

[2] in fact, the merging should occur also at a time $\hat{t}$ after the transition point. By symmetry, the freezing-out holds for a duration $\hat{t}$ in each side of the transition.

gases [91, 93]. In these cases, inherent non-homogeneities imply a dominant role of the causality principle [173], which in particular leads to a strong reduction of the number of topological defects and a major change in the scaling properties. Indeed, whereas, in presence of inhomogeneities, the transition occurs successively in the different regions of the gas, in the uniform case, coherence is established simultaneously over the whole cloud matching the previously described independent choice of order parameter per *frozen out* domains. Then a different and interesting regime can be achieved with our uniform configuration.

In a first part, I will present an overview of Kibble–Zurek predictions emphasizing on the specificity of uniform systems versus inhomogeneous ones and presenting some particularities of the applicability of KZ predictions to our experiments. Then I will present two experimental configurations in which we observed topological defects formation when quenching a gas successively through $\mathrm{BEC}_\perp$ and $\mathrm{BEC}_{\mathrm{full}}$/BKT transitions (see Chs. 1 and 7). We studied the lifetime, the probability of occurrences and the mean numbers of these defects and the scalings of the latter properties as a function of the quench time for both configurations, which we compare to KZ predictions:

- We observe nucleation of vortices in 2D uniform, simply connected gases. In this case, the vortices are revealed by expanding cores density holes after short 3D Time–of–Flight. In this case, we can in particular study the spatial distribution and the correlations of the vortices.
- We observe nucleation of persistent currents in an annular gas. In this case, the vortex phase windings are revealed by matter-wave interference with a central disk of atoms that serves as a phase reference. We are in this case able to characterize the sign and the charge of the corresponding vortices.

8.1. Kibble–Zurek Mechanism

8.1.1. General description of the mechanism

As introduced, Kibble–Zurek mechanism states than when approaching a transition point via a finite ramp of duration τ_Q of a control parameter T, independent coherent patches are formed prior to the transition crossing. Topological defects are nucleated when these patches merge into a unique coherent system, after the transition has occurred. Both scaling of the size of the independent patches $\hat{\xi}$ and of the number of the topological defects N_v or N_w as a function of the quench duration τ_Q are dictated by the divergences of both the correlation length ξ and the thermalization time τ at the transition. These divergences are typically[3] featured at equilibrium – or by extension in the adiabatic regime– by universal critical exponents ν and νz respectively:

---

[3] Note that for transitions of infinite order (as BKT), a quench would not lead to a power-law scaling of ξ and τ. It was nevertheless shown that Kibble–Zurek mechanism keeps applying then, leading to more a complicated scaling that was the object of recent theoretical analysis [174, 175].

$$\xi(\epsilon) = \frac{\xi_0}{|\epsilon|^{\nu}} \tag{8.1}$$

$$\tau(\epsilon) = \frac{\tau_0}{|\epsilon|^{\nu z}} \tag{8.2}$$

where ϵ is the distance to the transition point in terms of the control parameter T (T_c standing for its value at the transition):

$$\epsilon = \frac{T_c - T}{T_c}. \tag{8.3}$$

Values of critical exponents ν and z depend on the universality class of the transition considered.

If we perform a ramp of ϵ in a time τ_Q from $\epsilon(t = 0) > 0$ to $\epsilon(t = \tau_Q) \leq 0$, then as we approach the transition time t^* such as $\epsilon(t = t^*) = 0$, the thermalization time $\tau(t)[\equiv \tau(\epsilon(t))]$ diverges. As long as $\tau(t)$ stays small compared to the time before the transition crossing $|t^* - t| \gg \tau(t)$, then the adiabaticity of the evolution holds. Out of equilibrium dynamics arises when this adiabaticity condition is no longer verified: $|t^* - t| \lesssim \tau(t)$. We denote $\hat{t}$ the time distance to transition for which

$$\tau(t^* - \hat{t}) \approx \hat{t} \tag{8.4}$$

$\hat{t}$ is called the *freezing out* time as it matches the time distance to the transition point at which adiabaticity fails. At this moment physical parameters can no longer follow the dynamics imposed by the forced ramp of the control parameter.

In particular, at this time $\hat{t}$, the correlation length is frozen to the value $\xi(t^* - \hat{t})$. The system can not equilibrate on length scales larger than $\xi(t^* - \hat{t})$ and no coherence can then be established on larger scales. From this observation, Kibble and Zurek suggest that this *frozen out* correlation length $\xi(t^* - \hat{t})$ matches the size of the independent coherent domains that are formed due to this *freezing out* of the dynamics:

$$\hat{\xi} = \xi(t^* - \hat{t}) \tag{8.5}$$

Then the mean number (over a large number of realizations) of independent domains N_{d} formed and observed at the end is given by

$$N_{\mathrm{d}} \sim \frac{\mathcal{V}}{f\hat{\xi}^D} \tag{8.6}$$

where $f \gtrsim 1$ is a numerical factor correcting for non–independent choice of the order parameter value between the "initial" patches[4], for example due to diffusion during the freezing out period [176]; D is the dimension of the patches we consider and $\mathcal{V}$ is the

---

[4] The term "initial" patches here refers to the patches formed at time $t^* - \hat{t}$, whose mean number is $\mathcal{V}/\hat{\xi}^D$. Then, with this correction, N_{d} corresponds to the mean number of domains observed at time $\sim t^* + \hat{t}$, that is at the end of the freezing out period, just before the merging of the domains. This value of N_{d} is the relevant one to deduce the mean number of topological defects that are formed.

fluid volume in this space. For example:

— For a uniform 2D gas as considered in 8.2, patches are bi–dimensional ($D = 2$) and the volume is equal to the area of the box $\mathcal{V} = \mathcal{A}$.

— For an annular geometry as considered in 8.3, we will see that we can look at the patches as effectively[5] one-dimensional $D = 1$ and the volume is equal to the annulus circumference $\mathcal{V} = \mathcal{C}$.

On each coherent domain formed at the freezing out time, the phase φ of the wavefunction (that is the order parameter for BEC transition) is approximately constant and its value is chosen randomly and independently. Hence, there is a chance to find an accumulation of the phase around a closed loop that crosses some boundaries between several of theses patches. During the coarsening dynamics at the transition crossing, the patches merge together and the point around which the phase winds up forms a topological phase defect, namely a vortex. From Kibble–Zurek formalism described above, we can deduce the mean number of topological defects that are nucleated in the quench. We distinguish two specific geometries that we will later experimentally study, an annular and a bulk geometry:

— In an annular geometry, the domains numbered by $i \in [\![1;\ N_\mathrm{d}]\!]$ form a one dimensional chain around the annulus. The choice of the independent phases φ_i on each domain i may lead to a persistent current if the phase accumulated around the annulus $\Delta\varphi = \sum_{i=1}^{N_\mathrm{d}-1}(\varphi_{i+1} - \varphi_i)[2\pi]$ (where $[\,.\,]$ stands for the modulo operation) is a non–zero multiple n_w of 2π. Then the mean over a large number of realizations (noted $\langle\ .\ \rangle$) of flux quanta n_w ($\equiv \Delta\varphi/2\pi$) that are created is directly deduced from the number of domains N_d as, if $N_\mathrm{d} > 1$, the variation of the phase over the circumference can be seen as a random walk of N_d steps. The precise scaling law of $\Delta\varphi$ to N_d depends on the range of N_d. If the number of patches is large ($N_\mathrm{d} \gg 1$), $\Delta\varphi$ follows the law of large numbers and the winding number n_w verifies

$$\langle |n_\mathrm{w}| \rangle \sim \sqrt{\langle n_\mathrm{w}^2 \rangle} \propto \sqrt{N_\mathrm{d}}. \tag{8.7}$$

Such a scaling law has been checked by numerical simulations using Stochastic Gross–Pitaevskii Equation (SGPE) for instance in [177][6]. If $N_\mathrm{d} \ll 1$, then scaling law is modified [178, 179] in

$$\sqrt{\langle n_\mathrm{w}^2 \rangle} \sim N_\mathrm{d} \tag{8.8}$$

$$\langle |n_\mathrm{w}| \rangle \sim N_\mathrm{d}^2 \tag{8.9}$$

In experimental investigations of 8.3, we will consider $N_\mathrm{w} \equiv \langle |n_\mathrm{w}| \rangle$. If the number of patches is intermediate between these two regimes, the scaling law must transit between Eq. 8.7 and Eqs. 8.8– 8.9. Our experimental realization of 8.3 holds in this situation. We have implemented simple simulations to estimate the correction to the scaling law by performing random walks on relevant number N_d of patches and fitting the resulting averaged winding number toward N_d (see 8.3.3.2) .

---

[5] For considering so the characteristic patches size $\hat{\xi}$ must be larger than the width of the annulus.

[6] In this paper the smallest $\mathcal{C}/\hat{\xi}$ considered is 30. The critical exponent found is 0.126 very closed from MF prediction 0.125

— For the nucleation of topological defects in the volume of the fluids in our uniform 2D gas of 8.2, scaling law of the mean defect number N_v is more complex to infer. It has been shown experimentally and theoretically that when merging independent condensates of random phases, vortices are formed and their mean number N_v depends on the merging rate [180, 181]. If the merging is slow enough, the vortices can only formed at the intersection of several (≥ 3) domains, then the number of vortices observed in one configuration is set by the simple geometrical organizations of the phases φ_i around the various intersection points (via the geodesic argument [182]). However if the merging is too fast, vortices can be nucleated from interference at the boundary between two domains. These interferences create instabilities that may decay in vortex anti–vortex pairs. Some of the generated vortices or anti-vortices may then survives (and not annihilate) within the resulting cloud. It was shown [180, 181] that the nucleation efficiency can be embodied by a constant f_v that does not depend on the critical exponents so that

$$N_v = \frac{N_d}{f_v} \tag{8.10}$$

8.1.2. Specific description of the mechanism in our experiment.

In our experiment, the quench through a transition to a coherent state is realized by performing the final evaporation ramp of the micro–trap potential height U_{box} (see 2.1.3). During this ramp, we vary the temperature T (see 7.1) but also the 2D character of the gas. In this sense, nor defining the order parameter that is ramped neither pointing out the critical phenomenon that leads to the formation of a coherent state (and if crossed via a finite ramp to topological defects) are straightforward tasks. In this section, our aim is to clarify the way KZ mechanism applies in our case.

The measurements detailed in this chapter have been taken at $\omega_z = 2\pi \times 365\,\text{Hz} \approx k_B/\hbar \times 17\,\text{nK}$. The loading temperature is typically of the order of $T_{\text{load}} \sim 200\,\text{nK}$ such that the starting value of $\zeta = k_B T/\hbar\omega_z$ is $\zeta_{\text{load}} \approx 12 \gg 1$ and we are in the 3D regime. More precisely, we compute an initial occupation of the ground state of the z-motion of 23%. In contrary, the final temperature is $T_f \sim 10\,\text{nK}$ and $\zeta_f \approx 0.6 \leq 1$: we reach a 2D regime with a final occupation of the ground state of the z-motion of nearly 100%. As highlighted in Chapters 1 and 7, in this case two transitions occur successively (two-step condensation). First, at temperature $T_\perp$, the transverse condensation (BEC$_\perp$) occurs, leading to emergence of a 2D behavior of the gas, with a dominant population of the ground state of the z–motion. Second, at temperature $T_{\text{full}} < T_\perp$, in–plane condensation (BEC$_{\text{full}}$) or BKT transition are crossed leading to a "true" superfluid state. BEC$_\perp$ occurs at a 3D phase-space-density $\mathcal{D}^{(3D)} \approx 2.612$ as the gas is weakly interacting there (see 1.2.3.3), and we show that at this point, the 2D phase-space-density associated to the population of the ground state of the z-motion is of the order of $\mathcal{D}_0^{(2D)} \approx \ln(\zeta)$ that is of the order of 2 in our case (see 1.2.3.2). BEC$_{\text{full}}$ and BKT happens at a similar phase-space-density $\mathcal{D}_0^{(2D)} \approx 8$ in our configuration.

In 1.2.3.4 we theoretically demonstrated and in Ch. 7 we experimentally verified that the occurrence of the BEC$_\perp$ phenomenon leads to a state of increased coherence length compared to the thermal length λ_{T} both in the z-direction but also (more subtly) in-plane. Then the establishment of such an extended coherence at crossing of BEC$_\perp$ phenomenon makes it relevant for the KZ formalism: In our ramp, the topological defects that may be nucleated via a KZ-like mechanism must be formed when approaching the BEC$_\perp$ point, which corresponds to a sharp dimensional crossover. The temperature can be seen as the order parameter varied and $T_c = T_\perp$.

To understand the details of the application of KZ-like mechanism in this case, we must analyze how the coherence length ξ evolves close to the transition point. We will start from the case of a 3D condensation considering a similar geometry[7]. In this case the previously developed KZ formalism simply applies using BEC universality class exponents and leads to the formation of coherent domains of size $\hat{\xi}$ (Eq. 8.5) isotropic for the 3 directions of space. For a condensation arising in two steps (that is for traps with a higher anisotropy $L/\ell_z \gg 10$), the same description than for this 3D case applies up to the first step of the condensation. As the isotropy of the evolution keeps being relevant up to this first step, the size of the coherent domains must then be limited by the smallest dimension if the gas, that is to say its typical thickness. It thus sets a validity bound to the 3D description of the KZ mechanism for this two-step condensation. More insight (see 1.2.3.4 for more details and rigorous derivation) in such a bounding effect can be obtained by injecting the order of magnitude $\mathcal{D}_0^{(2D)} \approx \ln(\zeta)$ in the 2D coherence length formula $\ell_{\mathrm{c}} = \lambda_T e^{\mathcal{D}_0/2}/\sqrt{4\pi}$ (Eq. 1.22), we found an in-plane correlation length $\ell_{\mathrm{c}} \sim \ell_z/\sqrt{2}$ with $\ell_z = \sqrt{\hbar/m\omega_z}$ such that ℓ_{c} matches (in order of magnitude) the thickness of the ground-state of the z-motion: At the transverse condensation point, the in–plane coherence length is equal to the correlation length in the z-direction and is set by the characteristic thickness of the gas.

Then, for the fastest cooling ramps, KZ description for a BEC-type transition predicts domain sizes for a 3D fluid that are smaller than $\sim \ell_z/\sqrt{2}$, and it can thus provide a good description of our system. For a slower cooling, large coherent domains would be expected in 3D, but in this case, the 2D nature of our gas cuts the critical divergence of the correlation length (at the value $\hat{\xi} \gtrsim \ell_z$)[8] and slows down the emergence of the coherent patches. In this slow cooling regime, we thus expect to find an excess of topological defects with respect to the 3D KZ prediction and a reduced variation[9] of the numbers of domains toward the quench time above the corresponding threshold in τ_Q.

For the fast cooling regime, the number of patches scales according to the BEC uni-

---

[7] we consider a uniform in-plane confinement and a transverse harmonic one but with different numeric parameters: 3D condensation is relevant when the two described steps for the condensation are not distinguishable anymore. Quantitatively, it is the case when the characteristic size of the box potential L is of the order of the size of the harmonic oscillator $\ell_z = \sqrt{\hbar/m\omega_z}$ (see Eq. 1.51). In our case we have a ratio of 1 : 53 between the two rms size of the traps.

[8] such an effect can be seen as finite size effect in the transverse direction, see the corresponding subsection 8.1.5.

[9] Following literally our analysis, we deduced that this reduced variation should be a constant one. In reality this variation may be more sophisticatedly affected by the further evolution of the coherence, beyond the unique BEC$_\perp$ phenomenon. Then we can not rigorously conclude on the occurrence of a plateau. In our experimental investigation however, we do not reach a sufficient precision to distinguish a constant from a slow decay. For conveniency, we will use the plateau terminology rather a reduced dependency in the rest of this chapter for describing this divergence cut effect

versality class prediction. It can be described using a *Mean–Field* (*MF*) formulation[10] (*i.e.* Ginzburg-Landau theory) that gives $\nu = 1/2$ and $z = 2$ (see *e.g.* [**?**]). Beyond *Mean–Field* predictions have also been developed. In our case[11], we will considered the so–called *Model F* [185]. We summarize in Table 8.1, the different values of the exponents that could describe our gas.

Exponent	BEC, *MF*	BEC, *Model F*
ν	$1/2$	$2/3$
z	2	$3/2$

Table 8.1.: Prediction for critical exponents ν and z for BEC universality class described in a Mean–Field (BEC MF) approximation (Ginzburg–Landau theory) or beyond Mean–Field *Model F* [185].

Note that in our case, we are not studying the BKT transition. BKT transition would also lead to highly interesting physics as it is of infinite order and do not lead to a power-law scaling of ξ and τ. It was shown that Kibble–Zurek mechanism nevertheless keeps applying then, leading to a more complicated scaling that was the object of recent theoretical analysis [174, 175]. To reach such an interesting physics it is necessary to use higher transverse trapping frequencies and larger in-plane boxes to be able to make irrelevant the $\text{BEC}_\perp$ phenomenon and to separate the scales of BEC_full and BKT transitions compared to our current implementation.

In our case, pushing further the evaporation to reach the deep 2D regime is a simple mean to facilitate the visualization of the topological defects.

8.1.3. Homogeneous Kibble–Zurek mechanism

8.1.3.1. Linear ramp model

The historical argument by Kibble and Zurek bears on homogeneous systems. They consider a uniform quench of the temperature T (or more generally any control parameter) and they assume this ramp to be linear in time[12]:

$$T(t) = T_c \left(1 - \frac{t}{\tau_Q}\right) \tag{8.11}$$

---

[10] We note that such values of critical exponents are correct for space dimension larger or equal to 4. Then corrections must be taken into account in our 3D case for a more accurate description taking into account the enhanced role of fluctuations.

[11] Other predictions based on Monte Carlo calculations to compute z value can also be used [183, 184]. We note that the value of z coefficient depends on the dynamics considered and is not well characterized.

[12] Until now we considered τ_Q as the ramp time until the crossing of the transition. As we consider here a symmetric ramp around the transition, the value of τ_Q is only half the total duration of the ramp. In fact the rigorous definition of τ_Q for all ramp types is linked to the notion of quench rate that is the slope of the ramp in temperature divided by the temperature at the transition. Inversely, $\tau_Q = T_c \left|\frac{\mathrm{d}T}{\mathrm{d}t}(t^*)\right|^{-1}$. Then it simply extend to the non-linear case, see 8.1.3.2.

with t varying from $-\tau_Q$ to τ_Q so that $\epsilon(t) = t/\tau_Q$ and the transition time $t^* = 0$. Then, the *freezing out* time defined in Eq. 8.4 is given by

$$\tau(\hat{t}) = \frac{\tau_0}{|\hat{t}/\tau_Q|^{\nu z}} = \hat{t} \Rightarrow \hat{t} = \left(\tau_0 \tau_Q^{\nu z}\right)^{\frac{1}{1+\nu z}} \tag{8.12}$$

and we deduce the scaling of the characteristic size of the domains:

$$\hat{\xi} = \xi_0 \left(\frac{\tau_Q}{\tau_0}\right)^{\frac{\nu}{1+\nu z}} \tag{8.13}$$

We denote d the critical exponent for the domain size:

$$d = \frac{\nu}{1+\nu z} \tag{8.14}$$

For the considered description of the BEC class of universality summarized in Table 8.1, the possible values of the critical exponents for either looking at vortex nucleation in a 2D gas or at winding numbers around an annulus, are detailed in Table 8.2.

Quantity	power-law exponent	*MF*	*Model F*
$\hat{\xi}$	d	$1/4$	$1/3$
N_v	$-d_\mathrm{v} = -2d$	$-1/2$	$-2/3$
$\langle\lvert n_\mathrm{w}\rvert\rangle$ if $\hat{\xi} \ll \mathcal{C}$	$-d_\mathrm{w} = -d/2$	$-1/8$	$-1/6$
$\langle\lvert n_\mathrm{w}\rvert\rangle$ if $\hat{\xi} \gg \mathcal{C}$	$-d_\mathrm{w} = -2d$	$-1/2$	$-2/3$

Table 8.2.: Critical exponents for the characteristic size of domains $\hat{\xi}$, the mean number of vortices in a 2D gas N_v or the winding number N_w around an annulus in their dependency toward the quench time τ_Q. $\mathcal{C}$ denotes the circumference of the annulus so that the mean number of domains in the annulus is $N_\mathrm{d} = \mathcal{C}/\hat{\xi}$.

8.1.3.2. Some insights on non–linear ramps and application to our experimental ramp:

Experimentally, it may be complex to implement a linear ramp of the temperature T as it is not monitored directly but via an evaporative cooling control parameter. In our case this control parameter is the box–potential height U_box. We studied in detail the relation between T and U_box in 7.1 and showed an exponential dependency following Eq. 7.10 (due to loading condition influence). In the experiments described in this chapter, we will consider a linear ramp of the box–potential height U_box so that in the approximation of an adiabatic following of the temperature, the ramp on T results non–linear.

In this case, we have to reconsider the starting argument of Kibble and Zurek on the *freezing out* determination of the size of the domains (see Eqs. 8.4 and 8.5) and find new scaling laws of $\hat{t}$ and $\hat{\xi}$ with τ_Q. In a general way, this is a complex issue as the implicit relation defining the *freezing out* time in Eq. 8.4 cannot be generally solved. Nevertheless, as KZ scaling is fully determined by the physics happening between two times: the transition time t^* and the self–consistently defined *freezing out* time $t = t^* - \hat{t}$, conclusions can be drawn if the description of the evolution between these two times can be simplified. In particular, if the evolution of the control parameter can be approximated by a linear ramp in this range , then the KZ scaling law is unchanged. The quench time τ_Q will however take a local value characterizing this local evolution that may depend on the transition time t^*:

$$\frac{1}{\tau_Q^*} \equiv \frac{1}{T_c} \left| \frac{\mathrm{d}T}{\mathrm{d}t} (t^*) \right| \tag{8.15}$$

Such an approximation is valid if the slope of T does not vary too much between $t^* - \hat{t}$ and t^*, for instance:

$$\left| 1 - \frac{\mathrm{d}T/\mathrm{d}t\,(t^*)}{\mathrm{d}T/\mathrm{d}t\,\left(t^* - \hat{t}\right)} \right| \lesssim 1 \tag{8.16}$$

In our case, the ramp of U_{box} is set linear between a loading value $U(t=0) = U_{\mathrm{box}}^{\mathrm{load}}$ and a final value $U(t = \tau_Q) = U_{\mathrm{box}}^{f}$ very small compared to the initial one $U(\tau_Q) \ll U(0)$:

$$U(t) \approx U_{\mathrm{box}}^{\mathrm{load}} \left(1 - \frac{t}{\tau_Q} \right) \tag{8.17}$$

Assuming adiabatic following of the temperature along relation of Eq. 7.10 deduced in previous chapter, we find

$$\frac{\mathrm{d}T}{\mathrm{d}t}(t) = -\frac{U_{\mathrm{box}}^{\mathrm{load}}}{U_0} \frac{T_0}{\tau_Q} \exp\left(-\frac{U(t)}{U_0} \right) = -\frac{U_{\mathrm{box}}^{\mathrm{load}}}{U_0} \frac{T_0 - T(t)}{\tau_Q} \tag{8.18}$$

and deduce a local effective quench duration at time t

$$\begin{aligned} \tau_Q^{(\mathrm{loc})}(t) &\equiv T_c \left| \frac{\mathrm{d}T}{\mathrm{d}t}(t) \right|^{-1} && (8.19) \\ &= \frac{U_0}{U_{\mathrm{box}}^{\mathrm{load}}} \frac{T_c}{T_0 - T(t)} \tau_Q && (8.20) \\ &= \tau_Q \frac{T_c}{T_0} \frac{U_0}{U_{\mathrm{box}}^{\mathrm{load}}} \exp\left(\frac{U_{\mathrm{box}}^{\mathrm{load}}}{U_0} \left(1 - \frac{t}{\tau_Q} \right) \right). && (8.21) \end{aligned}$$

By applying condition of Eq. 8.16 and using latter expression of Eq. 8.21, the linear approximation is valid if the *freezing out* time separation is small compared to some fraction of the actual quench duration τ_Q:

$$\hat{t} \lesssim \frac{U_0}{U_{\mathrm{box}}^{\mathrm{load}}} \tau_Q \tag{8.22}$$

In Eq. 7.10, U_0 divides between the high and low potential–height values compared to the loading condition effect and is typically a fraction of $U_{\mathrm{box}}^{\mathrm{load}}$, $U_0 \sim U_{\mathrm{box}}^{\mathrm{load}}/3$.

If Eq. 8.22 is verified, then, using Eq. 8.20, the local quench time of interest defined in

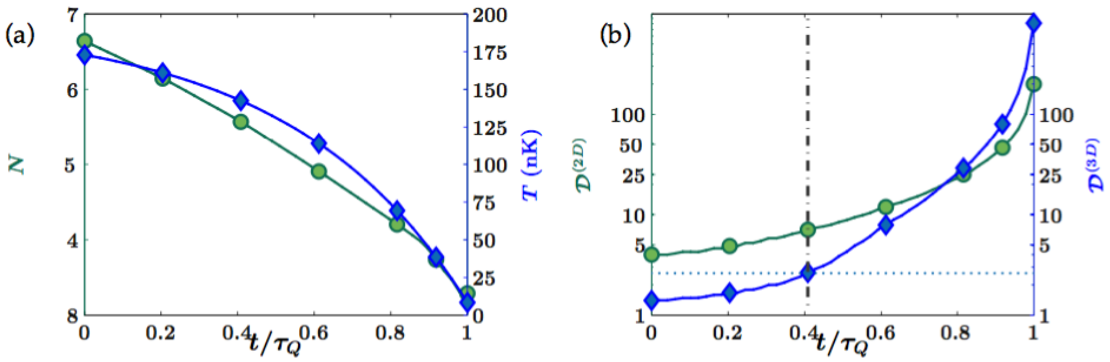

Figure 8.1.: **(a)** Evolution of cloud parameters N (green disks, left axis) and T (blue diamonds, right axis) along the evaporation ramp. t is the time along the ramp and τ_Q the ramp duration. **(b)** Deduced predictions using ideal Bose law calculations of the 2D phase-space-density associated to $|j_z = 0\rangle$ state $\mathcal{D}_0^{(2D)}$ (green disks, left label) and the 3D PSD at trap center $\mathcal{D}^{(3D)}$ (blue diamond, right axis). Grey dash-dotted line highlight the time where $\mathcal{D}^{(3D)} = 2.612$, matching the time at which $BECp$ occurs(see 1.2.3.3). We find that the relevant transition occurs at $t^* = 0.41\tau_Q$.

Eq. 8.15 is simply

$$\tau_Q^* \approx \tau_Q \frac{U_0}{U_{\text{box}}^{\text{load}}} \frac{T_c}{T_0 - T_c} \tag{8.23}$$

that is directly proportional to τ_Q. Then the scaling law predicted for the size of the domains – and thus for the resulting one for the topological defects observed – is unchanged compared to Eq. 8.13.

To study further applicability of linear approximation, we must study the value of $\hat{t}$. Assuming linear approximation and considering $\nu z = 1$ (see Table 8.1), Eq. 8.12 writes

$$\hat{t} = \sqrt{\tau_0 \tau_Q^*} \tag{8.24}$$

where τ_0 is the thermalization time of the normal gas and is typically identified with the collision time $\tau_0 \equiv \tau_{\text{coll}} \approx 4$ ms (see Annex I). τ_Q^* is given by Eq. 8.23 such that the condition of Eq. 8.22 reads

$$\tau_Q \gtrsim \frac{U_{\text{box}}^{\text{load}}}{U_0} \frac{T_c}{T_0 - T_c} \tau_0 \tag{8.25}$$

It depends on the value of the critical temperature T_c for the considered ramp. When performing a ramp on the box–potential height, the couple (N, T) of cloud parameters evolves when varying U_{box}. We show in Ch. 7, measurements of this couple for various trapping configurations and loading conditions. We consider here the evolution measured for the specific geometry presented in the following section 8.2 [13] and plot their time dependency in Fig. 8.1**(a)**.

---

[13] We can perform similar calculations for the geometry presented in 8.3 . Due to similarities in transverse trapping and in the size of the in-plane box (similar d_{max}, $\mathcal{A}$), it is then not drastically different. The former situation is nevertheless easier to describe due to a simpler geometry.

To study the $\mathrm{BEC}_{\perp}$ transition point on this ramp, we use ideal Bose law calculations as presented in Annex A for a square box of size $L = 30\,\mu\mathrm{m}$ and a transverse confinement frequency $\omega_z/2\pi = 365\,\mathrm{Hz}$. We deduce both the populations of the single-particle states and the extent of the gas in the transverse direction so that we can compute the 2D and 3D phase space densities $\mathcal{D}^{(2D)}$ and $\mathcal{D}^{(3D)}$. We plot their time evolution along the ramp in Fig. 8.1**(b)**. From these calculations, we found that $\mathcal{D}^{(3D)}$ raises above 2.612 at $t^* = 0.41\tau_Q$, defining the time at which $\mathrm{BEC}_{\perp}$ occurs. We deduce $T_c = 142$ nK while we measure $T_0 = 194$nK and $U_{\mathrm{box}}^{\mathrm{load}}/U_0 = 2.2$. In this case, Eq. 8.25 reads $\tau_Q \gtrsim 6\tau_0 \sim 24$ ms.

If we consider evaporation ramps longer than few tens of milliseconds, the linear approximation is valid in our configuration and KZ scalings summarized in Table 8.2 apply. We will only consider these cases in practice as the adiabatic following of the temperature along the ramp also requires quench times longer than a few collision times and $\tau_Q \gtrsim 25$ ms.

8.1.4. Specificity of transition crossing in homogeneous systems: some insights on the inhomogeneous KZ phenomenon

In most of the previous experiments testing KZ mechanism ([91, 93, 94, 170, 171], see [186] for a review), the systems under study is intrinsic non-homogeneous. In this section, we want to briefly highlight how inhomogeneities constitute a limitation in testing KZ mechanism along its original formulation and demonstrate – by contrast – the original input of our uniform setup. We point out the specificity of transition dynamics in uniform setups in which causality [173] is avoided by simultaneity of the transition over the whole cloud, recovering the original argument of KZ mechanism. Hence, dynamical features of transition crossing are expected to be strongly enhanced in uniform systems.

In this section, we will only present the main lines of the understanding of KZ mechanism in an inhomogeneous system without entering in the details of the calculations as it is not the main point of our experimental investigation presented further. In-depth proofs of the presented arguments can be found in [187].

In an inhomogeneous system, the critical temperature at which transition occurs depends on the location $\boldsymbol{r}$ via $T_c(\boldsymbol{r})$. Then as the temperature is commonly the same over the whole cloud, the crossing of the transition can be seen as the propagation of a coherent front. Regions with higher T_c are crossing the transition first and choose an initial arbitrary value of the order parameter. Neighboring regions will successively reach the transition point and then, if the transition is slow enough, the choice of the order parameter in these regions is dictated by proximity from the original choice of the most coherent regions. KZ mechanism is relevant in such traps only for regions where the transition front is too rapid so that the coherent parts have no time to impose their choice to the neighboring incoherent ones. We will called these regions, the *Kibble–Zurek (KZ) domain*. *KZ domain* limits are set by the condition of a local non–adiabatic propagation of the transition front.

For a finite quench time, such regions always exist as the gas always shows regions that locally look like an homogeneous system. In an harmonic trap, this would be the case in the central region where the density reaches its maximal value and so its gradient is zero and in the far outer region where the density asymptotically decays to zero. The size of the *KZ domain* then depends on the quench rate.

KZ prediction applies for each of the *KZ domain* components in which τ_Q, $\hat{t}$ and $\hat{\xi}$ take local values due to the spatial dependency of $T_c(\boldsymbol{r})$. Using Local Density Approximation (LDA), we can deduce a local density of topological defects $n_\text{v} \equiv N_\text{v}/\mathcal{V}$ by applying the uniform prediction obtained in previous section 8.1.1. Then the average total number of defects is computed by integrating $n_\text{v}(\boldsymbol{r})$ over the *KZ domain*:

$$N_\text{v} = \int_{\textit{KZ domain}} n_\text{v}(\boldsymbol{r}) d\boldsymbol{r} \tag{8.26}$$

For fast enough quenches (compared to some characteristics time deduced from the trap shape), *KZ domain* can match the entire cloud. In this case, the KZ scaling deduced for uniform clouds is not modified. For slower quenches however, some regions of the cloud will be excluded from *KZ domain*. In a typical harmonic trap, this excluded region forms a ring. Due to the ring radii dependency on the quench duration τ_Q, scaling of the number of vortices detected toward τ_Q is modified by the inhomogeneity. In the limit of very slow quench, we can approximately compute Eq. 8.26 (by considering only a very small central KZ domain). In an harmonic trap, we find for example a modified scaling

$$N_\text{v} \propto \left(\frac{\tau_0}{\tau_Q}\right)^{2(\nu(1+D/2)+1)/(1+\nu z)} \tag{8.27}$$

This limit corresponds to a power-law of greater exponent $d' = 2(\nu(1+D/2)+1)/(1+\nu z)$ than the homogeneous scaling described in Eqs. 8.10-8.13 whose exponent is $Dd = \nu D/(1+\nu z)$. In between these two limiting cases of extremely fast quenches and slow ones, the scaling of N_v to τ_Q must evolve from power-law scaling of exponent dD to exponent d'. We also point out in these calculations that the total number of vortices is strongly reduced compared to the homogeneous case as they can only be found in restricted parts of the gas.

We note that the KZ prediction has been extended to inhomogeneous systems by performing some approximations that enable one to deduce them from the original case of a uniform system. The KZ mechanism is then no longer universal but needs a non–adiabatic condition to be verified. The inhomogeneities lead to an ease of the adiabaticity thanks to the causality principle. Indeed, if the evolution is slow then the KZ domain is very limited and only a very small part of the gas evolves out of equilibrium at the transition crossing. The characteristics evolution rate for defining this slowness is here set by the comparison of the freezing-out correlation length $\hat{\xi}$ (at this rate) to the typical scale of the trap spatial variations. In a uniform gas adiabaticity of the evolution can be recovered only in case of a finite system (non-adiabaticity is always induced by the crossing of a transition in an infinite uniform gas, see 8.1.5 for an insight on finite size effects). Here out-of-equilibrium dynamics is prevented if $\hat{\xi}$ becomes larger than the cloud size itself. Thus considering gases of similar sizes, the characteristic slow evolution corresponds to a smaller rate (longer time scale) in the homogeneous case than in the non-homogeneous one. We conclude that homogeneous systems appear very promising in terms of studying out-of-equilibrium and dynamical phenomena.

Finally, we note that the KZ predictions for inhomogeneous systems are deduced from the original prediction by applying LDA. Such an approximation must be considered with care as we analyze physical phenomena close to a transition point where the characteristic length ξ diverges. In particular we deduce the scaling of the number of defects from a local value of the size of the coherent domains $\hat{\xi}(\boldsymbol{r})$ that may be larger than the characteristic length of the inhomogeneities of the potential. Such issues may be addressed by taking into account by the effect of finite size on scaling properties that we will not address in next paragraph but we will not further investigate this question latter on in this work.

8.1.5. Some insights on finite size effects on scaling properties

The scaling laws described above have been established considering an infinite system. However, experimental systems are always of finite size. We denote L the characteristic size of the system. We immediately grasp that when the characteristic size of the domains $\hat{\xi}$ deduced from the infinite system prediction becomes larger than L, the scaling law must be strongly modified. When $\hat{\xi} > L$, the influence of L must reduce the influence of $\hat{\xi}$ over the number of defects nucleated as then a vanishingly small number of topological defects are expected to be formed whatever the quench rate is. It has been more rigorously demonstrated that critical behavior of both homogeneous [188] and inhomogeneous [189, 190] gases is modified from the finite size of the system. A more in–depth study of the modification of the critical exponent can be performed using the Renormalization Group Theory (similarly to the works presented in the three last references) but goes beyond the scope of this manuscript.

8.2. Nucleation of vortices in a 2D uniform gas via Kibble–Zurek mechanism

We will now describe a first experiment in which we tested KZ mechanism on a 2D uniform gas. We use a similar geometry as the ones used to test establishment of coherence as a steady state property of our gases in Ch. 7. In that chapter, we studied the coherence as a function of the final equilibrium configuration (N, T) of the gas. Nevertheless, the finite duration of the evaporation ramp used to establish the coherent behavior also implies interesting dynamical features of the coherence establishment due to the crossing of the relevant transitions in a uniform 2D geometry, $\mathrm{BEC}_\perp$, $\mathrm{BEC}_{\mathrm{full}}$ and BKT.

In this section I present our test of KZ mechanism at crossing of $\mathrm{BEC}_\perp$ (see 8.1.2) by observing topological defects that survive in the coherent gas, namely vortices.

8.2.1. Characterizing vortices via Time–of–Flight measurements

8.2.1.1. Experimental sequence

For these measurements, we use a box potential of square shape and of length $L = 30\,\mu$m transversely confined in a harmonic trap of frequency $\omega_z/2\pi = 365\,$Hz. After

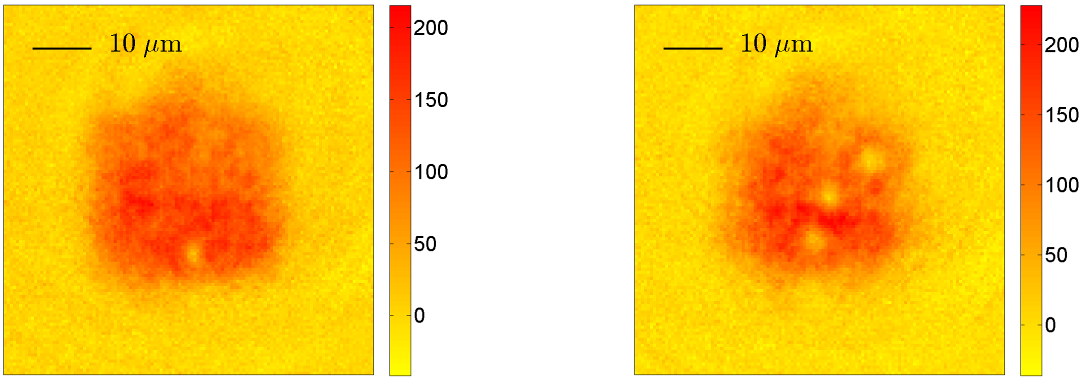

Figure 8.2.: Examples of density distribution after 4.5ms of ToF showing **(left)** 1 and **(right)** 3 hole(s) of high contrast, corresponding to topologically protected expanding vortex core(s).

loading these 2D traps from a 3D cold gas (see 2.1.3 and Fig. 2.1), we ramp down the box height U_{box} to its final value in a time t_{evap} and finally wait for a time t_{hold}. In this chapter, we consider fixed final end points for both the ramps performed within the hybrid trap (see 2.1.2) and within the 2D box-potential (see 2.1.3). Then, the final cloud configuration is fixed, the temperature is $T \approx 11\,\text{nK}$ (see 7.1) and the atomic density $n^{(2D)} \approx 50\ \text{at}/\ \mu\text{m}^2$.

In this configuration, topological defects expected from KZ mechanism are vortices (see last point of 8.1.1 and [91, 180**?**]). The predicted size of the vortex in–situ is determined by the healing length $\varsigma = 1/\sqrt{\tilde{g}n^{(2D)}}$. By performing 3D Gross–Pitaevskii calculations in imaginary time (see Annex B) , we deduce the 3D ground–state wave function in our trapping configuration taking into account interactions. As the final configuration of our gas is highly degenerate with $T_d/T \sim 150$ where $T_d = 2\pi\hbar^2 n/(k_B m)$ is the degeneracy temperature, the deduced ground–state gives a good approximation of the actual macroscopic wavefunction of the coherent part of our sample. We estimate ς along Eqs.B.23-B.25 and we assess $\varsigma \sim 0.7\,\mu\text{m}$ for the considered atomic density. As our imaging resolution is of the order of 1–2 μm, we expected the vortices not to be visible in situ and indeed we detect no density holes in the corresponding absorption images.

We then perform a short Time–of–Flight expansion and image our gas along the vertical axis with high intensity absorption imaging (see Ch. 3) to let the vortex cores widen. In the resulting density distribution, we observe deep density holes in arbitrary number per realization (up to 5) and located at random positions as shown in Fig. 8.2. We observed similar density holes for different cloud shapes (disk and square of smaller sizes) and confinement frequencies (as at frequency of $\omega_z/2\pi = 1460\,\text{Hz}$) but we only performed a systematic analysis on the above described configuration.

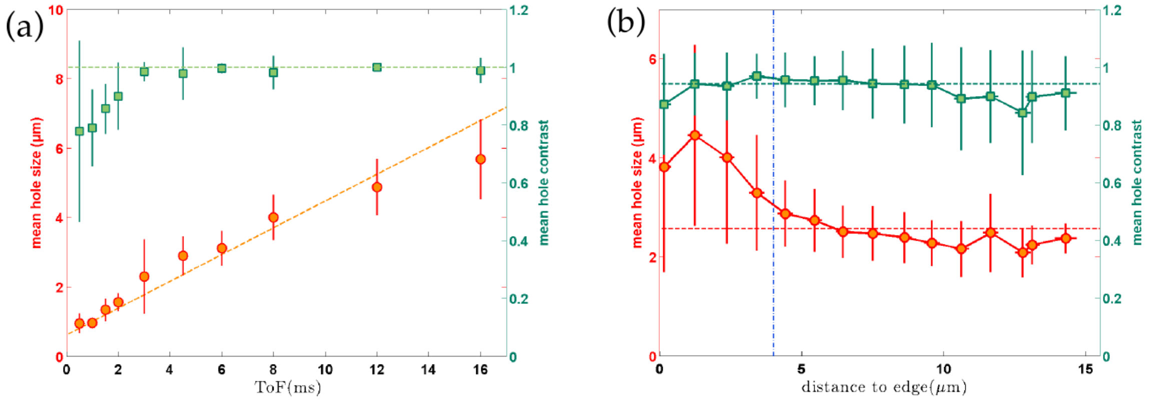

Figure 8.3.: **(a)**. Evolution of the fitted contrast c (green square, right axis) and of the average size ς (red circle, left axis) of the density holes with the expansion duration τ. We fit each density hole by an hyperbolic tangent deep (of contrast c and size ς) convoluted by of gaussian of waist $w = 1\,\mu$m corresponding to effect of imaging resolution and depth of field (Eq. 8.28). We fit w from a preliminary analysis of the holes as detailed in the text. For each τ, we fit in average 20 density holes. We note that ς increases with τ. The dashed red line is a linear fit of the variation of ς and serves as a guide to the eye. **(b)**. Evolution of c and of ς (same code as **(a)**) with the position on the cloud for a fixed $\tau = 4.5$ms. We fit 1430 vortices. The position on the cloud is denoted by the distance to the closest edge of the initial square-box and we binned the data around the abscissa of the shown dots. We note that vortices are distorted when close to the edges. For holes located at a distance larger than $4\,\mu$m from the edges (represented by the blue dashed-dotted line), the characteristics are independent from its position on the cloud (the dashed red line shows the mean value of ς in this case). In both cases, c is compatible with $c = 1$ (dashed green lines).

8.2.1.2. Identifying density holes to vortex cores.

We identify all relevant holes in the in–plane density distribution $n(x, y)$ by an automatized procedure. We first compute the average density over a large number of pictures for each Time–of–Flight duration τ, $n_m(x, y; \tau)$, and consider the difference[14] $\delta(x, y) = n_m(x, y; \tau)/\langle n_m\rangle(\tau) - n(x, y)/\langle n\rangle$ where $\langle . \rangle$ stands for the spatial average. We then analyze peaks of δ of high enough amplitude, more precisely we look at the sets of pixels (x, y) for which $\delta(x, y) \geq b \times \langle \delta(x, y)\rangle$ and typically $b = 10$. We will identify a set[15] of pixels to a physical defect if it is of large enough size (typically it must contain between 15 and 100 pixels for $\tau = 4.5$ ms) and of circular enough shape (the solidity[16] of the set of pixels considered must be greater than 0.5).

To identify the nature of these density holes, we perform a statistical analysis of the

---

[14] Considering here the difference and not the division enables a more reliable investigation of the wings of the cloud (where $n_m(x, y) \approx 0$) in these Time–of-Flight measurements.

[15] a set of pixel is defined as a connected component of the true regions in the boolean matrix $\delta(x, y) \geq b \times \langle \delta(x, y)\rangle$, after having performed some morphological operation to get rid of the noise of this boolean matrix.

[16] The solidity of a set of pixels is the proportion of pixels of the convex hull of the set that belong to the considered set, the convex hull being the smallest convex polygon that contains all the considered set.

hole properties. We perform a fit of the density distribution around each detected hole. The fitting function is:

$$\rho(x,y) = (\rho_0 * g)(x,y) \tag{8.28}$$

$$\text{with } g(x,y) = \frac{1}{\sqrt{2\pi}\sigma}\exp\left(-\frac{x^2+y^2}{2\sigma^2}\right) \tag{8.29}$$

$$\rho_0(x,y) = \rho_0\left((1-c)+c\tanh(r(x,y)/\varsigma)\right) \tag{8.30}$$

$$r(x,y) = \sqrt{(x\cos\theta+y\sin\theta)^2+\epsilon^2(y\sin\theta-x\sin\theta)^2} \tag{8.31}$$

where $*$ denotes the convolution operator. $g(x,y)$ is a Gaussian representing the effect of imaging imperfections (finite imaging resolution, finite depth of field) and $\rho_0(x,y)$ is the physical expectation of density dependency around a vortex core (for $c=1$).

We first estimate the size ς_i of the vortices for each τ by a manual method. We then consider the ratio $\rho_{\text{mes}}(x,y) = n(x,y)/n_m(x,y;\tau)$, on a square region of $1.5\times\varsigma_i(\tau)$ around each density hole (these domains are located inside the cloud so that $n_m(x,y;\tau)\neq 0$).

We perform a preliminary fit of $\rho_{\text{mes}}(x,y)$ to the simpler function $\rho_0(x,y)$ given in Eq. 8.30, neglecting imaging effects. From fitting the overall set of experimental vortices, we compute an expected relation between the fitted contrast c and the fitted size ς valid for the observed vortices.

To deduce the imaging imperfection function $g(x,y)$ (Eq. 8.29), and the physical contrast of the vortices c_{v}, we simulate a set of density distributions perturbed by a vortex (along Eq. 8.30) while varying the size ς_{s} and the contrast c_{s} of the vortices and convoluting it by a Gaussian $g(x,y)$ of varying width σ_{s}. We fit the resulting density distribution by the same procedure as the experimental vortices and deduce a theoretical relation between fitted parameters c and ς for a given contrast c_{s} and imaging width σ_{s} while varying the size ς_{s} of the simulated vortex (as it reproduces variations of τ for physical vortices). By computing the minimal distance between the simulated and experimental sets of (c,ς), we found the contrast of the vortices $c_{\text{v}}=1$ and the width of the imaging gaussian $\sigma = 1\,\mu$m.

We then perform a final fit of $\rho_{\text{mes}}(x,y)$ to the function given in Eq. 8.28 with fixed imaging width $\sigma=1\,\mu$m and fixed or varying contrast c. We analyze the variations of the resulting fit parameters ς and c for different Time–of–Flight durations and different locations in the cloud. We analyze the variations of c and ς at a fixed τ over the whole set of experimental realizations studied latter on in this chapter (corresponding to 1430 vortices at $\tau = 4.5$ ms). We note that all the observed holes show similar ς and c for all cloud realizations and all hole positions [17] on the cloud (Fig. 8.3 **(b)**). We analyze the variations of c and ς when varying τ. We use 10 values of τ between 0.5 ms and 16 ms, and record a set of 38 images for each τ corresponding to a number of fitted vortices varying from 15 to 25 (with an average vortex number per realization $N_{\text{v}} = 0.52$). The

---

[17] We however note a distortion of the vortices when they get to close to the edges. More specifically we observe elliptic vortices with long axis perpendicular to the edge and with larger area than bulk vortices (see Fig. 8.2). Such distortions must be due to effect of the short Time–of–Flight on density distribution. For holes located at a distance larger than 4 μm from the edges, we note that the influence of the edges is not perceptible anymore.

average ς shows a typical increase with τ and the measured contrast is compatible with $c = 1$ (Fig. 8.3 **(a)**).

All these observations are the signature that the density holes correspond to topologically protected expanding single vortex cores:

— They are not close vortex–antivortex pairs for which predicted evolution from Gross–Pitaevskii real time evolution simulations lead to an annihilation of the two defects in Time–of–Flight [18]. This process results in a decreasing c with τ that we do not observe here.

— They are not phonons as these phase defects would also create density hole of strongly varying sizes for different realizations due to the range of their possible momenta. They would also result in a lower average contrast (see for example [191–193]).

We now fix the Time–of–Flight duration to $\tau = 4.5\,\text{ms}$ for which the density holes are well visible and study in more details the statistics of the observed vortices.

8.2.2. Justifying dynamical origin of the vortices

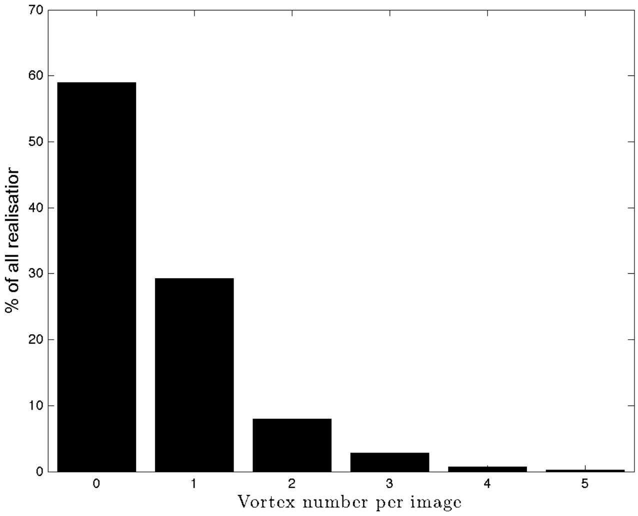

Figure 8.4.: Histogram of vortex number realization over the 2460 analyzed images. We note that most of the images (59%) show no vortices while the mean number of vortices over this set of image is 0.58 vortex per realization. Most of the images presenting some vortices only show one, with probability of 71%. We observe multiple vortices in 12% of all the cases.

In our measurement campaign, we studied vortex nucleation for varying experimental parameters and, in total, we analyze 2460 images corresponding to a total of 1430 vortices detected. On this set of images, we observe a number of vortices varying from

---

[18] simulations were performed for distances between the vortex and the anti-vortex up to a few healing lengths (typically 5)

shot-to-shot such that it indicates a stochastic nucleation mechanism. We measure up to 5 vortices per image and histograms of occurrences are given in Fig. 8.4.

To predict the mean vortex number expected from a steady–state thermal activation in the final configuration of our gas we use the *semi–classical field* predictions from [194]. Our final configuration corresponds to a temperature $T = 11\,\mathrm{nK}$ and an interaction energy per particle $\epsilon_{\mathrm{int}} \approx k_{\mathrm{B}} \times 5.5\mathrm{nK}$ (which we deduce from 3D Gross–Pitaevskii calculations in imaginary time along Eq. B.24, see 8.2.1 for validity).Such a highly degenerate configuration ($2k_{\mathrm{B}}T/\epsilon_{\mathrm{int}} \sim 1$) lies outside the range of parameters considered in [194] and the predictions obtained for a 1.5 times higher temperature leads to a vanishingly small mean number of vortices nucleated $N_{\mathrm{v}} \lesssim 5 \times 10^{-12}$. Then it is highly unlikely that vortices are nucleated from thermal activation in our final experimental configuration. Moreover, [194] also predicts that vortices must arrange in close pairs of vortices of opposite charge in this configuration as the correlation between pairs is predicted to be high at short distances and nearly zero at long range. The high occurrence of vortices detected as well as the non pairing of the observed vortices is in clear disagreement with this steady–state prediction. Such a high discrepancy fully excludes thermal excitations from the possible mechanisms that the vortices may originate from. The observed topological defects must then have a dynamical origin.

In the following, we study this dynamical origin by varying the two times that characterize the evolution of the gas, the duration of evaporation in the uniform trap t_{evap} and the hold duration after evaporation t_{hold} (see Fig. 2.1 for a summary of the experimental sequence and a schematic definition of these times).

8.2.3. Studying the quench dynamics

For the results presented in this section, we fixed $t_{\mathrm{hold}} = 500\,\mathrm{ms}$ and studied the evolution of the average vortex number N_{v} as a function of t_{evap}. The corresponding data, given in Fig. 8.5, show a decrease of N_{v} with t_{evap}, passing from $N_{\mathrm{v}} \approx 1$ for $t_{\mathrm{evap}} = 50\,\mathrm{ms}$ to $N_{\mathrm{v}} \approx 0.4$ for $t_{\mathrm{evap}} = 250\,\mathrm{ms}$. For longer evaporation times, N_{v} remains approximately constant within the error-bars [19], and we fit $N_{\mathrm{v}} = 0.40\,(3)$ (see legend of Fig. 8.5 for details). The decrease of N_{v} with t_{evap} suggests that the observed vortices are nucleated via a Kibble–Zurek (KZ) type mechanism, occurring when the transition to the phase coherent regime is crossed. Note that we observe a similar behavior for data taken at $t_{\mathrm{hold}} = 0\,\mathrm{ms}$. Such a behavior is in qualitative agreement with the expectations of 8.1.2.

8.2.3.1. Fit of critical exponent for the quench dynamics

For a quantitative analysis of KZ mechanism in our configuration, we fitted the expected power-law decay, $N_{\mathrm{v}} \propto t_{\mathrm{evap}}^{-d_{\mathrm{v}}}$, to the measured variations of N_{v} for $t_{\mathrm{evap}} \leq 250\,\mathrm{ms}$ (see Fig. 8.5). We performed a linear fit to the logarithmic quantities and took into account the errobars on N_{v} in the weights of the fit. The fitted exponent $d_{\mathrm{v}} = 0.69\,(17)$

---

[19] Error-bars are obtained from a bootstrap method [196]. For this we use 10 000 bootstrap data samples and compute the confidence interval at $1/e$ of the mean from the set of vortex numbers extracted for all realizations at given t_{hold} and t_{evap}. The same bootstrapping method will be applied for the data in the rest of this chapter.

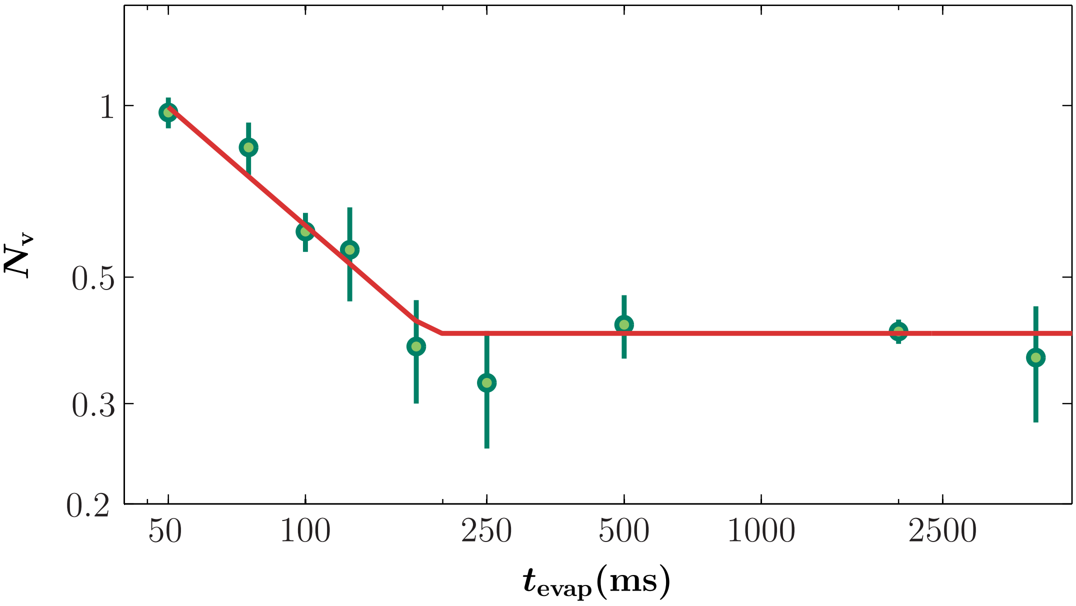

Figure 8.5.: Evolution of the mean number of vortices N_v with quench time t_evap for a fixed $t_\mathrm{hold} = 500\mathrm{ms}$ (green circle). The number of images per point ranges from 37 to 233 (mean number of images being 90 and median number 46). Error-bars are obtained from a bootstrapping approach (see footnote 19). We restrict to $t_\mathrm{evap} \geq 50\,\mathrm{ms}$ to ensure that local thermal equilibrium is reached at any time during the evaporation ramp ([195] and see Annex I for an estimation of the collision time in the weakly degenerate configurations). We fit of a power-law decay $N_\mathrm{v} \propto t_\mathrm{evap}^{-d_\mathrm{v}}$ to the short time data ($t_\mathrm{evap} \leq t_\mathrm{cut} \sim 250\,\mathrm{ms}$) and a plateau to the longer time data ($t_\mathrm{evap} > t_\mathrm{cut}$). The fit of the power-law decay restricted to $t_\mathrm{evap} \leq 250\,\mathrm{ms}$ gives an exponent $d_\mathrm{v} = 0.69\,(17)$. The simultaneous fit of the two behavior (red line) gives the same exponent $d_\mathrm{v} = 0.69\,(19)$, and a plateau at long time at $N_\mathrm{v} = 0.40\,(3)$. The threshold time between these two behaviors is fitted to $t_\mathrm{cut} = 189(56)\,\mathrm{ms}$.

is in good agreement with the prediction $d_\mathrm{v} = 2/3$ for the beyond *Mean–Field* prediction of *model F* given in 8.2 whereas the *MF* prediction for a pure mean-field transition, $d_\mathrm{v} = 1/2$, is notably lower than our result.

8.2.3.2. Description of the plateau at longer quench times

The non-zero plateau found for long t_evap may be the signature of the breakdown of the KZ model due to the restricted size of the gas in the transverse direction and the emergence of 2D physics as explained in 8.1.2. This emergence of 2D leads to a "cut" (or "smoothening") in the divergence of the coherence length ℓ_c at the characteristic gas thickness, of the order of the size of the transverse harmonic oscillator ground state ℓ_z. By proportionality, a similar "cut" is performed for the domain size $\hat{\xi}$ to some multiple of ℓ_z. We note $\hat{\xi} = q\ell_z$ and q set the proportionality factor at the plateau appearance[20]. As $\ell_z = 0.6\,\mu\text{m} \ll L$, then, the gas still holds an important number of domains in-plane, leading to a non-zero mean number of vortices nucleated. Due to the fixed size of the cut, this number remains constant with varying τ_Q, leading to a plateau.

From the value of the plateau $N_\text{v} \sim 0.4$, the deduced relation from laws of Eqs. 8.6 and 8.10, $\sqrt{ff_\text{v}}\,\hat{\xi} \sim L/\sqrt{N_\text{v}} = 47\,\mu\text{m}$ is compatible with usual range $f = 1$–5 ,$f_\text{v} = 5$–10 [176, 177, 186, 197] and choosing q within $12 - 40$ (see footnote 20 for validity of this range). We note that f_v must also take into account here some dissipation effects with the non-zero t_hold and may be greater than the range usually found in the literature, (typically by a factor $2 - 3$, see 8.2.4), this simply leads to a smaller range of $q = 4 - 20$. From these ranges, the whole picture appears to be consistent. It however seems difficult to conclude more assertively on the validity of the BEC$_\perp$ scenario by a quantitative analysis of the plateau value; such a limitation is in fact inherent to Kibble–Zurek formalism which sets proportionality relations more than accurate equalities.

8.2.4. Analyzing dissipation dynamics of the vortices

The variation of the number of vortices N_v with the hold time t_hold allows us to study the fate of vortices that have been nucleated during the evaporation. We quantitatively analyze this evolution (Fig. 8.6) after a short quench of $t_\text{evap} = 50\,\text{ms}$. We observe a decay of N_v with the hold time, from $N_\text{v} = 2.3$ initially to 0.3 at long hold time (2 s).

8.2.4.1. Principle of vortices dissipative dynamics simulations

To interpret this decay, we modeled the dynamics of the vortices in the gas. These simulations have been developed by a permanent member from our team, Sylvain Nascimbène. The modeled is based on two ingredients:

1. The conservative motion of a vortex in the velocity field created by the other vortices, including the vortex images from the boundaries of the box potential. Such image vortices, which are positioned outside the fluid are necessary to compensate for the velocity field created by a physical vortex (inside the fluid) at the edge of the gas and thus satisfy the boundary condition on the flow [198, 199]. Simulations are performed in a disk shape uniform trap of radius $R = \sqrt{\pi}L$ for conveniency of this geometry in terms of image determination. The velocity field generated by a vortex at distance $\boldsymbol{r}$ from the vortex core is [199]

$$\boldsymbol{u}(\boldsymbol{r}) = \pm\frac{\hbar}{m}\boldsymbol{u}_z \times \frac{\boldsymbol{r}}{\boldsymbol{r}^2} \tag{8.32}$$

---

[20] First we want to emphasis that as pointed out in 8.1.2 due to the further evolution of the 2D gas, this reasoning performed here to describe the plateau is a simplification. $\hat{\xi}$ may keep increasing after the crossing of the BEC$_\perp$ transition point but more slowly that what is expected for standard BEC. This must lead to correction and in particular q must be larger than our simple picture. In our simplified picture that matches well the observed variations of N_v, q has two origin: $\hat{\xi}$ must be a few correlation rms size ℓ_c, which itself must be of the order of magnitude of ℓ_z, typically $1 - 10 \times \ell_z$ (for ℓ_c a more precise estimate can be obtained using numerical computations as in 1.2.3.4, Table 1.1 and Fig. 1.3. However we cannot get a better insight on the dependency of $\hat{\xi}$ on ℓ_c from such simulations). Then q must roughly varies between 5 and 50.

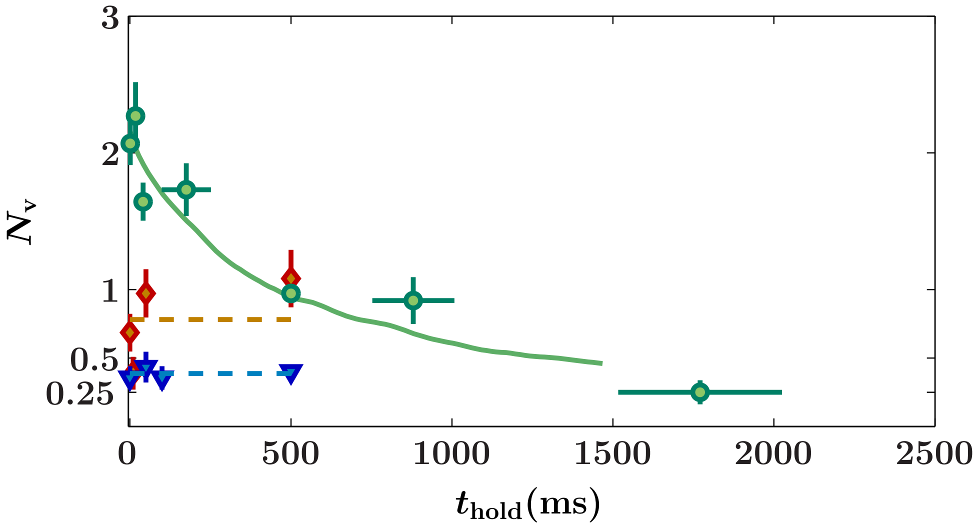

Figure 8.6.: Evolution of the mean vortex number N_v with the hold duration at the end of the evaporation ramp t_{hold}, for $t_{\mathrm{evap}} = 50\,\mathrm{ms}$ (green circles), $t_{\mathrm{evap}} = 200\,\mathrm{ms}$ (red diamonds), $t_{\mathrm{evap}} = 2000\,\mathrm{ms}$ (blue triangle). For the shortest quench time $t_{\mathrm{evap}} = 50\,\mathrm{ms}$, we note a decay of N_v decelerating with t_{hold}. Note that for this set of data, the number of images per point ranges from 24 to 181 (mean number of images being 59). We match this time evolution with simulations of vortices dynamics (see description in the text) and found damping coefficient $\alpha = 0.06(2)$ and initial vortex number $N_0 = 2.5(3)$. The green solid line shows the simulated evolution of N_v from the vortex dynamics dictated by the previously fitted coefficients and obtained from 100 initial cast. For $t_{\mathrm{evap}} = 200\,\mathrm{ms}$ (resp $t_{\mathrm{evap}} = 2000\,\mathrm{ms}$), the number of realizations is constant and equals to 36 (resp. ranges from 31 to 563). For longer quench times $t_{\mathrm{evap}} \gtrsim 200\,\mathrm{ms}$, we note absence of evolution of the mean vortex number within the error-bars (dashed line represent the weighted average value for each t_{hold} (same colors)). Error-bars are obtained from a bootstrapping approach (see footnote 19).

where $\boldsymbol{u}_z$ stands for the unitary vector along the vertical axis and the sign depends on the direction of the vortex phase winding. Then, in the presence of N vortices numbered by $i \in [\![1;\ N]\!]$, the velocity of the vortex j (in absence of dissipation) is given by

$$\boldsymbol{v}_j = \sum_{i \neq j} \boldsymbol{u}_i(\boldsymbol{r}_j - \boldsymbol{r}_i) \tag{8.33}$$

where r_i is the position of the vortex i and $\boldsymbol{u}_i(\boldsymbol{r})$ its velocity field given by Eq. 8.32.

2. The dissipation induced by the scattering of thermal excitations by the vortices, which results in a friction force [199]. Following calculations from [200], the effect of a vortex on the velocity of a second vortex distant from $\boldsymbol{r}$ can be grasped by a

modification of its velocity field $\boldsymbol{u}(\boldsymbol{r})$ given in Eq. 8.32 by adding

$$\delta\boldsymbol{u} = \frac{n_\mathrm{n}}{n_\mathrm{s}}\left(-\boldsymbol{u}(\boldsymbol{r}) + \sqrt{\frac{gn_0}{k_\mathrm{B}T}}\boldsymbol{u}(\boldsymbol{r}) \times \boldsymbol{u}_z\right) \tag{8.34}$$

where n_s, n_n and n_0 stands respectively for the superfluid, the non superfluid and the condensed density so that $n = n_\mathrm{s} + n_\mathrm{n}$. $g = \hbar^2\tilde{g}/m$ is the 2D interaction parameter. Then in the presence of N vortices, the velocity of the vortex j is modified along

$$\begin{aligned} \boldsymbol{v}_j &= \sum_{i\neq j}\left(\boldsymbol{u}_i(\boldsymbol{r}_j-\boldsymbol{r}_i) + \delta\boldsymbol{u}_i(\boldsymbol{r}_j-\boldsymbol{r}_i)\right) && (8.35)\\ &= \sum_{i\neq j}|\boldsymbol{u}_i(\boldsymbol{r}_j-\boldsymbol{r}_i)|\left[\left(1-\frac{n_\mathrm{n}}{n_\mathrm{s}}\right)\boldsymbol{u}_z \times \frac{\boldsymbol{r}_j-\boldsymbol{r}_i}{|\boldsymbol{r}_j-\boldsymbol{r}_i|} + \frac{n_\mathrm{n}}{n_\mathrm{s}}\sqrt{\frac{gn_0}{k_\mathrm{B}T}}\frac{\boldsymbol{r}_j-\boldsymbol{r}_i}{|\boldsymbol{r}_j-\boldsymbol{r}_i|}\right] && (8.36) \end{aligned}$$

Here, we will neglect the effect of the slowing down of the motion and only consider the arising of a transverse component to the velocity such that the velocity of the vortex j approximates to

$$\boldsymbol{v}_j \approx \sum_{i\neq j}\left(\boldsymbol{u}_i(\boldsymbol{r}_j-\boldsymbol{r}_i) + \frac{n_\mathrm{n}}{n_\mathrm{s}}\sqrt{\frac{gn_0}{k_\mathrm{B}T}}\,|\boldsymbol{u}_i(\boldsymbol{r}_j-\boldsymbol{r}_i)|\,\frac{\boldsymbol{r}_j-\boldsymbol{r}_i}{|\boldsymbol{r}_j-\boldsymbol{r}_i|}\right) \tag{8.37}$$

Then the friction is characterized phenomenologically by a unique damping coefficient $\alpha = \frac{n_\mathrm{n}}{n_\mathrm{s}}\sqrt{\frac{gn_0}{k_B T}}$.

To compare the predictions of this model to our data, we perform simulations of the evolution of an initial set of several vortices along the system of equations bearing on the vortex positions and velocities deduced from Eq. 8.37 (along with the straightforward relation $v_j = \mathrm{d}r_j/\mathrm{d}t$). The initial distribution of vortices is randomly cast with the following characteristics:

- the number of vortices per realization is a random number drawn from a Poissonian distribution of parameter N_0 that represent the mean vortex number at $t_\mathrm{hold} = 0\,\mathrm{ms}$.
- the positions of the vortices on the cloud are randomly chosen with an initial uniform probability for distributing the vortices on the cloud.
- the charges of the vortices are also randomly chosen without any correlation between them.

While varying t_hold along this simulated evolution, vortices move within the cloud and we "manually" annihilate them (*i.e.* erase from longer time evolution simulation) in two cases:

- when they get too close to the edges of the trap, that is their distance from the center is larger than $0.999R$. We then physically expect the vortex to be absorbed by the edges of the trap.
- when they get too close to an other vortex of opposite sign, that is when their distance become smaller than $0.001R$. We then physically expect that the two vortices merge together and annihilate.

8.2.4.2. Results of vortex dissipative dynamics simulations

We record a from numerical resolution of this model, the mean vortex number N_{v}, the occurrence of a given vortex number and the vortex positions from which we analyze individual locations and correlations (see following sections). In particular, it leads to a non-exponential, slowing down decay of N_{v}, with details that depend on the initial number of vortices N_0 and the cloud superfluid fraction n_{s}/n. We match this evolution to our experimental data by varying both N_0 and α and by minimizing the χ^2 distance of the simulated evolution to the experimental data (their confidence intervals are deduced by the analysis of the curvature of this χ^2). We take into account the effective initial value of t_{hold} induced in the end of the evaporation ramp of 32.5 ms as $t_{\mathrm{evap}} = 50$ ms (see 8.1.3.2). From this match, we find $\alpha = 0.06(2)$ and $N_0 = 2.5(2)$. In the following, we assume that α is a constant for all considered t_{evap} (due to local thermalization condition) so that we can predict the evolution for all initial value of the vortex number N_0. From the fitted value of α, we can then perform simulations and record vortex numbers, positions and correlations evolutions with t_{hold} for various t_{evap}.

For the estimating thermal fraction n_{n}/n in the final cloud configuration, we use an estimate of the 2D interaction parameter g from the 3D Gross–Pitaevskii imaginary time simulations (as in 8.2.1, see Annex B for details). For the considered atomic density $n = 50\,\mu\mathrm{m}^2$ and assuming $n_0 \sim n$ we found $g n_0 \approx k_{\mathrm{B}} \times 11\mathrm{nK}$. The resulting thermal fraction is $n_{\mathrm{n}}/n \approx 0.06(2)$.

8.2.4.3. Further observations on the evolution with t_{hold}

For longer quenches $t_{\mathrm{evap}} \gtrsim 200$ms, we note an absence of evolution of N_{v} with t_{hold}, within error-bars (see footnote 19). This is due to the fact that the fast start of the dissipative evolution is in reality hidden within the end of the evaporation ramp. Indeed, as computed in 8.1.3.2, we found that the transition occurs at $t^* = 0.35 t_{\mathrm{evap}}$ so that for t_{evap} of a fews hundreds of ms, the fast decay that is observed at $t_{\mathrm{hold}} \lesssim 100$ ms is fully hidden within the end of the evaporation ramp and the predicted slow decay is negligible.

We note that for $t_{\mathrm{evap}} = 50$ ms at short t_{hold}, the images of the clouds are quite fuzzy, probably because of the presence of important non thermal phononic excitations produced (in addition to vortices) by the evaporation ramp. This is the origin of the fluctuations of N_{v} at short t_{hold} visible in Fig. 8.6, as it is then difficult to make a precise counting of vortices. The choice $t_{\mathrm{hold}} = 500$ ms for studying the quench dynamics in Fig. 8.5 was made according to the two latter observations.

The finite lifetime of the vortices in our sample points to a general issue that one faces in the experimental studies on the KZ mechanism. In principle the KZ formalism gives a prediction on the state of the system within the freezing out period around the transition (*i.e.* $t \in [t^* - \hat{t}, t^* + \hat{t}]$). Experimentally we observe the system at a later stage, at a moment when the various domains have merged, and we detect the topological defects formed from this merging. In spite of their robustness, the number of vortices is not strictly conserved after the crossing of the transition, and its decrease depends on their initial positions. A precise comparison between our results and KZ theory should take this evolution into account, for example using stochastic mean-field methods [201, 202].

8.2.5. Complementary analysis

8.2.5.1. Evolution in occurrence of vortex numbers

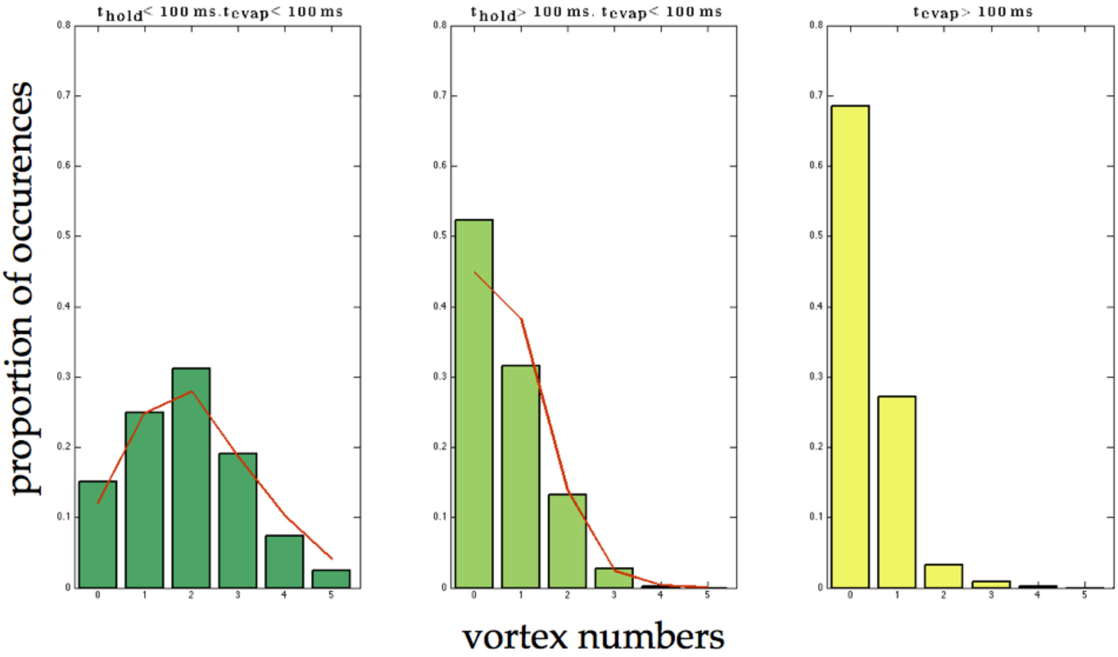

Figure 8.7.: Proportion of occurrence of vortex numbers for three ranges of couples(t_{hold},t_{evap}): **(left)** dark–green histogram for $t_{\text{evap}} \leq 100$ms, $t_{\text{hold}} \leq 100$ms (205 images) , **(middle)** middle–green histogram $t_{\text{evap}} \leq 100$ms, $t_{\text{hold}} > 100$ms (656 images), **(right)** yellow histogram for $t_{\text{evap}} > 100$ms, all t_{hold} (1499 images). Results of dissipative dynamics simulations for $N_0 = 2.5$ and $\alpha = 0.06$ (corresponding to the fit performed in Fig. 8.6 and so to $t_{\text{evap}} \sim 50$ ms) are plotted in red lines on the relevant histogram (that is $t_{\text{evap}} \leq 100$ms, see footnote 21). We perform evolution from 5000 initial casts. To obtained the simulated curves, we simulated various t_{hold} and we averaged the same proportion of evolutions at a given t_{hold} as in the experimental histograms.

We previously highlighted that the number of vortices detected per atomic realization varies from shot to shot, revealing their stochastic origin. We note that as N_{v} varies with both t_{hold} and t_{evap}, the probability of occurrence of a given number of vortices evolves similarly. In Fig. 8.7, we compare histograms of occurrence for long and short characteristics times. We note a strong evolution of the histogram for both short t_{hold} and t_{evap} compared to long t_{hold} or long t_{evap}.

The evolution with t_{hold} after a short quench time ($t_{\text{evap}} \leq 100$ ms) is embedding the fast decay analyzed in the previous subsection in terms of N_v and can be nicely reproduced by the previously presented dissipative dynamics simulations of 8.2.4.1[21]. For long quench times, there is no visible effect of holding the gas on the number occurrence. In this case, the initial fast decay of the vortex number is hidden within the end of the evaporation ramp. Then, we represented a unique histogram for all the value of t_{hold}.

The evolution of the size of the patches with the quench time is also embedded in the occurrence of a given vortex number for one cloud realization while varying t_{evap}. For short quench times ($t_{\text{evap}} \leq 100$ms), multiple vortices probability is non negligible whereas for long quench times ($t_{\text{evap}} > 100$ms), we usually excite only a single vortex or none.

8.2.5.2. Vortices location

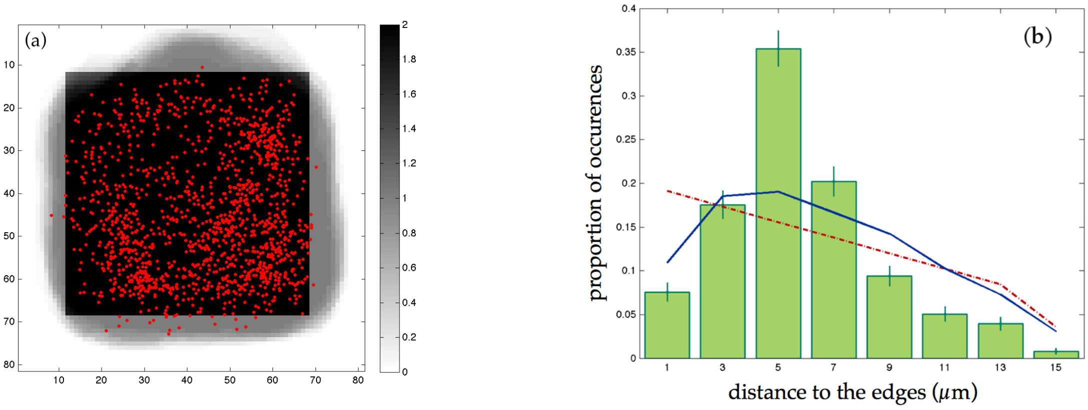

Figure 8.8.: (a) Positions of the detected density holes (red points) after a ToF expansion of 4.5 ms for $t_{\text{evap}} = 50$ms and all values of t_{hold}. We represent their position on a schematic representation of the initial square uniform trap (dark region) that we position by centering it on the center of mass of the detected atomic distribution. The mean region of non negligible density after the ToF expansion is represented in gray. **(b)** Histogram of the distances to the edges of the initial box for the same data set as in (a) (green histogram). Error-bar are obtained from a bootstrapping approach. The red line correspond to the histogram for random positions of the vortices over the square. The blue solid line is the result of dissipative dynamics simulation computed with $N_0 = 2.5$ and $\alpha = 0.06$ that are the fitted values for an evolution after a quench of $t_{\text{evap}} \sim 50$ ms. The histogram is obtained from 5000 initial draws. We simulated various t_{hold} and we averaged the results of these simulations by considering the same proportion of evolutions at a given t_{hold} as in the experimental histogram.

We characterize the position of the vortices in the cloud by their distance to the edges of the initial square box of length $L = 30\,\mu$m. We thus assume that:

---

[21] The fitted parameters $N_0 = 2.5$ and $\alpha = 0.06$ corresponding to the fit of experimental data taken with $t_{\text{evap}} = 50$ ms are only relevant for the short $t_{\text{evap}} \leq 100$ ms. For longer t_{evap}, a lower value of N_0 must be used to perform similar simulation. Such a value can not be deduced from our dissipative simulations. We must either perform a fit at longer t_{evap} or rely on the KZ scaling analyzed in 8.2.2.

— the center of mass of the ToF density distribution is the same as the original one.

— their displacement during the 4.5ms of ToF is negligible so that the detected position is a good estimation of their initial position.

In Fig. 8.8 we show the histogram of the distances to the edges of the box for all configurations of t_{hold} and for fixed $t_{\mathrm{evap}} = 50\,\mathrm{ms}$. We note a distortion compared to a perfectly randomly distributed set of vortices by both a depletion of the edges and of the center. From the dissipative dynamics simulation (see 8.2.4.1), we can predict the effect of the hold time on the vortex distribution. We perform such a statistical analysis of a high number (typically 5000) of simulated configurations initially drawn with $N_0 = 2.5$ and evolved with $\alpha = 0.06$. We average on the same t_{hold} spreading than experimental data (see Fig. 8.6 for more information on this data set). Such a simulation explains well the depletion from the edges but not the observed depletion of the center.

Such a depletion of central region may be linked to KZ mechanism itself. Indeed, as KZ mechanism is linked to a geometrical argument of phase patches spatial organization (see 8.1.1), it is easier to organize phase patches to create a vortex configuration (that is an organization where a phase winding around several patches is created) at the edges, as the absence of atoms intuitively reduces the constraint on the spatial organization of the patches (that are thus in lower number at the edges).

8.2.5.3. Correlation between the vortices

On the whole set of data (all t_{evap} and all t_{hold}), we also compute the mean distance to the closest vortex for all multiple vortices realizations while varying both t_{evap} and t_{hold} (Fig. 8.9). Such an analysis enables studying the dynamics of correlations between the vortices. We first note that the longer t_{hold} is, the further away the vortices are located. Such a moving apart of the vortices is well reproduced by dissipative dynamics simulation results performed as in previous paragraph. At this point of the analysis, it is not easy to comment on the specific shape of the distances distribution as statistic is not high enough and simulations are too naive.

8.2.6. Conclusion

In this section, we have presented measurements on the detection of free vortices in a strongly degenerate 2D gas. We showed that these vortices have a stochastic and dynamical origin that we identified as being due to the KZ mechanism. We performed a quantitative analysis of the scaling of the mean vortex number N_{v} as a function of the quench duration t_{evap} for both the short t_{evap} values at which we expect a power-law scaling and at long t_{evap} values at which we expect a significantly slower decay N_{v}. In our case the long time evolution is compatible with a plateau at $N_{\mathrm{v}} \sim 0.4$. The short-t_{evap} power-law fit reveals the universal behavior at $\mathrm{BEC}_{\perp}$ transition or crossover and is equals to $d_{\mathrm{v}} = 0.69(17)$, corresponding to a scaling for the domain size $\hat{\xi}$ of $d = 0.35(9)$, compatible with beyond *MF* predictions $d = 1/3$ (see 8.2). We noted that the dissipative dynamics of the vortices may constitute a limitation to our analysis and we performed a physical analysis of this process. We developed a modeling for this dissipative dynamics which account for the observed slowing-down decay of N_{v} and estimate the

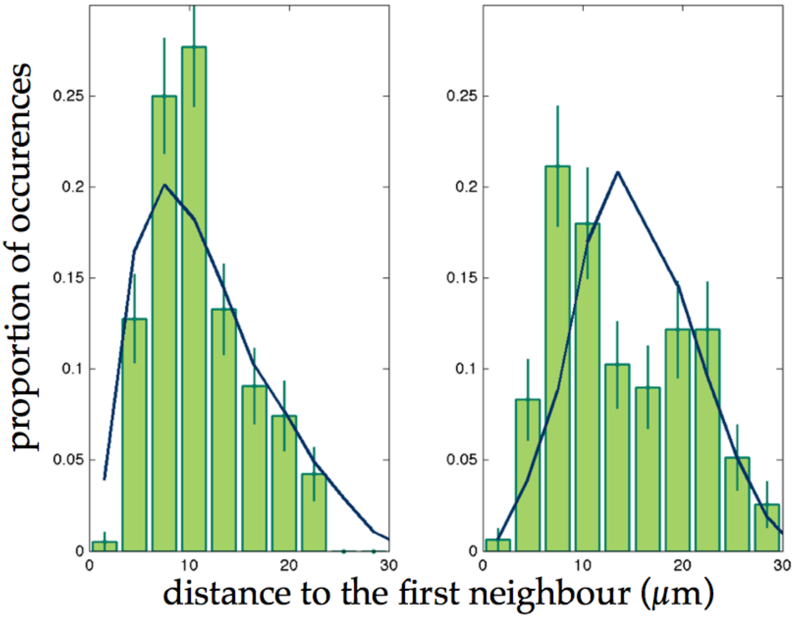

Figure 8.9.: Histograms of distances to the first neighboring vortex per atomic sample for all possible evaporation time and **(left)** $t_{\mathrm{hold}} \leq 100\,\mathrm{ms}$ **(right)** $t_{\mathrm{hold}} > 100\mathrm{ms}$. Histograms are made from 188 (resp. 158) distances for the different times domains. The blue solid lines are the result of dissipative dynamics simulation computed with $N_0 = 2.5$ and $\alpha = 0.06$ that are the fitted values for an evolution after a quench of $t_{\mathrm{evap}} \sim 50\,\mathrm{ms}$. The histogram is obtained from 5000 initial casts. We simulated various t_{hold} and we averaged the results of these simulations by considering the same proportion of evolutions at a given t_{hold} as in the respective experimental histograms they described.

superfluid fraction of our gas $n_s/n \approx 0.94(2)$. This model is however too limited to perform a quantitative correction of the scaling law exponent d. We noted that the finite size of the system may also induce some limitations to this scaling. Finally we performed some complementary but preliminary analysis on the vortex spatial distributions that would be interesting to push further in order to shed a new light on the nucleation process and the dissipation dynamics. In the next section, we will present another experimental study of the KZ physics based on the detection of supercurrents in an annular geometry. This second geometry allows us to complement the present analysis, leading to a second estimate of the scaling exponent d via the measurement of d_w. It will also give access to other properties such as the sign and the charge of the topological defects.

8.3. Nucleation of supercurrents in an annular Bose gas via Kibble–Zurek mechanism

In this section, we describe a second experimental procedure to study Kibble–Zurek mechanism. In this study we use a geometry reproducing the original argument considered by Zurek [89] by studying the phase winding of a (super-)fluid in an annular geometry. In this geometry, the phase winding of the macroscopic wavefunction around the annulus must be a multiple of 2π, ensuring the quantization of the circulation of the fluid velocity. Supercurrents in annular BECs are usually created in a deterministic way by using laser beams to impart angular momentum on the atoms [79, 81, 203] or by rotating a weak link along the annulus [204]. Here we study supercurrents that have a stochastic origin, justify it, describe their nucleation rate and compare it to KZ predictions. For each realization of the experiment, we use a novel method, based on matter-wave interferences between this annulus and a central disk acting as a phase reference, to measure the charge as well as the sign of the random supercurrent [22].

8.3.1. Characterizing vortices current by matter-wave interference in a target

8.3.1.1. Experimental sequence

For these measurements, we use a target-like box potential, consisting of a disk of radius $R_0 = 4.5\,\mu$m surrounded by a ring of inner (resp. outer) radius of $R_{\mathrm{in}} = 9\,\mu$m (resp. $R_{\mathrm{out}} = 15\,\mu$m) (see Fig. 6.9 for an example of in-situ density distribution). Transverse confinement is $\omega_z/2\pi = 365\,$Hz. As in the previous section, once the 2D traps are loaded we perform evaporative cooling by ramping down the box potential barrier height U_{box} in a time t_{evap} to its final value and hold it at this constant value for a time t_{hold}. The final temperature is $\sim 10\,$nK and the surface densities are similar in the ring and the disk and equal to $n^{(2D)} \approx 80\,\mu\mathrm{m}^{-2}$. From 3D imaginary time Gross Pitaevskii calculations (see Annex B), we deduce that typical interaction energy per atom is $\epsilon_{\mathrm{int}} \approx k_{\mathrm{B}} \times 8\,$nK (Eq. B.24), and the gas is marginally quasi-2D with $k_{\mathrm{B}}T$, $\epsilon_{\mathrm{int}} \lesssim \hbar\omega_z$. These parameters correspond to a large 2D phase-space-density, $\mathcal{D} = \rho\lambda^2 \geqslant 100$, so that the gas is deeply in the superfluid regime at the end of the evaporation ramp.

We use matter-wave interference to probe the relative phase distribution between the cloud in the central disk and the one in the ring by performing a 2D ToF, similar to the detection of the fringes in 7.3 except that in the present case the interaction energy of the gas is non negligible: We abruptly switch off the box-potential while keeping the confinement along the z-direction. The clouds experience a hydrodynamical expansion during which the initial interaction energy is converted into kinetic energy. After 7 ms of expansion, we record the interference pattern by imaging the atomic gas along the vertical direction.

---

[22] A similar method has recently been developed to investigate the supercurrent generated by a rotating weak link [205]

8.3.1.2. Identifying supercurrent from fringe patterns

Typical interference patterns are shown in Fig. 8.10. Most of them consist in concentric rings, as expected for a quasi-uniform phase distribution in the disk and the annulus. However we also observe a significant fraction of spiral patterns, revealing the presence of a phase winding in the wavefunction of one of the two clouds.

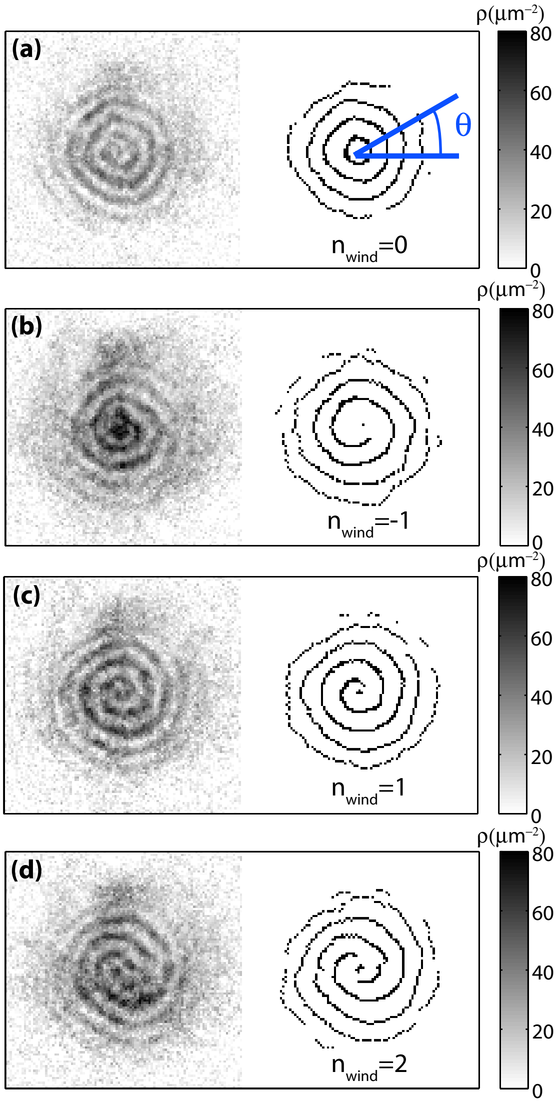

Figure 8.10.: Experimental interference patterns. Examples of interference patterns after expansion in the 2D plane, along with contrast-amplified pictures. (a) without phase winding, **(b)** with phase winding -2π, **(c)** with phase winding $+2\pi$, **(d)** with phase winding $+4\pi$.

We developed an automatized procedure to analyze these patterns, which reconstructs the phase $\phi(\theta)$ of the fringes along a line of azimuthal angle θ. This method has been implemented by a PhD student of our team, Laura Corman. For each picture, the center is determined manually. Then we proceed in two steps to reconstruct the phase profile: contrast amplification and fit.

To amplify the contrast, the pictures are first convoluted by a 2×2 matrix with constant coefficients. This filters out high frequency noise but does not blur the interference pattern. Then radial cuts with angle $\theta \in \{0, 2\pi/n, \cdots, 2\pi(1-1/n)\}$ are performed (typically $n = 150$), and the positions of local maxima are recorded, giving the contrast amplified picture.

To retrieve the phase, we perform a convolution of the contrast amplified picture with a gaussian of width 3 pixels and we fit the radial cuts of the convoluted, contrast-amplified pictures with the function:

$$f(r, k, \phi, A, c) = A \sin(kr + \phi) + c \tag{8.38}$$

for points with distance to the center $r \in [r_{\text{min}}, r_{\text{max}}]$. First, the parameter k is left as a free parameter to fit the radial cuts. Then the averaged k_{mean} over all fits is taken as a fixed parameter and all the radial cuts are fitted again. The phase ϕ is recorded as a function of the angle θ of the radial cut [23]. From the accumulated phase $\Delta\phi$ as the angle θ varies from 0 to 2π, we associate to each pattern a winding number $n_{\text{w}} = \Delta\phi/2\pi$, which is a positive, null or negative integer.

8.3.2. Studying the supercurrent origin

8.3.2.1. Stochastic Origin

We record n_{w} for many realizations of the same experimental sequence. It takes a random value varying from -2 to 2 (with a probability varying when varying t_{evap}). The average mean winding number over all the runs is compatible with a zero mean value. We show in Fig. 8.11 an example of measured probability distribution of n_{w} for the ensemble of data shown in Fig. 8.13. It corresponds to $\langle n_{\text{w}} \rangle = 0.001 \pm 0.012$. This confirms the stochastic nature of the mechanism at the origin of this phase winding.

8.3.2.2. Location of the phase winding

The phase winding at the origin of spiral-like interferences patterns can be due either to a vortex in the central disk or to a quantized persistent current in the outer ring. We can experimentally eliminate the first possibility by noticing that we never observe any vortex signature in the small disk of radius $R_0 = 4.5\mu$m by the method presented in 8.2, performing short 3D ToF. Hence we conclude that the spiral interference patterns reveal the presence of a supercurrent in the annulus, whose charge and orientation correspond to the modulus and sign of the winding number n_{w}.

By varying the hold duration t_{hold} at the end of the experimental sequence with a constant value of the evaporation duration t_{evap}, we measure the lifetime of this supercurrent. We perform this measurement for $t_{\text{evap}} = 2\,\text{s}$ and measure a lifetime of $7\,\text{s}$,

---

[23] ϕ is define up to a multiple of 2π. As we are interested in the difference $\phi(\theta = 2\pi(1-1/n)) - \phi(\theta = 0)$, we are not sensitive to the absolute value of ϕ but we take care of making this function continuous for θ varying from 0 to 2π by applying unwrapping procedure. This is that no jump of ϕ larger than 2π is tolerated for two successive θ, $\theta_j = 2\pi \times j/n$ and $\theta_{j+1} = 2\pi \times (j+1)/n$.

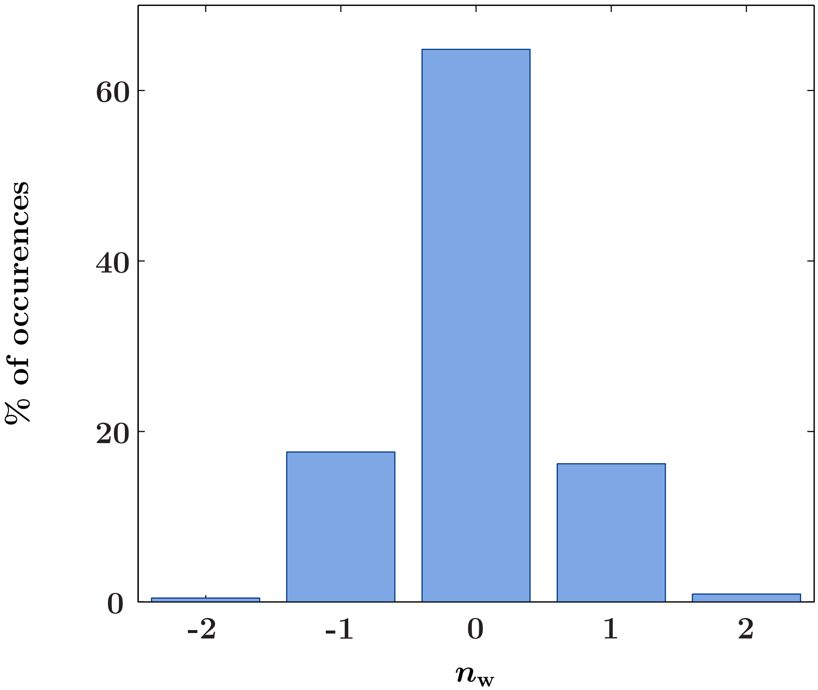

Figure 8.11.: Histogram showing the distribution of the winding numbers n_{w} for all data shown in 8.13, with $t_{\mathrm{hold}} = 0.5\,\mathrm{s}$ and t_{evap} varying from 25 ms to 2 s. In total, this graph includes 237 realizations and 6 different t_{evap}. It corresponds to an average of $\langle n_{\mathrm{w}} \rangle = 0.001 \pm 0.012$.

similar to the cloud lifetime (see Fig. 8.12).

8.3.2.3. Dynamical origin

As for the vortices observed in 8.2, the supercurrents can either be due to thermal excitations or result from the quench cooling. Similar to what was performed in 8.2.2, we show here that due to the high degeneracy of the final configuration, a thermal explanation of the observed probability of n_{w} is precluded. Indeed, if these currents had a thermal origin, their probability of occurrence would be given by the Boltzmann law $p(n_{\mathrm{w}}) \propto \exp\left[-E(n_{\mathrm{w}})\,/\,k_{\mathrm{B}}T\right]$, where the energy of the supercurrent is

$$E(n_{\mathrm{w}}) = n_{\mathrm{w}}^2 \, \frac{\pi\hbar^2 n}{m} \, \ln\left(R_{\mathrm{out}}/R_{\mathrm{in}}\right). \tag{8.39}$$

taking into account only the kinetic term [24]. This leads to

$$p(n_{\mathrm{w}}) \propto \left(R_{\mathrm{in}}/R_{\mathrm{out}}\right)^{n_{\mathrm{w}}^2 \mathcal{D}/2}, \tag{8.40}$$

---

[24] We neglect modification of the surface density n due to the presence of the vortices. This is a good approximation, especially in this geometry, as the effect of the vortex on the density extends over a size of the order of the healing length $\varsigma \sim 0.5\,\mu\mathrm{m}$ around the vortex core. Eq. 8.39 corresponds to a vortex core with the central region $r \leq R_{\mathrm{in}}$, then the modification of the density is negligible.

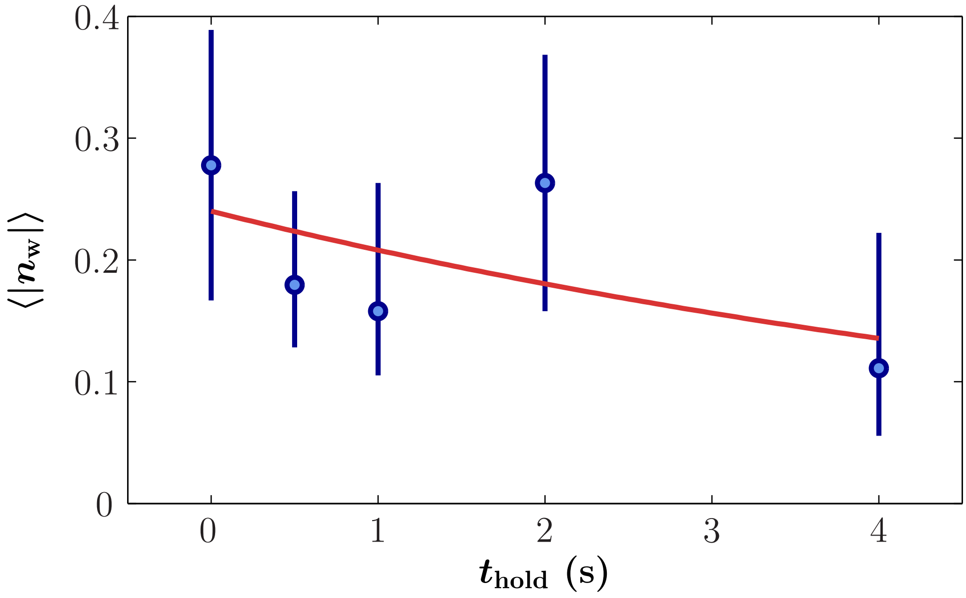

Figure 8.12.: Mean absolute winding number as a function of hold time ($t_\mathrm{evap} = 2\,\mathrm{s}$). Average number of realizations per point is 22.6. The data is fitted with an exponential with a time constant of 7 s.

which is vanishing small for $n_\mathrm{w} \neq 0$ for our large final phase space densities $\mathcal{D} \geq 100$, in clear disagreement with the typical 20-50% of pictures showing phase winding. Note that the probability for a vortex to appear in the central disk as a thermal excitation is even smaller than (8.40) because R_in and R_out should be replaced respectively by the healing length ς and R_0.

This simple calculation confirms the dynamical origin of the supercurrents observed within the ring. Both the dynamical and the stochastic natures of the nucleation mechanism strongly promote an explanation through KZ mechanism.

8.3.3. Studying the quench dynamics

8.3.3.1. Fit of the power-law exponent for quench dynamics.

To check that the quench cooling is indeed responsible for the formation of these supercurrents, we study the variation of $N_\mathrm{w} = \langle |n_\mathrm{w}| \rangle$ for evaporation times spanning two orders of magnitude. We summarize in Fig. 8.13 the experimental variation of N_w with t_evap. We note an overall decrease of N_w from 0.6 ($t_\mathrm{evap} = 0.025\,\mathrm{s}$) to 0.2 ($t_\mathrm{evap} = 2\,\mathrm{s}$). A power-law fit to the data, inspired by the prediction for the KZ mechanism, leads to $N_\mathrm{w} \propto t_\mathrm{evap}^{-d_\mathrm{w}}$ with $d_\mathrm{w} = 0.19(6)$. Such an exponent is in good agreement with beyond *Mean-Field* prediction of $d_\mathrm{w} \approx 0.17$ and slightly disagreed from *MF* predictions of $d_\mathrm{w} = 0.125$ obtained for a large number of domains $N_\mathrm{d} \gg 1$. We note that the average windings measured $0.2 \leq N_\mathrm{w} \leq 0.6$, must in fact correspond to moderately

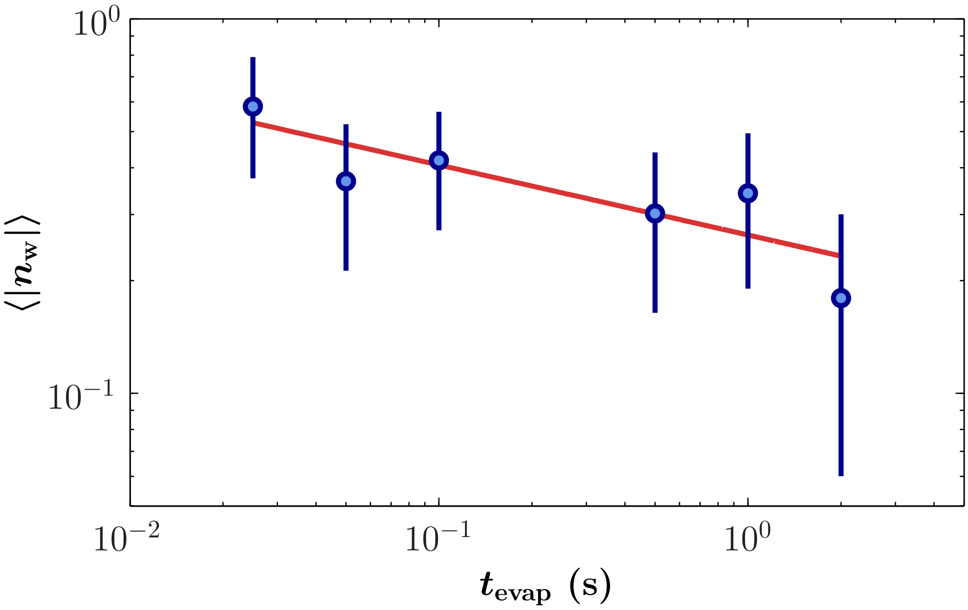

Figure 8.13.: Mean absolute winding number as a function of evaporation time. ($t_{\mathrm{hold}} = 0.5\,\mathrm{s}$) in log-log scale. Average number of realizations per point is 39.5. A power-law fit to the data, $\langle |n_{\mathrm{w}}| \rangle \propto t_{\mathrm{evap}}^{-d_{\mathrm{w}}}$, gives $d_{\mathrm{w}} = 0.19(6)$.

large values of N_{d}. Using the random-walk[25] relation $N_{\mathrm{d}} \sim 12N_{\mathrm{w}}^2$ (expected to be valid for $N_{\mathrm{d}} \gg 1$), we estimate that $N_{\mathrm{d}} \lesssim 10$. Then the power-law scaling must be modified and the exponent d_{w} predicted must then take an intermediate value between predictions of Eqs.8.8 and 8.7.

8.3.3.2. Estimation of domain numbers and corrections of the power-law scaling

To interpret our results we have developed a simple one-dimensional (1D) model following the KZ scenario presented in [89, 177]. This study has been carried out by a permanent member from our team, Jérôme Beugnon. We consider a 1D ring of perimeter L and we assume that, when $\mathrm{BEC}_\perp$ is crossed, N_{d} domains of uniform phase φ_j, $j \in [\![\, 1;\ N_{\mathrm{d}} \,]\!]$ are created. As we are interested in $\Delta\varphi = \sum_{j=1}^{N_{\mathrm{d}}-1} (\varphi_{j+1} - \varphi_j)[2\pi]$ (see 8.1.1), we consider the phase steps $\phi_j = (\varphi_{j+1} - \varphi_j)[2\pi]$ for $j \in [\![\, 1;\ N_{\mathrm{d}} - 1 \,]\!]$. Each run of the experiment is modeled by a set of $\{\phi_j\}$ where the phases ϕ_j are independent random variables uniformly drawn in $(-\pi, \pi]$. For each set of $\{\phi_j\}$ we calculate the total phase variation along the ring $\Delta\varphi = \sum_j \phi_j$ and define n_{w} as the nearest integer to $\Delta\varphi/2\pi$. We then average over many draws of the set $\{\phi_j\}$ and compute an average winding num-

---

[25] To obtain this relation we consider a one-dimensional random walk on the phase steps ϕ_i between neighboring patches (numbered i and $i+1$) as detailed in 8.3.3.2. Then all ϕ_i are random variables uniformly drawn in $(-\pi, \pi]$. Then $\Delta\varphi = |\sum_i \phi_i| \sim_{N_{\mathrm{d}} \gg 1} \sqrt{N_d}\, \Delta\phi$ where $\Delta\phi = \pi/\sqrt{3}$ is the standard deviation of the variables ϕ_i. Then $n_{\mathrm{w}} = \Delta\varphi/2\pi \sim_{N_{\mathrm{d}} \gg 1} \sqrt{N_{\mathrm{d}}/12}$

ber N_w. We report on Fig. 8.14 the computed variations of N_w as a function of N_d. For large values of N_d we find that N_w scales like $\sqrt{N_\mathrm{d}}$ as expected from Eq. 8.7.

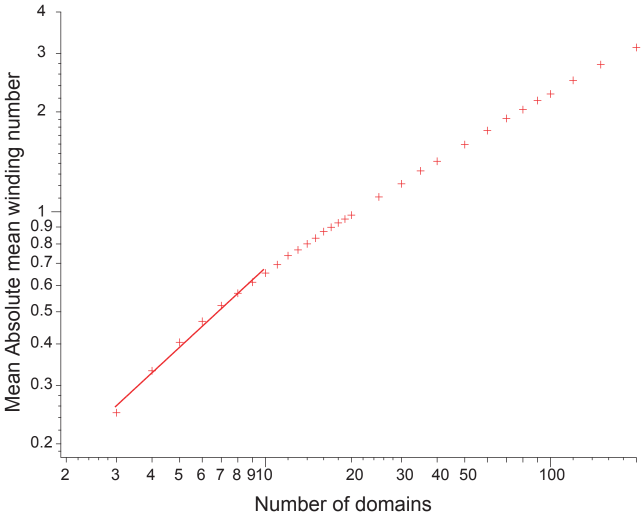

Figure 8.14.: Average absolute winding number as the number of phase domains is increased in log-log scale. The points are the results of the simulation and the line the power-law fit to points for the relevant regime for the experiments described here.

Our experimental range $0.2 \leq N_\mathrm{w} \leq 0.6$ is obtained for $3 \leq N_\mathrm{d} \leq 10$ in this model. In this domains, we do not expect to recover an exact power-law behavior but in first approximation a power-law fit to the predicted variations of N_w to N_d gives

$$N_\mathrm{w} \propto N_\mathrm{d}^{0.8} \, . \tag{8.41}$$

with an increase of the exponent from 0.5 to 0.8 compared to the large N_d case. Then the expected power-law scaling as a function of the quench time t_evap is $d_\mathrm{w} = 0.2$ for *MF* prediction and $d_\mathrm{w} = 0.27$ for beyond *MF* prediction. Such corrections make unclear with which model our data best agree with. In addition, other effects may also be considered such as the role of the predicted long time plateau (see 8.1.2 for a description of this effect) or other finite size effects.

We note from this model that the expected size $\hat{\xi}$ of the domains varies from 7 to 25 μm. Then $\hat{\xi}$ is larger than the transverse size of the annulus, which justifies the use of a 1D model. $\hat{\xi}$ is also larger than the size R_0 of the central disk, which confirms the fact that we do not observe any vortex in this small disk. The two main assumptions in these calculations are then auto-coherently verified. This model remains a simple insight on the phase winding establishment in the superfluid assuming independent choice of the phases on a given number of predefined domains. To better predict the phase winding scaling with the quench time more sophisticated calculations must be performed such as using Stochastic Gross–Pitaevskii Equation (SGPE) [177].

8.3.3.3. Corrections due to predicted long time plateau for quench through $\mathrm{BEC}_\perp$

As described in 8.1.2, the transition that leads to freezing out of coherent domains is the transverse condensation. In this crossing, the in-plane correlation length is limited by the transverse extension of the cloud and for long enough quench times, the number of domains created must be fixed only by ℓ_z and not by the quench rate. This would then result in a non-zero plateau for N_w. From the quality of our data we cannot distinguish such a plateau. However, the physical configuration studied in this section is not drastically different from the one studied in previous section 8.2 for which a plateau was clearly [26] observed for t_evap longer than several hundreds of ms. Assuming a similar threshold time appears compatible with the data of Fig. 8.13. If it is true that we expect a reduced variation of N_w at $t_\mathrm{evap} \gtrsim 250\,\mathrm{ms}$, the power-law fit for t_evap up to 2 s must underestimate the actual exponent d_w (for $t_\mathrm{evap} \lesssim 250\,\mathrm{ms}$) as it approximate the "kinky" variation in a straight one, slower than the actual start. Such an underestimate may conclude to a better agreement with beyond *MF* expectations of *Model F* while still considering corrections due to small N_d, compared to previous conclusions.

8.3.4. Other limitations

As for the vortex nucleation described in 8.2, limitations to the predicted scaling laws may come from:

- the modification of the power-law scaling due to the finite size of the box.
- the variation of the effective hold time with t_evap even though we note that in this case it must have less influence due to the long lifetime of the supercurrents observed
- the effects of inhomogeneities of the trap potential along the annulus (see 6 for a description of these non-homogeneities).

There is another assumption specific to this geometry that could limit the validity of the theoretical description of the annulus as a 1D chain of domains. Domains are in fact 3D patches of fluids and vortices can be generated in the volume of the fluid as described in the previous section 8.2. Such an event remains very seldom due to the size of the system: the transverse size along the annulus is $6\,\mu\mathrm{m}$ while the minimum average size of the domains deduced from simple modeling of 8.3.3.2 is $7\,\mu\mathrm{m}$, justifying the 1D description in first approximation.

8.3.5. Characterizing phonons from fringes patterns

In this last paragraph, we show that one can extract more information from the interference patterns, which goes beyond the determination of the topological number n_w. In particular the ripples of the fringes are related to the phase distribution of the fluids in the central disk and the ring, which is characterized by the one-body correlation function g_1. This function plays a specially important role for low-dimensional systems,

---

[26] Note that in this case the expected exponent $d_\mathrm{v} \sim 4d_\mathrm{w}$. This faster decay at short t_evap makes it easier to distinguish a change toward a slower decay at long t_evap and explains why a plateau is observable or not depending on the case.

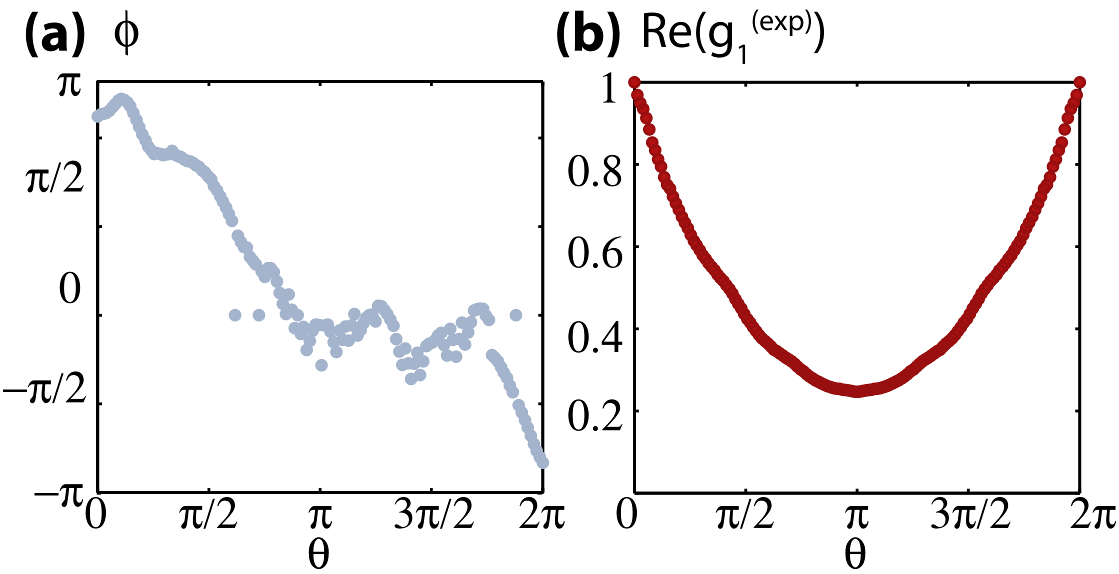

Figure 8.15.: (a) Typical phase distribution reconstructed from the phase profile $\phi(\theta)$ of the interference pattern of Fig. 8.10**(b)** showing a winding number of -1. **(b)** Real value of the angular correlation function reconstructed from the phase of the interference patterns with 18 realizations of $t_{\mathrm{evap}} = 2\,\mathrm{s}$ and $t_{\mathrm{hold}} = 4\,\mathrm{s}$. When $N_{\mathrm{d}} \neq 0$ the linear phase winding is subtracted before computing g_1.

since it indicates how long-range order is destroyed by thermal phonons. To give an estimate of g_1, we study the angular dependance of the phase of the fringes $\phi(\theta)$ as shown on Fig. 8.15a. In particular we consider the periodic function $\delta\phi(\theta) = \phi(\theta) - n_{\mathrm{w}}\,\theta$, which describes the deviation of the reconstructed phase from a perfect linear winding. We construct the angular correlation function:

$$g_1^{(\mathrm{exp})}(\theta) = \langle \mathrm{e}^{\mathrm{i}[\delta\phi(\theta') - \delta\phi(\theta'+\theta)]} \rangle_{\theta',\,\mathrm{realizations}} \tag{8.42}$$

where the average is taken over all images irrespective of the value of n_{w}, and which is expected to be real in the limit of a large number of realizations. A typical example for $\mathcal{R}\mathrm{e}[g_1^{(\mathrm{exp})}]$ is given in Fig. 8.15b, where the minimum for $\theta = \pi$ gives an indication of the phase coherence between diametrically opposite points. To relate quantitatively $g_1^{(\mathrm{exp})}(\theta)$ to the coherence properties of the gas in the ring, two hypotheses are needed:

- We suppose that the fluid in the central disk acts as a phase reference, so that the ripples of the fringes come essentially from the phase fluctuations in the ring. Indeed the small size of this disk guarantees that phonon modes are only weakly populated. Using Bogoliubov description of the excitations and a minimal phonon wavevector of $k \sim 1/R_0$, we fund a maximal population of the order of one atom per mode.
- We assume that the fluctuations of the phase of the fringe pattern directly reflect the phase of the atomic wave function along the ring. We check this hypothesis by simulating numerically the hydrodynamical expansion using 2D Gross Pitaevskii

simulations (see Annex B). These precise simulations have been performed by co-worker Sylvain Nascimbène. We first compute the ground state of $N = 5 \times 10^4$ atoms in the target potential using 2D imaginary time Gross-Pitaevskii calculations. A phase fluctuation $\delta\tilde{\phi}(\theta)$ is then added by hand to the wave function in the ring. We then simulate the hydrodynamical expansion by evolving the Gross-Pitaevskii equation in real time during 7 ms. The phase $\delta\phi(\theta)$ of the fringe pattern is finally obtained using the same procedure as for experimental pictures. A comparison between two typical phase distributions $\delta\tilde{\phi}(\theta)$ and $\delta\phi(\theta)$ is given in Fig. 8.16. Both phase profiles are similar, confirming that the phase reconstructed from the interference pattern corresponds in good approximation to the in-situ phase of the gas.

The measured angular correlation function $g_1^{(\mathrm{exp})}(\theta)$ can thus be used to reconstruct the first-order correlation function of the gas in the annulus. This correlation function could allow one to extract the evolution of the phonon distribution during the thermalization of the fluid.

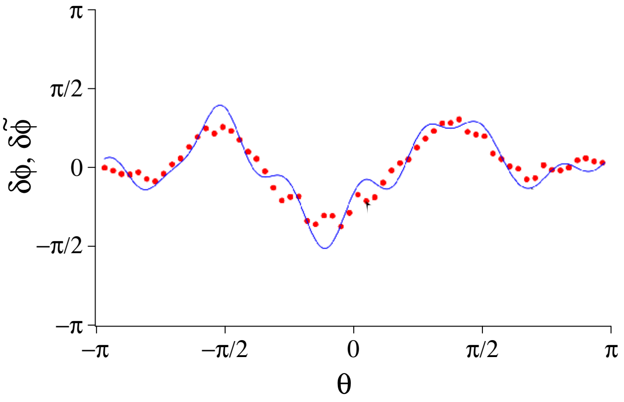

Figure 8.16.: Comparison between the phase fluctuations of an initial state in the annulus ($\delta\tilde{\phi}$, solid line) and the phase profile deduced with the interference method used in the experiment ($\delta\phi$, red points).

8.4. Conclusion

In this chapter, we presented two measurements testing Kibble–Zurek mechanism at the dimensional cross-over between 2D and 3D in a uniform 2D gas. We shown that topological defects can be nucleated at the transition crossing even for long evaporation ramps, highlighting the specificity of the specificity of the emergence of coherence in uniform gases. We have presented a quantitative analysis of the KZ scaling of the number of domains N_d with the quench time t_evap through the measurements of the mean number of topological defects N_v (number of vortex cores in a bulk geometry) or N_w (number of phase windings in an annular geometry). The measured exponent for the related power-law scaling of the number of coherent domains $N_\mathrm{d} \propto t_\mathrm{evap}^d$ gives respectively $d = 0.35(9)$ and $d = 0.38(12)$, in agreement with beyond *MF* prediction of $d = 1/3$.

In the presented studies we were able to test KZ scaling law only over a limited range of t_{evap} precluding a clear discrimination between *MF* from beyond *MF* predictions. This limitation is in fact intrinsic to the system under study. First, the range of study is limited for t_{evap} by two extreme effects:

— t_{evap} should be chosen long enough so that at any given time a local thermal equilibrium is achieved in the cloud (see Annex I). As the collision time at the crossing of the transition is $\tau_{\text{coll}} \approx 4\,\text{ms}$, we impose $t_{\text{evap}} \geq 25\,\text{ms}$ [27]

— The largest t_{evap} is set by the cloud lifetime that is of 6 s in our case. Then we impose $t_{\text{evap}} \leq 3\,\text{s}$.

In our case, we can then test 2 orders of magnitude of t_{evap} (and this relative range cannot be significantly modified). Moreover due to the expectation of a plateau of N_{d} for long quench times through the dimensional crossover, the range of study of the power-law scaling is actually more limited. In 8.2, we found a characteristic time for this plateau at $t_{\text{evap}} \approx 250\,\text{ms}$, restricting the range for power-law study to one order of magnitude in t_{evap}. Finally, as we work with a uniform system, the expected power-law exponent is smaller than 1, resulting in an even smaller accessible range for N_{d} (and the relative range that can be investigated in N_{d} is then fixed). It could be interesting to study situations with larger absolute values of N_{d}. For a given density the local equilibrium requirement limits the lower value of $\hat{\xi}$ and one can only increase the size of the system L in order to increase N_{d}. Within current experimental techniques, it should be possible to load one order of magnitude more atoms, leading to an increase of N_{d} by the same factor, assuming fixed transverse sizes.

In this study, we considered only the weakly interacting regime for which we showed that an extended quantum coherence emerges essentially due to ideal Bose statistics (see Ch. 7). Our work also motivates future research in the direction of strongly interacting 2D gases [206], for which the order of the various transitions could be interchanged. In particular the critical $\mathcal{D}$ for the BKT transition should decrease, and reach ultimately the universal value of the "superfluid jump", $\mathcal{D} = 4$ [122]. In this case, the emergence of extended coherence in the 2D gas would be essentially driven by the interactions. Indeed once the superfluid transition is crossed, the one-body correlation function is expected to decay very slowly, $g_1(r) \propto r^{-\alpha}$, with $\alpha < 1/4$. It would be interesting to revisit the statistics of formation of quench-induced topological defects in this case, for which significant deviations to the KZ power-law scaling have been predicted [174, 175].

---

[27] Note that a similar condition is imposed by the applicability of linear approximation in the quench in temperature, see 8.1.3.2

Concluding remarks

Summary

In this thesis, we studied experimentally the two-dimensional Bose gas starting from a local investigation of conventional harmonically confined samples to the development of a direct exploration of homogeneous gases. In the harmonic trapping case, we used the induced spatial dependency of the degree of degeneracy of the gas $\mathcal{D}$ to probe several homogeneous-equivalent configurations within a unique experimental realization. In the uniform configuration, we used the spatial independency of $\mathcal{D}$ to probe long distance effects. In the first case, we measured the equation of state around the BKT critical point and explored the transition from a thermal to a superfluid behavior. In the second case, we characterized the (extended) coherence range at equilibrium varying the degree of degeneracy of a 2D gas and the strength of the confinement along the third direction of space. We also tested the dynamics of the establishment of the in-plane coherence along the dimensional crossover.

The measurements on the uniform 2D traps that we presented in this manuscript constitute our first studies in this specific trapping configuration. Comparing to state-of-the-art achievements in our research community they are rather innovative. We want to push these investigations further and study in-depth the specially accessible properties in a homogeneous configuration. We are also eager to investigate other range of parameters for our cloud configuration (other transverse confinements, other interaction regimes, other in-plane sizes...). Finally, we also wish to implement new box geometries that will enable us to explore original physical phenomena. I detail here some of these further developments and directions of research.

Beyond coherence measurement, toward a characterization of the correlations and the fluctuations in a 2D uniform gas

In chapter 7, we were interested in a simple characterization of the $g_1(r)$ decay, extracting a single number that characterizes the coherence range from two much more complex sources of information, the 2D density spatial distribution of an expanding gas and the 2D fringes pattern resulting from the overlap of two initially independent gases. A more complete description of the correlations can be extracted from a more in-depth analysis of similar measurements. This is of particular interest in the uniform configuration since long range correlation analysis is relevant (*i.e.* it is not limited by the inhomogeneity range, only by the size of the cloud). Then a measure of the full $g_1(r)$ dependency may be achievable in our experiment. In this case if a high enough precision is achieved, we may expect (see 1.1.3.1 and 1.1.4.4) to observe a transition from a Gaussian behavior (predicted for the thermal gas) to a exponential decay (predicted from ideal Bose law) and/or to an algebraic decrease (as expected in the superfluid phase) with the increase of the degree of degeneracy of the gas. Moreover the BKT theory predicts an intimate link between the algebraic decay exponent η and the superfluid density n_s : $\eta = 1/(n_\mathrm{s}\ \lambda_\mathrm{T}^2)$. Then n_s can potentially be extracted from the measure of g_1 spatial dependency. We note that as the system size here limits the range of investigation and may perturb it we are willing to produce larger 2D traps.

From density distribution measurements higher-order correlation functions may also be measured [111, 207]. The second order correlation function, also called density-density correlation function g_2, is of special interest as it enables a description of both density and phase fluctuations (by performing either in situ or Time-of-Flight measurements) [192, 208]. A similar technique has been developed earlier for 1D gases [191]. In a (homogeneous) 2D gas, the specific behavior of the g_2 function in Time-of-Flight may also prove the algebraic decay of the g_1 correlations and gives access to the exponent η [192]. Some developments have also been carried out for 2D harmonically confined gases [105, 106, 111] but gave limited results due to the restrictions introduced by the spatial dependency of the gas properties. Here again, the specificity of the uniform configuration is to give access to a close to the text-book configuration along with permitting to carry out this study over large distances. By varying the degree of degeneracy, we may revisit the previously described evolution from a thermal to a quasi-condensate to a superfluid state by describing here the thermal excitations of the gas: It must evolve from a fully fluctuating gas to a regime where the density fluctuation are strongly suppressed over large scales while the phase remains fluctuating with a proliferation of phase windings defects, to a final state where the free vortices are precluded but the phase keeps fluctuating over long range (see 1.1.4.2). In the latter regime, a large scale analysis of the power spectrum of the resulting density fluctuations after a Time-of-Flight expansion may as announced give access to η and thus to n_s.

The observations of density and phase fluctuations are not limited to the equilibrium characterization of the 2D gas but is also of interest for describing the dynamical establishment of the coherence as alluded in 8.3.5. We may thus perform a precise correlation analysis in a quench through a transition toward a coherent state to investigate not only the robust topological defects that survives long after the quench as in chapter 8 but also the short lived excitations such as phonons [95]. Here we would need to look at the gas at times closer to the transition point. Their scaling properties would provide valuable insights on the thermodynamics transitions occurring in 2D [209, 210] and a more in-depth comprehension of the dynamics occurring from their quenched crossing.

We finally note that the recent development of single atom imaging techniques [211–214] enables a more in-depth investigation of the (high-order) correlations and may be implemented in our setup [111]. From this we may drastically gain information on the statistics of excitations.

Toward tighter confinement and strongly interacting gases

In our experimental study of the uniform gas performed up to this date, we have mainly focused on statistical effects. Indeed, we considered only loose transverse confinement with $\omega_z/2\pi \lesssim 1.5\,\mathrm{kHz}$ such that the 2D interaction parameters are restricted to weakly interacting values $\tilde{g} \lesssim 0.1$. This has several consequences on the physical properties that can potentially be investigated.

First, due to the limited energy spacing between the excited and the ground states for the z-motion, 2D is only marginally achieved, leading to a crucial role of the transverse excitations in the way 2D physics is established. Using this loosely confined configuration we pioneered investigations of the Bose-driven partial condensation phenomenon $\mathrm{BEC}_{\perp}$ in 2D. However it would also be interesting to study the opposite configuration of a deep 2D regime with $k_{\mathrm{B}}T \ll \hbar\omega_z$ over a large range of temperature. In this configuration we may also expect to achieve a better exploitation of the Time-of-Flight measurements, for example extracting a reliable value of the condensed fraction of the gas, due to the simplification of the theoretical model (where no sum over the z excited states is needed).

Second, in the weakly interacting regime, the superfluid BKT transition is expected at a relatively large value of the 2D phase-space-density (Eq. 1.35) $\mathcal{D}^{(2D)} \sim 8$ whereas in the strongly interacting case, this quantity tends toward its «superfluid jump» value of $\mathcal{D}^{(2D)} = 4$ [122]. In 2D, due to the ideal prediction of an exponential growth of the correlation length with $\mathcal{D}^{(2D)}$, extended coherence (compared to the thermally set range λ_T, with in our gas $\lambda_T \lesssim 1\,\mu$m) is expected for $\mathcal{D}^{(2D)} \sim 4$ (see Eq. 1.22 and 7.4). Then in the weakly interacting case, emergence of quantum coherence is essentially driven by a statistical effect; when the superfluid transition is crossed, the coherence length set by Bose statistics is comparable to our box size. In the strongly interacting case however, the emergence of an extended coherence in the 2D gas would be essentially driven by the interactions : close to the BKT point the characteristic length of the exponential decay diverges (see Eq. 1.37) and at the onset of the superfluid regime an algebraic decay of $g_1(r)$ establishes.

It would be interesting to revisit our study of the emergence of coherence in these deep 2D and/or strongly interacting regimes[28] both as a function of the equilibrium properties of the gas and following a quench evolution throughout a coherent state. The scaling of the number of topological defects nucleated along a quench in the strongly interacting regime is of particular interest. It is indeed extremely different from the configuration described in this manuscript as the relevant transition (that is the one that establishes an extended coherence) for this quench is the interaction-induced BKT transition. For such a transition of infinite order, the KZ mechanism keeps applying but the theoretical expectations happen to be vastly modified. In particular, the scaling of the defect number toward the quench rate is not expected to follow a power law variation [174, 175]. The observation of such an altered dependency would constitute an original investigation of the refined applicability of the KZ mechanism, beyond finite order transitions.

We highlight that such a tight confinement and strongly interacting regime can be achieved by the implementation of the new confinement setup presented in 2.3.

---

[28] Note that in our case, as we cannot vary the scattering length a_s (no Feshbach resonances) these two regimes are intimately linked

Toward other uniform geometries and transport measurements

A third direction for further study would be to vary the shape of our box potential. A first point is to vary the size of this trap. As noticed theoretically, due to the exponential growth of the coherence length, the finite size of the samples has a predominant role on the thermodynamical properties of the gas (see Eq. 1.23 for example). Changing this size may enable to study its effects. If we vary simultaneously the interaction strength, we can look at the order of the occurrence of either a (finite-size) statistic-driven or an interaction-driven condensation in 2D (see 1.1.4.4 and [111, 115]). Moreover, as highlighted in 8.4 to study further the quench scaling of the density of defects via KZ mechanism, as we can not change the relative range of the defect number, it is necessary to vary the size of the sample which modify the absolute defect number. We can then extend our KZ exponent determination by simultaneously fitting its scaling on data taken with different box sizes.

A more subtle change of geometry can be realized to study new physical phenomena. A particularly interesting idea is for example to use the two spatially-separated rectangular boxes geometry (see 7.3 and Fig. 6.9) and modify it by creating a small potential channel between the two gases. We can think of dynamically closing and opening this channel by tightly focusing a blue detuned laser beam on it. This beam would be similar in its experimental implementation to the stirring beam used to probe the superfluid behavior of our gas (see 5.1.1) for which we achieved a waist of 2 μm on the atoms. Compared to the distance between the two parallel rectangular clouds (of 4.5 μm), this beam provides the desired «gate» effect on the trapping potential. Opening and closing the channel enable to make the two linked clouds coherent or not. The statistical distribution of their relative phase can be tested by a repetitive measurement of the fringes patterns.

In this configuration, we can also study transport properties along the channel and their evolution for various degrees of degeneracy of the clouds. Such a measurement complements our probing of the superfluid behavior via the response to a moving defect detailed in chapter 5 but can also address a wider scope of problems. Recent experiments have initiated the exploration of transport properties with ultracold atom gases [80, 82–87]. They are of interest for example for quantum simulations purpose or atomtronics [215] as they provide an equivalent for the conduction phenomenon. By varying the intensity of the «gate beam» we can vary the importance of the leak between the two reservoirs and then reach the regime of a weak leak in which the transport occurs at the single quantum level. Then in the superfluid regime a Josephson like effect reveals [216]. We may investigate the transition from this Josephson transport to a hydrodynamical one according to the energy height of the channel by exploring for example the oscillations in the atom numbers of each box (see [84, 217, 218] for examples of experimental realizations). Following lines of [219], we may be interested in controlling the regime of transportation for the normal and the superfluid components independently. By adding a disorder potential in the channel, we can for example realized a specific regime of transport that is named the superleak : In this case, the transport of the normal part is prohibited and only the superfluid may be transported. The disorder potential can be created by using the speckle pattern of a laser beam. Further interesting properties from transport measurements may be accessed by controlling the population and/or the temperature of each of the boxes independently.

A. Ideal Bose description of the uniform 2D gases.

By neglecting the effects of the interactions between atoms and applying the ideal Bose predictions for the non-interacting single-particle Hamiltonian, we can deduce predictions for many of the gas properties at thermal equilibrium. In our uniform trap configurations, this approximation happens to be relevant in a large number of configurations around the critical points of interest (see Ch. 7-8). We can self-consistently check its validity by estimating the interaction energy per particle in a first order approximation.

A.1. Ideal description of the gas at thermal equilibrium

To apply the ideal Bose law predictions to our gas configuration, we consider a full quantum 3D treatment of the Hamiltonian eigenstates (as introduced in 1.2.2). The Hamiltonian has no interaction contribution and the confinement potentials are modeled as follow:

— The vertical confinement is purely harmonic of pulsation ω_z (We use two configurations $\omega_z/2\pi = 365\,\mathrm{Hz}$ and $\omega_z/2\pi = 1460\,\mathrm{Hz}$).

— We consider an in–plane confinement perfectly uniform and of square shape of size L. To reproduce the experimental configurations for which the box shape varies, we choose $L = \sqrt{\mathcal{A}}$ where $\mathcal{A}$ is the area of the considered box. This simplification is justified by the more thorough simulations performed by previous PhD student Rémi Desbuquois [111] taking into account exact levels description of a disk–shape uniform box. These simulations conclude in a dominant dependency on the area of the box potential and only small corrections coming from the exact geometry.

Here we consider the Dirichlet boundaries conditions. The eigenstates of the corresponding single-particle Hamiltonian are labelled by three integers $j_x, j_y \geq 1$, $j_z \geq 0$ and its energy and eigenfunction are (taking the energy of the ground-state to be zero):

$$E_{\boldsymbol{j}} = \frac{\pi^2\hbar^2}{2mL^2}(j_x^2 + j_y^2 - 2) + j_z\hbar\omega_z, \tag{A.1}$$

$$\psi_{\boldsymbol{j}}(\boldsymbol{r}) = \frac{1}{L\sqrt{\ell_z}} \sin(\pi j_x x/L)\ \sin(\pi j_y y/L)\ \chi_{j_z}(z/\ell_z), \tag{A.2}$$

where $\ell_z = \sqrt{\hbar/m\omega_z}$ and χ_j is the j-th Hermite function. If we consider a gas of N non-interacting particles at temperature T, the occupation factor of level $\boldsymbol{j} \equiv (j_x, j_y, j_z)$ is given by Bose statistics:

$$f_{\boldsymbol{j}} = \frac{1}{\exp\left[(E_{\boldsymbol{j}} - \mu)/k_{\mathrm{B}}T\right] - 1}, \tag{A.3}$$

where $\mu \leq 0$ is the chemical potential of the gas and $N = \sum_j f_j$.

A.2. Computing predictions

We perform numerical computations by considering all levels within $\boldsymbol{j} = (j_x \leq j_r^{max}, j_y \leq j_r^{max}, j_z \leq j_z^{max})$. Each quantum number j_x, j_y and j_z are upper bounded by a value that takes into account energies as high as $20 \times k_B T$:

$$j_r^{max} \equiv \frac{5\,L}{\lambda_{\mathrm{T}}}\ ,\ j_z^{max} \equiv \frac{20 k_{\mathrm{B}} T}{\hbar \omega_z} \tag{A.4}$$

From Eqs.A.1-A.3, we can estimate a wide range of parameters along the lines explained below.

A.2.1. Occupation of the single-particle states

Following Eq. A.3, we can characterize the state $|\psi\rangle$ of a gas of N particles at thermal equilibrium by its average over a large number of realizations. In average, it is populated along

$$|\langle \boldsymbol{j} | \psi \rangle|^2 = f_{\boldsymbol{j}} \tag{A.5}$$

Note: To relate this results to A.2.2 we note that $|\langle \boldsymbol{j}|\psi\rangle|^2 = \langle \hat{N}_{\boldsymbol{j}} \rangle$ where $\hat{N}_{\boldsymbol{j}}$ is the operator number of particles in state $\boldsymbol{j}$ and is given by $\hat{N}_{\boldsymbol{j}} = \hat{a}_{\boldsymbol{j}}^\dagger \hat{a}_{\boldsymbol{j}}$ ($\hat{a}_{\boldsymbol{j}}$ annihilates one particle in state $|\boldsymbol{j}\rangle$). Such a knowledge of the population of the single-particle states enables to calculate all the averages considered in the following sections.

In this manuscript, we are particularly interested in:

- the population of the overall ground-state $N_{(0,0,0)} = N\Pi_{(0,0,0)} = f_{(1,1,0)}$
- the population of the ground-state of the z-motion $|j_z = 0\rangle$ that is $N_{(0)} = \Pi_{(0)} N = \sum_{j_x, j_y} f_{(j_x, j_y, 0)}$.

A.2.2. Mean value of one-body observables

Using the second quantification formalism, the general expression of any one-body observable $\hat{A} = \sum_{\boldsymbol{j}_1, \boldsymbol{j}_2} A_{\boldsymbol{j}_1, \boldsymbol{j}_2}\, \hat{a}_{\boldsymbol{j}_1}^\dagger \hat{a}_{\boldsymbol{j}_2}$ (where $\hat{a}_{\boldsymbol{j}}$ stands for the annihilation operator in the $|\boldsymbol{j}\rangle$ state). Its average for a gas of N particles at thermal equilibrium can then be calculated along

$$\langle \hat{A} \rangle = \sum_{\boldsymbol{j}} f_{\boldsymbol{j}} A_{\boldsymbol{j},\boldsymbol{j}} \text{ (with } A_{\boldsymbol{j}_1, \boldsymbol{j}_2} = \langle \boldsymbol{j}_1 | \hat{A} | \boldsymbol{j}_2 \rangle). \tag{A.6}$$

For example, the variance of the in-plane velocity $v^2 = v_x^2 + v_y^2$ is given by:

$$\Delta v^2 \equiv \langle v^2 \rangle = \left(\frac{\pi \hbar}{L m} \right)^2 \sum_{\boldsymbol{j}} \frac{j_x^2 + j_y^2}{2} f_{\boldsymbol{j}} \tag{A.7}$$

The first order correlation function g_1 between the points $\boldsymbol{r}$ and $\boldsymbol{r}'$ writes

$$g_1(\boldsymbol{r},\boldsymbol{r}') \equiv \langle \hat{\psi}(\boldsymbol{r})^\dagger \hat{\psi}(\boldsymbol{r}') \rangle = \sum_j f_j \psi_j^*(\boldsymbol{r}) \psi_j(\boldsymbol{r}') \tag{A.8}$$

as the field operator is given by $\hat{\psi}(\boldsymbol{r}) = \sum_j \psi_j(\boldsymbol{r}) \hat{a}_j$ (with $\psi_j(\boldsymbol{r})$ given in Eq. A.2).

A.2.3. Mean value of two-body observables

In the same way, we can estimate the average value of a two-body observable whose general expression is $\hat{B} = \sum_{j_1,j_2,j_3,j_4} B_{j_1,j_2,j_3,j_4} \hat{a}^\dagger_{j_1} \hat{a}^\dagger_{j_2} \hat{a}_{j_3} \hat{a}_{j_4}$. It is then calculated along

$$\langle \hat{B} \rangle = \sum_{j_1,j_2} f_{j_1} f_{j_2} B_{j_2,j_1,j_1,j_2} \text{ (with } B_{j_1,j_2,j_3,j_4} = \langle \boldsymbol{j}_1 | \langle \boldsymbol{j}_2 | \hat{B} | \boldsymbol{j}_4 \rangle | \boldsymbol{j}_3 \rangle). \tag{A.9}$$

For example, the interaction potential operator (assuming the binary contact approximation with s-wave channel collisions) is defined as

$$\hat{V}_{\text{int}}(\boldsymbol{r}) \quad = \quad g^{(3D)} \hat{\psi}^\dagger(\boldsymbol{r}) \hat{\psi}^\dagger(\boldsymbol{r}) \hat{\psi}(\boldsymbol{r}) \hat{\psi}(\boldsymbol{r}) \tag{A.10}$$

where $g^{(3D)}$ is the 3D interaction parameter introduced in 1.1.4.1, $g^{(3D)} = \frac{4\pi\hbar^2}{m} a_s$. Then the first order approximation of this total interaction energy (in this non-interacting treatment) averages to

$$\begin{aligned} E_{\text{int}} &\equiv \frac{1}{2} \int \mathrm{d}^3 r \langle \hat{V}_{\text{int}}(\boldsymbol{r}) \rangle & \text{(A.11)} \\ &= \sum_{j,j'} f_j f_{j'} \frac{1}{2} g^{(3D)} \int \mathrm{d}^3 r |\psi_j(\boldsymbol{r})|^2 |\psi_{j'}(\boldsymbol{r})|^2. & \text{(A.12)} \end{aligned}$$

A.3. self-consistent validity of the non-interacting treatment

The estimate deduced from such a Bose law treatment is relevant only for gas configurations in which the interaction energy is negligible. We self-consistently verified this assumption, by estimating the first order contribution of an interaction energy value in the ideal approximation. Rather than calculating its average value by integrating Eq. A.12 we will consider its maximal (local) contribution to the Hamiltonian[1]. As highlighted in 1.1.4, a first order contribution of the interaction energy to the single-particle Hamiltonian can be estimated by the spatial dependent factor

$$h_{\text{int}} = g^{(3D)} \frac{\langle n^{(3D)}(\boldsymbol{r})^2 \rangle}{\langle n^{(3D)}(\boldsymbol{r}) \rangle} \tag{A.13}$$

---

[1] This choice is made for two reasons. First the integration of Eq. A.12 is a complex numerical task. Second we are interested in the perturbation that can induced the interaction energy in the population of the single-particle state. Then it is sensible to consider the importance of the contribution in the (single-particle) Hamiltonian to then estimate a first order correction to the eigenenergies and eigenstates by applying the perturbation theory for example.

while $\langle n^{(3D)}(\boldsymbol{r})^2\rangle$ varies from $2\langle n^{(3D)}(\boldsymbol{r})\rangle^2$ in a thermal gas to $\langle n^{(3D)}(\boldsymbol{r})\rangle^2$ in a highly degenerate regime (suppression of density fluctuations). We must then compare the value of $g^{(3D)}\langle n^{(3D)}(\boldsymbol{r})\rangle$, which gives the range of h_{int}, to the other characteristic energies of the gas. As the negligibility must be verified in all parts of the cloud, we estimate the maximal value of $g^{(3D)}\langle n^{(3D)}(\boldsymbol{r})\rangle$ over the cloud, which is obtained in $\boldsymbol{r} = \mathbf{0}$. We estimate $n^{(3D)}(\mathbf{0})$ from the ideal Bose law calculations. We will consider as relevant the ideal estimations for gases that self-consistently verify that $gn^{(3D)}(\mathbf{0})$ is smaller than a certain limit. This limit is usually set to a fraction of the thermal energy $k_{\mathrm{B}}T$ and of the level spacing for the transverse confinement $\hbar\omega_z$.

B. Gross-Pitaevskii simulations to estimate the gas parameters in the highly degenerate regime.

Along this work we use Gross-Pitaevskii simulations to compute the gas properties in the highly degenerated configurations. Gross-Pitaevskii simulations enable to take into account the interaction contribution using *Mean-Field* approximation. In these simulations we assume that all particles populate the ground state of the macroscopic Hamiltonian $\hat{H}$, then contributing to a macroscopic wavefunction (equivalently, we assume that the temperature of the gas is zero, $T = 0$). It thus provides a first order approximation to the treatment of interactions between atoms in the highly degenerate case.

B.1. Principle of GrossPitaevskii simulations

B.1.1. Time dependent Gross-Pitaevskii equations

To perform such a simulation we use the time-dependent Gross-Pitaevskii equation (GPE), also called non-linear Schrodinger equation (NLSE) in 3D:

$$\begin{aligned} i\hbar\frac{\partial\psi(\boldsymbol{r})}{\partial t} &= \left(\hat{D}+\hat{K}\right)\psi(\boldsymbol{r}) & \text{(B.1)}\\ \text{with } \hat{D}\,\psi(\boldsymbol{r}) &\equiv \left(V(\boldsymbol{r})+g^{(3D)}N|\psi(\boldsymbol{r})|^2\right)\psi(\boldsymbol{r}) & \text{(B.2)}\\ \hat{K}\,\psi(\boldsymbol{r}) &\equiv -\frac{\hbar^2}{2m}\frac{\partial^2}{\partial\boldsymbol{r}^2}\psi(\boldsymbol{r}) & \text{(B.3)} \end{aligned}$$

where $\boldsymbol{r}$ is the 3D position vector, $\psi(\boldsymbol{r})$ is the 3D macroscopic wavefunction with the normalization condition $\int|\psi(\boldsymbol{r})|^2\mathrm{d}^3r = 1$, N is the total number of atoms, $V(\boldsymbol{r})$ is the 3D-trapping potential; finally $g^{(3D)} = \frac{4\pi\hbar^2 a_s}{m}$ is the 3D interaction parameter. Then the macroscopic Hamiltonian is $\hat{H} = \hat{D}+\hat{K}$.

B.1.1.1. Defining the confining potential V

In our case the 3D potential has a dominant harmonic contribution of pulsation ω_z along z and a dominant uniform contribution in the xy-plane. We denote $\boldsymbol{\rho}$ the 2D position vector such that $\boldsymbol{r} = \boldsymbol{\rho} + z\boldsymbol{u}_z$ ($\boldsymbol{u}_z$ stands for the unit vector along z). Then we can write

$$\begin{aligned} V(\boldsymbol{r}) &= U(\boldsymbol{\rho}) + \frac{m}{2}\omega_z^2 z^2 + \delta V(\boldsymbol{r}) & \text{(B.4)}\\ \text{with } U(\boldsymbol{\rho}) &= U_{\text{barrier}}\,\Theta(\boldsymbol{\rho}\notin \text{Box}) & \text{(B.5)}\\ |\delta V(\boldsymbol{r})| &\ll |V(\boldsymbol{r})|. & \text{(B.6)} \end{aligned}$$

where Θ is the Heaviside function. $U(\boldsymbol{\rho})$ is thus a 2D perfectly uniform potential with infinitely sharp edges. In our simulations we commonly use disk-shape boxes for simplicity reasons, assuming then that the specific shape has a negligible influence. To reproduce the experimental configuration, we use a disk of same area as the box used in the experiment and populate it with the experimentally measured atom number N.

$\delta V(\boldsymbol{r})$ stands for all the corrections that can be made to the simple description detailed above. Several corrections may be included:

- As shown in 2.1.1, the use of a magnetic gradient for compensating gravity field along z simultaneously induces a shallow harmonic confinement in-plane. We take this correction into account by calculating the approximate harmonic trapping frequencies (Eq. 2.10) created by a magnetic gradient that perfectly compensates the gravity field along z ($b'_z = 15\,\mathrm{G/cm}$) and whose zero is perfectly at the vertical of the trap center, at a distance $d_{\mathrm{mag}} = 1.45\,\mathrm{mm}$ from this center. In the simulations used in this manuscript we took this correction into account.
- As shown in 2.2.3.1, the light-sheet beam creating the confinement along z also leads to a shallow harmonic trapping (or anti-trapping) in-plane. We take this correction into account, also considering for the actual distance d of the atoms compared to the focus of this beam (see Annex C).This distance is $d = 190\,\mu\mathrm{m}$ for configuration at $\omega_z/2\pi = 1460\,\mathrm{Hz}$ and $d = 840\,\mu\mathrm{m}$ for configuration at $\omega_z/2\pi = 365\,\mathrm{Hz}$. In our simulations, we took this correction into account.
- Due to the finite waist of the light-sheet beam in-plane $w_r = 50\,\mu\mathrm{m}$, the z-trapping frequency varies within the box. At the position $\boldsymbol{\rho}$, ω_z is proportional to the square root of the intensity of the beam at this position and then varies as $\exp(-\boldsymbol{\rho}^2/w_r^2)$ (see Eq. 2.13). In the 3D simulations performed in this work, we take this correction into account by using a local definition of the z-trapping frequency $\omega_z(\boldsymbol{r}) = \omega_z \exp(-\boldsymbol{\rho}^2/w_r^2)$.
- Non uniformity of the box-trap bottom (see 6.3.3.2) as well as non-harmonicities of the light-sheet confinement (see 2.2.3.2 for example) could also be added. We do not model such an effect in our simulations.

B.1.1.2. 2D approximation for the Gross-Pitaevskii equation

In our case as, the confinement along z is rather strong, we can assume that the chemical potential μ is negligible compare to $\hbar\omega_z$. With this assumption, we state that interactions have a negligible effect along z and we can then assume that only the single-particle ground-state of the z-motion is populated. In this approximation, we can then project this 3D equation in a 2D one using the decomposition:

$$\psi(\boldsymbol{r}) = \phi(\boldsymbol{\rho})\frac{\chi_0(z/\ell_z)}{\sqrt{\ell_z}} \tag{B.7}$$

where χ_0 stands for the zeroth Hermite function and $\ell_z = \sqrt{\hbar/m\omega_z}$ for the size of z-harmonic oscillator[1]. $\phi(\boldsymbol{\rho})$ is the 2D macroscopic wavefunction and the 3D normaliza-

---

[1] Here, we neglect the contribution of $\delta V(\boldsymbol{r})$ depending on z. It is possible to take into account this modification of $V(\boldsymbol{r})$ in Eq. B.8 by correcting according the integration performed. It translates quantita-

tion condition translates in the 2D condition $\int |\phi(\boldsymbol{\rho})|^2 \mathrm{d}^2\rho = 1$. Then Eq. B.1 integrates in :

$$\begin{aligned} i\hbar\frac{\partial\phi(\boldsymbol{\rho})}{\partial t} &= \left(\hat{\mathcal{D}} + \hat{\mathcal{K}}\right)\phi(\boldsymbol{\rho}) \quad &(B.8)\\ \text{with } \hat{\mathcal{D}}\,\phi(\boldsymbol{\rho}) &\equiv \left(U(\boldsymbol{\rho}) + \delta U(\boldsymbol{\rho}) + g^{(2D)}N|\phi(\boldsymbol{\rho})|^2\right)\phi(\boldsymbol{\rho}) \quad &(B.9)\\ \hat{\mathcal{K}}\,\phi(\boldsymbol{\rho}) &\equiv -\frac{\hbar^2}{2m}\frac{\partial^2}{\partial\boldsymbol{\rho}^2}\phi(\boldsymbol{\rho}) \quad &(B.10)\end{aligned}$$

where $\delta U(\rho)$ is the component of δV correcting the in-plane confinement; $g^{(2D)} = \frac{\sqrt{8\pi}\,\hbar^2 a_s}{m\ell_z}$ is the 2D interaction parameter, linked to the reduced one by $g^{(2D)} = \hbar^2\tilde{g}/m$.

As the 2D equation is an approximation of the 3D one, the resolution of Eq. B.1 is more rigorous than of Eq. B.8 (but necessitate more computations). In particular, it takes into account the modifications of the z macroscopic ground-state due to interactions between atoms. These can be important in our highly degenerate gases ($\mathcal{D}^{(2D)} > 100$) and relatively loose trapping of $\omega_z/2\pi = 365\,\mathrm{Hz}$. In most of the cases, we performed 3D calculations, except in 8.3.5 (for the qualitative justification of g_1 analysis).

B.1.2. Method for solving the time-dependent GPE

We solve Eq. B.1 (resp. Eq. B.8) by using a split-step method. In this method we perform an evolution by small time steps $\mathrm{d}t$ by successively solving over each small step the two partial evolutions:

1. in the direct spatial domain, we evolve ψ along :

$$i\hbar\frac{\partial\psi(\boldsymbol{r})}{\partial t} = \hat{D}\psi(\boldsymbol{r}) \quad (\text{resp. } i\hbar\frac{\partial\phi(\boldsymbol{\rho})}{\partial t} = \hat{\mathcal{D}}\phi(\boldsymbol{\rho})) \tag{B.11}$$

2. in the frequency one, we evolve ψ along :

$$i\hbar\frac{\partial\psi(\boldsymbol{r})}{\partial t} = \hat{K}\psi(\boldsymbol{r}) \quad (\text{resp. } i\hbar\frac{\partial\phi(\boldsymbol{\rho})}{\partial t} = \hat{\mathcal{K}}\phi(\boldsymbol{\rho})) \tag{B.12}$$

The two evolutions of Eqs. B.11 and B.12 are independently easily solvable in the specified spaces. In first approximation, they can be treated separately along the small time steps as then the commutator of $\mathrm{d}t\hat{D}$ (resp. $\mathrm{d}t\hat{\mathcal{D}}$) and $\mathrm{d}t\hat{K}$ (resp. $\mathrm{d}t\hat{\mathcal{K}}$) can be neglected: it contributes to terms of an order smaller in $\mathrm{d}t$. More rigorously, using Baker-Hausdorff formula in Eq. B.1, we find :

$$\psi(\boldsymbol{r}, t + \mathrm{d}t) = e^{i\mathrm{d}t(\hat{K}+\hat{D})/\hbar}\psi(\boldsymbol{r}, t) = e^{i\mathrm{d}t\hat{K}/\hbar}e^{i\mathrm{d}t\hat{D}/\hbar}\psi(\boldsymbol{r}, t) + o(\mathrm{d}t^2) \tag{B.13}$$

Then, if we choose a small enough value of $\mathrm{d}t$ so that $|\frac{\mathrm{d}t}{\hbar}\hat{K}\psi|$, $|\frac{\mathrm{d}t}{\hbar}\hat{D}\psi| \ll 1$. The solution of Eq. B.1 (resp. Eq. B.8) evolved between t and $t + \mathrm{d}t$ is well approximated by

---

tively in a modification of the 2D interaction parameter $g^{(2D)}$

:

$$\psi(\boldsymbol{r}, t+\mathrm{d}t) = TF^{-1}[\exp\left(-\frac{i\mathrm{d}t\hbar\boldsymbol{k}^2}{2m}\right) TF[e^{i\mathrm{d}t\hat{D}}\psi(\boldsymbol{r}, t)]] \tag{B.14}$$

$$\text{(resp. } \phi(\boldsymbol{\rho}, t+\mathrm{d}t) = TF^{-1}[\exp\left(-\frac{i\mathrm{d}t\hbar\boldsymbol{\kappa}^2}{2m}\right) TF[e^{i\mathrm{d}t\hat{\mathcal{D}}}\phi(\boldsymbol{\rho}, t)]] \text{).} \tag{B.15}$$

where TF is the Fourier transform operator and $\boldsymbol{k}$ (resp. $\boldsymbol{\kappa}$) is the variable conjugated to $\boldsymbol{r}$ (resp. $\boldsymbol{\rho}$) by Fourier transform. The evolution from $t = 0$ to $t = \hat{t}$ is performed using $\hat{t}/\mathrm{d}t$ successive steps.

B.2. Numerical computations

B.2.1. Computing the macroscopic ground state wavefunction for the trap sample

We compute the ground state wavefunction $\varphi_0(\boldsymbol{r})$ of the macroscopic Hamiltonian $\hat{H} = \hat{D} + \hat{K}$ of Eq. B.1 (resp. $\hat{\mathcal{H}} = \hat{\mathcal{D}} + \hat{\mathcal{K}}$ of Eq. B.8) by evolving the state along Eq. B.14 (resp. B.15) in imaginary time, that is replacing the time t of this equation along (so called Wick rotation):

$$t \to \tau = -it \tag{B.16}$$

We start the evolution from an arbitrary wavefunction $\psi(\boldsymbol{r}, t = 0) = \psi_0(\boldsymbol{r})$ that can be in a general way decomposed over the eigenstates $|\varphi_k\rangle$ of $\hat{H}$ (resp. $\hat{\mathcal{H}}$) along $|\psi_0\rangle = \sum_{k=0}^{\infty} c_k|\varphi_k\rangle$. We number the eigenstates in the increasing order of their energies ϵ_k and we set the origin of the energies to $\epsilon_0 = 0$. We also assume that the ground-state $|\varphi_0\rangle$ is not degenerate so that $\epsilon_k > 0$, $\forall k > 0$. Then, applying the propagation operator $\exp(-\frac{i\hat{H}t}{\hbar})$ after the transformation of Eq. B.16, we find :

$$\psi(\boldsymbol{r}, t = i\tau) = \sum_{k=0}^{\infty} c_k \exp(-\frac{\epsilon_k\tau}{\hbar})|\varphi_k\rangle \underset{\tau\to\infty}{\longrightarrow} c_0|\varphi_0\rangle \tag{B.17}$$

If we perform the evolution for a long enough time τ compared to the first excitation energy gap ϵ_1 (*i.e.* $\tau \gg \hbar/\epsilon_1$), then the evolved wavefunction is directly proportional to the ground state wavefunction $\varphi_0(\boldsymbol{r})$. As the evolution is performed in imaginary time, then the normalization is not implicitly conserved along the evolution. Then in our numerical procedure, we reestablished the normalization condition $\int |\psi(\boldsymbol{r}, i\tau)|^2\mathrm{d}^3r = 1$ (resp. $\int |\phi(\boldsymbol{\rho}, i\tau)|^2\mathrm{d}^2\rho = 1$) after each time step of duration $\mathrm{d}t$ by dividing $\psi(\boldsymbol{r}, i\tau)$ (resp. $\phi(\boldsymbol{\rho}, i\tau)$) by its norm $\sqrt{\int |\psi(\boldsymbol{r}, i\tau)|^2\mathrm{d}^3r}$ (resp. $\sqrt{\int |\phi(\boldsymbol{\rho}, i\tau)|^2\mathrm{d}^2\rho}$).

In the numerical calculation, we typically use time steps of 10^{-4} ms and compute the evolution for 10 ms. The 3D grid contains $152 \times 152 \times 32$ voxels, with a voxel size $0.52 \times 0.52 \times 0.26\,\mu\mathrm{m}^3$. The 2D grid contains 70×70 pixels, with a pixel size $0.52 \times 0.52\,\mu\mathrm{m}^2$.

B.2.2. Deducing the gas parameters

From the determination of the ground state of the macroscopic Hamiltonian, we are in particular interested in estimating the various contributions to the total energy. These are the potential energy E_{pot}, the kinetic energy E_{kin} and interaction energy E_{int} and they are given by the following integrals over the cloud:

$$\begin{aligned} E_{\text{pot}} &= N\int V(\boldsymbol{r})|\psi(\boldsymbol{r})|^2 \mathrm{d}^3 r, && \text{(B.18)} \\ E_{\text{kin}} &= \frac{\hbar^2 N}{2m}\int |\nabla\psi(\boldsymbol{r})|^2 \,\mathrm{d}^3 r, && \text{(B.19)} \\ E_{\text{int}} &= \frac{2\pi\hbar^2 a_s}{m} N^2 \int |\psi(\boldsymbol{r})|^4 \,\mathrm{d}^3 r. && \text{(B.20)} \end{aligned}$$

We can obtain the value of the chemical potential μ by taking the derivative of the total energy with respect to N and subtracting the single-particle ground state energy:

$$\mu = \frac{1}{N}\left(E_{\text{pot}} + E_{\text{kin}} + 2E_{\text{int}}\right) - \frac{h^2}{4mL^2} - \frac{1}{2}\hbar\omega_z. \tag{B.21}$$

We can also be interested in calculating the modification of characteristic parameters due to the interactions. For instance, the extent Δz of the atomic sample along z is modified compared to its ideal value $\ell_z/\sqrt{2}$ and is given by:

$$\Delta z^2 = \int |\psi(\boldsymbol{r})|^2 z^2 \mathrm{d}^3 r \tag{B.22}$$

The 2D interaction parameters is similarly modified and calculated along:

$$\tilde{g} = 4\pi a_s \mathcal{A}\int |\psi(\boldsymbol{r})|^4 \,\mathrm{d}^3 r. \tag{B.23}$$

so that the interaction energy per particle $\epsilon_{\text{int}} = E_{\text{int}}/N$ (Eq. B.20) writes

$$\epsilon_{\text{int}} = \frac{\hbar^2\tilde{g}}{2m} N/\mathcal{A} = g^{(2D)} n^{(2D)}/2. \tag{B.24}$$

Where $g^{(2D)} = \hbar^2\tilde{g}/m$ is the 2D interaction parameter and $n^{(2D)} = N/\mathcal{A}$ is the mean 2D density. Then we note that the contribution of E_{int} to μ is $g^{(2D)}n^{(2D)}$. From $\tilde{g}$ value we can deduced the modified healing length:

$$\varsigma = 1/\sqrt{\tilde{g}n^{(2D)}}. \tag{B.25}$$

Finally, we note also the in-plane extent of the cloud is slightly modified due to the effects of the healing length, which is the characteristic length scale for the variations of φ_0 at the edges of the trap, and due to the corrections to uniformity in $\delta V(\boldsymbol{r})$. These extents are given by similar integrations as in Eq. B.22, replacing $z \to x, y$ or $\boldsymbol{\rho}$.

For example, we performed a 3D Gross-Pitaevskii computation for a gas with a surface density of $n^{(2D)} = 50\,\mu\mathrm{m}^{-2}$ and trapped in disk of $R = 16.9\,\mu\mathrm{m}$ (corresponding to the same area than a square of $L = 30\,\mu\mathrm{m}$). We found :

:textbfEnergies	Values ($/k_{\mathrm{B}}$)	**Parameters**	Ideal values	Modified values
E_{kin}/N	3.4 nK	Δz	397 nm	479 nm
E_{pot}/N	6.66 nK	$\tilde{g}$	0.0455	0.0388
E_{int}/N	5.35 nK	ς	663 nm	718 nm
μ	12.0 nK	$\Delta\rho$	$11.968\,\mu\mathrm{m}$	$11.948\,\mu\mathrm{m}$

Table B.1.: Results of a GP simulation for an atomic sample confined in a harmonic trap along z of $\omega_z/2\pi = 365\,\mathrm{Hz}$ and a uniform disk in-plane of $R = 16.9\,\mu\mathrm{m}$. The surface density for the simulation is $n^{(2D)} = 50\,\mu\mathrm{m}^{-2}$. We compute the various energy contributions and the resulting chemical potential. We also highlight the various corrections to the characteristic cloud parameters.

B.2.3. Computing 2D and 3D Time-of-Flight evolutions of the wavefunction.

Using a real time evolution we can also compute the evolution of the macroscopic wavefunction after some brutal changes in the trapping configuration. For example, we can simulate an abrupt switching off of the box-trap potential U – this corresponds to evolution of a highly degenerate gas in a 2D ToF – or an abrupt switching off of the full potential V – this depicts evolution of $T = 0$ coherent gas in 3D ToF (see 2.1.3).

For these evolutions, we start from the previously computed $\varphi_0(\boldsymbol{r})$ ground-state wavefunction and perform further evolution in real time, taking into account the modified potential in B.14 (or B.15). In this case, the normalization of the wavefunction is conserved during the evolution and the size of the grid is imposed from the choice of the $\varphi_0(\boldsymbol{r})$ computation. We use the same time steps as for the imaginary-time evolution which is of 10^{-4} ms while typical ToF evolutions are from a few to a few tens of ms.

The evolution is performed for a given time $\hat{t}$ in order to reproduced the wanted experimental measurements. In this evolution, the temperature T of the gas does not play any role and the expansion is due to the conversion of the total energy of the ground state into kinetic energy. Usually we are interested in the in-plane spatial density distribution $n(x, y)$ after such a ToF evolution:

$$n(x,y) = \int |\psi(\boldsymbol{r})|^2 \,\mathrm{d}z. \tag{B.26}$$

C. Residual radial confinements for a decentered cloud compared to the light-sheet beam focus

This appendix details the calculations of the shift in the residual anti–confinement created by the light-sheet beam in the case where the cloud is not positioned at the focus center of this beam. We remind that the light-sheet (LS) beam is designed to create a tight confinement along the z-direction (see 2.2). A residual radial effect occurs from the radial dependency of the zero-point energy of the z-motion. Calculations have been carried out for a cloud confined in the center focus $(x, y) = (0, 0)$ of the beam in 2.2.3.1. In this annex we will detail a further analysis of the resulting trapping around the atomic sample center (x_c, y_c) differing from the beam center $(0, 0)$.

C.1. Decentering along the LS-beam propagation direction x

We pointed out in 2.2.2 that positioning the atom sample out of the LS beam focus (at $x_c \neq 0$) is compulsory to achieve satisfying experimental conditions. There, we stated that the focus of the beam must be displaced compared to the atom position by more than a Rayleigh length x_R. We will describe such a case by $x_c = \alpha x_R$ and in our optimal experimental configuration, we have $\alpha = 1.28$.

We can develop the radial potential $\hbar\omega_z(x, y)/2$ (engendered by the freezing out of the z motion) around $x = x_c$ instead of $x = 0$ (see 2.2.3.1) to deduce the shift in ω_x and ω_y. We first keep $y = 0$ so that only ω_x is modified and we set $\omega_z^c = \omega_z(x_c, 0) = \omega_z(0, 0)\ (1 + \alpha^2)^{-3/4}$. Then the trapping potential along x is

$$\frac{\hbar\omega_z}{2}(x, 0) \quad = \quad \frac{\hbar\omega_z^c}{2}\left(1 - \frac{3\alpha}{2(1+\alpha^2)x_R}(x - x_c) + \frac{3(5\alpha^2 - 2)}{8(1+\alpha^2)^2 x_R^2}(x - x_c)^2\right). \tag{C.1}$$

We see that :

- The main effect of Eq. C.1 is a potential gradient $U = -U'_x\ (x - x_c)$. We will compensate it on the experiment in our alignment procedure (based on making the 2D atomic density profile as much uniform as possible) by decentering the position of the magnetic zero x_{mag} from x_c. We will estimate latter in this section the displacement needed to exactly compensate this effect.
- The second order approximation leads to an important modification of the longitudinal deconfining frequency along:

$$\omega_{x\sim x_c} \quad = \quad \sqrt{\frac{3(5\alpha^2 - 2)}{8(1+\alpha^2)^2}}\ \frac{\sqrt{\hbar\omega_z^c/m}}{x_R}. \tag{C.2}$$

The deconfinement effect is lowered when we go away from the focus. If we displace the atoms by $|x_c| \geq \sqrt{2/5}x_R = 0.6x_R$, the resulting potential is in fact confining.

In our case, we found :

$$\omega_{x\sim x_c} = 0.578 \frac{\sqrt{\hbar\omega_z(x_0,0)/m}}{x_R} = -i\, 0.196\, \omega_y. \tag{C.3}$$

Now we estimate the displacement $x_{\text{mag}} \neq 0$ we need to impose to the magnetic zero position for compensating the linear dependency of the potential in the atom position $x - x_c$. The magnetic potential of Eq. 2.8 centered on $(x_{\text{mag}} \neq x_c, y_{\text{mag}})$ is:

$$V_{\text{mag}}(x,y) = \mu b_z' \left[d_z^2 + \frac{(x-x_{\text{mag}})^2}{4} + \frac{(y-y_{\text{mag}})^2}{4} \right]^{1/2}. \tag{C.4}$$

We want to approximate this potential around $x = x_c$ (we set $\Delta_x = x_{\text{mag}} - x_c$ and suppose $y_c = y_{\text{mag}} = 0$) :

$$\begin{aligned} V_{\text{mag}}(x,0) &= mgD_z - \frac{mg\Delta_x}{4D_z}(x-x_c) + \frac{mg}{8D_z}(x-x_c)^2 && \text{(C.5)} \\ \text{where } D_z &= \sqrt{d_z^2 + \Delta_x^2/4}. && \text{(C.6)} \end{aligned}$$

Then if we want that $V_{\text{mag}}(x,0)$ and $\hbar\omega_z(x,0)/2$ linear contributions cancel, we must impose:

$$\begin{aligned} \frac{3\hbar\omega_z^c}{8x_R^2}\frac{2\alpha x_R}{(1+\alpha^2)} &= -\frac{mg}{8D_z}\,2\Delta_x && \text{(C.7)} \\ \Delta_x &= -\left(\frac{\omega_{x\sim 0}(\omega_z^c)}{\omega_{\text{mag}}}\right)^2 \frac{\alpha}{1+\alpha^2} x_R && \text{(C.8)} \end{aligned}$$

where $\omega_{x\sim 0}(\omega_z^c)$ is the deconfining angular frequency calculated according to Eq. 2.19 (as if the atoms where at the LS focus) but with a reduced frequency ω_z^c calculated along Eq. C.2 in $x = x_c$ (which is its value at the actual position of the atoms x_c). As this frequency is typically lower than the magnetic confinement frequency (see 2.4), we find that we must move the zero of the magnetic field away from the cloud center by 4% to 30% of the Rayleigh length x_R for the highest frequencies used, and in the opposite direction compared to the displacement of the cloud center from the LS focus. We quantitatively find $|\Delta_x| \in [10, 40]\,\mu$m. Then, we can still consider $D_z \approx d_z$ and the magnetic trapping frequency ω_{mag} is not modified.

In conclusion, the defocusing of the light-sheet beam on the atoms creates:

— a potential gradient that can easily be compensated by a small decentering (compared to the cloud center) of the magnetic zero in the direction of the beam propagation and on a distance of some tens of micrometers.

— a deep change in the x-confinement due to the variation of the zero-point energy in x but no change in the magnetic confinement along x as the displacement are too small compared to the important vertical decentering of the magnetic zero in our configuration.

C.2. Decentering along the transverse and weakly direction, y

In general we do not want a decentering along x to occur but it can happen that $y_c \neq 0$ because of:

— a misalignment due to some flaws in the alignment procedure,

— a deliberate misalignment chosen to avoid the deep rugosities of the light-sheet potential at some position y in the beam (see 2.2.3.2).

In both cases, such a decentering is definitely smaller than the one studied along x axis, it is typically restricted to some percents (up to 20%) of the beam waist : $y_c = \beta w_y$ with $\beta \lesssim 0.2$.

As previously we approximate the radial potential $\hbar\omega_z(x, y)/2$ around $y = y_c$, first keeping $x = 0$. We set $\omega_z'^c = \omega_z(0, y_c) = \omega_z(0, 0)e^{-\beta^2}$. Then the potential along y writes

$$\frac{\hbar\omega_z(0, y)}{2} = \frac{\hbar\omega_z'^c}{2}\left(1 - \frac{2\beta}{w_y}(y - y_c) + \frac{2\beta^2 - 1}{w_y^2}(y - y_c)^2\right). \tag{C.9}$$

We see that :

— The first order effect is again a potential gradient $U = -U_y' \ (y - y_c)$. As previously, we will compensate it experimentally by decentering the position of the zero of the magnetic field y_{mag} from y_c. Once again, we deduce it value by equalizing the magnetic slope $\frac{mg}{8D_z}\ 2\Delta_y$ with the one $\beta\ \hbar\omega_z'^c/w_y$ resulting from the LS potential. This gives

$$\Delta_y = -\left(\frac{\omega_{y\sim 0}(\omega_z'^c)}{\omega_{\text{mag}}}\right)^2 \beta w_y \tag{C.10}$$

where $\omega_{y\sim 0}(\omega_z'^c)$ is the deconfining angular frequency calculated according to Eq. 2.19 (as if the atoms where at the LS focus) but with a reduced frequency $\omega_z'^c$ corresponding to the one at the actual position of the atoms y_c (see next item). Δ_y varies from 3 to 30 μm typically so that its amplitude is also negligible compared to d_z; hence the magnetic confinement is not affected.

— The second order effect leads to a modification of the y-deconfining frequency along :

$$\omega_{y\sim y_c} = \sqrt{2\beta^2 - 1}\ \frac{\sqrt{\hbar\omega_z'^c/m}}{w_y} \tag{C.11}$$

The multiplicative correction factor $\sqrt{2\beta^2 - 1}$ changes the anti–confinement into a confinement at $\beta = 1/\sqrt{2}$. As $\beta \lesssim 0.2$, the modification of ω_y stays small and the maximal absolute value of the correction factor is 0.96. We will then suppose that this modification is negligible.

In conclusion, the miscentering of the light-sheet beam in the y-direction leads to

— a potential gradient that can easily be compensated as previously by a small decentering (compared to the cloud center) of the magnetic zero y_{mag} on a distance of some μm.

— a negligible modification of both the trapping frequencies associated with the zero-point energy and with magnetic gradient.

C.3. Decentering along both x and y directions

We should note that if the cloud is decentered in both x and y directions ($x_c = \alpha x_R \neq 0$, $y_c = \beta w_y \neq 0$), a coupling term proportional to $(x - x_c)(y - y_c)$ appears. We can define a corresponding coupling frequency by equalizing the coupling term to $\frac{1}{2} m \omega_{xy}^2 (x - x_c)(y - y_c)$

If we combine both development of the potential given in Eq. C.2 and Eq. C.11, we find :

$$\begin{aligned} \frac{\hbar\omega_z(x,y)}{2} &= \frac{\hbar\omega_z^{''c}}{2} \left(1 - \frac{2\beta}{w_y}(y - y_c) + \frac{2\beta^2 - 1}{w_y^2}(y - y_c)^2\right) && \text{(C.12)} \\ & \left(1 - \frac{3\alpha}{2(1+\alpha^2)x_R}(x - x_c) + \frac{3(5\alpha^2 - 2)}{8(1+\alpha^2)^2 x_R^2}(x - x_c)^2\right) && \text{(C.13)} \end{aligned}$$

where $\omega_z^{''c} = \omega_z(0,0)\ (1+\alpha^2)^{-3/4}\ e^{-\beta^2}$. Then the coupling frequency is

$$\begin{aligned} \omega_{xy\sim(x_c,y_c)} &= \sqrt{\frac{3\alpha\beta}{1+\alpha^2}}\ \frac{\sqrt{\hbar\omega_z^{''c}/m}}{\sqrt{x_R w_y}} && \text{(C.14)} \\ &= \sqrt{\frac{3\alpha\beta}{1+\alpha^2}}\ \sqrt{\frac{w_y}{x_R}}\ \omega_{y\sim 0}(\omega_z^{''c}) && \text{(C.15)} \end{aligned}$$

where $\omega_{y\sim 0}(\omega_z^{''c})$ is the deconfining angular frequency calculated according to Eq. 2.19 (as if the atoms where at the LS focus) but with a reduced frequency $\omega_z^{''c}$ corresponding to the one at the actual position of the atoms (x_c, y_c). For now on, we suppose that the cloud is always decentered along x with a typical $\alpha = 1.28$. The coupling frequency then depends on the square root of decentering along y direction $\sqrt{\beta}$ (that can be wanted or unwanted but remains small $\beta \lesssim 0.2$). Then,

$$|\omega_{xy\sim(x_c,y_c)}| \lesssim 0.31\ \omega_{y\sim 0}(\omega_z^{''c}) \qquad \text{(C.16)}$$

Such an oscillation remains small compared to the anti–confinement in y-direction $\omega_{y\sim y_c} \approx \omega_{y\sim 0}(\omega_z^{''c})$ but is of the same order than the confinement along x. From this coupling term, we can infer a new oscillation axis for which the oscillations are decoupled. Such axes X and Y are defined by the angle θ they make with the original axis from the experiment x and y:

$$\begin{aligned} X &= (x - x_c)\cos\theta + (y - y_c)\sin\theta && \text{(C.17)} \\ Y &= -(x - x_c)\sin\theta + (y - y_c)\cos\theta && \text{(C.18)} \\ \text{and}\quad \frac{\hbar\omega_z(x,y)}{2} &= \frac{\hbar\omega_z^{''c}}{2} + U'_X X + U'_Y Y + \frac{m}{2}\left(\Omega_X^2 X^2 + \Omega_Y^2 Y^2\right) && \text{(C.19)} \end{aligned}$$

By developing the quadratic term we find :

$$\begin{aligned} \tan 2\theta &= \frac{\omega_{xy}^2}{\omega_y^2 - \omega_x^2} && \text{(C.20)} \\ &= \frac{-\alpha\beta}{\left[\frac{(1-2\beta^2)(1+\alpha^2)}{3}\frac{x_R}{w_y} + \frac{(5\alpha^2-2)}{8(1+\alpha^2)}\frac{w_y}{x_R}\right]} && \text{(C.21)} \end{aligned}$$

As both the collinear and coupling frequencies are small compared to the transverse one : $\omega_x^2, \omega_{xy}^2 \ll \omega_y^2$, the axis of decoupling is nearly the same than the experimental one. We found $\theta = -0.05$. The resulting frequencies are also approximately equal to the x, y ones:

$$\begin{aligned} \Omega_X &= i0.201\omega_{y\sim 0}(\omega_z^{''c}) = 1.027\omega_{x\sim x_c} && \text{(C.22)} \\ \Omega_Y &= 0.955\omega_{y\sim 0}(\omega_z^{''c}) = 0.996\omega_{y\sim y_c} && \text{(C.23)} \end{aligned}$$

In conclusion, the coupling between the collinear (x) and transverse (y) axes to the propagation of the light-sheet beam can always be neglected.

D. Conventional imaging of an atomic ensemble, limitations due to bi–dimensionality

The following annex was initially published in [136], and is reproduced without modifications except for introducing remarks and words within brackets

In this annex we present a theoretical analysis of the absorption imaging technique used to determine the atomic density $n(\boldsymbol{r})$ of a 2D cloud. Previous experimental works of our group [139] shown that the absorption imaging in the low intensity regime ($I \ll I_{\text{sat}}$) interpreted along Beer Lambert law (Eq. D.1) leads to underestimating n in the dense regions of a 2D gases (*i.e.* $n \gg \sigma^{-1}$ where σ stands for the photon scattering cross-section). In order to understand this phenomenon and be able to use absorption imaging to investigate the physical properties of our gases, we developed a theoretical model for this effect. In this annex, we first present our modeling of the atom-light interaction, using both the two-level (with a $J = 0$ ground state and a $J = 1$ excited state) and the rotating wave approximations. Then we explain the principle of the calculation for the absorption of a weak probe beam crossing the atom slab, we only consider a single-photon interacting with a (dense) atom assembly (thus neglecting any collective effects between photons and/or multiplication of excited atoms). Finally we present our numerical results in which we observed an effective reduction of the optical density (OD) compared to Beer Lambert prediction in the case of high densities.

D.1. Theoretical analysis of the multiple scattering effect

To access the atomic density $n(\boldsymbol{r})$, one usually relies on the interaction of the atoms with quasi-resonant laser light. The most common method is absorption imaging, in which the shadow imprinted by the cloud on a low intensity probe beam is imaged on a camera. The simplest modelling of absorption imaging is based on a mean-field approach, in which one assumes that the local value of the electric field driving an atomic dipole at a given location depends only on the average density of scatterers. One can then relate the attenuation of the laser beam to the column atomic density $n^{(\text{col})}(x,y) = \int n(\boldsymbol{r})\, dz$ along the line-of-sight z. The optical density of the cloud $\mathcal{D}(x,y) \equiv \ln[I_{\text{in}}(x,y)/I_{\text{out}}(x,y)]$ is given by the Beer–Lambert law

$$\mathcal{D}_{\text{BL}}(x,y) = \sigma\, n^{(\text{col})}(x,y), \tag{D.1}$$

where σ is the photon scattering cross-section, and I_{in} (resp. I_{out}) are the incoming (resp. outgoing) intensity of the probe laser in the plane xy perpendicular to the propagation axis. For a closed two-level atomic transition of frequency $\omega_0 = ck_0$, σ depends on the wavelength $\lambda_0 = 2\pi/k_0$ associated to this transition and on the detuning $\Delta = \omega - \omega_0$

between the probe light frequency ω and the atomic frequency:

$$\sigma = \frac{\sigma_0}{1+\delta^2}, \qquad \sigma_0 = \frac{3\lambda_0^2}{2\pi}, \qquad \delta = \frac{2\Delta}{\Gamma} \,. \tag{D.2}$$

Here Γ represents the natural line width of the transition (*i.e.*, Γ^{-1} is the natural life time of the excited state of the transition). Eq. D.2 assumes that the intensity of the probe beam is much lower than the saturation intensity of the atomic transition. Quasi-resonant absorption imaging is widely used to measure the spatial distribution of atomic gases after a long time-of-flight, when the density has dropped sufficiently so that the mean-field approximation leading to Eq. D.1 is valid.

One can also use absorption imaging to probe *in situ* samples, at least in the case where $\sigma\, n^{(\mathrm{col})}$ is not very large so that the output intensity is not vanishingly small. This is in particular the case for low dimensional gases. Consider for example a 2D gas, such that the translational degree of freedom along z has been frozen. For a probe beam propagating along this axis, one can transpose the Beer–Lambert law of Eq. D.1 by simply replacing the column density by the surface density $n^{(2\mathrm{D})}$ of the gas. This 2D Beer–Lambert law can be heuristically justified by treating each atom as a disk of area σ that blocks every photon incident on it. In an area $A \gg \sigma$ containing $N = An^{(2\mathrm{D})} \gg 1$ randomly placed atoms, the probability that a photon is not blocked by any of the disks is $(1-\sigma/A)^N \approx \exp(-\sigma n^{(2\mathrm{D})})$.

In a quasi-2D gas there is however an important limitation on the optical densities to which one may apply the Beer-Lambert prediction of Eq.D.1. Already for $\sigma_0 n^{(2\mathrm{D})} = 1$ the mean interparticle distance is only $0.7\,\lambda_0$ and one may expect that the optical response of an atom strongly depends on the precise location of its neighbours. More precisely the exchange of photons between closely spaced atoms induces a resonant van der Waals interaction that significantly shifts the atomic resonance frequency with respect to its bare value ω_0. The optical density of the gas at resonance may then be reduced with respect to Eq. D.1, and this was indeed observed in a series of experiments performed with a degenerate ^{87}Rb gas [70, 139].

The general subject of the propagation of a light wave in a dense atomic sample, where multiple scattering plays an essential role, has been the subject of numerous experimental and theoretical works (see *e.g.* [220, 221] in the context of cold atoms, and [222] for a review). Here we present a quantitative treatment of the collective effects that appear when a weak probe beam interacts with a quasi-2D atomic gas. We consider an ensemble of N atoms at rest with random positions and we investigate the transmission of quasi-resonant light by the atom sheet. We model the resonance transition between the atomic ground (g) and excited (e) states by a $J_g = 0 \leftrightarrow J_e = 1$ transition. We present two equivalent approaches; the first one is based on the calculation of the field radiated by an assembly of N dipoles, where each dipole is driven by an external field plus the field radiated by the $N-1$ other dipoles; the second one uses the standard T matrix formalism of scattering theory. We show that in both cases the optical density of the medium can be determined by solving the same $3N \times 3N$ linear system. A similar formalism has been previously used for the study of light propagation in small 3D atomic samples, in the presence of multiple scattering (see *e.g.* [223–230]). However its application to quasi-2D samples has (to our knowledge) not yet been investigated, except in the context of Anderson localisation of light [224]. Our numerical calculations are performed for $N = 2048$ atoms, which is sufficient to reach the 'thermodynamic limit' for the range of parameters that is relevant for experiments. We show in particular that even for moderate values of $\sigma_0 n^{(\mathrm{col})}$, the optical density is notably reduced compared to what is expected from the Beer-Lambert law (*e.g.*, more than 20 % reduction for $\sigma_0 n^{(\mathrm{col})} = 1$). We investigate how the absorption line shape is modified by the resonant van der Waals interactions and we also show how the result Eq. D.1 is recovered when one increases the thickness of the gas, for a given column density $n^{(\mathrm{col})}$. Note that our simulations are performed with a much smaller atom number than in real experiments (N is up to 10^5 in [70, 139]). However we expect our results to be relevant for addressing experimental realisations, since the light attenuation can be treated in the local density approximation. Indeed in the 'thermodynamic limit' mentioned above, the optical density $\mathcal{D}$ at a point (x, y) depends only on the spatial density $n(x, y, z)$ along the line of sight, and not on the overall density distribution $n(x', y', z')$ in the sample.

D.2. Modelling the atom-light interaction

D.2.1. The electromagnetic field

We use the standard description of the quantised electromagnetic field in the Coulomb gauge [231], and choose periodic boundary conditions in the cubic-shaped quantisation volume $\mathcal{V} = L_x L_y L_z$. We denote $a_{\boldsymbol{q},\boldsymbol{s}}$ the destruction operator of a photon with wave vector $\boldsymbol{q}$ and polarisation $\boldsymbol{s}$ ($\boldsymbol{s} \perp \boldsymbol{q}$). The Hamiltonian of the quantised field is

$$H_{\mathrm{F}} = \sum_{\boldsymbol{q},\boldsymbol{s}} \hbar c q \, a^{\dagger}_{\boldsymbol{q},\boldsymbol{s}} a_{\boldsymbol{q},\boldsymbol{s}} \; , \tag{D.3}$$

and the transverse electric field operator reads $\boldsymbol{E}(\boldsymbol{r}) = \boldsymbol{E}^{(+)}(\boldsymbol{r}) + \boldsymbol{E}^{(-)}(\boldsymbol{r})$ with

$$\boldsymbol{E}^{(+)}(\boldsymbol{r}) = i \sum_{\boldsymbol{q},\boldsymbol{s}} \sqrt{\frac{\hbar c q}{2\varepsilon_0 \mathcal{V}}} \, a_{\boldsymbol{q},\boldsymbol{s}} \, e^{i\boldsymbol{q}\cdot\boldsymbol{r}} \, \boldsymbol{s} \; , \tag{D.4}$$

and $\boldsymbol{E}^{(-)}(\boldsymbol{r}) = \left(\boldsymbol{E}^{(+)}(\boldsymbol{r})\right)^{\dagger}$. The wave vectors $\boldsymbol{q}$ are quantised in the volume $\mathcal{V}$ as $q_i = 2\pi n_i / L_i$, $i = x, y, z$, where n_i is a positive or negative integer.

D.2.2. The atomic medium

We consider a collection of N identical atoms at rest in positions $\boldsymbol{r}_j$, $j = 1, \ldots N$. We model the atomic resonance transition by a two-level system with a ground state $|g\rangle$ with angular momentum $J_g = 0$ and an excited level of angular momentum $J_e = 1$. We choose as a basis set for the excited manifold the three Zeeman sublevels $|e_\alpha\rangle$, $\alpha = x, y, z$, where $|e_\alpha\rangle$ is the eigenstate with eigenvalue 0 of the component J_α of the atomic angular momentum operator. We denote $\hbar\omega_0$ the energy difference between e and g. The atomic

Hamiltonian is thus (up to a constant)

$$H_\mathrm{A} = \sum_{j=1}^{N} \sum_{\alpha=x,y,z} \hbar\omega_0 \, |j:e_\alpha\rangle\langle j:e_\alpha| . \tag{D.5}$$

The restriction to a two-level approximation is legitimate if the detuning Δ between the probe and the atomic frequencies is much smaller than ω_0. The modelling of this transition by a $J_g = 0 \leftrightarrow J_e = 1$ transition leads to a relatively simple algebra. The transitions that are used for absorption imaging in real experiments often involve more Zeeman states ($J_g = 2 \leftrightarrow J_e = 3$ for Rb atoms in [70, 139]), but are more complex to handle [232, 233] and they are thus out of the scope of this [work]. However we believe that the most salient features of multiple scattering and resonant van der Waals interactions are captured by our simple level scheme.

D.2.3. The atom-light coupling

We treat the atom-light interaction using the electric dipole approximation (length gauge), which is legitimate since the resonance wavelength of the atoms λ_0 is much larger than the atomic size. We write the atom-light coupling as:

$$V = -\sum_j \boldsymbol{D}_j \cdot \boldsymbol{E}(\boldsymbol{r}_j), \tag{D.6}$$

where $\boldsymbol{D}_j$ is the dipole operator for the atom j. We will use the rotating wave approximation (RWA), which consists in keeping only the resonant terms in the coupling:

$$V \approx -\sum_j \boldsymbol{D}_j^{(+)} \cdot \boldsymbol{E}^{(+)}(\boldsymbol{r}_j) + \text{h.c.} , \tag{D.7}$$

where h.c. stands for Hermitian conjugate. Here $\boldsymbol{D}_j^{(+)}$ represents the raising part of the dipole operator for atom j:

$$\boldsymbol{D}_j^{(+)} = d \sum_{\alpha=x,y,z} |j:e_\alpha\rangle\langle j:g| \, \hat{\boldsymbol{u}}_\alpha , \tag{D.8}$$

where d is the electric dipole associated to the $g-e$ transition and $\hat{\boldsymbol{u}}_\alpha$ is a unit vector in the direction α.

When a single atom is coupled to the electromagnetic field, this coupling results in the modification of the resonance frequency (Lamb shift) and in the fact that the excited state e acquires a non-zero width Γ

$$\Gamma = \frac{d^2\omega_0^3}{3\pi\varepsilon_0\hbar c^3} . \tag{D.9}$$

For simplicity we will incorporate the Lamb shift in the definition of ω_0. Note that the proper calculation for this shift requires that one goes beyond the two-level and the rotating wave approximations. The linewidth Γ on the other hand can be calculated from the above expressions for V using the Fermi golden rule.

The RWA provides a very significant simplification of the treatment of the atom-light coupling, in the sense that the total number of excitations is a conserved quantity. The annihilation (resp. creation) of a photon is always associated with the transition of one of the N atoms from g to e (resp. from e to g). This would not be the case if the non-resonant terms of the electric dipole coupling $\boldsymbol{D}_i^{(+)} \cdot \boldsymbol{E}^{(-)}$ and $\boldsymbol{D}_i^{(-)} \cdot \boldsymbol{E}^{(+)}$ were also taken into account. For a single atom, the small parameter associated to the RWA is Δ/ω_0, which is in practice in the range $10^{-6} - 10^{-9}$. For a collection of atoms, the RWA is still an excellent approximation if the shifts introduced by resonant van der Waals interactions are small compared to atomic frequencies. In practice this requires that the interatomic distances remain very large compared to the atom size (Bohr radius).

Formally the use of the electric dipole interaction implies to add to the Hamiltonian an additional contact term between the dipoles (see *e.g.* [223, 234]). This term will play no role in our numerical simulations because we will surround the position of each atom by a small excluded volume, which mimics the short range repulsive interaction between atoms. We checked that the results of our numerical calculations (see Sec. D.4) do not depend on the size of the excluded volume, and we can safely omit the additional contact term in the present work.

D.3. Interaction of a probe laser beam with a dense quasi-2D atomic sample

We present in this section the general formalism that allows one to calculate the absorption of a quasi-resonant laser beam by a slab of N atoms. We address this question using two different approaches. The first one maps the problem onto the collective behaviour of an assembly of N oscillating dipoles [223]. The equation of motion for each dipole is obtained using the Heisenberg picture for the Hamiltonian presented in section D.2. It contains two driving terms, one from the incident probe field and one from the field radiated by all the other dipoles at the location of the dipole under study. The steady-state of this assembly of dipoles is obtained by solving a set of $3N$ linear equations. The second approach uses the standard quantum scattering theory [235], which is well suited for perturbative calculations and partial resummations of diagrams. We suppose that one photon is incident on the atomic medium and we use resummation techniques to take into account the multiple scattering events that can occur before the photon emerges from the medium. The relevant quantity in this approach is the probability amplitude T_{ii} that the outgoing photon is detected in the same mode as the incident one [225, 228], and we show that T_{ii} is obtained from the same set of equations as the values of the dipoles in the first approach.

D.3.1. Wave propagation in an assembly of driven dipoles.

In this section we assume that the incident field is prepared in a coherent state corresponding to a monochromatic plane wave $E_\mathrm{L}\, \boldsymbol{\epsilon}\, e^{i(kz-\omega t)}$. We choose the polarization $\boldsymbol{\epsilon}$ to be linear and parallel to the x axis ($\boldsymbol{\epsilon} = \hat{\boldsymbol{u}}_{\boldsymbol{x}}$). Since we consider a $J_g = 0 \leftrightarrow J_e = 1$ transition, this choice does not play a significant role and we checked that we recover essentially the same results with a circular polarisation. Note that the situation would be different for an atomic transition with larger J_g and J_e since optical pumping processes would then depend crucially on the polarisation of the probe laser.

The amplitude $E_{\rm L}$ is supposed to be small enough that the steady-state populations of the excited states $e_{j,\alpha}$ are small compared to unity. This ensures that the response of each atomic dipole is linear in $E_{\rm L}$; this approximation is valid when the Rabi frequency $dE_{\rm L}/\hbar$ is small compared to the natural width Γ or the detuning Δ.

Using the atom-light coupling of Eq. D.6, the equations of motion for the annihilation operators $a_{q,s}$ in the Heisenberg picture read:

$$\dot{a}_{\boldsymbol{q},\boldsymbol{s}}(t) = -i\,cq\,a_{\boldsymbol{q},\boldsymbol{s}}(t) + \sqrt{\frac{cq}{2\hbar\varepsilon_0\mathcal{V}}}\sum_{j'}\boldsymbol{s}^*\cdot\boldsymbol{D}_{j'}(t)\,e^{-i\boldsymbol{q}\cdot\boldsymbol{r}_{j'}}\,. \tag{D.10}$$

This equation can be integrated between the initial time t_0 and the time t, and the result can be injected in the expression for the transverse field to provide its value at any point $\boldsymbol{r}$:

$$\begin{aligned} E_\alpha(\boldsymbol{r},t) \;&=\; E_{\text{free},\alpha}(\boldsymbol{r},t) + \sum_{j',\alpha'}\sum_{\boldsymbol{q},\boldsymbol{s}}\int_0^{t-t_0} d\tau\,\frac{cq}{2\varepsilon_0\mathcal{V}} \\ &\qquad \left[iD_{j',\alpha'}(t-\tau)\,e^{i\boldsymbol{q}\cdot(\boldsymbol{r}-\boldsymbol{r}_{j'})-icq\tau}\,s_\alpha s^*_{\alpha'} + \text{h.c.}\right]\;, \end{aligned} \tag{D.11}$$

where $\boldsymbol{E}_{\text{free}}$ stands for the value obtained in the absence of atoms. We now take the quantum average of this set of equations. In the steady-state regime the expectation value of the dipole operator $\boldsymbol{D}_j(t)$ can be written $\boldsymbol{d}_j e^{-i\omega t}$ + c.c., and the average of $\boldsymbol{E}_{\text{free}}(\boldsymbol{r},t)$ is the incident field $E_{\rm L}\,\boldsymbol{\epsilon}\,e^{i(kz-\omega t)}$ + c.c. . We denote the average value of the transverse field operator in $\boldsymbol{r}$ as $\langle\boldsymbol{E}(\boldsymbol{r},t)\rangle = \bar{\boldsymbol{E}}(\boldsymbol{r})\,e^{-i\omega t}$ + c.c., and we obtain after some algebra (see *e.g.* [223, 236])

$$\bar{E}_\alpha(\boldsymbol{r}) = E_{\rm L}\,\epsilon_\alpha\,e^{ikz} + \frac{k^3}{6\pi\varepsilon_0}\sum_{j',\alpha'} g_{\alpha,\alpha'}(\boldsymbol{u}_{j'})\,d_{j',\alpha'}\;, \tag{D.12}$$

where we set $\boldsymbol{u}_j = k(\boldsymbol{r}-\boldsymbol{r}_j)$ (with $k \approx k_0$),

$$g_{\alpha,\alpha'}(\boldsymbol{u}) = \delta_{\alpha,\alpha'}h_1(u) + \frac{u_\alpha u_{\alpha'}}{u^2}h_2(u), \tag{D.13}$$

and

$$h_1(u) = \frac{3}{2}\frac{e^{iu}}{u^3}(u^2+iu-1), \qquad h_2(u) = \frac{3}{2}\frac{e^{iu}}{u^3}(-u^2-3iu+3). \tag{D.14}$$

The function $g_{\alpha,\alpha'}(k\boldsymbol{r})$ is identical to the one appearing in classical electrodynamics [237], when calculating the field radiated in $\boldsymbol{r}$ by a dipole located at the origin.

We proceed similarly for the equations of motion for the dipole operators $\boldsymbol{D}_j^{(-)}$ and take their average value in steady-state. The result can be put in the form [223]

$$(\delta+i)d_{j,\alpha} + \sum_{j'\neq j,\,\alpha'} g_{\alpha,\alpha'}(\boldsymbol{u}_{jj'})d_{j',\alpha'} = -\frac{6\pi\varepsilon_0}{k^3}\,E_{\rm L}\,\epsilon_\alpha\,e^{ikz_j}\;, \tag{D.15}$$

where the reduced detunig $\delta = 2\Delta/\Gamma$ has been defined in Eq. D.2 and $\boldsymbol{u}_{j,j'} = k(\boldsymbol{r}_{j'} - \boldsymbol{r}_j)$. This can be written with matrix notation

$$[M]|X\rangle = |Y\rangle \tag{D.16}$$

where the $3N$ vectors $|X\rangle$ and $|Y\rangle$ are defined by

$$X_{j,\alpha} = -\frac{k^3}{6\pi\epsilon_0 E_L} d_{j,\alpha}, \qquad Y_{j,\alpha} = \epsilon_\alpha e^{ikz_j} , \tag{D.17}$$

and where the complex symmetric matrix $[M]$ has its diagonal coefficients equal to $\delta + i$ and its off-diagonal coefficients (for $j \neq j'$) given by $g_{\alpha,\alpha'}(\boldsymbol{u}_{jj'})$. This matrix belongs to the general class of Euclidean matrices [238], for which the (i, j) element can be written as a function $F(\boldsymbol{r}_i, \boldsymbol{r}_j)$ of points $\boldsymbol{r}_i$ in the Euclidean space. The spectral properties of these matrices for a random distribution of the $\boldsymbol{r}_i$'s (as it will be the case in this work, see Sec. D.4) have been studied in [238–241].

Eq. D.15 has a simple physical interpretation: in steady-state each dipole $\boldsymbol{d}_j$ is driven by the sum of the incident field E_L and the field radiated by all the other dipoles. This set of $3N$ equations was first introduced by L. L. Foldy in [242] who named it, together with Eq. D.12, “the fundamental equations of multiple scattering". Indeed for a given incident field, the solution of Eq. D.16 provides the value of each dipole $\boldsymbol{d}_j$, which can then be injected in Eq. D.12 to obtain the value of the total field at any point in space.

D.3.2. Absorption signal

From the expression of the average value of the dipoles we now extract the absorption coefficient of the probe beam and the optical density of the gas. We suppose that the N atoms are uniformly spread in a cylinder of radius R along the z axis and located between $z = -\ell_z/2$ and $z = \ell_z/2$. We can consider two experimental setups to address this problem. The first one, represented in Fig. D.1a, consists in measuring after the atomic sample the total light intensity with the same momentum $\boldsymbol{k} = k\hat{\boldsymbol{u}}_z$ as the incident probe beam. This can be achieved by placing a lens with the same size as the atomic sample, in the plane $z = \ell' > \ell_z/2$ just after the sample. The light field at the focal point of the lens F gives the desired attenuation coefficient. We refer to this method as ‘global’, since the field $\boldsymbol{E}(F)$ provides information over the whole atomic cloud. One can also use the setup sketched in Fig. D.1b, which forms an image of the atom slab on a camera and provides a ‘local’ measurement of the absorption coefficient. In real experiments local measurements are often favored because trapped atomic sample are non homogeneous and it is desirable to access the spatial distribution of the particles. However for our geometry with a uniform density of scatterers, spatial information on the absorption of the probe beam is not relevant. Therefore we only present the formalism for global measurements, which is simpler to derive and leads to slightly more general expressions. We checked numerically that we obtained very similar results when we modelled the local procedure.

We assume that the lens in Fig. D.1a operates in the paraxial regime, *i.e.*, its focal length f is much larger than its radius R. We relate the field at the image focal point of

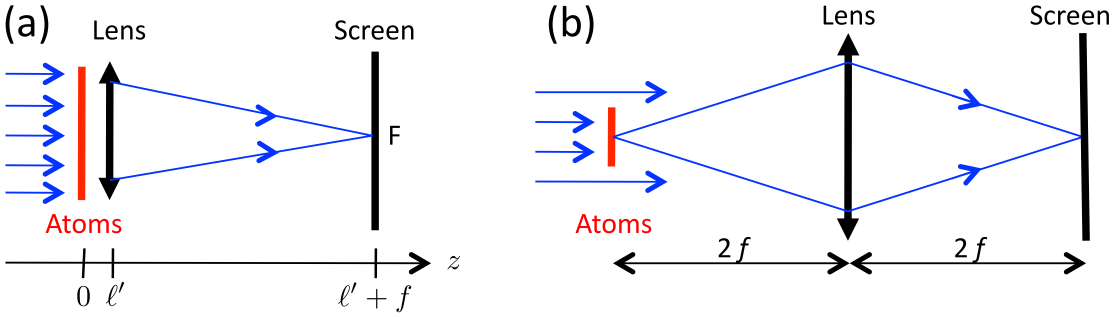

Figure D.1.: Two possible setups for measuring the absorption of an incident probe beam by a slab of atoms using a lens of focal f. a) Global probe. b) Local probe.

the lens to the field in the plane $z = \ell'$ just before the lens:

$$\boldsymbol{E}(F) = -\frac{ie^{ikf}}{\lambda_0 f}\int_{\mathcal{L}} \boldsymbol{E}(x, y, \ell')\, dx\, dy, \tag{D.18}$$

where the integral runs over the lens area. Since the incident probe beam is supposed to be linearly polarised along x, we calculate the x component of the field in F. Plugging the value of the field given in Eqs. D.12-D.17 we obtain the transmission coefficient

$$\mathcal{T} \equiv \frac{E_x(F)|_{\text{with atoms}}}{E_x(F)|_{\text{no atom}}} = 1 - \frac{e^{-ik\ell'}}{\pi R^2}\sum_{j,\alpha} X_{j,\alpha}\int_{\mathcal{L}} g_{x,\alpha}[k(\boldsymbol{r} - \boldsymbol{r}_j)]\, dx\, dy\, . \tag{D.19}$$

This result can be simplified in the limit of a large lens by using an approximated value for the integral appearing in Eq. D.19. We suppose that $k\ell' \gg 1$ so that the dominant part in $g_{x,\alpha}$ is the e^{iu}/u contribution to h_1. More precisely the domain in the lens plane contributing to the integral for the dipole j is essentially a disk of radius $\sqrt{\lambda(\ell' - z_j)} \sim \sqrt{\lambda\ell'}$ centered on (x_j, y_j). When this small disk is entirely included in the lens aperture, *i.e.*, the larger disk of radius R centered on $x = y = 0$, we obtain

$$\int_{\mathcal{L}} g_{x,\alpha}[k(\boldsymbol{r} - \boldsymbol{r}_j)]\, dx\, dy \approx \frac{3i\pi}{k^2}\delta_{x,\alpha}e^{ik(\ell' - z_j)}\, . \tag{D.20}$$

We use the result Eq. D.20 for all atoms, which amounts to neglect edge effects for the dipoles located at the border of the lens, and we obtain:

$$\mathcal{T} = 1 - \frac{i}{2}\sigma_0 n^{(\text{col})}\Pi, \tag{D.21}$$

with $n^{(\text{col})} = N/\pi R^2$ and where the coefficient Π is defined by

$$\Pi = \frac{1}{N}\sum_j X_{j,x}e^{-ikz_j}. \tag{D.22}$$

This coefficient captures the whole physics of multiple scattering and resonant van der

Waals interactions among the N atoms. Indeed one takes into account all possible couplings between the dipoles when solving the $3N \times 3N$ system $[M]|X\rangle = |Y\rangle$. Once $\mathcal{T}$ is known the optical density is obtained from

$$\mathcal{D} \equiv \ln |\mathcal{T}|^{-2} . \tag{D.23}$$

As an example, consider the limit of a very sparse sample where multiple scattering does not play a significant role ($\sigma_0 n^{(\mathrm{col})} \ll 1$). All non-diagonal matrix elements in $[M]$ are then negligible and $[M]$ is simply the identity matrix, times $i + \delta$. Each $X_{j,x}$ solution of the system of Eq. D.16 is equal to $e^{ikz_j}/(i+\delta)$, and we obtain as expected:

$$\sigma_0 n^{(\mathrm{col})} \ll 1 : \quad \mathcal{T} \approx 1 - \frac{1}{2(1-i\delta)} \sigma_0 n^{(\mathrm{col})} , \quad \mathcal{D} \approx \frac{\sigma_0 n^{(\mathrm{col})}}{1+\delta^2} . \tag{D.24}$$

D.3.3. Light absorption as a quantum scattering process

In order to study the attenuation of a weak probe beam propagating along the z axis when it crosses the atomic medium, we can also use quantum scattering theory. The Hamiltonian of the problem is

$$H = H_0 + V , \qquad H_0 = H_\mathrm{A} + H_\mathrm{F}, \tag{D.25}$$

and we consider the initial state where all atoms are in their ground state and where a single photon of wave vector $\boldsymbol{k} = k\hat{\boldsymbol{u}}_z$ and polarisation $\boldsymbol{\epsilon} = \hat{\boldsymbol{u}}_x$ is incident on the atomic medium

$$|\Psi_\mathrm{i}\rangle = |\mathcal{G}\rangle \otimes |\boldsymbol{k}, \boldsymbol{\epsilon}\rangle, \tag{D.26}$$

with $|\mathcal{G}\rangle \equiv |1:g,\ 2:g,\ \ldots, N:g\rangle$. The state $|\Psi_\mathrm{i}\rangle$ is an eigenstate of H_0 with energy $\hbar\omega$. The interaction of the photon with the atomic medium, described by the coupling V, can be viewed as a collision process during which an arbitrary number of elementary scattering events can take place. Each event starts from a state $|\mathcal{G}\rangle \otimes |\boldsymbol{q}, \boldsymbol{s}\rangle$ and corresponds to:

(i) The absorption of the photon in mode $\boldsymbol{q}, \boldsymbol{s}$ by atom j, which jumps from its ground state $|j:g\rangle$ to one of its excited states $|j:e_\alpha\rangle$. The state of the system is then

$$|\mathcal{E}_{j,\alpha}\rangle = |1:g,\ \ldots, j:e_\alpha, \ldots, N:g\rangle \otimes |\mathrm{vac}\rangle, \tag{D.27}$$

where $|\mathrm{vac}\rangle$ stands for the vacuum state of the electromagnetic field. The subspace spanned by the states $|\mathcal{E}_{j,\alpha}\rangle$ has dimension $3N$.

(ii) The emission of a photon in the mode $(\boldsymbol{q}', \boldsymbol{s}')$ by atom j, which falls back into its ground state.

Finally a photon emerges from the atomic sample, and we want to determine the probability amplitude to find this photon in the same mode $|\boldsymbol{k}, \boldsymbol{\epsilon}\rangle$ as the initial one.

The T matrix defined as

$$T(E) = V + V \frac{1}{E - H + i0_+} V , \tag{D.28}$$

where 0_+ is a small positive number that tends to zero at the end of the calculation, provides a convenient tool to calculate this probability amplitude. Generally

$$T_{if} = \langle \Psi_f | T(E_i) | \Psi_i \rangle \tag{D.29}$$

gives the probability amplitude to find the system in the final state $|\Psi_f\rangle$ after the scattering process. The states $|\Psi_i\rangle$ and $|\Psi_f\rangle$ are eigenstates of the unperturbed Hamiltonian H_0, with energy E_i. Here we are interested in the element T_{ii} of the T matrix, corresponding to the choice $|\Psi_f\rangle = |\Psi_i\rangle$. Using the definition of Eq.D.28 we find

$$T_{ii} = \frac{\hbar\omega_{\mathrm{L}} d^2}{2\varepsilon_0 \mathcal{V}} \sum_{j,j'} e^{ik(z_j - z'_j)} \, \langle \mathcal{E}_{j',x} | \frac{1}{\hbar\omega_{\mathrm{L}} - H + i0_+} | \mathcal{E}_{j,x} \rangle . \tag{D.30}$$

We now have to calculate the $(3N) \times (3N)$ matrix elements of the operator $1/(z - H)$, with $z = \hbar\omega_{\mathrm{L}} + i0_+$, entering into Eq. D.30. We introduce the two orthogonal projectors P and Q, where P projects on the subspace with zero photon, and Q projects on the orthogonal subspace. We thus have

$$P|\mathcal{E}_{j,\alpha}\rangle = |\mathcal{E}_{j,\alpha}\rangle \qquad P|\mathcal{G}\rangle \otimes |\boldsymbol{k}, \boldsymbol{\epsilon}\rangle = 0, \tag{D.31}$$

$$Q|\mathcal{E}_{j,\alpha}\rangle = 0 \qquad Q|\mathcal{G}\rangle \otimes |\boldsymbol{k}, \boldsymbol{\epsilon}\rangle = |\mathcal{G}\rangle \otimes |\boldsymbol{k}, \boldsymbol{\epsilon}\rangle . \tag{D.32}$$

We define the displacement operator

$$R(z) = V + V \frac{Q}{z - QH_0Q - QVQ} V \tag{D.33}$$

and use the general result [231]

$$P \frac{1}{z - H} P = \frac{P}{z - H_{\mathrm{eff}}} , \tag{D.34}$$

where the effective Hamiltonian H_{eff} is

$$H_{\mathrm{eff}} = P \left(H_0 + R(z) \right) P. \tag{D.35}$$

For the following calculations, it is convenient to introduce the dimensionless matrix $[M]$ proportional to the denominator of the right hand side of Eq. D.34:

$$[M]_{(j',\alpha'),(j,\alpha)} = \frac{2}{\hbar\Gamma} \langle \mathcal{E}_{j',\alpha'} | z - H_{\mathrm{eff}} | \mathcal{E}_{j,\alpha} \rangle . \tag{D.36}$$

It is straightforward to check [1] that for $z \to \hbar\omega$ this matrix coincides with the symmetric matrix appearing in Eq. D.16. Indeed the matrix elements of $R(z)$ are

$$\langle \mathcal{E}_{j',\alpha'}|R(z)|\mathcal{E}_{j,\alpha}\rangle = \frac{\hbar d^2}{2\varepsilon_0 \mathcal{V}} \sum_{\boldsymbol{q},s} cq\, s_\alpha^* s_{\alpha'} \frac{e^{i\boldsymbol{q}\cdot(\boldsymbol{r}_{j'}-\boldsymbol{r}_j)}}{z-\hbar\omega}, \tag{D.37}$$

which can be calculated explicitly. For $j = j'$, the real part of this expression is the Lamb shift that we reincorporate in the definition of ω_0, and its imaginary part reads:

$$\langle \mathcal{E}_{j,\alpha'}|R(z)|\mathcal{E}_{j,\alpha}\rangle = -i\frac{\hbar\Gamma}{2}\,\delta_{\alpha,\alpha'}\,. \tag{D.38}$$

For $j \neq j'$, the sum over $(\boldsymbol{q}, \boldsymbol{s})$ appearing in Eq.D.37 is the propagator of a photon from an atom in $\boldsymbol{r}_j$ in internal state $|e_\alpha\rangle$, to another atom in $\boldsymbol{r}_{j'}$ in internal state $|e_{\alpha'}\rangle$. This is nothing but (up to a multiplicative coefficient) the expression that we already introduced for the field radiated in $\boldsymbol{r}_{j'}$ by a dipole located in $\boldsymbol{r}_j$:

$$\langle \mathcal{E}_{j',\alpha'}|R(z)|\mathcal{E}_{j,\alpha}\rangle = -\frac{\hbar\Gamma}{2} g_{\alpha,\alpha'}(\boldsymbol{u}_{j,j'}), \tag{D.39}$$

where the tensor $g_{\alpha,\alpha'}$ is defined in Eqs. D.13-D.14.

Suppose now that the atoms are uniformly distributed over the transverse area $L_x L_y$ of the quantisation volume. We set $n^{(\mathrm{col})} = N/(L_x L_y)$ and we rewrite the expression of Eq.D.30 of the desired matrix element T_{ii} as

$$\frac{T_{ii}L_z}{\hbar c} = \frac{1}{2N}\sigma_0 n^{(\mathrm{col})} \sum_{j,j'} e^{ik(z_j - z_{j'})}\, [M^{-1}]_{(j,x),(j',x)} = \frac{1}{2}\sigma_0 n^{(\mathrm{col})}\Pi\,, \tag{D.40}$$

where the coefficient Π has been defined in Eq.D.22. The result Eq.D.40 combined with Eq. D.21 leads to

$$\mathcal{T} = 1 - i\frac{T_{ii}L_z}{\hbar c}\,, \tag{D.41}$$

which constitutes the 'optical theorem' for our slab geometry, since it relates the attenuation of the probe beam $\mathcal{T}$ to the forward scattering amplitude T_{ii}.

The emergence of resonant van der Waals interactions is straightforward in this approach. Let us consider for simplicity the case where only $N = 2$ atoms are present. The effective Hamiltonian H_{eff} is a 6×6 matrix that can be easily diagonalized and its eigenvectors, with one atom in $|e\rangle$ and one in $|g\rangle$, form in this particular case an orthogonal basis, although H_{eff} is non-Hermitian [243, 244]. For a short distance r between the atoms ($kr \ll 1$), the leading term in $h_1(u)$ and $h_2(u)$ is u^{-3} and the energies (real parts of the eigenvalues) of the six eigenstates vary as $\sim \pm\hbar\Gamma/(kr)^3$ (resonant dipole-dipole interaction). The imaginary parts of the eigenvalues, which give the inverse of the radiative lifetime of the states, tend either to Γ or 0 when $r \to 0$, which correspond to the superradiant and subradiant states for a pair of atoms, respectively [245].

---

[1] As for the derivation leading from Eq. D.10 to Eq. D.12, one must take into account the non-resonant terms that are usually dropped in the RWA, in order to ensure the proper convergence of the sum of Eq.D.37 and obtain the tensor $g_{\alpha\alpha'}$.

For $N > 2$ the eigenvectors of the non-Hermitian Euclidean matrix H_{eff} are in general non orthogonal, which complicates the use of standard techniques of spectral theory in this context [240, 241]. More precisely, one could think of solving the linear system of Eq.D.16, or equivalently calculating T_{ii} in Eq. D.30, by using the expansion of the column vector $|Y\rangle$ defined in Eq. D.17 on the left ($|\alpha_j\rangle$) and right ($\langle\beta_j|$) eigenvectors of H_{eff}. Then one could inject this expansion in the general expression of the matrix element T_{ii}, to express it as a sum of the contributions of the various eigenvalues of H_{eff}. However the physical discussion based on this approach is made difficult by the fact that since H_{eff} is non-Hermitian, the $\{|\alpha_j\rangle\}$ and the $\{|\beta_j\rangle\}$ bases do not coincide. Hence the weight $\langle\beta_j|Y\rangle\langle Y|\alpha_j\rangle$ of a given eigenvalue in the sum providing the value of T_{ii} is not a positive number, and this complicates the interpretation of the result.

As a final comment we note that our approach does not make use of the quite common concept of self-energy. In the context of the propagation of waves in a random medium [222], the self-energy Σ appears by averaging the relation $G = G_0 + G_0VG$ over disorder , where $G = 1/(z - H)$ and $G_0 = 1/(z - H_0)$. The average $\tilde{G}$ of G then satisfies $\tilde{G} = G_0 + G_0\Sigma\tilde{G}$, where Σ is an infinite sum of irreducible diagrams. Here we choose a different but equivalent route, which consists in solving exactly the scattering problem for N atoms and 1 photon for a given realisation of the disorder, *i.e.*, a given draw $\{\boldsymbol{r}_j\}$ of the positions of the atoms, obtain the attenuation $\mathcal{T}$ of the sample, and subsequently average this result over several realisations of the disorder (see § D.4).

D.3.4. Beyond the sparse sample case: 3D vs. 2D

For a sparse sample, we already calculated the optical density at first order in density (Eq. D.24) and the result is identical for a strictly 2D gas and a thick one. The approach based on quantum scattering theory is well suited to go beyond this first order approximation and look for differences between the 2D and 3D cases. The basis of the calculation is the series expansion of Eq. D.34, which gives

$$P\frac{1}{z-H}P = \frac{P}{z-H_0} + \sum_{n=1}^{\infty} \frac{P}{z-H_0}\left(PR(z)P\frac{1}{z-H_0}\right)^n . \tag{D.42}$$

Consider the case of a resonant probe $\delta = 0$ for simplicity. The result $\mathcal{T} \approx 1 - \sigma_0 n^{(\text{col})}/2$ obtained for a sparse sample in Eq. D.24 corresponds to the first term $[P/(z - H_0)]$ of this expansion. Here we investigate the next order term and explain why one can still recover the Beer-Lambert law for a thick (3D) gas, but not for a 2D sample.

Double scattering diagrams for a thick sample ($k\ell_z \gg 1$). We start our study by adding the first term ($n = 1$) in the expansion of Eq.D.42 to the zero-th order term already taken into account in Eq. D.24. This amounts to take into account the diagrams where the incident photon is scattered on a single atom, and those where the photon 'bounces' on two atoms before leaving the atomic sample. Injecting the first two terms of the expansion of Eq.D.42 into Eq. D.40, we obtain

$$\frac{T_{ii}L_z}{\hbar c} = \frac{1}{2}\sigma_0 n^{(\mathrm{col})}\left[-i + \frac{1}{N}\sum_j \sum_{j'\neq j} e^{ik(z_j - z_{j'})} g_{xx}(\boldsymbol{u}_{jj'})\right] . \tag{D.43}$$

We now have to average this result on the positions of the atoms j and j'. There are $N(N-1) \approx N^2$ couples (j, j'). Assuming that the gas is dilute so that the average distance between two atoms (in particular $|z_j - z_{j'}|$) is much larger than k^{-1}, the leading term in g_{xx} is the e^{iu}/u contribution of $h_1(u)$ in Eqs. (D.13)-(D.14). We thus arrive at

$$\frac{T_{ii}L_z}{\hbar c} = \frac{1}{2}\sigma_0 n^{(\mathrm{col})}\left[-i + \frac{3N}{2k}\langle e^{ik(z-z')}\frac{e^{ik|\boldsymbol{r}-\boldsymbol{r}'|}}{|\boldsymbol{r}-\boldsymbol{r}'|}\rangle\right] , \tag{D.44}$$

where the average is taken over the positions $\boldsymbol{r}$ and $\boldsymbol{r}'$ of two atoms. We first calculate the average over the xy coordinates and we get (cf. Eq. (D.20))

$$\frac{T_{ii}L_z}{\hbar c} = \frac{1}{2}\sigma_0 n^{(\mathrm{col})}\left[-i + \frac{i}{2}\sigma_0 n^{(\mathrm{col})}\langle e^{ik(z-z')}e^{ik|z-z'|}\rangle\right] . \tag{D.45}$$

For a thick gas ($k\ell_z \gg 1$) the bracket in this expression has an average value of $\approx 1/2$. Indeed the function to be averaged is equal to 1 if $z < z'$, which occurs in half of the cases, and it oscillates and averages to zero in the other half of the cases, where $z > z'$. We thus obtain the approximate value of the transmission coefficient:

$$k\ell_z \gg 1: \quad \mathcal{T} = 1 - i\frac{T_{ii}L_z}{\hbar c} \approx 1 - \frac{1}{2}\sigma_0 n^{(\mathrm{col})} + \frac{1}{8}\left(\sigma_0 n^{(\mathrm{col})}\right)^2 , \tag{D.46}$$

where we recognize the first three terms of the power series expansion of $\mathcal{T} = \exp(-\sigma_0 n^{(\mathrm{col})}/2)$, corresponding to the optical density $\mathcal{D} = \sigma_0 n^{(\mathrm{col})}$.

Double scattering diagrams for a 2D gas ($\ell_z = 0$). When all atoms are sitting in the same plane, the evaluation of the second order term (and the subsequent ones) in the expansion of T_{ii} in powers of the density is modified with respect to the 3D case. The calculation starts as above and the second term in the bracket of Eq. (D.43) can now be written

$$\frac{1}{N}\sum_j \sum_{j'\neq j} g_{xx}(u_{jj'}) = n^{(2\mathrm{D})} \int g_{xx}(\boldsymbol{u})\, d^2u . \tag{D.47}$$

If we keep only the terms varying as e^{iu}/u in h_1 and h_2 (Eq. (D.14)), we can calculate analytically the integral in (D.47) and find the same result as in 3D, *i.e.*, $i\sigma_0 n^{(2\mathrm{D})}/4$. If this was the only contribution to (D.47), it would lead to the Beer–Lambert law also in 2D, at least at second order in density. However one can check that a significant contribution to the integral in (D.47) comes from the region $u = kr < 1$. In this region, it is not legitimate to keep only the term in e^{ikr}/kr in h_1, h_2, since the terms in $e^{ikr}/(kr)^3$, corresponding to the short range resonant van der Waals interaction, are actually dominant. Therefore the expansion of the transmission coefficient $\mathcal{T}$ in powers of the density differs from (D.46), and one cannot recover the Beer–Lambert law at second order in density. Calculating analytically corrections to this law could be done following the procedure of [223]. Here we will use a numerical method to determine the deviation with respect to the Beer–Lambert law (see section D.4.2).

Remark. For a 3D gas there are also corrections to the second term in Eq. (D.45) due the $1/r^3$ contributions to h_1 and h_2. However these corrections have a different scaling with the density and can be made negligible. More precisely their order of magnitude is $\sim n^{(3D)}k^{-3}$, to be compared with the value $\sim n^{(\mathrm{col})}k^{-2}$ of the second term in Eq. (D.45). Therefore one can have simultaneously $n^{(3D)}k^{-3} \ll 1$ and $n^{(\mathrm{col})}k^{-2} \gtrsim 1$, if the thickness ℓ_z of the gas along z is $\gg 1/k$.

D.4. Absorption of light by a slab of atoms

In order to study quantitatively the optical response of a quasi-2D gas, we have performed a Monte Carlo calculation of the transmission factor $\mathcal{T}$ given in Eq. (D.21), and of the related optical density $\mathcal{D} = \ln |\mathcal{T}|^{-2}$. We start our calculation by randomly drawing the positions of the N atoms, we then solve numerically the $3N \times 3N$ linear system (D.16), and finally inject the result for the N dipoles in the expression of $\mathcal{T}$.

The atoms are uniformly distributed in a cylinder of axis z, with a radius R and a thickness ℓ_z. The largest spatial densities considered in this work correspond to a mean inter-particle distance $\approx k^{-1}$. Around each atom we choose a small excluded volume with a linear size $a = 0.01\,k^{-1}$. We varied a by a factor 10 around this value and checked that our results were essentially unchanged. Apart from this excluded volume we do not include any correlation between the positions of the atoms. This choice is justified physically by the fact that, in the case of large phase space densities which motivates our study, the density fluctuations in a 2D Bose gas are strongly reduced and the two-body correlation function $g_2(\boldsymbol{r}, \boldsymbol{r}')$ is such that $g_2(\boldsymbol{r}, \boldsymbol{r}) \approx 1$ [124].

In this section we first determine the value of N that is needed to reach the 'thermodynamic limit' for our problem: for a given thickness ℓ_z, $\mathcal{D}$ should not be an independent function of the number of atoms N and the disk radius R, but should depend only of the ratio $N/\pi R^2 = n^{(\mathrm{col})}$. We will see that this imposes to use relatively large number of atoms, typically $N > 1000$, for the largest spatial densities considered here. All subsequent calculations are performed with $N = 2048$. We then study the dependence of $\mathcal{D}$ with the various parameters of the problem: the column density $n^{(\mathrm{col})}$, the thickness of the gas ℓ_z, and the detuning Δ. In particular we show that for a given $n^{(\mathrm{col})}$ we recover the 3D result of Eq. D.1 when the thickness ℓ_z is chosen sufficiently large.

D.4.1. Reaching the 'thermodynamic limit'

We start our study by testing the minimal atom number that is necessary to obtain a faithful estimate of the optical density. We choose a given value of $n^{(\mathrm{col})} = N/\pi R^2$ and we investigate how $\mathcal{D}$ depends on N either for a strictly 2D gas ($\ell_z = 0$) or for a gas extending significantly along the third direction ($\ell_z = 20\,k^{-1}$). We consider a resonant probe for this study ($\Delta = 0$). We vary N by multiplicative steps of 2, from $N = 8$ up to $N = 2048$ and we determine how large N must be so that $\mathcal{D}$ is a function of $n^{(\mathrm{col})}$ only.

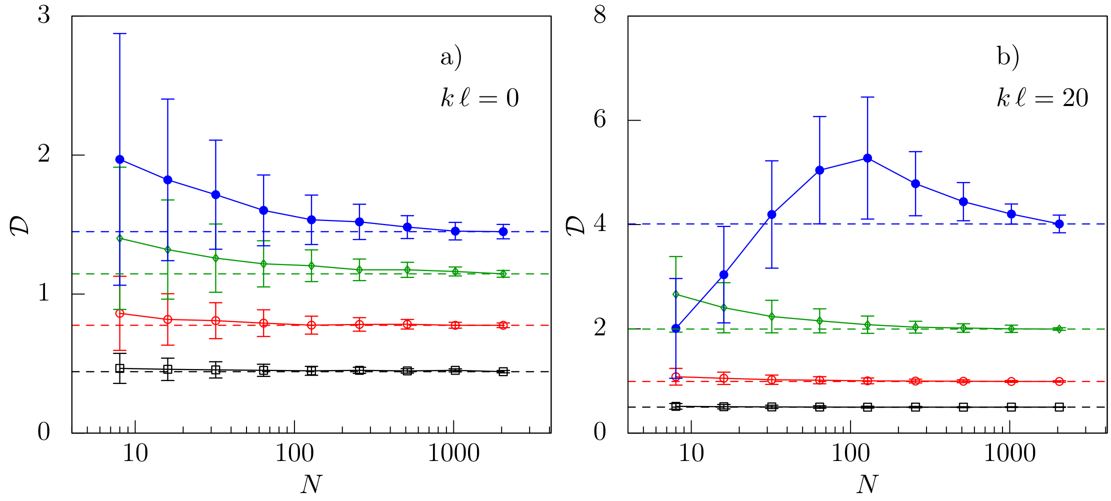

Figure D.2.: Variation of the optical density $\mathcal{D} = \ln|\mathcal{T}|^{-2}$ calculated from (D.21) as function of the number of atoms N, for $\ell_z = 0$ (a) and $\ell_z = 20\,k^{-1}$ (b), and for 4 values of the density: $\sigma_0 n^{(2D)} = 0.5$ (black empty squares), 1 (red empty circles), 2 (green diamonds) and 4 (blue filled circles). The bars indicate the standard deviations. The dotted lines give the value obtained for our largest value of N ($N = 2048$). The results have been obtained at resonance ($\Delta = 0$).

The results are shown in Fig. D.2a and Fig. D.2b, where we plot $\mathcal{D}$ as a function of N. We perform this study for four values of the density $n^{(\mathrm{col})}$, corresponding to $\sigma_0 n^{(\mathrm{col})} = 0.5, 1, 2$ and 4. Let us consider first the smallest value $\sigma_0 n^{(\mathrm{col})} = 0.5$. For each value of N we perform a number of draws that is sufficient to bring the standard error below 2×10^{-3} and we find that the calculated optical density is independent of N (within standard error) already for $N \gtrsim 100$, for both values of ℓ_z. Consider now our largest value $\sigma_0 n^{(\mathrm{col})} = 4$; for a strictly 2D gas ($\ell_z = 0$), $\mathcal{D}$ reaches an approximately constant value independent of N for $N \gtrsim 1000$. For $\sigma_0 n^{(\mathrm{col})} = 4$ and a relatively thick gas ($\ell_z = 20\,k^{-1}$, blue squares in Fig. D.2b), reaching the thermodynamic limit is more problematic since there is still a clear difference between the results obtained with 1024 and 2048 atoms. This situation thus corresponds to the limit of validity of our numerical results. In the remaining part of the [annex] we will show only results obtained with $N = 2048$ atoms for column densities not exceeding $\sigma_0 n^{(\mathrm{col})} = 4$. The number of independent draws of the atomic positions (at least 8) is chosen such that the standard error for each data point is below 2%.

D.4.2. Measured optical density vs. Beer–Lambert prediction

We now investigate the variation of the optical density $\mathcal{D} = \ln|\mathcal{T}|^{-2}$ as function of the column density of the sample $n^{(\mathrm{col})}$, or equivalently of the Beer–Lambert prediction $\mathcal{D}_{\mathrm{BL}} = n^{(\mathrm{col})}\sigma$. We suppose in this section that the probe beam is resonant ($\Delta = 0$), and we address the cases of a strictly 2D gas ($\ell_z = 0$) and a thick slab ($\ell_z = 20\,k^{-1}$).

Consider first the case of a strictly 2D case, $\ell_z = 0$, leading to the results shown in

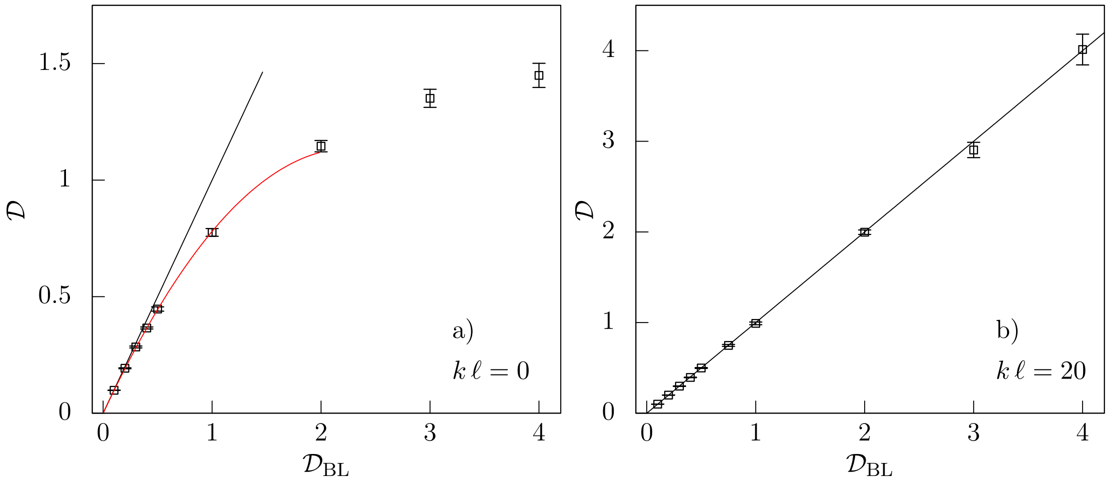

Figure D.3.: Variations of the optical density $\mathcal{D}$ as function of the Beer–Lambert prediction $\mathcal{D}_{\rm BL}$ for $\ell_z = 0$ (a) and $\ell_z = 20\,k^{-1}$ (b). The black dotted line is the straight line of slope 1. In (a) the continuous red line is a quadratic fit $\mathcal{D} = \mathcal{D}_{\rm BL}\,(1 - \mu\,\mathcal{D}_{\rm BL})$ with $\mu = 0.22$ to the data points with $\mathcal{D}_{\rm BL} \leq 1$. The calculations are done for $N = 2048$, $\Delta = 0$ and the bars indicate standard deviations.

Fig. D.3a. We see that $\mathcal{D}$ differs significantly ($\sim$ 25%) from $\mathcal{D}_{\rm BL}$ already for $\mathcal{D}_{\rm BL}$ around 1. A quadratic fit to the calculated variation of $\mathcal{D}$ for $\sigma_0 n^{(2\rm D)} < 1$ (continuous red line) gives

$$\mathcal{D} \approx \mathcal{D}_{\rm BL}\,(1 - 0.22\,\mathcal{D}_{\rm BL})\,. \tag{D.48}$$

The discrepancy between $\mathcal{D}$ and $\mathcal{D}_{\rm BL}$ increases when the density increases: for $\mathcal{D}_{\rm BL} = 4$, the calculated $\mathcal{D}$ is only ≈ 1.4. For such a large density the average distance between nearest neighbours is $\approx k^{-1}$ and the energy shifts due to the dipole-dipole interactions are comparable to or larger than the linewidth Γ. The atomic medium is then much less opaque to a resonant probe beam than in the absence of dipole-dipole coupling.

Consider now the case of a thick sample, $\ell_z = 20\,k^{-1}$ (Fig. D.3b). The calculated optical density is then very close to the Beer–Lambert prediction over the whole range that we studied. This means that in our chosen range of optical densities, the mean-field approximation leading to $\mathcal{D}_{\rm BL}$ is satisfactory as soon as the sample thickness exceeds a few optical wavelengths $\lambda = 2\pi/k$.

It is interesting to characterize how the optical density evolves from the value for a strictly 2D gas to the expected value from the Beer–Lambert law $\mathcal{D}_{\rm BL}$ when the thickness of the gas increases. We show in Fig. D.4 the variation of $\mathcal{D}$ as function of ℓ_z for three values of the column density corresponding to $\mathcal{D}_{\rm BL} = 1, 2$ and 4. An exponential fit $\mathcal{D} = \alpha + \beta \exp(-\ell_z/\ell_c)$ to these data for $2\,k^{-1} \leq \ell_z \leq 20\,k^{-1}$ gives a good account of the observed variation over this range, and it provides the characteristic thickness ℓ_c needed to recover the Beer–Lambert law. We find that $\ell_c \approx 3.0\,k^{-1}$ for $\mathcal{D}_{\rm BL} = 1$, $\ell_c \approx 3.5\,k^{-1}$ for $\mathcal{D}_{\rm BL} = 2$, and $\ell_c \approx 4.4\,k^{-1}$ for $\mathcal{D}_{\rm BL} = 4$.

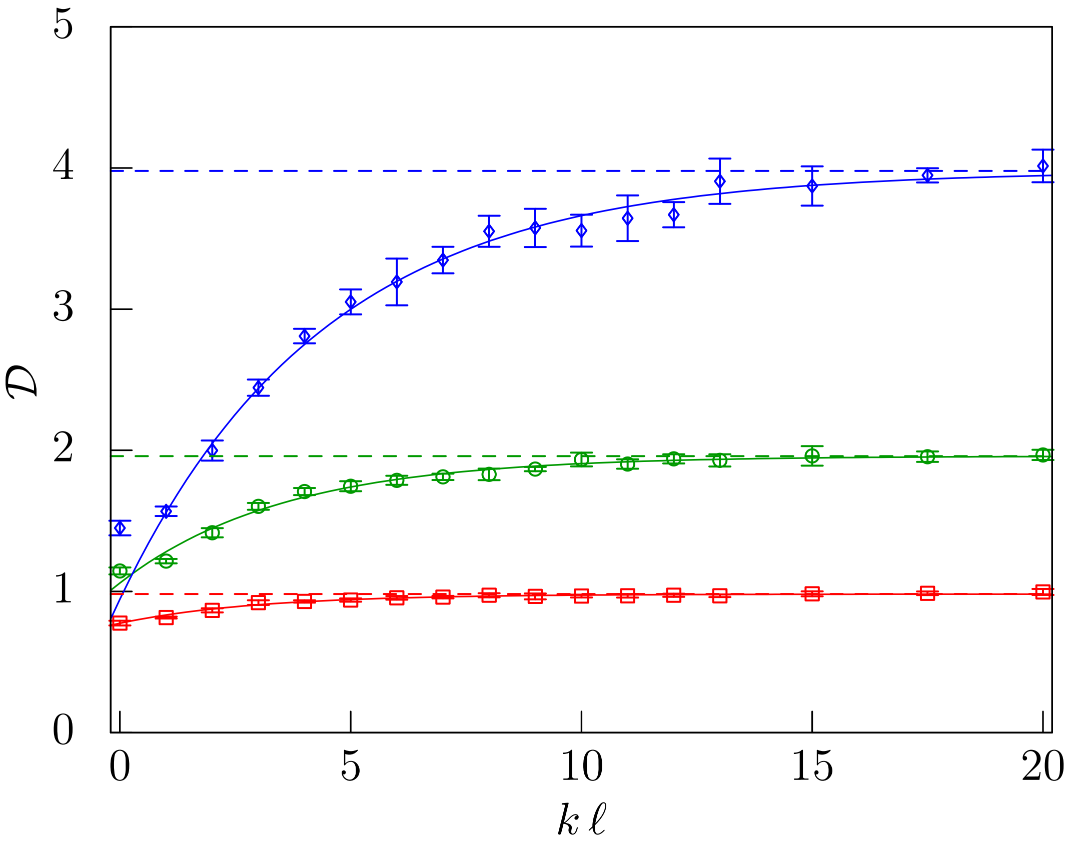

Figure D.4.: Variation of $\mathcal{D}$ with the thickness ℓ_z of the gas for various column densities corresponding to $\mathcal{D}_{\text{BL}} = 1$ (red squares), 2 (green circles), 4 (blue diamonds). The continuous lines are exponential fits to the data. The dotted lines give the Beer–Lambert result. The calculations are done for $N = 2048$, $\Delta = 0$ and the bars indicate standard deviations.

Remark. For the largest value of the column density considered here ($n^{(\text{col})}\sigma_0 = 4$) we find that $\mathcal{D}$ increases slightly above the value $\mathcal{D}_{\text{BL}}$ when ℓ_z is chosen larger than $20\,k^{-1}$ (upper value considered in Fig. D.4). We believe that this is a consequence of the edge terms that we neglected when approximating Eq. (D.19) by Eq. (D.21). These terms become significant for $\mathcal{D}_{\text{BL}} = 4$ because for our atom number $N = 2048$, the sample radius $R \approx 55\,k^{-1}$ is then not very large compared to its thickness for $\ell_z \gtrsim 20\,k^{-1}$. In order to check this assumption, we also calculated numerically the result of Eq. (D.19) (instead of Eq. (D.21)) for practical values of the parameters (position and radius) of the lens represented in Fig. D.1a. The results give again $\mathcal{D} \approx \mathcal{D}_{\text{BL}}$, but now with $\mathcal{D}$ remaining below $\mathcal{D}_{\text{BL}}$. Since our emphasis in this [annex] is rather put on the 2D case, we will not explore this aspect further here.

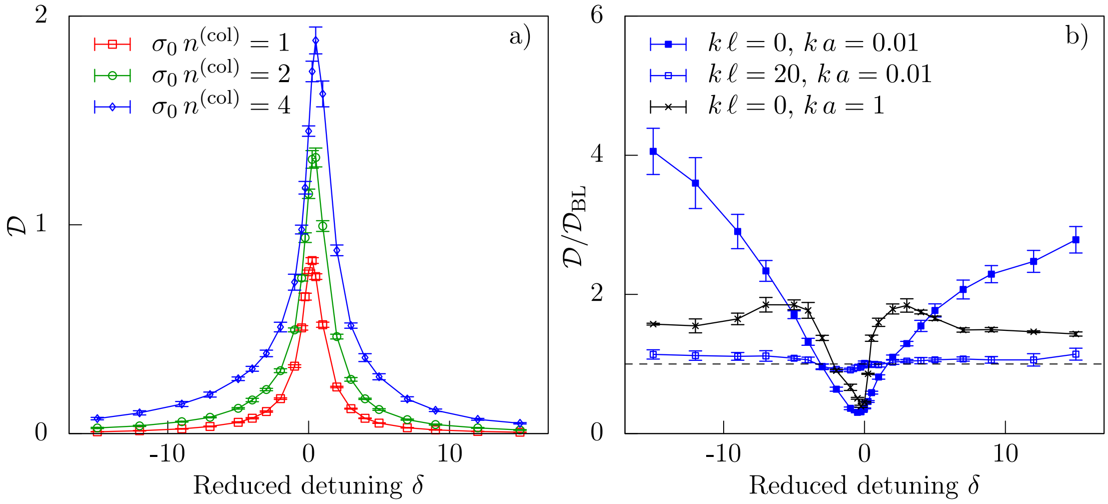

Figure D.5.: (a) Variation of $\mathcal{D}$ with the reduced detuning $\delta = 2\Delta/\Gamma$ of the probe laser in the case of a 2D gas ($\ell_z = 0$), for three values of the column density $\sigma_0 n^{(\mathrm{col})} = 1$ (red squares), 2 (green circles), and 4 (blue diamonds). (b) Blue full squares: same data as in (a), now plotted for $\mathcal{D}/\mathcal{D}_{\mathrm{BL}}$ as function of δ. Blue open squares: $\mathcal{D}/\mathcal{D}_{\mathrm{BL}}$ for a thick gas ($\ell_z = 20\,k^{-1}$). Black stars: $\mathcal{D}/\mathcal{D}_{\mathrm{BL}}$ for a 2D gas ($\ell_z = 0$) and a large exclusion region around each atom ($a = k^{-1}$). All data in (b) correspond to $\sigma_0 n^{(\mathrm{2D})} = 4$. The calculations are done with $N = 2048$ atoms and the bars indicate standard deviations.

D.4.3. Absorption line shape

Resonant van der Waals interactions manifest themselves not only in the reduction of the optical density at resonance but also in the overall line shape of the absorption profile. To investigate this problem we have studied the variations of $\mathcal{D}$ with the detuning of the probe laser. We show in Fig. D.5a the results for a strictly 2D gas ($\ell_z = 0$) for $n^{(\mathrm{col})}\sigma_0 = 1, 2$ and 4. Several features show up in this series of plots. First we note a blue shift of the resonance, which increases with $n^{(\mathrm{2D})}$ and reaches $\Delta \approx \Gamma/4$ for $\sigma_0 n^{(\mathrm{2D})} = 4$. We also note a slight broadening of the central part of the absorption line, since the full-width at half maximum, which is equal to Γ for an isolated atom, is $\simeq 1.3\Gamma$ for $n^{(\mathrm{col})}\sigma_0 = 4$. Finally we note the emergence of large, non-symmetric wings in the absorption profile. This asymmetry is made more visible in Fig. D.5b, where we show with full blue squares the same data as in Fig. D.5a for $n^{(\mathrm{col})}\sigma_0 = 4$, but now plotting $\mathcal{D}/\mathcal{D}_{\mathrm{BL}}$ as function of δ. For a detuning $\delta = \pm 15$, the calculated optical density exceeds the Beer–Lambert prediction by a factor 4.1 (resp. 2.8) on the red (resp. blue) side.

In order to get a better understanding of these various features, we give in Fig. D.5b two additional results. On the one hand we plot with empty blue squares the variations of $\mathcal{D}/\mathcal{D}_{\mathrm{BL}}$ for a thick gas ($\ell_z = 20\,k^{-1}$) with the same column density $n^{(\mathrm{col})}\sigma_0 = 4$. There are still some differences between $\mathcal{D}$ and $\mathcal{D}_{\mathrm{BL}}$ in this case, as already pointed out in [228], but they are much smaller than in the $\ell_z = 0$ case. This indicates that the strong deviations with respect to the Beer–Lambert law that we observe in Fig. D.5a are specific 2D features. On the other hand we plot with black stars the variations of $\mathcal{D}/\mathcal{D}_{\rm BL}$ for a 2D gas ($\ell_z = 0$) in which we artificially increased the exclusion radius around each atom up to $a = k^{-1}$ instead of $a = 0.01\,k^{-1}$ (blue full squares) for the other results in this [annex]. This procedure, which was suggested to us by Robin Kaiser, allows one to discriminate between effects due to isolated pairs of closely spaced atoms, and many-body features resulting from multiple scattering of photons among larger clusters of atoms. The comparison of the results obtained for $a = 0.01\,k^{-1}$ and $a = k^{-1}$ suggests that the blue shift of the resonance line, which is present in both cases, is a many-body phenomenon, whereas the large amplitude wings with a blue-red asymmetry, which occurs only for $a = 0.01\,k^{-1}$, is rather an effect of close pairs.

This asymmetry in the wings of the absorption line in a 2D gas can actually be understood in a semi-quantitative manner by a simple reasoning. We recall that for two atoms at a distance $r \ll k^{-1}$, the levels involving one ground and one excited atom have an energy (real part of the eigenvalues of $H_{\rm eff}$) that is displaced by $\sim \pm\hbar\Gamma/(kr)^3$. A given detuning δ can thus be associated to a distance r between the two members of a pair that will resonantly absorb the light. To be more specific let us consider a pair of atoms with $kr \ll 1$, and suppose for simplicity that it is aligned either along the polarization axis of the light (x) or perpendicularly to the axis (y). In both cases the excited state of the pair that is coupled to the laser is the symmetric combination $(|1:g;2:e_x\rangle + |1:e_x;2:g\rangle)/\sqrt{2}$. If the pair is aligned along the x axis, this state has an energy $\hbar\omega_0 - 3\hbar\Gamma/2(kr)^3$, hence it is resonant with red detuned light such that $\delta = -3/(kr)^3$. If the pair axis is perpendicular to x, the state written above has an energy $\hbar\omega_0 + 3\hbar\Gamma/4(kr)^3$, hence it is resonant with blue detuned light such that $\delta = 3/2(kr)^3$. This clearly leads to an asymmetry between red and blue detuning; indeed the pair distance r needed for ensuring resonance for a given $\delta > 0$, $r_{\rm blue} = (3/2|\delta|)^{1/3}\,k^{-1}$, is smaller than the value $r_{\rm red} = (3/|\delta|)^{1/3}\,k^{-1}$ for the opposite value $-\delta$. Since the probability density for the pair distance at small r is $\mathcal{P}(r) \propto r$ in 2D for randomly drawn positions, we expect the absorption signal to be stronger for $-\delta$ than for $+\delta$. In a 3D geometry the variation of the probability density at small r is even stronger ($\mathcal{P}(r) \propto r^2$), but it is compensated by the fact that the probability of occurrence of pairs that are resonant with blue detuned light is dimensionally increased. For example in our simplified modelling where the pair axis is aligned with the references axes, a given pair will be resonant with blue detuned light in 2/3 of the cases (axis along y or z) and resonant with red detuned light only in 1/3 of the cases (axis along x). This explains why the asymmetry of the absorption profile is much reduced for a 3D gas in comparison to the 2D case.

D.5. Conclusion

We have presented in this [annex] a detailed analysis of the scattering of light by a disordered distribution of atoms in a quasi-two dimensional geometry. The particles were treated as fixed scatterers and their internal structure was modeled as a two-level system, with a $J = 0$ ground state and a $J = 1$ excited state. In spite of these simplifying assumptions the general trend of our results is in good agreement with the experimental finding of [139], where a variation of the measured optical density similar to that of

Fig. D.3 was measured.

Several improvements in our modeling can be considered in order to reach a quantitative agreement with theory and experiment. The first one is to include the relatively complex atomic structure of the alkali-metal species used in practice, with a multiply degenerate ground state; this could be done following the lines of [232, 233]. A second improvement consists in taking into account the atomic motion. This is in principle a formidable task, because it leads to a spectacular increase in the dimension of the relevant Hilbert space. This addition can however be performed in practice in some limiting cases, for example if one assumes that the particles are tightly bound in a lattice [246, 247]. When the atom-light interaction is used only to probe the spatial atomic distribution of the gas, neglecting the particle motion should not be a major problem. Indeed the duration of the light pulse is quite short ($\sim$ 10 microseconds only). Each atom scatters only a few photons in this time interval and its displacement is then smaller than the mean interatomic spacing for the spatial densities encountered in practice. The acceleration of the atoms under the effect of resonant van der Waals interaction should also have a minor effect under relevant experimental conditions.

Finally another aspect that could be valuably studied is the interaction of the gas with an intense laser beam [137]. One could thus validate the intuitive idea that saturation phenomena reduce the effects of resonant van der Waals interactions [69, 70], and are thus helpful to provide a faithful estimate of the atomic density from the light absorption signal. A first step in this direction consists in implementing the tools developed in [248, 249], which allow one to study the modification of the coherent propagation of light in an dilute medium, due to the non-linear optical response of the scatterers. In particular it would be interesting to investigate if the instabilities found in [249] can play a significant role in absorption imaging of dense atomic clouds.

E. Historical procedure and results for the calibration of the α imaging coefficient

In this annex, I will present the "historical" procedure to calibrate the value of the imaging coefficient α, which has been introduced in chapter 3 (see for example Eq. 3.9). This procedure was initially developed by G. Reinaudi [137] and used for the previous calibration on our experiment, which has been performed by T. Yefsah [110] in 2010. I will present such an analysis for the data taken during our new calibration campaign whose reasons and details have been presented in 3.3.3.1 and 3.3.3.2. As stated in this latter section, we actually started by implementing this "historical" analysis on our set of data but the surprising results obtained led us to build up a new and more straightforward procedure for computing α. The results of this new analysis are presented in 3.3.3 and complete the overall imaging calibration procedure. The development presented in this annex are thus unnecessary for the completeness of the calibration but it reveals profitable to analyze them thoroughly: First, we note that its conclusions are in agreement with the new analysis (see *e.g* Fig. 3.6 and Fig. E.2) and so the calibration performed with this new campaign is not intrinsically different from its previous realizations. Second, it is interesting to highlight the lack of understanding we get from using this method and how this is fixed by the new procedure developed in the main text (see 3.3.3.4).

E.1. Principle

As introduced in 3.3.3, the principle of any analysis for the calibration of α^* (which denotes the physical value of the parameter α of Eq. 3.9) is to find the value of this coefficient for which the optical density distribution $d_\alpha(x, y; s, \tau)$ over one cloud configuration (whose spatial dependency is embodied by the variables (x, y)) is a constant toward the variations of the imaging parameters, namely the intensity of the probe beam $I = sI_{\text{sat}}$ and its pulse duration τ. We remind that d_α is given by:

$$d_\alpha = \alpha d_{\log} + d_{\text{diff}} \tag{E.1}$$

$$\text{where } d_{\log} = -\ln\left(\frac{I_{\text{f}} - 2\gamma}{I_{\text{i}} - \gamma}\right) \tag{E.2}$$

$$\text{and } d_{\text{diff}} = \frac{I_{\text{i}} - I_{\text{f}} + \gamma}{\eta I_{\text{sat}}}. \tag{E.3}$$

where I_{i} and I_{f} denote the distributions of the light intensity arriving or going out of the cloud, γ and η are constants of our imaging setup introduced in 3.3.1 and 3.3.2 respectively.

In the "historical" procedure presented here, one deduces α^* by minimizing the deviation of the optical densities d_α (toward α) over a set of N images taken in the same cloud configuration but with varying s and τ. For this minimization, an intermediate quantity is computed on which a fit is ultimately performed. Such an indirect method somehow hides the defects of the experimental data and makes the analysis of the experimental errors more complex.

In practice, the procedure is the following :

1. As explained in the main text in the case of the new method, we have at our disposal a set of N absorption images of a cloud always prepared in the same configuration. The images are taken successively, repeating the same preparation sequence several times and varying at the end of each production stage the imaging parameters s and τ used to take an absorption picture of the gas.
2. For each image k of this set, we compute the azimuthal average[1] of the optical density $d_\alpha\,(r;k)$ for a given range of α (manually introduced along Eq. E.1).
3. We compute the standard deviation, noted $\sigma(r,\alpha)$, of this optical density $d_\alpha\,(r;k)$ over the whole set of N images: $\sigma(r,\alpha) = std_{k\in[1,N]}\,[d_\alpha(r;k)]$. $\sigma(r,\alpha)$ thus estimates the variations of the optical density computed with a given α on a given radius r over the range of the considered couples (s,τ) and taking into account their numerous repetitions.
4. For each radius r, $\sigma(r,\alpha)$ typically shows a minimum at a given value of α called $\alpha^*(r)$. We fit $\sigma(r,\alpha)$ variations to

   $$\sigma(r,\alpha) = \sqrt{\sigma_{\min}(r)^2 + C(r)^2(\alpha - \alpha^*(r))^2} \tag{E.4}$$

   The fitted parameter $\alpha^*(r)$ is an estimate of the physical value α^* we want to calibrate at the radius r.

   Note: This fit generally gives a perfect match to the computed standard deviation in terms of α. Indeed, σ is representing the fluctuations according to a smoothly varying parameter α that we artificially introduced (see step 2 of the procedure). Hence, from this artifact, $\sigma(r,\alpha)$ shows a noiseless variation versus α perfectly described by the hyperbolic model of Eq. E.4. Nevertheless, such a perfect match does not give any indication on the quality of the experimental data themselves. No errorbars can be extracted directly from this fit and a more sophisticate analysis of the data set must be carried out to evaluate the experimental deviations within this method.
5. For the radii r where this analysis is valid, we expect $\alpha^*(r)$ to be equal to the physical value of the coefficient α. It must then be a constant with r and its averaged value must not depend on the set of data considered. We thus complete this analysis, by selecting a set of relevant r for which our previous analysis is accurate. These radii should correspond to a specified range of atomic densities $n(r)$:
   — $n(r)$ must not be too low so that the determination of α^* is not too sensitive to the intensity shot noise of the probe beam;

---

[1] For an explanation of the use of the azimuthal average,see 3.3.3.2. The aim is to lower the noise compared to a pixel-wise comparison of the optical density by performing an averaging on comparable cloud regions.

— $n(r)$ must not be too high so that we are not sensitive to the collective effects (see Annex D) and thus Eq. E.1 demonstrated in 3.1.2 remains valid for all the probing intensities ($I = sI_{\text{sat}}$) considered.

The cloud configuration we considered for the recent calibration campaign (see 3.3.3.1 and 3.3.3.3) used a free expansion of the atomic distribution (2D and if necessary 3D) which is uniform in-situ. Then framing the value of $n(r)$ simply translates into selecting a continuous range of radii : $r \in [r_{\min}, r_{\max}]$ for each of the calibration set taken. We then deduce the global value of α^* by averaging $\alpha^*(r)$ on this range of radii.

E.2. Results

As detailed in the main text (see 3.3.3.3), the ensemble of data for the new calibration campaign is composed of four different sets of images. Roughly, two were taken in a "hot" cloud configuration and the other two in a "cold" one, enabling thus to investigate an enlarged range of optical densities.

In Fig. E.1, we show, for one of these four data sets (the set numbered 2 in Table E.1), the extracted values of $\alpha^*(r)$ and $\sigma_{\min}(r)$ from fitting of the set of $\sigma(r, \alpha)$ to Eq. E.4 (see E.1). In this figure, we also show an estimate of the optical density $d_{\alpha=3.7}(r)$ that is computed along Eq. E.1 with a fixed[2] $\alpha = 3.7$ and averaged over all the images: $d_{\alpha=3.7}(r) = \langle d_{\alpha=3.7}(r; k)\rangle_{n\in[1,N]}$.

We then want to average the values of the first fitting parameter $\alpha^*(r)$ on a given range of radii $r \in [r_{\min}, r_{\max}]$ to estimate α^* (see E.1), independently for each of our four data sets. In order to set $[r_{\min}, r_{\max}]$ we compare for each r, the value of the second fitting parameter $\sigma_{\min}(r)$ to the estimated optical density $d_{\alpha=3.7}(r)$. $\sigma_{\min}(r)$ assesses the deviation of the optical density d_α of Eq. E.1 computed with $\alpha = \alpha^*(r)$ at the radius r. We thus consider the relative deviation of the density $\bar{\sigma}(r) = \sigma_{\min}(r)/d_{\alpha=3.7}(r)$ at a fixed r. As the absolute value of $\bar{\sigma}(r)$ depends on the set of images considered, we compare it to the minimal value it takes $\bar{\sigma}_0$ over this given set. Then to distinguish the relevant r from the irrelevant ones for the calibration, we arbitrarily fix a maximal value f to the ratio $\bar{\sigma}(r)/\bar{\sigma}_0$. Relevant r's are those for which $\bar{\sigma}(r) \leq f\bar{\sigma}_0$ (not too high variations of the density). Typically, we choose $f = 1.4$ and this corresponds to a range $[r_{\min}, r_{\max}]$ spanning typically 2 gaussian widths of the atomic cloud.

As shown in Fig. E.1 where relevant data are represented in blue (and irrelevant ones in red), we note that the value of $\alpha^*(r)$ is well approximated by a constant in the extracted range of r (as expected theoretically). In Fig. E.1, we show the average value of this blue points and its error. We denote α^*_{fit} the estimate of the physical value of α assessed through this average.

In Table E.1, we summarize all the fitted values α^*_{fit} for the four data sets available. We found different values of α^*_{fit} according to the set considered. At this point of the analysis, we could not distinguish if such an intriguing result was due to the overall

---

[2] We choose such a value as we expect it to be close to the physical value α^*. We could also define an expected optical density per radius directly from the fits, by $d_{std}(r) = \alpha^*(r)d_{\log}(r) + d_{\text{diff}}(r)$ where $\alpha^*(r)$ is the value of α deduced from the fit for each radius r. The following results are not drastically changed by this choice.

data quality, to few outlier data points or to a physical effect. This uncertainty led us to develop a new analysis.

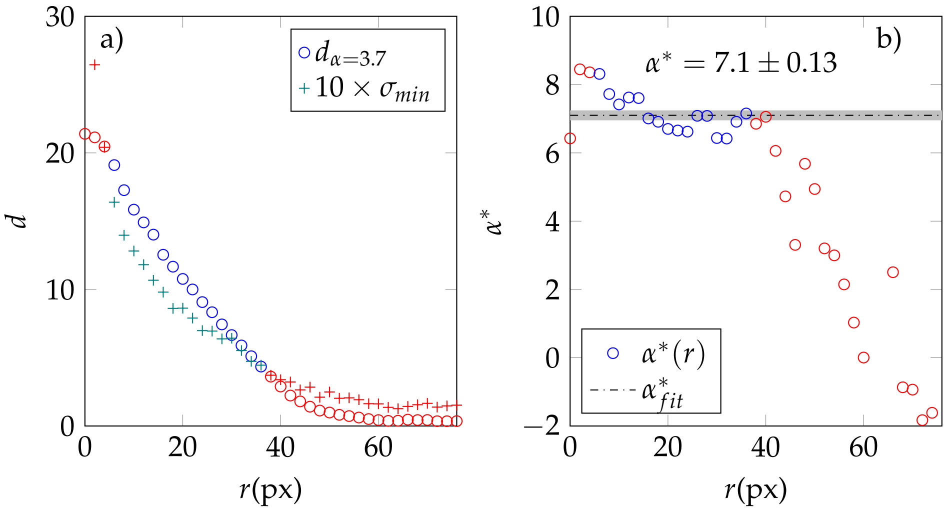

Figure E.1.: Fitted values of σ_{min} (**a**) and α^* (**b**) for the set **2** as function of the distance to the cloud center r. In (**a**) we also show an estimate of the optical density given by choosing an ab-initio value of α, $\alpha = 3.7$ (see text). To be on a comparable scale, we multiply the minimum of the standard deviation σ_{min} by 10 on this representation. In both graphs, we represented in red the discarded data. As described in the text, These are point showing a too high σ_{min} value compared to their optical density $d_{\alpha=3.7}(r)$. In (**b**), we also show the result of fitting $\alpha^*(r)$ by a constant on the relevant domain $\alpha^* = 7.1\,(1)$.

series Number	Cloud Conf.	Fitted α^*
1	"hot"	$3.0\,(1)$
2	"cold"	$7.1\,(1)$
3	"hot"	$4.8\,(1)$
4	"cold"	$6.4\,(1)$

Table E.1.: Summary of all the fitted values of α^* on the 4 data sets.

To conclude this "historical" analysis and further highlight the need for a new analysis, we also represent here our data in the same way it is commonly done in the new calibration procedure developed in the main text (see 3.3.3 and Fig. 3.6). In this representation, we compare the results of these four data sets by representing all the fitted $\alpha^*(r)$ as a function of the estimated optical density d. Here (*i.e.* in the "historical" analysis case, we use the previously described estimate of the optical density $d_{\alpha=3.7}(r;k)$. Such a representation is shown in Fig. E.2.

With this representation, we find that for a given d, all the data of the four sets are approximately compatible with each other whereas all the average values α^*_{fit} computed above are not. In this representation, we roughly identify two separated plateaus, as shown in Fig. E.2, one at high d with a higher value of α^* that we denote α^*_{high}, and a second one at low d corresponding to a lower value of α^* that we name α^*_{low}. A weighted average of $\alpha^*(d)$ for $d \in [0.5; 5]$ gives $\alpha^*_{\text{low}} = 3.60\,(14)$ and for $d \geq 5$ gives $\alpha^*_{\text{high}} = 6.84\,(13)$.

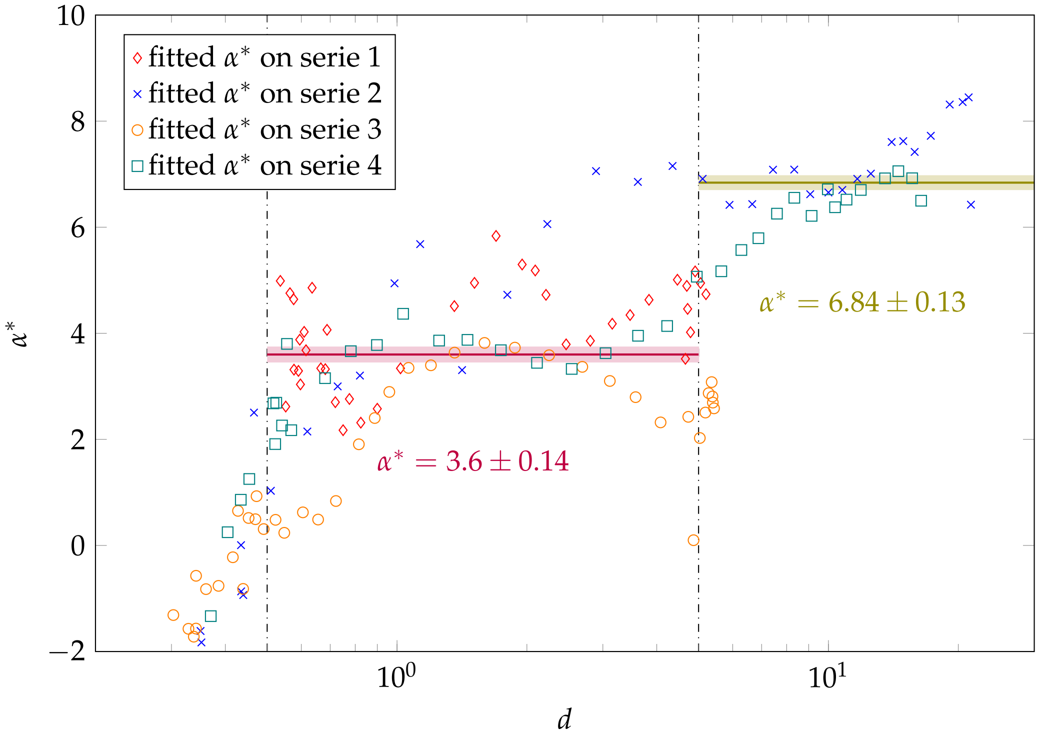

Figure E.2.: Fitted values of α^* for all data sets plotted as function of an estimate of the optical density given, as stated previously by choosing an ab-initio value of α, $\alpha = 3.7$. We saw two separated plateaus according to the density values. The dotted black lines identify the separation between the plateaus. The thick solid lines shows the averaged constant values for each plateaus. We found $\alpha^*_{\text{low}} = 3.60\,(14)$ for $d \in [0.5; 5]$ and $\alpha^*_{\text{high}} = 6.84\,(13)$ for $d \geq 5$

In fact, we came up with the new analysis idea as this last representation gives the intuition that α^* depends on the atomic density. As this historical sophisticated procedure does not easily enable an inspection of the experimental data quality or the detection of outliers in our data, we were in need for a better understanding of this unusual and unexpected behavior of our coefficient α, varying with d. The new procedure which results in a more straightforward manipulation of the experimental data enables this inspection. In particular it gives an insight into all the experimental points leading to a given $\alpha^*(d)$ as shown in Fig. 3.5.

F. A conventional analysis of equation of state of the two-dimensional Bose gas

As introduced in Ch. 4, a first measurement of the equation of state (EoS) of a 2D uniform Bose gas was performed in 2011 following a conventional analysis method based on a thermometry of individual images [70]. The main parts of this article are reproduced here, while a novel and more accurate determination of this same EoS is presented in the main text (along with the description of the experimental preparation of the gases).

F.1. Analysis of the images

The following experimental investigation of the EoS of a 2D Bose gas has been performed on a similar set of data as in the investigation of 4.2. The sequence for the preparation of the 2D samples as the experimental parameters are detailed in 4.2.1 and are thus not reproduced here. At the end of the data acquisition process we have for each atomic configuration two images successively taken in the high and in the low intensity regime (see Ch. 3) as illustrated in Fig. F.1. Here we will extract from each pair of images the temperature T, the chemical potential at center μ and the density $n(\boldsymbol{\rho})$ in any pixel of the image.

The following section was initially published as part of the supplemental material of [70], and is reproduced without modifications

From the density profile of the low-intensity image, we determine the temperature T and the chemical potential μ by fitting the low density region with the prediction of the Hartree–Fock mean field theory (HFMF). Our fitting function takes into account the residual excitation of the z degree of freedom. Actually, this fit of the whole set of images also provides the value of the detection efficiency $\beta = 0.40\,(2)$. The high-intensity image provides us with the density profile $n(\boldsymbol{\rho})$.

Once T and μ are known, we self-consistently determine the population of the excited states using the method described in [103, 118], assuming the atoms in the excited states $j \geq 1$ of the z motion to be in the HFMF regime. In practice we restrict the analysis to the first ten levels. In order to give an estimation of the contribution of the various levels $j \geq 1$ to the total density, we show in Fig. F.2a numerical results obtained by applying this procedure to a numerically generated profile, produced using the prediction [125] with $T = 100\,\text{nK}$ and $\mu/k_{\mathrm{B}}T = 0.45$. This temperature is on the high side of our experimental range, where the influence of the atoms in the excited states along z is expected to be the most important. We plot in Fig. F.2a the phase space density of the excited states $\mathcal{D}^{(\text{exc})}$, distinguishing the contribution of the state(s) $j = 1$, $j = (1,2)$, $j = (1,2,3)$, etc. For

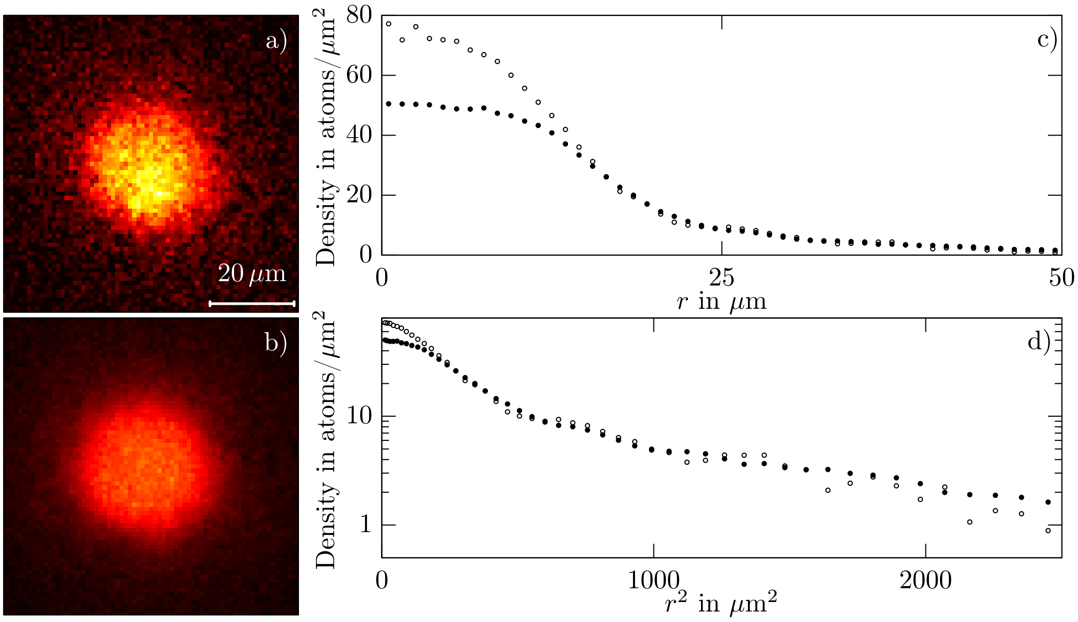

Figure F.1.: Absorption imaging of quasi-2D clouds of ^{87}Rb atoms. (a) Image obtained with a short pulse ($\sim 2\mu$s) of an intense probe beam ($I/I_{\text{sat}} = 40$) . (b) Image obtained with a longer pulse (50 μs) of a weak probe beam ($I/I_{\text{sat}} = 0.5$). The processing of images (a) and (b) is detailed in [Ch. 3]. (c) and (d) Radial density profiles for image (a) (hollow circles ○) and image (b) (filled circles ●) in linear (c) and logarithmic (d) scales. The solid line combines the predictions of the HFMF theory, of [125] in the intermediate regime and of the Thomas–Fermi approximation $\mu = \hbar^2 \tilde{g} n/m$ in the central region ($T = 133\,$nK, $\mu/k_B = 47\,$nK).

comparison we also plot the profile $D(0)$ obtained from [125], associated to the atoms in the ground state. Note that the contribution of the states $j > 4$ is already negligible. The phase space density associated to each excited state is lower than 0.5, which justifies to treat the atoms in these states within the HFMF approximation. The flattened shape of the density distributions in the central region is due to the repulsive interaction with the atoms in the ground state of the z motion. This procedure also allows us to calculate the effective potential felt by the atoms in $j = 0$, when the repulsive potential $W(\boldsymbol{\rho})$ created by the atoms in $j \geq 1$ is taken into account. Plotting together $W(\boldsymbol{\rho})$ and the trapping potential $V(\boldsymbol{\rho})$ (Fig. F.2b) we see that $W(\boldsymbol{\rho})$ is essentially negligible ($\lesssim 1\,$nK) and one can thus consider the density $n0(\boldsymbol{\rho})$ to be insensitive to the presence of the atoms in $j \geq 1$

F.2. Thermodynamic analysis

The following section was initially published in [70], and is reproduced without modifications

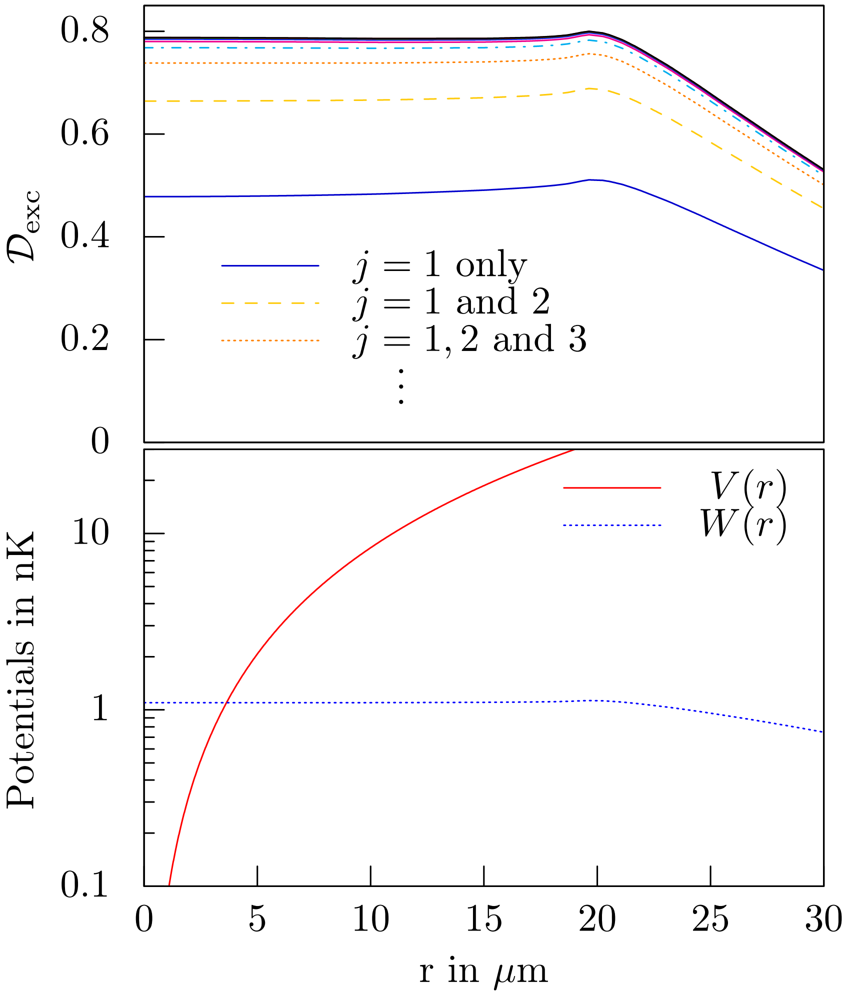

Figure F.2.: (a) Phase space density of the ground (solid red line) and excited state(s) of the z-motion. The n-th line from the bottom corresponds to the contributions of excited levels 1 to n. (b) Comparison of the trapping potential (red solid line) and the repulsive potential created by the excited atoms on the population in the ground state (blue dotted line).

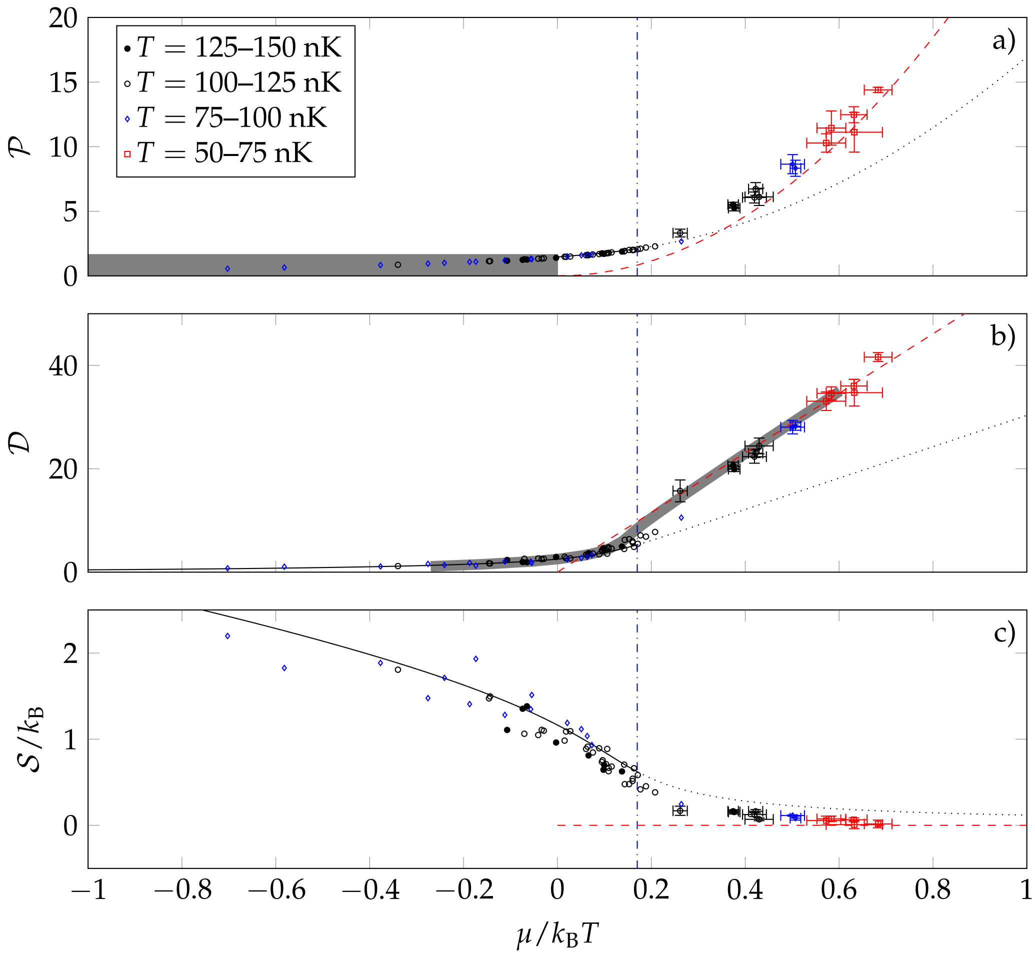

Figure F.3.: Equations of state for (a) the reduced pressure $\mathcal{P}$, (b) the phase space density $\mathcal{D}$ and (c) the entropy per particle $\mathcal{S}$. The HFMF prediction is plotted in black full line and extended in dotted line beyond the expected superfluid transition. The dashed red line is the Thomas-Fermi prediction. In (a) the grey area indicates the region of parameter space accessible to an ideal gas. In (b) the thick grey line indicates the prediction from [125]. For $\mu/k_BT > 0.2$, data obtained for the same control parameters (trap loading time and evaporative cooling ramp) have been grouped and error bars indicate standard deviation of the measurement. For $\mu/k_BT < 0.2$, data are displayed for individual images, thus with no error bar. The vertical dash-dotted line (blue) indicates the prediction [124] for the superfluid transition.

F.2.1. EoS for the pressure

We start our thermodynamic analysis by inferring the pressure $P(\mu, T)$ of the homogeneous gas from our measurements. Here we adapt to the 2D case the technique presented in [65], which has been used successfully in 3D for Fermi gases [66]. We show that $P(\mu, T)$ is directly related to the atom number $N_0 = \int n_0(\boldsymbol{\rho})\, d^2r$ in our harmonic trap. Indeed, the LDA relates $n_0(\boldsymbol{\rho})$ to the density of the homogenous gas

$n^{(2D)}_{\rm hom}[\mu - V(\boldsymbol{\rho}), T]$[1]. For an isotropic harmonic potential $V(\boldsymbol{\rho}) = m\omega^2 r^2/2$ the total atom number is

$$N_0 = \frac{2\pi}{m\omega^2} \int_{-\infty}^{\mu} n^{(2D)}_{\rm hom}(\mu', T)\, d\mu', \tag{F.1}$$

and using the thermodynamic relation $n^{(2D)}_{\rm hom} = (\partial P/\partial\mu)_T$, we find $N_0 = (2\pi/m\omega^2)$ $P(\mu, T)$. Introducing the dimensionless quantity $\mathcal{P} = P\lambda_{\rm T}^2/k_{\rm B}T$, which we refer to as the reduced pressure, we then obtain

$$\mathcal{P}(\mu, T) = \left(\frac{\hbar\omega}{k_{\rm B}T}\right)^2 N_0, \tag{F.2}$$

where ω is to be replaced by the geometrical mean of ω_x and ω_y for an non-isotropic potential. Our results are summarized in Fig. F.3a, where we plot $\mathcal{P}$ deduced from Eq. (F.2) as function of $\mu/k_{\rm B}T$. The temperatures of the data entering in this plot range from 40 nK to 150 nK. The fact that all data points collapse on the same line show that $\mathcal{P}$ is a function of the ratio $\mu/k_{\rm B}T$ only, as expected from the scale invariance of the system. The HFMF theory is represented by a continuous line in the normal region and by a dotted line in the superfluid region. The dashed line is the Thomas–Fermi prediction at zero temperature $\mathcal{P} = \pi(\mu/k_{\rm B}T)^2/\tilde{g}$. The grey area is the parameter subspace accessible to an ideal Bose gas. Interestingly, although the phase space density $\mathcal{D}$ can take arbitrarily large values, one can show in the ideal gas case that the reduced pressure $\mathcal{P} = g_2(z) \leq \pi^2/6$, where g_2 is the dilogarithm function and $z = \exp(\mu/k_{\rm B}T)$ ($z \leq 1$ for an ideal Bose gas).

F.2.2. EoS for the phase space density

We show in Fig. F.3b our measurements for the phase space density $\mathcal{D}$, obtained from the central density of each cloud. In wide gray line we plot the prediction of [125], which is in good agreement with our results. A further confirmation of this agreement is shown in Fig. F.1c, where we plot in full line the numerically generated profile using [125] for the fitted T and μ. A measurement of $\mathcal{D}(\mu/k_{\rm B}T, \tilde{g})$ was also reported in [69] for a quasi-2D Cesium gas, for $\tilde{g}$ ranging from 0.05 to 0.26. Our results agree well with those measurements over the covered range ($\mathcal{D} < 20$ in [69] for $\tilde{g}$ similar to ours).

F.2.3. EoS for the entropy

From our measurements of $\mathcal{P}$ and $\mathcal{D}$ we also obtain the equation of state for the entropy per particle $\mathcal{S}(\mu, T)$:

$$\frac{\mathcal{S}}{k_{\rm B}} = 2\frac{\mathcal{P}}{\mathcal{D}} - \frac{\mu}{k_{\rm B}T}\,, \tag{F.3}$$

which can be derived starting from the entropy per unit area $s = (\partial P/\partial T)\,|_{\mu}$, assuming the EoS for $\mathcal{P}$ to be scale invariant[2]. The corresponding result is shown in Fig. F.3c.

---

[1] The LDA holds for short range interactions when the spatial density is nearly constant over the microscopic length scales set by $\lambda_{\rm T}$ and by the healing length $\xi = (\tilde{g}n)^{-1/2}$.

[2] A similar method has been used for a 3D Fermi gas at unitarity, Martin Zwierlein, private communication, February 2011.

As expected, $\mathcal{S}$ is large in the non-degenerate regime and rapidly decreases around $\mu/k_\mathrm{B}T \approx 0.17$, where the superfluid transition is expected for our value of $\tilde{g}$ [124]. Finally $\mathcal{S}$ tends to zero in the Thomas–Fermi regime. Our data points with the largest phase-space density ($\mu/k_\mathrm{B}T > 0.5$) correspond to $\mathcal{S} = 0.06\,(1)\,k_\mathrm{B}$ only. For comparison the entropy per particle reported in [250] for a 2D Mott insulator is $\sim 0.3\,k_\mathrm{B}$. Note that since the BKT transition is of infinite order, one does not expect any discontinuous change for $\mathcal{P}$, $\mathcal{D}$ or $\mathcal{S}$ at the superfluid transition for an infinite homogeneous fluid, although the superfluid density jumps suddenly from 0 to $4/\lambda_\mathrm{T}^2$ [122].

F.3. Measuring the interaction energy

The following section was initially published in [70], and is reproduced without modifications

We now turn to the last part of our study, where we illustrate how to measure the various contributions to the energy of our trapped 2D gases: potential energy E_p in the external trapping potential, kinetic energy of the particles E_k, and interaction energy between atoms E_i. We first point out the simple relation $E_\mathrm{p} = E_\mathrm{k} + E_\mathrm{i}$, obtained from virial theorem assuming 2D contact interaction. We measure $E_\mathrm{p} = \int n_0(\boldsymbol{\rho})\, V(\boldsymbol{\rho})\, d^2r$ from an *in situ* image, but we still need to disentangle the contributions of E_k and E_i to the total energy. This can be done by abruptly switching off interactions at time $t = 0$, either via a Feshbach resonance or effectively by using a "one dimensional" (1D) ToF described below. Each particle then undergoes a free harmonic motion $\boldsymbol{\rho}(t) = \cos(\omega t)\,\boldsymbol{\rho}(0) + \sin(\omega t)\,\boldsymbol{v}(0)/\omega$. The potential energy after a time t following the switching off of the interactions is

$$E_\mathrm{p}(t) = E_\mathrm{p}(0)\cos^2(\omega t) + E_\mathrm{k}(0)\sin^2(\omega t), \tag{F.4}$$

where we used the fact that the correlation $\langle \boldsymbol{\rho}(0) \cdot \boldsymbol{v}(0) \rangle$ is zero at thermal equilibrium. Thus we can extract $E_\mathrm{k}(0)$ from the time evolution of E_p, which we obtain from the density profiles at different times t.

In order to implement this procedure, we perform the 1D ToF mentioned above by switching off abruptly the laser providing the confinement along z while keeping the magnetic confinement in the xy plane. The gas then expands very fast along the initially strongly confined direction z, as shown in figures F.4a to F.4d, and interactions between particles drop to a negligible value after a time of a few ω_z^{-1}, where $\omega_z^{-1} \sim 100\,\mu$s. The subsequent evolution in the xy plane occurs on a longer time scale given by $\omega^{-1} \sim 8$ ms. From Eq. (F.4) and $E_\mathrm{k}(0) < E_\mathrm{p}(0)$, we expect the size of the gas to decrease for $t \lesssim \omega^{-1}$, which can be understood in simple physical terms. The equilibrium state of the 2D gas results from a balance between the trapping potential, which tends to compress the gas, and the kinetic and interaction energies, which tend to increase its area. When interaction energy drops to zero the equilibrium is broken and the gas implodes in the xy plane. A similar 1D ToF technique was used recently in Boulder with the value of t fixed at $\pi/2\omega$ [103]. For this particular choice the initial momentum distribution is converted into position distribution and can thus be measured accurately [251].

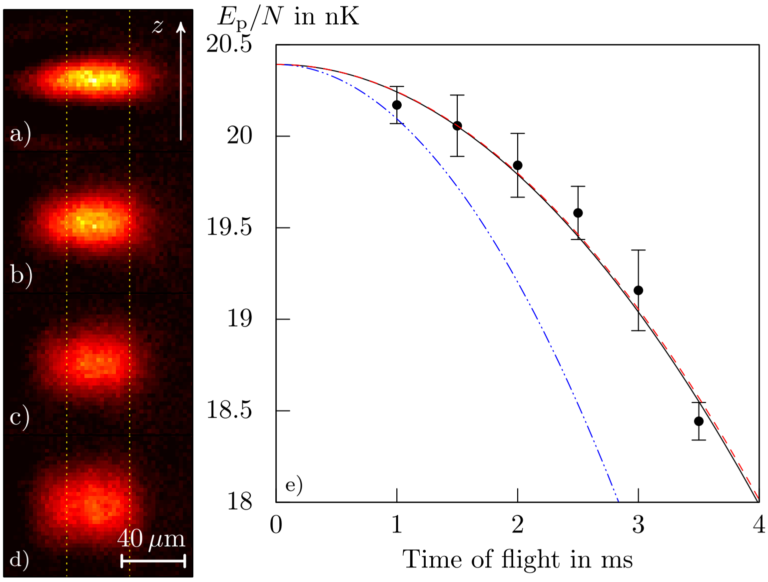

Figure F.4.: (a) to (d) Side view of a cloud initially in the 2D regime and expanding along z once the laser providing the confinement in this direction has been switched off. (a) $t = 1\,$ms; (b) $t = 2\,$ms; (c) $t = 3\,$ms; (d) $t = 4\,$ms. (e) Time evolution of the potential energy E_p. The different lines represent a fit to the data of a parabola (solid black line), the time evolution assuming flattened density fluctuations (dashed red line) and the one expected for a dilute non-condensed gas (dash-dotted green line).

We show in figure F.4e an example of measurement of $E_\mathrm{p}(t)$ for a gas with $N_0 = 6.1\,10^4$, $T = 72\,$nK, and $\mu/k_\mathrm{B}T = 0.59$. From the contraction of the gas, we infer $E_\mathrm{k}/E_\mathrm{p} = 0.56\,(3)$, from which we deduce $E_\mathrm{i}/E_\mathrm{p} = 0.44\,(3)$ using virial theorem. This configuration is thus neither completely in the very dilute regime ($E_\mathrm{i} \ll E_\mathrm{k} \sim E_\mathrm{p}$) nor in the Thomas–Fermi regime ($E_\mathrm{k} \ll E_\mathrm{i} \sim E_\mathrm{p}$) and contains comparable thermal and quasi-coherent fractions.

The measurement of E_i is of particular interest in this case since it gives access to the density fluctuations in the gas. Indeed, by definition $E_\mathrm{i} = (\hbar^2\tilde{g}/2m)\int\langle n_0^2(\boldsymbol{\rho})\rangle\, d^2r = (\hbar^2\tilde{g}/2m)\mathcal{F}\int\langle n_0(\boldsymbol{\rho})\rangle^2\, d^2r$ [252], where we have introduced the parameter $\mathcal{F}$ that characterizes the degree to which density fluctuation are reduced. In the limiting case of a dilute, non-condensed gas, one expects $\mathcal{F} = 2$, since $\langle n_0^2\rangle = 2\langle n_0\rangle^2$, while in the opposite limit of a 'flattened' density profile $\mathcal{F}$=1. Since our measurement provides us with E_i, we can infer the value of $\mathcal{F}$, from the comparison with the quantity $(\hbar^2\tilde{g}/2m)\int\langle n_0(\boldsymbol{\rho})\rangle^2\, d^2r$, calculated using the *in situ* density profile n_0. For the conditions of figure F.4e, we find $\mathcal{F} = 1.1\,(1)$, very close to the value 1 for flattened density fluctuations. Note that this is obtained for a gas still far from the Thomas–Fermi limit since $E_\mathrm{k} \sim E_\mathrm{i}$. This "early" reduction of density fluctuations is an important ingredient for the proper operation of the BKT mechanism. This presuperfluid phase, whose existence was also inferred by different methods in [69, 102, 103], constitutes a medium that can support vortices, which pair at the superfluid threshold.

F.4. Conclusion

The following section was initially published in [70], and is reproduced without modifications

In conclusion we presented in this Letter various aspects of the thermodynamics of a 2D Bose gas, investigating first the EoS's for the pressure, the phase space density and the entropy. Our results confirm the scale invariance that was discussed theoretically in [125] and observed in [69] for $\mathcal{D}$. We point out that the entropy per particle drops notably below $0.1\,k_{\mathrm{B}}$ beyond the transition point. With such a low entropy a 2D Bose gas can constitue excellent coolants for other quantum fluids such as a 2D Fermi gas [253]. We also presented a method that allows one to extract the various contributions to the total energy of the system. By applying it to a degenerate but not fully coherent 2D cloud, we find that density fluctuation are nearly frozen, marking the presuperfluid phase.

G. Aperture effect on the uniform trap implementation via dark mask imaging.

In this annex, we give some insights about the effect of a finite aperture in the dark mask imaging setup used to create the uniform potential as described in Chapter 6. Such a finite aperture can be due to the finite size of the lens (or other blocking elements on the path of the beam). In our setup it results in fact from a diaphragm set on the path of the beam, just after the second lens of the telescope[1], as described in 6.3.2. In this annex, we simulate the effect of a similar diaphragm placed in between the two lenses of the telescope (for simplicity of the simulation and of the modeling) on the resulting potential by modeling the beam propagation along the imaging setup. We analyze the intensity profile imaged at the position where the atoms are trapped as it is proportional to the generated trapping potential. We are particularly interested in the resulting modifications on the uniform trap properties, namely the trap bottom uniformity and its edges steepness. We will characterize them quantitatively and compare the results to the specifications required experimentally, as described in 6.1.2.

G.1. Principle of the simulation

G.1.1. Simulating the beam propagation

In the goal introduced above, we simulate the beam propagation after its transmission across the glass plate holding the dark spot imprints and over a modeled imaging setup until a location equivalent to the one of the atomic cloud. For this simulation, we model the experimental imaging setup that is described in 6.3.2 with the scheme represented in Fig. G.1. Then, the simulation procedure is as follow:

1. The light beam just before the glass plate holding the dark spots is assumed to be gaussian and non-elliptic. We set its waist to $w_0 = 50\,\mu$m (we also checked that this value does not affect the conclusions on the trap uniformity by few complementary analysis at $w_0 = 150\,\mu$m).
2. The dark spot is assumed to be perfectly opaque and presenting infinitely sharp edges. Then the electric field just after the plate writes.

$$E_i(x, y) \propto e^{-r^2/w_0^2}\, t(x, y) \tag{G.1}$$

where $t(x, y) = 0$ if (x, y) is inside the mask shape and $t(x, y) = 1$ elsewhere. We set the mask to be centered on the beam and we choose a characteristic half–

---

[1] The diaphragm is considered close enough from the second lens so that it is equivalent to position it inside the telescope, as modeled here

length of the mask to be $R_{\mathrm{mask}} = 40\,\mu\mathrm{m}$ so that it matches to the usual values in our experimental setup.

3. In the whole simulation, we will assume that the propagation is well described within paraxial approximation.
4. The imaging setup is composed of a two–lenses telescope. We suppose that the lenses are well described within the thin lens approximation. We assume in this simulation that they both have the same focal length $f = 500\,\mathrm{mm}$. We perform such a simplification in order to facilitate the grid definitions for the Fourier transform and not affect the final resolution of the simulation at a given grid size. Then, the resulting telescope has a magnification of $\mathcal{M}_{\mathrm{sim}} = 1$ instead of $\mathcal{M}_{\mathrm{exp}} = 0.3$ in the experimental setup. In the resulting intensity profile, it simply translates by a rescaling of an overall factor of $\mathcal{M}_{\mathrm{sim}}/\mathcal{M}_{\mathrm{exp}} = 10/3$ compared to the experimental one but no shape modification are expected from this substitution.
5. The mask is set at the focus of the first lens so that the electric field just after this lens is
$$E_1(x,y) \propto e^{-\frac{ik}{2f}r^2}\tilde{E}_i(k_x = \frac{kx}{f}, k_y = \frac{ky}{f}) \tag{G.2}$$
where $k = 2\pi/\lambda$ is the wave number of the beam ($\lambda = 532\,\mathrm{nm}$), $\tilde{E}_i(k_x, k_y)$ is the Fourier transform of the electric field just after the mask given in Eq. G.1.
6. Both lenses are separated by a distance d along which the beam propagates freely according to :
$$\tilde{E}_d(k_x,k_y) \propto e^{-\frac{i(k_x^2+k_y^2)}{2k}d}\tilde{E}_1(k_x,k_y) \tag{G.3}$$
where $\tilde{E}_1(k_x,k_y)$ (resp. $\tilde{E}_d(k_x,k_y)$) is the Fourier transform of the electric field just after the first lens given in Eq. G.2 (resp. after the propagation over the distance d). In the presented simulation results, we took $d = 100\,\mathrm{cm}$. We also checked that the results are not drastically modified if we choose $d = 500\,\mathrm{cm}$ or $d = 50\,\mathrm{cm}$.
7. After this propagation, we model a circular diaphragm aperture of radius R_{diaphr} that cuts the electric field outside its range:
$$E_{dd}(x,y) = E_d(x,y)\ \mathcal{D}(x,y) \tag{G.4}$$
where $\mathcal{D}(x,y) = 1$ if (x,y) is inside the diaphragm aperture and $\mathcal{D}(x,y) = 0$ elsewhere. We set this diaphragm to be centered on the beam and on the mask so that
$$\mathcal{D}(r) = \begin{cases} 1 & \text{if } r \leq R_{\mathrm{diaphr}} \\ 0 & \text{if } r > R_{\mathrm{diaphr}} \end{cases} \tag{G.5}$$
8. Finally, we image the beam at the focus of the second lens as it must match the position of the atoms. The final electric beam is then:
$$E_2(x,y) \propto e^{-\frac{ik}{2f}r^2}\tilde{E}_{dd}\left(k_x = \frac{kx}{f}, k_y = \frac{ky}{f}\right) \tag{G.6}$$
where $\tilde{E}_{dd}(k_x,k_y)$ is the Fourier transform of the electric field just after diaphragm.

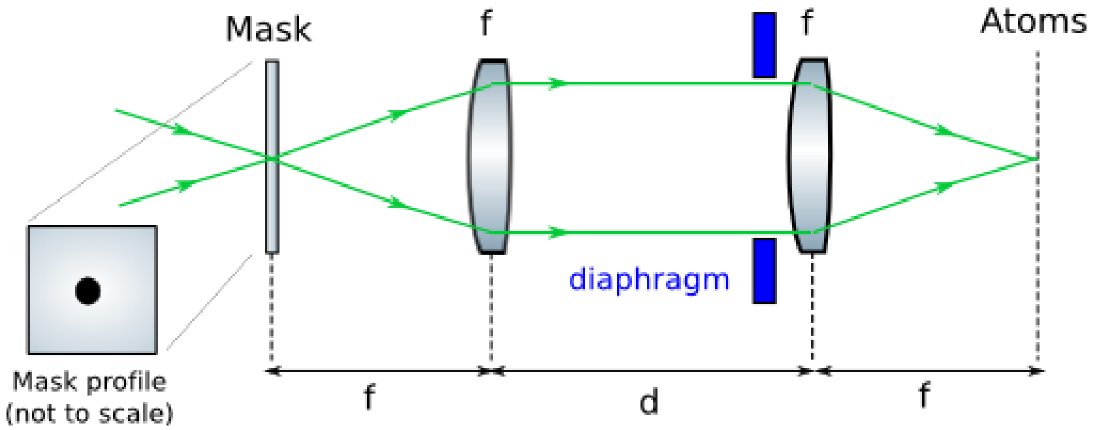

Figure G.1.: Schematic representation of the optical setup simulated. We describe this setup in paraxial approximation and using thin lenses model. In this setup we use to lenses of focal lengths $f = 500\,\mathrm{mm}$. The mask imprinted on a initially gaussian beam is at focus of the first lens. We compute the resulting intensity profile at the focus of the second lens. Just before this lens, we cut the electric field distribution but a circular aperture of radius R_{diaphr} which account for both the effect of the slit and of the diaphragm of the experimental setup of Fig.6.5.

For this simulation we use a 4096 × 4096 grid. We represent the input beam in a grid varying from $-10w_0$ to $10w_0$ (it results being the same for the output beam as the magnification of the simulated setup is $\mathcal{M}_{\text{sim}} = 1$).

G.1.2. Analyzing the simulated intensity profile

At the end of this process we analyze the output intensity profile $I_{\text{sim}}(x,y) = |E_2(x,y)|^2$ in terms of its resulting uniform trapping quality as introduced in chapter 6 and summarized here:

1. We characterize the trap bottom variations by computing :
   - — The difference δI between the value of the potential inside the inner trapping region and its average value I_{bottom}. This inner region is defined by the simply connected domain where the potential is less than $I_{\text{min}} = I_{\text{bottom}} + (I_{\text{barrier}} - I_{\text{bottom}})/20$ where I_{barrier} is the intensity maximum on the edges of this region. We characterize δI in percentage of $(I_{\text{barrier}} - I_{\text{bottom}})$. We may consider the maximum of δI over the the inner trapping region, we denote this quantity δI_{max} .
   - — We can also describe the trap bottom quality in terms of the standard deviation of δI over the whole central trapping region. We denote this quantity δI_{std}.
2. We characterize the edges steepness by computing:
   - — The characteristic length η within which the intensity varies from I_{min} to $I_{\text{max}} = I_{\text{bottom}} + (I_{\text{barrier}} - I_{\text{bottom}})/4$ as for the experimental characterization.
   - — The power law fitted exponent using fitting function of Eq. 6.4 of these edges from $r = 0$ to $r = r_{\text{max}}$, the position where $I = I_{\text{max}}$.

G.2. Results on a disk

G.2.1. Intensity Profiles

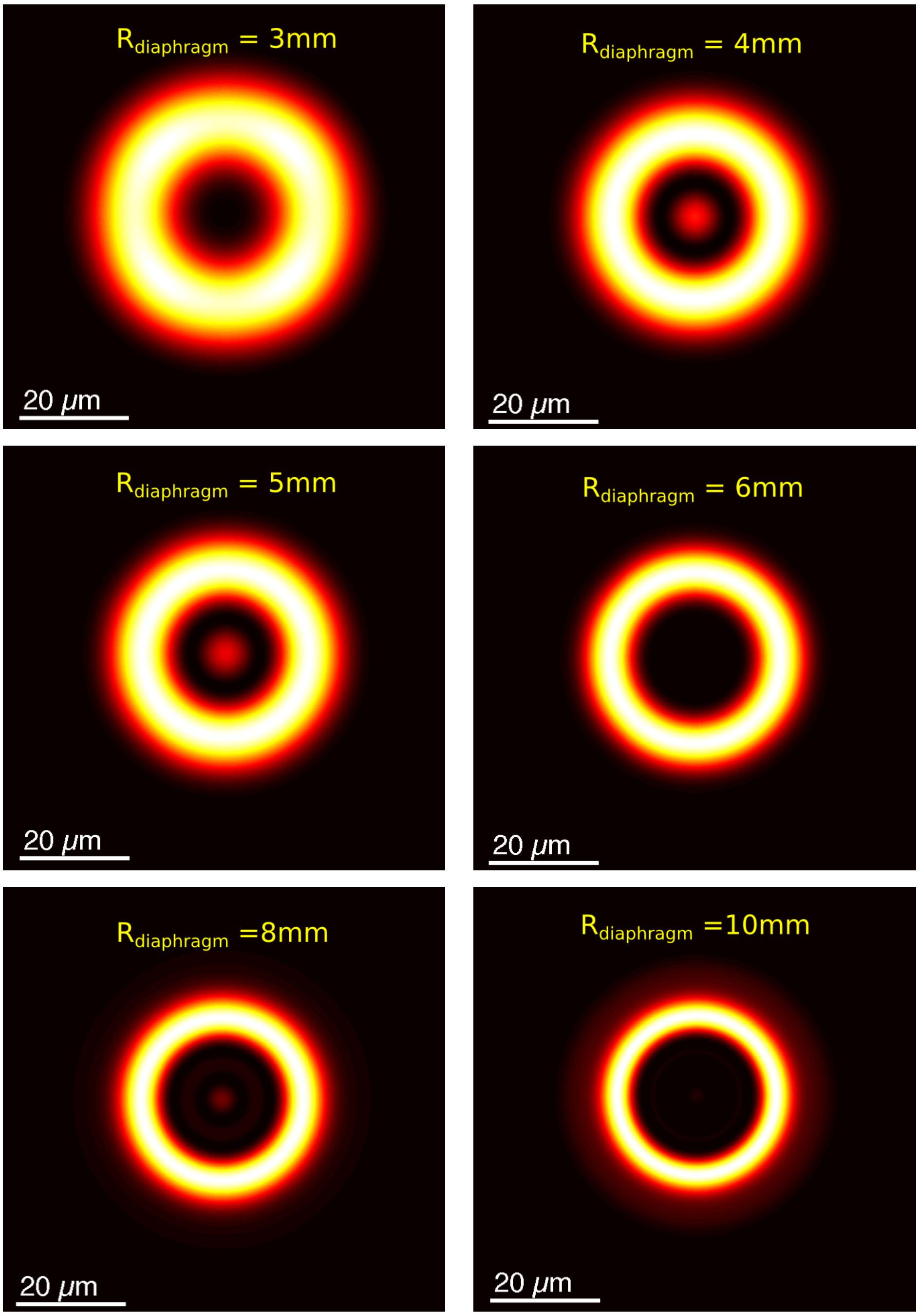

Figure G.2.: Examples of simulated intensity profiles with various diaphragm apertures $R_{\text{diaphr}} = 3,\ 4,\ 5,\ 6,\ 8$ and $10\,\text{mm}$. We use a initially disk shaped mask of radius $R_{\text{mask}} = 40\,\mu\text{m}$. It is imaged via a 1 to 1 telescope made up with two lenses of focal $f = 500\,\text{mm}$.

We first select a unique mask configuration and look at the effects of a variation of the diaphragm aperture R_{diaphr} on the simulated intensity profile at the position of the atoms. We choose a disk shape mask as it is the easiest to analyze: it indeed preserves the beam symmetry and offers the possibility of using radial averaging. The mask is then defined by:

$$t(r) = 1 \text{ , if } r > R_{\text{mask}} = 40\,\mu\text{m} \qquad \text{or} \qquad t(r) = 0 \text{ , if } r \leq R_{\text{mask}} = 40\,\mu\text{m} \tag{G.7}$$

Typically we vary the radius of the diaphragm from $R_{\text{diaphr}} = 3\,\text{mm}$ to $R_{\text{diaphr}} = 30\,\text{mm}$ (which are relevant for our experimental configuration in which $R_{\text{diaphr}} = 9\,\text{mm}$). For apertures $R_{\text{diaphr}} \leq 2.8\,\text{mm}$, we note that the intensity profile does not show any trapping region. In Fig. G.2, we show six examples of intensity distributions obtained via this simulation procedure using six different value of R_{diaphr}. In these six images, we see that the intensity structures appearing in the trap center change with the diaphragm aperture. For the largest R_{diaphr}, they tend to disappear. For the short R_{diaphr}, a central bump appears but its intensity does not vary monotonically with R_{diaphr}. More precisely, we note by varying both the mask radius R_{mask} and the diaphragm one R_{diaphr} that this peak appears and disappears according to the relative position of the aperture cut compared to the various order peaks in the diffraction pattern imposed by the mask in the intensity profile at the position of the diaphragm. It appears that being able to select the precise radius at which we cut the distribution is a fundamental feature for optimizing the uniformity of the resulting trapping potential, similar to a (rough)-apodization.

G.2.2. Characterizing trap properties

To confirm these preliminary observations, we characterize the trapping properties quantitatively. We plotted the resulting values in Fig. G.3 for the uniformity of the trap bottom and the steepness of the edges. There, we renormalize the length scales by the experimental magnification $\mathcal{M}_{\text{exp}} = 0.3$. In these plots, we note an overall tendency to recover the uniformity and the sharpness of the edges with an increasing R_{diaphr}.

1. We note that a sufficiently high stiffness is reached even at very short aperture $R_{\text{diaphr}} \gtrsim 3\,\text{mm}$. For example, the power law coefficient β is larger than 5 for $R_{\text{diaphr}} \geq 3.2\,\text{mm}$. Indeed, the sharpness is expected to be affected if we cut spatial frequencies of the order of $k \approx \mathcal{M}/\eta$ where η is the required stiffness at the position of the atoms. In 6.1 we impose $\eta \lesssim R_{\text{box}}/3 = \mathcal{M}R_{\text{mask}}/3 = 4\,\mu\text{m}$ for $R_{\text{mask}} = 40\,\mu\text{m}$ and $\mathcal{M} = \mathcal{M}_{\text{exp}} = 0.3$. We deduce that the corresponding aperture is $R_{\text{diaphr}} = \frac{3f\lambda}{2\pi R_{\text{mask}}} = 3.2\,\text{mm}$.
2. The limiting aspect is then the variations of the potential inside the trapping region. For $R_{\text{diaphr}} \gtrsim 15\,\text{mm}$, the maximal defect in the trap bottom verified $\delta U_{\text{max}} \leq 5\%$ as specified. For smaller apertures, we note that the trap-bottom defect oscillates with R_{diaphr} and can reach values, as high as $\delta U_{\text{max}} \approx 40\%$ for $R_{\text{diaphr}} \approx 4.5\,\text{mm}$ with this specific mask. Nevertheless we note that whatever the radius is we can always reduce the aperture size to find a configuration where the

> trap-bottom defect complies with the specifications (apodization). In our experimental setup, the aperture set by the rough optical setup (in the absence of the adjustable diaphragm) is $R_{\text{diaphr}} \approx 9\,\text{mm}$ (see 6.3.2). It then lies in this "apodization" range and we complement our optical setup by adding a diaphragm of adjustable aperture inside the telescope to perform the desired optimization on the trap quality. We note that for the mask considered in this simulation, $R_{\text{diaphr}} \approx 9\,\text{mm}$ is close to an optimum.

In fact we notice that all features show oscillations with the aperture and we precisely describe the extrema positions in terms of the diaphragm aperture R_{diaphr}. We first note that the maximal (resp. minimal) values of the trap bottom variations (as represented by δU_{std}, δU_{max} or U_{bottom}) match the position of the minimal (resp. maximal) values of the stiffness of the potential η. We can then only consider one of these variables to represent the global variations of the trap characteristics. From now on, we describe the oscillations of the trapping properties by the variation of δU_{std} with the diaphragm aperture R_{diaphr}.

Following the qualitative conclusions of G.2.1, we can compare these oscillations to the azimuthal average of the intensity profile juste before the diaphragm. From this, we infer the cut realized by our circular diaphragm. For getting an insight on this intensity profile, we note the similarity of the optical setup considered to the Fraunhofer diffraction by a disk–shaped aperture that results in an Airy pattern:

$$I_{\text{Airy}}(r) \propto \left(\frac{J_1(x)}{x}\right)^2 \quad \text{where } x = \frac{2\pi r R_{\text{mask}}}{\lambda f} \tag{G.8}$$

We can also numerically estimate this intensity profile using our previous model for the light propagation and by considering the profile:

$$I_d(r) = |E_d(r)|^2 \tag{G.9}$$

where $E_d(r)$ is the azimuthal average of the field calculated in Eq. G.3 just before the diaphragm cutting.

First, we notice that the oscillation of the trapping properties occurs at a length scale corresponding to the diffraction pattern modulation obtained from Airy function or from the more accurately simulated intensity profile $I_d(r)$. For R_{diaphr} varying from 3 mm to 30 mm, the average spacing of the extrema is $\sim 3.3\,\text{mm}$ for all these oscillations. We also note an "inversion" between the largest spacing [2] from maxima in intensity to minima in the trap bottom variations.

For a quantitative comparison, we plot in Fig. G.4 the variations of the trap characteristics for an aperture R_{diaphr} along with the intensity value at the cutting radius $r = R_{\text{diaphr}}$ as function of this radius. We note that the maxima in δU_{std} are located at radii close to, but greater than, the intensity minima. On the selected range of R_{diaphr}, the distance between these two successive extrema is, in average, $\delta_{\text{max}} = 180\,\mu\text{m}$. We note in the same way, that the minima in δU_{std} are located at radii close to, but greater

---

[2] Indeed the spacing of the maxima is not rigorously equal th the spacing of the minima for each of the considered oscillations.

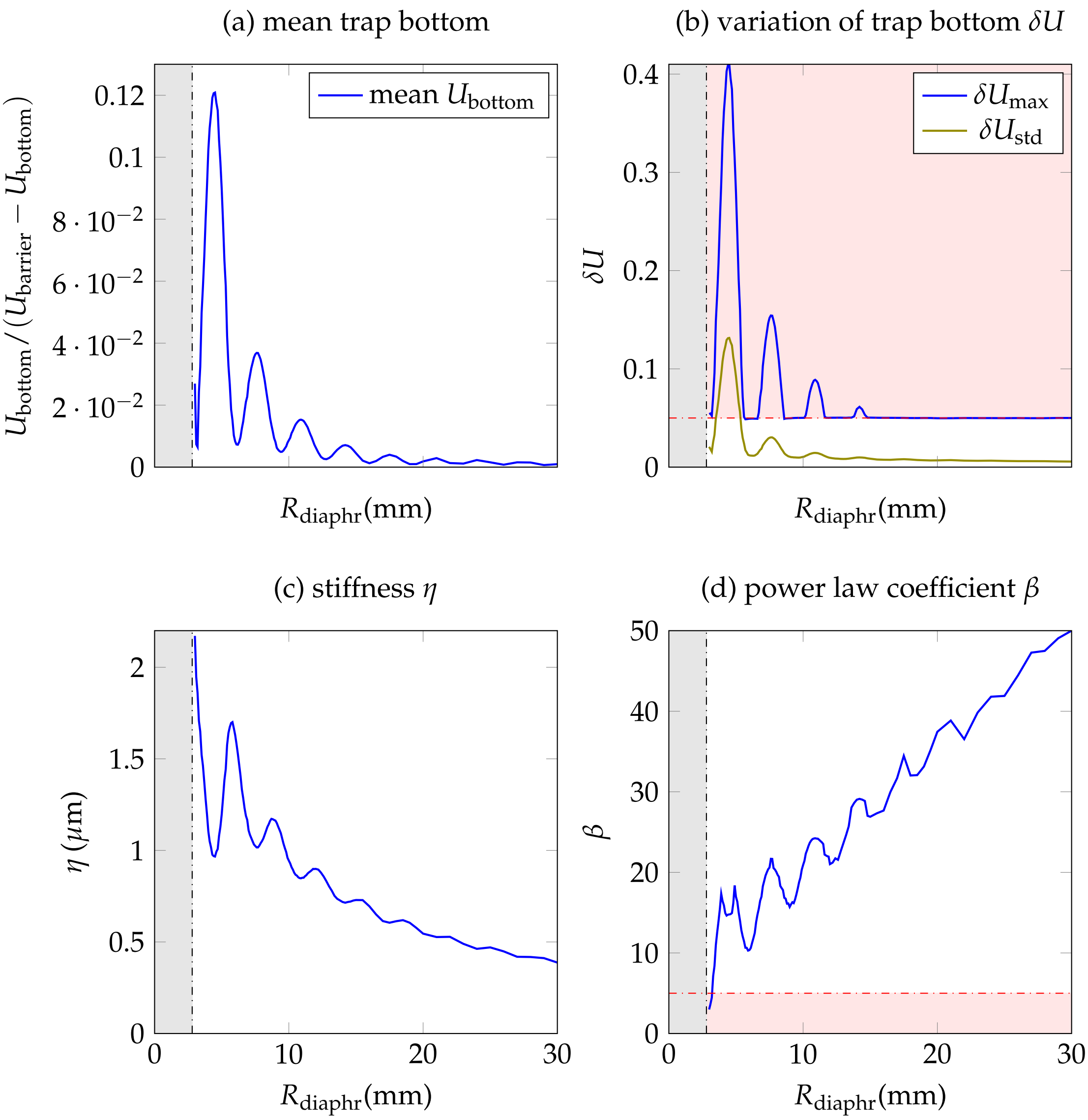

Figure G.3.: **(a)-(b)** :Evolution of the uniformity of the trap bottom with$R_{\text{diaphr.}}$: (a) mean value of the potential in the trapping region, (b) maximal (blue) and rms (green) variations of the potential in this region. The red area is the forbidden domain where the variation of the trap bottom is more than 5% of the trap barrier (Note that by definition of the trapping region, $\delta U_{\text{max}} \geq 0.05$). **(c)-(d)**: Evolution of the steepness of the edges with R_{diaphr}: (c) fitted stiffness on the simulated intensity profile, (d) power law coefficient obtained from the fit of its elliptic average. The red area corresponds to the forbidden domain where $\beta \leq 5$. The gray area corresponds to the domain where no trapping region is found in the resulting intensity distribution.

than, the intensity maxima. On the selected range of radii, the distance between these two successive extrema is, in average, $\delta_{\text{min}} = 700\,\mu$m.If the diaphragm cuts the electric field distribution close to a minimum of the diffraction pattern then the resulting

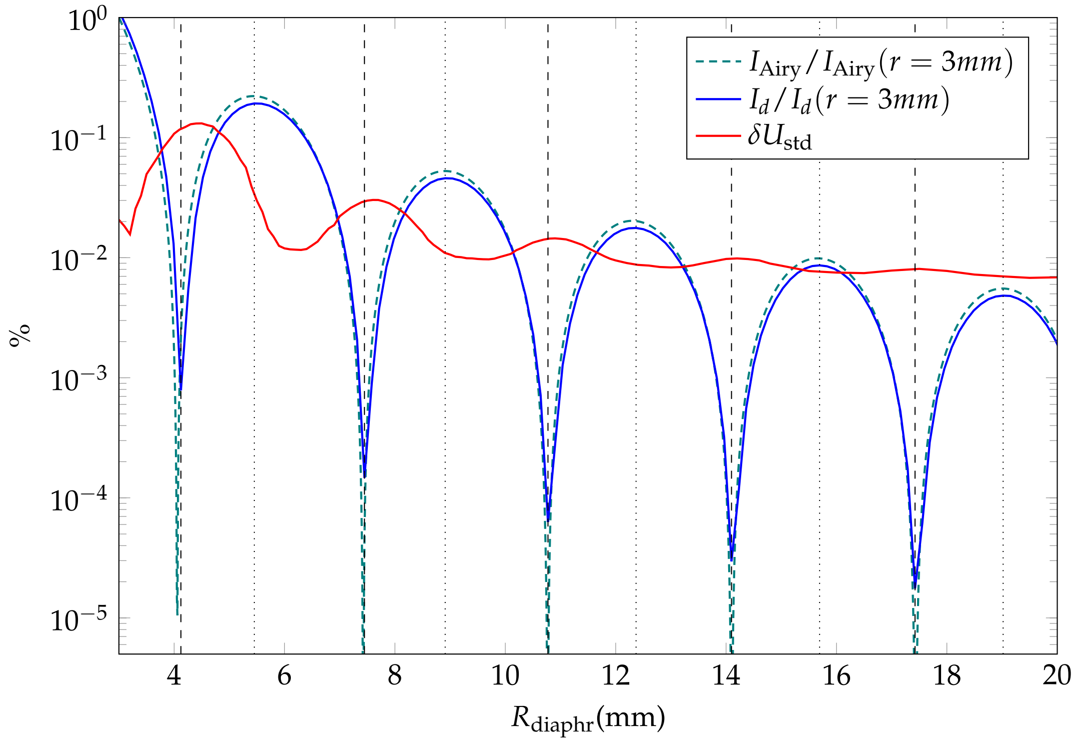

Figure G.4.: Comparison of the evolution of the trap properties and of the diffracted intensity at the edge of the diaphragm in terms of the diaphragm radius R_{diaphr} itself. For visibility we renormalize the intensity profile by their value at the minimally used radius for the cut $R_{\text{diaphr}} = 3\,\text{mm}$

trap shows the highest discrepancies to a box–like one; whereas it results very close to the expected quality of a uniform trap when the cut is made near a maximum of the distribution.

G.2.3. auxiliary effects: varying the size and the shape of the mask

By performing similar simulations while varying the mask functions $t(x,y)$, we note that these conclusions hold for various mask shapes and sizes. More precisely, the conclusions are qualitatively the same but the quantitative results are modified.

First, we note that if we perform a simple rescaling of the mask then the quantitative description of the trapping quality is the same up to a basic rescaling of the diaphragm aperture. Indeed, from previous analysis, we pointed out the intimate link between the position of the cut in the diffraction pattern and the resulting trap quality. As understood from the previous simplified description using Airy pattern, the cutting effect can be expressed in terms of the dimensionless quantity $x = 2\pi R_{\text{diaphr}} R_{\text{mask}}/\lambda f$. Then, when changing R_{mask} by a multiplicative factor γ, the conclusions hold for the rescaled aperture R_{diaphr}/γ.

We performed simulations for various mask types – square, rectangle and annulus. In each case, we note the appearance and disappearance of intensity bumps inside the inner trapping region though not always simply located at the center. Their position and their number change according to the precise intensity pattern in the plane of the diaphragm and on the order of the cut maxima in this pattern. However, we computed that they similarly result in an oscillatory behavior in the characteristics of the trap uniformity. The positions of the extrema are shifted compared to the simple case of the disk shape mask for which the beam symmetry is preserved by the mask cut and thus a unique length scale R_{mask} is introduced by this cut.

We show in Fig. G.5 an example of the intensity defects appearing when cutting the diffraction pattern resulting from the use of a square-shaped mask of half side length of 40 μm. We rescale the intensity to 15% of the barrier in order to enhance the trap bottom variations. We point out the evolution of the number of the intensity peaks in the trapping domain with the diaphragm aperture. Apart from these geometry changes, we also notice a variation in the maximum and standard deviation of the intensity of these defects with the radius. This translates in oscillations in the uniform trap quality as previously observed with the disk-shaped mask. We note from unshown simulations that for $R_{\text{diaphr}} \lesssim 5\,\text{mm}$ the resulting beam profile presents smooth corners and is intermediate between a square and a disk shape. It also shows an important bump at the center of the distribution. For $R_{\text{diaphr}} = 3\,\text{mm}$, the potential is equivalent to the diffraction by a disk–shaped mask.

G.3. Conclusion

In conclusion, we showed that a diaphragm placed just in front of the second lens of the telescope used for imaging our dark mask has a drastic effect on the uniform trap quality. For the characteristic sizes of our setup, these modifications are non-negligible in terms of atomic sensitivity for radii $R_{\text{diaphr}} \lesssim 15\,\text{mm}$ which is the case in our setup. In this case, the limiting feature for identifying our trap to a box-like one is the trap bottom uniformity, that is to say the importance of the variations of the intensity in the central region (where the atoms are confined) compared to the height of the barrier that bounds this region. For an aperture smaller than $R_{\text{diaphr}} \lesssim 15\,\text{mm}$, we note that we can still reach a satisfying regime by fine-tuning the effective aperture of our optical system, for example by setting it to a smaller value by adding a diaphragm of adjustable aperture on the path of the beam. This technique is similar to an rough apodization process. Indeed, the trap quality shows an oscillatory behavior with the aperture size due to the specific position of the cut performed by the diaphragm within the diffraction pattern (position compared to the local intensity minima or maxima.) shown by the beam inside the telescope.

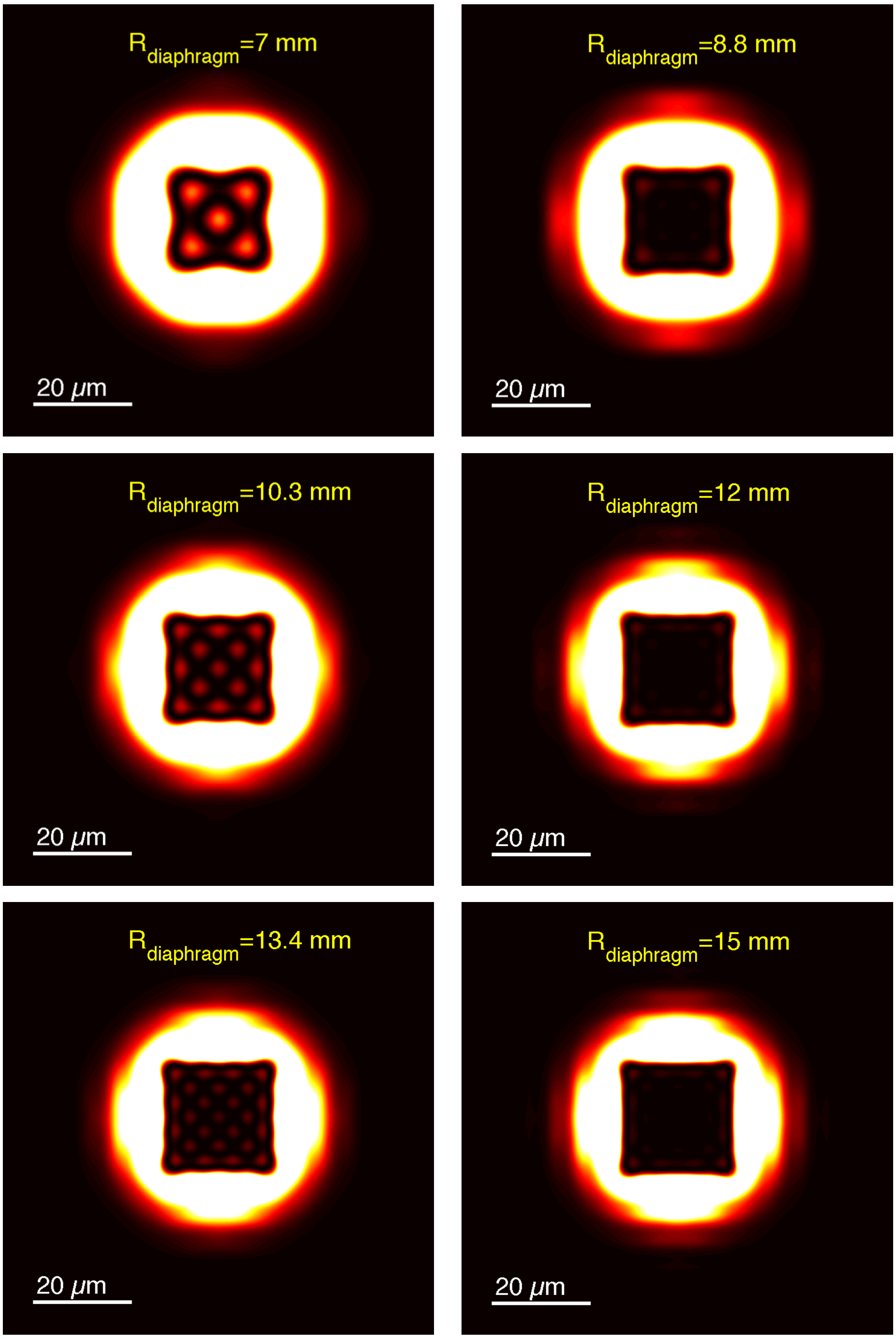

Figure G.5.: Examples of simulated intensity profiles for a square–shaped mask when varying R_{diaphr}. We simulate the intensity profile using the procedure described in G.1.1. We use $R_{\mathrm{diaphr}} = 7,\ 8.8,\ 10.3,\ 12,\ 13.4$ and 15 mm which correspond to the detected extrema (alternatively maxima and minima) of δI_{std}. We rescale the intensity to 15% of the barrier to enhance the trap bottom defects.

H. Procedure for Initialization of fringe pattern fit

In 7.3.2, we are interested in characterizing quantitatively the evolution of the fringe pattern resulting from matter-wave interference between two similar but independent rectangular clouds set parallel and coplanar, with the cloud parameters. The interferences result in roughly linear fringes aligned along the separation between the two clouds, roughly matching the vertical axis of our imaging camera. As described in the main text, we characterize the fringes contrast by performing an initial fit of the density on each line l of pixels $n(x,y_l)$ to Eq. 7.22 which reads:

$$n(x) = n_0\left(e^{-x^2/2\sigma_0^2} + ce^{-x^2/2\sigma^2}\cos(k_0x+\phi)\right) \tag{H.1}$$

This fit function has six free parameters:

1. n_0 is the central density on the line l,
2. σ_0 is the gaussian width of the overall cloud,
3. σ is the gaussian width of the interference domain,
4. k_0 is the momentum component associated with the fringe spacing $\lambda = 2\pi/k_0$,
5. ϕ is the fringe phase,
6. c is the fringe contrast.

The most challenging part of our contrast characterization lies in the quality performance of this fit for each line of the initial density $n(x,y_l)$ whereas the data may show important shot noise (from photonics noise inherent to absorption imaging technique) making each fit very sensitive to the initial condition. To enhance the performance our fitting procedure, we performed a sophisticated initialization using several preliminary fits. We detail this procedure here.

Firstly, we initialize the phase ϕ and the fringe momentum k_0 by using a **contrast enhancement** method and by fitting each line of the resulting contrast–enhanced picture. We first convolute the 2D density distribution by a 2×2 matrix with constant coefficients so that the high–frequency noise is filtered out but the fringes are not blurred. On this smooth picture, we detect local maxima of each line and produce a resulting boolean matrix of local–line–maxima (showing 1 at each detected maxima). We smooth out this intermediate matrix by convoluting it with a gaussian whose width is selected [1] to filter out the noise without merging the different fringes and thus produce a contrast–amplified picture. We finally iterate once this contrast enhancement procedure on the first contrast–amplified picture. To initialize the phase ϕ and the momentum k_0 of the fit of $n(x,y_l)$, we fit the corresponding lines of the final contrast–amplified picture by a pure sinusoid:

$$n(x) = n_0\left(1 + c_0\cos(k_0x+\phi)\right) \tag{H.2}$$

---

[1] The precise value of this width depends on Time–of–Flight duration τ used

Note that the contrast c_0 of the fitted sinusoid has no link to the initial fringes contrast c.

Secondly, we initialize the contrast c and the gaussian widths σ_0 and σ, and a second test value of fringe momentum k_0 by fitting the norm of the **1D Fourier transform** of each line of pixels $|\tilde{n}(k_x, y_l)|^2$. This transform enables to get ride of the phase parameter and to isolate the interesting momentum domain. This decouples better the noise component from the fringe component than the direct space signal. We fit $|\tilde{n}(k_x, y_l)|^2$ by a sum of three gaussian peaks:

$$|\tilde{n}(k_x)|^2 = \tilde{n}_0^2 \left(e^{-k_x^2/\tilde{\sigma}_0{}^2} + \frac{c^2}{4} \left(e^{-(k_x-k_0)^2/\tilde{\sigma}^2} + e^{-(k_x+k_0)^2/\tilde{\sigma}^2} \right) \right) + b \tag{H.3}$$

The peak centered on $k_x = 0$ corresponds to the cloud density itself. The fringes reveals in two symmetric peaks centered on $\pm k_0$ and of reduced amplitude compared to the central peak by a factor $c^2/4$, c equaling the fringes contrast in real space. We note that photonic shot noise contributes to $|\tilde{n}(k_x)|^2$ as a constant offset. The parameter $b \geq 0$ added in Eq. H.3 aims in accounting for such a contribution. Note that such an effect of the shot noise blurs the signal of the fringes pattern by leading to random fluctuations of the order of b for any k. The effect is thus more important as n_0 and c are small.

We initialize the various parameters of the preliminary fits of Eqs. H.2 and H.3 either with constant preselected values or, if it exists, with the results of the previously performed fit of the above line $n(x, y_{l-1})$ along Eq. H.1. We choose the best matching [2] result between these two initializations.

Finally, we perform three fits of the initial density $n(x, y_l)$ along Eq. H.1, with three different initializations:

1. We initialize all six parameters with the results of the previously performed fit of the above line $n(x, y_{l-1})$ along Eq. 7.22.
2. We initialize the phase ϕ, and the fringe momentum k_0 from the **contrast-enhanced fit**. The contrast c, the widths σ_0 and σ and the density n_0 are initialized from preselected constant values.
3. We initialize the contrast c, the widths σ_0 and σ, and the fringe momentum k_0 from the **Fourier-transform fit** and the phase ϕ and n_0 from the "second-initialization" fit detailed in the last point.

We then choose the best matching (defined as in footnote 2) result between the three fits and deduce the values of γ from Eq. 7.23 from which we ultimately obtain the fringe coherence parameter Γ via Eq. 7.24.

---

[2] The best match is defined here by the highest value of the R^2 determination coefficient that is the normalized difference between the total sum of square SS_{tot} and the residual sum of square SS_{res}: $R^2 \equiv 1 - \frac{SS_{\text{res}}}{SS_{\text{tot}}}$ with, if we denotes n_i the experimental data at pixel i, f_i the fitted value at same pixel and N the total number of pixel in a line, $SS_{\text{res}} = \sum_i (n_i - f_i)^2$, $SS_{\text{tot}} = \sum_i (n_i - \bar{n})^2$ and $\bar{n} = \frac{1}{N} \sum_{i=1}^{N} n_i$

I. Estimate of the collision time in a thermal cloud

In this annex, we define and calculate the collision time τ_{coll} for a thermal cloud confined in-plane in a uniform trap and along z by an harmonic potential. The estimate of this characteristic time reveals important for accurately defining time scale over which thermalization occurs and then setting the experimental time variables accordingly. It is also significant for the study of its dynamical properties as the one presented in Chapter 8. First it gives the scale for a local equilibrium to be set and so a temperature to be defined (it must be a few τ_{coll}). Second it is a key variable in the general Kibble-Zurek (KZ) formalism (which study the quench dynamic at the crossing of a transition point) used in Chapter 8: It enters as the characteristic scale of the thermalization time divergence of Eq. 8.2 which is used to analyze the "freezing-out" of the dynamics at the vicinity of the transition point. Estimating this characteristic time is then useful to determine the range of durations over which it is relevant to consider a ramp in temperature in our investigation of the KZ mechanism (see 8.1.3.2).

I.1. Definition

We define the average collision time τ_{coll} as :

$$\tau_{\text{coll}} = \frac{1}{\bar{n}\sigma\bar{v}} \tag{I.1}$$

where

- σ is the elastic cross-section. For a Bose gas of identical particles, cold enough for the inter-particle interactions to be characterized in the contact approximation by a unique scattering length a_s, the cross-section simply follows $\sigma = 8\pi a_s^2$. For ^{87}Rb the s-wave scattering length is $a_s = 5.1\,\text{nm}$.
- $\bar{n}$ is the average density defined by

  $$\bar{n} = \frac{1}{N}\int n^2(\boldsymbol{r})d^3r \tag{I.2}$$

  Here and for the rest of the Annex, $n(\boldsymbol{r})$ stands for the 3D spatial density.
- $\bar{v}$ is the average velocity of the colliding particles. It is defined by

  $$\bar{v} = \frac{1}{\tilde{m}}\frac{\int p\tilde{n}(\boldsymbol{p})d^3p}{\int \tilde{n}(\boldsymbol{p})d^3p} \tag{I.3}$$

  where $\tilde{m}$ is the reduced mass of the colliding particles. $\tilde{n}(\boldsymbol{p})$ is the density in the conjugated space for the reduced particle (of mass $\tilde{m}$), deduced from integration of the global phase space density $d(\boldsymbol{r},\boldsymbol{p})$: $\tilde{n}(\boldsymbol{p}) = \int d(\boldsymbol{r},\boldsymbol{p})d^3r$ while $n(\boldsymbol{r}) =$

$\int d(\boldsymbol{r},\boldsymbol{p})d^3p$ (d is precisely defined by the choice of a normalization condition).

I.2. Calculation using Boltzmann predictions

I.2.1. Average velocity

In the ideal case, we have $\tilde{n}(\boldsymbol{p}) \propto \exp\frac{-p^2}{2\tilde{m}k_\mathrm{B}T}$ and :

$$\bar{v} = \frac{1}{\tilde{m}}\left(\frac{1}{2\pi k_\mathrm{B}T\tilde{m}}\right)^{3/2}\int p\exp\frac{-p^2}{2\tilde{m}k_\mathrm{B}T}d^3p \tag{I.4}$$

For identical particles the reduced mass is $\tilde{m} = m/2$ and thus we have

$$\bar{v} = \sqrt{\frac{16k_\mathrm{B}T}{\pi m}}. \tag{I.5}$$

I.2.2. Average density

For a classical thermal gas trapped in a potential $V(\boldsymbol{r})$, we have $n(\boldsymbol{r}) = n(0)\exp\left(-\frac{V(\boldsymbol{r})}{k_\mathrm{B}T}\right)$ where $n(0)$ is the density at the trap center. We consider a transverse harmonic confinement of frequency $\omega_z/2\pi$ and a perfectly uniform in-plane confinement of area $\mathcal{A}$. Then :

$$n(0) = \frac{N}{\sqrt{2\pi}\sigma_z\mathcal{A}} \text{ with } \sigma_z = \sqrt{\frac{k_\mathrm{B}T}{m\omega_z^2}} \tag{I.6}$$

and

$$\bar{n} = \frac{n(0)}{\sqrt{2}}. \tag{I.7}$$

We can express this average density in terms of the average velocity given in Eq. I.5 and find :

$$\bar{n} = \frac{N}{\mathcal{A}}\frac{2\omega_z}{\pi\bar{v}}. \tag{I.8}$$

I.2.3. Collision time

Reinjecting the previous expression in Eq. I.1, we find :

$$\tau_\mathrm{coll} = \frac{1}{16n^{(2D)}a_s^2\omega_z}. \tag{I.9}$$

where $n^{(2D)}$ denotes the two-dimensional uniform density of the gas $N/\mathcal{A}$. The result is remarkably independent of the temperature.

As a reference point, we will first use the BEC$_\perp$ transition point. We however already point out that, due to the intrinsically non negligible Bose stimulation, Boltzmann predictions developed here lead to an overestimate of the actual collision time. Using $\omega_z/2\pi = 365\,\mathrm{Hz}$ and typical[1] surface density $n^{(2D)} = 75\,\mu\mathrm{m}^{-2}$, we find $\tau_\mathrm{coll} = 14\,\mathrm{ms}$.

---

[1] it matches the BEC$_\perp$ transition point of interest in 8.1.2. In this study, we consider a gas confined in

For configuration deep in the thermal regime, which would be more reliably described by the previous development (negligible Bose stimulation) and which is of interest for a quantitative description of the KZ argument (for example in 8.1.3.2), the surface density would be much higher and thus τ_{coll} shorter. Indeed, in our uniform geometry, the surface of gas is constant, while evaporative cooling leads to a loss of atoms. The value of τ_{coll} in this classical calculation is then reduced by the same factor than N is higher.

I.3. Calculation using Bose Law

In order to go further in the estimate of τ_{coll}, we will now use Bose statistics instead of Boltzmann approximation, still applying the definition of Eq. I.1, for a set of independent particles. This approximation must give a better estimate close to the $\text{BEC}_\perp$ transition point that is of interest here (as in 8.1.2) as then the effect of Bose statistics can not be neglected (at least as far as the description of z-motion is concerned). We consider the same trapping potential $V(\boldsymbol{r})$ as in the previous section (sum of a transverse harmonic confinement of frequency $\omega_z/2\pi$ and a perfectly uniform in-plane confinement of area $\mathcal{A}$). We perform Bose computations as described in Annex A using a full quantum 3D treatment of the states. In this calculation, the spatial density is given by:

$$n^{\text{Bose}}(\boldsymbol{r}) = N\langle\hat{\psi}^\dagger(\boldsymbol{r})\hat{\psi}(\boldsymbol{r})\rangle = \sum_{\boldsymbol{j}} f_{\boldsymbol{j}}|\psi_{\boldsymbol{j}}(\boldsymbol{r})|^2 \tag{I.10}$$

where $\psi_{\boldsymbol{j}}(\boldsymbol{r})$ is the wavefunction for the state $\boldsymbol{j} = (j_x, j_y, j_z)$ and is given by (Eq. A.2)

$$\psi_{\boldsymbol{j}}(\boldsymbol{r}) = \frac{1}{L\sqrt{\ell_z}}\sin(\pi j_x x/L)\ \sin(\pi j_y y/L)\ \chi_{j_z}(z/\ell_z), \tag{I.11}$$

in the case of a square box, with $\ell_z = (\hbar/m\omega_z)^{1/2}$ and χ_j is the j-th Hermite function. $f_{\boldsymbol{j}}$ stands for the occupation factor of the same state $\boldsymbol{j}$ and is given by ideal Bose law formula (Eq. A.3):

$$f_{\boldsymbol{j}} = \frac{1}{\exp\left[(E_{\boldsymbol{j}}-\mu)/k_{\text{B}}T\right]-1} \tag{I.12}$$

$$\text{with } E_{\boldsymbol{j}} = \frac{\pi^2\hbar^2}{2mL^2}(j_x^2+j_y^2-2) + j_z\hbar\omega_z \tag{I.13}$$

The value of the mean velocity $\bar{v}$ must also be modified. It can be approximated to the mean value:

$$\bar{v}^{\text{Bose}} = \frac{1}{\tilde{m}}\sqrt{\langle\hat{p}^2\rangle} = \left(\frac{1}{N}\sum_{\boldsymbol{j}} f_{\boldsymbol{j}}\left[\left(\frac{\pi\hbar}{\tilde{m}L}\right)^2(j_x^2+j_y^2) + (j_z+\frac{1}{2})\frac{\hbar\omega_z}{\tilde{m}}\right]\right)^{1/2} \tag{I.14}$$

in which we replaced the mass m by the reduced mass $\tilde{m}$. Such a formula is easily

---

a square of $L = 30\,\mu$m and the $\text{BEC}_\perp$ transition point corresponds to a temperature is $T = 148\,$nK and a atom number $N = 65700$.

summable and we check that using Boltzmann prediction for f_j (instead of Bose formula), we numerically recover the prediction of Eq. I.5. For the parameters given in footnote 1, we found $\bar{v}^{\text{Bose}} = 9.38\,\text{mm/s}$ instead of $\bar{v} = 8.47\,\text{mm/s}$ using Boltzmann prediction.

I.3.1. Approximating spatial density dependency

Performing numerical summations to deduce the full dependency of the density is an involved task but to have an insight on the modifications of the collision time due to Bose statistics, we can perform some approximations. We first assume that :

1. the in-plane density is uniform so that $n(\boldsymbol{r}) = n(z)$.
2. the z-dependency of the density can still be encompassed by a gaussian but with a modified width σ_z^{Bose} compared to the thermal value of σ_z given in Eq. I.6.

We compute the modified width σ_z^{Bose} by inverting Eq. I.6 which is valid within previous approximations and using the central 3D density $n^{\text{Bose}}(0)$ deduced from Bose law along Eq. I.10:

$$\sigma_z^{\text{Bose}} = \frac{N}{\sqrt{2\pi}\, n^{\text{Bose}}(0)\mathcal{A}} \tag{I.15}$$

For the parameters given in footnote 1, we found $\sigma_z^{\text{Bose}} = 0.84\,\mu\text{m}$ instead of $\sigma_z = 1.63\,\mu\text{m}$. We deduce the simple rescaling relation : $\bar{n}^{\text{Bose}} = \frac{\sigma_z}{\sigma_z^{\text{Bose}}}\bar{n}$ and $\tau_{\text{coll}}^{\text{Bose}} = \frac{\sigma_z^{\text{Bose}}}{\sigma_z}\frac{\bar{v}}{\bar{v}^{\text{Bose}}}\tau_{\text{coll}}$. The collision time is then reduced to $\tau_{\text{coll}}^{\text{Bose}} = 6.6\,\text{ms}$.

Using Bose law, it is easy to characterize a configuration away from the transition point by simply considering a (relatively) small value of the fugacity z. For example, we choose $z = 0.96$ (at the transition point we had $z = 0.998$ for the considered parameters). Using a typical temperature of $T = 250\,\text{nK}$ (characteristic of our loading conditions, see 7.1) we deduce $N = 1.4 \times 10^5$ and found $\tau_{\text{coll}}^{\text{Bose}} = 3.9\,\text{ms}$.

In conclusion, the characteristic collision time typically verifies $\tau_{\text{coll}}^{\text{Bose}} \lesssim 10\,\text{ms}$ in a 2D thermal cloud above or around the $\text{BEC}_\perp$ transition point and for our typical experimental parameters.

Bibliography

[1] A. Einstein. *Quantentheorie des einatomigen idealen Gases*. Sitzungsberichte/Physikalische Klasse, Preussische Akademie der Wissenschaften **22**, 261 (1924).

[2] S. N. Bose. *Plancks Gesetz und Lichtquantenhypothese*. Z. Phys. **26**, 178 (1924).

[3] L. de Broglie. *Recherches sur la théorie des quant*. Ann. phys. (paris) 3, 22 (1925)., Paris (1925).

[4] P. Kapitza. *Viscosity of liquid helium below the λ-point*. Nature **141**, 74 (1938).

[5] F. London. *The λ -phenomenon of liquid helium and the Bose–Einstein degeneracy*. Nature **141**, 643 (1938).

[6] V. F. Sears and E. C. Svensson. *Pair correlations and the condensate fraction in superfluid* ^{4}He. Phys. Rev. Lett. **43**, 2009–2012 (1979).

[7] H. K. Onnes. *Further experiments with liquid helium. C. On the change of electric resistance of pure metals at very low temperatures etc. IV. The resistance of pure mercury at helium temperatures*. In *KNAW, Proceedings*, volume 13, pages 1910–1911 (1911).

[8] F. London. *On the Problem of the Molecular Theory of Superconductivity*. Phys. Rev. **74**, 562–573 (1948). URL `http://link.aps.org/doi/10.1103/PhysRev.74.562`.

[9] D. D. Osheroff, R. C. Richardson, and D. M. Lee. *Evidence for a New Phase of Solid* He^3. Phys. Rev. Lett. **28**, 885–888 (1972). URL `http://link.aps.org/doi/10.1103/PhysRevLett.28.885`.

[10] D. D. Osheroff, W. J. Gully, R. C. Richardson, and D. M. Lee. *New Magnetic Phenomena in Liquid* He^3 *below 3 mK*. Phys. Rev. Lett. **29**, 920–923 (1972). URL `http://link.aps.org/doi/10.1103/PhysRevLett.29.920`.

[11] T. H. Mainman. *Stimulated Optical Radiation in Ruby*. Nature **187**, 493–494 (1960). URL `http://dx.doi.org/10.1038/187493a0`.

[12] H. Deng, G. Weihs, C. Santori, J. Bloch, and Y. Yamamoto. *Condensation of semiconductor microcavity exciton polaritons*. Science **298**, 199–202 (2002).

[13] J. Kasprzak, M. Richard, S. Kundermann, A. Baas, P. Jeambrun, J. Keeling, F. Marchetti, M. Szymańska, R. Andre, J. Staehli, et al. *Bose–Einstein condensation of exciton polaritons*. Nature **443**, 409–414 (2006).

[14] R. Balili, V. Hartwell, D. Snoke, L. Pfeiffer, and K. West. *Bose-Einstein condensation of microcavity polaritons in a trap*. Science **316**, 1007–1010 (2007).

[15] S. Demokritov, V. Demidov, O. Dzyapko, G. Melkov, A. Serga, B. Hillebrands, and A. Slavin. *Bose–Einstein condensation of quasi-equilibrium magnons at room temperature under pumping*. Nature **443**, 430–433 (2006).

[16] J. Klaers, J. Schmitt, F. Vewinger, and M. Weitz. *Bose-Einstein condensation of photons in an optical microcavity*. Nature **468**, 545–548 (2010). URL `http://dx.doi.org/10.1038/nature09567`.

[17] M. H. Anderson, J. R. Ensher, M. R. Matthews, C. E. Wieman, and E. A. Cornell. *Observation of Bose-Einstein condensation in a dilute atomic vapor*. Science **269**, 198 (1995).

[18] K. B. Davis, M.-O. Mewes, M. R. Andrews, N. J. van Druten, D. S. Durfee, D. M. Kurn, and W. Ketterle. *Bose–Einstein condensation in a gas of sodium atoms*. Phys. Rev. Lett. **75**, 3969 (1995).

[19] C. C. Bradley, C. A. Sackett, J. J. Tollett, and R. G. Hulet. *Evidence of Bose–Einstein condensation in an atomic gas with attractive interactions*. Phys. Rev. Lett. **75**, 1687 (1995).

[20] A. L. Schawlow and C. H. Townes. *Infrared and Optical Masers*. Phys. Rev. **112**, 1940–1949 (1958). URL `http://link.aps.org/doi/10.1103/PhysRev.112.1940`.

[21] B. DeMarco and D. D. Jin. *Onset of Fermi degeneracy in a trapped atomic gas*. Science **285**, 1703 (1999).

[22] A. Truscott, K. Strecker, W. McAlexander, G. Partridge, and R. G. Hulet. *Observation of Fermi pressure in a gas of trapped atoms*. Science **291**, 2570 (2001).

[23] F. Schreck, L. Khaykovich, K. L. Corwin, G. Ferrari, T. Bourdel, J. Cubizolles, and C. Salomom. *Quasipure Bose-Einstein condensate immersed in a Fermi sea*. Phys. Rev. Lett. **87**, 080403 (2001).

[24] M. R. Andrews, C. G. Townsend, H. J. Miesner, D. S. Durfee, D. M. Kurn, and W. Ketterle. *Observation of interference between two Bose condensates*. Science **275**, 637 (1997).

[25] I. Bloch, T. W. Hänsch, and T. Esslinger. *Measurement of the spatial coherence of a trapped Bose gas at the phase transition*. Nature **403**, 166 (2000).

[26] M. R. Matthews, B. P. Anderson, P. C. Haljan, D. S. Hall, C. E. Wieman, and E. A. Cornell. *Vortices in a Bose–Einstein condensate*. Phys. Rev. Lett. **83**, 2498 (1999).

[27] K. W. Madison, F. Chevy, W. Wohlleben, and J. Dalibard. *Vortex formation in a stirred Bose–Einstein condensate*. Phys. Rev. Lett. **84**, 806 (2000).

[28] J. R. Abo-Shaeer, C. Raman, J. M. Vogels, and W. Ketterle. *Observation of vortex lattices in Bose–Einstein condensates*. Science **292**, 476–479 (2001).

[29] P. Courteille, R. Freeland, D. Heinzen, F. van Abeelen, and B. Verhaar. *Observation of a Feshbach resonance in cold atom scattering*. Phys. Rev. Lett **81**, 69 (1998).

[30] S. Inouye, M. Andrews, J. Stenger, H. J. Miesner, D. M. Stamper-Kurn, and W. Ketterle. *Observation of Feshbach resonances in a Bose Einstein condensate*. Nature **392**, 151 (1998).

[31] S. Jochim, M. Bartenstein, A. Altmeyer, G. Hendl, S. Riedl, C. Chin, J. Hecker-Denschlag, and R. Grimm. *Bose–Einstein Condensation of molecules*. Science **302**, 2101 (2003).

[32] M. Greiner, C. A. Regal, and D. S. Jin. *Emergence of a molecular Bose–Einstein condensate from a Fermi gas*. Nature **426**, 537 (2003).

[33] M. W. Zwierlein, C. A. Stan, C. H. Schunk, S. M. F. Raupach, S. Gupta, Z. Hadzibabic, and W. Ketterle. *Observation of Bose–Einstein condensation of molecules*. Phys. Rev. Lett. **91**, 250401 (2003).

[34] J. Cubizolles, T. Bourdel, S. J. J. M. F. Kokkelmans, G. V. Shlyapnikov, and C. Salomon. *Production of Long-Lived Ultracold Li_2 Molecules from a Fermi Gas*. Phys. Rev. Lett. **91**, 240401 (2003).

[35] T. Bourdel, L. Khaykovich, M. E. Cubizolles, J. Zhang, F. Chevy, M. Teichmann, L. Tarruell, M. F. K. S. J. H, and C. Salomon. *Experimental study of the BEC-BCS crossover region in Lithium 6*. Phys. Rev. Lett. **93**, 050401 (2004).

[36] M. Bartenstein, A. Altmeyer, S. Riedl, S. Joachim, C. Chin, J. Hecker-Denschlag, and R. Grimm. *Crossover from a molecular Bose–Einstein condensate to a degenerate Fermi Gas*. Phys. Rev. Lett. **92**, 120401 (2004).

[37] C. A. Regal, M. Greiner, and D. S. Jin. *Observation of resonance condensation of fermionic atom pairs*. Phys. Rev. Lett. **92**, 040403 (2004).

[38] M. W. Zwierlein, C. A. Stan, C. H. Schunck, S. M. F. Raupach, A. J. Kerman, and W. Ketterle. *Condensation of pairs of fermionic atoms near a Feshbach resonance*. Phys. Rev. Lett. **92**, 120403 (2004).

[39] R. P. Feynman. *Simulating physics with computers*. International Journal of Theoretical Physics **21**, 467–488 (1982).

[40] B. Paredes, A. Widera, V. Murg, O. Mandel, S. Fölling, J. I. Cirac, G. V. Shlyapnikov, T. W. Hänsch, and I. Bloch. *Tonks-Girardeau gas of ultracold atoms in an optical lattice*. Nature **429**, 277 – 281 (2004).

[41] T. Kinoshita, T. Wenger, and D. S. Weiss. *Observation of a one-dimensional Tonks-Girardeau gas*. Science **305**, 1125–1128 (2004).

[42] Z. Hadzibabic, P. Krüger, M. Cheneau, B. Battelier, and J. Dalibard. *Berezinskii-Kosterlitz-Thouless crossover in a trapped atomic gas*. Nature **441**, 1118–1121 (2006).

[43] D. Jaksch, C. Bruder, J. I. Cirac, C. W. Gardiner, and P. Zoller. *Cold bosonic atoms in optical lattices*. Phys. Rev. Lett **81**, 3108 (1998).

[44] M. Greiner, M. O. Mandel, T. Esslinger, T. Hänsch, and I. Bloch. *Quantum phase transition from a superfluid to a Mott insulator in a gas of ultracold atoms*. Nature **415**, 39 (2002).

[45] T. Stöferle, H. Moritz, C. Schori, M. Köhl, and T. Esslinger. *Transition from a strongly interacting 1D superfluid to a Mott insulator*. Phys. Phys. Lett. **92**, 130403 (2004).

[46] I. B. Spielman, W. D. Phillips, and J. V. Porto. *The Mott insulator transition in two dimensions*. Phys. Rev. Lett. **98**, 080404 (2007).

[47] M. Köhl, H. Moritz, T. Stöferle, C. Schori, and T. Esslinger. *Superfluid to Mott insulator transition in one, two, and three dimensions*. Journal of Low Temperature Physics **138**, 635 (2005).

[48] R. Jördens, N. Strohmaier, K. Günter, H. Moritz, and T. Esslinger. *A Mott insulator of fermionic atoms in an optical lattice*. Nature **455**, 204–207 (2008).

[49] A. L. Gaunt, T. F. Schmidutz, I. Gotlibovych, R. P. Smith, and Z. Hadzibabic. *Bose-Einstein Condensation of Atoms in a Uniform Potential*. Phys. Rev. Lett. **110**, 200406 (2013). URL `http://link.aps.org/doi/10.1103/PhysRevLett.110.200406`.

[50] P. W. Anderson. *Absence of diffusion in certain random lattices*. Phys. Rev. **109**, 1492–1505 (1958). URL `http://dx.doi.org/10.1103/PhysRev.109.1492`.

[51] J. Billy, V. Josse, Z. Zuo, A. Bernard, B. Hambrecht, P. Lugan, D. Clement, L. Sanchez-Palencia, P. Bouyer, and A. Aspect. *Direct observation of Anderson localization of matter waves in a controlled disorder*. Nature **453**, 891–894 (2008). URL `http://dx.doi.org/10.1038/nature07000`.

[52] G. Roati, C. D/'Errico, L. Fallani, M. Fattori, C. Fort, M. Zaccanti, G. Modugno, M. Modugno, and M. Inguscio. *Anderson localization of a non-interacting Bose-Einstein condensate*. Nature **453**, 895–898 (2008). URL `http://dx.doi.org/10.1038/nature07071`.

[53] J. Chabé, G. Lemarié, B. Grémaud, D. Delande, P. Szriftgiser, and J. C. Garreau. *Experimental observation of the Anderson metal-insulator transition with atomic matter waves*. Physical review letters **101**, 255702 (2008).

[54] V. Bretin, S. Stock, Y. Seurin, and J. Dalibard. *Fast rotation of a Bose–Einstein condensate*. Phys. Rev. Lett. **92**, 050403 (2004).

[55] V. Schweikhard, I. Coddington, P. Engels, V. P. Mogendorff, and E. A. Cornell. *Rapidly Rotating Bose-Einstein Condensates in and near the Lowest Landau Level*. Phys. Rev. Lett. **92**, 040404 (2004). URL `http://link.aps.org/doi/10.1103/PhysRevLett.92.040404`.

[56] Y. Lin, R. L. Compton, K. Jiménez-García, J. V. Porto, and I. B. Spielman. *Synthetic magnetic fields for ultracold neutral atoms*. Nature **462**, 628–632 (2009).

[57] J. Struck, C. Ölschläger, R. Le Targat, P. Soltan-Panahi, A. Eckardt, M. Lewenstein, P. Windpassinger, and K. Sengstock. *Quantum Simulation of Frustrated Classical Magnetism in Triangular Optical Lattices*. Science **333**, 996–999 (2011). URL `http://www.sciencemag.org/content/333/6045/996.abstract`.

[58] J. Struck, C. Ölschläger, M. Weinberg, P. Hauke, J. Simonet, A. Eckardt, M. Lewenstein, K. Sengstock, and P. Windpassinger. *Tunable Gauge Potential for Neutral and Spinless Particles in Driven Optical Lattices*. Phys. Rev. Lett. **108**, 225304 (2012). URL `http://link.aps.org/doi/10.1103/PhysRevLett.108.225304`.

[59] M. Aidelsburger, M. Atala, S. Nascimbène, S. Trotzky, Y.-A. Chen, and I. Bloch. *Experimental Realization of Strong Effective Magnetic Fields in an Optical Lattice*. Phys. Rev. Lett. **107**, 255301 (2011). URL `http://link.aps.org/doi/10.1103/PhysRevLett.107.255301`.

[60] A. Griesmaier, J. Werner, S. Hensler, J. Stuhler, and T. Pfau. *Bose–Einstein Condensation of Chromium*. Phys. Rev. Lett. **94**, 160401 (2005).

[61] T. Lahaye, T. Koch, B. Frohlich, M. Fattori, J. Metz, A. Griesmaier, S. Giovanazzi, and T. Pfau. *Strong dipolar effects in a quantum ferrofluid*. Nature **448**, 672–675 (2007). URL `http://dx.doi.org/10.1038/nature06036`.

[62] P. Schausz, M. Cheneau, M. Endres, T. Fukuhara, S. Hild, A. Omran, T. Pohl, C. Gross, S. Kuhr, and I. Bloch. *Observation of spatially ordered structures in a two-dimensional Rydberg gas*. Nature **491**, 87–91 (2012). URL `http://dx.doi.org/10.1038/nature11596`.

[63] S. Ospelkaus, K.-K. Ni, D. Wang, M. H. G. de Miranda, B. Neyenhuis, G. Quéméner, P. S. Julienne, J. L. Bohn, D. S. Jin, and J. Ye. *Quantum-State Controlled Chemical Reactions of Ultracold Potassium-Rubidium Molecules*. Science **327**, 853–857 (2010). URL `http://www.sciencemag.org/content/327/5967/853.abstract`.

[64] Y.-i. Shin. *Determination of the equation of state of a polarized Fermi gas at unitarity*. Phys. Rev. A **77**, 041603 (2008). URL `http://link.aps.org/doi/10.1103/PhysRevA.77.041603`.

[65] T.-L. Ho and Q. Zhou. *Obtaining the phase diagram and thermodynamic quantities of bulk systems from the densities of trapped gases*. Nature Physics **6**, 131 (2009).

[66] S. Nascimbène, N. Navon, K. J. Jiang, F. Chevy, and C. Salomon. *Exploring the thermodynamics of a universal Fermi gas*. Nature **463**, 1057 (2010).

[67] N. Navon, S. Piatecki, K. J. Günter, B. Rem, T.-C. Nguyen, F. Chevy, W. Krauth, and C. Salomon. *Dynamics and Thermodynamics of the Low-Temperature Strongly Interacting Bose Gas*. arXiv:1103.4449 (2011).

[68] K. Van Houcke, F. Werner, E. Kozik, N. Prokof'ev, B. Svistunov, M. Ku, A. Sommer, L. Cheuk, A. Schirotzek, and M. Zwierlein. *Feynman diagrams versus Fermi-gas Feynman emulator*. Nature Physics **8**, 366–370 (2012).

[69] C.-L. Hung, X. Zhang, N. Gemelke, and C. Chin. *Observation of scale invariance and universality in two-dimensional Bose gases*. Nature **470**, 236 (2011).

[70] T. Yefsah, R. Desbuquois, L. Chomaz, K. J. Günter, and J. Dalibard. *Exploring the thermodynamics of a two-dimensional Bose gas*. Phys. Rev. Lett. **107**, 130401 (2011).

[71] M. J. H. Ku, A. T. Sommer, L. W. Cheuk, and M. W. Zwierlein. *Revealing the Superfluid Lambda Transition in the Universal Thermodynamics of a Unitary Fermi Gas*. Science **335**, 563–567 (2012).

[72] S. Stringari. *Collective excitations of a trapped Bose-condensed gas*. Phys. Rev. Lett. **77**, 2360 (1996).

[73] D. S. Jin, J. R. Ensher, M. R. Matthews, C. E. Wieman, and E. A. Cornell. *Collective Excitations of a Bose–Einstein Condensate in a Dilute Gas*. Phys. Rev. Lett. **77**, 420 (1996).

[74] C. Raman, M. Köhl, R. Onofrio, D. S. Durfee, C. E. Kuklewicz, Z. Hadzibabic, and W. Ketterle. *Evidence for a critical velocity in a Bose–Einstein condensed gas*. Phys. Rev. Lett. **83**, 2502 (1999).

[75] R. Onofrio, C. Raman, J. M. Vogels, J. R. Abo-Shaeer, A. P. Chikkatur, and W. Ketterle. *Observation of Superfluid Flow in a Bose-Einstein Condensed Gas*. Phys. Rev. Lett. **85**, 2228–2231 (2000).

[76] C. Raman, R. Onofrio, J. Vogels, J. Abo-Shaeer, and W. Ketterle. *Dissipationless Flow and Superfluidity in Gaseous Bose-Einstein Condensates*. Journal of Low Temperature Physics **122**, 99–116 (2001). ISSN 0022-2291.

[77] P. Engels and C. Atherton. *Stationary and Nonstationary Fluid Flow of a Bose-Einstein Condensate Through a Penetrable Barrier*. Phys. Rev. Lett. **99**, 160405 (2007).

[78] D. E. Miller, J. K. Chin, C. A. Stan, Y. Liu, W. Setiawan, C. Sanner, and W. Ketterle. *Critical Velocity for Superfluid Flow across the BEC-BCS Crossover*. Phys. Rev. Lett. **99**, 070402 (2007).

[79] C. Ryu, M. Andersen, P. Cladé, V. Natarajan, K. Helmerson, and W. Phillips. *Observation of persistent flow of a Bose-Einstein condensate in a toroidal trap*. Physical review letters **99**, 260401 (2007).

[80] A. Ramanathan, K. C. Wright, S. R. Muniz, M. Zelan, W. T. Hill, C. J. Lobb, K. Helmerson, W. D. Phillips, and G. K. Campbell. *Superflow in a Toroidal Bose-Einstein Condensate: An Atom Circuit with a Tunable Weak Link*. Phys. Rev. Lett. **106**, 130401 (2011).

[81] S. Moulder, S. Beattie, R. P. Smith, N. Tammuz, and Z. Hadzibabic. *Quantized supercurrent decay in an annular Bose-Einstein condensate*. Physical Review A **86**, 013629 (2012).

[82] F. Jendrzejewski, S. Eckel, N. Murray, C. Lanier, M. Edwards, C. Lobb, and G. Campbell. *Resistive flow in a weakly interacting Bose-Einstein condensate*. arXiv preprint arXiv:1402.3335 (2014).

[83] C.-L. Hung, X. Zhang, N. Gemelke, and C. Chin. *Slow Mass Transport and Statistical Evolution of an Atomic Gas across the Superfluid–Mott-Insulator Transition*. Phys. Rev. Lett. **104**, 160403 (2010). URL `http://link.aps.org/doi/10.1103/PhysRevLett.104.160403`.

[84] L. J. LeBlanc, A. B. Bardon, J. McKeever, M. H. T. Extavour, D. Jervis, J. H. Thywissen, F. Piazza, and A. Smerzi. *Dynamics of a Tunable Superfluid Junction*. Phys. Rev. Lett. **106**, 025302 (2011). URL `http://link.aps.org/doi/10.1103/PhysRevLett.106.025302`.

[85] J.-P. Brantut, J. Meineke, D. Stadler, S. Krinner, and T. Esslinger. *Conduction of Ultracold Fermions Through a Mesoscopic Channel*. Science **337**, 1069–1071 (2012). URL `http://www.sciencemag.org/content/337/6098/1069.abstract`.

[86] D. Stadler, S. Krinner, J. Meineke, J.-P. Brantut, and T. Esslinger. *Observing the drop of resistance in the flow of a superfluid Fermi gas*. Nature **491**, 736–739 (2012). URL `http://dx.doi.org/10.1038/nature11613`.

[87] E. L. Hazlett, L.-C. Ha, and C. Chin. *Anomalous thermoelectric transport in two-dimensional Bose gas*. arXiv preprint arXiv:1306.4018 (2013).

[88] T. W. Kibble. *Topology of cosmic domains and strings*. Journal of Physics A: Mathematical and General **9**, 1387 (1976).

[89] W. Zurek. *Cosmological experiments in superfluid helium?* Nature **317**, 505–508 (1985).

[90] L. E. Sadler, J. M. Higbie, S. R. Leslie, M. Vengalattore, and D. M. Stamper-Kurn. *Spontaneous symmetry breaking in a quenched ferromagnetic spinor Bose-Einstein condensate*. Nature **443**, 312–315 (2006).

[91] C. N. Weiler, T. W. Neely, D. R. Scherer, A. S. Bradley, M. J. Davis, and B. P. Anderson. *Spontaneous vortices in the formation of Bose–Einstein condensates*. Nature **455**, 948–951 (2008).

[92] D. Chen, M. White, C. Borries, and B. DeMarco. *Quantum Quench of an Atomic Mott Insulator*. Phys. Rev. Lett. **106**, 235304 (2011). URL `http://link.aps.org/doi/10.1103/PhysRevLett.106.235304`.

[93] G. Lamporesi, S. Donadello, S. Serafini, F. Dalfovo, and G. Ferrari. *Spontaneous creation of Kibble-Zurek solitons in a Bose-Einstein condensate*. Nature Physics **9**, 656–660 (2013).

[94] S. Braun, M. Friesdorf, S. Hodgman, M. Schreiber, J. Ronzheimer, A. Riera, M. del Rey, I. Bloch, J. Eisert, and U. Schneider. *Emergence of coherence and the dynamics of quantum phase transitions*. arXiv preprint arXiv:1403.7199 (2014).

[95] Z. Hadzibabic. Private communication (2014).

[96] N. D. Mermin and H. Wagner. *Absence of ferromagnetism or antiferromagnetism in one- or two-dimensional isotropic Heisenberg models*. Phys. Rev. Lett. **17**, 1133 (1966).

[97] P. C. Hohenberg. *Existence of long-range order in one and two dimensions*. Phys. Rev. **158**, 383 (1967).

[98] R. E. Peierls. *Quelques propriétés typiques des corps solides*. Ann. Inst. Henri Poincaré **5**, 177 (1935).

[99] S. T. Bramwell and P. C. W. Holdsworth. *Magnetization: A characteristic of the Kosterlitz-Thouless-Berezinskii transition*. Phys. Rev. B **49**, 8811–8814 (1994).

[100] V. L. Berezinskii. *Destruction of long-range order in one-dimensional and two-dimensional system possessing a continuous symmetry group - II. quantum systems*. Soviet Physics JETP **34**, 610 (1971).

[101] J. M. Kosterlitz and D. J. Thouless. *Ordering, metastability and phase transitions in two dimensional systems*. J. Phys. C: Solid State Physics **6**, 1181 (1973).

[102] P. Cladé, C. Ryu, A. Ramanathan, K. Helmerson, and W. D. Phillips. *Observation of a 2D Bose gas: from thermal to quasicondensate to superfluid*. Phys. Rev. Lett. **102**, 170401 (2009).

[103] S. Tung, G. Lamporesi, D. Lobser, L. Xia, and E. A. Cornell. *Observation of the presuperfluid regime in a two-dimensional Bose gas*. Phys. Rev. Lett. **105**, 230408 (2010).

[104] J.-Y. Choi, S. W. Seo, and Y.-I. Shin. *Observation of thermally activated vortex pairs in a quasi-2D Bose gas*. arXiv:cond-mat/1211.5649v2 (2012).

[105] J.-y. Choi, S. W. Seo, W. J. Kwon, and Y.-i. Shin. *Probing Phase Fluctuations in a 2D Degenerate Bose Gas by Free Expansion*. Phys. Rev. Lett. **109**, 125301 (2012). URL `http://link.aps.org/doi/10.1103/PhysRevLett.109.125301`.

[106] S. W. Seo, J.-y. Choi, and Y.-i. Shin. *Scaling behavior of density fluctuations in an expanding quasi-two-dimensional degenerate Bose gas*. Phys. Rev. A **89**, 043606 (2014). URL `http://link.aps.org/doi/10.1103/PhysRevA.89.043606`.

[107] B. Battelier. *Gaz bidimensionnel de bosons ultra-froids Nouvelle expérience de condensation de Bose-Einstein*. PhD thesis, Université Pierre et Marie Curie (2007).

[108] M. Cheneau. *Transition superfluide et potentiels géométriques dans le gaz de Bose bidimensionnel*. PhD thesis, Université Pierre et Marie Curie (2009).

[109] S. P. Rath. *Production and investigation of quasi-two-dimensional Bose gases*. PhD thesis, Université Pierre et Marie Curie (2010).

[110] T. Yefsah. *Thermodynamique du gaz de Bose à deux dimensions*. PhD thesis, Université Pierre et Marie Curie (2011).

[111] R. Desbuquois. *Thermal and superfluid properties of the two–dimensional Bose gas*. PhD thesis, Université Pierre et Marie Curie (2013).

[112] R. Desbuquois, T. Yefsah, L. Chomaz, C. Weitenberg, L. Corman, S. Nascimbène, and J. Dalibard. *Determination of Scale-Invariant Equations of State without Fitting Parameters: Application to the Two-Dimensional Bose Gas Across the Berezinskii-Kosterlitz-Thouless Transition*. Phys. Rev. Lett. **113**, 020404 (2014). URL `http://link.aps.org/doi/10.1103/PhysRevLett.113.020404`.

[113] R. Desbuquois, L. Chomaz, T. Yefsah, J. Léonard, J. Beugnon, C. Weitenberg, and J. Dalibard. *Superfluid behaviour of a two-dimensional Bose gas*. Nature Physics **8**, 645–648 (2012).

[114] I. Bloch, J. Dalibard, and W. Zwerger. *Many-body physics with ultracold gases*. Rev. Mod. Phys **80**, 885 (2008).

[115] Z. Hadzibabic and J. Dalibard. *Two-dimensional Bose fluids: An atomic physics perspective*. In R. Kaiser and D. Wiersma, editors, *Nano optics and atomics: transport of light and matter waves*, volume CLXXIII of *Proceedings of the International School of Physics Enrico Fermi, 2009*. IOS Press (2010). arXiv:0912.1490.

[116] N. N. Bogoliubov. Physica **26**, S1 (1960).

[117] O. Penrose and L. Onsager. *Bose–Einstein condensation and liquid helium*. Phys. Rev. **104**, 576 (1956).

[118] Z. Hadzibabic, P. Krüger, M. Cheneau, S. P. Rath, and J. Dalibard. *The trapped two-dimensional Bose gas: from Bose–Einstein condensation to Berezinskii–Kosterlitz–Thouless physics*. New Journal of Physics **10**, 045006 (2008).

[119] D. S. Petrov, M. Holzmann, and G. V. Shlyapnikov. *Bose–Einstein condensation in quasi-2D trapped gases*. Phys. Rev. Lett. **84**, 2551 (2000).

[120] D. S. Petrov and G. V. Shlyapnikov. *Interatomic collisions in a tightly confined Bose gas*. Phys. Rev. A **64**, 012706 (2001).

[121] J.-y. Choi, S. W. Seo, and Y.-i. Shin. *Observation of Thermally Activated Vortex Pairs in a Quasi-2D Bose Gas*. Phys. Rev. Lett. **110**, 175302 (2013). URL `http://link.aps.org/doi/10.1103/PhysRevLett.110.175302`.

[122] D. R. Nelson and J. M. Kosterlitz. *Universal jump in the superfluid density of two-dimensional superfluids*. Phys. Rev. Lett. **39**, 1201 (1977).

[123] D. J. Bishop and J. D. Reppy. *Study of the superfluid transition in two-dimensional* ^{4}*He films*. Phys. Rev. Lett. **40**, 1727–1730 (1978).

[124] N. V. Prokof'ev, O. Ruebenacker, and B. V. Svistunov. *Critical point of a weakly interacting two-dimensional Bose gas*. Phys. Rev. Lett. **87**, 270402 (2001).

[125] N. V. Prokof'ev and B. V. Svistunov. *Two-dimensional weakly interacting Bose gas in the fluctuation region*. Phys. Rev. A **66**, 043608 (2002).

[126] M. Holzmann, G. Baym, J. P. Blaizot, and F. Laloë. *Superfluid transition of homogeneous and trapped two-dimensional Bose gases*. P.N.A.S. **104**, 1476 (2007).

[127] M. Holzmann, M. Chevallier, and W. Krauth. *Semiclassical theory of the quasi two-dimensional trapped gas*. Europhys. Lett. **82**, 30001 (2008).

[128] R. N. Bisset, D. Baillie, and P. B. Blakie. *Analysis of the Holzmann-Chevallier-Krauth theory for the trapped quasi-two-dimensional Bose gas*. Phys. Rev. A **79**, 013602 (2009).

[129] N. J. van Druten and W. Ketterle. *Two-step condensation of the ideal Bose gas in highly anisotropic traps*. Phys. Rev. Lett. **79**, 549–552 (1997).

[130] A. Keshet and W. Ketterle. *A distributed, graphical user interface based, computer control system for atomic physics experiments*. Rev. Sci. Instrum. **84**, 015105 (2013).

[131] Y.-J. Lin, A. R. Perry, R. L. Compton, I. B. Spielman, and J. V. Porto. *Rapid production of* ^{87}*Rb Bose-Einstein condensates in a combined magnetic and optical potential*. Phys. Rev. A **79**, 063631 (2009).

[132] R. Dubessy, K. Merloti, L. Longchambon, P.-E. Pottie, T. Liennard, A. Perrin, V. Lorent, and H. Perrin. ^{87}*Rb Bose-Einstein condensate in an optically plugged quadrupole trap*. Phys. Rev. A **85**, 013643 (2012).

[133] M. Greiner, I. Bloch, T. Hänsch, and T. Esslinger. *Magnetic transport of trapped cold atoms over a large distance*. Phys. Rev. A **63**, 031401 (2001).

[134] N. L. Smith, W. H. Heathcote, G. Hechenblaikner, E. Nugent, and C. J. Foot. *Quasi-2D confinement of a BEC in a combined optical and magnetic potential*. Journal of Physics B **38**, 223 (2005).

[135] T. C. Li, H. Kelkar, D. Medellin, and M. G. Raizen. *Real-time control of the periodicity of a standing wave: an optical accordion*. Opt. Express **16**, 5465–5470 (2008). URL `http://www.opticsexpress.org/abstract.cfm?URI=oe-16-8-5465`.

[136] L. Chomaz, L. Corman, T. Yefsah, R. Desbuquois, and J. Dalibard. *Absorption imaging of a quasi-two-dimensional gas: a multiple scattering analysis*. New Journal of Physics **14**, 055001 (2012).

[137] G. Reinaudi, T. Lahaye, Z. Wang, and D. Guéry-Odelin. *Strong saturation absorption imaging of dense clouds of ultracold atoms*. Optics Letters **32**, 3143 (2007).

[138] N. Navon, S. Nascimbène, F. Chevy, and C. Salomon. *The Equation of State of a Low-Temperature Fermi Gas with Tunable Interactions*. Science **328**, 729–732 (2010). URL `http://www.sciencemag.org/content/328/5979/729.abstract`.

[139] S. P. Rath, T. Yefsah, K. J. Günter, M. Cheneau, R. Desbuquois, M. Holzmann, W. Krauth, and J. Dalibard. *Equilibrium state of a trapped two-dimensional Bose gas*. Phys. Rev. A **82**, 013609 (2010).

[140] A. Rançon and N. Dupuis. *Universal thermodynamics of a two-dimensional Bose gas*. Phys. Rev. A **85**, 063607 (2012). URL `http://link.aps.org/doi/10.1103/PhysRevA.85.063607`.

[141] A. J. Leggett. *Quantum Liquids*. Oxford University Press (2006).

[142] T. W. Neely, E. C. Samson, A. S. Bradley, M. J. Davis, and B. P. Anderson. *Observation of Vortex Dipoles in an Oblate Bose-Einstein Condensate*. Phys. Rev. Lett. **104**, 160401 (2010).

[143] G. E. Astrakharchik and L. P. Pitaevskii. *Motion of a heavy impurity through a Bose-Einstein condensate*. Phys. Rev. A **70**, 013608 (2004).

[144] A. D. Chepelianskii, F. Chevy, and E. Raphaël. *Capillary-Gravity Waves Generated by a Slow Moving Object*. Phys. Rev. Lett. **100**, 074504 (2008).

[145] J. S. Langer and M. E. Fisher. *Intrinsic Critical Velocity of a Superfluid*. Phys. Rev. Lett. **19**, 560–563 (1967).

[146] T. Frisch, Y. Pomeau, and S. Rica. *Transition to Dissipation in a Model of Superflow*. Phys. Rev. Lett. **69**, 1644 (1992).

[147] T. Winiecki, J. F. McCann, and C. S. Adams. *Pressure Drag in Linear and Nonlinear Quantum Fluids*. Phys. Rev. Lett. **82**, 5186 (1999).

[148] J. S. Stiessberger and W. Zwerger. *Critical Velocity of Superfluid Flow past Large Obstacles in Bose-Condensates*. Phys. Rev. A **62**, 061601(R) (2000).

[149] M. Crescimanno, C. G. Koay, R. Peterson, and R. Walsworth. *Analytical Estimate of the Critical Velocity for Vortex Pair Creation in Trapped Bose Condensates*. Phys. Rev. A **62**, 063612 (2000).

[150] F. Dalfovo, S. Giorgini, M. Guilleumas, L. Pitaevskii, and S. Stringari. *Collective and single-particle excitations of a trapped Bose gas*. Phys. Rev. A **56**, 3840–3845 (1997).

[151] P. O. Fedichev and G. V. Shlyapnikov. *Critical velocity in cylindrical Bose-Einstein condensates*. Phys. Rev. A **63**, 045601 (2001).

[152] A. Amo, J. Lefrere, S. Pigeon, C. Adrados, C. Ciuti, I. Carusotto, R. Houdre, E. Giacobino, and A. Bramati. *Observation of Superfluidity of Polaritons in Semiconductor Microcavities*. Nature Physics **5**, 805 (2009).

[153] T. Kuga, Y. Torii, N. Shiokawa, T. Hirano, Y. Shimizu, and H. Sasada. *Novel Optical Trap of Atoms with a Doughnut Beam*. Phys. Rev. Lett. **78**, 4713–4716 (1997). URL `http://link.aps.org/doi/10.1103/PhysRevLett.78.4713`.

[154] R. Ozeri, L. Khaykovich, and N. Davidson. *Long spin relaxation times in a single-beam blue-detuned optical trap*. Phys. Rev. A **59**, R1750–R1753 (1999). URL `http://link.aps.org/doi/10.1103/PhysRevA.59.R1750`.

[155] T. P. Meyrath, F. Schreck, J. L. Hanssen, C.-S. Chuu, and M. G. Raizen. *Bose-Einstein condensate in a box*. Phys. Rev. A **71**, 041604 (2005). URL `http://link.aps.org/doi/10.1103/PhysRevA.71.041604`.

[156] A. Jaouadi, N. Gaaloul, B. Viaris de Lesegno, M. Telmini, L. Pruvost, and E. Charron. *Bose-Einstein condensation in dark power-law laser traps*. Phys. Rev. A **82**, 023613 (2010). URL `http://link.aps.org/doi/10.1103/PhysRevA.82.023613`.

[157] Y. B. Ovchinnikov, I. Manek, and R. Grimm. *Surface Trap for Cs atoms based on Evanescent-Wave Cooling*. Phys. Rev. Lett. **79**, 2225–2228 (1997). URL `http://link.aps.org/doi/10.1103/PhysRevLett.79.2225`.

[158] A. Kaplan, N. Friedman, and N. Davidson. *Optimized single-beam dark optical trap*. J. Opt. Soc. Am. B **19**, 1233–1238 (2002). URL `http://www.opticsinfobase.org/josab/abstract.cfm?URI=josab-19-6-1233`.

[159] N. Friedman, L. Khaykovich, R. Ozeri, and N. Davidson. *Compression of cold atoms to very high densities in a rotating-beam blue-detuned optical trap*. Phys. Rev. A **61**, 031403 (2000). URL `http://link.aps.org/doi/10.1103/PhysRevA.61.031403`.

[160] J. Liesener, M. Reicherter, T. Haist, and H. Tiziani. *Multi-functional optical tweezers using computer-generated holograms*. Optics Communications **185**, 77 – 82 (2000). ISSN 0030-4018. URL `http://www.sciencedirect.com/science/article/pii/S0030401800009901`.

[161] W. Ketterle, D. Durfee, and D. Stamper-Kurn. *Making, probing and understanding Bose-Einstein condensates*. arXiv preprint cond-mat/9904034 **5** (1999).

[162] F. S. Dalfovo, L. P. Pitaevkii, S. Stringari, and S. Giorgini. *Theory of Bose–Einstein condensation in trapped gases*. Rev. Mod. Phys. **71**, 463 (1999).

[163] S. Hofferberth, I. Lesanovsky, B. Fischer, T. Schumm, and J. Schmiedmayer. *Non-equilibrium coherence dynamics in one-dimensional Bose gases*. Nature **449**, 324–327 (2007).

[164] C. Kohstall, S. Riedl, E. R. S. Guajardo, L. A. Sidorenkov, J. H. Denschlag, and R. Grimm. *Observation of interference between two molecular Bose–Einstein condensates*. New Journal of Physics **13**, 065027 (2011). URL `http://stacks.iop.org/1367-2630/13/i=6/a=065027`.

[165] A. Polkovnikov, E. Altman, and E. Demler. *Interference between independent fluctuating condensates*. Proc. Natl. Acad. Sci. USA **103**, 6125 (2006).

[166] M. Holzmann, M. Chevallier, and W. Krauth. *Universal correlations and coherence in quasi-two-dimensional trapped Bose gases*. Phys. Rev. A **81**, 043622 (2010).

[167] I. Chuang, R. Durrer, N. Turok, and B. Yurke. *Cosmology in the laboratory: Defect dynamics in liquid crystals*. Science **251**, 1336–1342 (1991).

[168] V. M. H. Ruutu, V. B. Eltsov, A. J. Gill, T. W. B. Kibble, M. Krusius, Y. G. Makhlin, B. Placais, G. E. Volovik, and W. Xu. *Vortex formation in neutron-irradiated superfluid 3He as an analogue of cosmological defect formation*. Nature **382**, 334–336 (1996). URL http://dx.doi.org/10.1038/382334a0.

[169] C. Bäuerle, Y. M. Bunkov, S. Fisher, H. Godfrin, and G. Pickett. *Laboratory simulation of cosmic string formation in the early Universe using superfluid 3 He*. Nature **382**, 332–334 (1996).

[170] S. Ulm, J. Roßnagel, G. Jacob, C. Degünther, S. Dawkins, U. Poschinger, R. Nigmatullin, A. Retzker, M. Plenio, F. Schmidt-Kaler, et al. *Observation of the Kibble–Zurek scaling law for defect formation in ion crystals*. Nature communications **4** (2013).

[171] K. Pyka, J. Keller, H. Partner, R. Nigmatullin, T. Burgermeister, D. Meier, K. Kuhlmann, A. Retzker, M. Plenio, W. Zurek, et al. *Topological defect formation and spontaneous symmetry breaking in ion Coulomb crystals*. Nature communications **4** (2013).

[172] R. Monaco, J. Mygind, R. Rivers, and V. Koshelets. *Spontaneous fluxoid formation in superconducting loops*. Physical Review B **80**, 180501 (2009).

[173] W. H. Zurek. *Causality in condensates: gray solitons as relics of BEC formation*. Physical review letters **102**, 105702 (2009).

[174] J. Dziarmaga and W. H. Zurek. *Quench in 1D Bose-Hubbard model: Topological defects and excitations from Kosterlitz-Thouless phase transition dynamics*. arXiv preprint arXiv:1312.5139 (2013).

[175] A. Jelić and L. F. Cugliandolo. *Quench dynamics of the 2d XY model*. Journal of Statistical Mechanics: Theory and Experiment **2011**, P02032 (2011).

[176] P. Laguna and W. H. Zurek. *Density of Kinks after a Quench: When Symmetry Breaks, How Big are the Pieces?* Phys. Rev. Lett. **78**, 2519–2522 (1997). URL http://link.aps.org/doi/10.1103/PhysRevLett.78.2519.

[177] A. Das, J. Sabbatini, and W. H. Zurek. *Winding up superfluid in a torus via Bose Einstein condensation*. Scientific reports **2** (2012).

[178] R. Monaco, J. Mygind, R. J. Rivers, and V. P. Koshelets. *Spontaneous fluxoid formation in superconducting loops*. Phys. Rev. B **80**, 180501 (2009). URL http://link.aps.org/doi/10.1103/PhysRevB.80.180501.

[179] W. Zurek. *Topological relics of symmetry breaking: winding numbers and scaling tilts from random vortex–antivortex pairs*. Journal of Physics: Condensed Matter **25**, 404209 (2013).

[180] D. R. Scherer, C. N. Weiler, T. W. Neely, and B. P. Anderson. *Vortex Formation by Merging of Multiple Trapped Bose-Einstein Condensates*. Phys. Rev. Lett. **98**,

110402 (2007). URL http://link.aps.org/doi/10.1103/PhysRevLett.98.110402.

[181] R. Carretero-González, B. P. Anderson, P. G. Kevrekidis, D. J. Frantzeskakis, and C. N. Weiler. *Dynamics of vortex formation in merging Bose-Einstein condensate fragments*. Phys. Rev. A **77**, 033625 (2008). URL http://link.aps.org/doi/10.1103/PhysRevA.77.033625.

[182] M. V. Berry. *The adiabatic phase and Pancharatnam's phase for polarized light*. Journal of Modern Optics **34**, 1401–1407 (1987).

[183] M. Campostrini, M. Hasenbusch, A. Pelissetto, and E. Vicari. *Theoretical estimates of the critical exponents of the superfluid transition in* ^{4}He *by lattice methods*. Phys. Rev. B **74**, 144506 (2006). URL http://link.aps.org/doi/10.1103/PhysRevB.74.144506.

[184] A. Pelissetto and E. Vicari. *Critical phenomena and renormalization-group theory*. Physics Reports **368**, 549–727 (2002).

[185] P. C. Hohenberg and B. I. Halperin. *Theory of dynamic critical phenomena*. Reviews of Modern Physics **49**, 435 (1977).

[186] A. del Campo and W. H. Zurek. *Universality of phase transition dynamics: Topological defects from symmetry breaking*. International Journal of Modern Physics A **29** (2014).

[187] A. del Campo, A. Retzker, and M. B. Plenio. *The inhomogeneous Kibble-Zurek mechanism: vortex nucleation during Bose-Einstein condensation*. New Journal of Physics **13**, 083022 (2011). URL http://stacks.iop.org/1367-2630/13/i=8/a=083022.

[188] M. E. Fisher and M. N. Barber. *Scaling Theory for Finite-Size Effects in the Critical Region*. Phys. Rev. Lett. **28**, 1516–1519 (1972). URL http://link.aps.org/doi/10.1103/PhysRevLett.28.1516.

[189] M. Campostrini and E. Vicari. *Critical behavior and scaling in trapped systems*. Physical review letters **102**, 240601 (2009).

[190] M. Collura and D. Karevski. *Critical quench dynamics in confined systems*. Physical review letters **104**, 200601 (2010).

[191] S. Dettmer, D. Hellweg, P. Ryyty, J. J. Arlt, W. Ertmer, K. Sengstock, D. S. Petrov, G. V. Shlyapnikov, H. Kreutzmann, L. Santos, and M. Lewenstein. *Observation of phase fluctuations in elongated Bose–Einstein condensates*. Phys. Rev. Lett **87**, 160406 (2001).

[192] A. Imambekov, I. E. Mazets, D. S. Petrov, V. Gritsev, S. Manz, S. Hofferberth, T. Schumm, E. Demler, and J. Schmiedmayer. *Density ripples in expanding low-dimensional gases as a probe of correlations*. Phys. Rev. A **80**, 033604 (2009).

[193] J. Choi, S. W. Seo, W. J. Kwon, and Y. Shin. *Probing phase fluctuations in a 2D degenerate Bose gas by free expansion*. Phys. Rev. Lett. **109**, 125301 (2012).

[194] L. Giorgetti, I. Carusotto, and Y. Castin. *Semiclassical field method for the equilibrium Bose gas and application to thermal vortices in two dimensions*. Phys. Rev. A **76**, 013613 (2007).

[195] W. Ketterle and N. Van Druten. *Evaporative cooling of trapped atoms*. Advances in atomic, molecular, and optical physics **37**, 181–236 (1996).

[196] B. Efron. *Better bootstrap confidence intervals*. Journal of the American statistical Association **82**, 171–185 (1987).

[197] A. Yates and W. H. Zurek. *Vortex Formation in Two Dimensions: When Symmetry Breaks, How Big Are the Pieces?* Phys. Rev. Lett. **80**, 5477–5480 (1998). URL `http://link.aps.org/doi/10.1103/PhysRevLett.80.5477`.

[198] C. Muirhead, W. Vinen, and R. Donnelly. *The Nucleation of Vorticity by Ions in Superfluid* ^{4} *He: I. Basic Theory*. Philosophical Transactions of the Royal Society of London. Series A, Mathematical and Physical Sciences **311**, 433–467 (1984).

[199] R. J. Donnelly. *Quantized vortices in helium II*. Cambridge University Press, Cambridge (1991).

[200] P. O. Fedichev and G. V. Shlyapnikov. *Dissipative dynamics of a vortex state in a trapped Bose-condensed gas*. Phys. Rev. A **60**, R1779–R1782 (1999). URL `http://link.aps.org/doi/10.1103/PhysRevA.60.R1779`.

[201] R. N. Bisset, M. J. Davis, T. P. Simula, and P. B. Blakie. *Quasicondensation and coherence in the quasi-two-dimensional trapped Bose gas*. Phys. Rev. A **79**, 033626 (2009).

[202] L. Mathey and A. Polkovnikov. *Light cone dynamics and reverse Kibble-Zurek mechanism in two-dimensional superfluids following a quantum quench*. Phys. Rev. A **81**, 033605 (2010). URL `http://link.aps.org/doi/10.1103/PhysRevA.81.033605`.

[203] S. Beattie, S. Moulder, R. J. Fletcher, and Z. Hadzibabic. *Persistent currents in spinor condensates*. Physical review letters **110**, 025301 (2013).

[204] K. Wright, R. Blakestad, C. Lobb, W. Phillips, and G. Campbell. *Driving phase slips in a superfluid atom circuit with a rotating weak link*. Physical review letters **110**, 025302 (2013).

[205] S. Eckel, F. Jendrzejewski, A. Kumar, C. Lobb, and G. Campbell. *Direct measurement of the current-phase relationship of a superfluid weak link*. arXiv preprint arXiv:1406.1095 (2014).

[206] L.-C. Ha, C.-L. Hung, X. Zhang, U. Eismann, S.-K. Tung, and C. Chin. *Strongly Interacting Two-Dimensional Bose Gases*. Phys. Rev. Lett. **110**, 145302 (2013). URL `http://link.aps.org/doi/10.1103/PhysRevLett.110.145302`.

[207] C.-L. Hung, X. Zhang, L.-C. Ha, S.-K. Tung, N. Gemelke, and C. Chin. *Extracting density–density correlations from in situ images of atomic quantum gases*. New Journal of Physics **13**, 075019 (2011). URL `http://stacks.iop.org/1367-2630/13/i=7/a=075019`.

[208] E. Altman, E. Demler, and M. D. Lukin. *Probing many-body states of ultracold atoms via noise correlations*. Phys. Rev. A **70**, 013603 (2004).

[209] B. Yurke, A. N. Pargellis, T. Kovacs, and D. A. Huse. *Coarsening dynamics of the XY model*. Phys. Rev. E **47**, 1525–1530 (1993). URL `http://link.aps.org/doi/10.1103/PhysRevE.47.1525`.

[210] L. Mathey, K. J. Günter, J. Dalibard, and A. Polkovnikov. *Dynamic Kosterlitz-Thouless transition in 2D Bose mixtures of ultra-cold atoms*. arXiv preprint arXiv:1112.1204 (2011).

[211] K. D. Nelson, X. Li, and D. S. Weiss. *Imaging single atoms in a three-dimensional array*. Nature Physics **3**, 556–560 (2007).

[212] M. Karski, L. Förster, J. M. Choi, W. Alt, A. Widera, and D. Meschede. *Nearest-neighbor detection of atoms in a 1D optical lattice by fluorescence imaging*. Phys. Rev. Lett. **102**, 053001 (2009).

[213] W. S. Bakr, A. Peng, M. E. Tai, R. Ma, J. Simon, J. I. Gillen, S. Fölling, L. Pollet, and M. Greiner. *Probing the superfluid-to-Mott insulator transition at the single-atom level*. Science **329**, 547–550 (2010).

[214] C. Weitenberg, M. Endres, J. F. Sherson, M. Cheneau, P. Schauß, T. Fukuhara, I. Bloch, and S. Kuhr. *Single-spin addressing in an atomic Mott insulator*. Nature **471**, 319–324 (2011).

[215] B. T. Seaman, M. Krämer, D. Z. Anderson, and M. J. Holland. *Atomtronics: Ultracold-atom analogs of electronic devices*. Phys. Rev. A **75**, 023615 (2007). URL `http://link.aps.org/doi/10.1103/PhysRevA.75.023615`.

[216] K. K. Likharev. *Superconducting weak links*. Rev. Mod. Phys. **51**, 101–159 (1979). URL `http://link.aps.org/doi/10.1103/RevModPhys.51.101`.

[217] Y. Sato and R. Packard. *Superfluid helium quantum interference devices: physics and applications*. Reports on Progress in Physics **75**, 016401 (2012).

[218] M. Albiez, R. Gati, J. Fölling, S. Hunsmann, M. Cristiani, and M. Oberthaler. *Direct observation of tunneling and nonlinear self-trapping in a single bosonic Josephson junction*. Phys. Rev. Lett. **95**, 10402 (2005).

[219] D. Papoular, L. Pitaevskii, and S. Stringari. *Fast thermalization and Helmholtz oscillations of an ultracold Bose gas*. arXiv preprint arXiv:1405.6026 (2014).

[220] G. Labeyrie, F. de Tomasi, J.-C. Bernard, C. A. Müller, C. Miniatura, and R. Kaiser. *Coherent Backscattering of Light by Cold Atoms*. Phys. Rev. Lett. **83**, 5266–5269 (1999). URL `http://link.aps.org/doi/10.1103/PhysRevLett.83.5266`.

[221] G. Labeyrie, E. Vaujour, C. A. Müller, D. Delande, C. Miniatura, D. Wilkowski, and R. Kaiser. *Slow Diffusion of Light in a Cold Atomic Cloud*. Phys. Rev. Lett. **91**, 223904 (2003). URL `http://link.aps.org/doi/10.1103/PhysRevLett.91.223904`.

[222] E. Akkermans and G. Montambaux. *Mesoscopic Physics of Electrons and Photons*. Cambridge University Press, Cambridge, England (2007).

[223] O. Morice, Y. Castin, and J. Dalibard. *Refractive index of a dilute Bose gas*. Phys. Rev. A **51**, 3896 (1995).

[224] F. A. Pinheiro, M. Rusek, A. Orlowski, and B. A. van Tiggelen. *Probing Anderson localization of light via decay rate statistics*. Phys. Rev. E **69**, 026605 (2004). URL `http://link.aps.org/doi/10.1103/PhysRevE.69.026605`.

[225] A. Gero and E. Akkermans. *Superradiance and multiple scattering of photons in atomic gases*. Phys. Rev. A **75**, 053413 (2007). URL `http://link.aps.org/doi/10.1103/PhysRevA.75.053413`.

[226] A. A. Svidzinsky, J.-T. Chang, and M. O. Scully. *Dynamical Evolution of Correlated Spontaneous Emission of a Single Photon from a Uniformly Excited Cloud of N Atoms*. Phys. Rev. Lett. **100**, 160504 (2008). URL `http://link.aps.org/doi/10.1103/PhysRevLett.100.160504`.

[227] E. Akkermans, A. Gero, and R. Kaiser. *Photon Localization and Dicke Superradiance in Atomic Gases*. Phys. Rev. Lett. **101**, 103602 (2008). URL `http://link.aps.org/doi/10.1103/PhysRevLett.101.103602`.

[228] I. M. Sokolov, M. D. Kupriyanova, D. V. Kupriyanov, and M. D. Havey. *Light scattering from a dense and ultracold atomic gas*. Phys. Rev. A **79**, 053405 (2009).

[229] M. O. Scully. *Collective Lamb Shift in Single Photon Dicke Superradiance*. Phys. Rev. Lett. **102**, 143601 (2009). URL `http://link.aps.org/doi/10.1103/PhysRevLett.102.143601`.

[230] A. Goetschy and S. E. Skipetrov. *Euclidean matrix theory of random lasing in a cloud of cold atoms*. EPL (Europhysics Letters) **96**, 34005 (2011). URL `http://stacks.iop.org/0295-5075/96/i=3/a=34005`.

[231] C. Cohen-Tannoudji, J. Dupont-Roc, and G. Grynberg. *Atom-Photon Interactions*. Wiley, New York (1992).

[232] T. Jonckheere, C. A. Müller, R. Kaiser, C. Miniatura, and D. Delande. *Multiple Scattering of Light by Atoms in the Weak Localization Regime*. Phys. Rev. Lett. **85**, 4269–4272 (2000). URL `http://link.aps.org/doi/10.1103/PhysRevLett.85.4269`.

[233] C. A. Müller and C. Miniatura. *Multiple scattering of light by atoms with internal degeneracy*. Journal of Physics A: Mathematical and General **35**, 10163 (2002).

[234] C. Cohen-Tannoudji, J. Dupont-Roc, and G. G. *Photons and Atoms–Introduction to Quantum Electrodynamics*. Wiley, New-York (1989).

[235] A. Messiah. *Quantum Mechanics*, volume II, Chapter XIX. North-Holland Publishing Company, Amsterdam (1961).

[236] M. O. *tomes refroidis par laser : du refroidissement sub-recul à la recherche d'effets quantiques collectifs*. PhD thesis, Université Pierre et Marie Curie (1995).

[237] J. D. Jackson. *Classical electrodynamics*. John Wiley, New York (1998).

[238] M. Mézard, G. Parisi, and A. Zee. *Spectra of Euclidean random matrices*. Nuclear Physics B **559**, 689–701 (1999).

[239] M. Rusek, J. Mostowski, and A. Orłowski. *Random Green matrices: From proximity resonances to Anderson localization*. Phys. Rev. A **61**, 022704 (2000). URL `http://link.aps.org/doi/10.1103/PhysRevA.61.022704`.

[240] S. Skipetrov and A. Goetschy. *Eigenvalue distributions of large Euclidean random matrices for waves in random media*. arXiv preprint arXiv:1007.1379 (2010).

[241] A. Goetschy and S. Skipetrov. *Non-Hermitian Euclidean random matrix theory*. Physical Review E **84**, 011150 (2011).

[242] L. L. Foldy. *The multiple scattering of waves. I. General theory of isotropic scattering by randomly distributed scatterers*. Physical Review **67**, 107 (1945).

[243] M. Stephen. *First-Order Dispersion Forces*. The Journal of Chemical Physics **40**, 669–673 (1964).

[244] D. Hutchinson and H. Hameka. *Interaction effects on lifetimes of atomic excitations*. The Journal of Chemical Physics **41**, 2006–2011 (1964).

[245] R. H. Dicke. *Coherence in Spontaneous Radiation Processes*. Phys. Rev. **93**, 99 (1954).

[246] M. Antezza and Y. Castin. *Spectrum of Light in a Quantum Fluctuating Periodic Structure*. Phys. Rev. Lett. **103**, 123903 (2009). URL `http://link.aps.org/doi/10.1103/PhysRevLett.103.123903`.

[247] M. Antezza and Y. Castin. *Fano-Hopfield model and photonic band gaps for an arbitrary atomic lattice*. Phys. Rev. A **80**, 013816 (2009). URL `http://link.aps.org/doi/10.1103/PhysRevA.80.013816`.

[248] T. Wellens and B. Grémaud. *Coherent propagation of waves in dilute random media with weak nonlinearity*. Phys. Rev. A **80**, 063827 (2009). URL `http://link.aps.org/doi/10.1103/PhysRevA.80.063827`.

[249] B. Grémaud and T. Wellens. *Speckle Instability: Coherent Effects in Nonlinear Disordered Media*. Phys. Rev. Lett. **104**, 133901 (2010). URL `http://link.aps.org/doi/10.1103/PhysRevLett.104.133901`.

[250] J. Sherson, C. Weitenberg, M. Endres, M. Cheneau, I. Bloch, and S. Kuhr. *Single-atom-resolved fluorescence imaging of an atomic Mott insulator*. Nature **467**, 68–72 (2010).

[251] I. Shvarchuck, C. Buggle, D. S. Petrov, K. Dieckmann, M. Zielonkowski, M. Kemmann, T. G. Tiecke, W. von Klitzing, G. V. Shlyapnikov, and J. T. M. Walraven. *Bose–Einstein condensation into nonequilibrium states studied by condensate focusing*. Phys. Rev. Lett. **89**, 270404 (2002).

[252] W. Ketterle and H.-J. Miesner. *Coherence properties of Bose–Einstein condensates and atom lasers*. Phys. Rev. A **56**, 3291 (1996).

[253] B. Fröhlich, M. Feld, E. Vogt, M. Koschorreck, W. Zwerger, and M. Köhl. *Radio-Frequency Spectroscopy of a Strongly Interacting Two-Dimensional Fermi Gas*. Phys. Rev. Lett. **106**, 105301 (2011).

Résumé

La dimensionnalité d'un système affecte fortement ses propriétés physiques ; les transitions de phase qui s'y déroulent ainsi que le type d'ordre qui y apparaît dépendent de la dimension. Dans les systèmes de basse dimension, la cohérence s'avère plus difficile à établir car les fluctuations thermiques et quantiques y jouent un rôle plus important. Le fluide de Bose à deux dimensions est particulièrement intéressant car, même si un ordre total est exclu, un ordre résiduel à « quasi-longue » portée s'établit à basse température. Deux ingrédients ont un effet significatif sur l'état du système : (i) la taille finie d'un système réel permet de retrouver une occupation macroscopique d'un état à une particule ; (ii) les interactions entre particules conduisent à l'apparition d'un type non-conventionnel de transition de phase vers un état superfluide.

Dans cette thèse, nous présentons une étude expérimentale du gaz de Bose bidimensionnel (2D) utilisant deux types de paysages énergétiques pour piéger nos atomes. Dans la première partie, nous utilisons la dépendance spatiale de certaines propriétés locales d'un gaz inhomogène pour caractériser l'état du système homogène équivalent. Nous extrayons son équation d'état des profils de densité et nous testons son comportement superfluide en mesurant le chauffage induit par le mouvement d'une perturbation locale. Dans la deuxième partie, nous observons et caractérisons l'émergence d'une cohérence de phase étendue dans un gaz 2D homogène, en particulier via le passage de trois dimensions à deux (croisement dimensionnel). Nous étudions l'établissement dynamique de la cohérence par un passage rapide du croisement dimensionnel et nous observons des défauts topologiques dans l'état superfluide final. Nous comparons nos résultats avec les prédictions du mécanisme de Kibble–Zurek.

Mots-clés : Condensation de Bose–Einstein, basse dimension, équation d'état, superfluidité, gaz uniforme, cohérence de phase quantique.

Abstract

The dimensionality of a system strongly affects its physical properties; the phase transitions that take place and the type of order that arises depend on the dimension. In low dimensional systems phase coherence proves more difficult to achieve as both thermal and quantum fluctuations play a stronger role. The two-dimensional Bose fluid is of particular interest as even if full order is precluded, a residual "quasi-long" range order arises at low temperatures. Then two ingredients have a significant effect on the state of the system: (i) the finite size of a real system enables one to recover of a macroscopic occupation of a single-particle state; (ii) the interactions between particles lead to the emergence of a non-conventional type of phase transition toward a superfluid state.

In this thesis, we present an experimental study of the two-dimensional (2D) Bose gas using two different energy landscapes to trap our atoms. In the first part, we use the spatial dependence of some local properties of an inhomogeneous gas to characterize the state of the equivalent homogeneous system. We extract its equation of state with a high accuracy from the gas density profiles and test its superfluid behavior by measuring the heating induced by a moving local perturbation. In the second part, we observe and characterize the emergence of an extended phase coherence in a 2D homogeneous gas in particular via a 3D-to-2D dimensional crossover. We investigate the dynamical establishment of the coherence via a rapid crossing of the dimensional crossover and observe topological defects in the final superfluid state. We compare our findings with the predictions for the Kibble–Zurek mechanism.

Key words: Bose–Einstein condensation, low dimension, equation of state, superfluidity, uniform gas, quantum phase coherence.